PHYSICS REPORTS (Review Section of Physics Letters) 107, Nos. 2–5 (1984) 59–324. North-Holland, Amsterdam

e^+e^- PHYSICS AT PETRA – THE FIRST FIVE YEARS

Sau Lan WU

*Department of Physics, University of Wisconsin, Madison, Wisconsin, USA**

and

Deutsches Elektronen-Synchrotron DESY, Hamburg, Germany

Received 8 December 1983

Contents:

1. PETRA and the detectors 61
1.1. Introduction 61
1.2. PETRA 62
1.3. Detectors 70
1.4. CELLO 71
1.5. JADE 76
1.6. MARK J 81
1.7. PLUTO 87
1.8. TASSO 92
2. Hadronic events in e^+e^- annihilation 100
2.1. Orientation 100
2.2. Experimental data on total hadronic cross section 103
2.3. Hadronic events at PETRA 108
2.4. Quark picture and quantum chromodynamics 110
2.5. Momentum tensor 114
2.6. Thrust 118
2.7. Spin of the quarks 120
2.8. Field–Feynman fragmentation 122
2.9. Experimental determination of the Field–Feynman parameters 123
2.10. Long-range charge correlation in opposite jets 124
3. Three-jet events and properties of the gluon 127
3.1. Three-jet events 127
3.2. Methods of three-jet analysis used at PETRA 127
3.3. Observation of three-jet events 140
3.4. Determination of the quark–gluon coupling constant α_s 149
3.5. Properties of the gluon 160
4. Single-particle inclusive cross sections of hadrons 169
4.1. Introduction 169
4.2. Charged-particle multiplicity and neutral fraction 171
4.3. Inclusive cross section of charged hadrons and scale breaking 175
4.4. Charged-particle inclusive distribution with respect to the jet axis 177
4.5. Particle identification and over-all view 179
4.6. Inclusive cross section of π^0 186
4.7. Inclusive cross section of $\pi^\pm$ 191
4.8. Inclusive cross section of $K^\pm$ 194
4.9. Inclusive cross section of K^0 197
4.10. Inclusive cross section of ρ^0 198
4.11. Inclusive cross section of proton 201
4.12. Inclusive cross section of Λ 203
4.13. Inclusive cross section of Ξ^- 208
4.14. Inclusive cross section of $D^{*\pm}$ 210
4.15. Fragmentation functions for heavy quarks 213
5. Electroweak interaction 215
5.1. Introduction 215

* Supported in part by the US Department of Energy, Contract number DE-AC02-76ER00881.

e^+e^- PHYSICS AT PETRA – THE FIRST FIVE YEARS

Sau Lan WU

Department of Physics, University of Wisconsin, Madison, Wisconsin, USA

and

Deutsches Elektronen-Synchrotron DESY, Hamburg, Germany

NORTH-HOLLAND PHYSICS PUBLISHING–AMSTERDAM

5.2. Standard model 216
5.3. Bhabha scattering $e^-e^+ \to e^-e^+$ 221
5.4. Total cross section of μ-pair creation 224
5.5. Total cross section for $e^-e^+ \to \tau^-\tau^+$ and branching ratios 224
5.6. Forward–backward asymmetry in $e^-e^+ \to \mu^-\mu^+$ 227
5.7. Forward–backward asymmetry in $e^-e^+ \to \tau^-\tau^+$ 230
5.8. Overall fit of the leptonic vector and axial-vector weak couplings 230
5.9. Determination of the Weinberg angle θ_w from the total hadronic cross section 232
5.10. Forward–backward asymmetry in $e^-e^+ \to c\bar{c}$ 234
5.11. QED tests and search for a second neutral intermediate vector boson 235
6. Two-photon physics 237
6.1. Physical significance 237
6.2. Kinematics 242
6.3. QED tests 243
6.4. $\gamma\gamma$ total cross section 244
6.5. $e^+e^- \to e^+e^-\eta'$ 249
6.6. $e^+e^- \to e^+e^-f^0$ 249
6.7. $e^+e^- \to e^+e^-A_2$ 255
6.8. $e^+e^- \to e^+e^-f'$ 255
6.9. $e^+e^- \to e^+e^-\rho^0\rho^0$ 259
6.10. $e^+e^- \to e^+e^-p\bar{p}$ 260
6.11. High p_T jets 264
6.12. Deep inelastic $e\gamma$ scattering 268
7. Search for new particles 272
7.1. Introduction 272
7.2. Search for the top quark 272
7.3. Search for charged technipions and Higgs 279
7.4. Search for supersymmetric particles 284
7.5. Search for new heavy leptons 288
7.6. Search for magnetic monopoles and free quarks 295
Acknowledgements 297
References 298
Appendix 308
A1. Publications of the CELLO Collaboration 308
A2. Publications of the JADE Collaboration 311
A3. Publications of the MARK J Collaboration 314
A4. Publications of the PLUTO Collaboration at PETRA 317
A5. Publications of the TASSO Collaboration 320

Abstract:

PETRA (Positron–Electron Tandem Ring Accelerator) is located at DESY in Hamburg, Germany, and is the highest energy electron–positron storage ring in the world. This report gives a global review of the experimental investigations carried out at PETRA for the first five years of its operation beginning in 1978 by the five Collaborations CELLO, JADE, MARK J, PLUTO and TASSO. The physics objectives in the original proposals have largely been fulfilled. The emphasis of this review, based mainly on journal publications before July 15, 1983 (the fifth anniversary of the first successful storage of an electron beam at PETRA), is on the physics results, ranging over strong, electromagnetic and weak interactions. The topics covered include quark and gluon physics, inclusive particle production, electroweak interference, two-photon physics, and search for new particles.

Although cited for comparison, no attempt has been made for any systematic coverage of the corresponding results from PEP of SLAC.

1. PETRA and the detectors

1.1. Introduction

It has been just over five years since the electron beam was first successfully stored in PETRA. The purpose of this review is to summarize the experimental physics at PETRA during these five years. Throughout this period, PETRA (Positron–Electron Tandem Ring Accelerator) has been the highest energy electron–positron storage ring in the world. The maximum center-of-mass energy reached is above 43 GeV.

Another motivation for this review is the realization that the physics objectives in the original proposals have been largely fulfilled, although the results are not always positive. The most exciting results from PETRA include the following three:

(A) Discovery of the gluon and the determination of the quark–gluon coupling constant, to be discussed in chapter 3;

(B) First observation of the interference between weak and electromagnetic interactions in $e^+e^- \to \mu^+\mu^-$, chapter 5; and

(C) Copious production of baryons, chapter 4.

The third result is entirely unexpected. The greatest disappointment is without doubt the failure so far

to find the top quark, chapter 7. This search is being continued, and we hope that the properties of this top quark will be the most important topics of the next review of PETRA physics.

The table of contents gives the list of all the topic covered in this review. Nevertheless, it remains useful to have a brief summary of each of the chapters.

This chapter gives a short description of the storage ring PETRA and the five detectors: CELLO, JADE, MARK J, PLUTO and TASSO. Since the emphasis of this review is on the physics and the analyses that lead to these results, the descriptions in this chapter are quite brief. In particular, very little information will be given about the mechanical constructions.

Most of the hadronic events (i.e., $e^-e^+ \to$ hadrons) at PETRA are in the form of two back-to-back jets, naturally interpreted as the production of a quark–antiquark pair. The measurement of the total hadronic cross section and the properties of these two-jet events is presented in chapter 2. Further evidence for this quark interpretation is the experimental observation of the long-range charge correlation in opposite jets.

Chapter 3 reviews the discovery of the gluon in the form of a jet, rather similar to the quark jet. The resulting events therefore take the form of three jets, and hence provide a handle to the experimental measurement of the quark–gluon coupling constant α_s. From the distribution of these three-jet events, the spin of the gluon has been found to be 1, in agreement with gauge theory.

In chapter 4, the inclusive production cross sections of identified particles are presented. They are π^0, $\pi^\pm$, $K^\pm$, K_s^0, ρ^0, p, Λ, Ξ^- and $D^{*\pm}$. As already mentioned, one of the most unexpected results from PETRA is the copious production of baryons. The mechanism for this production has not yet been completely clarified. It is expected that many other particles, such as Σ, F, J/ψ and perhaps unexpected ones, will be identified in the future.

Chapter 5 gives the observation of the interference of weak and electromagnetic interactions. This is most successful in the pair production of muons $e^-e^+ \to \mu^-\mu^+$, the forward–backward asymmetry being almost ten standard deviations away from zero.

Chapter 6 deals with the so-called two-photon physics, which refers to processes where the incoming electron and positron each emit a photon, and the two photons interact to produce leptons or hadrons. Unfortunately, the new results from PLUTO, the detector that specialized in two-photon physics, are not yet published.

The last chapter, chapter 7, enumerates the unsuccessful particle searches at PETRA. They range from the eminently reasonable to the rather wild. In particular, the method of search for the toponium (i.e., the bound state of a top quark with an anti-top quark) is discussed in some detail, because it may remain useful in the future.

In the preparation of this review, the emphasis is mostly on the journal publications of the five Collaborations. At various places, however, efforts are made to update the results when more data become available after publication and the method of analysis is at most only slightly modified. Since the rapid rate of publication from these Collaborations keeps on delaying the completion of this review which was originally planned as "The First Three Years of PETRA", it has been decided to use the cutoff date July 15, 1983 – the fifth anniversary of the first successful storage of an electron beam at PETRA. Any publications which appear after this date are included only if they can be implemented easily into this report.

1.2. PETRA

1.2.1. Short history

PETRA is located in the German National Laboratory called Deutsches Elektronen-Synchrotron

(DESY), in a west suburb of Hamburg, Germany. This name, Deutsches Elektronen-Synchrotron, is derived from the first accelerator in the Laboratory, a 7 GeV alternating gradient electron synchrotron. This Laboratory was established in 1959 under the direction of Jentschke, and has played a crucial role in the re-emergence of Germany as one of the leading countries in physics.

The proposal for the project to construct PETRA was submitted to the government of the German Federal Republic in November 1974 [1.1]. Due to the diligent efforts of Schopper, the director of DESY at that time, approval was granted one year later. Shortly thereafter, on January 27, 1976, the foundation "stone", actually an aluminum vacuum chamber, was laid. Under the direction of Voss, the construction of PETRA proceeded very rapidly. The electron beam was first stored on July 15, 1978, more than nine months earlier than originally scheduled. In September 1978, collisions were first observed; a month later, three detectors, PLUTO, MARK J and TASSO (Two-Arm Spectrometer SOlenoid) were moved into place. On November 18, 1978, the first hadronic event was observed by PLUTO, at a center-of-mass total energy of 13 GeV. Since then, PETRA has been operating regularly, reliably and well.

As shown in fig. 1.1, PETRA is housed in a 2.3 kilometer tunnel and is composed of eight straight sections and eight identical curved sections consisting of quadrupole magnets, sextupole magnets and 5.5 meter bending magnets with a bending radius of 192 meters. Of the eight straight sections, four are long for rf accelerating cavities, and four are short for experiments: CELLO and PLUTO in Hall NE, JADE (JApan, Deutschland and England) in Hall NW, MARK J in Hall SW, and TASSO in Hall SE. JADE was moved in the beam in February 1979. CELLO was moved in to replace PLUTO in March 1980; PLUTO was moved back in August 1981 but was replaced by CELLO again in August 1982. PLUTO is not expected to move into the beam again. DORIS (DOuble RIng Storage) was used initially as an intermediate accumulator for positrons. On July 4, 1979, PIA (Positron Intensity Accumulator) came into operation, freeing DORIS to continue on lower-energy e^+e^- physics, in particular upsilon physics. Up to the summer of 1982, the maximum PETRA c.m. energy for luminosity operation was 36.7 GeV with 4.4 MW of rf power. By April 1983, the rf power had been increased to 8.8 MW by doubling the

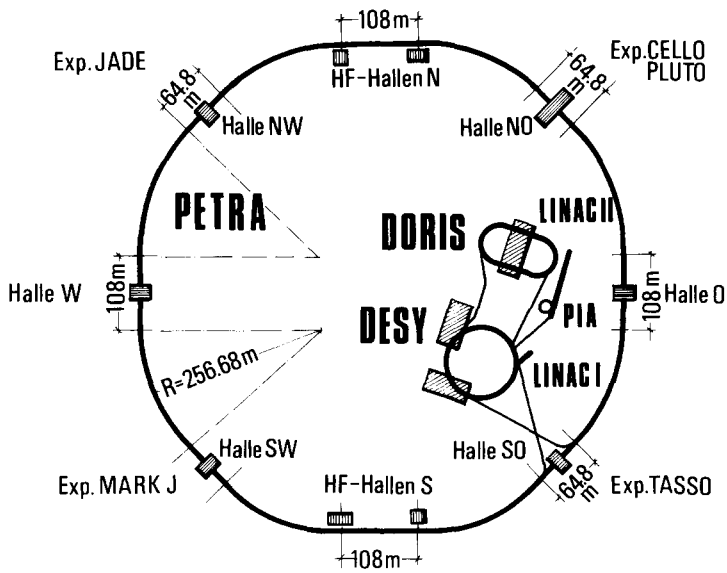

Fig. 1.1a. PETRA (Positron–Electron Tandem Ring Accelerator).

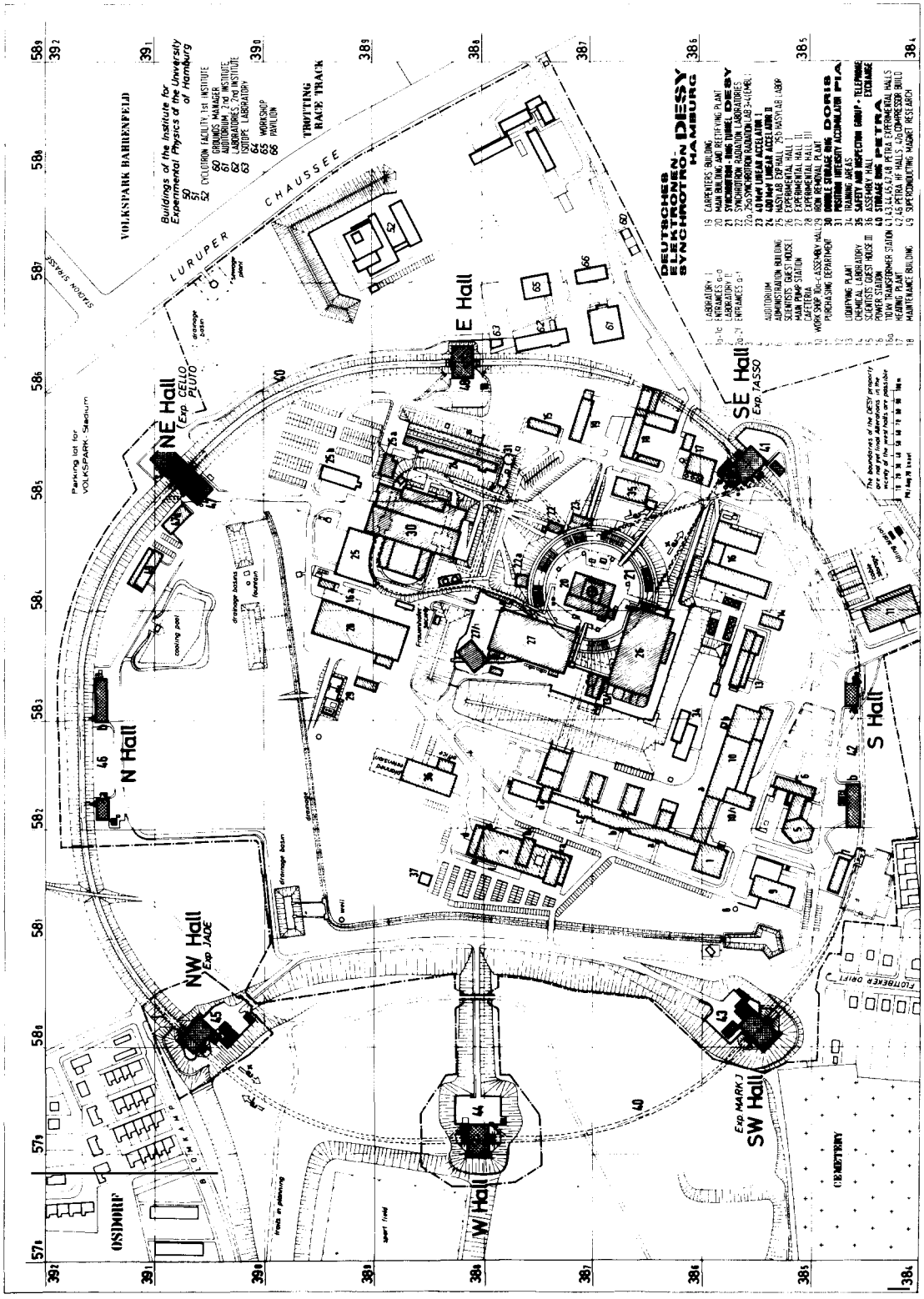

Fig. 1.1b. PETRA (Positron–Electron Tandem Ring Accelerator) and its surroundings.

number of klystrons from 8 to 16, and additional cavities had been installed, increasing the c.m. energy to 43 GeV [1.2]. A further increase to 45 GeV is planned at the end of 1983.

There are many inventions and innovations at PETRA. One of the most remarkable inventions is the so-called mini-beta scheme [1.3], installed in March 1981. In the classic configuration for solenoid detectors, it was considered essential to have compensating magnets. The main effect of an uncompensated solenoid is to increase the coupling K of the betatron oscillations in the vertical (y) and radial (x) directions. This leads to an increase in beam height and hence a reduction in luminosity. The presence of the compensating magnets is the main obstacle to increasing the luminosity by reducing the space between the final focussing elements. However, a detailed study of accelerator physics shows that the different solenoidal detectors can compensate each other [1.4]. The situation at PETRA is complicated by the fact that MARK J has no field on the beam. Fortunately, mutual compensation can still be achieved with the other three detectors: JADE with half the field of CELLO (at 90 degrees) and TASSO with the other half of CELLO (also at 90 degrees). With the chosen betatron frequencies at

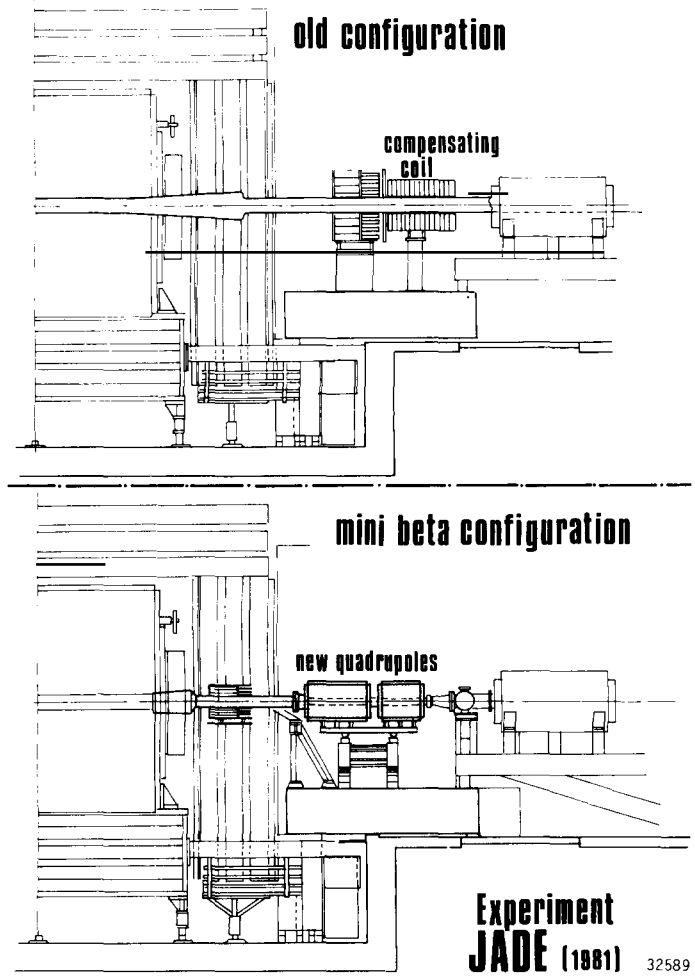

Fig. 1.2. Substitution of the compensating coils of the JADE detector by the quadrupoles for the mini-beta scheme.

PETRA, it is important that all three fields are directed the same way along the beam. In this way, all compensating magnets can be removed, and new quadrupoles are installed for all four interaction regions. With JADE as the example, the change in the detector is shown in fig. 1.2 [1.5]. It is remarkable that this new mini-beta scheme does not degrade any machine parameter. In particular, both the beam lifetime of several hours and the ratio K of about 1 to 2% have remained unchanged. The net effect is a gain in luminosity by a factor of 2.5 to 3. This mini-beta scheme will be described further in section 1.2.2.

There has been a proposal to carry the mini-beta scheme one step further by using air-core superconducting quadrupoles [1.3]. It is estimated that the luminosity can be further increased by another factor of perhaps 4. This scheme is compatible with the future maximum total c.m. energy of 45 GeV or even 60 GeV with superconducting cavities, but no date for its implementation has been set.

1.2.2. Luminosity performance with the mini-beta scheme

The presence of the mini-beta quadrupoles, as shown in fig. 1.2, for example, decreases the amplitude functions at the interaction points as follows [1.3]:

β_y: from 20 cm to 8 cm

and

β_x: from 2.6 m to 1.3 m.

Since the luminosity is proportional to $(\beta_y\beta_x)^{-1/2}$, these decreases by themselves give a theoretical gain of a factor of 2.2 for the same currents. Due to improvements of the operating condition at PETRA, the

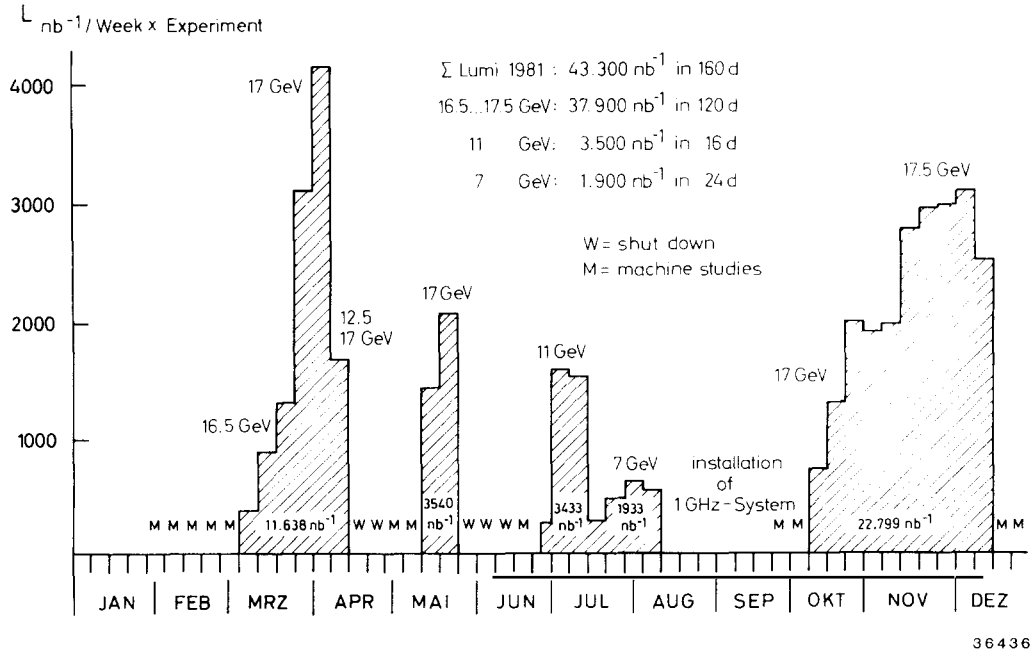

Fig. 1.3. Weekly integrated luminosity at PETRA in 1981 for each experiment.

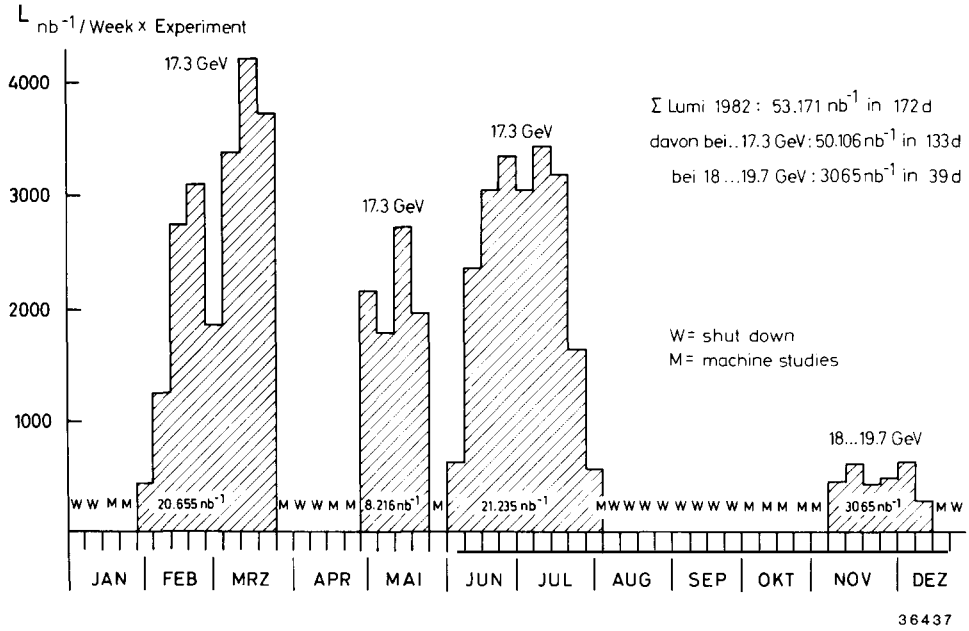

Fig. 1.4. Weekly integrated luminosity at PETRA in 1982 for each experiment.

total gain after the implementation of the mini-beta scheme is somewhat higher. As seen from fig. 1.2., the space available for the detector is slightly reduced. After gaining some experience, beam currents up to 5 mA per bunch are reached again. Fig. 1.3 and fig. 1.4 show the luminosity performance in 1981 and 1982 [1.5] respectively. The highest luminosity so far reached is $1.7 \times 10^{31}\ \mathrm{cm}^{-2}\,\mathrm{sec}^{-1}$.

1.2.3. Radio-frequency power and superconducting cavities

The frequency of the basic rf accelerating system at PETRA is 500 MHz. In the ten month period from October 1981 to July 1982, the experiments were carried out mostly at 2×17.3 GeV. Thus each beam is about 1 GeV below the maximum energy in order to avoid limiting the stored current due to the lack of rf power. Table 1.1 [1.5] gives, for various times, the available rf power, the numbers of accelerating cavities, the maximum accelerating voltage and energy.

During the eight week shut-down in August and September, 1982, the transmitter power was doubled by the addition of four 500 MHz, 1.1 MW rf transmitters in the East and West Halls, which were not used until then. Unfortunately, this increase of the accelerating voltage from 80 MV to 110 MV pushed the accelerating cavities to their power limit, causing the breaking of some coupling windows and the overloading of cooling circuits. This problem was mostly solved by the addition of 32 accelerating cavities in March 1983.

In August 1981, a 1 GHz radio-frequency system of lower power was first tested. These tests confirmed the lengthening of the bunches by a factor of 3 to 4 and the reduction of the troublesome influences of satellite resonances and vertical instabilities [1.6]. Some features of this additional system are also given in table 1.1.

At PETRA, beam energies significantly higher than 22.5 GeV can be reached if the copper cavities are replaced by superconducting resonators. Even without increasing the energy, the use of superconducting accelerating cavities is in any case of economic interest, because half of the power consumed is lost in the copper cavities.

Table 1.1
The radio-frequency systems of PETRA. These two systems, at 500 MHz and 1 GHz, are used together to permit longer bunches and to reduce instability

		1981 version	spring 1983 version	planned (autumn 1983)
Number of 5 cell cavities	500 MHz	60	60	56
Number of 7 cell cavities	500 MHz	–	32	56
Number of 7 cell cavities	1 GHz	–	8	8
Number of 6 cell cavities	1 GHz	–	16	16
Number of transmitters		4	8	8
Total rf power installed (only 80% of this power is available at the cavities)	500 MHz	4.4	8.8*	8.8
	1 GHz	–	0.6	0.6
Peak rf voltage per revolution	500 MHz MV	83	150*	180
	1 GHz MV	–	13	13
Max. beam energy in GeV with zero current		19	22	23

* A lower power and voltage limit is set by the maximum power dissipation per cavity (7.4 MW, 138 MV).

Two superconducting cavities [1.7] have been tested at PETRA, first in 1982 a one-cell cavity built at the Kernforschungszentrum Karlsruhe (Nuclear Research Center of Karlsruhe), and then in 1983 a five-cell cavity built at CERN. Both cavities are made of niobium sheet material, and are equipped with all the facilities needed for operation within a storage ring: a high-power coupler, higher order mode couplers and a tuner system. The result of the first test using the Karlsruhe cavity for six weeks at various beam currents is most encouraging. The Q-value (10^9) of the cavity is affected by neither the beam current of 20 mA nor the synchrotron radiation of 1.5 W which hit the cavity. The maximum field strength is 2.9 MV/m. The CERN five-cell cavity also performed well. It is impressive that a beam could be injected and stored using only the superconducting rf-cavities. With the 1-cell Karlsruhe cavity a beam was stored at 5 GeV and with the 5-cell CERN cavity at 7 GeV.

1.2.4. Beam polarization

For high-energy physics, synchrotron radiation is a nuisance. However, there is a benefit from synchrotron radiation. Because of the guiding magnetic field, electrons with spin antiparallel to the magnetic field have lower energy than those parallel to the magnetic field. Because of synchrotron radiation, the electrons eventually become predominantly antiparallel and the positron parallel to the

magnetic field. Theoretically [1.8], the polarization buildup as a function of time is given by

$$P(t) = P_0(1 - e^{-t/t_0}) \tag{1.1}$$

where

$$P_0 = \frac{8}{5\sqrt{3}} = 92.4\% \tag{1.2}$$

and

$$t_0 = \frac{8}{5\sqrt{3}} \frac{\alpha}{r_0^2} \frac{\rho^2 R}{\gamma^5} \frac{1}{c} . \tag{1.3}$$

In (1.3), $r_0 = 2.818 \times 10^{-13}$ cm is the classical radius of the electron, ρ is the bending radius and R the average radius of the guiding field, γ is the ratio of the beam energy to the electron mass and c is of course the velocity of light. For example, at a beam energy of 15 GeV, the PETRA and PEP time constant t_0 is about 20 minutes.

In writing down the theoretical expectations (1.1)–(1.3), we have ignored many complications. For example, machine resonances tend to destroy the polarization. Thus the actual polarization depends crucially on the small orbital deviations in the vertical direction. Using a method developed at PETRA to compensate for these perturbations, single-beam polarization of 80% of the theoretical maximum of

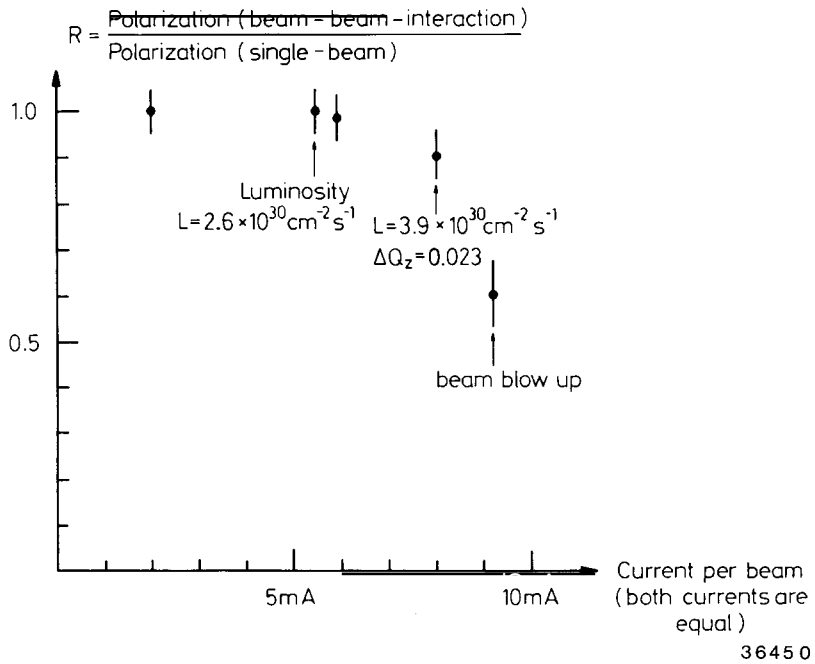

Fig. 1.5. Observed polarization as a function of beam current and luminosity. The electron and the positron currents are equal.

(1.2) has been reached [1.9]. Secondly, beam–beam interaction also tends to destroy the polarization. After careful compensation, a polarization of over 60% was reached at a luminosity larger than $3 \times 10^{30}\,\mathrm{cm}^{-2}\,\mathrm{sec}^{-1}$, as shown in fig. 1.5.

Unfortunately, these are not all the problems. The polarization also tends to be destroyed by the solenoidal magnetic field of the experiment [1.9]. This problem has not yet been solved in a practical way.

The polarization is well suited for an absolute measurement of the energy E of the stored beam. Resonating depolarization destroys the polarization at well defined frequencies [1.9]. The most important resonances occur when the spin-resonance frequency f_s is an integer multiple of the revolution frequency f. The condition is

$$f_s/f = E(g-2)/2m = \text{integer}\,,$$

where m is the electron mass and $g-2$ is the anomalous magnetic moment of the electron, numerically

$$m = 5.11003 \times 10^{-4}\,\mathrm{GeV} \qquad \tfrac{1}{2}(g-2) = 1.159652 \times 10^{-3}\,.$$

Measurements at PETRA have demonstrated that the energy values used previously which come from magnetic field measurements agree with the new energy calibrations to about 0.07%.

1.3. Detectors

Colliding beam accelerators give much lower event rates than fixed target machines; colliding electron machines give much lower event rates than colliding proton machines. At PETRA, the events are clean and yield much physics information, but the rate is relatively low. For example, at beam energy of 18 GeV, the total rate for the process

$$e^+e^- \rightarrow \text{hadrons}$$

is only about 11 per hour even at the exceptionally high luminosity of $1000\,\mathrm{nb}^{-1}/\mathrm{day}$.

Because of this low rate, the basic philosophy of designing detectors for PETRA is vastly different from that for fixed target machines. Instead of selecting one or more particular processes to be studied, all PETRA detectors are general-purpose detectors, which venture to record all events of interest. The main differences between the detectors stem from the emphasis on the various types of information. For example, CELLO is optimized for electron and photon detection at the expense of extensive particle identification, while TASSO opts for particle identification. In this way, the perception of the experimentalists as to what physics will be most important plays a fundamental role.

On October 19, 1976, the Physics Research Committee of PETRA approved five experiments: CELLO, JADE, MARK J, PLUTO and TASSO, in alphabetical order. In the next five sections, these five detectors are described in this order with emphasis on their capability. However, the reader should be cautioned against any naive comparison between the detectors, especially those concerning angular coverage and resolution. The usefulness of a large angular coverage depends among other factors, on the uniformity of the performance of the detector within the coverage. The resolutions given are those from the Collaborations themselves, and the methods used to arrive at these numbers are different for the different Collaborations, some being more conservative than others. The performance of a

Collaboration should be judged by the priority and correctness of the physics discoveries, not the dubious claimed prowess of the detector.

For each Collaboration, the name of the member institutions and the physicists are also given. We have ventured to follow the following rules. If a person has moved from one institution to another within the Collaboration, his name is given under only one institution. Also, former members of the PLUTO Collaboration who have recently joined another Collaboration are still listed under PLUTO.

The detectors necessarily have a number of similar features, including luminosity monitors and muon identification which is affected by placing wire chambers behind iron shields. None of the detectors has had any serious problem with synchrotron radiation.

1.4. CELLO

1.4.1. Members of the CELLO Collaboration

(A) Deutsches Elektronen-Synchrotron, DESY, Hamburg, Germany:
H.-J. Behrend, Ch. Chen, H. Fenner, J.H. Field, U. Gümpel, M.-J. Schachter, V. Schröder, H. Sindt.

(B) Kernforschungszentrum Karlsruhe and Universität Karlsruhe, Germany:
O. Achterberg, G. D'Agostini, W.-D. Apel, S. Banerjee, J. Bodenkamp, D. Chrobaczek, J. Engler, G. Flügge, B. Forstbauer, D.C. Fries, W. Fues, K. Gamerdinger, Th. Henkes, G. Hopp, M. Krüger, H. Küster, F. Mönnig, H. Müller, H. Randoll, G. Schmidt, H. Schneider.

(C) Max-Planck-Institut für Physik und Astrophysik, München, Germany:
W. de Boer, G. Buschhorn, G. Grindhammer, P. Grosse-Wiesmann, B. Gunderson, C. Kiesling, R. Kotthaus, U. Kruse, H. Lierl, D. Lüers, T. Meyer, L. Moss, H. Oberlack, P. Schacht, A. Snyder, H. Steiner.

(D) Laboratoire de l'Accelerateur Lineaire, Orsay, France:
G. Bonneaud, P. Colas, M. Cohen, A. Cordier, M. Davier, D. Fournier, J.F. Grivaz, J. Haissinski, V. Journé, A. Klarsfeld, F. Laplanche, F. Le Diberder, U. Mallik, E. Ros, J.-J. Veillet, A. Weitsch.

(E) Laboratoire de la Physique Nucleaire et Hautes Energies, University of Paris, France:
J.H. Field, R. George, M. Goldberg, B. Grossetête, O. Hamon, F. Kapusta, F. Kovacs, G. London, R. Pain, L. Poggioli, M. Rivoal.

(F) Centre d'Etudes Nucleaires, Saclay, France:
R. Aleksan, J. Bouchez, G. Carnesecchi, G. Cozzika, Y. Ducros, A. Gaidot, S. Jadach, P. Jarry, Y. Lavagne, J. Pamela, J.P. Pansart, F. Pierre.

1.4.2. Features of the CELLO detector

Fig. 1.6 shows two schematic views of the CELLO detector [1.10], which was first moved into the PETRA beam in March 1980. Fig. 1.7 shows the mounting of one of the 16 modules of the cylindrical liquid argon (LA) calorimeter into the cryostat [1.11]. This photograph was taken more than one year before the detector was moved into the beam.

A main feature of the CELLO detector is that the high current density superconducting coil of novel design has a wall thickness of only 0.5 radiation length, including cryostat and insulating material, and thus does not seriously interfere with the detection of electrons and photons in a fine-grain lead liquid argon calorimeter outside the coil.

The functions of the main components of this detector are:

– to measure the momenta of charged particles, over a solid angle of 97% of 4π, by a system of

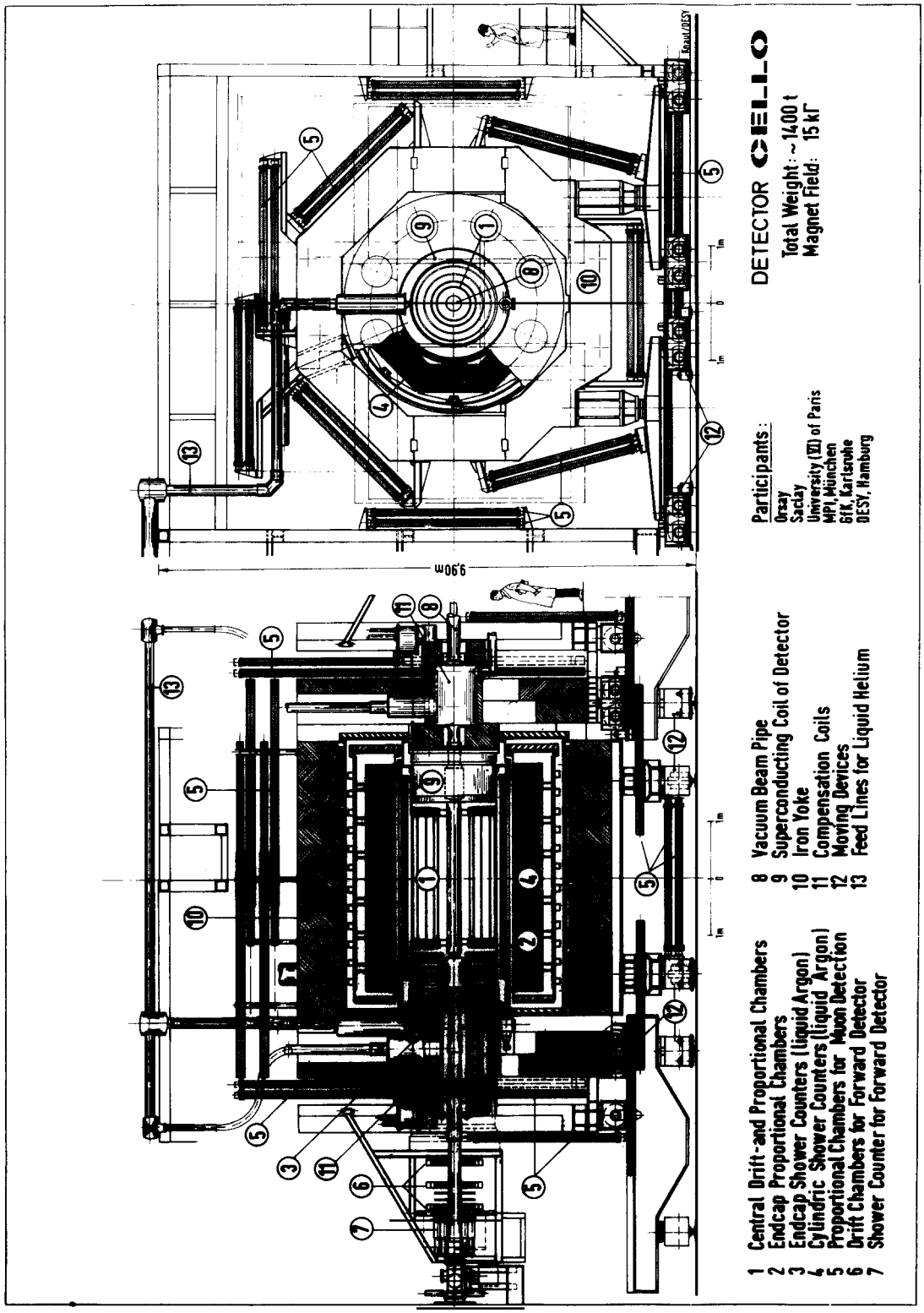

Fig. 1.6. Side view and end view of the CELLO detector.

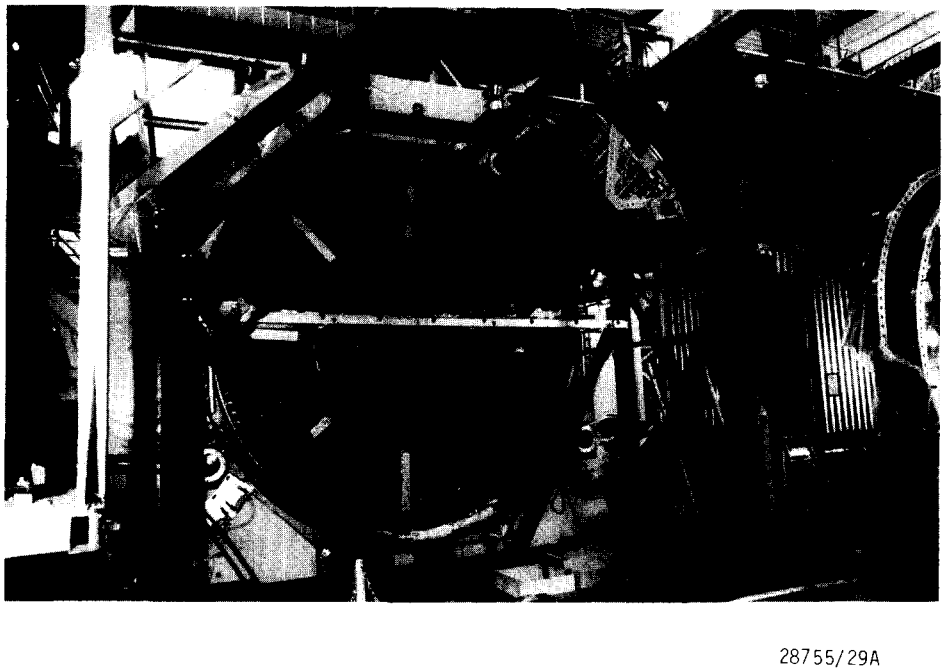

Fig. 1.7. End view of the CELLO detector showing the mounting of one of the 16 modules of the cylindrical argon calorimeter into the cryostat.

interleaved cylindrical and drift chambers mounted inside a superconducting solenoidal magnet of 13 kG and by a set of planar end cap drift chambers;

– to measure the energy of photons and to identify electrons by a system of barrel and end-cap lead liquid argon electromagnetic calorimeter outside the magnet coil over a solid angle of 96% of 4π;

– to identify muons by a system of hadron filter and drift chambers over a solid angle of 92% of 4π;

– to measure luminosity and to tag electrons in two-photon interaction by a forward detector consisting of drift chambers, scintillation counter hodoscopes and lead glass shower counters in the angular range between 25 mrad to 50 mrad with respect to the beam.

1.4.3. Central tracking detector

The CELLO central tracking detector consists of cylindrical proportional wire chambers (PC) interleaved with drift chambers (DC). As seen from fig. 1.8, there are five layers of PC and seven layers of DC, both concentric with respect to the beam axis. Tracking devices of this type all tend to have very accurate resolution in the $r\phi$ plane, i.e., the plane perpendicular to the direction of the beam axis (z axis), but comparatively worse resolution in the z direction. In the case of the CELLO detector, this problem is solved by equipping each of the PCs with two cylindrical cathodes which are finely segmented in strips oriented at 90° and 30° with respect to the cylinder axis. These cathode strips have analog readouts and provide very accurate z determination. The reconstruction of the space points is further facilitated by the pulse height correlation between the induced signals on the 90° and 30° cathode strips. The resulting resolutions are 440 μm in the z direction and 170 μm in the $r\phi$ plane, which is of course also the plane of magnetic deflection.

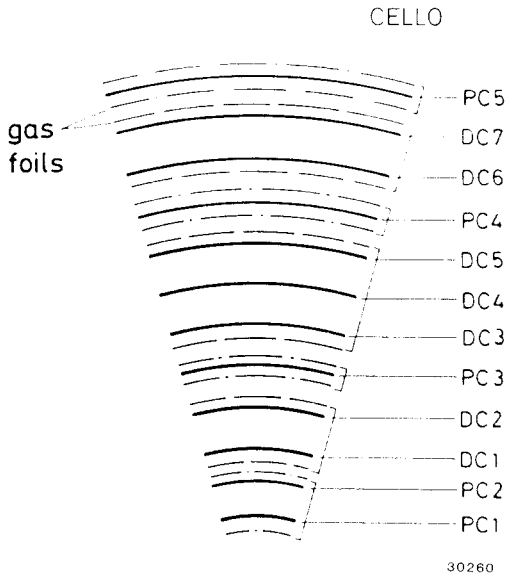

Fig. 1.8. Layer structure of the central tracking detector of CELLO.

For all chambers the wire length is 2.2 m, and the anode wire layers are located at radii between 17 and 70 cm, giving a visible radial track length of 53 cm. The solid angle covered by at least 8 wire layers is 91% of 4π. The anode wire spacing of the five PCs varies between 2.09 and 2.86 mm, and there is a total of 5120 wires, their diameter being 20 μm.

For the cylindrical drift chambers, an entirely open drift cell structure has been chosen in order to keep the number of potential wires at a minimum. The drift cells are arranged on cylindrical surfaces, as already seen from fig. 1.8. Adjacent sense wires, which are gold-plated tungsten wires of 20 μm diameter, are separated electrostatically by a triplet of copper–beryllium potential wires of 50 and 100 μm diameter. There are no further field-shaping electrodes in order to reduce multiple Coulomb scattering as much as possible. The small cell width of 15 mm is dictated by the strong axial magnetic field (13 kG) of the superconducting magnet and the required double-track resolution for jet events with high local track density. Single-hit electronics are used with an amplifier/discriminator hybrid directly mounted on the chamber and a TDC which consists of a low-noise amplifier and an 8 bit ADC to digitize a maximum time interval of 810 ns. A gas mixture of 90% argon and 10% methane is used.

The end-cap multiwire proportional chambers of the CELLO detector are placed at the ends of the cylindrical part of the central tracking device. They cover the acceptance region of $153 < \theta < 428$ milliradians.

1.4.4. Lead liquid argon calorimeter

As seen from fig. 1.7, each of the 16 stacks of the central lead liquid argon calorimeter has a trapezoidal cross section corresponding to a sector of an octagon. The dimensions are: length of 2 m, width of 85 cm in the first and 121 cm in the last layer, and depth of 43 cm, which is equivalent to 20 radiation lengths. Fig. 1.9 shows the details of a stack.

Lead strips of 1.2 mm in thickness alternate with continuous lead plates of the same thickness with an argon gap of 3.6 mm. The strips are held at a positive high voltage relative to the plates. As seen from fig. 1.9, the strips in the central lead liquid argon calorimeter run in three directions, which are

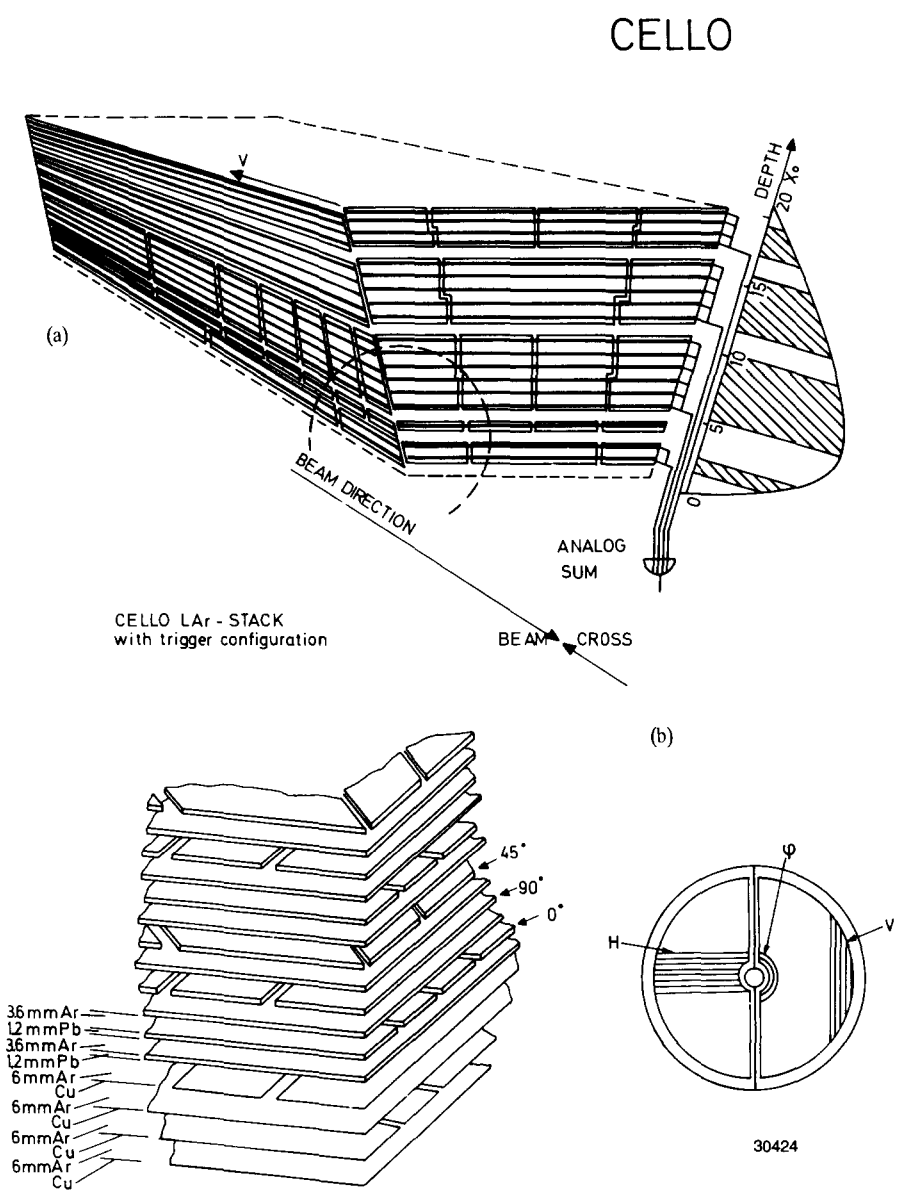

Fig. 1.9. Layout of the lead liquid argon calorimeter of CELLO. (a) Structure of a stack in the central liquid argon calorimeter and groupings of strips inside a stack for the neutral trigger. (b) Orientation of the strips in an end-cap liquid argon calorimeter module.

respectively 0°, 45° and 90° to the beam axis. The 0° and the 90° strips are 2.3 cm wide, whereas the 45° strips are 3.25 cm wide. In front of each stack, there are two additional layers which serve as dE/dx gaps. These layers are built of copper foils glued to epoxy plates with a gap width of 6 mm, as also shown in fig. 1.9. The overall dead areas of the stacks amount to less than 3.5% of the total solid angle covered. The number of electronic channels is 384 per stack.

Each module in the end-cap lead liquid argon calorimeter consists of 42 layers of lead strips interleaved with full plates. The strips are alternatively vertical, horizontal, and circular, see fig. 1.9b.

The thickness of the lead is 1.2 mm and the argon gap 4 mm. The corresponding strips form sectors pointing to the interaction point. This end-cap calorimeter is 21 radiation lengths in total thickness, covers the angular range $5° < \theta < 30°$, and is equipped in front with three planes of copper foils glued on epoxy for dE/dx measurement. The number of electronic channels is 368 per module.

Before installation at PETRA, one full-size stack was tested in a hadron/electron beam at CERN and in an electron/photon beam at DESY. The resolution measured in these tests was degraded by material in front of the calorimeter: 0.6 radiation length for the CERN test and one radiation length for the DESY test. Both the CERN test result and the value obtained from the Bhabha events $e^-e^+ \to e^-e^+$ at the PETRA beam energy of 18.25 GeV are in agreement with the resolution

$$\sigma_E/E = 0.101/\sqrt{E}$$

with E in GeV. Extrapolating to zero material the resolution is

$$\sigma_E/E = 0.085/\sqrt{E}\,.$$

1.5. JADE

1.5.1. Members of the JADE Collaboration

(A) Deutsches Elektronen-Synchrotron, DESY, Hamburg, Germany:
W. Bartel, L. Becker, C. Bowdery, T. Canzler, D. Cords, P. Dittmann, R. Eichler, R. Felst, E. Gadermann, D. Haidt, H. Krehbiel, B. Naroska, L.H. O'Neill, J. Olsson, P. Steffen, P. Warming, H. Wenninger, W.L. Yen, Y. Zhang.

(B) II. Institut für Experimentalphysik der Universität Hamburg, Germany:
G. Dietrich, E. Elsen, G. Heinzelmann, M. Helm, H. Kado, K. Meier, A. Petersen, H. Riege, U. Schneekloth, G. Weber.

(C) Physikalisches Institut der Universität Heidelberg, Germany:
S. Bethke, A. Dieckmann, H. Drumm, W. Farr, J. Heintze, K.H. Hellenbrand, R.D. Heuer, S. Kawabata, S. Komamiya, J. von Krogh, P. Lennert, H. Matsumura, H. Rieseberg, J. Spitzer, A. Wagner.

(D) University of Lancaster, England:
A. Bell, D.C. Darvill, A. Finch, F. Foster, G. Hughes, T. Nozaki, H. Wriedt.

(E) University of Manchester, England:
J. Allison, J. Armitage, J. Baines, A.H. Ball, G. Bamford, R. Barlow, J. Chrin, I.P. Duerdoth, I. Glendinning, J.F. Hassard, B.T. King, F.K. Loebinger, A.A. Macbeth, H. McCann, H.E. Mills, D. Mercer, P.G. Murphy, H.B. Prosper, P. Rowe, K. Stephens.

(F) Rutherford Appleton Laboratory, Chilton, England:
D. Clarke, M.C. Goddard, R. Hedgecock, R. Marshall, G.F. Pearce, J.B. Whittaker.

(G) Lab. of Int. Coll. on Elementary Particle Physics and Department of Physics, University of Tokyo, Japan:
M. Imori, J. Kanzaki, T. Kawamoto, T. Kobayashi, S. Komamiya, M. Koshiba, M. Minowa, M. Nozaki, S. Odaka, S. Orito, A. Sato, T. Suda, H. Takeda, T. Takeshita, Y. Totsuka, Y. Watanabe, S. Yamada, C. Yanagisawa.

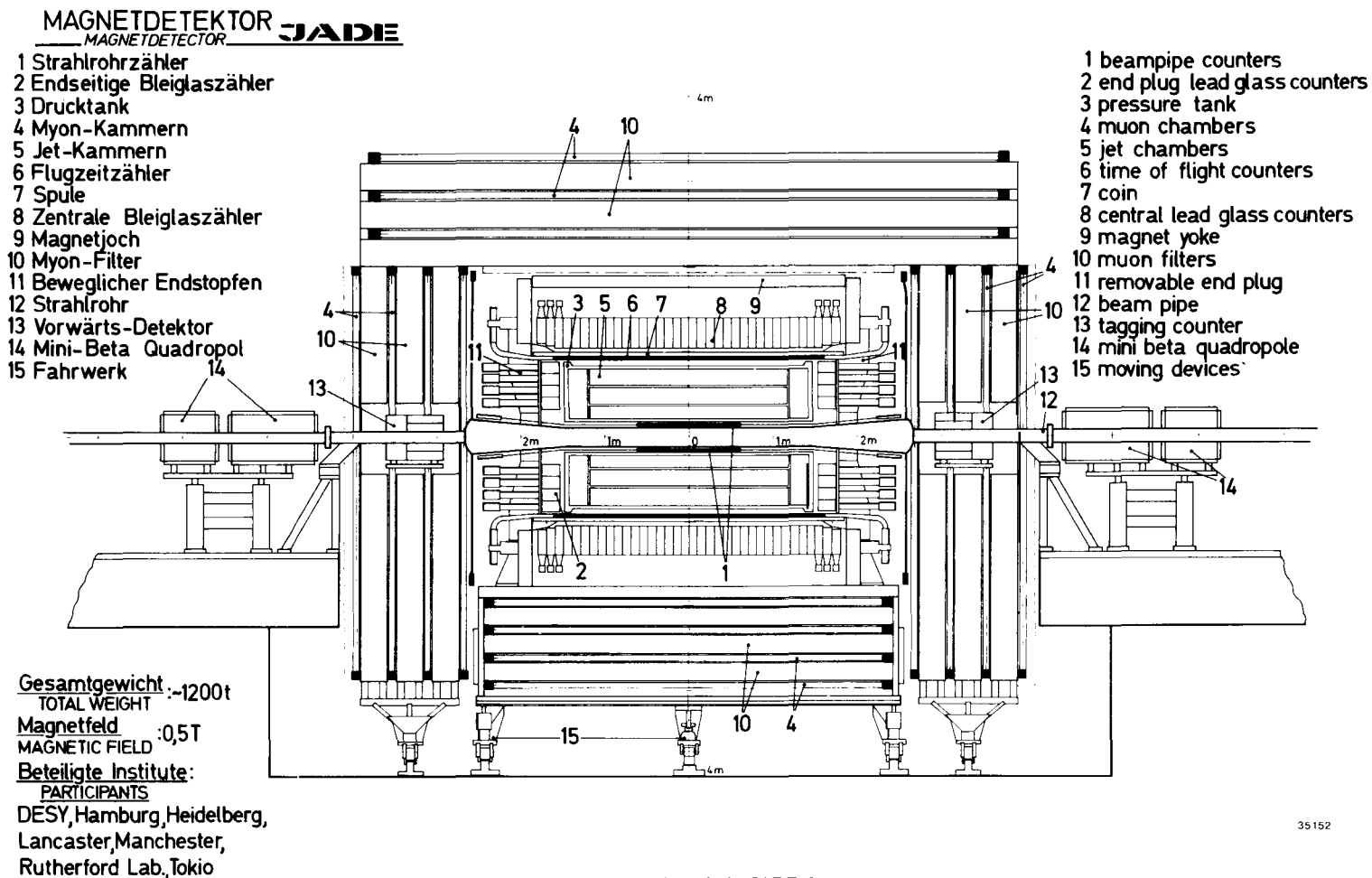

Fig. 1.10. Cross section through the JADE detector.

1.5.2. Features of the JADE detector

Fig. 1.10 shows the side view of the JADE detector [1.11, 1.12], which was moved into the PETRA beam in February 1979. Fig. 1.11 shows the assembly of the JADE central detector, called the "jet chamber", in progress in the dust-free room at Heidelberg University.

This jet chamber [1.13], which is a special type of high-pressure (4 atmospheres) drift chamber, is a main feature of the JADE detector. It is situated within the 4.8 kG magnetic field of the solenoid, and at least eight points on a track are obtained over 97% of 4π.

The functions of the main components of this detector are:

- to measure the momenta of charged particles with this jet chamber;
- to separate π, K and p in the non-relativistic region and to identify π in the region of relativistic rise by measuring dE/dx in the jet chamber;
- to measure the energies of photons and to identify electrons by a system of barrel and end-cap lead glass shower counters outside the magnet coil over a solid angle of 90% of 4π [1.14];
- to identify muons by a segmented system with five layers of iron/concrete absorber and drift chambers covering a solid angle of 92% of 4π [1.15];
- to measure luminosity and to tag electrons in two-photon interactions by a forward detector consisting of a lead glass, scintillator and drift chamber system in the angular range between 34 mrad to 75 mrad [1.16].

1.5.3. Jet chamber

The concept of the jet chamber was developed in 1976 at the University of Heidelberg [1.13]. It is a

Fig. 1.11. The assembly of the JADE central detector in progress in the dust-free room at Heidelberg University.

drift chamber with closely spaced sense wires but relatively long drift distance. The sensitive volume is a cylinder surrounding the beam pipe: outer diameter 1.6 m, inner diameter 0.4 m, and length 2.4 m. The chamber is subdivided into 24 modules, each subtending an angle of 15°. As seen from fig. 1.12 which shows two of the modules, each module contains 4 cells arranged in the 1–1–2 configuration, and each cell contains 16 anode wires. Since $\tan^{-1} 1.6/2.4 = 34°$, in the polar angular region $34° < \theta < 146°$ 48 points are measured along each track, which is 57 cm long in the radial direction. As already mentioned, and as is readily seen from the dimensions given, in 97% of 4π the track traverses at least half a cell, giving 8 points of measurement.

The drift trajectories are up to 8 cm long. At each point of measurement the spatial coordinates r, ϕ and z are given by the wire position, the drift time, and the charge division measurement. In this charge division method, the integrated charge from each hit is measured separately from each end of the anode wire. The ratio of these measurements determines the position of the hit along the wire, and the sum gives the energy loss dE/dx of the particle. As shown in fig. 1.12, the field shaping electrodes are located on the surface of the module, and the resulting electric field is perpendicular to the plane containing the anode wires. Therefore, the magnetic field of 4.8 kG provided by the warm solenoidal magnet is orthogonal to the electric drift field and causes a rotation of the drift trajectory by a Lorentz angle of

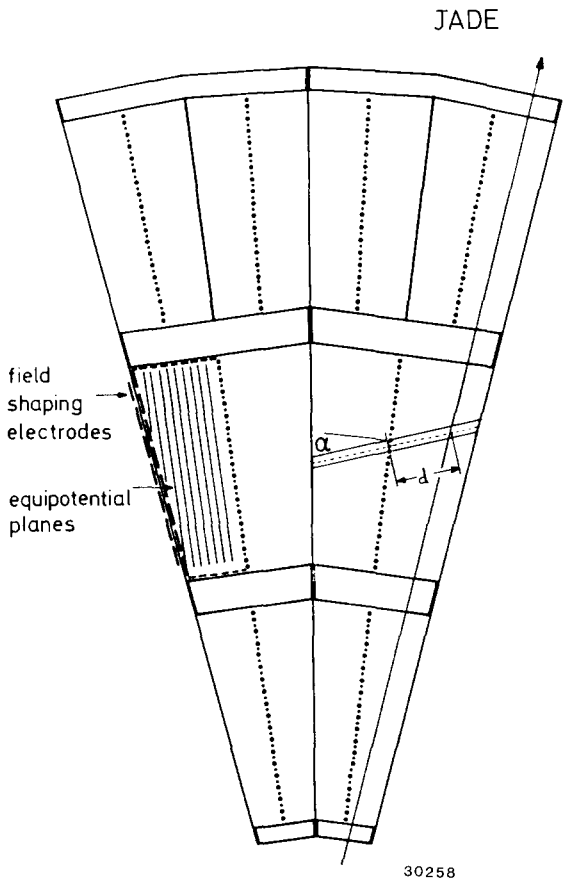

Fig. 1.12. Cross section through two segments of the JADE jet chamber. d is the length of the drift path, α the Lorentz angle. The position of the anode wires (small points) and of the potential wires (large points) are indicated.

20°, also shown in fig. 1.12. The average values of the space resolution of the jet chamber are 160 μm in the $r\phi$ plane and 13 mm in the z direction. The average transverse-momentum resolution, which does not depend on the z resolution, is

$$\Delta p_T/p_T = 2.2\% \cdot p_T$$

with p_T in GeV/c.

The jet chamber operates with a gas mixture of argon (88.7%), methane (8.5%) and isobutane (2.8%) at a pressure of 4 atmospheres. The pressure dictates the wall thickness. The electronics connected to each of the 1536 wires of the jet chamber consists of preamplifiers on both ends of the wire, a discriminator-integrator and fast analog and time memories with a capacity of 8 hits per wire. The double-track resolution is 7 mm.

A feature of the jet chamber is that the 48 dE/dx measurements are used for particle identification. It has been used to separate $\pi^{\pm}$, $K^{\pm}$, and p, $\bar{p}$ in the non-relativistic region, and also for the determination of the $\pi/(K+p)$ ratio in the region of the relativistic rise. This dE/dx resolution is limited by three factors: statistical fluctuation in energy loss, statistical fluctuation in the gas amplification ($\sim 4 \times 10^4$), and systematic errors. Both types of statistical fluctuations are determined by the choice of gas mixture and pressure. With the observed relativistic rise of 1.48, the dE/dx resolution of electrons from Bhabha scattering is

$$\frac{\sigma(dE/dx)}{dE/dx} = 5.7\%$$

or (13–14)% full width half maximum. The dE/dx resolution obtained in high-multiplicity events is somewhat worse:

$$\frac{\sigma(dE/dx)}{dE/dx} = 9.4\%$$

or 22% FWHM.

1.5.4. Lead glass shower counters

Another feature of the JADE detector is the extensive use of lead glass Schott SF 5 and SF 7 shower counters shown in fig. 1.13. They consist of two parts: a cylindrical portion (marked as 8 in fig. 1.10) located between the coil and the return iron yoke of the magnet, and two circular end caps (2 in fig. 1.10). The angles covered are respectively $|\cos\theta| < 0.82$ and $0.89 < |\cos\theta| < 0.97$. Taken together, the solid-angle coverage is 90% of 4π. Fine granularity is achieved by dividing the cylindrical portion into 2520 separate counters and the end caps into 2×96 counters. This fine granularity allows an accurate measurement of the emission angle, typically $\Delta\theta = \pm 0.6°$ using the known interaction point. All the lead glass counters were tested and calibrated at the test beam facility at DESY. The energy resolution of the individual counters was measured to be [1.14]

$$\sigma_E/E = 6\%/\sqrt{E}$$

up to $E = 6$ GeV. The overall energy resolution actually achieved for 17 GeV electron showers is 2%.

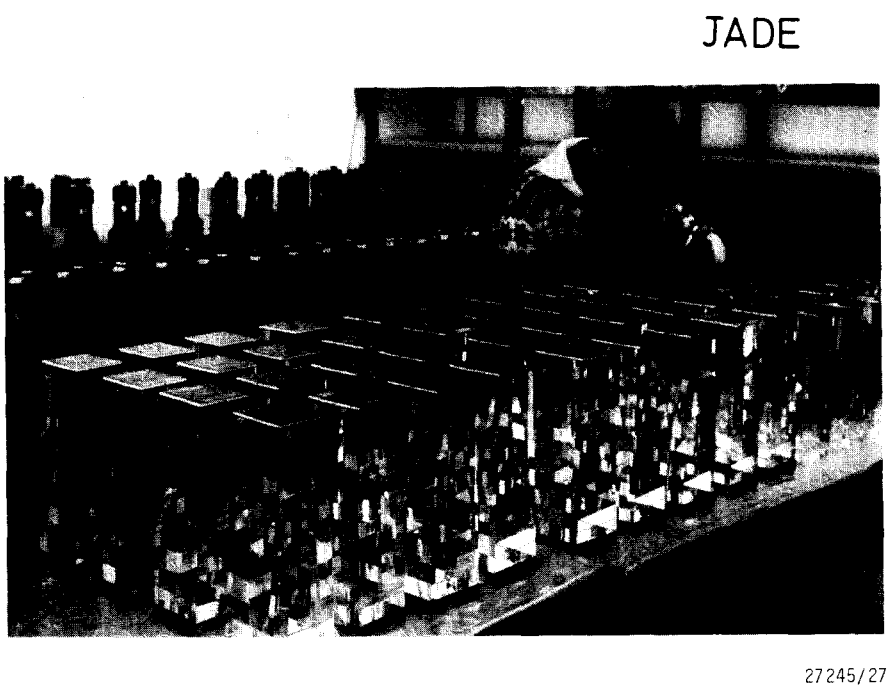

Fig. 1.13. Lead glass blocks from the JADE shower counters.

1.6. MARK J

1.6.1. Members of the MARK J Collaboration

(A) III. Physikalisches Institut, Technische Hochschule Aachen, Germany;
(B) Deutsches Elektronen-Synchrotron DESY, Hamburg, Germany;
(C) Laboratoire de Physique des Particules (LAPP), Annecy-le-Vieux, France;
(D) Laboratory for Nuclear Science, Massachusetts Institute of Technology, Cambridge, Massachusetts, U.S.A.;
(E) Junta de Energia Nuclear, Madrid, Spain;
(F) Nationaal Instituut voor Kernfysica en Hoge-Energiefysica, Amsterdam, The Netherlands;
(G) California Institute of Technology, Pasadena, California, U.S.A.;
(H) Institute of High Energy Physics, Chinese Academy of Science, Beijing, People's Republic of China.

The physicists are:

B. Adeva, D. P. Barber, U. Becker, G.D. Bei, J. Berdugo, H. Benda, G. Berghoff, A. Böhm, J.G. Branson, J. Bron, D. Buikman, J.D. Burger, M. Capell, M. Cerrada, C.C. Chang, G.F. Chen, H.S. Chen, M. Chen, M.L. Chen, M.Y. Chen, C.P. Cheng, Y.S. Chu, R. Clare, E. Deffur, M. Demarteau, P. Duinker, G.Y. Fang, Z.Y. Feng, H.S. Fesefeldt, D. Fong, M. Fukushima, J.C. Guo, A. Hariri, D. Harting, T. Hebbeker, G. Herten, M.C. Ho, H.K. Hsu, T.T. Hsu, M.M. Ilyas, D.Z. Jiang, R.W. Kadel, D. Kooijman, W. Krenz, P. Kuiger, J. Li, Q.Z. Li, M. Lu, D. Luckey, E.J. Luit, C.M. Ma, D.A. Ma, C. Maña, M.A. Marquina, G.G.G. Massaro, T. Matsuda, R. Mount, H. Newman, J. Paradiso, M. Pohl, F.P. Poschmann, R.R. Rau, J.P. Revol, S. Rodriguez, M. Rohde, J.A. Rubio, H. Rykaczewski, J. Salicio, I. Schulz, K. Sinram, M. Steuer, G.M. Swider, H.W. Tang, L.G. Tang, D. Teuchert, Samuel

C.C. Ting, K.L. Tung, F. Vannucci, M.Q. Wang, X.R. Wang, Y.X. Wang, J. Warnock, P.S. Wei, M. White, G.H. Wu, H.G. Wu, S.X. Wu, T.W. Wu, B. Wyslouch, J.P. Xi, P.C. Yang, C.C. Yu, X.H. Yu, Y.Q. Zeng, N.L. Zhang, B. Zhou, R.Y. Zhu, Y.C. Zhu.

1.6.2. Features of the MARK J detector

Fig. 1.14 shows the side view and the end view of the MARK J detector [1.17], which was moved into the PETRA beam in October 1978. Unlike the other four detectors at PETRA, the central part of the MARK J detector has a square instead of a circular cross section. This is readily seen from both fig. 1.14 and fig. 1.15 [1.11]. The underlying reason for this difference is that, for MARK J, there is no magnetic field in the central detector and the magnetic field is supplied by magnetized iron rather than a solenoid. Fig. 1.16 [1.11] shows the MARK J detector at the time of moving into the PETRA beam.

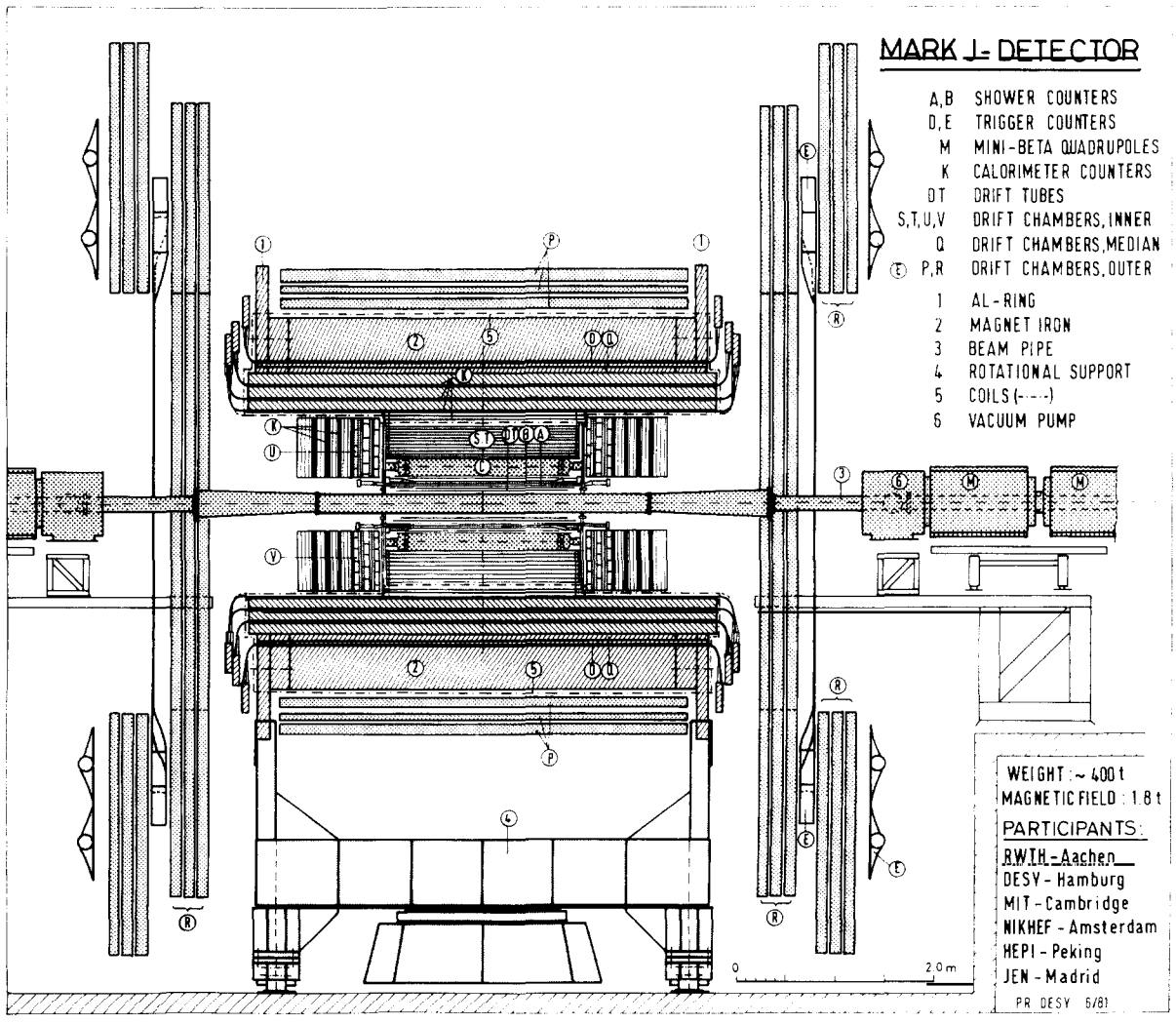

Fig. 1.14a. Side view of the MARK J detector.

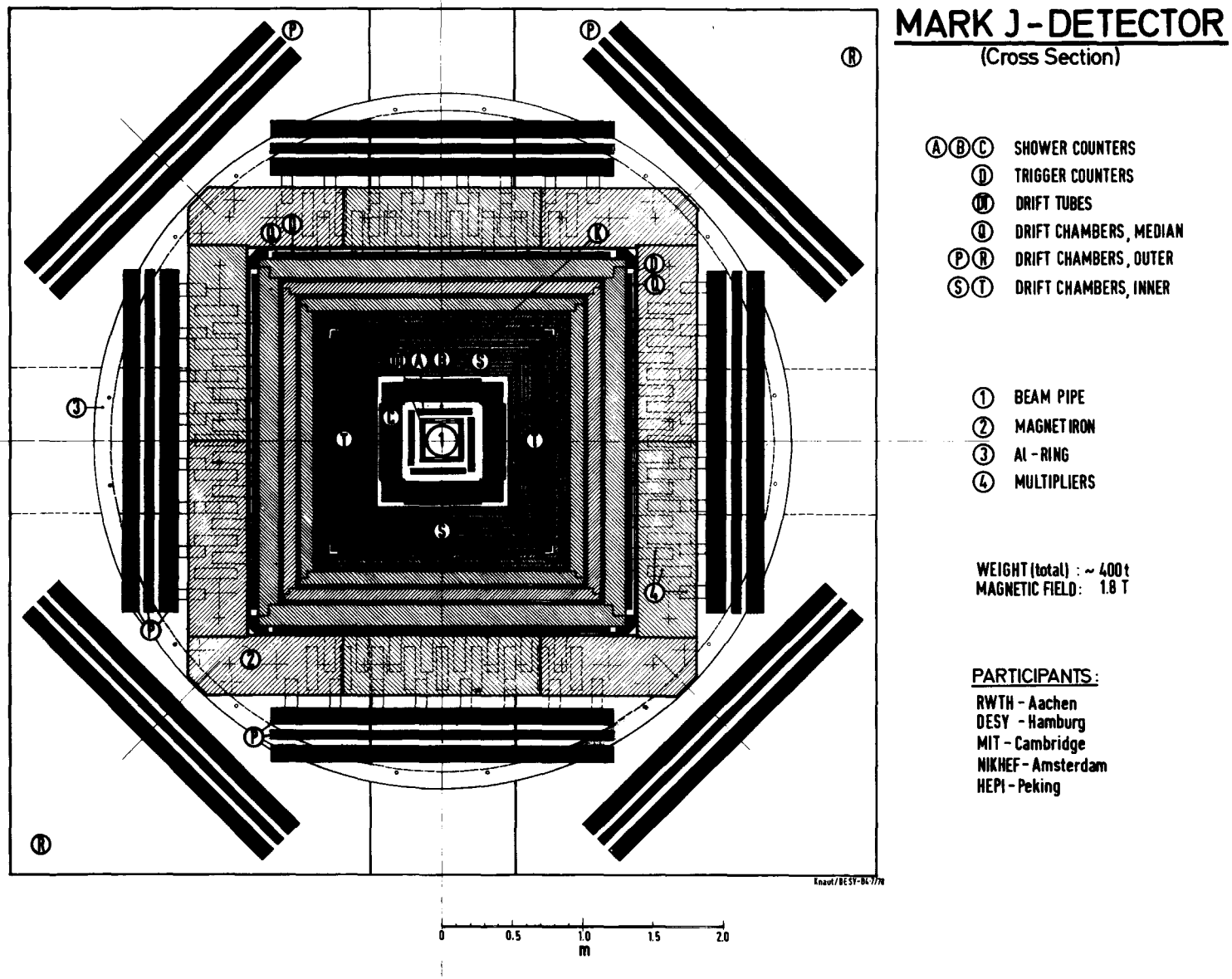

Fig. 1.14b. End view of the MARK J detector.

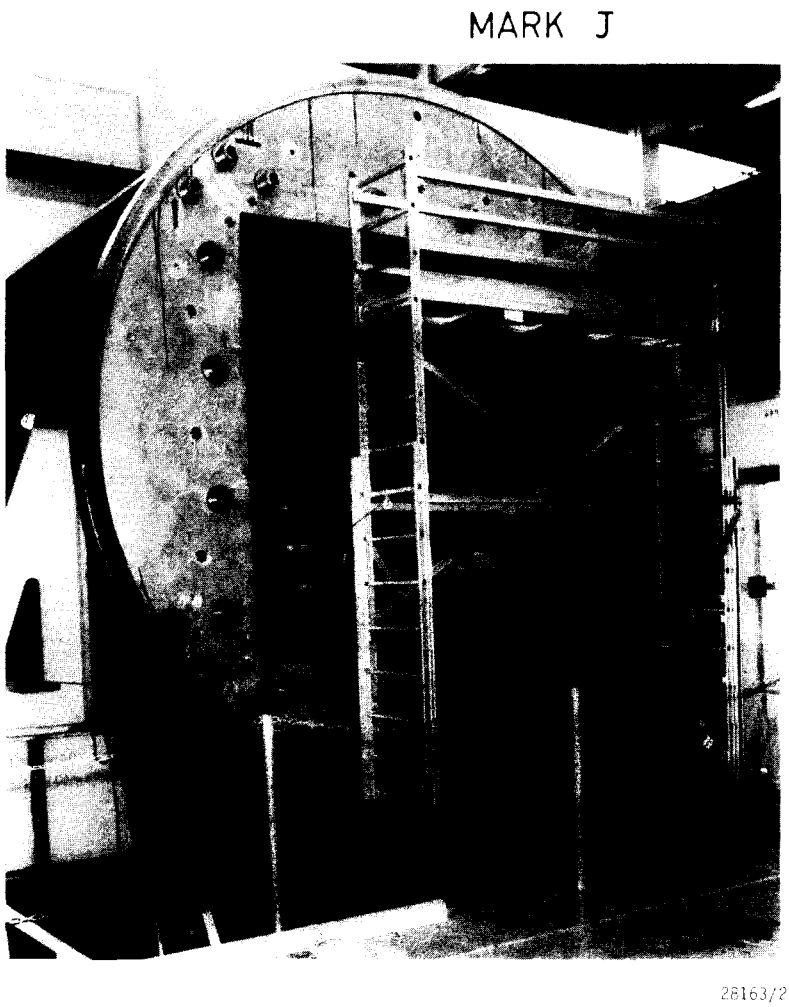

Fig. 1.15. The just assembled magnet iron of the MARK J detector in 1978.

A main feature of the MARK J detector is the special rotational support. This support permits the rotation of the entire MARK J detector in order to cancel the small systematic effects due to variations in chamber efficiency and counter gain, and also the slight asymmetry in mechanical construction. By disconnecting and reconnecting the cables, the detector can be rotated azimuthally about the beam line by ±90°; by cutting the beam pipe, it can be rotated about the vertical axis by 180°.

The functions of the main components of this detector are:

– to measure the energies of neutral and charged particles by a system of lead-scintillator sandwich shower counters and hadron calorimeters consisting of magnetized-iron-scintillator sandwiches (individual momenta of charged particles in a jet are not measured);

– to identify and measure the momenta of muons using magnetized iron with an integrated bending power of 17 kG-meter at $\theta = 90°$, the muon chamber coverage being 90% of 4π [1.18];

– to measure luminosity by a forward detector consisting of scintillators and lead glass blocks designed to measure Bhabha events at small scattering angles (~30 mrad).

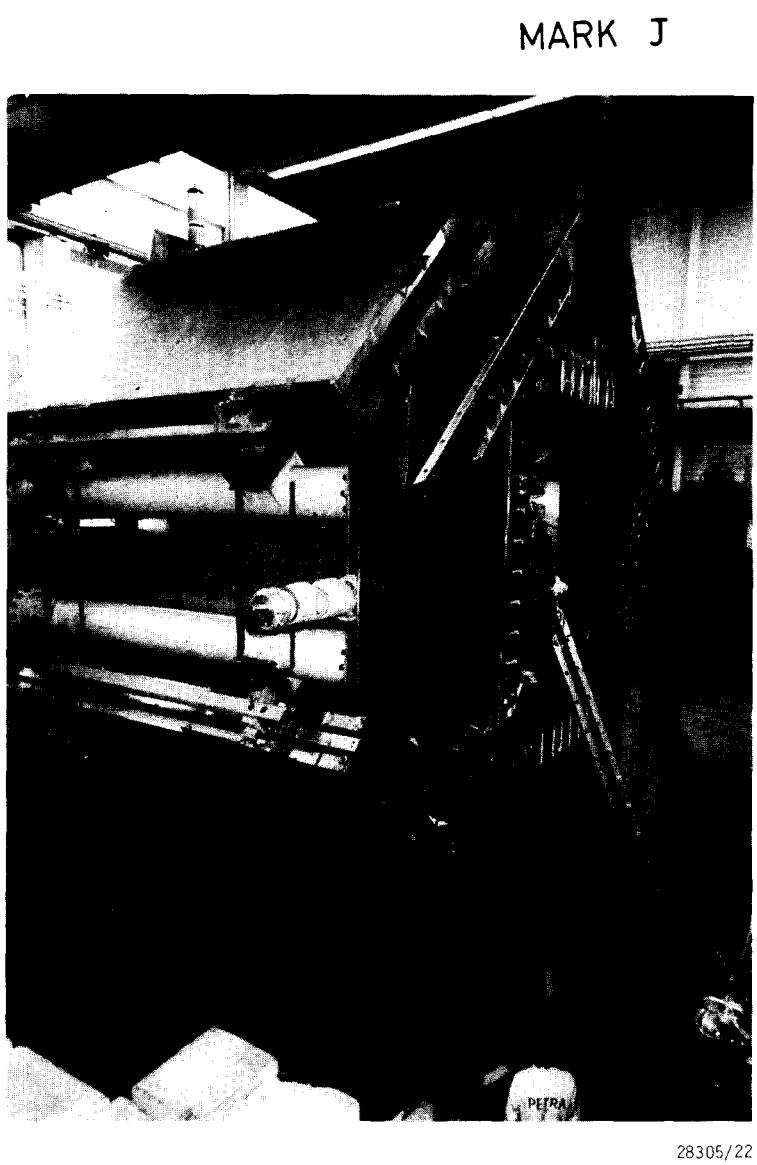

Fig. 1.16. The MARK J detector when it was moved into PETRA beam line in 1978. The muon drift chambers are clearly seen.

1.6.3. Non-magnetic inner detector

During the first nine months of operation, a ring of 32 lucite Čerenkov counters covered the angular region $9° < \theta < 171°$ around the beam pipe. These counters were divided at $\theta = 90°$, 16 to each side, to permit a crude determination of the momentum balance between the forward and the backward hemispheres. They were replaced by a four-layer inner tracking detector composed of 992 drift tubes. These tubes, which are 0.3 m long and 1 cm wide, are arranged perpendicular to the beam line, leading to the square cross section mentioned earlier. The angular range covered is $30° < \theta < 150°$, and the spatial resolution of 300 μm perpendicular to the anode wire makes it possible to reconstruct the position of the event vertex along the beam line in the z direction to an accuracy of 2 mm.

Particles produced in e^-e^+ annihilation then pass through 18 radiation lengths of shower counters for energy measurement, as shown in fig. 1.17. This inner calorimeter is divided into three layers A, B and C, each constructed of 5 mm thick pieces of scintillator alternated with 5 mm thick lead plates. At $\theta = 90°$, the thicknesses of the three layers are respectively 3, 3 and 12 radiation lengths. The A and B layers consist of 20 and 24 identical shower counters each 2 m long and cover the angular regions $12° < \theta < 168°$ and $16° < \theta < 164°$ respectively. All the counters in these three layers are aligned along the z direction, and have a phototube at each end. The pulse height and time differences measured by these phototubes are used to determine the position of the track along the z direction. The azimuthal angle ϕ is determined by the position of the shower counters in space. For an individual hit, the resulting accuracies are

$$\Delta z = 25\,\text{mm} \qquad \text{and} \qquad \Delta\phi = 7°\,.$$

Since this inner detector is non-magnetic, energies of individual tracks close to each other are not separately measured. Instead, from the pulse height and position information of groups of hits occurring within a cone of 20° opening angle emanating from the interaction point, the vector energy flow is computed. The weights used in this summation of pulse heights are different for hadronic and electromagnetic showers. For hadron events, the resolution in the total observed energy is ~20% at $W \approx 30$ GeV.

As seen in fig. 1.17, the three layers A, B and C of shower counters are followed by twelve planes of drift chambers to measure the angle of the particles that penetrate through. Since these drift chambers are located behind the shower counters, the amount of material in the chamber along the path of the

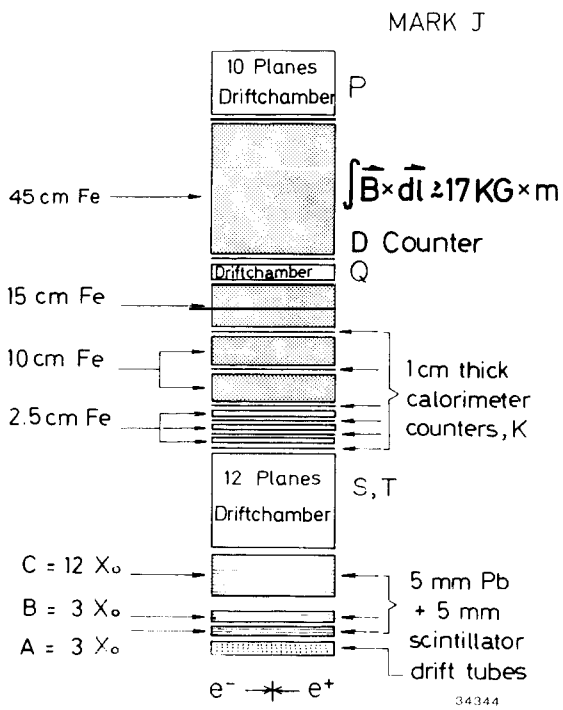

Fig. 1.17. The structure of the MARK J detector as seen by a particle emerging from the interaction point at a right angle to the beam axis.

particles is not a consideration in their design. Thus they consist of 10 cm cells formed by two field shaping I-beams glued with insulators between two aluminum ground plates. The resolution for individual cells is 400 μm for perpendicular tracks, and 600 μm when averaged over all angles of incidence. A gas mixture of argon (75%) and isobutane (25%) is used.

1.6.4. Magnetized iron toroids

Another feature of the MARK J detector is the extensive use of magnetized iron, which constitutes the bulk of the total weight of the detector. There are five magnetized iron toroids surrounding the non-magnetic inner detector described in the last section. The thickness of these five toroids are respectively 7.5 cm, 10 cm, 10 cm, 15 cm and 45 cm, as is most readily seen from fig. 1.17. The innermost one is separated into three sections, each of thickness 2.5 cm, with scintillation counters in-between. The total thickness of the iron is thus 87.5 cm, and the total bending power is approximately 17 kG-meters. The typical bending angle for a 15 GeV muon is 30 mrad. The trajectory of the muon is measured by three drift chambers, one with 12 planes already mentioned, a second one with 2 planes before the last toroid, and finally one with 10 planes behind the last toroid.

At a muon momentum $p = 17.5\ \mathrm{GeV}/c$, the inverse-momentum resolution is found to be [1.18]

$$\sigma_k/k = 30\% ,$$

where $k = 1/p$. This means approximately that

$$\sigma_p/p \sim 30\% .$$

After the installation of the end-cap muon chambers, the muon acceptance was increased to 90% of 4π.

1.7. PLUTO

1.7.1. Members of the PLUTO Collaboration

(A) I. Physikalisches Institut der RWTH Aachen, Germany:
Ch. Berger, H. Genzel, R. Grigull, W. Lackas, J. Pielorz, F. Raupach, W. Wagner.

(B) University of Bergen, Norway:
L.H. Fløl o, A. Klovning, E. Lillestöl, E. Lillethun, J.M. Olsen.

(C) Deutsches Elektronen-Synchrotron, DESY, Hamburg, Germany:
H. Ackermann, J. Bürger, L. Criegee, Ch. Dehne, A. Deuter, R. Devenish, A. Eskreys, F. Ferrarotto, G. Flügge, G. Franke, W. Gabriel, M. Gaspero, Ch. Gerke, G. Horlitz, U. Jacobs, G. Knies, E. Lehmann, B. Lewendel, U. Maurus, H.D. Mertiens, J. Meyer, U. Michelsen, B. Neumann, K.H. Pape, H.D. Reich, B. Stella, T.N. Ranga Swamy, U. Timm, P. Waloschek, G.G. Winter, S.T. Xue, S. Wolff, M. Zachara, W. Zimmermann, M. Greco.

(D) University of Glasgow, U.K.:
P.J. Bussey, S.L. Cartwright, J.B. Dainton, B.T. King, C. Raine, J.M. Scarr, I.O. Skillicorn, K.M. Smith, J.C. Thomson.

(E) II. Institut für Experimentalphysik der Universität Hamburg, Germany:
O. Achterberg, V. Blobel, L. Boesten, D. Burkart, K. Diehlmann, M. Feindt, V. Hepp, H. Kapitza, B. Koppitz, M. Krüger, B. Lewendel, W. Lührsen, R. Maschuw, M. Poppe, H. Spitzer, R. van Staa.

(F) University of Maryland, U.S.A.:
C.Y. Chang, R.G. Glasser, R.G. Kellogg, K.H. Lau, S.J. Maxfield, R.O. Polvado, B. Sechi-Zorn, J.A. Skard, A. Skuja, A.J. Tylka, G. Welch, G.T. Zorn.

(G) Universität-Gesamthochschule Siegen, Germany:
F. Almeida, A. Bäcker, F. Barreiro, S. Brandt, K. Derikum, A. Diekmann, C. Grupen, H.J. Meyer, H. Müller, B. Neumann, M. Rost, K. Stupperich, G. Zech.

(H) Tel-Aviv University, Israel:
G. Alexander, G. Bella, Y. Gnat, J. Grunhaus.

(I) Universität-Gesamthochschule Wuppertal, Germany:
T. Azemoon, H.J. Daum, H. Junge, K. Kraski, C. Maxeiner, H. Maxeiner, H. Meyer, O. Meyer, M. Rössler, D. Schmidt, K. Wacker.

1.7.2. Features of the PLUTO detector

Fig. 1.18 shows a side view of the PLUTO detector [1.19] at the time it was moved into the PETRA beam in October 1978. PLUTO is the first detector moved into the beam, and is also the first detector to observe a hadronic event at PETRA, on November 18, 1978. Previously it was used extensively at DORIS, but a number of new components were added before being moved to PETRA. Fig. 1.19 shows the central detector of PLUTO in June 1978.

The functions of the main components of this detector are:

– to measure the momenta of charged particles over a solid angle of 87% of 4π by a set of cylindrical proportional chambers inside a superconducting solenoid of magnetic field 16.5 kG;

– to measure the energies of photons and to identify electrons by a system of barrel and end-cap lead-scintillator shower counters over a solid angle of 96% of 4π;

– to identify muons by the iron yoke acting as the hadron absorber and a set of proportional tube chambers over a solid angle of 80% of 4π;

– to measure luminosity and to tag electrons for two-photon processes by a forward detector consisting of a set of lead-scintillator shower counters covering the angular region $70 < \theta < 260$ mrad (large angle tagger LAT) and a matrix of lead glass blocks for $23 < \theta < 70$ mrad (small angle tagger SAT).

1.7.3. Inner track chambers

The track chambers and the shower counters of the inner detector are located inside a superconducting solenoid of 1.40 m diameter and 1.05 m in length. The barrel shower counters consist of two layers, and are described in the next section. Inside these barrel shower counters, there are 12 cylindrical proportional chambers with a wire spacing of 2–4 mm, an active length of 0.94 m, and diameters ranging from 0.225 m to 1.125 m. In 87% of 4π, the track traverses at least six wire layers. The cathodes are built of cylinders of epoxy fibre glass of 0.017 radiation length in thickness, coated with 35 μm of copper. This copper coating is segmented into stripes which are tilted at various angles to the wires. For every discharge, a wire signal plus two pulses induced on the stripes are read out. This layout produces a high density of space coordinates along a track, at the price of multiple scattering affecting the resolution for low-momentum particles. The momentum resolution for pions which are constrained to the beam line is given at high momenta by

$$\sigma_p/p = 3\% \cdot p$$

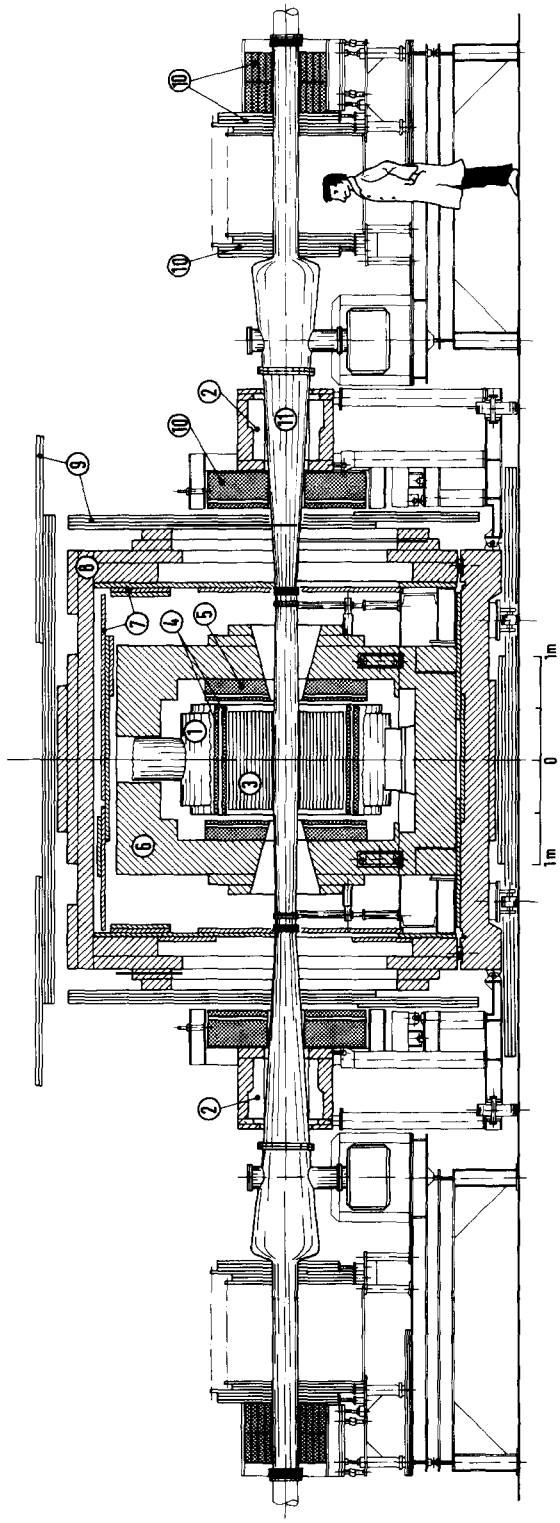

Fig. 1.18. Side view of the PLUTO detector at PETRA. Part of the detector was previously used at DORIS.

Fig. 1.19. Central detector of PLUTO in June 1978 during installation at PETRA.

with p in GeV/c. The resolution is about constant over 60% of the solid angle, but deteriorates rapidly towards the forward and backward directions.

1.7.4. Shower counters

These 12 cylindrical proportional chambers are enclosed by lead-scintillator shower counters which measure neutral energy within a solid angle of 96% of 4π. These shower detectors are segmented in the azimuth angle ϕ, every 6° for the barrel and every 12° for the end-cap shower counters. Each has a layer of wire chambers to locate the shower origin.

The barrel shower detector consists of 60 modules of lead-scintillator sandwiches arranged in two layers, both inside the superconducting solenoid. The lengths of both layers are 0.81 m, the diameters 1.20 m and 1.34 m respectively [1.20]. As shown in fig. 1.20, the thickness of the two layers, with helix tube chambers in-between, are 3.9 and 4.7 radiation lengths. This total thickness of 8.6 radiation lengths is marginal for sampling the showers due to electrons and photons of energy around 10 GeV or higher, but does give a fair measure of the neutral energy of hadronic events, which is predominantly emitted via low-energy photons (<4 GeV) from π^0 decay. Since the geometry chosen does not allow optimum light collection, another limitation on the resolution is due to photon statistics. For electrons the energy resolution is [1.19]

$$\sigma_E/E = 35\%/\sqrt{E}$$

with E in GeV. The helix tube chambers, shown in fig. 1.20, provide an angular resolution of

$$\sigma_\phi = 1.3° \quad \text{and} \quad \sigma_\theta = 1.4°$$

for isolated showers.

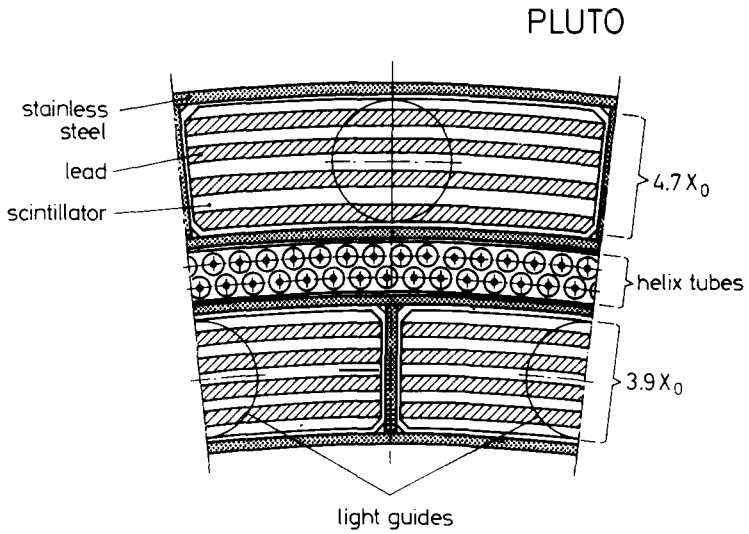

Fig. 1.20. Cross section through barrel shower counter of PLUTO with lead-scintillator sandwiches and helix tubes.

Each of the two end-cap shower counters consists of 30 pie-shaped lead-scintillator sandwiches of 10.3 radiation lengths. The energy resolution is

$$\sigma_E/E = 19\%/\sqrt{E}\,.$$

The single layer of multiwire proportional chambers inserted in the sandwiches provides a measurement of the polar angle with the resolution

$$\sigma_\theta = 1^\circ\,.$$

1.7.5. Forward spectrometer

The so-called two-photon process $e^+e^- \to e^+e^-$ hadrons, where the hadrons are produced via two photons, is studied in chapter 6. These reactions can be "tagged" by measuring the outgoing e^+ and/or e^-, which are produced predominantly in directions near the beam line. For this purpose, the PLUTO detector is equipped with two taggers each in the forward and backward directions, the SAT and the LAT as already described in section 1.7.2.

Each of the SAT's consists of 96 blocks of lead glass, 12.5 radiation lengths thick. The energy resolution is

$$\sigma_E/E = 8.5\%/\sqrt{E}\,.$$

Charged particles are tracked by four planes of proportional wire chambers in front of each SAT.

Each of the LAT's consists of 18 lead-scintillator sandwiches, 14.5 radiation lengths thick. The energy resolution is

$$\sigma_E/E = 11\%/\sqrt{E}\,.$$

Charged particles are tracked and showers are localized by four layers of proportional tube chambers, two in front and two inside the shower counters.

What has been described here is actually the PLUTO forward spectrometer in the pre-1981 configuration. All the PLUTO data reported in this review have been taken in this configuration. During the period from March 1980 to August 1981, when PLUTO was out of the PETRA beam and CELLO was taking data at Hall NE, the PLUTO forward spectrometers were almost completely rebuilt and thus upgraded to allow momentum measurement and particle identification. These new forward spectrometers have been used to take data for one year from August 1981 to August 1982. However, these new data are not included in this review because they are not published before the fifth anniversary of the first PETRA electron beam.

Fig. 1.21 shows the PLUTO detector with the forward spectrometers in the post-1981 configuration.

1.8. TASSO

1.8.1. Members of the TASSO Collaboration

(A) I. Physikalisches Institut der RWTH Aachen, Germany:
M. Althoff, R. Brandelik, W. Braunschweig, B. Jaax, V. Kadansky, F.J. Kirschfink, K. Lübelsmeyer, H.-U. Martyn, G. Peise, J. Rimkus, P. Rosskamp, H.G. Sander, D. Schmitz, A. Schultz von Dratzig, H. Siebke, W. Wallraff.

(B) Physikalisches Institut der Universität Bonn, Germany:
H. Boerner, H.M. Fischer, H. Hartmann, W. Hillen, A. Jocksch, G. Knop, L. Köpke, H. Kolanoski, W. Korbach, H. Kück, V. Mertens, F. Roth, W. Rühmer, R. Wedemeyer, N. Wermes, M. Wollstadt.

(C) Deutsches Elektronen-Synchrotron, DESY, Hamburg, Germany:
R. Bühring, H. Burkhardt, D.G. Cassel, S. Cooper, J. Franzke, K. Gather, H. Hultschig, P. Joos, W. Koch, P. Koehler, U. Kötz, H. Kowalski, A. Ladage, B. Löhr, D. Lüke, H.L. Lynch, P. Mättig, K.H. Mess, D. Notz, R.J. Nowak, J. Pyrlik, D.R. Quarrie, R. Riethmüller, M. Rushton, M. Schliwa, W. Schütte, P. Söding, D. Trines, G. Wolf, Ch. Xiao.

(D) II. Institut für Experimentalphysik der Universität Hamburg, Germany:
R. Fohrmann, E. Hilger, T. Kracht, H.L. Krasemann, P. Leu, E. Lohrmann, D. Pandoulas, G. Poelz, K.U. Pösnecker, J. Ringel, O. Römer, R. Rüsch, P. Schmüser, B.H. Wiik.

(E) Department of Physics, Imperial College, London, England:
I. Al-Agil, R. Beuselinck, D.M. Binnie, A.J. Campbell, P.J. Dornan, N.A. Downie, B. Foster, D.A. Garbutt, C. Jenkins, T.D. Jones, W.G. Jones, J. McCardle, A. Pevsner, J. Sedgbeer, R.A. Stern, J. Thomas, W.A.T. Wan Abdullah, S. Yarker.

(F) Department of Nuclear Physics, Oxford University, England:
R.J. Barlow, K.W. Bell, M.G. Bowler, I. Brock, P. Bull, R. Carnegie, R.J. Cashmore, P.E.L. Clarke, R. Devenish, P. Grossmann, C.M. Hawkes, J. Illingworth, S.L. Lloyd, M. Ogg, B. Roe, G.L. Salmon, T.R. Wyatt, C. Youngman.

(G) Rutherford Appleton Laboratory, Chilton, England:
W. Chinowsky, G.E. Forden, J.C. Hart, J. Harvey, D.K. Hasell, J. Proudfoot, D.H. Saxon, P.L. Woodworth.

(H) Fachbereich Physik der Universität-Gesamthochschule Siegen, Germany:
F. Barreiro, M. Dittmar, D. Heyland, M. Holder, G. Kreutz, B. Neumann.

(I) Weizmann Institute, Rehovot, Israel:
E. Duchovni, Y. Eisenberg, D. Hochman, U. Karshon, E. Kogan, G. Mikenberg, R. Mir, D. Revel, E. Ronat, A. Shapira, G. Yekutieli.

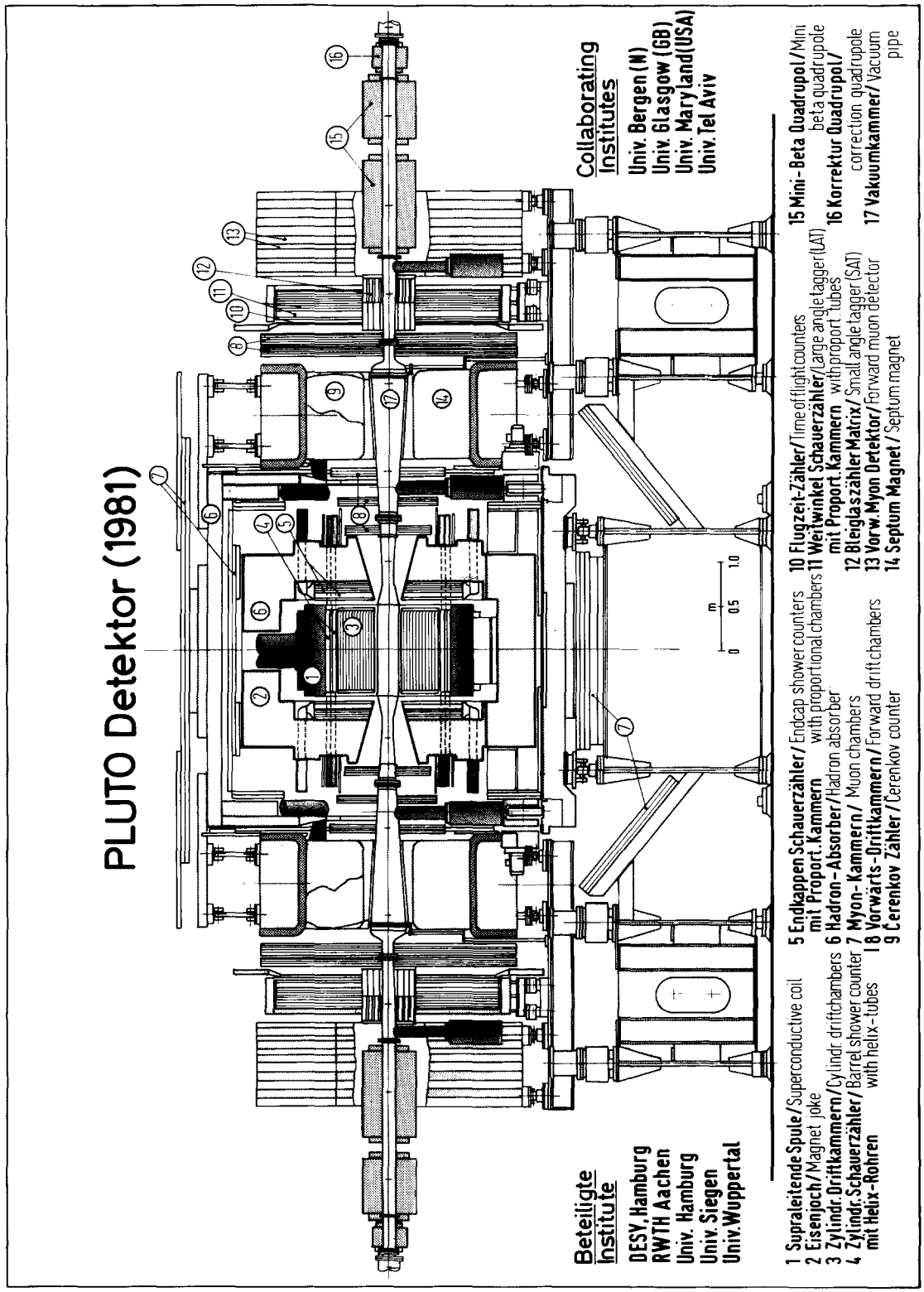

Fig. 1.21. PLUTO 1981 with upgraded forward spectrometers, consisting of analyzing magnet (14), drift chambers, Čerenkov counter (9), small angle tagger (SAT) and enlarged large angle tagger (LAT). The long quadrupoles (15) are part of the 'mini-β^*' focussing system, while the short ones (16) compensate the field of the central and the forward magnets.

(J) Department of Physics, University of Wisconsin, Madison, Wisconsin, U.S.A.:
G. Baranko, T. Barklow, A. Caldwell, M. Cherney, J. Freeman, J.M. Izen, P. Lecomte, M. Mermikides, T. Meyer, G. Rudolph, D. Strom, M. Takashima, H. Venkataramania, E. Wicklund, Sau Lan Wu, G. Zobernig.

1.8.2. Features of the TASSO detector

Figs. 1.22 and 1.23 show the three different views of the TASSO detector [1.11, 1.21], which was moved into the PETRA beam in October 1978. A main feature of the TASSO detector is the two-arm spectrometer, which leads to the name TASSO (section 1.2.1) and is clearly seen in the end and plane views of fig. 1.23. The two arms cover a solid angle of 20% of 4π, and each of them consists of a plane drift chamber, three types of Čerenkov counters with aerogel, freon 114 and CO_2 respectively, time-of-flight counters, lead-scintillator shower counters, and an iron wall to filter muons followed by proportional tube muon chambers. They are used for particle identification.

The functions of the main components of this detector are:

– to measure the momenta of charged particles, over a solid angle of 87% of 4π, by a set of cylindrical proportional chambers and drift chambers inside a solenoid magnet of 5 kG;

– to measure the energies of photons and to identify electrons by a system of barrel and end-cap lead liquid argon shower counters and lead-scintillator shower counters covering a solid angle of 90% of 4π;

– to identify muons by a system of hadron filters and proportional tube chambers over a solid angle of 45% of 4π [1.22];

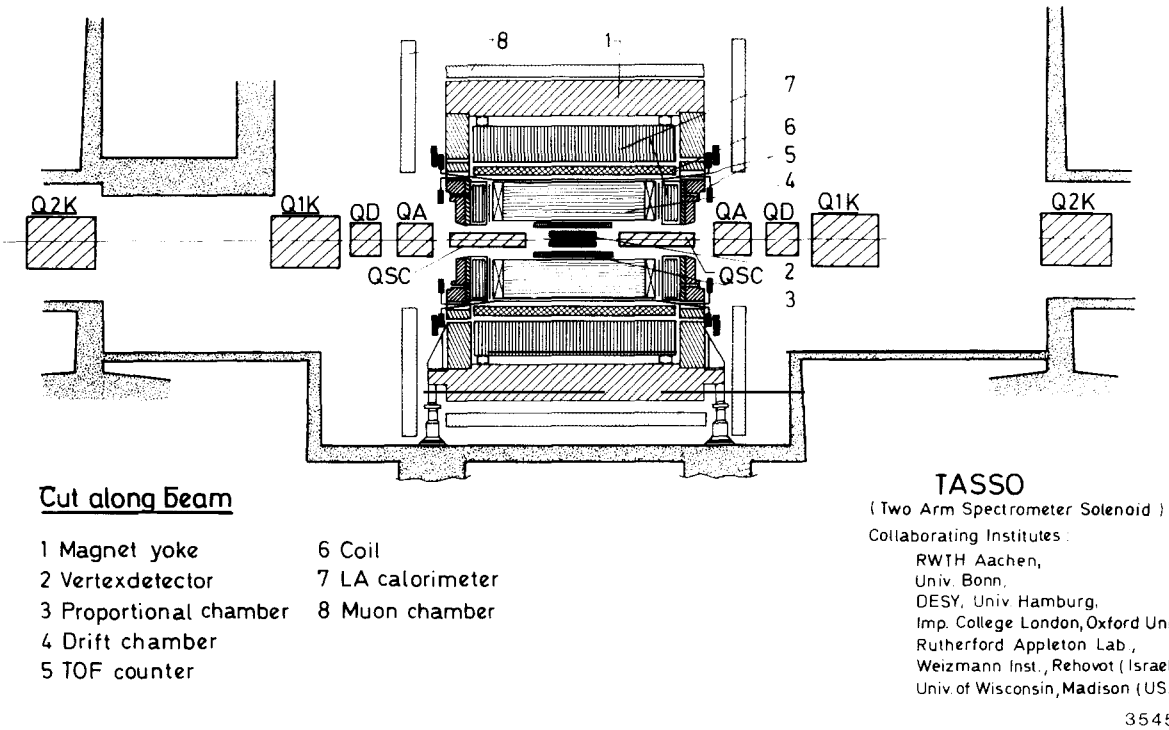

Fig. 1.22. Cut-along-beam view of the TASSO detector.

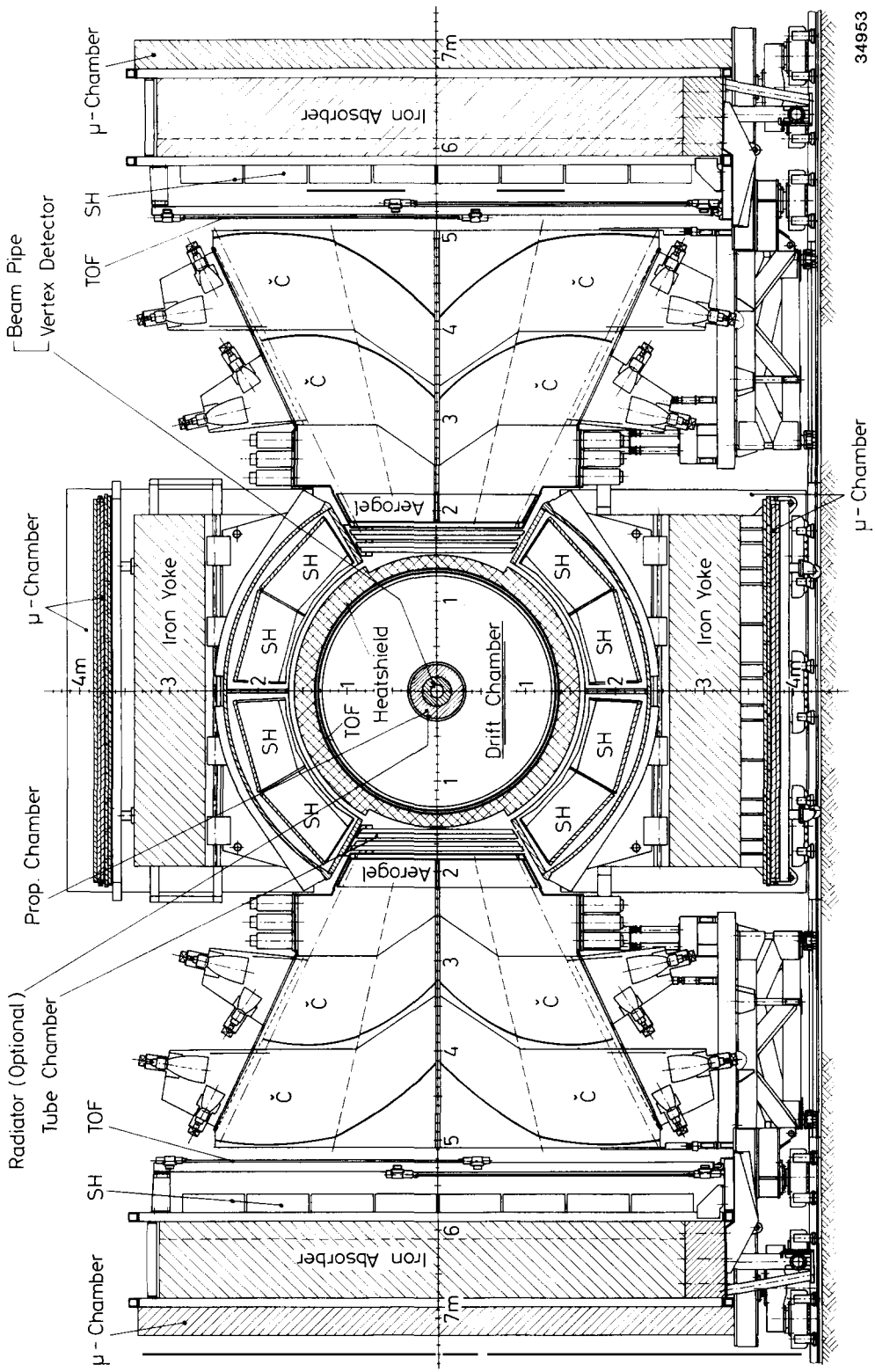

Fig. 1.23a. End view of the TASSO detector.

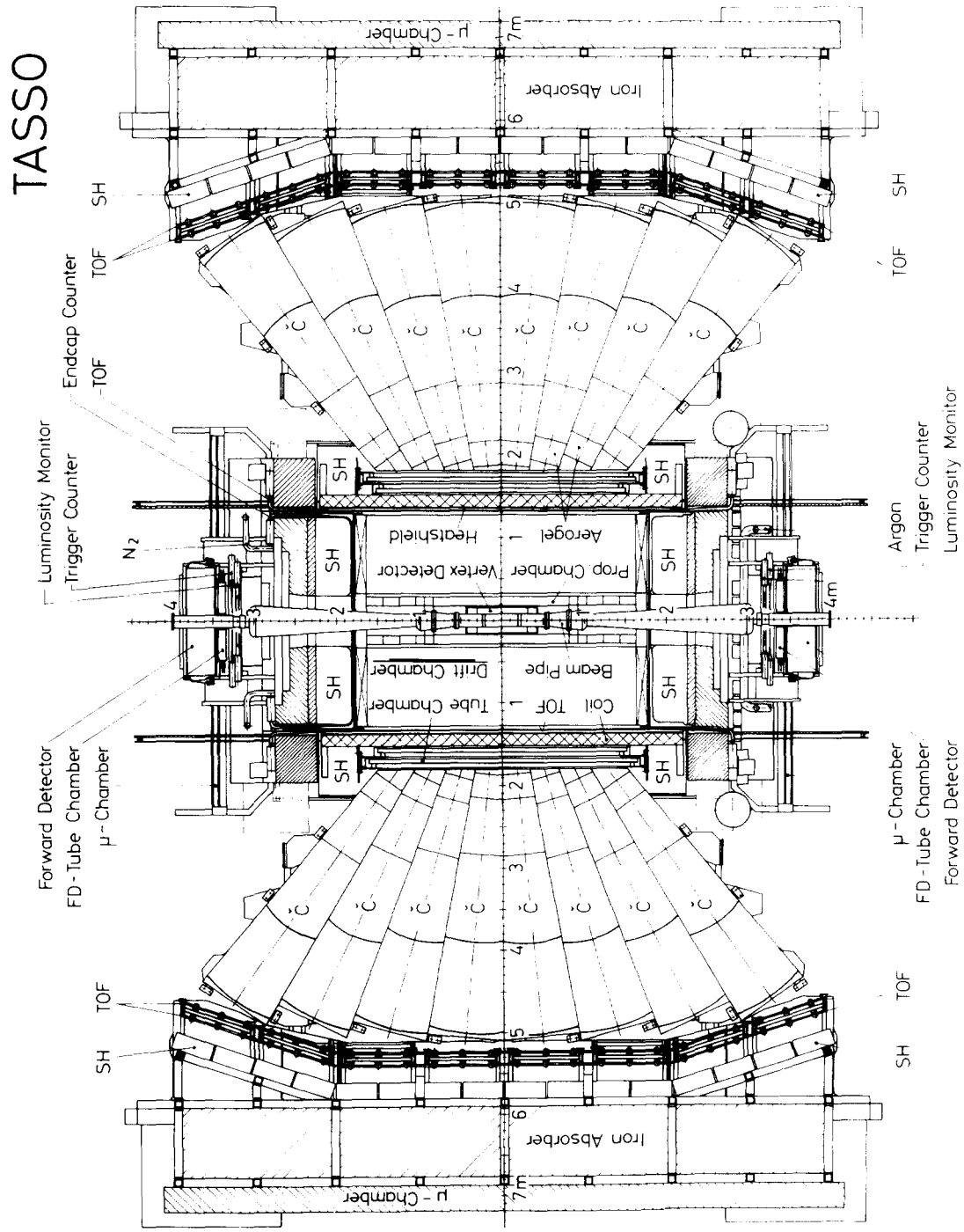

Fig. 1.23b. Top view of the TASSO detector.

– to identify $e^{\pm}$, $\pi^{\pm}$, $K^{\pm}$, p and $\bar{p}$ by the spectrometer arms (20% of 4π) together with inner time-of-flight systems (82% of 4π) [1.22];

– to measure luminosity and to tag electrons in two-photon interactions by forward detectors consisting of acceptance-defining scintillator counters, lead glass shower counters, and proportional chamber in the angular range between 24 mrad and 60 mrad with respect to the beam [1.23].

1.8.3. Central tracking detector

As seen from fig. 1.23, the central tracking detector consists of the proportional chamber, the large drift chamber, and the time-of-flight counters.

The proportional chamber [1.24] is 1.4 m long with inner and outer diameter of 36 and 57 cm. It is made of concentric styrofoam shells each 1.6 cm thick forming 4 active gaps of 1.4 cm each. In each gap, there are 480 anode wires mounted parallel to the beam axis, together with 120 inner and 120 outer cathode strips forming helices of opposite sense of rotation and average pitch of 36.5°. The strips are made by etching copper-coated Kapton film with an average width of 8 mm.

The drift chamber [1.24, 1.25] has a sensitive length of 3.23 m with inner and outer diameter of 0.734 and 2.444 m. There are in total 15 layers, as shown in fig. 1.24a, 9 with the sense wires parallel to the axis and 6 with the sense wires oriented at an angle of approximately ±4° for three-dimensional track reconstruction. The chamber has 2340 identical drift cells, as shown in fig. 1.24b, each with radial and azimuthal dimensions of 1.2 and 3.2 cm respectively. The gas mixture was argon (90%) and methane (10%) and later has been changed to argon (50%) and ethane (50%).

The average value of the space resolution of the drift chamber is about 200 μm in the $r\phi$ plane perpendicular to the beam axis. From the process $e^-e^+ \to \mu^-\mu^+$, the momentum resolution of the drift chamber is found to be (p in GeV/c) [1.22]

$$\sigma_p/p = 1.7\% \cdot p$$

for p not too low and without using the vertex constraint; and [1.26]

$$\sigma_p/p = 1.0\% \cdot \underline{\sqrt{2.9 + p^2}}$$

using the average beam position as a constraint for track reconstruction.

A set of 48 time-of-flight counters [1.27] is mounted around the drift chamber. Each scintillator ($390 \times 17 \times 2\ \mathrm{cm}^3$) is viewed from both ends by photomultipliers. In addition, 24 sector-shaped time-of-flight counters cover each end of the drift-chamber flange. These counters have an average time resolution of 0.38 nsec, and are used for π/K/p separation.

In the summer of 1982, a small high-resolution drift chamber (vertex chamber) with a beryllium beam pipe of 1.8 mm in thickness and 6.5 cm in radius replaced the original aluminum beam pipe. The chamber has 8 cylindrical layers of signal wires at radii between 8.1 and 14.9 cm with a total of 720 sense wires. Data based on this vertex chamber are not included in this review because they are not yet published.

1.8.4. Lead liquid argon calorimeter

Liquid argon shower counters [1.28, 1.29] cover the solenoid at both ends and two thirds of its circumference. As shown in fig. 1.25, they are made of stacks of 2 mm lead plates separated by gaps of 3 mm (end-cap counters) and 5 mm (barrel counters) widths filled with liquid argon. The total

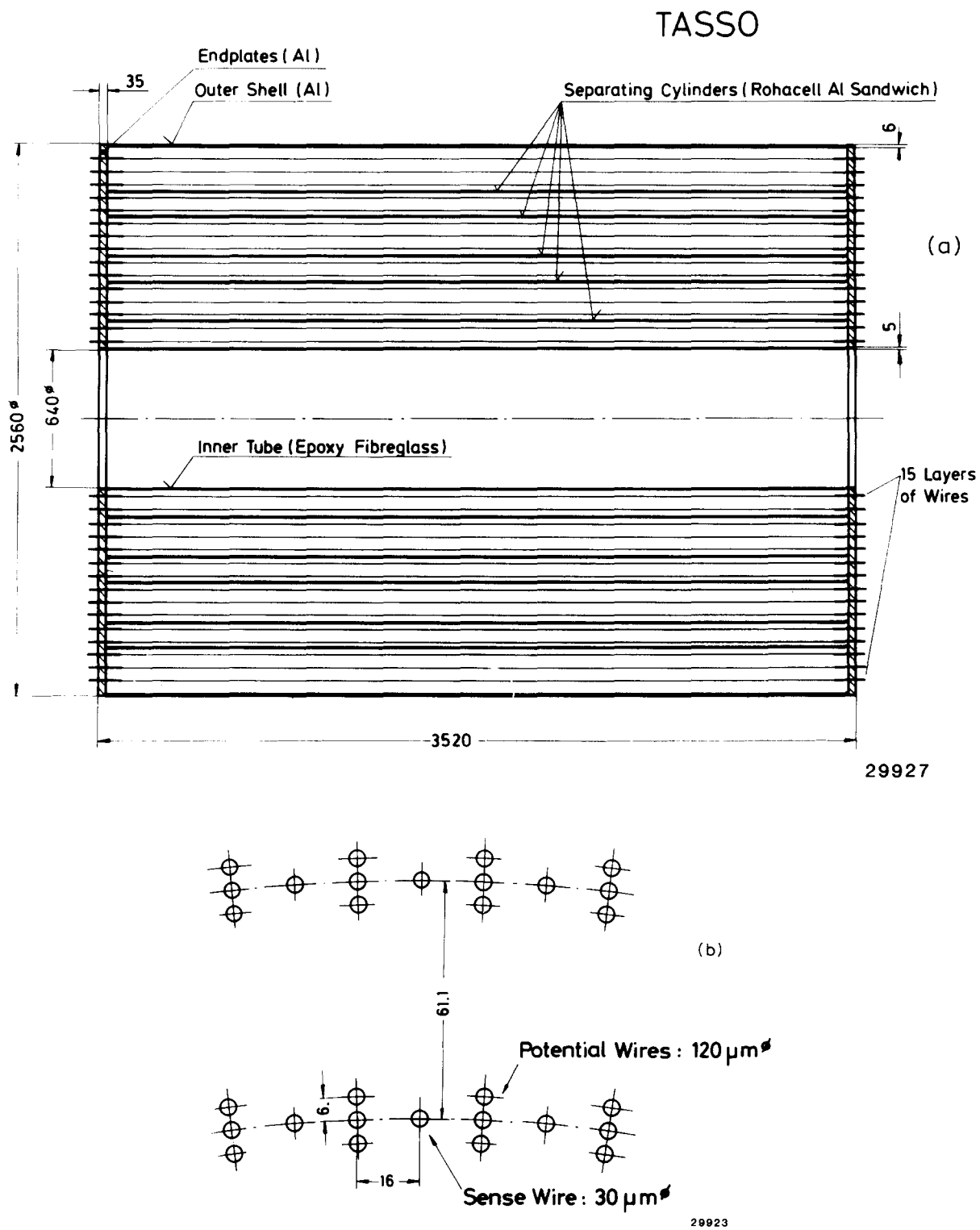

Fig. 1.24. (a) Schematic drawing of the TASSO drift chamber (dimension in mm). (b) Drift cell geometry.

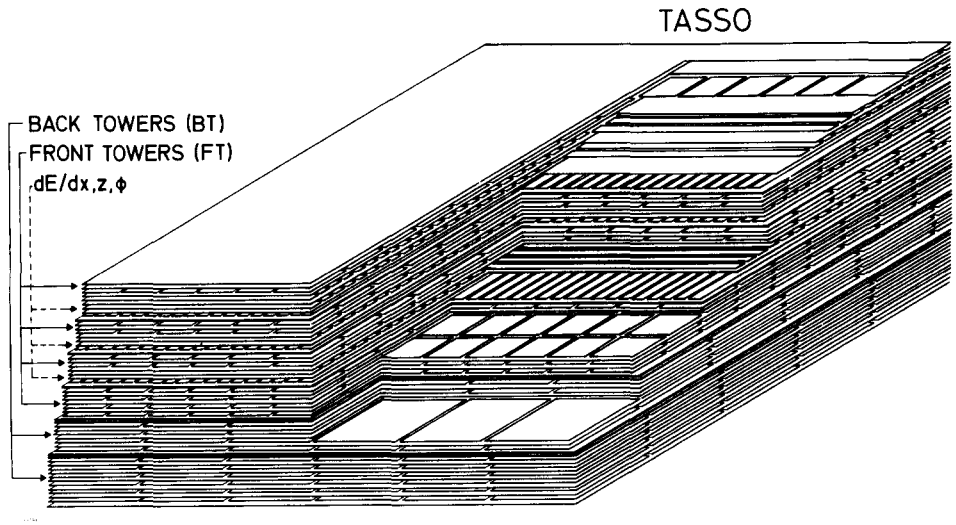

Fig. 1.25. A cut-away of a part of a TASSO liquid argon calorimeter submodule. The positions of the front towers, back towers and of the strips for dE/dx, z and ϕ measurements are marked.

thicknesses are 12.6 and 14 radiation lengths respectively. The energy deposited by a shower is measured by 5088 front towers and 1248 back towers in the barrel shower counters and 1444 front towers and 872 back towers in the end cap. Each front tower subtends 0.8 (barrels) and 1.5 (end cap) mster and are directed towards the interaction point. There are in addition two special gaps for dE/dx measurements at the entrance of the module and 2 cm wide strip electrodes for more precise shower localisation. The total number of electronic channels is 4400 for the end caps and 12000 for the barrel counters.

With the 1.6 radiation lengths of material in front of the calorimeter including the tank wall, the resulting energy resolution for photons at normal incidence for the barrel shower counters is given approximately by

$$\sigma_E/E = [0.11 + 0.02/(E - 0.5)]/\sqrt{E}$$

for $E > 1$ GeV. [Without absorber material in front of the module $\sigma_E/E = 0.09/\sqrt{E}$ has been obtained in test beam for electrons with $E > 0.8$ GeV.] The angular resolution is

$$\sigma_\phi = 4 \text{ mrad} \quad \text{and} \quad \sigma_\theta = 6 \text{ mrad}$$

for photons of energy near 1 GeV, and

$$\sigma_\phi = \sigma_\theta = 3 \text{ mrad}$$

for electrons of energy above 10 GeV. The detection efficiency for photons as determined from EGS studies is 50% at 55 MeV rising to >90% above 160 MeV.

1.8.5. Two-arm spectrometer

The two-arm spectrometer, which is a main feature of TASSO, is already shown in fig. 1.23 and

briefly described in section 1.8.2. The indices of refraction for the Čerenkov materials are 1.025 (aerogel), 1.0014 (freon 114) and 1.00043 (CO_2). The thresholds in GeV/c are thus respectively 0.7, 2.7 and 4.8 for pions; 2.3, 9.5 and 17 for kaons; and 4.4, 18 and 32 for p, $\bar{p}$. This is the first detector that uses aerogel in a large scale, the total quantity being $11.4\,m^2 \times 13.5\,cm$ thick [1.30].

The Čerenkov counters are subdivided into 16 mechanically separate cells per arm, each covering a range of about 10° in θ and 26° in ϕ. Each gas cell is further subdivided by two mirrors collecting the light onto different phototubes. For the aerogel Čerenkov counters, the produced light is diffused and is collected, not by mirrors, but by highly reflecting millipore paper.

Together with the time-of-flight counters, particle separation is possible for most of the energies up to the PETRA beam energy. The main exceptions are, as discussed in section 4.7, two gaps where K/p separation cannot be effected.

2. Hadronic events in e^+e^- annihilation

After the description of the accelerator and the five detectors in chapter 1, we begin to give a summary of the numerous experimental results obtained so far. There are many possible ways to arrange the order of presentation; we choose here as the guiding philosophy to go from the general features to the specific channels. Since the various results are intimately related to each other, it is neither desirable nor possible to adhere to this philosophy too rigidly.

2.1. Orientation

When an electron and a positron interact with each other, many different phenomena may occur. For purposes of orientation, we show in fig. 2.1 a rather coarse-grained classification of such events. This classification is not meant to be exhaustive. For ease of reference, the reactions listed are numbered. In the left two columns labelled as electron and photon, the well-known QED processes are given together with some of their Feynman diagrams. The amplitudes for such reactions are conveniently classified according to their orders in the electromagnetic coupling constant e. Thus to order e^2 there are only Bhabha scattering [2.1]

$$e^+e^- \to e^+e^-$$

labelled as 1e in fig. 2.1 and annihilation into photons

$$e^+e^- \to \gamma\gamma$$

labelled as 1γ there. To order e^3, the only possibilities involve merely the addition of a photon to the final state. Thus 2e and 2γ refer respectively to the processes

$$e^+e^- \to e^+e^-\gamma$$

and

$$e^+e^- \to \gamma\gamma\gamma\,.$$

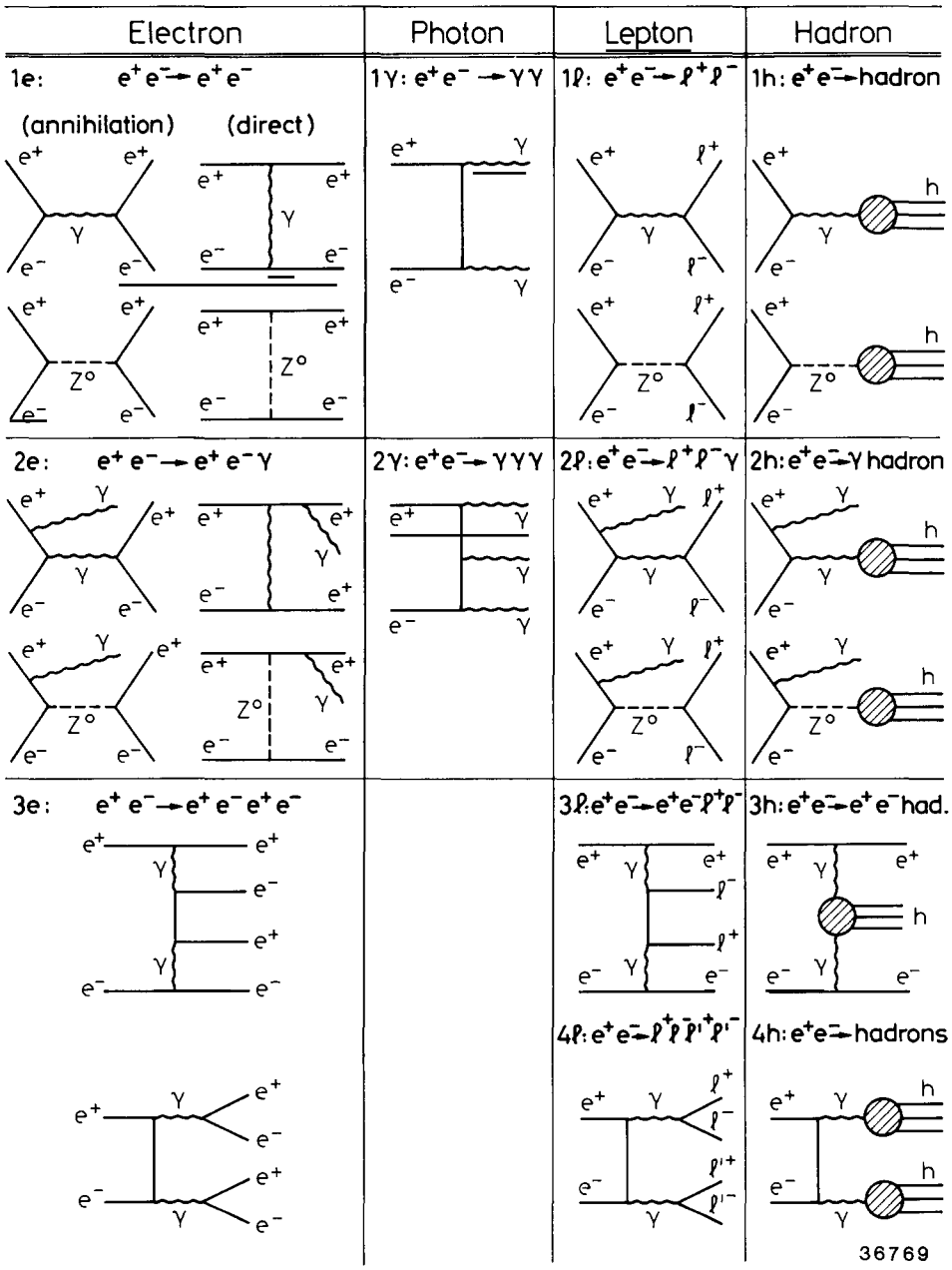

Fig. 2.1. Classification of e^+e^- reactions.

Some of the Feynman diagrams for these processes are shown in fig. 2.1 and the others may be obtained by attaching the photon line to another segment of the electron line or by permuting the photon lines.

To order e^4, it is possible to add a further photon to the final state, leading to

$$e^+e^- \to e^+e^-\gamma\gamma$$

and

$$e^+e^- \to \gamma\gamma\gamma\gamma$$

respectively. These processes are not shown in fig. 2.1. However, these are not the only possibilities. To this order, a new phenomenon occurs. The incoming electron and the incoming positron can each emit a virtual photon, and then the two virtual photons annihilate to give a new electron–positron pair. Although this process $e^+e^- \to e^+e^-e^+e^-$ is of fourth order in the coupling constant e, at the high energies available at PETRA, the two virtual photons can be very close to the mass shell so that the cross section is quite sizeable. We also show in the left column of fig. 2.1 one of the numerous other Feynman diagrams for this process 3e; because of the absence of the enhancement factors due to the photons, such additional diagrams give negligible contributions to the integrated cross sections. The other diagrams in the left column involving Z^0 [2.2] will be discussed later in this section.

With this understanding of the QED processes involving only electrons and photons, it is now straightforward to carry out an entirely similar classification of other e^+e^- reactions. First, the electron and the positron in the final state can be replaced by another lepton pair, either the muon or the τ [2.3] which was discovered at SPEAR several years ago, or perhaps some other charged lepton yet to be found. The resulting reactions are listed in the third column of fig. 2.1 under the heading "lepton". This differs from the first column in two respects: the "direct" diagrams with a photon exchange in the cross channel are no longer allowed; and the two diagrams given under 3e lead to different reactions after the replacement of the electron by other leptons. For the upper diagram, only one e^+e^- pair can be replaced by $\ell^+\ell^-$ and hence the reaction $e^+e^- \to e^+e^-\ell^+\ell^-$ results. This is enhanced at high energies by the small virtual masses of the photons as discussed above. From the lower diagram, $e^+e^- \to \ell^+\ell^-\ell'^+\ell'^-$ is allowed but not enhanced, where ℓ and ℓ' may be μ and μ, τ and τ, or μ and τ.

Finally, the lepton pairs may be replaced by hadrons, and the resulting diagrams are shown in the last column of fig. 2.1. While the electromagnetic interaction of leptons is theoretically understood and experimentally well verified, both before PETRA and at PETRA, that of hadrons is much more complicated and will be the central subject of study in the next several chapters. Accordingly, in fig. 2.1, the electromagnetic interaction of hadrons is shown merely as a blob. Reaction 4ℓ evolves into one with only hadrons in the final state, designated as 4h.

So far we have discussed only reactions that are mediated by a virtual photon. Fifteen years ago, in unifying the electromagnetic and weak interactions [2.2], Weinberg and Salam proposed a neutral massive vector meson Z^0. Recently the direct observation of this Z^0 has been accomplished at the CERN proton–antiproton collider [2.4]. Thus all these reactions can also proceed with the virtual photon replaced by a virtual Z^0. Because of the large mass of Z^0, measured to be about 95 GeV, diagrams with a virtual Z^0 are much less important, even at PETRA energies. For this reason, in fig. 2.1 these additional diagrams are shown only for the processes 1e, 1ℓ, 1h, 2e, 2ℓ and 2h. For other processes, the replacement of a virtual photon by a virtual Z^0 leads to negligible correction, because of both the large Z^0 mass and the removal of the enhancement factor which depends crucially on the massless nature of the photon.

It is not the intention of fig. 2.1 to give exhaustively all e^+e^- reactions with sizeable cross sections. Two examples are shown in fig. 2.2 for additional reactions, one actual and one speculative. The reaction of fig. 2.2a, $e^+e^- \to e^+e^-\gamma\gamma$, is expected to give a small but observable correction to luminosity measurements at PETRA. That of fig. 2.2b involves a neutral vector boson Z_1^0, which is present in some theoretical models of electroweak interaction and is just like Z^0, but with a lower mass.

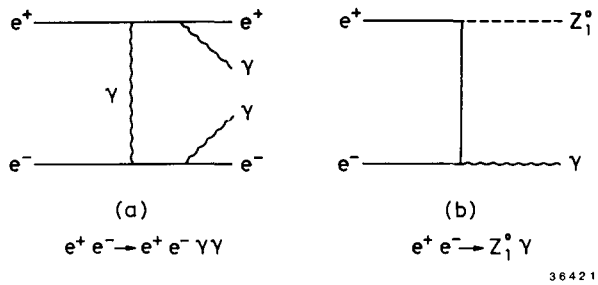

Fig. 2.2. Possible additional reactions not included in fig. 2.1. (b) can occur at PETRA only if the neutral vector meson Z_1^0 exists and is of sufficiently low mass.

2.2. Experimental data on total hadronic cross section

The e^+e^- reactions shown in fig. 2.1 can be broadly classified into two types: those where hadrons are produced, as shown in the right column, and those where only leptons and photons are in the final states, as shown in the other three columns. Of the second type, the cross sections are given by QED, modified by the presence of Z^0. Radiative corrections should of course be taken into account. Processes of the first type, on the other hand, involve the blob, or more precisely, two kinds of blobs:

(A) γ–hadron coupling

and

(B) $\gamma\gamma$–hadron coupling.

Here (B) appears only in 3h, while (A) appears in all the rest. This process 3h, $e^+e^- \to e^+e^-$ hadrons, is called the two-photon process and will be studied in detail in chapter 6, while this chapter and the next two chapters are devoted to 1h, $e^+e^- \to$ hadrons. Following the guidelines of going from general features to specific properties, we begin with the total cross section for $e^+e^- \to$ hadrons.

Because of the similarity of this process 1h to 1ℓ, $e^+e^- \to \ell^+\ell^-$, it is often convenient to use the ratio of these processes. Thus the R for the total hadronic cross section is defined as the ratio

$$R = \frac{\text{total cross section for } e^+e^- \to \text{hadrons}}{\text{total cross section for } e^+e^- \to \mu^+\mu^-} \tag{2.1}$$

at the same energy. More precisely, the denominator is *not* the actual total cross section for $e^+e^- \to \mu^+\mu^-$, but rather the theoretical total cross section in the lowest-order QED without weak interactions, i.e., without the Z^0 diagram shown under 1ℓ of fig. 2.1. This theoretical total cross section is

$$\sigma(e^+e^- \to \mu^+\mu^-) = \frac{2\pi\alpha^2}{3s}\beta\,(3-\beta^2), \tag{2.2}$$

where β is the velocity of the produced muons, and the mass of the electron has been neglected. α is the fine-structure constant and s is the square of the center-of-mass energy.

In (2.2) the factor $\beta(3-\beta^2)$ is extremely close to 2; it is for example $(2-10^{-4})$ for a beam energy of 1 GeV. Replacing this factor by 2, the result is

$$\sigma(e^+e^- \to \mu^+\mu^-) = \frac{86.856}{s}\,\text{nb} \tag{2.3}$$

with s in units of GeV^2. Therefore

$$R = \frac{s \text{ in GeV}^2}{86.856}\,(\text{total cross section for } e^+e^- \to \text{hadrons in nb}). \tag{2.4}$$

The precise determination therefore involves the careful identification of hadronic events, subtraction of backgrounds, calculation of acceptance, measurement of luminosity, etc., but not any experimental determination of the total cross section for μ-pair production.

We discuss briefly the experimental selection of hadronic events, not limited to the determination of the total cross section. This selection depends in detail on the characteristics of the detectors, and indeed is different for different purposes with the same detector. However, the general principle is as follows.

Since the processes 2h and 4h have relatively small cross sections, the purpose of the method of selection is to discriminate 1h against the following:

(i) Photon and lepton processes as shown in the left three columns of fig. 2.1,

(ii) $\gamma\gamma$ process 3h : $e^+e^- \to e^+e^-$ hadrons; and

(iii) Interaction of the beams with either the residual gas in the beam pipe or the beam pipe itself.

With the notable exception of the production of $\tau^+\tau^-$ pairs, background (i) is characterized mostly by the presence of, at most, two charged particles entering the detector. Therefore a requirement is imposed to have more than two tracks. Since the enhancement of the cross section for background (ii) is due to the virtual photons being near their mass shells, most of the time the electron and positron in the final state are nearly in the direction of the incident beams and hence go down the beam pipes. Accordingly, both background (ii) and background (iii) can be suppressed by requiring sufficiently high total energy of the detected particles, called the total visible energy.

Fig. 2.3 gives an overall view of the measured values of R from low energies to the highest available energy with significant amount of data. This figure is based on the compilation by the TASSO Collaboration [2.5]. From the data [2.6] obtained before PETRA, it is seen that, at low energies, the behavior of R is rather complicated, showing peaks at the masses of the vector mesons ρ, ω and ϕ. With increased energy, there are two sets of high peaks, one between 3 and 4 GeV at the masses of J/ψ and ψ' [2.7] and the other set around 10 GeV at the masses of the upsilons Υ, Υ' and Υ'' [2.8]. In both cases, immediately above the high peaks, there are other peaks attributed to the various resonances such as ψ (3770) and Υ (10570) [2.7, 2.8]. In the PETRA energy range of 12 GeV and above, the data are from CELLO [2.9], JADE [2.10, 2.11], MARK J [2.12], PLUTO [2.13] and TASSO [2.14, 2.15]. It is seen that PETRA has reached the energy range above the known resonances and hence the R value is nearly constant. These PETRA data are also tabulated in table 2.1. The theoretical lines will be discussed in section 2.4.

Since the JADE [2.11] value is the most accurate one in the energy range of PEP and PETRA, it is described in this section. The various contributions to the systematic error of JADE are shown in table 2.2. When added in quadrature, the total is 3% for the center-of-mass energies W between 22 and

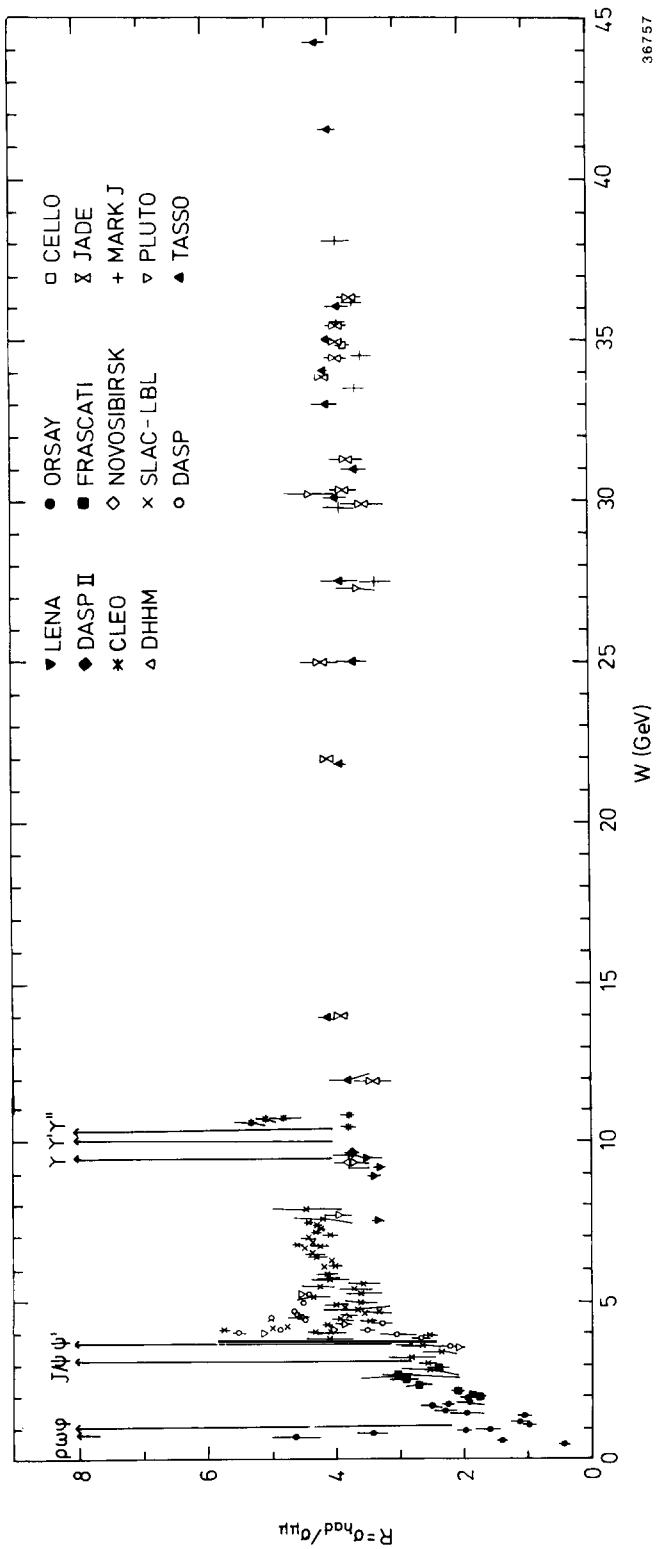

Fig. 2.3. The ratio of $R = \sigma(e^+e^- \to \text{hadrons})/\sigma_{\mu\mu}$ where $\sigma_{\mu\mu} = 4\pi\alpha^2/3s$. The data are taken from a compilation in ref. [2.5].

Table 2.1a
Values for R from JADE [2.11]. The errors quoted include the statistical and point-to-point systematic errors

W (GeV)	number of events	Luminosity (nb^{-1})	$R \pm \Delta R$	
12.00	219	106.39	3.45	0.27
14.04	2649	1462.62	3.94	0.14
22.00	1871	2405.87	4.11	0.13
25.01	290	470.81	4.24	0.29
27.66	84	181.90	3.85	0.48
29.93	101	276.24	3.55	0.40
30.38	642	1664.35	3.85	0.19
31.29	251	693.09	3.83	0.28
33.89	3785	11279.52	4.16	0.10
34.50	570	1880.32	3.93	0.20
35.01	4162	13951.49	3.93	0.10
35.45	679	2362.49	3.93	0.18
36.38	420	1623.35	3.71	0.21

Table 2.1b
Values for R from TASSO [2.15] as a function of c.m. energy for runperiod I (1979, 1980) and runperiod II (1981). The errors quoted include the statistical as well as the point-to-point systematic error. An overall uncertainty of ±4.5% has to be added. The relative uncertainty between the two runperiods is ±2%

W [GeV]	$\bar{W}$ [GeV]	Luminosity (nb^{-1})	number of events	R
Runperiod I				
12.0	12.0	96.3	186	3.80 ± 0.28
27.4–27.7	27.5	337.0	141	3.91 ± 0.32
29.9–30.5	30.1	1309.4	460	3.94 ± 0.18
30.5–31.5	31.1	1317.6	407	3.66 ± 0.18
32.5–33.5	33.2	762.6	262	4.48 ± 0.28
33.5–34.5	34.0	1422.2	410	4.09 ± 0.20
34.5–35.5	35.0	2224.4	592	4.03 ± 0.17
35.5–36.7	36.1	2213.3	543	3.93 ± 0.17
Runperiod II				
14.0	14.0	1631.0	2704	4.14 ± 0.30
22.0	22.0	2785.4	1889	3.89 ± 0.17
25.0	25.0	454.9	231	3.72 ± 0.38
33.0	33.0	817.9	220	3.73 ± 0.27
34.0	34.0	11143.0	3269	4.13 ± 0.13
35.0	35.0	15786.5	4532	4.22 ± 0.09

37 GeV. In fig. 2.4a, the measured distribution in the number of charged prongs is compared with the Monte Carlo simulation. In fig. 2.4b, the distribution of the vertex along the beam direction is given. In both cases, the cuts used are also shown and are quite far in the tails of the distributions.

As already mentioned, a cut is introduced in the total visible energy in order to remove the backgrounds (ii) and (iii). For the JADE detector, the total visible energy is the sum of energies carried by the charged tracks and photons. The observed distributions, the Monte Carlo simulation and the cuts used, are all shown in fig. 2.5 as functions of the ratio of the total visible energy to the beam energy.

Table 2.1c
Values for R from MARK J [2.12]

W (GeV)	$R \pm \Delta R$
13	$4.6 \pm 0.5 \pm 0.7$
17	$4.9 \pm 0.6 \pm 0.7$
27.4 to 27.7	$3.8 \pm 0.3 \pm 0.6$
31.57	$4.0 \pm 0.5 \pm 0.6$
33	$2.9 \pm 0.6 \pm 0.3$
35	$3.8 \pm 0.4 \pm 0.4$
35.8	$4.4 \pm 0.7 \pm 0.4$
37.94 to 38.63	$3.91 \pm 0.19 \pm 0.3$

Table 2.1d
Values for R from PLUTO [2.13]

W (GeV)	$R \pm \Delta R$
13	5.0 ± 0.5
17	4.3 ± 0.5
22.0	3.41 ± 0.73
27.6	3.64 ± 0.31
30.0	4.38 ± 0.37
31.6	3.59 ± 0.52

Table 2.1e
Values for R from CELLO [2.9]

W (GeV)	$R \pm \Delta R$
33.0 to 36.7	$3.85 \pm 0.12 \pm 0.31$

Table 2.2
Systematic errors of the JADE [2.11] measurement of R

	$E_{c.m.} \leqq 14$ GeV	22–37 GeV
Background subtraction	±1.6%	±1.6%
Radiative corrections	1.1	0.8
Detection efficiency	2.5	1.5
Luminosity, point-to-point	1.0	1.0
Luminosity, overall normalization	1.5	1.5
Total	3.6%	3.0%
Point-to-point	2.7%	1.8%
Overall normalization	2.4%	2.4%

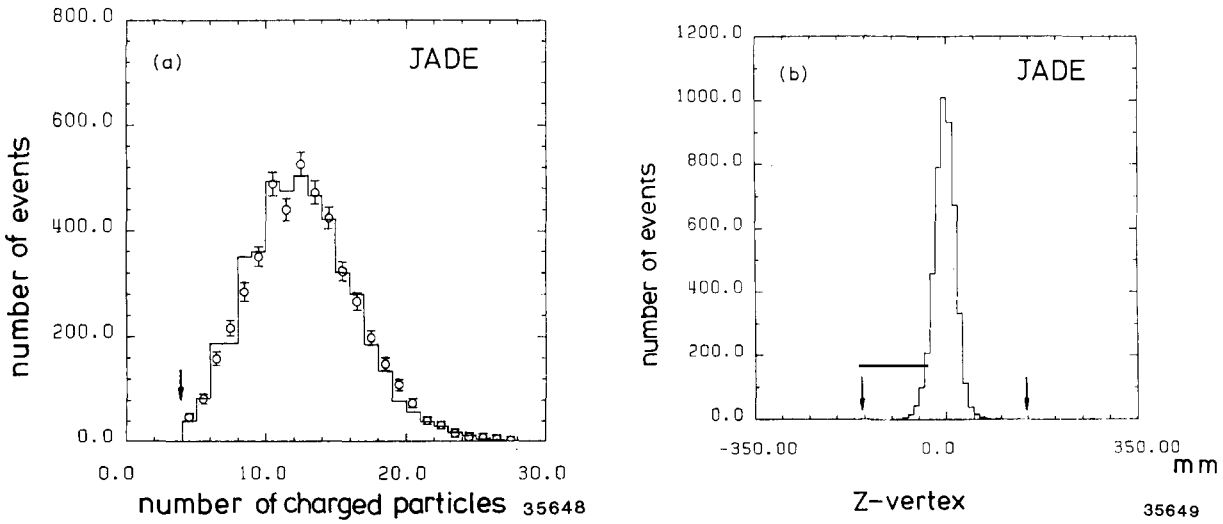

Fig. 2.4. (a) JADE [2.11] distribution of the number of observed charged tracks. The histogram shows the prediction from the Monte Carlo simulation. (b) The z-vertex distribution after all other cuts.

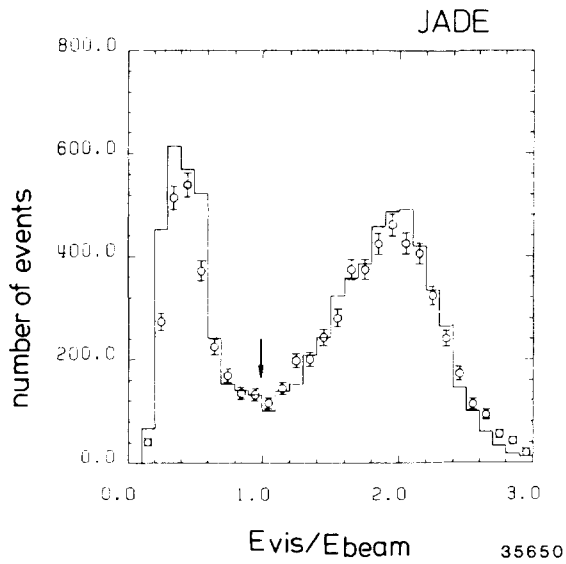

Fig. 2.5. JADE [2.11] distribution of the visible energy. The histogram shows the prediction from the Monte Carlo simulations which include the hadron production process via single photon annihilation and the VDM-like γ–γ interaction process.

The peak on the right is due to the hadronic events of interest, while that on the left is due to two-photon processes. Because of the good agreement between the experimental data and the Monte Carlo simulation, changing the position of the cut has relatively little effect on the value of R. For example, even with the rather extreme cuts at 1.0 and 1.6, R changes by less than one per cent.

The TASSO [2.15] and JADE [2.11] results on R are shown as functions of energy, in fig. 2.6 and fig. 2.7 respectively. The data between 12.0 and 36.4 GeV are consistent with a constant value of R with an average value $\langle R\rangle = 3.97 \pm 0.05 \pm 0.10$ (the second error is the overall normalization error) for JADE and $\langle R\rangle = 4.01 \pm 0.03 \pm 0.20$ for TASSO.

2.3. Hadronic events at PETRA

It is seen from the preceding section that experimentally the total cross section for e^+e^- hadrons is approximately constant in the range of W from 12 GeV to 37 GeV. What kind of final states contributes to this total cross section?

At lower energies, it is customary to list the exclusive channels that are important. At the high energies of PETRA, it is neither possible nor even necessarily desirable to try to measure the cross sections of exclusive channels. Two of the reasons for this assertion are that the number of important final states is too large to be usefully enumerated and that the percentage of hadronic events where all the particles in the final state are detected is quite small. Both are, of course, closely related to the observed large multiplicity.

In order to give some idea about the hadronic events at PETRA, we show in this section some examples of such events. As already seen at SPEAR [2.16] but much more apparent at PETRA, the majority of the hadronic events consists of two back-to-back jets, where the term "jet" is used to describe a group of particles moving in nearly the same direction. An example of such two-jet events from CELLO is shown in fig. 2.8. These two-jet events will be studied in detail in the remainder of this chapter.

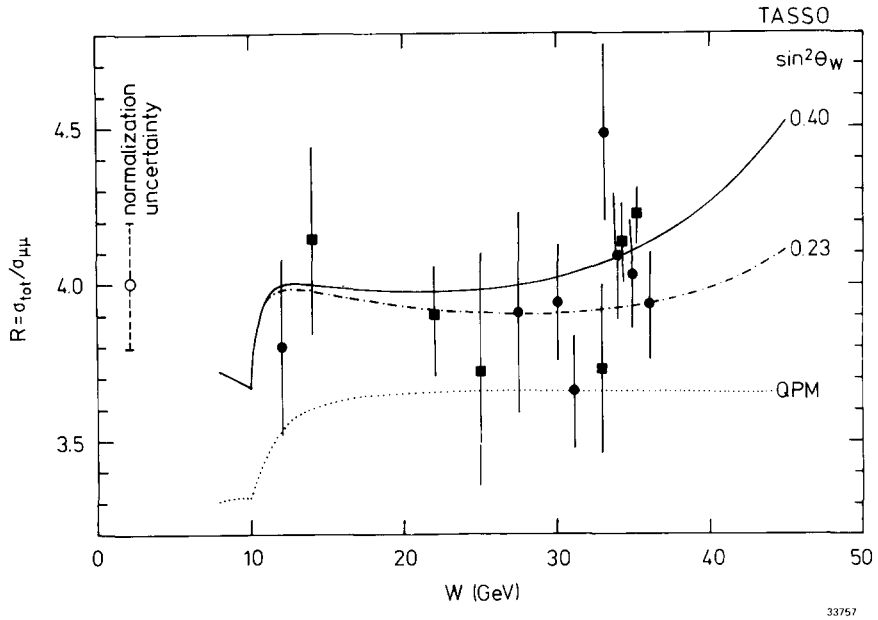

Fig. 2.6. TASSO [2.15] results on R for total hadronic cross section. The points marked by a circle are from the runs in 1979 and 1980, while those marked by a square are from 1981. The errors shown include the statistical and point-to-point systematic uncertainty, while the overall normalization uncertainty is indicated separately on the left. The dotted line shows the expectation from the quark–parton model (QPM). The full line represents the best fit including weak contributions, while the dash-dotted line was computed with α_s (s = 1000 GeV^2) = 0.18 and $\sin^2\theta_w$ = 0.23.

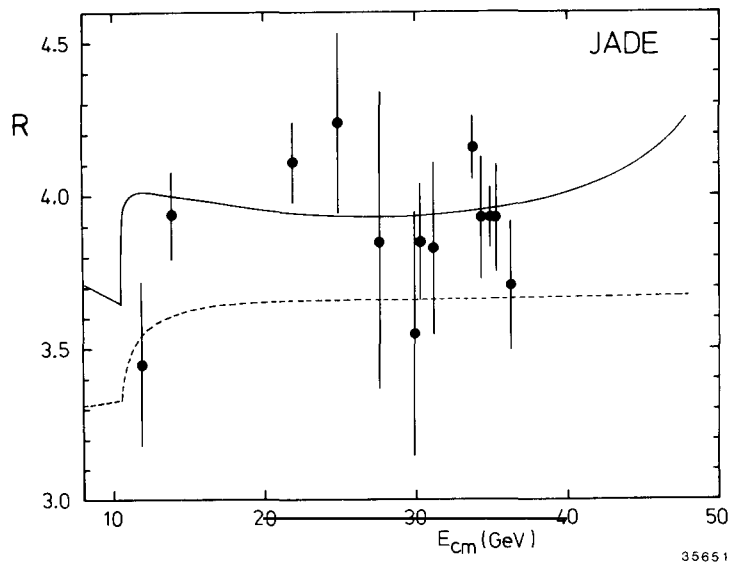

Fig. 2.7. JADE [2.11] results on R for total cross section. The error bars include the statistical and the point-to-point systematic errors. The solid curve represents the best fit with α_s (s = 1000 GeV^2) = 0.20 and $\sin^2\theta_w$ = 0.23. The prediction from the simple quark–parton model is also shown by the dashed curve.

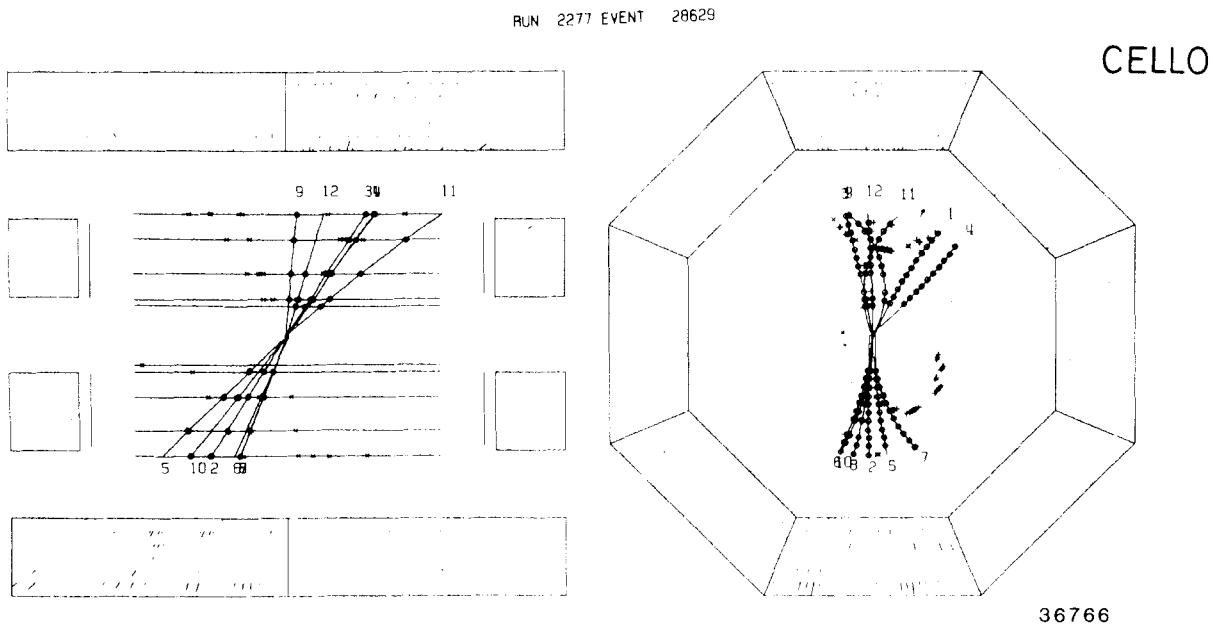

Fig. 2.8. Two-jet event from CELLO.

In fig. 2.9 a three-jet event is shown from TASSO. It is, in fact, the observation of three-jet events from electron–positron annihilation at PETRA that lead to the discovery of the gluon. The properties of the three-jet events and the gluon are described in the next chapter.

Since the majority of the hadronic events consists of two jets and a sizeable fraction consists of three jets, it is natural to expect to see some four-jet events. Such an example from JADE is shown in fig. 2.10.

In fig. 2.8 and fig. 2.9, what has been shown are the views from the beam axis, and the bending of the tracks is, of course, due to the solenoidal magnetic field. There is no guarantee in general that a two-jet event does look like a two-jet event in this particular view. For example, if the axis of the back-to-back jets is close to the beam direction, then such an event does not look like a two-jet event from this view down the beam line, but of course, does look that way from a perpendicular direction. For these figures, the events have been chosen to show clearly their jet characteristics, and thus cannot be said to be typical.

In fig. 2.11 we give an event of the type 3h, $e^+e^- \to e^+e^-$ hadrons from PLUTO. Since the e^+ and e^- in the final state go down the beam pipe and are hence not detected, the view in fig. 2.11 perpendicular to the beam bears a great deal of resemblance to the same view in fig. 2.8. Actually, these two-photon events are quite different: the two-hadron jets are coplanar with the beam axis, but not colinear as in two-jet events, and the total visible energy is relatively small, as seen from fig. 2.5. As already mentioned, properties of these two-photon events will be described in chapter 6.

2.4. *Quark picture and quantum chromodynamics*

The predominance of two-jet events indicates that something is pair produced, as represented by the Feynman diagrams of fig. 2.12. If it is a point fermion, then the matrix element is proportional to its

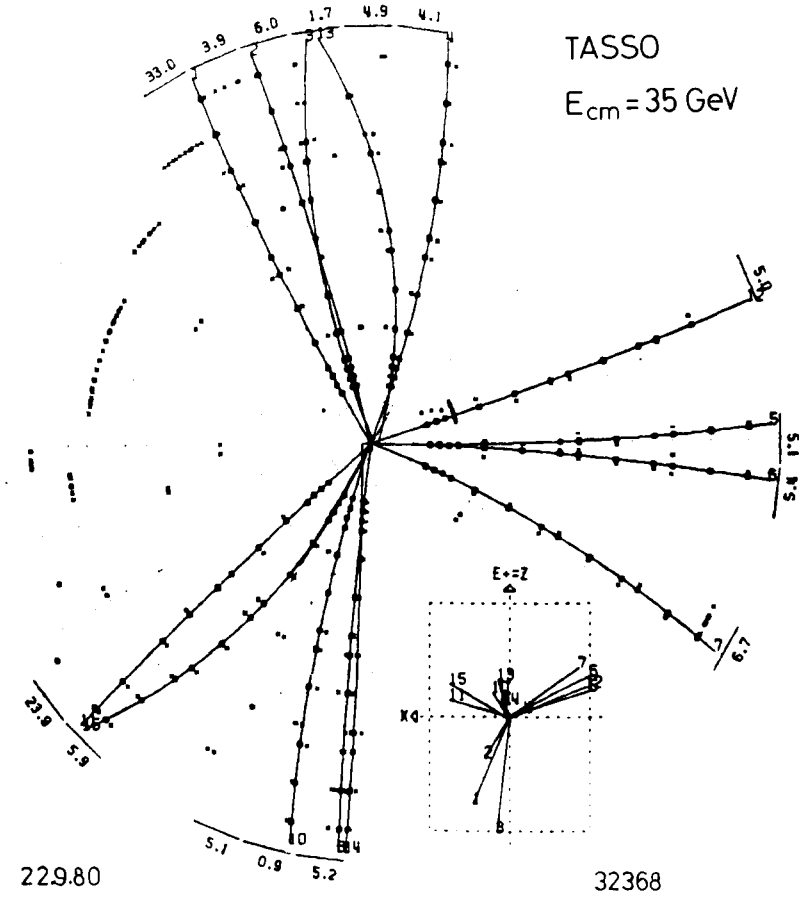

Fig. 2.9. Three-jet event from TASSO.

charge e_f, and hence

$$\sigma(e^+e^- \to f\bar{f})/\sigma(e^+e^- \to \mu^+\mu^-) = e_f^2/e^2 \tag{2.5}$$

when the center-of-mass energy is much larger than the fermion mass.

Quarks were invented in 1964 by Gell-Mann and Zweig [2.17] to explain the SU(3) multiplet structure of the observed hadrons. They are fermions with fractional charge and fractional baryon number. For reasons of statistics, the quark has a new internal quantum number called the color, which can take on three values. Since the cross section for the production of a quark pair with a given color is given by (2.5), the total cross section for the production of quark pairs of all colors is larger by a factor of 3:

$$\sigma(e^+e^- \to q\bar{q})/\sigma(e^+e^- \to \mu^+\mu^-) = 3e_f^2/e^2 \tag{2.6}$$

again on the basis of the diagram of fig. 2.12.

Since the discovery of the upsilon [2.8], there are five known quarks, as listed in table 2.3, together with some of their elementary properties. If (2.6) is used to get the total cross section for producing

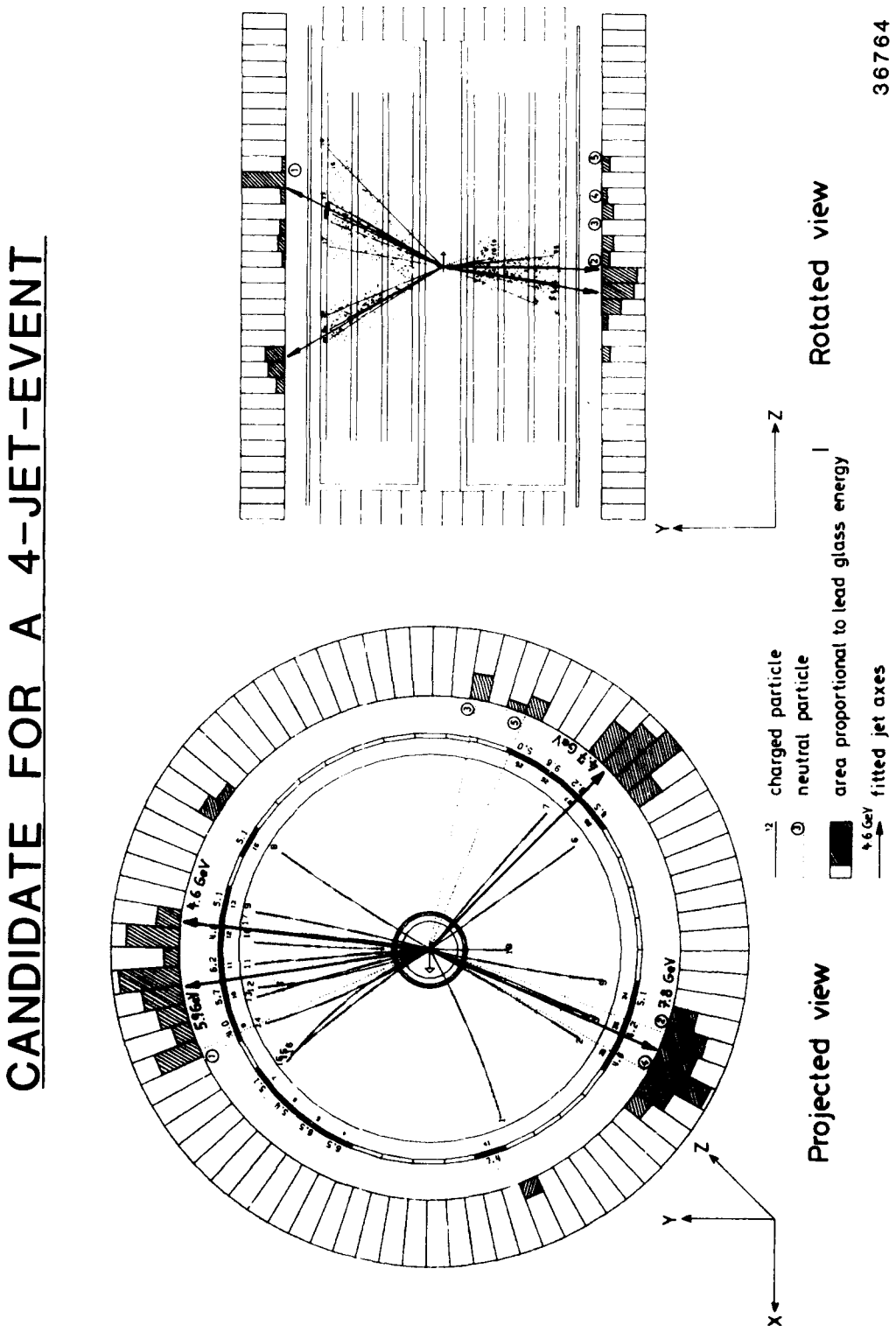

Fig. 2.10. Four-jet event from JADE.

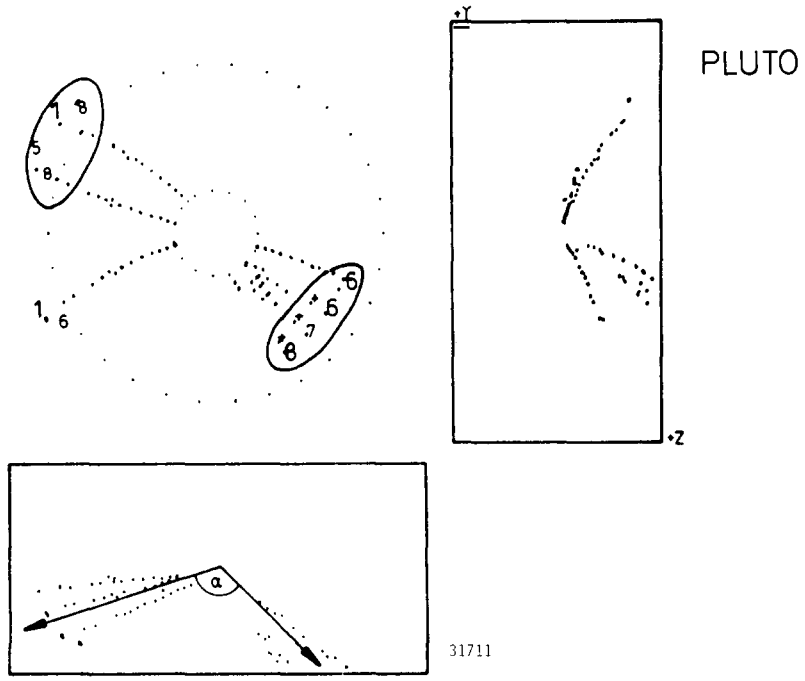

Fig. 2.11. Two-photon event $e^+e^- \to e^+e^-$ hadrons from PLUTO. The e^+ and e^- in the final state are not detected.

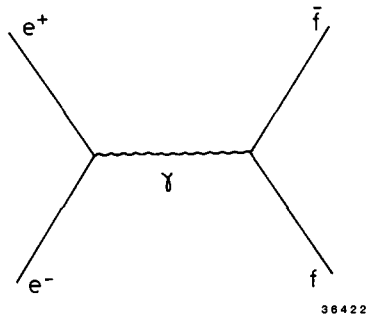

Fig. 2.12. Feynman diagram for the production of a pair of charged particles.

Table 2.3
Elementary properties of five quarks

quark	u	d	c	s	b
baryon number	$\frac{1}{3}$	$\frac{1}{3}$	$\frac{1}{3}$	$\frac{1}{3}$	$\frac{1}{3}$
charge	$\frac{2}{3}e$	$-\frac{1}{3}e$	$\frac{2}{3}e$	$-\frac{1}{3}e$	$-\frac{1}{3}e$
isospin I	$\frac{1}{2}$	$\frac{1}{2}$	0	0	0
I_z	$\frac{1}{2}$	$-\frac{1}{2}$	0	0	0
mass (GeV)	small	small	1.9	0.5	5.3

pairs of these five types of quarks, the result is

$$\frac{\sigma(e^+e^- \to u\bar{u}, d\bar{d}, c\bar{c}, s\bar{s}, b\bar{b})}{\sigma(e^+e^- \to \mu^+\mu^-)} = 3[(\tfrac{2}{3})^2 + (\tfrac{1}{3})^2 + (\tfrac{2}{3})^2 + (\tfrac{1}{3})^2 + (\tfrac{1}{3})^2] = \tfrac{11}{3}. \tag{2.7}$$

This compares favorably with the observed R as given in table 2.1 and figs. 2.3, 2.6 and 2.7.

Because of color symmetry, the quarks must interact through a Yang–Mills [2.18] non-Abelian gauge field called the gluon. Similar to QED, but much more complicated, the theory of the interaction between quarks and gluons is called quantum chromodynamics, or QCD for short. On the basis of QCD, first order radiative correction to $e^+e^- \to q\bar{q}$ gives an extra factor of $1 + \alpha_s/\pi$ [2.19]:

$$\frac{\sigma(e^+e^- \to u\bar{u}, d\bar{d}, c\bar{c}, s\bar{s}, b\bar{b})}{\sigma(e^+e^- \to \mu^+\mu^-)} = \frac{11}{3}\left(1 + \frac{\alpha_s}{\pi}\right) \tag{2.8}$$

where α_s is the so-called running coupling constant for the strong interaction between quarks and gluons. The experimental determination of this fundamental coupling constant at PETRA energies will be discussed in the next chapter. Theoretically

$$\alpha_s(s) = \frac{12\pi}{(33 - 2N_f)\ln(s/\Lambda^2)} \tag{2.9}$$

where N_f is the number of quarks with mass below the beam energy, and Λ is a characteristic strong interaction mass, believed to be about a few hundred MeV. Using the experimentally determined value of α_s, the PETRA data on the total hadronic cross section are in good agreement with the simple picture of pair producing five types of quarks, especially if the lowest-order QCD correction is included.

In table 2.3, there are three quarks of charge $-\frac{1}{3}$, but only two of charge $\frac{2}{3}$. Therefore many physicists expect the existence of a sixth quark, called t, with baryon number $\frac{1}{3}$, charge $\frac{2}{3}$, and isospin $I = I_z = 0$. The search for this t quark will be summarized in section 7.2.

2.5. Momentum tensor

As shown in the preceding section, the quark picture on the basis of the diagram of fig. 2.12 leads to eq. (2.7) which is in good agreement with the experimental measured value of R for the total cross section at PETRA energy. Yet these produced quark pairs of fractional charge have never been observed directly. This dilemma leads to the working hypothesis that somehow the quarks turn into a group of hadrons through strong interactions. Another way of stating this hypothesis is that quarks are "confined" so that in the final state each quark must combine with other quarks or antiquarks to form hadrons. We shall accept this working hypothesis in this and the next chapters.

Independent of the mechanism of turning the quark into hadrons, the hadrons are expected to retain some memory of the quark momentum. In other words, if the quark is produced in the x direction, the resulting hadrons are expected to have, on the average, larger momenta in the x direction than the y or z direction, especially at high energies. This situation is illustrated in fig. 2.13. From this point of view, the occurrence of jets is natural. If the hadron momenta transverse to the quark direction of flight are limited and the number of produced hadrons grows only slowly with energy, the emitted hadrons will be more and more collimated around the primary quark direction as the total energy increases.

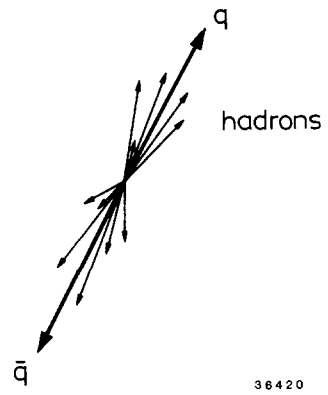

Fig. 2.13. e^+e^- annihilation in the quark model: Production of a $q\bar{q}$ pair followed by hadronization.

Motivated by such considerations, the jet structure in e^+e^- annihilation was first looked for and found at SPEAR [2.16]. Their method is based on the analog with the problem of the moment of inertia in classical mechanics. For a system of particles or a rigid body, the moment of inertia, as a function of the direction of axis of rotation, is an ellipsoid. If the rigid body is cigar shaped, then this ellipsoid of inertia is a pancake such that the momenta of inertia is small when rotated in the direction of the cigar. Thus the SPEAR group calculated for each event the momentum analog of the inertia tensor [2.20]

$$T_{\alpha\beta} = \sum_j (\delta_{\alpha\beta} \boldsymbol{p}_j^2 - p_{j\alpha} p_{j\beta}) \tag{2.10}$$

where the summation is over all detected particles and α and β refer to the three spatial components of each particle momentum $\boldsymbol{p}_j$. Since $T^{\alpha\beta}$ is a symmetrical tensor, it can be diagonalized to give the eigenvalues $\bar{\lambda}_1, \bar{\lambda}_2$ and $\bar{\lambda}_3$. If $\bar{\lambda}_3$ is the smallest of the three, then the sphericity S is defined as

$$S = \frac{3\bar{\lambda}_3}{\bar{\lambda}_1 + \bar{\lambda}_2 + \bar{\lambda}_3} = \frac{3(\Sigma_i p_{Ti}^2)_{\min}}{2\,\Sigma_i \boldsymbol{p}_i^2}. \tag{2.11}$$

S approaches 0 for events with bounded transverse momenta and approaches 1 for events with large multiplicity and isotropic phase-space particle distributions. The jet structure is established by studying the energy dependence of sphericity.

Sphericity gives essentially the relative magnitude of $\bar{\lambda}_3$ compared with the other two. If we want to analyze the shape of the event in more detail, it is useful to study the relative magnitudes of all the three eigenvalues. These eigenvalues $\bar{\lambda}_1$, $\bar{\lambda}_2$ and $\bar{\lambda}_3$ satisfy the triangular inequalities, i.e.

$$\bar{\lambda}_1 \leqq \bar{\lambda}_2 + \bar{\lambda}_3 \tag{2.12}$$

etc. Since triangular inequalities are not easy to deal with, it is more convenient to use the momentum tensor [2.21, 2.22]

$$M_{\alpha\beta} = \sum_j p_{j\alpha} p_{j\beta}. \tag{2.13}$$

Let λ_1, λ_2, λ_3 be the eigenvalues and $\hat{n}_1$, $\hat{n}_2$, $\hat{n}_3$ the corresponding eigenvectors of M which are ordered by

$$0 \leq \lambda_1 \leq \lambda_2 \leq \lambda_3 , \tag{2.14}$$

and are related to those of T by

$$\bar{\lambda}_i = (\lambda_1 + \lambda_2 + \lambda_3) - \lambda_i \tag{2.15}$$

for $i = 1, 2, 3$. Thus (2.15) guarantees the triangular inequalities (2.12). Since

$$\lambda_1 + \lambda_2 + \lambda_3 = \sum_j \boldsymbol{p}_j^2 , \tag{2.16}$$

let

$$Q_k = \lambda_k \Big/ \sum_j \boldsymbol{p}_j^2 . \tag{2.17}$$

These normalized eigenvalues Q_k satisfy

$$Q_1 + Q_2 + Q_3 = 1 \tag{2.18}$$

and

$$0 \leq Q_1 \leq Q_2 \leq Q_3 , \tag{2.19}$$

and their physical meanings are as follows:

$Q_1 = \min_{\hat{n}} \sum_j (\boldsymbol{p}_j \cdot \hat{n})^2 \Big/ \sum_j \boldsymbol{p}_j^2$ gives the flatness of the event ($\hat{n} = \hat{n}_1$),

$Q_2 = \min_{\hat{n}_\perp \hat{n}_1} \sum_j (\boldsymbol{p}_j \cdot \hat{n})^2 \Big/ \sum_j \boldsymbol{p}_j^2$ gives the width of the event ($\hat{n} = \hat{n}_2$), and

$Q_3 = \max_{\hat{n}} \sum_j (\boldsymbol{p}_j \cdot \hat{n})^2 \Big/ \sum_j \boldsymbol{p}_j^2$ gives the length of the event ($\hat{n} = \hat{n}_3$).

Colinear events are characterized by $Q_2 \ll Q_3$, and similarly coplanar events by $Q_1 \ll Q_2$. In terms of the Q's, the sphericity S is

$$S = \tfrac{3}{2}(Q_1 + Q_2) . \tag{2.20}$$

A triangular plot, with the coordinate variables chosen to be S and $Y = \sqrt{3}\,(Q_2 - Q_1)/2$, can be used to separate two-jet, three-jet and non-coplanar events as shown in fig. 2.14. The aplanarity A is naturally defined as

$$A = \tfrac{3}{2} Q_1 . \tag{2.21}$$

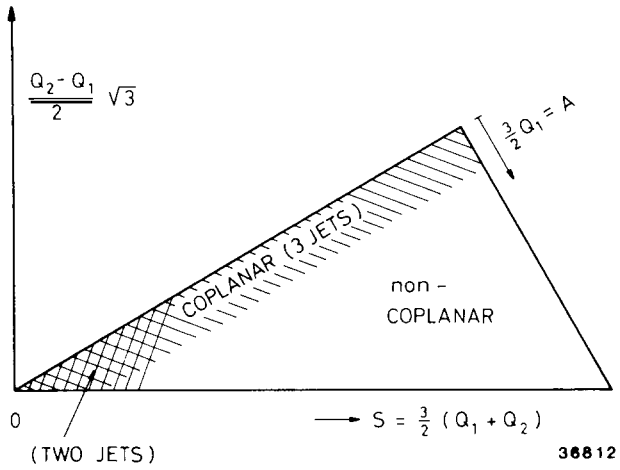

Fig. 2.14. Triangular plot to separate two-jet, three-jet and non-coplanar events.

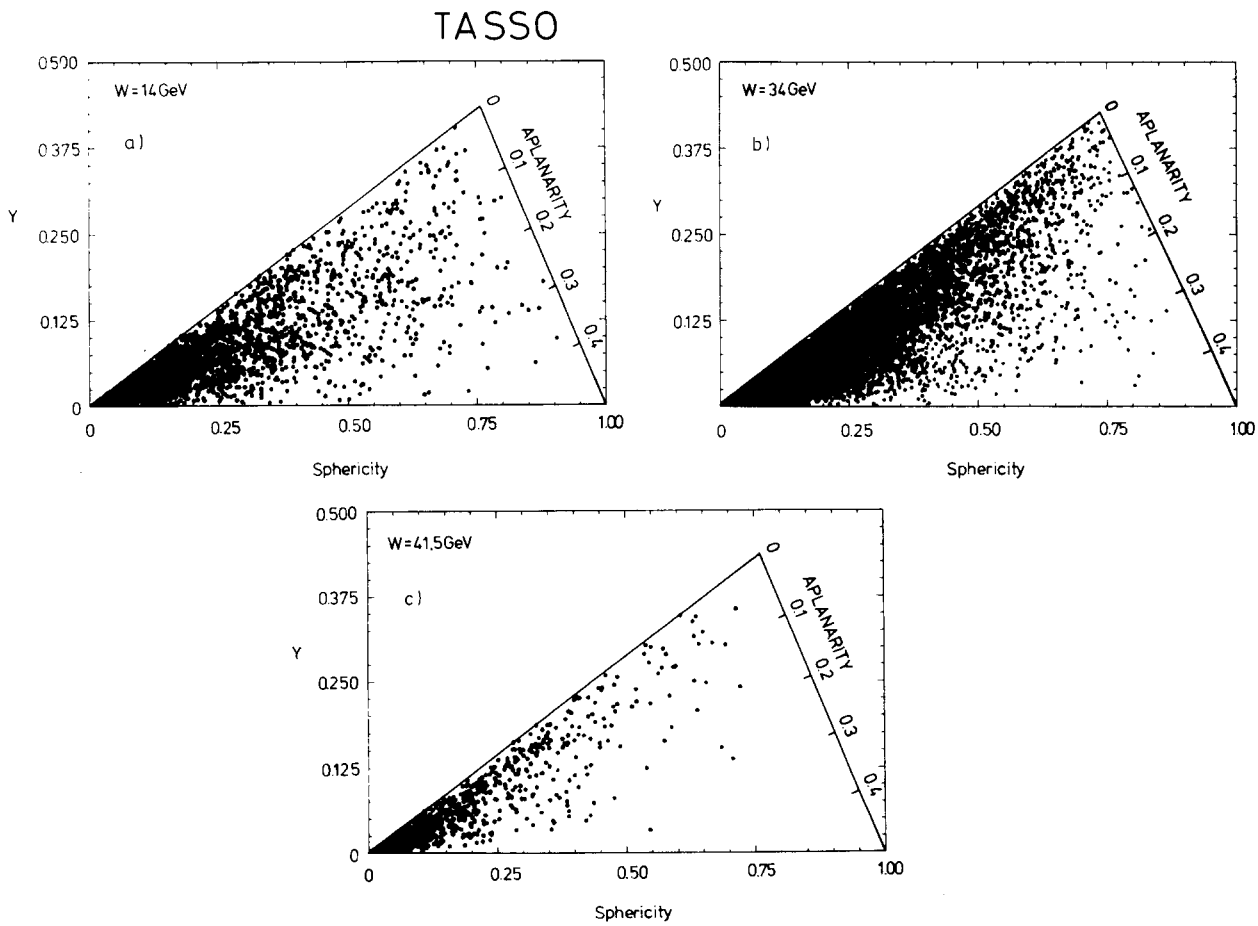

Fig. 2.15. The TASSO [2.5] distribution of sphericity versus aplanarity at W = 14, 34 and 41.5 GeV.

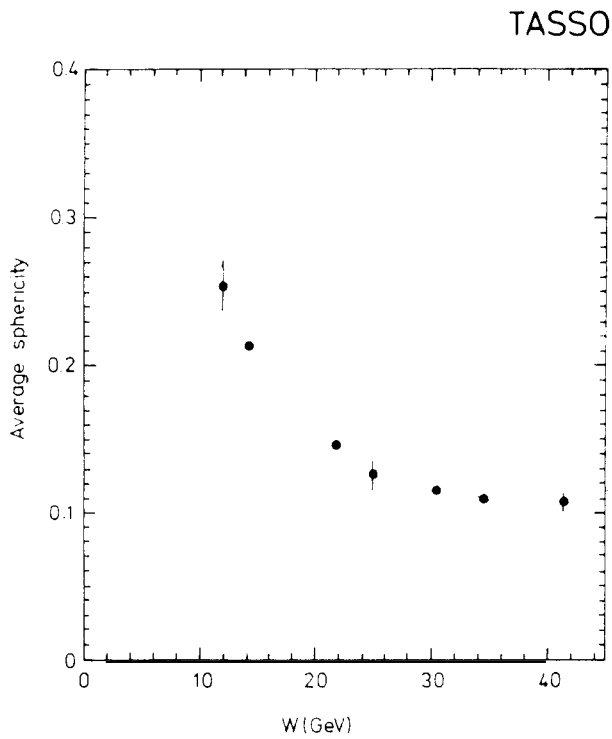

Fig. 2.16. The average sphericity as a function of the center-of-mass energy from TASSO [2.5].

Fig. 2.15 shows the event distribution on the triangular plot for $W = 14$, 34 and 41.5 GeV. Fig. 2.16 shows the energy dependence of the average sphericity $\langle S \rangle$ as measured at PETRA [2.5]. As shown in this figure, $\langle S \rangle$ decreases rapidly with increasing W, i.e., the particles become more and more collimated in clear distinction to a phase space behavior. Fig. 2.17 shows the sphericity distribution measured at $W = 14$, 22 and 34 GeV [2.5]. The strong preference for small S values is clearly seen, 80% of the events have $S < 0.25$. This shows clearly that two-jet events dominate at PETRA energies.

2.6. *Thrust*

In the context of electron–positron annihilation, the usefulness of thrust, defined by

$$T = \max_{\hat{n}} \frac{\Sigma_i |\boldsymbol{p}_i \cdot \hat{n}|}{\Sigma_i |\boldsymbol{p}_i|} \tag{2.22}$$

where $\hat{n}$ is a unit vector, was first discussed by Farhi [2.23]. This same quantity was used previously by Brandt et al. [2.24] in connection with an attempt to analyze high energy hadronic collisions in order to test the "intermediate bodies" model.

As explained by Farhi, the reason for using T is entirely theoretical. The underlying question is: what quantities can be reliably calculated in quantum chromodynamics (QCD) by perturbation theory? Some theoreticians believe that the working hypothesis stated at the beginning of section 2.5 can be derived from QCD, but no clear derivation has yet been given. The difficulty of applying perturbative

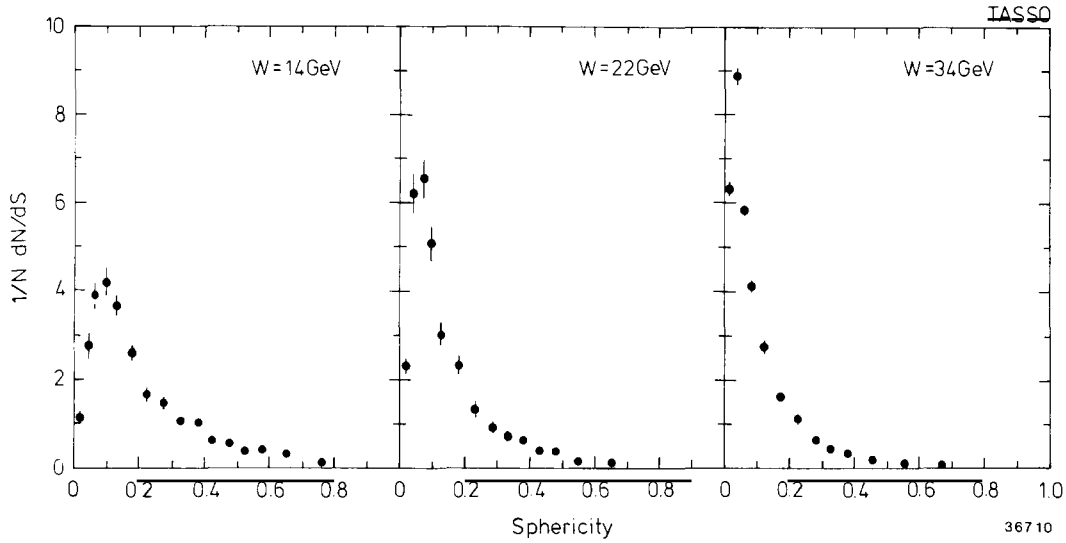

Fig. 2.17. The normalized sphericity distributions at W = 14, 22 and 34 GeV from TASSO [2.5].

QCD to e^+e^- annihilation is, however, of an entirely different nature, namely the uncertainty about quark masses.

For definiteness, consider the QCD correction to the two-body process $e^+e^- \to q\bar{q}$, as shown in fig. 2.12. Thus it is necessary to study the three-body process $e^+e^- \to q\bar{q}g$, where g stands for the gluon. To the lowest order, the diagrams are those of fig. 2.18 and the calculations are entirely similar to, but simpler than those of quantum electrodynamics (QED) for $e^+e^- \to \mu^+\mu^-\gamma$. Since in both cases gauge invariance obtains only for all fermions on their respective mass shells, it is necessary to know the masses of the quarks. Since quarks have never been observed directly, their masses are not known. More precisely, while good estimates of the masses of the s, c and b quarks can be obtained from the ϕ, the J/ψ, and the Υ mesons, there is a great deal of uncertainty about the masses of the u and d quarks, which may be as light as 10 or 20 MeV (see table 2.3).

In view of this difficulty, there are at least two distinct approaches. The more straightforward approach is to introduce quantities that cannot be calculated within the framework of perturbative QCD, such as quark and gluon fragmentation functions into hadrons. An alternative approach is to restrict attention to quantities that do not depend critically on the masses of the u and d quarks. In particular, perturbative QCD is to be applied only to quantities which have the property of being finite order by order in the unphysical limit where the quark mass m approaches zero [2.25].

On a purely theoretical level, this second approach is perhaps to be preferred. Practically, however,

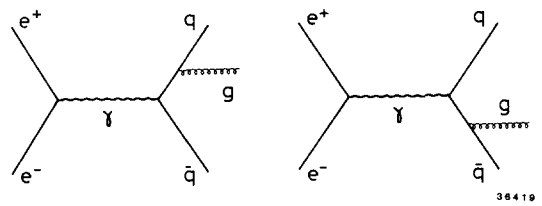

Fig. 2.18. Feynman diagrams for $e^+e^- \to q\bar{q}g$.

the two approaches are not entirely different, because fragmentation functions are in any case needed for the analysis of experimental data.

It is on the basis of the second approach that Farhi introduced the thrust [2.23]. As he puts it, the basis is a physical assumption yet to be contradicted: quantities which in the massless case are physically sensible, i.e., measurable in principle, will have a perturbative expansion free of $m \to 0$ singularities. The main problem with massless particles is that they are kinematically allowed to split into several massless particles all moving in the original direction. Therefore only quantities that do not change under this splitting can be used in perturbative QCD. The thrust T of (2.22) indeed has this property. Roughly speaking, what is needed is linearity in the momenta.

The energy dependence of the average thrust $\langle T \rangle$ is shown in fig. 2.19, and the normalized thrust distributions at $W = 14$, 22 and 34 GeV are presented in fig. 2.20. A comparison with figs. 2.16 and 2.17 shows that the spericity and thrust behave in the same way. Similar data have been obtained by all other PETRA Collaborations. At PETRA, both sphericity and thrust are used extensively, and they are about equally useful.

2.7. Spin of the quarks

On the basis of the angular distribution of the sphericity axis $\hat{n}_3$, Hanson et al. [2.16] found the spin of quarks to be 1/2 from the SPEAR data at $W = 7.4$ GeV. When W is increased by a factor of five to PETRA energies, this angular distribution, as shown in fig. 2.21 remains $1 + \cos^2\theta$, where θ is the angle between the beam direction and the sphericity axis. When the thrust axis is used instead of the sphericity axis $\hat{n}_3$, there is no substantial change in the angular distribution. Since the angular

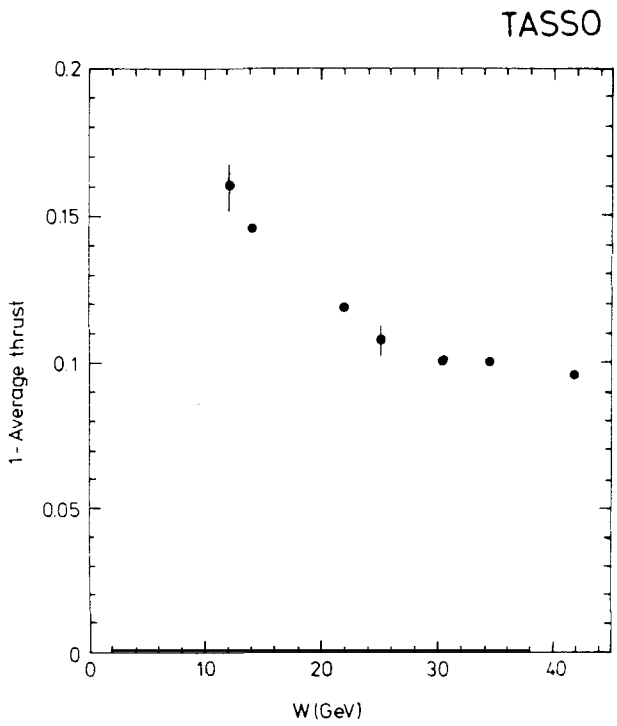

Fig. 2.19. The average value of 1-thrust, $\langle 1 - T \rangle$, as a function of the c.m. energy W from TASSO [2.5].

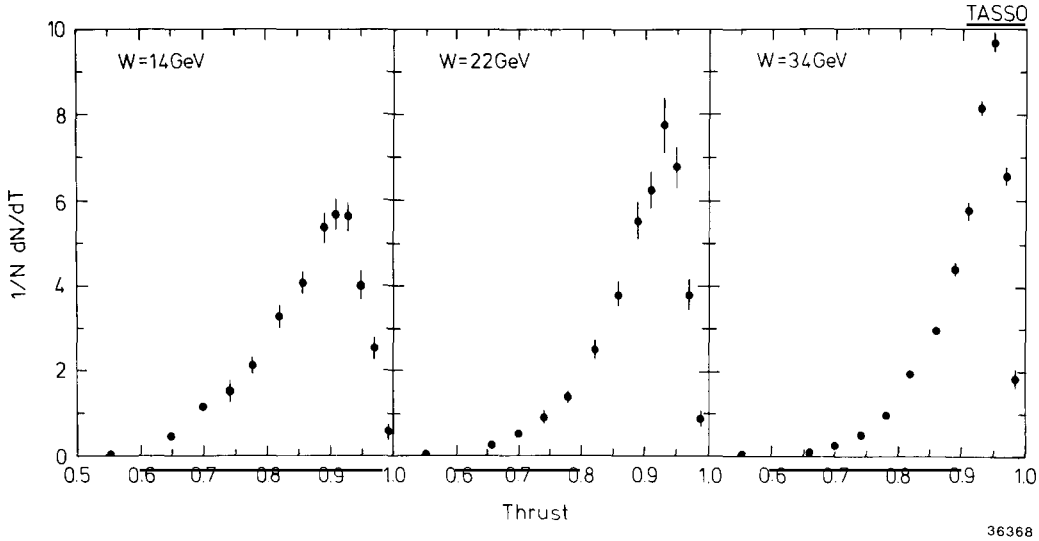

Fig. 2.20. The normalized thrust distributions at W = 14, 22 and 34 GeV from TASSO [2.5].

distribution of the jet axis is

$$\begin{cases} 1+\cos^2\theta & \text{for a quark of spin 1/2} \\ \sin^2\theta & \text{for a quark of spin 0} \end{cases} \tag{2.23}$$

on the basis of the Feynman diagrams of fig. 2.12, the spin of the quarks is verified to be 1/2 in agreement with the earlier SPEAR result.

Strictly speaking, since there are five quarks instead of one, this data by itself is not sufficient to give

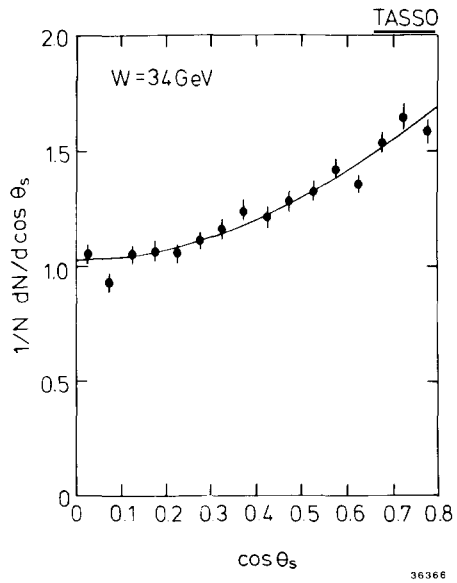

Fig. 2.21. The angular distribution of the jet axis determined by sphericity. The curves are proportional to $1+\cos^2\theta_s$.

the spins of the quarks separately. However, there is by now so much information about the quarks that the spin is no longer much of an issue, since it is related to numerous quantities, such as the step in R and the properties of the $q\bar{q}$ bound states.

2.8. Field–Feynman fragmentation

In section 2.5, the working hypothesis is introduced that somehow the quarks turn into a group of hadrons through strong interactions. In the absence of a theory based on first principles, Field and Feynman [2.27] pioneered the development of a phenomenological description of this fragmentation process. This work of Field and Feynman is of fundamental importance to the analysis of the experimental data from PETRA.

Field and Feynman assume that quark jets can be analyzed on the basis of a recursive principle. The ansatz is based on the idea that a quark of type "a" coming out at some momentum creates a color field in which new quark–antiquark pairs are produced. Quark "a" then combines with an antiquark, say "$\bar{b}$", from the new pair $b\bar{b}$ to form a meson "$a\bar{b}$" leaving the remaining quark "b" to combine with further antiquarks. The "meson" $a\bar{b}$, called the primordial or primary meson state, may be directly observed as a pseudoscalar meson, or it may be a vector or higher spin unstable resonance which subsequently decays into the observed mesons.

Fig. 2.22 of Field and Feynman gives a clear illustration of the phenomenological description.

In the original paper of Field and Feynman, only three quarks namely u, d and s are taken into account. The inclusion of the known c and b quarks and even the hypothetical top quark t has been carried out first by Meyer [2.28] of the TASSO Collaboration.

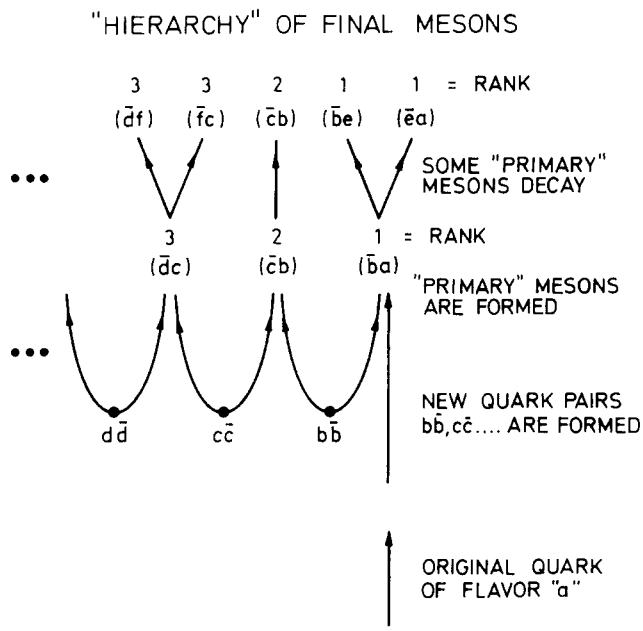

Fig. 2.22. Illustration of the "hierarchy" structure of the final mesons produced when a quark of type "a" fragments into hadrons in the Field–Feynman scheme [2.27]. New quark pairs $b\bar{b}$, $c\bar{c}$, etc., are produced and "primary" mesons are formed. The "primary" meson $\bar{b}a$ that contains the original quark is said to have "rank" one and primary meson $\bar{c}b$ rank two, etc. Finally, some of the primary mesons decay and all the decay products are assigned to have the rank of the parent. The order in "hierarchy" is *not* the same as order in momentum or rapidity.

The description of the fragmentation process involves the following three parameters:

(i) σ_q. The distribution of the transverse momentum k_T of the quarks in the jet cascade is assumed to be $\sim\exp(-k_T^2/2\sigma_q^2)$.

(ii) $P/(P+V)$. Here P/V is the ratio of primordial pseudoscalar mesons to vector mesons produced in the fragmentation process.

(iii) a_F. The primordial quark fragmentation function $f^h(z)$ of a quark into a hadron h in the Field–Feynman model is taken to be the same for u, d and s quarks,

$$f^h(z) = 1 - a_F + 3a_F(1-z)^2\,, \tag{2.24}$$

where

$$z = (E + p_\parallel)_h/(E + p_\parallel)_q\,. \tag{2.25}$$

The primordial fragmentation functions of the c and b quarks are discussed in section 4.15.

It is a peculiarity of the Field–Feynman fragmentation that only mesons are produced in the hadronic events of e^+e^- annihilation, but not baryons. The reason is that, in this type of models, it is quite difficult to bring three quarks or three antiquarks together. Indeed, it was one of the major surprises from PETRA that experimentally baryons are produced rather copiously. This point will be discussed in detail in chapter 4.

2.9. Experimental determination of the Field–Feynman parameters

The TASSO Collaboration [2.29] has determined the Field–Feynman parameters a_F, σ_q and $P/(P+V)$ from their experimental data. They use only the data from the region sphericity $S < 0.25$, where two-jet events dominate and gluon bremsstrahlung is of minor importance. It is noted that the average squared transverse momentum $\langle p_T^2\rangle_{out}$ $(=\langle(\boldsymbol{p}\cdot\hat{n}_1)^2\rangle)$ perpendicular to the event plane is most sensitive to σ_q, the single particle fractional momentum distribution dN/dx_p (where x_p = momentum of particle/beam momentum) is most sensitive to a_F, and the distribution of charged multiplicity n_{ch} is most sensitive to $P/(P+V)$. These distributions are well described by the parameters

$$a_F = 0.57 \pm 0.20\,, \qquad \sigma_q = 0.32 \pm 0.04\ \text{GeV}/c\,, \qquad P/(P+V) = 0.56 \pm 0.15\,. \tag{2.26}$$

These parameters are used in the determination of the quark–gluon coupling constant α_s, as to be discussed in section 3.4. With (2.26) and the value of α_s, numerous comparisons have been carried out between the experimental data and QCD with Field–Feynman fragmentation. The agreement is generally excellent. Some examples of these comparisons are shown in fig. 2.23.

Actually, in these and other comparisons, there is a fourth parameter related to the fragmentation of the gluon. As the gluon is assumed to split into a quark–antiquark pair, the distribution of the transverse momentum q_T of the quarks with respect to the gluon is taken to be $\exp(-q_T^2/2\sigma_g^2)$. However, the result of the analysis is insensitive to the value of this parameter, the reason being that in the gluon jets, the transverse momentum spread due to σ_g and that due to σ_q from the hadronization of quarks are hardly distinguishable. Changing σ_g from 0 to 0.5 GeV/c makes almost no difference in the results.

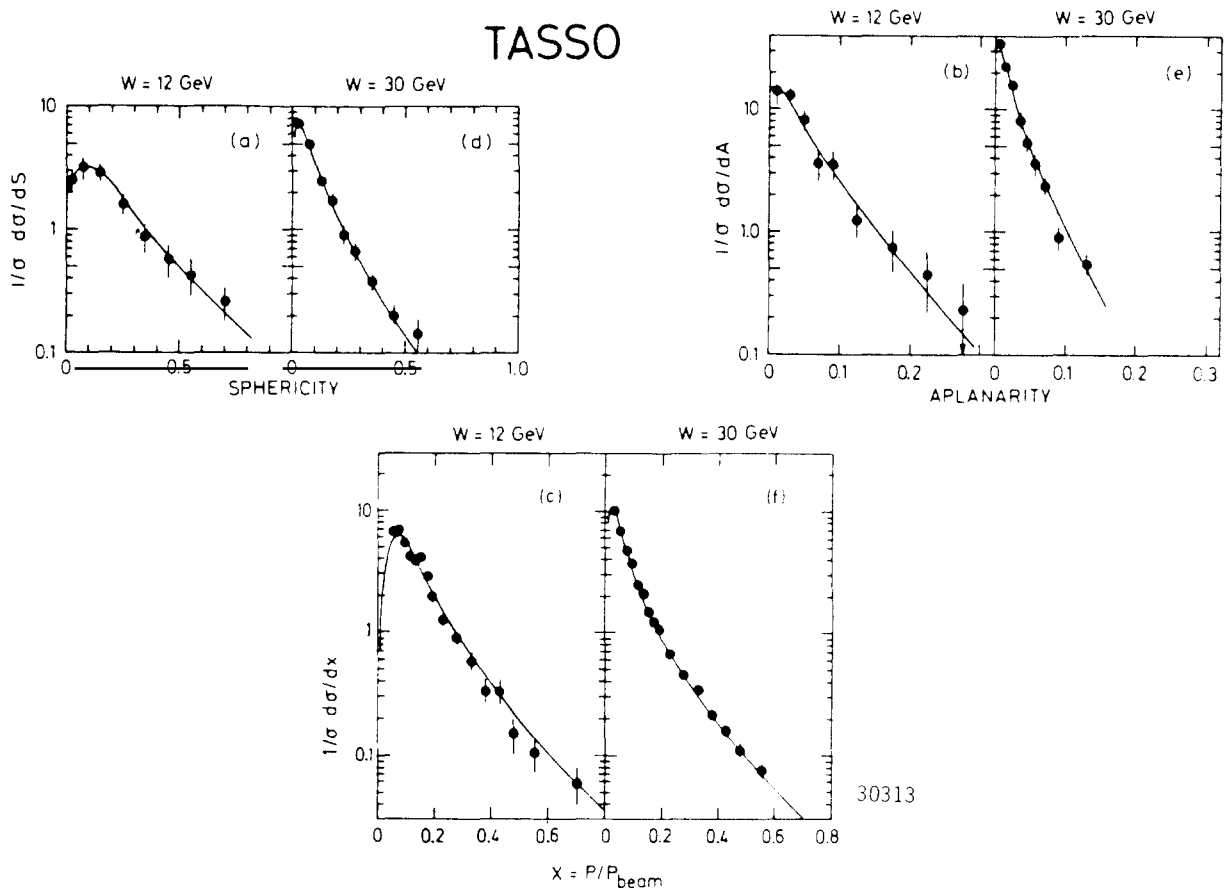

Fig. 2.23. Comparison of the TASSO [2.29] data with the QCD model (curves) at $W = 12$ GeV for (a) sphericity S, (b) aplanarity A and (c) the single particle inclusive x distribution for charged particles; and at $W = 30$ GeV for (d) S, (e) A, and (f) x. The experimental as well as the theoretical distributions are corrected for acceptance and radiative effects.

2.10. *Long-range charge correlation in opposite jets*

As shown in fig. 2.22, Field–Feynman fragmentation applies to each quark, or antiquark, separately. Actually quarks are never produced singly. In particular, in electron–positron annihilation, a $q\bar{q}$ pair is produced as shown in fig. 2.12. Therefore a better representation of the fragmentation process is shown schematically in fig. 2.24, where for simplicity the decays of the primordial mesons are omitted. Also the charged mesons are numbered as $h_1, h_2, \ldots$ but the neutral ones are not numbered. Since the quark charges are $-1/3$ and $+2/3$, we have with this ordering $e_1 = 1$, $e_2 = -1$, $e_3 = 1$, $e_4 = -1$, etc. Although this ordering cannot be determined experimentally, it is strongly correlated with the rapidity ordering. Accordingly, the presence of a negative charge for large negative y increases the probability of the presence of a positive charge for large positive y', and vice versa, where the rapidity y is defined as usual by $y = \frac{1}{2}\ln[(E + p_\parallel)/(E - p_\parallel)]$, with $p_\parallel$ the component of the momentum parallel to the jet axis. In other words it is a prediction of this picture of jet formation via a $q\bar{q}$ pair as shown in fig. 2.24 that there is a long-range charge correlation in opposite jets.

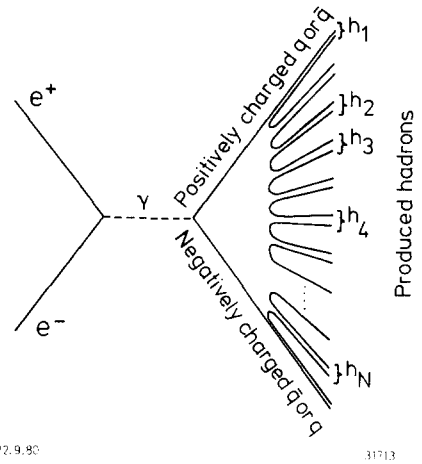

Fig. 2.24. A schematic diagram of hadron production in e^+e^- annihilation.

From the two-jet events, the TASSO Collaboration [2.30, 2.31] has observed this long-range charged correlation. If n is the charged multiplicity of the event, then we define a charge correlation function, the compensating charge flow $\bar{\phi}$ by

$$\bar{\phi}(y, y') = -\frac{1}{\Delta y\, \Delta y'} \left\langle \frac{1}{n} \sum_{k=1}^{n} \sum_{i \neq k} e_i(y)\, e_k(y') \right\rangle \tag{2.27}$$

where, for example, for the ith particle with rapidity y_i, $e_i(y) = +1$ or -1 according to the charge of this particle if y_i is inside an interval Δy around y and $e_i(y) = 0$ otherwise. Here $\langle\ \rangle$ means averaging over all events.

This charge correlation function is to be compared with the corresponding particle density function defined by

$$\bar{\rho}(y, y') = \frac{1}{\Delta y\, \Delta y'} \left\langle \frac{1}{n(n-1)} \sum_{k=1}^{n} \sum_{i \neq k} |e_i(y)|\, |e_k(y')| \right\rangle \tag{2.28}$$

where the sum is over all charged particles. The denominators n and $n(n-1)$ in (2.27) and (2.28) are chosen such that

$$\int dy \int dy'\, \bar{\phi}(y, y') = \int dy \int dy'\, \bar{\rho}(y, y') = 1 \tag{2.29}$$

because

$$\sum_{i \neq k} e_i e_k = -n \qquad \text{and} \qquad \sum_{i \neq k} |e_i|\, |e_k| = n^2 - n\,. \tag{2.30}$$

Let $P(y_+, y'_-)$, for example, be the probability of having a positively charged particle with rapidity y and a negatively charged particle with rapidity y'. In terms of this probability, $\bar{\rho}$ and $\bar{\phi}$ are

$$\bar{\rho}(y, y') \propto P(y_+, y'_-) + P(y_-, y'_+) + P(y_+, y'_+) + P(y_-, y'_-) \tag{2.31}$$

and

$$\bar{\phi}(y, y') \propto P(y_+, y'_-) + P(y_-, y'_+) - P(y_+, y'_+) - P(y_-, y'_-) . \tag{2.32}$$

For practical purposes, it is more convenient to plot instead

$$\rho(y, y') = \bar{\rho}(y, y') \Big/ \int dy\, \bar{\rho}(y, y') \tag{2.33}$$

and

$$\phi(y, y') = \bar{\phi}(y, y') \Big/ \int dy\, \bar{\phi}(y, y') \tag{2.34}$$

such that

$$\int dy\, \rho(y, y') = \int dy\, \phi(y, y') = 1 . \tag{2.35}$$

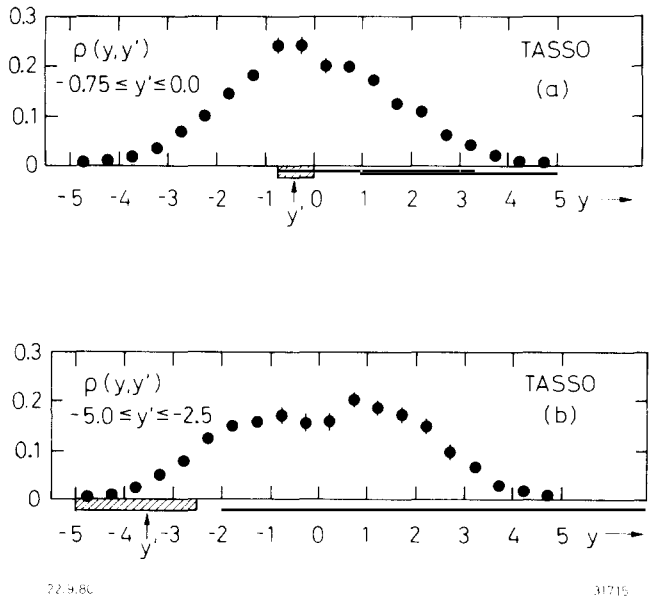

Fig. 2.25. The particle density function $\rho(y, y')$ as a function of y for (a) $-0.75 \leqq y' \leqq 0$ and (b) $-5 \leqq y' \leqq -2.5$. Here y and y' are the rapidity variables for charged particles. The data are from center-of-mass energies of 27 to 36 GeV by TASSO [2.30, 2.31].

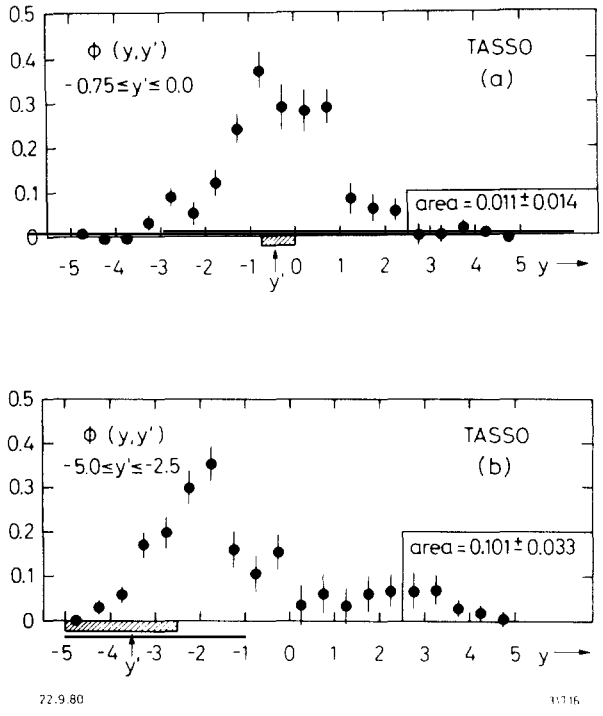

Fig. 2.26. The charge correlation function $\phi(y, y')$ as a function of y for (a) $-0.75 \leqq y' \leqq 0$ and (b) $-5 \leqq y' \leqq -2.5$. Here y and y' are the rapidity variables for charged particles. The data are from center-of-mass energies of 27 to 36 GeV by TASSO [2.30, 2.31].

Thus $\rho(y, y')$ is the probability that a charged particle with rapidity y' finds another charged particle with rapidity y, while $\phi(y, y')$ is the probability that the charge of a particle with rapidity y' is compensated by another particle of opposite charge with rapidity y.

Using the TASSO data with the additional cut that the total observed charge is 0 or ± 1, $\rho(y, y')$ is plotted in fig. 2.25 for (a) $-0.75 \leqq y' \leqq 0$ and (b) $-5 \leqq y' \leqq -2.5$. Also $\phi(y, y')$ is plotted in fig. 2.26 for (a) $-0.75 \leqq y' \leqq 0$ and (b) $-5 \leqq y' \leqq -2.5$. A comparison of these figures shows the following features.

(A) For small values of y', fig. 2.25a shows a broad distribution while fig. 2.26a shows a narrower distribution which peaks at $y \sim y'$. This is the evidence for a short range charge correlation. Moreover as y' becomes larger, there exhibits a peak adjacent to y' as shown in fig. 2.26b but not so in fig. 2.25b. This provides further evidence for short range charge correlation.

(B) As shown in fig. 2.26b, there is a noticeable rise in the ϕ distribution near large positive y when y' is large and negative. The area beyond $y \geqq 2.5$ is 0.101 ± 0.033 from fig. 2.26b compared with the corresponding value of 0.011 ± 0.014 from fig. 2.26a for small y'. This is the evidence of a long-range charge correlation in opposite jets from e^+e^- annihilation.

3. Three-jet events and properties of the gluon

3.1. Three-jet events

As discussed in the preceding chapter, at PETRA energies most of the hadronic events consist of two back-to-back jets, and are interpreted as the production of a quark–antiquark pair: $e^+e^- \to q\bar{q}$. In May 1979, for the first time PETRA had a run at center-of-mass energy above 27 GeV. The TASSO Collaboration, using the three-jet analysis method of Wu and Zobernig [3.1], found from their data the first few events with distinctly different shapes. The first such event, with three jets instead of two, was reported [3.2] late that spring, and several more such events shortly thereafter [3.3].

By late summer, the number of observed three-jet events had increased rapidly [3.4 to 3.7]. By now, there are several thousand such events from each of the PETRA experiments; the precise number is not well defined and depends on the somewhat artificial formulation adopted, because a three-jet event gradually changes over to a two-jet event if the angle between two of the jets is reduced. In spite of this ambiguity, or perhaps because of it, these three-jet events are most naturally explained by hard non-colinear gluon bremsstrahlung $e^+e^- \to q\bar{q}g$ [3.8], where the quark, the antiquark, and the gluon each materialize as a jet of hadrons with limited transverse momentum.

The three-jet events therefore give the most direct way to study the properties of the gluon, including in particular the quark–gluon coupling constant α_s. The Feynman diagrams for $e^+e^- \to q\bar{q}g$ are already given in fig. 2.18.

3.2. Methods of three-jet analysis used at PETRA

3.2.1. Wu–Zobernig method

Hansen et al. [3.9] discovered the two-jet structure of hadrons produced in e^+e^- annihilation by studying sphericity. In view of this success, Wu and Zobernig devised the method [3.1] of generalized sphericity in order to discover three-jet events. This method has been widely used by the TASSO Collaboration [3.4, 3.10].

The momentum tensor has been discussed in section 2.5, and the unit vector $\hat{n}_3$ defined there is

identified as the direction of the two back-to-back jets. This treatment of two-jet events can be reformulated as follows such that it can be generalized to three-jet events. Let $\hat{m}_1$ and $\hat{m}_2$ be two unit vectors for the directions of the two jets; since they are back-to-back, $\hat{m}_1$ and $\hat{m}_2$ satisfy

$$\hat{m}_1 = -\hat{m}_2 . \tag{3.1}$$

The momenta $\boldsymbol{p}_j$ are partitioned into two non-overlapping sets S_1 and S_2 such that

$$\begin{aligned} &\boldsymbol{p}_j \cdot \hat{m}_1 \geqq 0 \qquad \text{if } \boldsymbol{p}_j \text{ is in } S_1 , \\ &\boldsymbol{p}_j \cdot \hat{m}_2 \geqq 0 \qquad \text{if } \boldsymbol{p}_j \text{ is in } S_2 . \end{aligned} \tag{3.2}$$

Then $\hat{m}_1$ and $\hat{m}_2$ are determined, under the constraints (3.1) and (3.2), by maximizing the sum

$$\sum_{S_1} (\boldsymbol{p}_j \cdot \hat{m}_1)^2 + \sum_{S_2} (\boldsymbol{p}_j \cdot \hat{m}_2)^2 . \tag{3.3}$$

Because of (3.1), for the two-jet events the partition does not matter, and hence $\hat{m}_1$ or $\hat{m}_2$ can be identified with $\hat{n}_3$.

To generalize this formulation to three-jet events, let $\hat{m}_1$, $\hat{m}_2$ and $\hat{m}_3$ be three unit vectors for the directions of the three jets. By momentum conservation, $\hat{m}_1$, $\hat{m}_2$ and $\hat{m}_3$ must be coplanar; in other words, there is a unit vector $\hat{N}$ such that $\hat{N}$ is perpendicular to all three $\hat{m}$'s;

$$\hat{m}_1 \cdot \hat{N} = \hat{m}_2 \cdot \hat{N} = \hat{m}_3 \cdot \hat{N} = 0 . \tag{3.4}$$

This is the generalization of (3.1). The momenta $\boldsymbol{p}_j$ are partitioned into three non-overlapping sets S_1, S_2 and S_3 such that

$$\begin{aligned} &\boldsymbol{p}_j \cdot \hat{m}_1 \geqq 0 \qquad \text{if } \boldsymbol{p}_j \text{ is in } S_1 , \\ &\boldsymbol{p}_j \cdot \hat{m}_2 \geqq 0 \qquad \text{if } \boldsymbol{p}_j \text{ is in } S_2 , \\ &\boldsymbol{p}_j \cdot \hat{m}_3 \geqq 0 \qquad \text{if } \boldsymbol{p}_j \text{ is in } S_3 . \end{aligned} \tag{3.5}$$

This is the generalization of (3.2). The three-jet axes $\hat{m}_1$, $\hat{m}_2$ and $\hat{m}_3$ are determined, under the constraints (3.4) and (3.5), by maximizing the sum

$$\sum_{S_1} (\boldsymbol{p}_j \cdot \hat{m}_1)^2 + \sum_{S_2} (\boldsymbol{p}_j \cdot \hat{m}_2)^2 + \sum_{S_3} (\boldsymbol{p}_j \cdot \hat{m}_3)^2 . \tag{3.6}$$

This is the generalization of (3.3).

Unfortunately, this formulation is not useful practically, because the maximization of (3.6) is very difficult even on modern high-speed computers. The trouble stems entirely from the exceedingly large number of partitions: the number of ways to partition N observed tracks into three non-empty sets is

$$(3^{N-1} - 2^N + 1)/2 . \tag{3.7}$$

For example, this is 5.8×10^8 for $N = 20$, 1.4×10^{11} for $N = 25$, and 3.4×10^{13} for $N = 30$.

It is the basic idea of the procedure of Wu and Zobernig to use the following approximation

$$\hat{N} = \hat{n}_1 . \tag{3.8}$$

In other words, the approximation is that the three jet axes $\hat{m}_1$, $\hat{m}_2$ and $\hat{m}_3$ are taken to lie in the plane defined by $\hat{n}_2$ and $\hat{n}_3$ of section 2.5, called the event plane.

In general (3.8) is not exact; but it is exact in some limiting cases. Clearly it is exact in the case where all $\boldsymbol{p}_j$ are in the event plane. It is also exact if each $\boldsymbol{p}_j$ in the set S_α ($\alpha = 1, 2, 3$) is of the form

$$\boldsymbol{p}_j = a_j \hat{l}_\alpha + b_j \hat{n}_1 , \tag{3.9}$$

where $\hat{l}_1$, $\hat{l}_2$ and $\hat{l}_3$ are three unit vectors in the event plane, and b_j are sufficiently small in the sense

$$\sum_{S_\alpha} b_j^2 < \sum_{S_\alpha} a_j^2 . \tag{3.10}$$

In other words, (3.8) is exact when there is no spread out of the event plane *or* there is no spread in the event plane. Roughly speaking, the error of the approximation (3.8) is of the order of the product of the spreads of the jets in and perpendicular to the event plane. At PETRA energies, this error is quite small.

With this approximation (3.8), three-jet analysis becomes very much simpler because the components of $\boldsymbol{p}_j$ in the direction of $\hat{n}_1$ are no longer relevant. Let $\boldsymbol{q}_j$ be the projection of $\boldsymbol{p}_j$ into the event plane P. The important point here is that vectors in a plane, unlike those in a three-dimensional space, are naturally arranged in a cyclic order according to the polar angle. With this cyclic ordering, in the maximization of (3.6), or equivalently of

$$\sum_{S_1} (\boldsymbol{q}_j \cdot \hat{m}_1)^2 + \sum_{S_2} (\boldsymbol{q}_j \cdot \hat{m}_2)^2 + \sum_{S_3} (\boldsymbol{q}_j \cdot \hat{m}_3)^2 , \tag{3.11}$$

it is sufficient to consider only partitions where each of the three sets S_1, S_2 and S_3 consists of contiguous momenta. This reduces the number of partitions from (3.7) to

$$\binom{N}{3} = N(N-1)(N-2)/6 . \tag{3.12}$$

This is 1140 for $N = 20$, 2300 for $N = 25$ and 4060 for $N = 30$; or reductions by factors of 5×10^5, 6×10^7 and 8×10^9 respectively.

Let the rectangular and polar coordinates of $\boldsymbol{q}_j$ be respectively (q_{j1}, q_{j2}) and (q_j, θ_j), and let the N momenta be labeled such that

$$0 \leqq \theta_1 \leqq \theta_2 \leqq \theta_3 \leqq \theta_N < 2\pi . \tag{3.13}$$

The three sets S_1, S_2 and S_3 are specified as

$$\begin{aligned} S_1 &= \{N_1, N_1 + 1, \ldots, N_2 - 1\} , \\ S_2 &= \{N_2, N_2 + 1, \ldots, N_3 - 1\} , \\ S_3 &= \{N_3, N_3 + 1, \ldots, N, 1, 2, \ldots, N_1 - 1\} , \end{aligned} \tag{3.14}$$

where

$$1 \leqq N_1 < N_2 < N_3 \leqq N . \tag{3.15}$$

Furthermore, the conditions (3.5) imply the restrictions

$$\begin{aligned} &\theta_{N_2-1} - \theta_{N_1} < \pi , \\ &\theta_{N_3-1} - \theta_{N_2} < \pi , \\ &2\pi + \theta_{N_1-1} - \theta_{N_3} < \pi . \end{aligned} \tag{3.16}$$

In case $N_1 = 1$, θ_0 is defined to be $\theta_N - 2\pi$.

The second step is to define three 2×2 matrices $M^{(1)}$, $M^{(2)}$ and $M^{(3)}$ by

$$M^{(\tau)}_{\alpha\beta} = \sum_{j \text{ in } S_\tau} q_{j\alpha} q_{j\beta} \tag{3.17}$$

for $\alpha, \beta = 1, 2$ and $\tau = 1, 2$ and 3. For each of these three 2×2 matrices, let $A^{(\tau)}$ be the larger eigenvalue and $\hat{m}_\tau$ the corresponding normalized eigenvector. Hence $A^{(\tau)}$ is given explicitly by

$$A^{(\tau)} = \tfrac{1}{2}\{M^{(\tau)}_{11} + M^{(\tau)}_{22} + [(M^{(\tau)}_{11} - M^{(\tau)}_{22})^2 + 4(M^{(\tau)}_{12})^2]^{1/2}\} .$$

In terms of these $A^{(\tau)}$, we maximize

$$A(N_1, N_2, N_3) = A^{(1)} + A^{(2)} + A^{(3)} \tag{3.18}$$

over all partitions where (3.5) is satisfied. This maximizing partition gives the three jets and the corresponding $\hat{m}_1$, $\hat{m}_2$ and $\hat{m}_3$ the directions of the jet axes. From these directions, the total energies of the jets can be easily found if the approximation is made that the invariant masses of the jets are neglected. Let

$$\begin{aligned} \alpha_1 &= \sin(\phi^{(3)} - \phi^{(2)}) \\ \alpha_2 &= \sin(\phi^{(1)} - \phi^{(3)}) \\ \alpha_3 &= \sin(\phi^{(2)} - \phi^{(1)}) \end{aligned}$$

where the $\phi^{(\tau)}$'s are the polar angular coordinates in the event plane for $\hat{m}_\tau$ for the particular partition N_1, N_2, N_3 that maximizes $A(N_1, N_2, N_3)$. From the directions of the three jet axes, one obtains the total energy $E^{(\tau)}$ of each jet by

$$E^{(\tau)} = W\alpha_\tau/(\alpha_1 + \alpha_2 + \alpha_3) \tag{3.19}$$

where W is the center-of-mass energy.

As a measure of how three-jet like an event is, it is useful to define the quantity trijettiness J_3 by

$$J_3 = \frac{1}{N-3} \sum_{\tau=1,2,3} \left\{ \sum_{j \text{ in } S_\tau} \frac{(\boldsymbol{q}_j \times \hat{m}_\tau)^2}{\Delta_\tau^2} \right\} \tag{3.20}$$

where $\Delta_\tau^2 = \frac{1}{2}\langle p_T^2 \rangle_\tau$. $\langle p_T^2 \rangle_\tau$ is the average transverse momentum squared of a jet with energy E_τ and may be assumed to be equal to that for two-jet events. An alternative possibility is to use

$$J_3' = \frac{1}{2N-5} \sum_{\tau=1,2,3} \left\{ \sum_{j \text{ in } S_\tau} \frac{(\boldsymbol{p}_j \times \hat{m}_\tau)^2}{\Delta_\tau^2} \right\} . \tag{3.21}$$

As emphasized in the original paper, this procedure has the following desirable features:

(1) All three jet axes are determined.

(2) It is not necessary to have the momenta of all produced particles. For example, this procedure can be used where there is no detection of neutral particles. Of course the loss of information leads to a larger error.

(3) All measured momenta can be used; in other words, there is no need to introduce a cutoff for low momenta.

(4) Computer time is moderate.

3.2.2. Brandt–Dahmen method

In the three-jet analysis of Brandt and Dahmen [3.11], first used by the PLUTO Collaboration [3.6], the quantity to be maximized is the generalized thrust

$$\sum_{S_1} \boldsymbol{p}_j \cdot \hat{m}_1 + \sum_{S_2} \boldsymbol{p}_j \cdot \hat{m}_2 + \sum_{S_3} \boldsymbol{p}_j \cdot \hat{m}_3 , \tag{3.22}$$

instead of (3.6). This maximization is to be taken over all choices of $\hat{m}_1$, $\hat{m}_2$ and $\hat{m}_3$, and also over all admissible partitions.

Brandt and Dahmen consider a case where the N measured momenta $\boldsymbol{p}_j$ satisfy

$$\sum_j \boldsymbol{p}_j = 0 . \tag{3.23}$$

This is true when the momenta of all produced particles are measured. In this case, the $\hat{m}$'s can be found as follows. Given S_τ the maximum of $\Sigma_{S_\tau} \boldsymbol{p}_j \cdot \hat{m}_\tau$ over $\hat{m}_\tau$ is

$$\max_{\hat{m}_\tau} \sum_{S_\tau} \boldsymbol{p}_j \cdot \hat{m}_\tau = \left| \sum_{S_\tau} \boldsymbol{p}_j \right| . \tag{3.24}$$

The choice of $\hat{m}_\tau$ is

$$\hat{m}_\tau = \left(\sum_{S_\tau} \boldsymbol{p}_j \right) \Big/ \left| \sum_{S_\tau} \boldsymbol{p}_j \right| . \tag{3.25}$$

The important point here is that the condition (3.23) guarantees that the $\hat{m}$'s satisfy (3.4), i.e. they are coplanar.

For any experimental data, (3.23) is almost never satisfied. It is therefore necessary to introduce a fictitious momentum $\boldsymbol{p}_{N+1}$ defined by

$$\boldsymbol{p}_{N+1} = -\sum_{j=1}^{N} \boldsymbol{p}_j . \tag{3.26}$$

Thus the $N+1$ momenta, taken together, do satisfy (3.23). If these $N+1$ momenta are partitioned into three non-empty sets S_1, S_2 and S_3 then (3.25) can be used, and the quantity to be maximized over all such partitions is

$$\left|\sum_{S_1} \boldsymbol{p}_j\right| + \left|\sum_{S_2} \boldsymbol{p}_j\right| + \left|\sum_{S_3} \boldsymbol{p}_j\right| . \tag{3.27}$$

A measure of the jettiness of a three-jet event is then the triplicity defined by

$$T_3 = \frac{|\Sigma_{S_1} \boldsymbol{p}_j| + |\Sigma_{S_2} \boldsymbol{p}_j| + |\Sigma_{S_3} \boldsymbol{p}_j|}{\sum_{j=1}^{N+1} |\boldsymbol{p}_j|} \tag{3.28}$$

for the maximizing partition of the $N+1$ momenta into the sets S_1, S_2 and S_3.

Because of the fictitious $\boldsymbol{p}_{N+1}$, the problem of the large number of partitions to be considered is further aggravated. This number is obtained by the replacement $N \to N+1$ in (3.7): $(3^N - 2^{N+1} + 1)/2$. This is 261625 even for $N = 12$, 7×10^6 for $N = 15$ and 1.9×10^8 for $N = 18$. Accordingly, for multiplicities commonly seen at PETRA, it is practically not possible to search through all partitions. The procedure actually followed is to take about the 16 or 17 largest momenta, carry through the analysis by ignoring the rest, and then reintroduce the neglected momenta one by one. Even with this procedure, the computer time needed is quite extensive.

3.2.3. Combined methods

It is clear that the methods described in the previous two subsections (sections 3.2.1 and 3.2.2) can be combined in a variety of ways. A bewildering array of such combinations, has been tried at one time or another. Among these numerous possibilities, only two will be described and discussed in this section.

(A) *Modified Brandt–Dahmen method*

The conservation of momentum, as expressed by (3.23), is of central importance in the Brandt–Dahmen method, but not in the Wu–Zobernig method. The fictitious momentum $\boldsymbol{p}_{N+1}$ is introduced for this reason in the Brandt–Dahmen method, and is treated on equal footing with the actually measured momenta. The question is therefore naturally raised whether this fictitious momentum $\boldsymbol{p}_{N+1}$ can be avoided.

Since the constraints (3.5) are of no importance, $\boldsymbol{p}_{N+1}$ can be avoided by reverting to the initial statement of the procedure, namely to maximize (3.22) under the constraint (3.4). Given a partition, let

$$\boldsymbol{P}_\tau = \sum_{S_\tau} \boldsymbol{p}_j \tag{3.29}$$

for $\tau = 1, 2, 3$, then $\hat{N}$ is determined by maximizing

$$|\boldsymbol{P}_1 \times \hat{N}| + |\boldsymbol{P}_2 \times \hat{N}| + |\boldsymbol{P}_3 \times \hat{N}| . \tag{3.30}$$

This expression (3.30) can also be written as

$$[\boldsymbol{P}_1^2 - (\boldsymbol{P}_1 \cdot \hat{N})^2]^{1/2} + [\boldsymbol{P}_2^2 - (\boldsymbol{P}_2 \cdot \hat{N})^2]^{1/2} + [\boldsymbol{P}_3^2 - (\boldsymbol{P}_3 \cdot \hat{N})^2]^{1/2} \tag{3.31}$$

and therefore $\hat{N}$ satisfies

$$\sum_\tau [\boldsymbol{P}_\tau^2 - (\boldsymbol{P}_\tau \cdot \hat{N})^2]^{-1/2} (\boldsymbol{P}_\tau \cdot \hat{N}) \boldsymbol{P}_\tau = \text{constant } \hat{N}. \tag{3.32}$$

While (3.32) is not difficult to solve numerically, it is nevertheless too complicated because it needs to be solved for each choice of partition. Hence the approximation is introduced to expand each term of (3.31) by the binominal theorem and keep only the first non-trivial term. In this approximation, $\hat{N}$ is determined by minimizing

$$(\boldsymbol{P}_1 \cdot \hat{N})^2 / |\boldsymbol{P}_1| + (\boldsymbol{P}_2 \cdot \hat{N})^2 / |\boldsymbol{P}_2| + (\boldsymbol{P}_3 \cdot \hat{N})^2 / |\boldsymbol{P}_3| . \tag{3.33}$$

In other words,

$$\hat{N} = \text{the } \hat{n}_1 \text{ for the three momenta } |\boldsymbol{P}_1|^{-1/2} \boldsymbol{P}_1 , \quad |\boldsymbol{P}_2|^{-1/2} \boldsymbol{P}_2 \quad \text{and} \quad |\boldsymbol{P}_3|^{-1/2} \boldsymbol{P}_3 . \tag{3.34}$$

When (3.23) is satisfied, $\boldsymbol{P}_1 + \boldsymbol{P}_2 + \boldsymbol{P}_3 = 0$, and clearly $\hat{N}$ is normal to the plane determined by $\boldsymbol{P}_1$, $\boldsymbol{P}_2$ and $\boldsymbol{P}_3$.

So far as computer time is concerned, this modified Brandt–Dahmen method is comparable to the original Brandt–Dahmen method of triplicity. The modification reduces the number of partitions by roughly a factor of 3, but the computation of $\hat{N}$ via (3.34) takes some additional time. The modified triplicity T_3' is

$$T_3' = \frac{|\Sigma_{S_1} \boldsymbol{p}_j| + |\Sigma_{S_2} \boldsymbol{p}_j| + |\Sigma_{S_3} \boldsymbol{p}_j| - \lambda_1}{\sum_{j=1}^N |\boldsymbol{p}_j|} \tag{3.35}$$

for the maximizing partition of the N observed momenta $\boldsymbol{p}_j$ into the sets S_1, S_2 and S_3, when λ_1 is the λ_1 defined by (2.14) for the three momenta of (3.34) with (3.29).

(B) *Modified Wu–Zobernig method*

The basic idea of the Wu–Zobernig method is to reduce the three-dimensional momentum vectors to two-dimensional ones so that the cyclic ordering can be used to reduce drastically the number of partitions. Once this reduction is carried out, the method is not limited to maximizing the generalized sphericity (3.6). A natural modification is to replace the generalized sphericity by the generalized thrust (3.22). However, this modification is not as straightforward as it may seem.

The difficulty stems from the fact that the fundamental Wu–Zobernig approximation (3.8) $\hat{N} = \hat{n}_1$ is accurate only for the generalized sphericity, as discussed in the paragraph containing eqs. (3.9) and (3.10). For the generalized thrust, this approximation (3.8) is exact only when there is no spread out of the event plane, not when there is no spread in the event plane, as clearly demonstrated in connection with the modified Brandt–Dahmen method. Therefore, in the modified Wu–Zobernig method where generalized thrust is used, an iterative procedure is needed.

The steps are as follows.

(a) From the momentum tensor, calculate $\hat{n}_1$, $\hat{n}_2$ and $\hat{n}_3$ as usual.

(b) Let $\boldsymbol{q}_j$, $j = 1, 2, \ldots, N$, be the projections of $\boldsymbol{p}_j$ into the $\hat{n}_2 - \hat{n}_3$ plane. Put these $\boldsymbol{q}_j$ in cyclic order and define the contiguous partitions S_1, S_2 and S_3 of (3.14) in accordance with the Wu–Zobernig procedure. Maximize, over these contiguous partitions, the quantity

$$\left|\sum_{S_1} \boldsymbol{q}_j\right| + \left|\sum_{S_2} \boldsymbol{q}_j\right| + \left|\sum_{S_3} \boldsymbol{q}_j\right| . \tag{3.36}$$

(c) Using the maximizing partition found in the preceding step, define the three vectors

$$\sum_{S_\tau} \boldsymbol{p}_j \Big/ \sqrt{\left|\sum_{S_\tau} \boldsymbol{p}_j\right|} \tag{3.37}$$

for $\tau = 1, 2, 3$. Recalculate $\hat{n}_1$, $\hat{n}_2$, $\hat{n}_3$ using these three momentum vectors of (3.37).

(d) On the basis of these new $\hat{n}$'s, repeat step (b). Iterate if necessary.

(e) From the final maximizing partition S_1, S_2 and S_3 and the final $\hat{n}_2 - \hat{n}_3$ plane, a measure of the jettiness of the three-jet event is the modified triplicity

$$T_3'' = \left\{\left|\sum_{S_1} \boldsymbol{q}_j\right| + \left|\sum_{S_2} \boldsymbol{q}_j\right| + \left|\sum_{S_3} \boldsymbol{q}_j\right|\right\} \Big/ \sum_{j=1}^{N} |\boldsymbol{p}_j| \tag{3.38}$$

and the three-jet axes are given by the unit vectors

$$\hat{m}_\tau = \sum_{S_\tau} \boldsymbol{q}_j \Big/ \left|\sum_{S_\tau} \boldsymbol{q}_j\right| \tag{3.39}$$

for $\tau = 1, 2, 3$.

So far as computer time is concerned, this modified method is comparable to the original method. While the iteration increases the computer time, it is faster to calculate (3.36) than (3.18). Methods intermediate between the original and the modified versions have also been used at PETRA [3.12].

3.2.4. Ellis–Karliner method

In the four methods of three-jet analysis discussed so far, the three jets are always treated on equal footing. While it is highly desirable to maintain this symmetry, it is not absolutely compelling. In the Ellis–Karliner method [3.13], this symmetry is not maintained. Indeed, the method was originally devised for the determination of the spin of the gluon, and will play an important role in section 3.5.1.

This method consists of the following steps.

(A) Determine the thrust axis $\hat{n}$ by (2.22). At this stage, the sign of $\hat{n}$ remains arbitrary.

(B) Designate one of the two jets as thin while the other one as fat according to the relative magnitudes of

$$\sum_{\boldsymbol{p}\cdot\hat{n}>0} |\boldsymbol{p}_j \times \hat{n}| \quad \text{and} \quad \sum_{\boldsymbol{p}\cdot\hat{n}<0} |\boldsymbol{p}_j \times \hat{n}| .$$

Choose the sign of $\hat{n}$ such that $\hat{n}$ is in the direction of the thin jet.

(C) Carry out a Lorentz transformation to the center of mass of the fat jet. In this new coordinate system and with only the tracks associated with the fat jet, determine again the thrust axis. In this way the fat jet is split into two jets.

(D) Go back to the laboratory system by reversing the Lorentz transformation.

The Lorentz transformation used in this procedure is shown schematically in fig. 3.1.

Let us compare in more detail this Ellis–Karliner method [3.13] with those of the preceding sections. Aside from the asymmetrical treatment of the three jets as already mentioned, the main feature of this method is the application of Lorentz transformation. Therefore, at least in principle, not only the $\boldsymbol{p}_j$ but also the corresponding E_j are needed. Since experimentally E_j can be found only with particle identification, all particles are assumed to be pions. The Ellis–Karliner method is used in section 3.3.4 by the JADE Collaboration [3.7], and in section 3.5.1 for spin determination by the TASSO Collaboration [3.14].

By contrast, in applying the method of Wu–Zobernig, Brandt–Dahmen or their modifications, we are instructed to remain in the center-of-mass system. Indeed, it is only in this system that sphericity, thrust, etc. are defined. Nevertheless, it is reasonable to raise the question whether there is a natural measure of the jettiness of a three-jet event with Lorentz invariance maintained. With the question posed in this way, a possible answer is the jet mass. More precisely, in the spirit of (3.6) and (3.22), the optimal partition of the four-momenta $(E_j, \boldsymbol{p}_j)$ into three non-overlapping sets S_1, S_2 and S_3 is determined by minimizing

$$M_1 + M_2 + M_3 \tag{3.40}$$

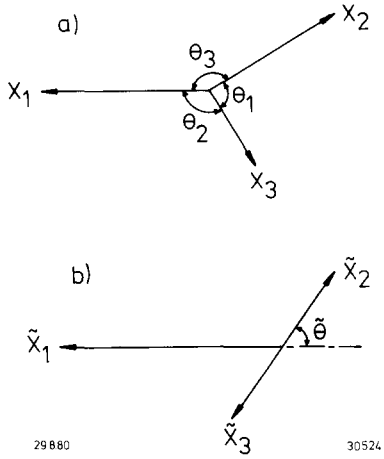

Fig. 3.1. (a) Momenta and angles of a qq̄g three-jet final state in the center-of-momentum frame. (b) The qq̄g final state transformed to the rest frame of jets 2 and 3.

where the jet masses M_τ are defined by

$$M_\tau^2 = \left(\sum_{S_\tau} E_j\right)^2 - \left(\sum_{S_\tau} \boldsymbol{p}_j\right)^2 . \tag{3.41}$$

Since such methods have not been developed systematically, it is not known what the advantages and shortcomings are.

3.2.5. Cluster analysis

In this and the next subsections, we shall describe two other methods of jet analysis, which do not use the full information of the events as those of the preceding four subsections. These methods are the cluster analysis and energy flow. While the method of energy flow has low discriminating power and uses excessive computer time, there is a distinct possibility that the method of cluster analysis may become the most suitable method for HERA, LEP, pp and $p\bar{p}$ colliders.

In the present context, the basic idea of cluster analysis is to avoid as an input the number of jets, i.e., to let the procedure determine the number of jets. Hence cluster analysis is the application of pattern recognition to identify clusters. As such the method has wide applications in many areas, including library science, visual scene analysis, medicine, and pattern recognition in spark and bubble chambers. There is a great deal of literature on this subject, including a textbook [3.15]; more recently, there are also several papers [3.16 to 3.19] in the specific context of electron–positron annihilation. The fact that the details are quite different in these papers means that cluster analysis for e^+e^- annihilation is quite flexible. We begin with a general discussion.

As before, let $\boldsymbol{p}_j$ be the momenta of the observed particles. For each pair $i \neq j$, a number ρ_{ij} is assigned as a measure of the likelihood that the particles with momenta $\boldsymbol{p}_i$ and $\boldsymbol{p}_j$ are in the same jet. In general $\rho_{ij} = \rho_{ji}$ and the smaller the ρ_{ij}, the more likely for them to be in the same jet. The obvious first question is: how should ρ_{ij} be chosen? There are at least two distinct types of answers:

(A) The values ρ_{ij} should give only a relative ordering of the likelihood. More precisely, if $\rho' = f(\rho)$ is a strictly increasing function of ρ, then the cluster analysis should give the same answer independent of whether ρ_{ij} or $\rho'_{ij} = f(\rho_{ij})$ is used. This philosophy is advocated especially by Lanius, Roloff and Schiller [3.19].

(B) The values of ρ_{ij} are themselves meaningful. In the language of pattern recognition, these $\boldsymbol{p}_j$ are embedded in the so-called feature space, and ρ_{ij} is identified with the metric in this feature space [3.20]. However, it is interesting to note that, in some of the recent papers [3.16, 3.17], the ρ_{ij} used do not satisfy the triangular inequality $\rho_{ij} + \rho_{jk} \geqq \rho_{ik}$.

In addition to the choice of ρ_{ij}, the proposed procedures to determine the jets are widely different. Indeed, even for each of the procedures, there are several parameters that need to be chosen. For example, the procedures of [3.17] and [3.18] have each four parameters. Accordingly, some of the interesting questions concerning cluster analysis are the following. (i) How should the ρ_{ij} be chosen? In particular, are there desirable properties that they should have? (ii) Given ρ_{ij}, how can the quality of a proposed procedure be evaluated? and (iii) Given a proposed procedure, how can its parameters be chosen?

The procedure of Daum, Meyer and Bürger [3.18] is the one actually used at PETRA, for example by the PLUTO and JADE Collaborations [3.21, 3.22]. This procedure is based on a two-step algorithm in which

(1) all particles – charged and neutrals – are used. The particle is taken to have momentum $\boldsymbol{p}_i$, direction $\hat{n}_i = \boldsymbol{p}_i/|\boldsymbol{p}_i|$ and energy E_i.

In the first step preclusters are defined such that

(2) each particle is a member of only one precluster,

(3) any two particles i, k $(i \neq k)$ belong to the same precluster if

$$\rho_{ik} = \hat{n}_i \cdot \hat{n}_k > \cos\alpha \tag{3.42}$$

for a predefined value of α. Thus the choice of ρ_{ij} here is such that it depends only on the directions, but not the magnitudes, of the momenta involved. A typical value for α is 30°.

The direction of the precluster D_i is defined by

$$\hat{n}_{D_i} = \sum_{k \in D_i} \boldsymbol{p}_k \Big/ \Big| \sum_{k \in D_i} \boldsymbol{p}_k \Big| \,. \tag{3.43}$$

In the second step the preclusters are concatenated to clusters

(4) each precluster is a member of exactly one cluster,

(5) any two preclusters D_i, D_k $(i \neq k)$ belong to the same cluster if

$$\hat{n}_{D_i} \cdot \hat{n}_{D_k} > \cos\beta \tag{3.44}$$

for a predefined value of $\beta \geqq \alpha$. A typical value for β is 45°.

The energy and the direction of a cluster C_i are defined by

$$E_{C_i} = \sum_{k \in C_i} E_k \qquad \text{and} \qquad \hat{n}_{C_i} = \sum_{k \in C_i} \boldsymbol{p}_k \Big/ \Big| \sum_{k \in C_i} \boldsymbol{p}_k \Big| \,. \tag{3.45}$$

Finally some cuts are made to define a jet:

(6) the multiplicity of clusters n_c is defined by the minimal number of clusters which fulfill

$$\sum_{i=1}^{n_c} E_{C_i} > E_{\text{tot}} \cdot (1 - \varepsilon) \tag{3.46}$$

for a predefined value of ε, where E_{tot} is the energy sum of all particles. The clusters are accepted if they belong to the set of n_c most energetic clusters.

(7) Each accepted cluster is called a jet if $E_{C_i} > E_{\text{th}}$ for a predefined value of E_{th}.

While this procedure forms the basis of cluster analysis used at PETRA, various modifications are sometimes used in actual application. For example, neutral particles are not always included, see (1) above. Although theoretical questions can be readily raised, this cluster analysis works well in practice.

3.2.6. Method of energy flow

The method of energy flow to find three-jet events was originally proposed by De Rujula, Ellis, Floratos and Gaillard [3.23]. However, the method of energy flow actually used by MARK J at PETRA is quite different in detail. In this section, only the version used by MARK J [3.5] will be discussed. So far as we know, the original version has never been employed to analyze e^+e^- data, and hence may not have the features of the MARK J version.

The momentum tensor discussed in section 2.5 gives not only the jet axis $\hat{n}_3$ but also an orthonormal system $\hat{n}_1$, $\hat{n}_2$ and $\hat{n}_3$. By contrast, the thrust as defined by (2.22) gives only the jet axis but not a

coordinate system. In the method of energy flow, the first step is to construct an orthonormal system $\hat{e}_1$, $\hat{e}_2$ and $\hat{e}_3$, using the energies and directions of the observed particles instead of the momentum vectors. More precisely, instead of $\boldsymbol{p}_j$, define the energy flow

$$\boldsymbol{E}_j = (E_j/|\boldsymbol{p}_j|)\boldsymbol{p}_j \,. \tag{3.47}$$

The unit vector $\hat{e}_1$ is defined analogous to the thrust T:

$$F_{\text{thrust}} = \max \frac{\Sigma_i |\boldsymbol{E}_i \cdot \hat{e}_1|}{\Sigma_i E_i} \,. \tag{3.48}$$

The orthonormal system is defined through $\hat{e}_2$ and $\hat{e}_3 = \hat{e}_1 \times \hat{e}_2$, such that

$$F_{\text{major}} = \max \frac{\Sigma_i |\boldsymbol{E}_i \cdot \hat{e}_2|}{\Sigma_i E_i} \qquad \hat{e}_2 \perp \hat{e}_1 \,, \tag{3.49}$$

and

$$F_{\text{minor}} = \frac{\Sigma_i |\boldsymbol{E}_i \cdot \hat{e}_3|}{\Sigma_i E_i} \,. \tag{3.50}$$

The oblateness O is defined by

$$O = F_{\text{major}} - F_{\text{minor}} \,. \tag{3.51}$$

The method of energy flow used by MARK J [3.5] consists of the following. First make a cut in F_{thrust}. For these events with F_{thrust} not close to 1, project the $\boldsymbol{E}_i$ into the thrust-major plane. Orient these projections such that the longest jet is near the direction of $\hat{e}_1$ at 0° and the second longest jet is in a chosen half-plane. Make one energy-flow plot by superimposing all events, and look for three-lobe structure in this plot.

It was originally thought that the method of energy flow allowed a non-magnetic detector to have a quick look into jet physics. However this method is less effective for a number of reasons. For example, the jet axes are not determined event by event. But the most undesirable feature is that, as pointed out by the MARK J Collaboration [3.5] and to be discussed in section 3.3.2, this procedure introduces three-lobe structure even if none is actually present.

3.2.7. Four-jet analysis

Since there are three-jet events, there should also be four-jet events. With the three-jet events interpreted as gluon bremsstrahlung, double gluon bremsstrahlung leads to four-jet events:

$$e^+e^- \to q\bar{q}gg \,.$$

Alternatively, the bremsstrahlung gluon may materialize into a $q\bar{q}$ pair,

$$e^+e^- \to q\bar{q}q\bar{q} \,.$$

The lowest-order QCD diagrams for these two types of four-jet events are shown respectively in fig. 3.2a and fig. 3.2b.

From the point of view of physics, four-jet events are important for the following reason. The most fundamental difference between Abelian and non-Abelian gauge theories is the presence of self-interactions of the gauge particle in the non-Abelian case. For e^+e^- annihilation at high energies, this self-interaction is important not in three-jet events but in four-jet events, as shown in the last two diagrams of fig. 3.2a.

The major difficulty of four-jet analysis is again the large number of possible partitions. The number of ways to partition N observed tracks into four non-empty sets is

$$\tfrac{1}{6}(4^{N-1} - 3^N + 3 \cdot 2^{N-1} - 1), \tag{3.52}$$

which is even much larger than (3.7). It is for example 4.5×10^{10} for $N = 20$ and 4.7×10^{13} for $N = 25$.

The basic idea of the four-jet analysis to be presented here is, taking the inspiration from Ellis and Karliner [3.13], to apply the three-jet analysis twice. The actual procedure followed by TASSO [3.25, 3.26] is as follows:

(A) Use either the original or the modified Wu–Zobernig program for the three-jet analysis [3.1].

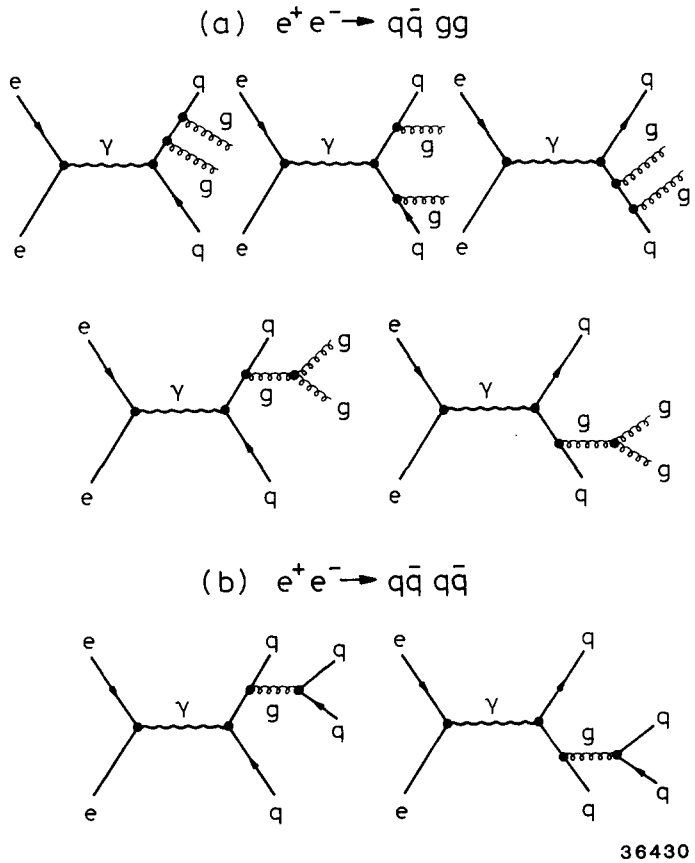

Fig. 3.2. Feynman diagrams for four-jet events.

(B) Determine the three jet axes by adding the momenta of the tracks in the jet. In general these three jet axes are not coplanar.

(C) Find the average transverse momenta for the three jets with respect to their own jet axes as defined above. To avoid possible confusion with the average transverse momenta used in the three-jet analysis, let us call them $\langle PT' \rangle$.

(D) Among the three jets being considered so far, define jet A as the one with the smallest value of $\langle PT' \rangle$.

(E) Remove all the tracks of jet A, and study the remaining tracks, i.e. the tracks that are not in jet A.

(F) Add up the energies and momenta of these remaining tracks to find the motion of the center-of-mass. Perform a Lorentz transformation to the center-of-mass system of these remaining tracks.

(G) Apply three-jet analysis to the transformed momenta for these remaining tracks. This gives the three new partitions. In particular, determine whether this is itself a three-jet event.

(H) If these remaining tracks form an acceptable three-jet event, go back to the original laboratory coordinate system.

(I) In the laboratory coordinate system, determine the four jet axes by adding up the momenta of the tracks in each jet.

(J) Find the angles between all the momentum directions and all the four jet axes. Each momentum should make the smallest angle with respect to the jet axis that it belongs to. If this is indeed the case, then the jet axes have been found properly.

(K) If not, such a momentum should be reassigned to the jet that gives the smallest angle. After reassignment, repeat steps I and J.

(L) The energies of the four jets are determined under the assumption that the jet masses can be neglected. Let $\hat{n}_i$ with $i = 1, 2, 3$ and 4 be the unit vectors in the directions of the jet axes, then the energies E_i of the jets are determined by the energy-momentum conservation

$$\sum_{i=1}^{4} E_i \hat{n}_i = 0 , \qquad \sum_{i=1}^{4} E_i = E_{\text{c.m.}} . \tag{3.53}$$

A variation of eq. (3.53) by introducing the observed jet mass is given in ref. [3.26].

This procedure of four-jet analysis has all the four advantages listed at the end of section 3.2.1 for the Wu–Zobernig three-jet analysis. It has the further advantage that it requires very little additional programming on the computer. The computer time required is dominated by the two three-jet analyses of steps A and G. Since there are fewer momenta in step G than step A, the computer time of four-jet analysis is not much more than that of three-jet analysis for the same number of observed tracks.

3.3. Observation of three-jet events

The first three-jet event, interpreted as $e^+e^- \to q\bar{q}g$, was discovered in the spring of 1979 at PETRA. As already mentioned, by now each of the PETRA and PEP experiments has thousands of three-jet events. It is however extremely interesting to retrace the historical excitements of the first observation of these events by each of the PETRA experiments.

3.3.1. TASSO

The TASSO Collaboration is the first group to observe three-jet events [3.2, 3.3, 3.4]. In the spring of 1979 when the center-of-mass energy of PETRA reached 27 GeV, the computer program based on the Wu–Zobernig method [3.1] was used and the first three-jet event observed is shown in fig. 3.3. This first event was presented by Wiik of the TASSO Collaboration [3.2] at the Bergen Conference in late spring, and was much discussed there. As seen from fig. 3.3, it had three clear, well separated jets, and was considered to be more convincing than a good deal of statistical analysis. Indeed, before the question of statistical fluctuation could be seriously raised, TASSO found a number of other three-jet events. Less than two weeks after the Bergen Conference, several further three-jet events from TASSO, shown in fig. 3.4, were presented by Söding [3.3] at the EPS Conference in Geneva. Comparisons of event shape distributions with the QCD predictions were also included. These additional events further demonstrated unambiguously the existence of planar three-jet events.

At the Fermilab Conference [3.27] several months later, all four experiments at PETRA gave more extensive data, confirming the earlier observation of TASSO. Since these experiments were run simultaneously, the amounts of data were the same within about 10–20%. In a period of three months, between August 29 and December 7, these more extensive data were submitted for publication by TASSO [3.4], MARK J [3.5], PLUTO [3.6] and JADE [3.7].

With the three-jet events understood as $e^+e^- \to q\bar{q}g$ [3.1 to 3.8], no sharp separation between two-jet and three-jet events is expected: when the angle between two of the jets becomes smaller and smaller (or alternatively when the momentum of one of the jets becomes less and less) the three-jet event looks

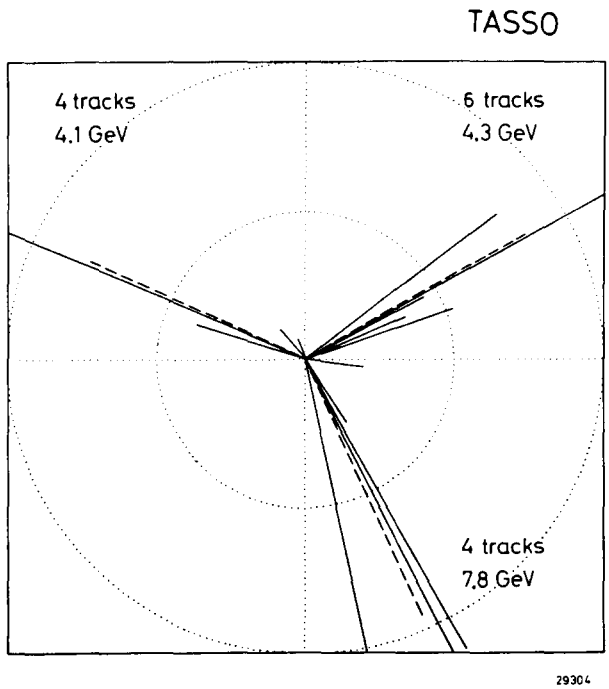

Fig. 3.3. The first three-jet event [3.2] observed at PETRA (TASSO run 447, event 13177). Plotted are the momentum vectors of the charged particles projected on the $\hat{n}_2 - \hat{n}_3$ event plane. The dotted lines show the directions of the jet axes found by the Wu–Zobernig method [3.1]. The center-of-mass energy is 27.4 GeV, and only charged particles are observed.

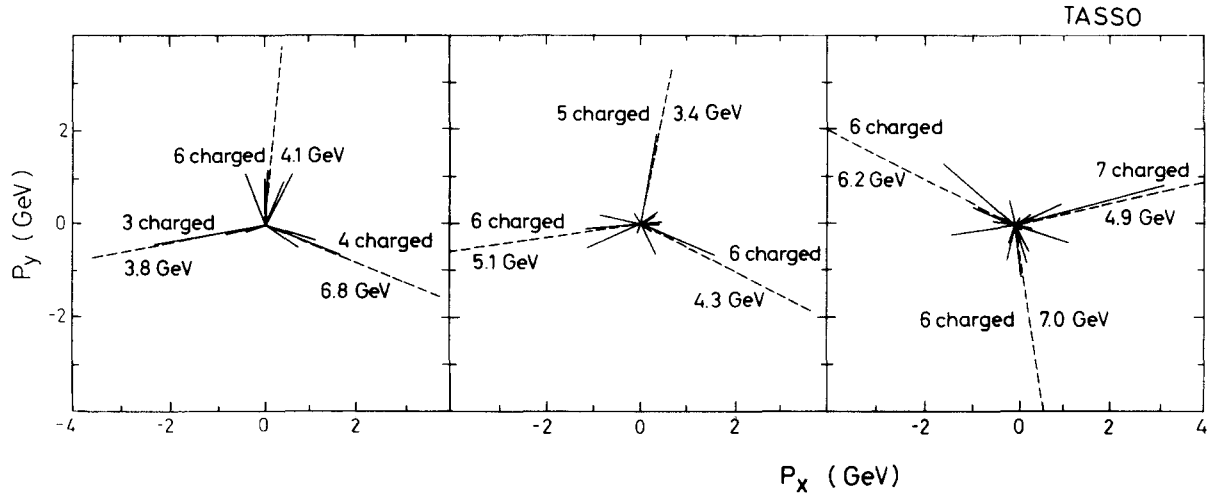

Fig. 3.4. Further three-jet events [3.3] observed by TASSO projected in the event plane. The center-of-mass energy is 27.4 GeV, and only charged particles are observed.

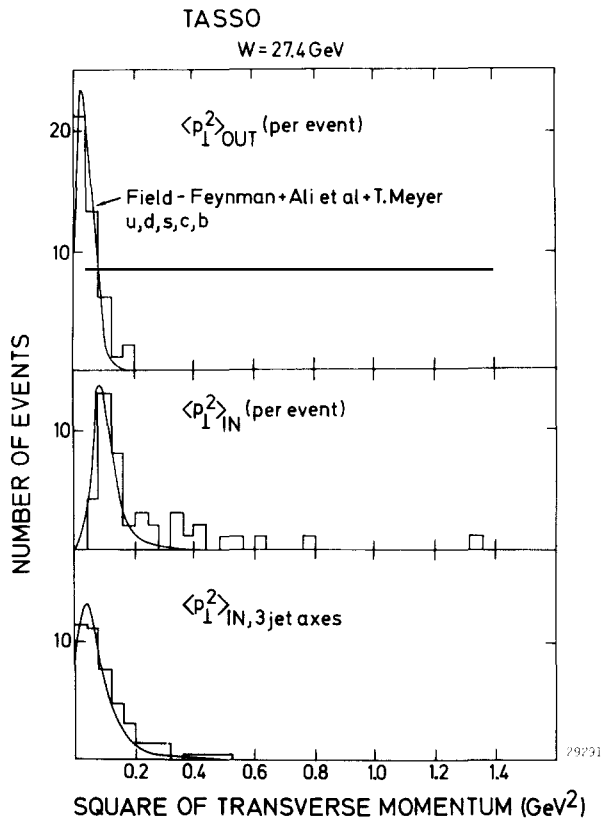

Fig. 3.5. TASSO distribution [3.3] of the average squared transverse momentum component *out* of the event plane (top), and *in* the event plane (center), for events at $W = 27.4$ GeV (averaging over charged hadrons only). The curves are for $q\bar{q}$ jets without gluon bremsstrahlung. The bottom figure shows $\langle p_\perp^2 \rangle$ per jet when three jet axes are fitted, again compared with the q jet model.

more and more like a two-jet event. One simple way to see this gradual transition is shown in fig. 3.5 [3.3], which compares, on the basis of the very early TASSO data, the distribution of

$$\langle p_T^2\rangle_{out} = \frac{1}{N}\sum_j (\boldsymbol{p}_j \cdot \hat{n}_1)^2 = Q_1\langle p^2\rangle \tag{3.54}$$

(= square of momentum component normal to the event plane averaged over the charged particles in one event) with that of

$$\langle p_T^2\rangle_{in} = \frac{1}{N}\sum_j (\boldsymbol{p}_j \cdot \hat{n}_2)^2 = Q_2\langle p^2\rangle \tag{3.55}$$

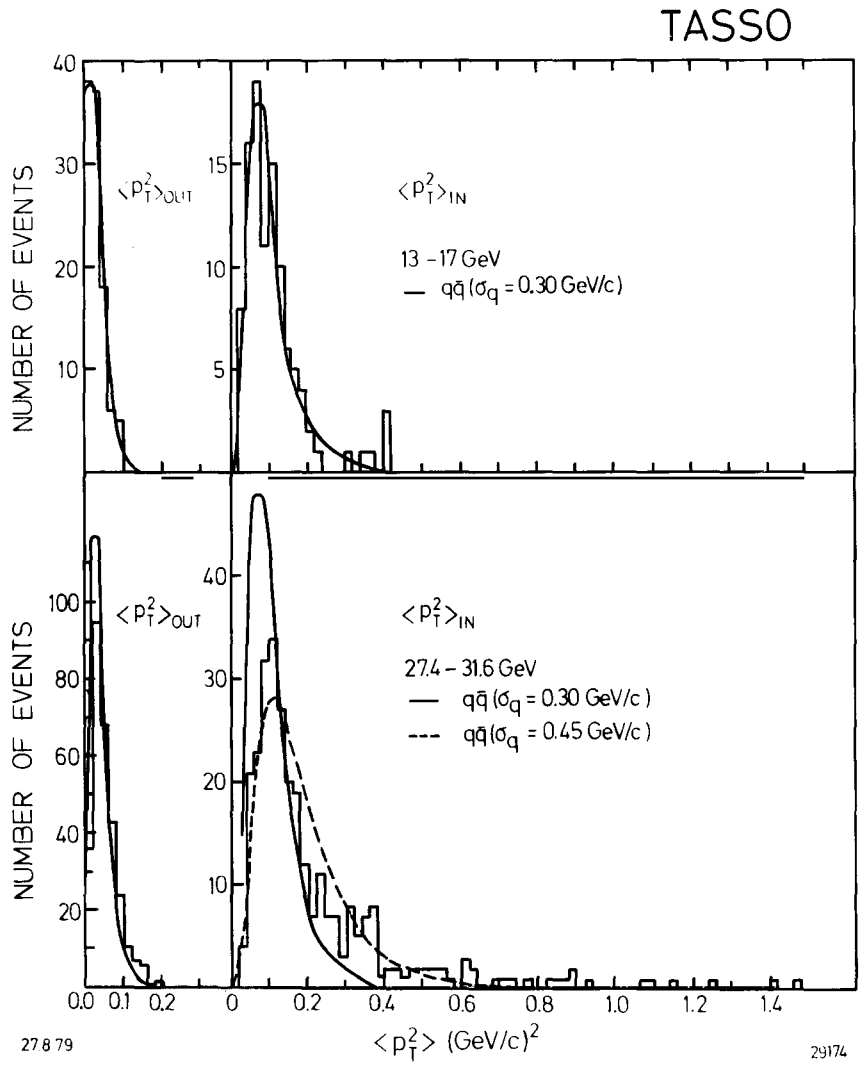

Fig. 3.6. The mean transverse momentum squared normal to the event plane $\langle p_T^2\rangle_{out}$ and in the event plane $\langle p_T^2\rangle_{in}$ per event for the low-energy and the high-energy TASSO data [3.4]. The predictions from the qq̄ model are shown assuming $\sigma_q = 0.30$ GeV/c (solid curves) and $\sigma_q = 0.45$ GeV/c (dotted curves). The model includes u, d, s, c and b quarks.

(= square of momentum component in the event plane and perpendicular to the jet axis averaged the same way). Also shown in fig. 3.5 is $\langle p_T^2 \rangle_{\text{in, 3 jet axes}}$, which is defined the same way as (3.55) but, for each jet, the jet axis found by the Wu–Zobernig method is used. For comparison, the corresponding results from Monte Carlo calculations on the basis of $q\bar{q}$ jets [3.28] are also given. Fig. 3.6 [3.4] gives the energy dependence of the $\langle p_T^2 \rangle_{\text{in}}$ and $\langle p_T^2 \rangle_{\text{out}}$ distributions on the basis of a larger data sample. While there is little change in the $\langle p_T^2 \rangle_{\text{out}}$ distribution from low ($W = 13$, 17 GeV) to high energies ($W = 27.4$, 31.6 GeV), the distribution of $\langle p_T^2 \rangle_{\text{in}}$ becomes much wider at high energies; there is a long tail of events with large $\langle p_T^2 \rangle_{\text{in}}$.

Hadrons resulting from pure $q\bar{q}$ jets will on the average be distributed uniformly around the jet axis. However, some asymmetry between $\langle p_T^2 \rangle_{\text{in}}$ and $\langle p_T^2 \rangle_{\text{out}}$ is caused by the bias introduced in choosing the axes. Good agreement with the $q\bar{q}$ model using $\sigma_q = 0.3$ GeV/c is found at low center-of-mass energies for both distributions and also at high energies for the $\langle p_T^2 \rangle_{\text{out}}$ distribution, but the $q\bar{q}$ model fails to reproduce the long tail of the $\langle p_T^2 \rangle_{\text{in}}$ distribution at high energies, as shown in fig. 3.6. Furthermore, as seen from the bottom histogram of fig. 3.5, the planar events exhibit three axes, the average transverse momentum of the hadrons with respect to these axes being the same 0.3 GeV/c. Indeed, the data are in agreement with predictions based on perturbative QCD.

Fig. 3.7 [3.10] compares the transverse momentum distribution, with respect to the individual jet axis, of three-jet events at the center-of-mass energy W of 30 GeV with that of two-jet events at $W = 12$ GeV. They are virtually identical. Also shown is the distribution of trijettiness J_3, defined by eq. (3.20). The peak at low J_3 values is a consequence of the strong collimation of the particles around the three jet axes. For fig. 3.7, cuts have been made in sphericity and aplanarity: $S > 0.25$ and $A < 0.08$ (see section 2.5).

3.3.2. MARK J

The MARK J Collaboration [3.5] used the method of energy flow as described in section 3.2.6. The central quantity that the MARK J Collaboration uses is the oblateness O defined by (3.51). Fig. 3.8a shows the event distribution as a function of this oblateness for their data at $W = 17$ GeV. The data agrees with both the $q\bar{q}$ and the $q\bar{q}g$ models. Fig. 3.8b shows the event distribution as a function of oblateness at $27.4 \leqq W \leqq 31.6$ GeV as compared with the predictions of the $q\bar{q}$ and the $q\bar{q}g$ models. For the $q\bar{q}$ model, MARK J uses both $\langle p_T \rangle = 0.325$ GeV/c and $\langle p_T \rangle = 0.425$ GeV/c. The data have more oblate events than the $q\bar{q}$ model predicts, but agree with the $q\bar{q}g$ model very well. The situation is therefore similar to that of the $\langle p_T^2 \rangle_{\text{in}}$ distributions of figs. 3.5 and 3.6.

More detailed analysis is carried out by MARK J by dividing the energy distribution of each event into two hemispheres using the plane defined by the major and minor axes $\hat{e}_2$ and $\hat{e}_3$. The forward hemisphere contains the narrow jet and the other contains the broader jet just as in the Ellis–Karliner method [3.13] of section 3.2.4. From the broader jet by itself, F^b_{major}, F^b_{minor} and

$$O_b = 2(F^b_{\text{major}} - F^b_{\text{minor}}) \tag{3.56}$$

are calculated [3.29]. The events from $W = 27.4$, 30 and 31.6 GeV are used with the cuts

$$F_{\text{thrust}} < 0.8 \quad \text{and} \quad O_b > 0.1\,. \tag{3.57}$$

From these events, the resulting energy-flow plot (see section 3.2.6) is shown in fig. 3.9a. Although three-jet structure can be clearly seen in this plot, it was already emphasized in the original paper of

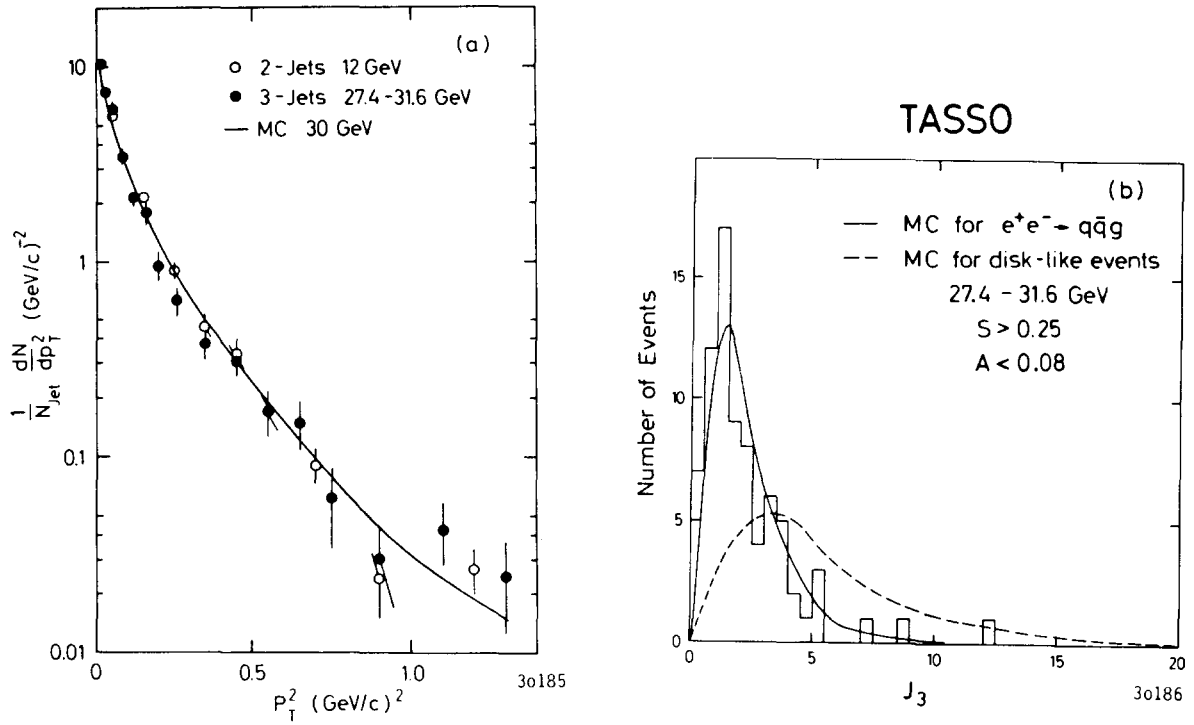

Fig. 3.7. (a) Observed transverse momentum distribution of the hadrons from the planar region ($S > 0.25$, $A < 0.08$) with respect to the three axes found with the Wu–Zobernig method [3.1], at $W = 30$ GeV (●). It is compared with the transverse momentum distribution relative to the sphericity axis for *all* events (no S or A cut) at $W = 12$ GeV, analyzed as two-jet events (○). It is also compared with the result from the QCD model at 30 GeV (curve). (b) Comparison of the trijettiness distribution for the planar event ($S > 0.25$, $A < 0.08$) sample at $W = 30$ GeV, with the distribution for disk-like events (dashed curve) and the QCD model (solid curve). The curves are normalized to the number of observed events. These data are from TASSO [3.10].

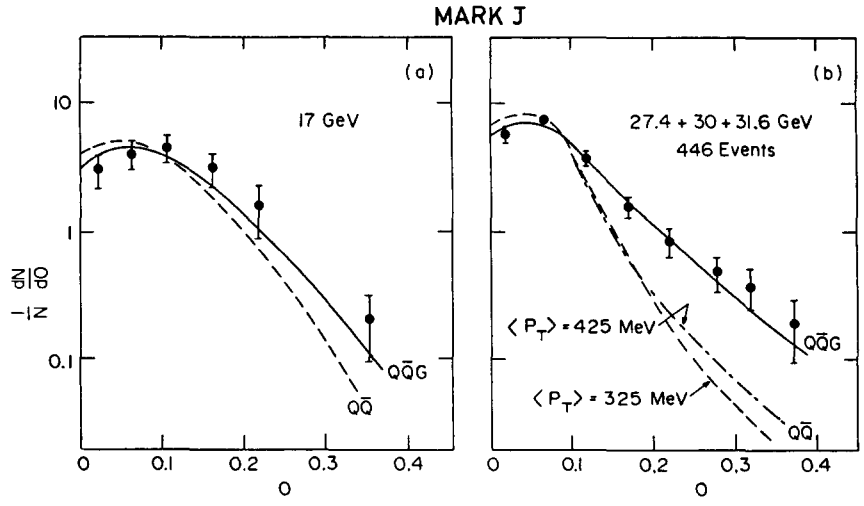

Fig. 3.8. (a) The MARK J [3.5] distribution $N^{-1}\,dN/dO$ as function of oblateness at $W = 17$ GeV. (b) The distribution $N^{-1}\,dN/dO$ as function of oblateness at $W = 27.4$–31.6 GeV. In both (a) and (b) the solid curves are the predictions based on the $q\bar{q}g$ model and the dashed curve is based on the standard $q\bar{q}$ model with $\langle p_T \rangle = 325$ MeV/c. The dash-dotted curve in (b) is the $q\bar{q}$ model prediction with $\langle p_T \rangle = 425$ MeV/c.

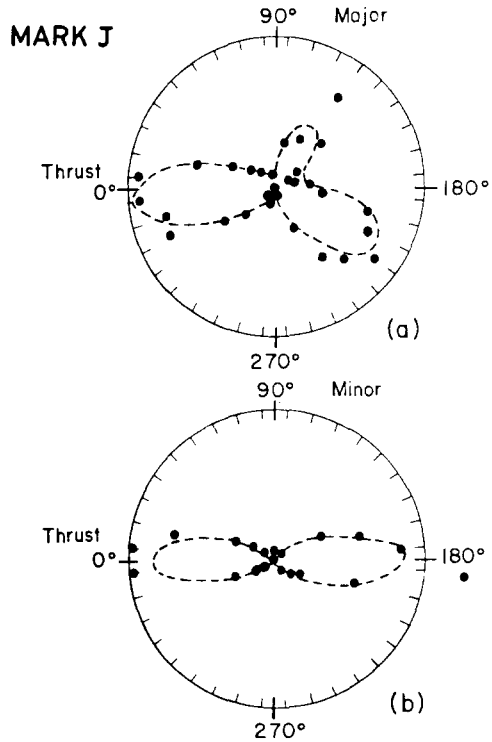

Fig. 3.9. (a) Energy distribution from MARK J [3.5] in the plane as defined by the thrust and the major axes for all the events with thrust <0.8 and oblateness >0.1 at $W = 27.4$, 30 and 31.6 GeV. The energy value is proportional to the radial distances. The superimposed dashed line represents the distribution calculated with the $q\bar{q}g$ model. (b) The measured and calculated energy distribution in the plane as defined by the thrust and the minor axes.

MARK J [3.5] that "phase-space distribution will show three nearly identical lobes due to the method of selection used".

This vital point is later discussed in great detail [3.24]. In this study with high statistics and higher energies W between 33 and 36.7 GeV, the cuts used are slightly different. The additional quantities used are F^{n}_{thrust} for narrow jet and θ_{minor}, which is the angle between the minor axis and the beam direction. The results are shown in fig. 3.10. It is seen clearly from fig. 3.10d that the phase-space model also gives three jets due to the method of selection used. However as seen from the same figure the solid curve (QCD) fits the data best.

The question may be raised why the method of energy flow was employed in the first place. The original reason was that, since individual tracks were not necessarily measured separately in the MARK J detector, it was thought that the method of energy flow was less sensitive to the combination of tracks. Actually, none of the methods described in section 3.2 is sensitive to this possible lack of resolution. Even in the Wu–Zobernig method, while the values of Q_1, Q_2 and Q_3 are sensitive to the combination of tracks (i.e. the replacement of say $\boldsymbol{p}_1$ and $\boldsymbol{p}_2$ by $\boldsymbol{p}_1 + \boldsymbol{p}_2$), the jet directions $\hat{m}_1$, $\hat{m}_2$ and $\hat{m}_3$ are much less sensitive.

It is instructive to compare the early data of TASSO and MARK J taken in 1979. Since moving into the beam in October 1978, both Collaborations had been struggling to get the various components to function properly. During the spring and summer of 1979 after PETRA energy reached 27 GeV, MARK J accumulated a somewhat higher integrated luminosity by about 10–20%, and hence a larger

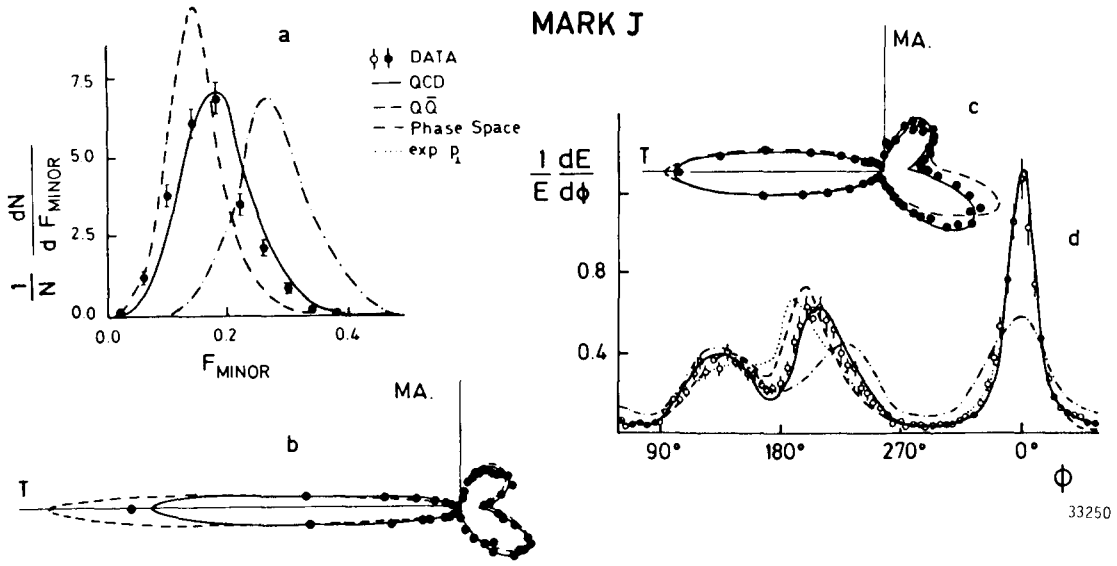

Fig. 3.10. (a) The MARK J [3.24] distribution $N^{-1}\,dN/dF_{minor}$ in the fraction of the visible energy flow of the entire event which is projected along the minor axis (perpendicular to the event plane). (b) Comparing the data with QCD, and $q\bar{q}$ models, using energy flow diagrams in the thrust major event plane for events with $O_B > 0.3$, $F^n_{thrust} > 0.98$ or $\theta_{minor} > 60°$. (c) Same as (b) but with $F^n_{thrust} < 0.98$ and $\theta_{minor} < 60°$. (d) The unfolded energy flow diagram of (c) compared with the models of QCD, $q\bar{q}$, phase space, and a $q\bar{q}$ model with a $\exp(-P_T/650\,\text{MeV}/c)$ fragmentation distribution.

number of total hadronic events. However it is not meaningful to compare the total number of three-jet events. While the event of fig. 3.3 consists clearly of three jets, reduction of the angle between two of the jets changes smoothly to a two-jet event. Thus the number of three-jet events depends sensitively on the cut used. The MARK J [3.29] advantage of having a slightly larger number of hadronic events compared with TASSO is, however, more than offset by the more effective method of three-jet analysis employed by TASSO.

3.3.3. PLUTO

The analysis of the PLUTO data [3.6] was carried out by the method of Brandt and Dahmen [3.11] described in section 3.2.2. In this method, three-jet events are characterized by a high triplicity T_3 but a relatively low thrust T, say <0.8. The original results of PLUTO are shown in fig. 3.11, where for $\tau = 1$, 2, 3 C^*_τ denotes the partition S_τ of section 3.2.2 that gives the triplicity. An example of a three-jet event from PLUTO is shown in fig. 3.12, where the triplicity plane denotes of course the plane determined by the three $\hat{m}_\tau$ of (3.25).

As an independent approach, the PLUTO group has also analyzed [3.21] all hadronic events in terms of separate hadronic jets as obtained by a cluster analysis method described in section 3.2.5. The specific procedure followed is the one by Daum, Meyer and Bürger [3.18]. The result is shown in fig. 3.13. It is seen from this figure that the number of three-jet events is about 45% of that of two-jet events. This ratio gives a clear demonstration of the fact that the number of three-jet events depends sensitively on the cut used, as discussed in section 3.3.2. This cluster analysis also gives a fair number of four-jet events, but virtually no five-jet or six-jet events.

3.3.4. JADE

An example of the JADE three-jet events is shown in fig. 3.14 [3.30]. The data on the planarity

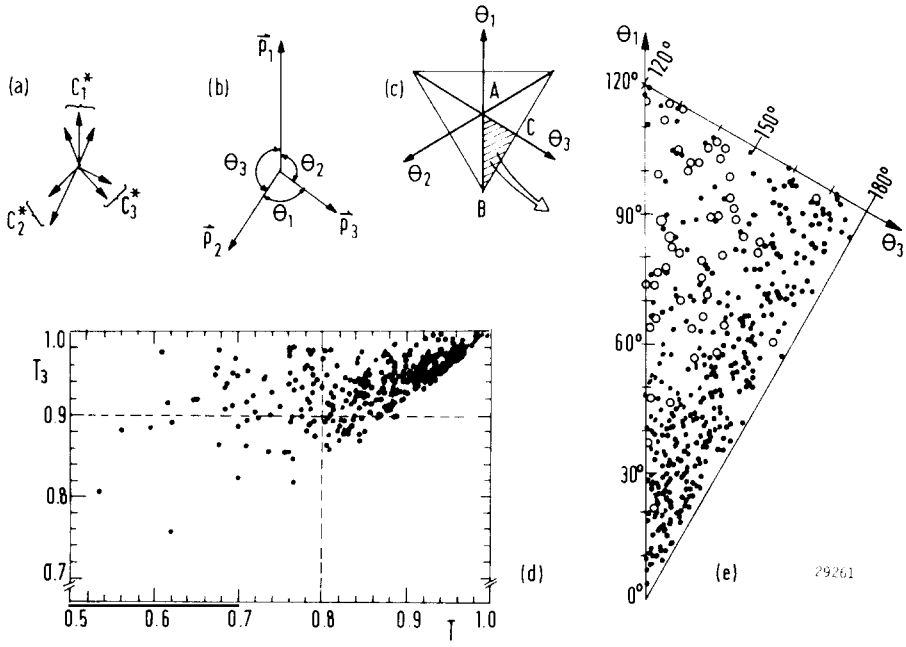

Fig. 3.11. Momentum configuration of hadrons (a) and jets (b) obtained by grouping hadrons into three classes according to the Brandt–Dahmen method [3.11]. A Dalitz plot (c) can be spanned by the angles between the jets whose shaded area only is populated. Nearly symmetrical three-jet events will be situated near point A. The data at $W = 27.6$, 30 and 31.6 GeV are shown in a scatter diagram of triplicity T_3 versus thrust T (d) and in the angular Dalitz plot (e). In (d) planar events will be in the upper left of the plot characterized by low thrust and high triplicity, e.g., $T < 0.8$ and $T_3 > 0.9$. Events falling in this category show up as large circles in (e). The data are from PLUTO [3.6].

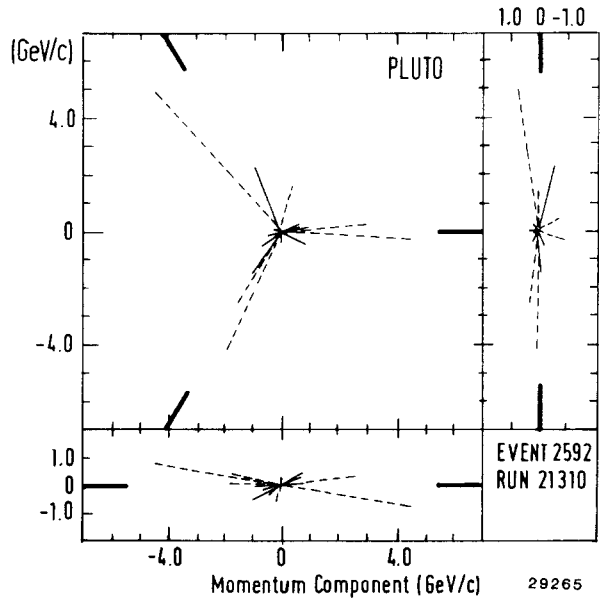

Fig. 3.12. Momentum vectors of a PLUTO [3.6] event ($W = 31.6$ GeV) with high triplicity and low thrust projected onto the triplicity plane (top left), onto a perpendicular plane normal to the fastest jet (top right) and onto a plane containing the direction of the fastest jet (bottom). Solid and dotted lines correspond to charged and neutral particles, respectively. The directions of the jet axes are indicated as fat bars near the margins of the figures.

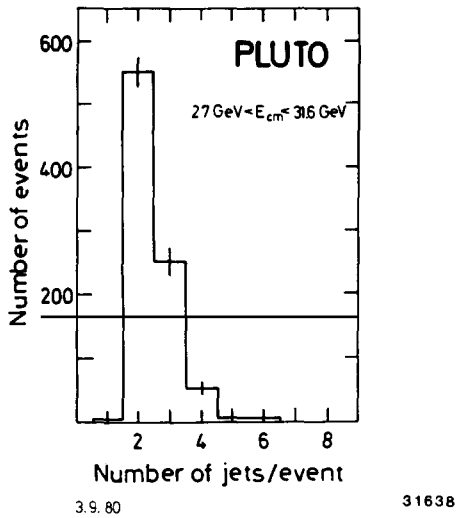

Fig. 3.13. PLUTO [3.21] distribution of number of jets as reconstructed by the cluster algorithm from the combined $W = 27$–32 GeV data.

$Q_2 - Q_1$ distribution (see section 2.5) is given in fig. 3.15 [3.7]. JADE has also used the Ellis–Karliner method [3.13] described in section 3.2.4. In this method, the thrust of the jets 2 and 3 in their own center-of-mass system is called T^* (see fig. 3.1). Assuming that all observed particles are massless, JADE made the interesting comparison between the T^* at $W = 30$ GeV for planar non-colinear events defined by $Q_2 - Q_1 > 0.07$ with the thrust T of all events at $W = 12$ GeV. This comparison is shown in fig. 3.16. The two distributions fall on top of each other, leading to the same conclusion as drawn from fig. 3.5, namely, for high-energy planar events the particles are as collimated around three axes as particles are collimated around the common jet axis at lower energies.

3.3.5. CELLO

By the time the CELLO detector was moved into the beam in March 1980 each of the other Collaborations had already collected a large number of three-jet events. We present here only one figure based on their data [3.31]. In fig. 3.17, the p_T and thrust distributions are compared with $q\bar{q}$ models with two different fragmentation processes. That both models fail to describe the data implies again the necessity of including $e^+e^- \to q\bar{q}g$.

Although the data presented in this section are taken from the early publications and hence the statistics are relatively low, all the conclusions discussed here are supported by later data with much larger numbers of events.

3.4. Determination of the quark–gluon coupling constant α_s

3.4.1. Results

The MARK J Collaboration is the first group to determine the quark–gluon strong coupling constant α_s, defined in a way analogous to the fine-structure constant α of QED. By now, each of the five Collaborations at PETRA has published at least one determination of α_s, mostly at center-of-mass energy W around 30 GeV. The results are listed in table 3.1 arranged in the order of publication. Only journal publications with the entire Collaboration as the author have been included, but not the numerous conference reports and summaries.

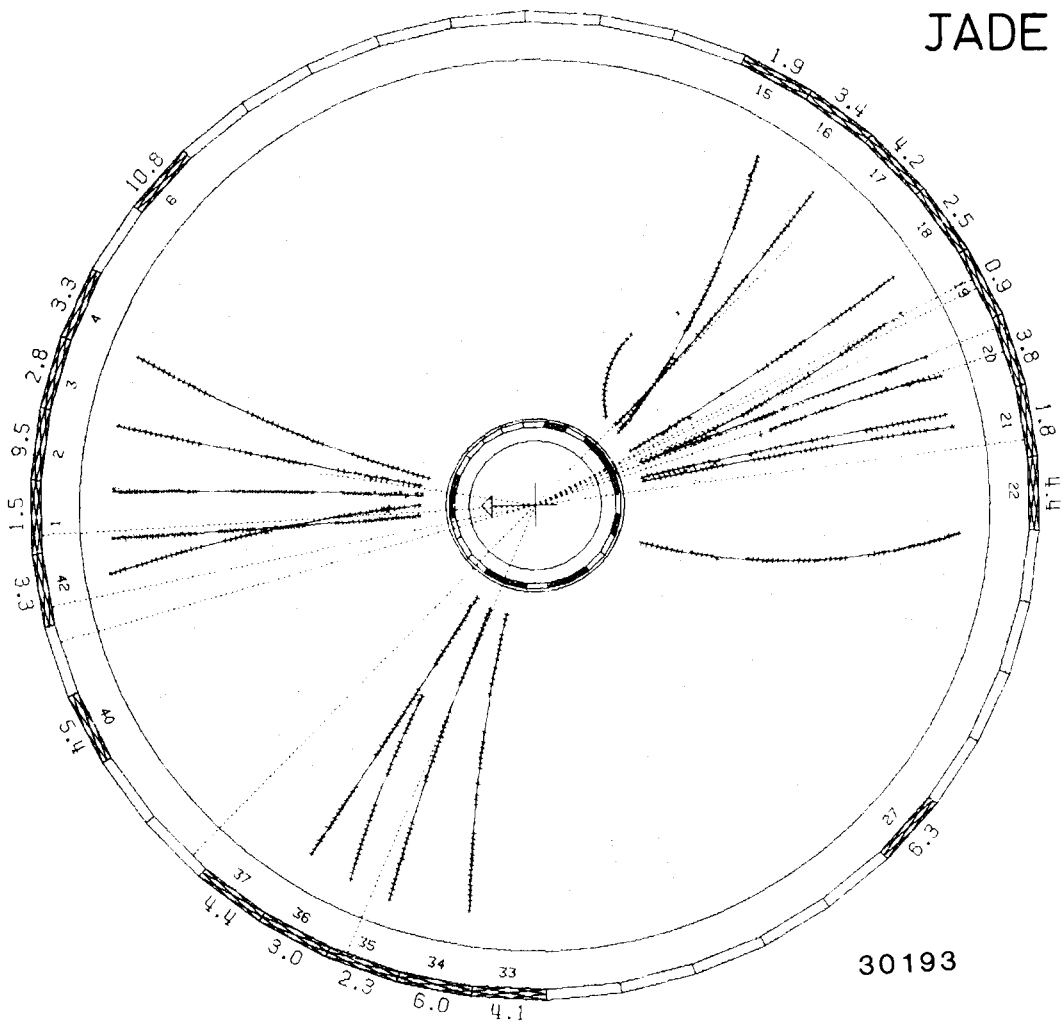

Fig. 3.14. A JADE three-jet event viewed along the beam axis.

Theorists tell us that it is very easy to determine α_s: it is essentially the ratio of the numbers of three-jet to two-jet events. Actually it is not so simple due to the fragmentation of quarks and gluons and the resulting ambiguity between two- and three-jet events already mentioned in section 3.1.

Consequently, the actual procedure of obtaining α_s, to be explained in section 3.4.4, is quite complicated. This is to be contrasted with the observations of the three-jet events discussed in section 3.3. There, once a three-jet analysis is used to determine the direction along which the event should be viewed, the three jets are clearly visible to the naked eye, as illustrated for example in fig. 3.3. Different track fitting programs may give slightly different momenta, and different three-jet analyses may give slightly different directions, but that the event has a qualitatively different topology from the two-jet events remains unchanged. Here, to find the value of α_s, we must at least ascertain a suitable cut, fit for the fragmentation parameters, and select a QCD model for comparison. Consequently, intimate acquaintance with the details of the experimental apparatus and data is essential.

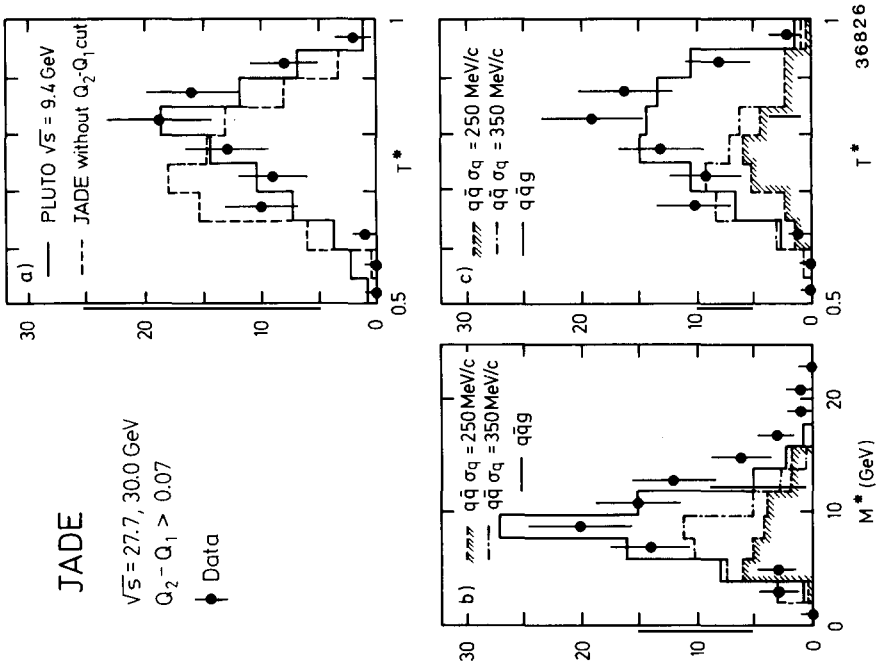

Fig. 3.16. The three-jet nature of the "planar" $(Q_2 - Q_1 > 0.07)$ events of JADE [3.7]. (a) The observed distribution of T^* (the thrust of the fat jet in its rest system) for the planar events compared with the two-jet thrust distribution obtained by PLUTO at $W = 9.4$ GeV (full-line histogram). The broken-line histogram shows the normalized T^* distribution for all events without the planarity cut. (b) The observed invariant mass (M^*) distribution of the fat jet system for the planar events compared with the distributions expected from the $q\bar{q}$ model with $\sigma_q = 250$ MeV/c (shaded, broken-line histogram) and with $\sigma_q = 350$ MeV/c (dot-dashed histogram). The full-line histogram represents the M^* distribution predicted by the $q\bar{q}g$ model. (c) The same observed T^* distribution as shown in (a) compared with the predictions of the $q\bar{q}$ and $q\bar{q}g$ models.

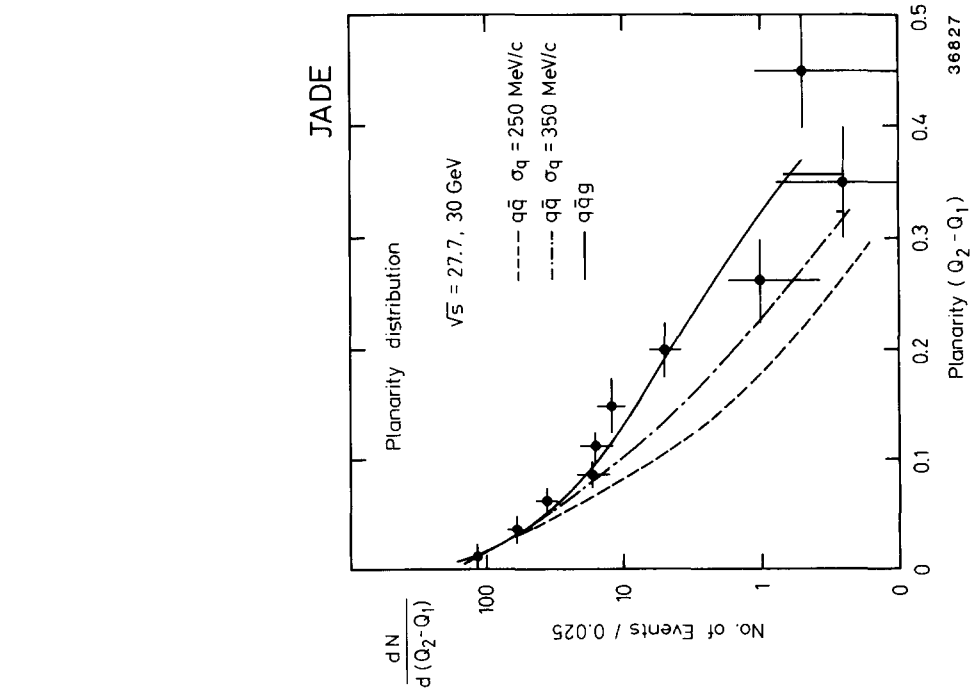

Fig. 3.15. The JADE [3.7] planarity distribution compared with model predictions.

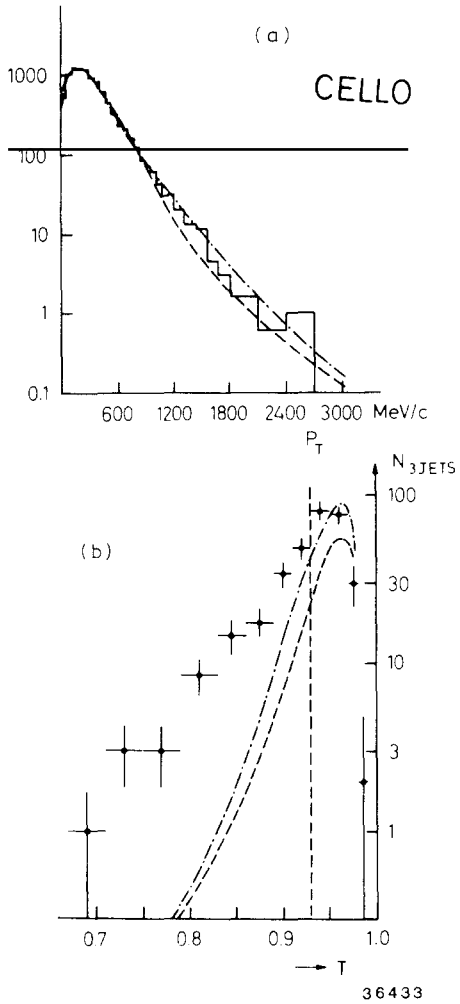

Fig. 3.17. Comparison of CELLO [3.31] data with different $q\bar{q}$ fragmentation models. (a) Distribution of p_T in a jet for charged particles in the 2-jet sample. (i) (histogram) experimental distribution, (ii) (dashed curve) Gaussian dependence in the fragmentation process with $\sigma_q = 300$ MeV/c. (iii) (dash-dotted) exponential dependence with $\sigma_q = 420$ MeV/c. High p_T values are overestimated. (b) Distribution of thrust T calculated from the jet momenta in 3-jet events. Experimental distribution and $q\bar{q}$ model calculations (dashed and dash-dotted curves) using the p_T distribution (ii) and (iii) described in (a). Both models fail to describe the data.

3.4.2. QCD diagrams

Before describing the QCD models useful in the experimental determination of α_s, we describe briefly the Feynman diagrams involved.

The lowest-order diagram for $e^+e^- \to q\bar{q}$ is shown once again in fig. 3.18a. For radiative correction to the order α_s, there are, as shown in fig. 3.18b, three diagrams, two of which (the second and third ones) have the radiative correction on the external legs. To avoid drawing too large a number of diagrams, those with radiative corrections on the external legs are omitted for radiative corrections to order α_s^2; the rest are shown in fig. 3.18c.

Similarly, for the process $e^+e^- \to q\bar{q}g$, the lowest-order QCD diagrams are shown once again in fig.

Table 3.1
List of experimental results on the quark–gluon coupling constant α_s published by the Collaborations at PETRA. The symbol * means that the systematic error is not given in the original publication

Coll.	Values of α_s	Order	Method of analysis	Date of recept by journal	Ref.
MARK J	$0.23 \pm 0.02 \pm 0.04$	First order	Oblateness distribution	November 1979	[3.32]
JADE	$0.17 \pm 0.04 \pm$ *	First order	Planarity distribution	December 1979	[3.7]
TASSO	$0.17 \pm 0.02 \pm 0.03$	Partial second order	Sphericity and aplanarity distribution	May 1980	[3.10]
PLUTO	$0.15 \pm 0.03 \pm 0.02$	First order	Cluster analysis and parton thrust (x_1) distribution	October 1980	[3.21]
PLUTO	$0.20 \pm 0.02 \pm$ *	First order	Energy–energy correlation	November 1980	[3.33]
CELLO	$0.16 \pm 0.01 \pm 0.03$	First order	Thrust and oblateness distribution	April 1982	[3.34]
CELLO	$0.21 \pm 0.01 \pm$ *	First order	Energy–energy correlation	May 1982	[3.35]
CELLO	$0.15 \pm 0.02 \pm$ *	First order	Energy–energy correlation asymmetry	May 1982	[3.35]
JADE	$0.16 \pm 0.015 \pm 0.03$	Second order	Cluster analysis and parton thrust (x_1 and $x_\perp$) distributions	September 1982	[3.36]
CELLO	See text and reference	First order	Various methods of analysis	October 1982	[3.37]
MARK J	$0.13 \pm 0.01 \pm 0.02$	Second order	Energy–energy correlation asymmetry	May 1983	[3.38]

3.19a while those for radiative correction to order α_s are given in fig. 3.19b. The QCD diagrams for the four-jet processes $e^+e^- \to q\bar{q}gg$ and $e^+e^- \to q\bar{q}q'\bar{q}'$ are shown in fig. 3.2.

Any differential cross section is calculated from the square of the corresponding matrix element, obtained by adding together the contributions from various Feynman diagrams. We list here the various interferences that contribute orders of α_s^0, α_s and α_s^2 in the cross sections. For brevity, we omit the words "the diagrams of"; thus for example "3.18a and 3.18b" means the contributions to the cross section from the interference of the diagrams of fig. 3.18a with those of 3.18b.

To order α_s^0: $e^+e^- \to q\bar{q}$ only from the square of 3.18a.

To order α_s: (i) two jets – 3.18a and 3.18b.
(ii) three jets – square of 3.19a.

To order α_s^2: (i) two jets – square of 3.18b, 3.18a and 3.18c.
(ii) three jets – 3.19a and 3.19b.
(iii) four jets – square of 3.2a; square of 3.2b.

3.4.3. QCD models

The value of α_s is determined by comparing the experimental data with a suitable QCD model. By a

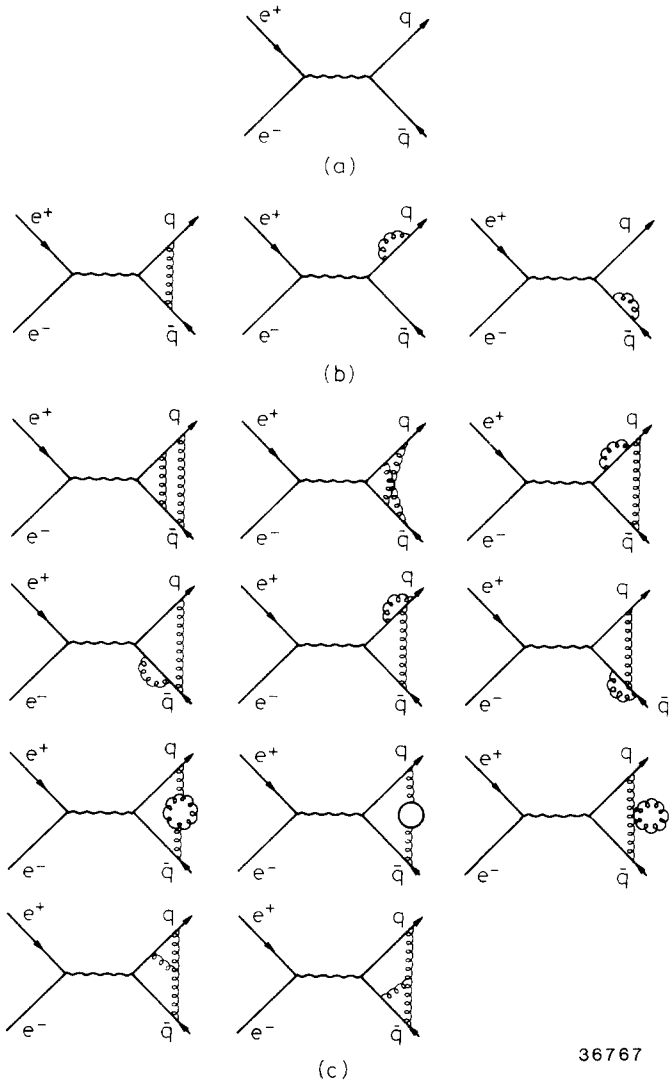

Fig. 3.18. Diagrams for $e^+e^- \to q\bar{q}$: (a) lowest order; (b) radiative correction to order α_s; and (c) radiative correction to order α_s^2.

QCD model, we mean a perturbative QCD calculation followed by a fragmentation scheme. Unavoidably, some parameters are needed to describe quark fragmentation, and further ones for gluon fragmentation. These parameters are also determined by the experimental data.

There are two general classes of QCD models used at PETRA: the Hoyer et al. or independent fragmentation models, and the Lund or string models. We describe both classes.

(A) *Hoyer et al. or independent fragmentation models*

The pioneering work on QCD model is due to Hoyer, Osland, Sander, Walsh and Zerwas [3.39]. They use the complete first-order theory [3.8], and apply a Field–Feynman jet fragmentation [3.28] independently to the quark, the antiquark, and the gluon. Their original program has been improved by Meyer [3.28] of the TASSO Collaboration with the inclusion of heavy quarks. At both PETRA and PEP, this improvement is used in all applications.

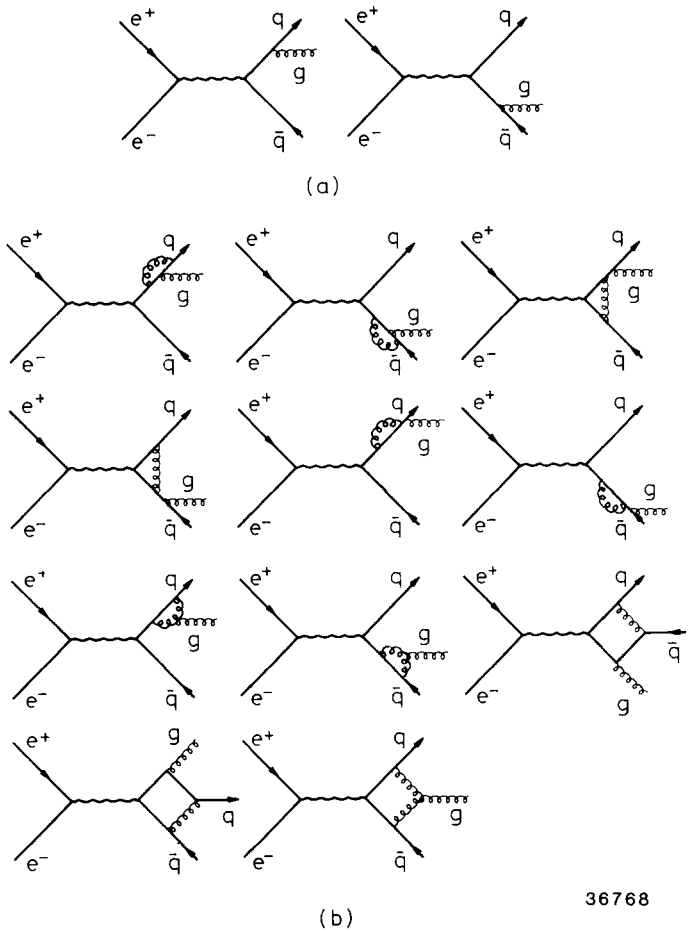

Fig. 3.19. Diagrams for $e^+e^- \to q\bar{q}g$: (a) lowest order; (b) radiative correction due to the gluon to order α_s.

The basic idea of the models of this type is shown schematically in fig. 3.20a. Later improvements of the original model include taking more QCD perturbative diagrams into account. Three general versions are currently in use at PETRA.

(a) First order. This is the original version of Hoyer et al., with the Meyer improvement.

(b) Partial second order. Ali, Pietarinen, Kramer and Willrodt [3.40] have modified the above first-order model by including the effects of producing four jets. In other words, with reference to the list of section 3.4.2 for the order α_s^2, (iii) is included but not (ii). Such a partial inclusion of α_s^2 effects require a more detailed discussion.

In QED, the masslessness of the photon leads to infrared divergences. Similarly, in QCD the masslessness of the gluon leads to infrared divergences of a somewhat more complicated nature. Physically meaningful results are obtained through cancellations in cross sections, such as between (ii) and (iii) of order α_s^2. Because of this necessary cancellation, in principle it is not acceptable to include (iii) but not (ii). Ali, Pietarinen, Kramers and Willrodt get around this problem by introducing an

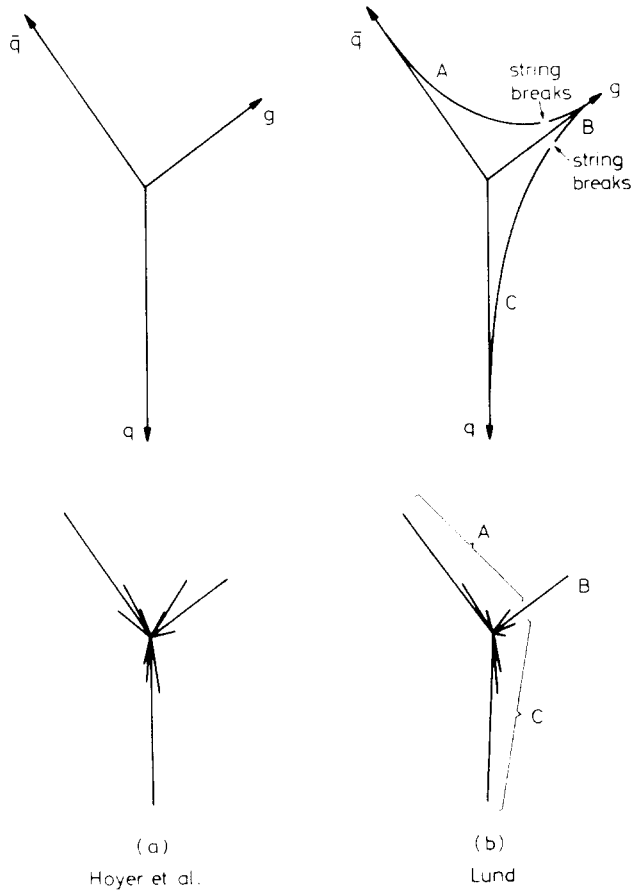

Fig. 3.20. Schematic representation of fragmentation models.

acoplanarity cut of

$$A > 0.05$$

for four jets. Thus this partial second-order model contains this additional parameter.

(c) Second order. It is clearly desirable to have a complete second-order model. The computation of the large number of Feynman diagrams shown in fig. 3.19b, which contribute to (ii) of order α_s^2, requires a heroic effort. Such a complete second-order QCD calculation was first accomplished by Ellis, Ross and Terrano [3.41], and also later by Vermaseren, Gaemers and Oldham [3.42] and by Fabricius, Schmitt, Kramer and Schierholz [3.43]. With reference to table 3.1, the version of Fabricius et al. is used by the JADE Collaboration [3.36], while that of Ellis et al. is used by the MARK J Collaboration [3.38] in their respective second-order determination of α_s. Because the jets fragment independently, the case of four jets is essentially the same as that of three jets.

(B) *Lund or string models*

The Lund group of Andersson, Gustafson and Sjoestrand [3.44] had the idea of combining fragmentation with the concept of the color string, which is stretched from the quark via the gluon to the

antiquark. This color string is envisaged to break first to produce a hadron carrying a sizeable fraction of the gluon energy. The remainder of the gluon energy is then shared between the two pieces of the broken string, which are fragmented independently in their respective center-of-mass systems [3.44]. This Lund fragmentation process is shown schematically in fig. 3.20b.

(a) First order. This is the original version, and is used extensively at PETRA.

(b) Second order. This is obtained by combining the Lund idea with the complete second-order QCD calculation mentioned above [3.41, 3.42, 3.43]. However, unlike the Hoyer et al. or independent fragmentation model, the extension of the Lund or string model to the case of four jets is not entirely straightforward. The basic problem is the following. For the process $e^+e^- \to q\bar{q}gg$, the Lund model requires the specification of the way the color string is stretched from the quark to one of the gluons, to the other gluon, and finally to the antiquark. As discussed in section 3.4.2, however, the second-order cross section comes from two matrix elements, which may have different specifications for the ordering of the color string. A solution to this mismatch is to introduce a further parameter specifying the relative probability for the ordering of the two gluons in the color string. This type of problem is to be expected because the perturbative QCD is carried out quantum mechanically while the fragmentation is semi-classical.

Finally, we add the remark that in QCD the value of α_s depends on the renormalization scheme. In all these QCD models, the $\overline{\text{MS}}$ scheme (modified minimum subtraction scheme) is used. Therefore α_s always means α_s in this $\overline{\text{MS}}$ scheme.

3.4.4. Procedures to determine α_s

It is seen from table 3.1 that the first determination of α_s by the MARK J Collaboration gives a result significantly larger than those obtained by the other Collaborations using Hoyer et al. or independent fragmentation models. The reason remains unclear; it is doubtful that the method of energy flow is to be blamed.

In the comparison of experimental data with the QCD models for the purpose of determining α_s, the following point deserves emphasis. Both the incident electron and the incident positron may emit a photon, leading to e^+e^- annihilation at a lower energy. This initial state radiation must be taken into account, as discussed in [3.45].

We give here briefly three examples of the procedures used in the determination of α_s.

(A) TASSO [3.10]. The TASSO Collaboration used the partial second order of Ali et al. [3.40]. The determination is based on the S–A (sphericity–aplanarity) distribution of their high sphericity data ($S > 0.25$). These data are analyzed by two different procedures.

In the first procedure, α_s is determined without any assumptions on the parameters of jet fragmentation. As shown in table 3.2 the value of α_s is totally insensitive to the values of the fragmentation parameters, and the result is $\alpha_s = 0.16 \pm 0.04$ (statistical).

In the second procedure, this statistical error is reduced by using the fragmentation parameters of section 2.9. The resulting value of α_s is the one given in table 3.1.

(B) JADE [3.36]. The JADE Collaboration uses the second-order QCD result of Fabricius et al. [3.43]. The determination is based on the distributions as functions of x_1 and $x_\perp$, defined as follows. x_1 is the largest fractional energy of the jets

$$x_1 = \frac{2}{W} \max_\tau E^{(\tau)}, \tag{3.58}$$

where the $E^{(\tau)}$ are given by (3.19). Remember that, in the derivation of (3.19), the jet masses are

Table 3.2
Fitted values of α_s and σ_q obtained by TASSO [3.10] for different input values of a_F and $P/(P+V)$. The fits are performed with the S–A distribution of the high sphericity data ($S > 0.25$)

	$P/(P+V)$				
a_F	0.1	0.3	0.5	0.7	0.9
0.1	$\alpha_s = 0.17 \pm 0.03$ $\sigma_q = 0.44 \pm 0.11$	0.17 ± 0.03 0.46 ± 0.10	0.17 ± 0.03 0.47 ± 0.10	0.16 ± 0.03 0.48 ± 0.09	0.16 ± 0.03 0.48 ± 0.08
0.3	$\alpha_s = 0.17 \pm 0.04$ $\sigma_q = 0.42 \pm 0.12$	0.16 ± 0.04 0.44 ± 0.11	0.16 ± 0.04 0.46 ± 0.10	0.15 ± 0.04 0.47 ± 0.09	0.15 ± 0.04 0.48 ± 0.08
0.5	$\alpha_s = 0.17 \pm 0.04$ $\sigma_q = 0.35 \pm 0.12$	0.16 ± 0.04 0.38 ± 0.12	0.16 ± 0.04 0.41 ± 0.12	0.15 ± 0.04 0.43 ± 0.10	0.14 ± 0.04 0.44 ± 0.09
0.7	$\alpha_s = 0.17 \pm 0.03$ $\sigma_q = 0.28 \pm 0.09$	0.17 ± 0.04 0.30 ± 0.10	0.16 ± 0.04 0.33 ± 0.10	0.15 ± 0.05 0.36 ± 0.10	0.14 ± 0.05 0.39 ± 0.09
0.9	$\alpha_s = 0.17 \pm 0.03$ $\sigma_q = 0.21 \pm 0.08$	0.17 ± 0.04 0.23 ± 0.08	0.16 ± 0.04 0.26 ± 0.08	0.15 ± 0.04 0.30 ± 0.09	0.14 ± 0.05 0.33 ± 0.08

neglected, and therefore $E^{(\tau)}$ is the same as the magnitude of the corresponding momentum $\boldsymbol{P}^{(\tau)}$. With this notation, $x_\perp$ is defined to be $2/W$ times the magnitude of the component of momenta of the other two jets perpendicular to the direction of x_1.

The comparison of the experimental and theoretical distributions in these two variables x_1 and $x_\perp$ is shown in fig. 3.21. The final value of α_s is the one given in table 3.1.

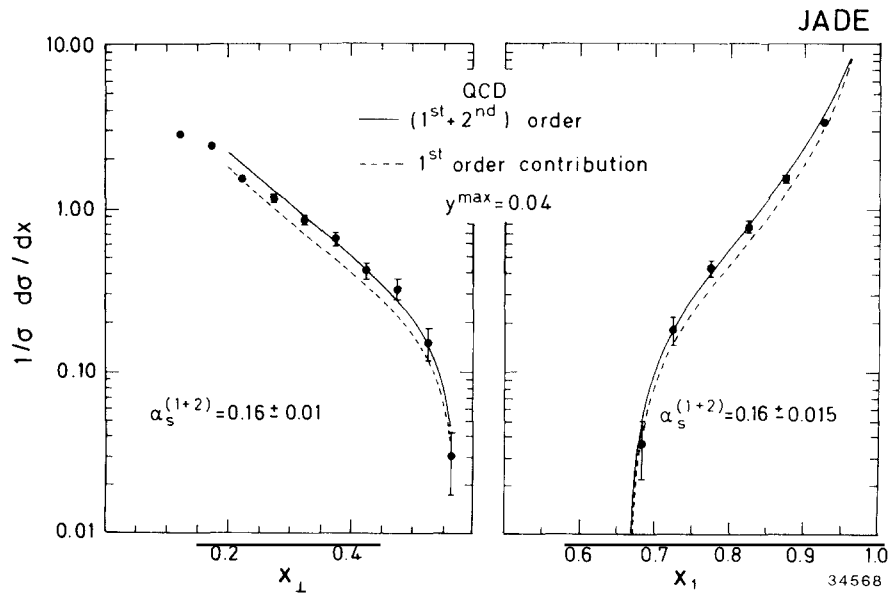

Fig. 3.21. The JADE [3.36] corrected x_1 and $x_\perp$ distributions together with the second-order QCD best fit. The first-order contribution of this fit is indicated by the broken curve. The fit does not include data above $x_1 = 0.85$ for the x_1-fit and below $x_\perp = 0.30$ for the $x_\perp$-fit.

(C) MARK J [3.38]. The MARK J Collaboration uses the calculation of Ali et al. [3.40] and completes it by doing a Monte Carlo integration of the second-order virtual contributions computed by Ellis et al. [3.41]. The determination is based on the asymmetry in the energy–energy correlation function defined by [3.46].

$$A(\cos\chi) = \frac{1}{\sigma}\left\{\frac{\mathrm{d}\Sigma}{\mathrm{d}\cos\chi}(\pi-\chi) - \frac{\mathrm{d}\Sigma}{\mathrm{d}\cos\chi}(\chi)\right\} \tag{3.59}$$

with

$$\frac{1}{\sigma}\frac{\mathrm{d}\Sigma}{\mathrm{d}\cos\chi} = \frac{1}{N}\sum_{\text{event}}^{N}\sum_{i,j}\frac{E_iE_j}{E_{\text{vis}}^2}\delta(\cos\chi_{ij} - \cos\chi)\,, \tag{3.60}$$

where the sum is over all hadronic events, E_i is the energy measured in a given solid angle element i, E_{vis} is the total event energy, and χ_{ij} is the angle separating the directions of the energy depositions. This definition used by MARK J differs from the usual one in the appearance of E_{vis} instead of W. The energy–energy correlation function has previously been used for the determination of α_s by PLUTO, MARK II, MAC and CELLO [3.47].

The comparison of the experimental and theoretical energy–energy correlation function is shown in fig. 3.22. The final value of α_s is the one given in table 3.1.

3.4.5. Comparison of Hoyer et al. and Lund models

The question of the influence of the fragmentation model used, Hoyer et al. or independent

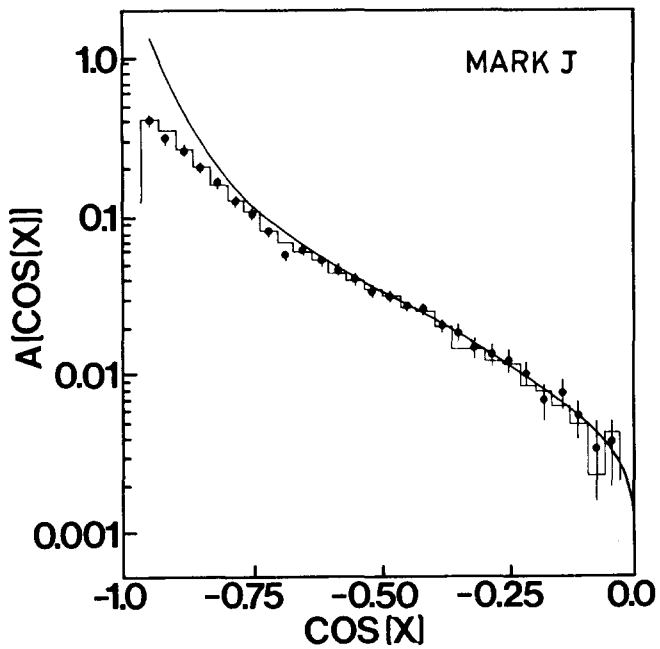

Fig. 3.22. MARK J [3.38] asymmetry data compared with predictions at parton level (curve) for $\alpha_s = 0.13$ and predictions for the two fragmentation models (Lund, Ali et al.; histogram) for the best fit values of α_s. These two histograms are indistinguishable.

fragmentation vs. Lund or string, on the value of α_s has been studied in first order by both the JADE [3.36] and CELLO [3.37] Collaborations. Their analyses reach different conclusions. JADE uses both fragmentation models to determine the corrected x_1 and $x_\perp$ distributions, and has found that the corrections are, within the errors, independent of the fragmentation scheme used [3.36]. On the other hand, CELLO has found that, depending on the distribution used, the Lund model gives α_s between 28% to 67% higher than the model of Hoyer et al. The two extreme cases are:

Smallest difference: three-jet fraction from events with oblateness larger than 0.3

Lund	$\alpha_s = 0.255 \pm 0.050$	
Hoyer et al.	$\alpha_s = 0.200 \pm 0.035$	ratio = 1.28

Largest difference: energy–energy correlation function

Lund	$\alpha_s = 0.25 \pm 0.04$	
Hoyer et al.	$\alpha_s = 0.15 \pm 0.02$	ratio = 1.67 .

In particular, this result from CELLO implies that, contrary to the earlier hope, the energy–energy correlation function is sensitive to fragmentation.

3.5. Properties of the gluon

3.5.1. Spin of the gluon

Since QCD is a gauge theory, its gluon must have spin 1. Experimentally, the gluon spin has been determined to be 1 by three Collaborations at PETRA: TASSO [3.14], PLUTO [3.21] and CELLO [3.31].

Before fragmentation, the $q\bar{q}g$ Dalitz plot can be described by the fractional energy variables

$$x_i = E_i/E_b \tag{3.61}$$

where E_i is the energy of quark or gluon i and $E_b = \frac{1}{2}W$ is the incident beam energy, so that

$$x_1 + x_2 + x_3 = 2 . \tag{3.62}$$

We choose to order them such that

$$x_3 \leqq x_2 \leqq x_1 \tag{3.63}$$

which implies

$$\tfrac{2}{3} \leqq x_1 \leqq 1 . \tag{3.64}$$

If the quarks and the gluon have negligible masses relative to E_b, the x_i are determined by the angles θ_i

shown in fig. 3.1:

$$x_i = \frac{2 \sin \theta_i}{\sin \theta_1 + \sin \theta_2 + \sin \theta_3}. \tag{3.65}$$

[The x_1 here is the same as the x_1 of (3.58), and (3.65) is essentially (3.19) rewritten in different notations, where the θ_i are the $\phi^{(i)}$ rearranged such that (3.63) is satisfied.]

Fig. 3.1b shows the angle $\tilde{\theta}$ suggested by Ellis and Karliner [3.13] to discriminate between vector and scalar gluons. In this figure, the $q\bar{q}g$ system has been Lorentz boosted to the center-of-momentum frame of partons 2 and 3. Assuming negligible quark and gluon masses, $\cos \tilde{\theta}$ is given by

$$|\cos \tilde{\theta}| = \frac{x_2 - x_3}{x_1} = \frac{\sin \theta_2 - \sin \theta_3}{\sin \theta_1}. \tag{3.66}$$

The distribution functions for the x_i in QCD and in the scalar gluon model, after averaging over the production angles relative to the incident e^+e^- beams, are given by [3.8]

$$\text{vector:} \quad \frac{1}{\sigma_0}\left(\frac{d\sigma}{dx_1\, dx_2}\right)_V = \frac{2\alpha_s}{3\pi}\left[\frac{x_1^2 + x_2^2}{(1-x_1)(1-x_2)} + \text{cyclic permut. of } 1,2,3\right] \tag{3.67}$$

$$\text{scalar:} \quad \frac{1}{\sigma_0}\left(\frac{d\sigma}{dx_1\, dx_2}\right)_S = \frac{\tilde{\alpha}_s}{3\pi}\left[\frac{x_3^2}{(1-x_1)(1-x_2)} + \text{cyclic permut. of } 1,2,3\right]. \tag{3.68}$$

To avoid a number of difficulties associated with the singularities of these distributions at $x_1 = 1$, the TASSO Collaboration [3.14] uses the kinematic region defined by $x_1 < 0.9$. In the three-jet region so defined, the distributions are not strongly peaked either for vector or scalar gluons, making the dependence on fragmentation smearing small. As a further precaution, only distributions normalized to the number of events in *this* kinematic region are used. This means that the distinction between vector and scalar gluons is made only on the basis of the difference in *shape* of the two distributions in the three-jet region. In this way one eliminates, on the parton level, all dependence of the spin analysis on the values of the strong coupling constant α_s and $\tilde{\alpha}_s$ for vector and scalar gluons, respectively.

TASSO has applied the Wu–Zobernig [3.1] three-jet analysis to 16000 hadronic events, and computed the x_i using (3.65). After a cut of $x_1 < 0.9$, which implies a minimum angle of 70° between the jets, 1600 events survive. In fig. 3.23 these events, which include higher statistics than those given in [3.14], are plotted as a function of the Ellis–Karliner angle, and compared with the Monte Carlo predictions under the two assumptions of spin 1 and spin 0. Spin 0 is clearly ruled out.

An alternative method of analysis [3.48] uses the variable

$$\begin{aligned}\xi &= 2\left[\frac{x_3^2}{(1-x_1)(1-x_2)} + \text{permut.}\right] \Big/ \left[\frac{x_1^2 + x_2^2}{(1-x_1)(1-x_2)} + \text{permut.}\right] \\ &= 2\left(\frac{x_1^2 + x_2^2 + x_3^2}{x_1^3 + x_2^3 + x_3^3} - 1\right)\end{aligned} \tag{3.69}$$

which is obtained from the right-hand sides of (3.67) and (3.68).

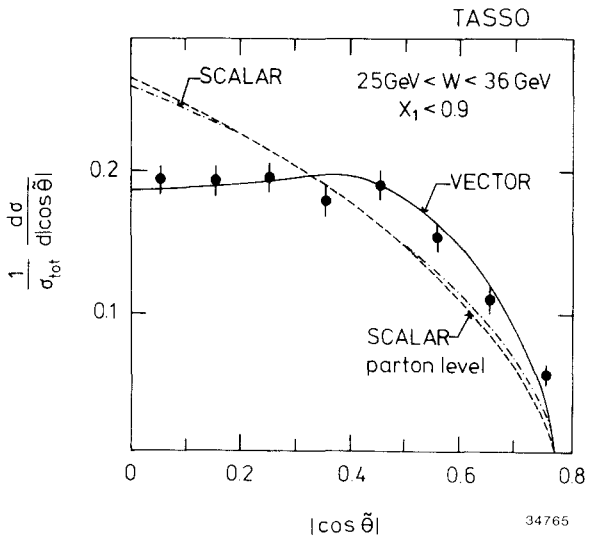

Fig. 3.23. Observed distribution of the TASSO data [3.14] in the region $x_1 < 0.9$ as a function of the Ellis–Karliner angle $\tilde{\theta}$. The solid line shows the QCD Monte Carlo prediction, the dashed line the prediction for the scalar gluons (--- for Monte Carlo scalar model; -·-·- for scalar model of parton level). All curves are normalized to the number of observed events.

Using the cluster analysis method, the PLUTO Collaboration [3.21] has plotted the x_1 distributions of the three-jet events as shown in fig. 3.24(a and b). The solid curve in fig. 3.24a is the prediction from first order QCD for vector gluons. A fit of the scalar gluon prediction to the data points yields a χ^2/D.F. = 9.1/4 as shown in fig. 3.24b (dashed curve). If one averages the x_1 distribution for $\frac{2}{3} < x_1 < 0.95$, the predictions for vector and scalar gluons are 0.891 and 0.871 respectively. For the data obtained by PLUTO $\langle x_1 \rangle = 0.893 \pm 0.005$. Hence the hypothesis of scalar gluons is disfavored. Similar plot from the CELLO data [3.31] is shown in fig. 3.25.

3.5.2. Angular distribution of particles in three-jet events

The JADE Collaboration [3.12] has found an interesting and subtle effect in the distribution of hadrons in the three-jet events as a function of the angular variable in the event plane. Their study is motivated by a comparison between the independent fragmentation model of Hoyer et al. [3.39] and the string model of the Lund group [3.44]. In the model of Hoyer et al., the quark, the antiquark, and the gluon fragment independently of each other in essentially identical ways, producing final state mesons with limited momentum transverse to the directions of the original partons.

In the Lund model the fragmentation proceeds along the color flux lines as the primary partons move apart. For $q\bar{q}g$ events, these flux lines are not strung between quark and antiquark directly, but via the gluon as intermediary (see figs. 3.20 and 3.26), because the quark is a color triplet while the gluon is a color octet. For example, if the quark is red (r) while the antiquark is antiblue ($\bar{b}$), then in order to get a color singlet, the gluon must be antired–blue ($\bar{r}b$). Thus the red color line runs from the quark to the gluon, while in the same way the blue color line runs from the gluon to the antiquark. The Lund model is formulated in terms of strings and is kinematically equivalent to a treatment of the gluon as a colinear quark–antiquark pair ($q', \bar{q}'$) with the momentum shared between q' and $\bar{q}'$. Each of the two gluon components form a $q\bar{q}'$ or $q'\bar{q}$ two-jet system with the primary $\bar{q}$ or q, and these two-jet systems are treated in their respective center-of-mass systems, not in the laboratory system (which is also the $q\bar{q}g$

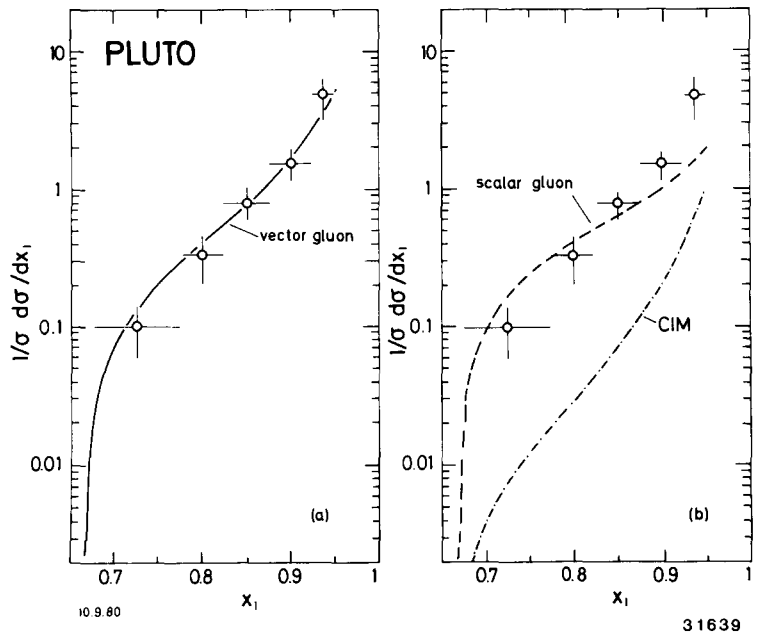

Fig. 3.24. PLUTO [3.21] distribution of the relative energy of the fastest parton (x_1). The data points are corrected for detector acceptance, radiation and hadronisation. The curves are (a) first order QCD, (b) dashed: scalar gluon hypothesis and dash-dotted: CIM (Constituent Interchange Model).

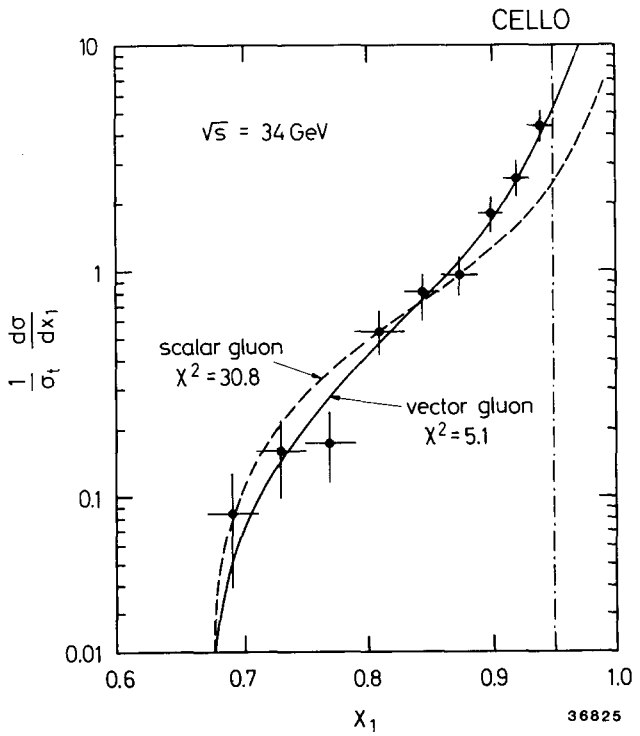

Fig. 3.25. CELLO [3.31] differential cross section of three-jet events with respect to the energy fraction x_1 carried by the most energetic parton. Data are compared to the QCD prediction of vector gluons (full curve) and a scalar gluon model (dashed curve).

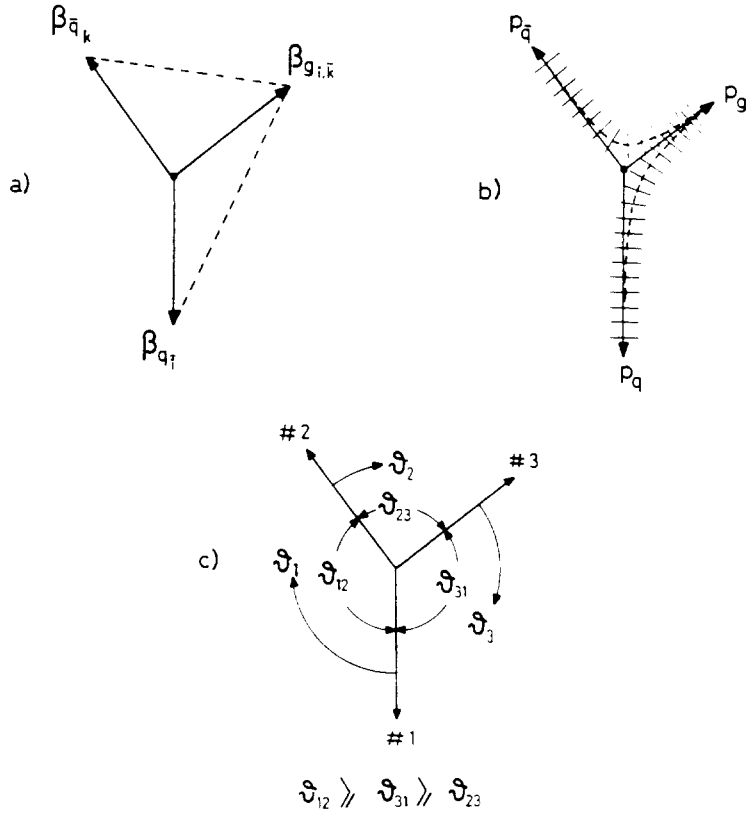

Fig. 3.26. Sketch of the quark and gluon velocities and of the color–anticolor axes (a). Fragmentation along these axes, neglecting transverse momenta, yields particles of the same mass distributed in momentum space along two hyperbolas, as indicated in (b). The broadening due to different masses and transverse momenta is also indicated. The ordering scheme of the observed jets is sketched in (c). θ_{ik} is the angle between the jet axes $\#i$ and $\#k$ projected onto the event plane. This figure is from JADE [3.12].

center-of-mass system). Aside from this Lorentz boost, the mesons within these jets are distributed according to the prescription of Field and Feynman [3.28] (see section 2.8), a special treatment being made only for the leading meson at the gluon corner. Neglecting transverse momenta with respect to the $q\bar{q}'$ and $q'\bar{q}$ jet axes final state particles of the same mass are distributed along hyperbolas in the overall c.m. momentum space as sketched in fig. 3.26b. Therefore the Lund model predicts the production of more particles in the angular region between the gluon and the quark or the antiquark than between the quark and the antiquark.

Fig. 3.27a shows the JADE result [3.12] on the angular distributions of the particles from their three-jet events. The average number of charged and neutral particles per event is plotted as a function of the normalized projected angle θ_i and θ_{ik} are defined in fig. 3.26c. The two model predictions are also shown in fig. 3.27a, and compared in fig. 3.27b.

Apart from the region between jets No. 1 and No. 2, both models describe the data reasonably well. In this region, which is the region between the two quark jets for the majority of events, the model of Hoyer et al. predicts more particles than the Lund model, and the experimental data are in better agreement with the Lund model than with the model of Hoyer et al.

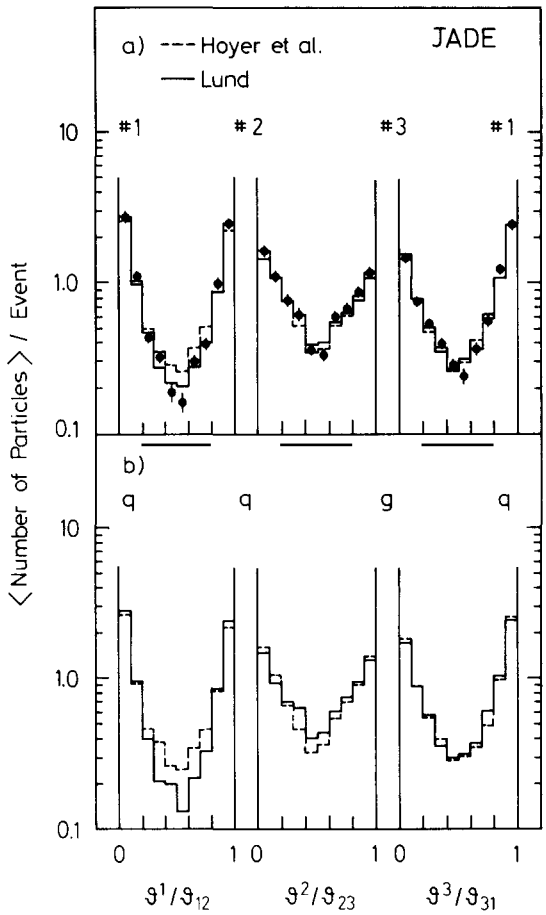

Fig. 3.27. The average number of particles per event between the indicated jet axes versus the normalized projected angle. The data together with the corresponding model predictions are shown in (a), the model predictions, ordered for quark and gluon jets, in (b). The data are from JADE [3.12].

3.5.3. Difference between quark and gluon jets

Ever since the first observation of gluon jets, an intriguing question is: how do we distinguish a gluon jet from a quark jet? Although some differences are expected from QCD, these two kinds of jets turn out to be remarkably similar. For example, JADE has measured the ratio of photon energy to charged particle energy separately for the three jets, and the results are [3.49]

Jet 1: 0.47 ± 0.01

Jet 2: 0.46 ± 0.01

Jet 3: 0.44 ± 0.02

where the errors are statistical but the systematic errors are expected to be small.

Recently, the JADE Collaboration has found experimental evidence that the mean transverse momentum $\langle p_T \rangle$ of particles within a jet is larger for the gluon jet than for the quark jet [3.50]. Since the spin of the gluon is 1 (section 3.5.1), jet 3, which is the least energetic one, is most likely to be the gluon

jet. More precisely, on the basis of Monte Carlo calculation at center-of-mass energies of 33 GeV (22 GeV) the probability for jet #1, #2 and #3 being closest to the gluon direction is 12% (9%), 22% (20%) and 51% (34%), respectively. The probabilities do not add up to 100%; residual $q\bar{q}$ events faking three-jet structures account for the difference. Fig. 3.28 shows the probabilities η_j for jet j being closest to the gluon direction as a function of $E_j = x_j W/2$ at $W = 33$ GeV. Note that

$$W/3 \leqq E_1 < W/2\,, \qquad W/4 \leqq E_2 < W/2 \qquad \text{and} \qquad E_3 \leqq W/3\,. \tag{3.70}$$

Therefore, for any given W, the overlap between E_1 and E_2 is from $W/3$ to $W/2$, that between E_2 and E_3 from $W/4$ to $W/3$, but E_1 and E_3 never overlap.

On the basis of 2048 planar three-jet events (out of 18424 hadronic events) at W between 29 and 36.4 GeV and 307 planar three-jet events (out of 1945 hadronic events) at $W = 22$ GeV, the JADE result for the average transverse momentum of a jet is shown in fig. 3.29a. The g = q model calculation using Hoyer et al. [3.39] shown in fig. 3.29b does not give any larger transverse momentum for jet 3, indicating that there is no significant bias in the selection of events. The experimentally observed larger transverse momentum for jet 3 can be reproduced by increasing the σ_q for the gluon from 330 MeV/c to 500 MeV/c (independent of energy), or by using the Lund model [3.44]. In this fig. 3.29, the overlaps of the energy ranges for the three jets are much more than those kinematically allowed for any given W, as discussed in the preceding paragraph and fig. 3.28. The reason is of course that the values of W range from 22 GeV to 36.4 GeV. In particular, the five data points indicated by arrows in fig. 3.29a are from $W = 22$ GeV. Accordingly, as emphasized by the JADE Collaboration, the comparison is made between jet 3 at $W = 29$ to 36.4 GeV and jet 2 at $W = 22$ GeV. For this comparison, jet 3 has significantly larger average transverse momentum than jet 2 for the same jet energy.

3.5.4. Four-jet events

The three-jet events have been analyzed in various other ways [3.51], including the utilization of such variables as total transverse momentum and jet mass. Instead of going into these further analyses, we now turn our attention to four-jet events.

An interesting variable introduced by Nachtmann and Reiter [3.52] and applied by the JADE Collaboration [3.53] to distinguish the case of four jets against those of two and three jets is the

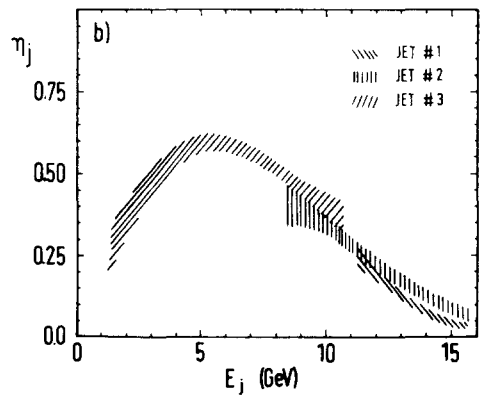

Fig. 3.28. The probability η_j given by JADE [3.49] for jet j being closest to the gluon direction as a function of the reconstructed jet energy E_j obtained from model calculations at a fixed c.m. energy of 33 GeV. The widths of the shaded areas indicate the statistical errors.

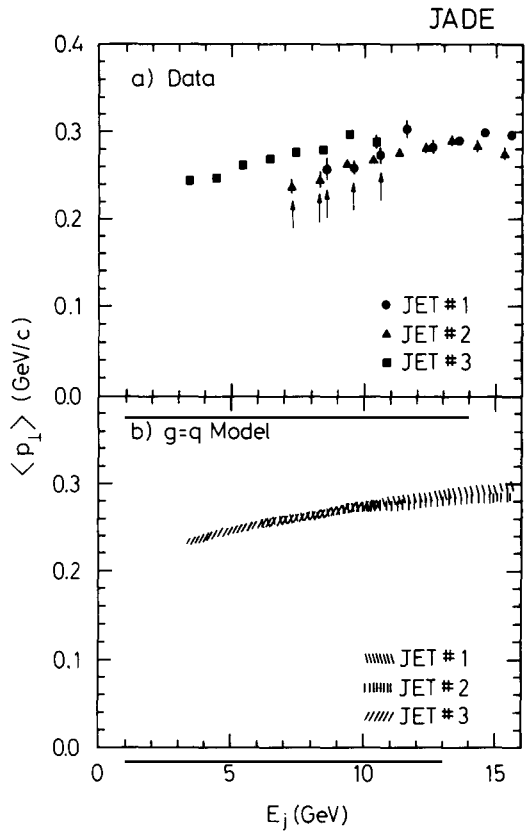

Fig. 3.29. Average p_T distribution from JADE [3.50] for the highest-energy jets (E_1), medium-energy jets (E_2) and lowest-energy jets (E_3) as a function of the jet energy E_j calculated from the angles between the three jets. The center-of-mass energy is between 22 and 36.7 GeV. (a) is from the experimental data, where the arrows indicate the data points at $W = 22$ GeV. (b) is the prediction of the q = g Monte Carlo model.

tripodity D_3:

$$D_3 = 2 \max\left(\sum_i |\boldsymbol{p}_i^T| \cos^3 \sphericalangle(\hat{n}, \boldsymbol{p}_i^T) \Big/ \sum_i |\boldsymbol{p}_i| \right), \tag{3.71}$$

where the $\boldsymbol{p}_i^T$ are the particle or parton momenta projected onto the plane perpendicular to the event thrust axis, and $\hat{n}$ is a unit vector in this plane, oriented such that the quantity in brackets is maximized.

D_3 measures the symmetry of the momentum distribution in the plane normal to the thrust axis. If this distribution is symmetric with respect to the interaction point, $D_3 = 0$. The allowed range of D_3 is most easily understood for events without fragmentation of quarks and gluons. For two- and three-jet events, D_3 vanishes due to a symmetric distribution. Four-jet events fall into two separate classes: events in class I have two parton momenta on each side of the plane normal to the thrust axis, which leads to a symmetric distribution and vanishing D_3. Events in class II have one high momentum in one hemisphere and the three remaining ones in the opposite one, leading to $D_3 \geqq 0$ with a maximum value of 0.324 [3.51].

In fig. 3.30 the JADE tripodity and acoplanarity distributions are shown and compared with the theoretical expectations based on a combination of Ali et al. [3.43] and Lund [3.44]. Because of

fragmentation, initial state radiation, and resolution as well as the fact that four axes are fitted to events with two or three jet structures, the expectation for two- and three-jet events alone (curves labelled L23) extends to large values of D_3. Inclusion of four-jet events (curves labelled L234) gives a significantly better fit to the data for $W = 33$ GeV. The conclusion is therefore reached that, for center-of-mass energy W above 30 GeV, the experimental distributions of the jet parameters acoplanarity and tripodity show significant deviations from the expectations for two- and three-jet events alone, and that the inclusion of four-jet events removes these deviations.

Examples of four-jet events observed by JADE and TASSO are shown in figs. 2.10 and 3.31 respectively.

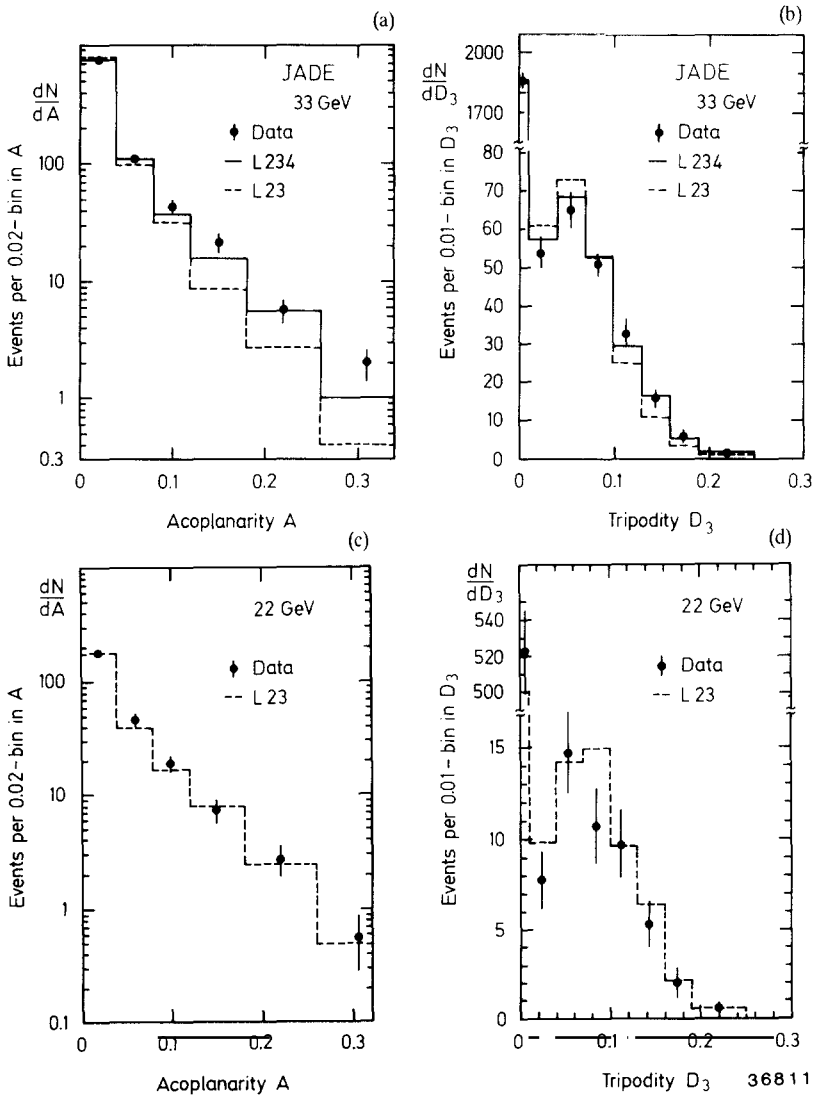

Fig. 3.30. JADE [3.52] experimental D_3-distribution for all events and A-distribution for the events with $D_3 < 0.01$. The variables D_3 and A were calculated from four reconstructed axes. (a) and (b) are for $W = 33$ GeV, (c) and (d) for $W = 22$ GeV. L23 is the model expectation for two- and three-jet events alone. L234 includes in addition four-jet events (5% at generation). Both L23 and L234 are normalized to the total number of events.

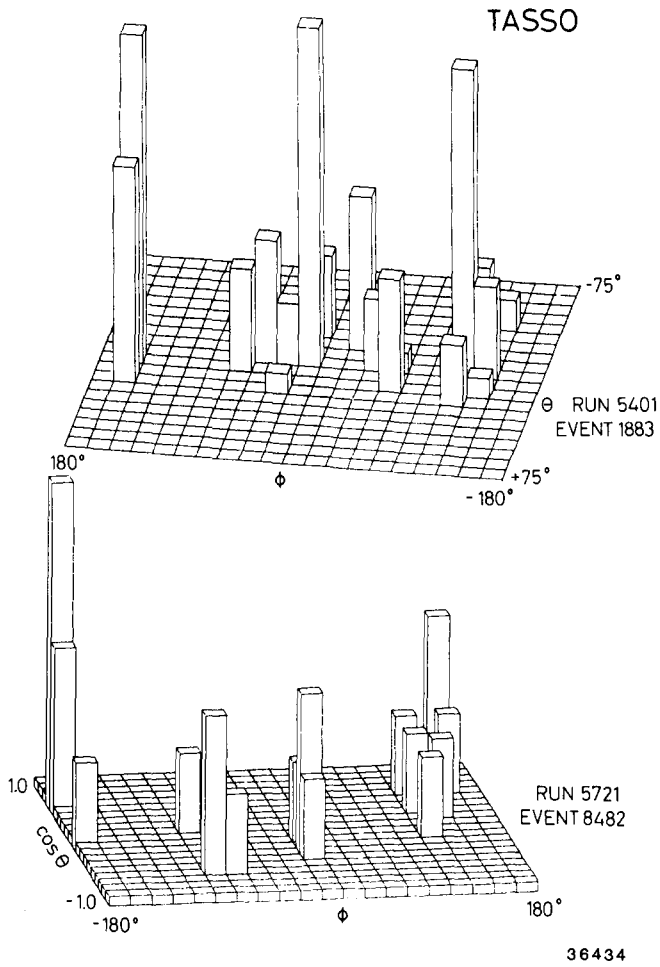

Fig. 3.31. Two examples of the many four-jet events observed at PETRA. These examples are from TASSO.

4. Single-particle inclusive cross sections of hadrons

4.1. Introduction

In the study of hadronic events so far, all the observed particles have been treated as equal. Examples are the calculation of sphericity, thrust, and all the three-jet analyses. In this chapter the inclusive spectra of various particles, π^0, $\pi^{\pm}$, K_s^0, $K^{\pm}$, ρ^0, p, Λ, Ξ^- and $D^{*\pm}$ are to be studied. Unlike the previous three chapters, particle identification in various forms plays a central role here. The study of hadronic final states with particle identification is a topic of current interest and is being pursued vigorously with rapidly increasing sophistication. For example, π^0 and K_s^0 have been successfully identified at PETRA, but many other particles, such as the bottom mesons, have not yet been identified. The observation of these and other particles in the hadronic final states of electron–positron annihilation is a prerequisite to a proper understanding of the underlying physics. As an example of our

present state of ignorance, even though we know that for two-jet events the quark pairs $u\bar{u}$, $d\bar{d}$, $s\bar{s}$, $c\bar{c}$ and $b\bar{b}$ contribute roughly in the ratio of 4:1:1:4:1 at PETRA energies, there is as yet no way of ascertaining which event comes from which quark pair, except the <1% events where a D^{*+} or D^{*-} has been identified. Even the supposedly relatively easy problem of identifying the $b\bar{b}$ pair has not yet been solved. We look forward eagerly to major progress in these and other related problems in the near future.

Let E and p be respectively the energy and the magnitude of the momentum of a particle. The single-particle inclusive cross section is $d\sigma_j/dE$ or $d\sigma_j/dp$, where j denotes the particle or groups of particles under consideration. Thus, for example j may denote π^0, or all neutral particles, or all particles together. When there is no confusion, this subscript is often omitted. $d\sigma_j/dE$ and $d\sigma_j/dp$ are functions of E (or p), the c.m. energy W, and j. For purposes of normalization, the variables E and p are sometimes replaced by

$$x_E = E/E_b = 2E/W \tag{4.1}$$

and

$$x_p = p/p_b = pc/E_b = 2pc/W, \tag{4.2}$$

where E_b and p_b are respectively the energy and momentum of the incoming electron and positron beams. For completeness, we have here kept explicitly the factor of the velocity of light c.

Let us list some of the simple properties of the single-particle inclusive cross sections.

(i) In the limit of small p the spectrum is controlled by phase space.

Thus

$$d\sigma_j/dp \to \text{const. } p^2. \tag{4.3}$$

(ii) Since

$$dx_E/dx_p = dE/c\, dp = cp/E = \beta, \tag{4.4}$$

the two forms of the cross sections are related by

$$c\beta\, d\sigma_j/dE = d\sigma_j/dp \tag{4.5}$$

and

$$\beta\, d\sigma_j/dx_E = d\sigma_j/dx_p. \tag{4.6}$$

These relations are useful only when the particles under consideration all have the same mass.

(iii) Let $j = 0$ denote the case of all hadrons, then

$$\int E\, d\sigma_0 = \int_0^{E_b} E \frac{d\sigma_0}{dE} dE = \int_0^{p_b} E \frac{d\sigma_0}{dp} dp = W\sigma, \tag{4.7}$$

where $\sigma = \sigma(e^+e^- \to \text{hadrons})$ is the total hadronic cross section. This is a consequence of the conservation of energy. Furthermore,

$$\int d\sigma_0 = \int_0^{E_b} \frac{d\sigma_0}{dE} dE = \int_0^{p_b} \frac{d\sigma_0}{dp} dp = \sigma\langle n\rangle \tag{4.8}$$

where $\langle n\rangle$ is the mean multiplicity of hadrons produced.

(iv) Similarly, if j = ch denotes the case of all charged hadrons, then

$$\int d\sigma_{ch} = \sigma \langle n_{ch}\rangle , \tag{4.9}$$

where $\langle n_{ch}\rangle$ is the mean charged particle multiplicity. Moreover, similar to (4.7),

$$\int E\, d\sigma_{ch} = \sigma\, W \rho_{ch} , \tag{4.10}$$

where ρ_{ch} is the mean fraction of energy carried by the charged hadrons.

(v) Since the top quark, as discussed in section 7.2, is not yet discovered, the hadronic cross section σ is proportional to $1/s$ from above the upsilon region to the highest PETRA energy. Accordingly, by (iii) and (iv), it is useful to multiply the single-particle inclusive cross section $d\sigma_0/dx_E$ or $d\sigma_j/dx_p$ by s to remove most of the energy dependence. In particular, when particles of different masses are considered together, x_p is more useful than x_E, and hence $s\, d\sigma_j/dx_p$ is sometimes referred to as "scale-invariant cross section". As discussed in section 4.3, this is not quite justified, and the variation of $s\, d\sigma_j/dx_p$ with respect to s for fixed x_p is referred to as scaling violation.

(vi) When j refers to a single type of particles such as π^0 or more generally particles of the same mass, the most useful form to express the single-particle inclusive cross section is

$$\frac{s}{\beta}\frac{d\sigma_j}{dx_E} .$$

As already explained, the factor s takes care of most of the energy dependence. By (4.3) and (4.6), the factor $1/\beta$ removes the zero at low momenta, so that this combination remains finite and non-zero over the entire physical range of x_E.

4.2. Charged-particle multiplicity and neutral fraction

In connection with single-particle cross sections, by (4.9) and (4.10) two quantities of interest are the average charged-particle multiplicity $\langle n_{ch}\rangle$ and the neutral fraction $1 - \rho_{ch}$. We discuss first these two gross features of the hadronic final states.

Table 4.1 gives the average charged-particle multiplicity $\langle n_{ch}\rangle$ measured by TASSO [4.1] and JADE [4.2]. This average multiplicity $\langle n_{ch}\rangle$ includes the contributions from decay products of particles with a lifetime smaller than 3×10^{-10} sec. For example, the pion fraction includes the $\pi^{\pm}$ coming from $K_s^0 \to \pi^+\pi^-$ decay. These results, together with the data from PLUTO, ADONE, SPEAR and DORIS

Table 4.1
Average charged-particle multiplicity by TASSO [4.1] and JADE [4.2]. This average charged multiplicity $\langle n_{ch} \rangle$ includes the $\pi^\pm$ coming from $K_s^0 \to \pi^+\pi^-$ decay

Collaboration	W (GeV)	$\langle n_{ch} \rangle$
TASSO	12	8.48 ± 0.21
	14	9.08 ± 0.05
	22	11.22 ± 0.07
	25	11.69 ± 0.24
	30.5	12.79 ± 0.13
	34.5	13.48 ± 0.03
	41.5	14.41 ± 0.24
(The systematic error is ± 0.25 at $W = 14$ GeV increasing to ± 0.45 at $W = 35$ GeV and ± 0.5 at $W = 41$ GeV)		
JADE	12	$8.4 \pm 0.3 \pm 0.6$
	30	$13.1 \pm 0.3 \pm 0.6$
	35	$13.6 \pm 0.3 \pm 0.6$

[4.1 to 4.6] are plotted in fig. 4.1. Above 7 GeV the multiplicity is seen to rise faster than at lower energies.

This faster rise can be partially understood as follows. If there were only two-jet events, then the ansatz of Field and Feynman [4.7], as discussed in section 2.8, leads to the multiplicity formula $\langle n_{ch} \rangle = a + b \ln s$. The presence of three-jet events leads to a faster increase.

We discuss next the fluctuation of this charged-particle multiplicity in terms of the ratio $\langle n_{ch} \rangle / D_{ch}$,

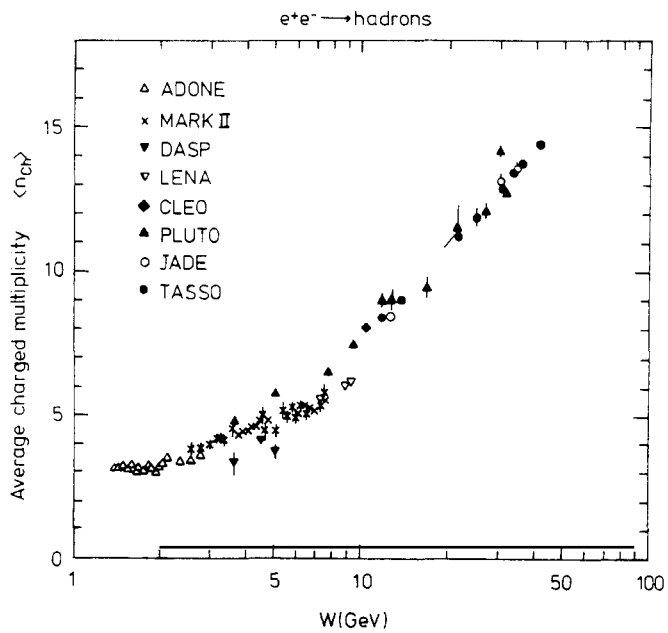

Fig. 4.1. Energy dependence of the average charged multiplicity.

where D_{ch} is the dispersion defined as usual by

$$D_{ch} = [\langle n_{ch}^2 \rangle - \langle n_{ch} \rangle^2]^{1/2} . \tag{4.11}$$

The result is plotted in fig. 4.2 [4.1], and is nearly a constant from 7 GeV up. The detailed charged-particle distribution (KNO plot [4.9]) from JADE [4.2] is shown in fig. 4.3a and from TASSO [4.1] and PLUTO [4.3] in fig. 4.3b. Here $P(n_{ch})$ is the probability of observing the charged-particle multiplicity n_{ch}.

We have refrained from comparing the PETRA e^+e^- annihilation data with either pp or $p\bar{p}$ data. Such comparisons are likely to be misleading, because of the major qualitative difference between the topologies of the hadronic events in these cases.

A second gross feature of the hadronic final state is the fraction of energies carried by neutrals. Measurements have been carried out by JADE [4.10] and CELLO [4.11], who can both detect photons in 90% of the 4π solid angle, JADE with lead glass shower counters and CELLO with liquid argon shower counters.

Two energy fractions are defined as follows: the neutral energy fraction ρ_N is the fraction of energy not carried by charged particles

$$\rho_N = 1 - \sum_j E_j^{ch}/\sqrt{s} = 1 - \rho_{ch} \tag{4.12}$$

and the photon fraction by

$$\rho_\gamma = \sum_j E_j^\gamma/\sqrt{s} . \tag{4.13}$$

The major contribution to ρ_γ is, of course, due to π^0. Both quantities have to be carefully corrected. For example, ρ_N includes contributions from K_s^0 and Λ, while for ρ_γ the energy deposited in the shower counters by charged particles must be subtracted out.

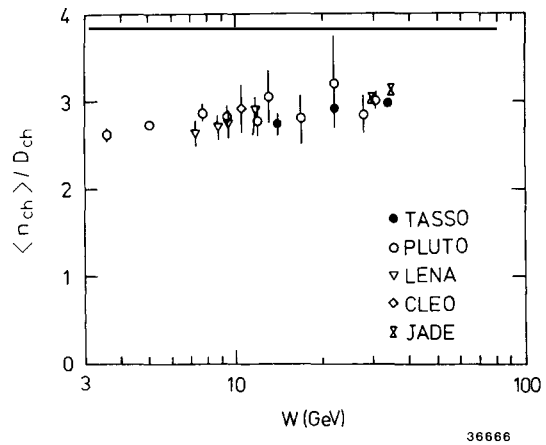

Fig. 4.2. Energy dependence of $\langle N_{ch} \rangle / D_{ch}$.

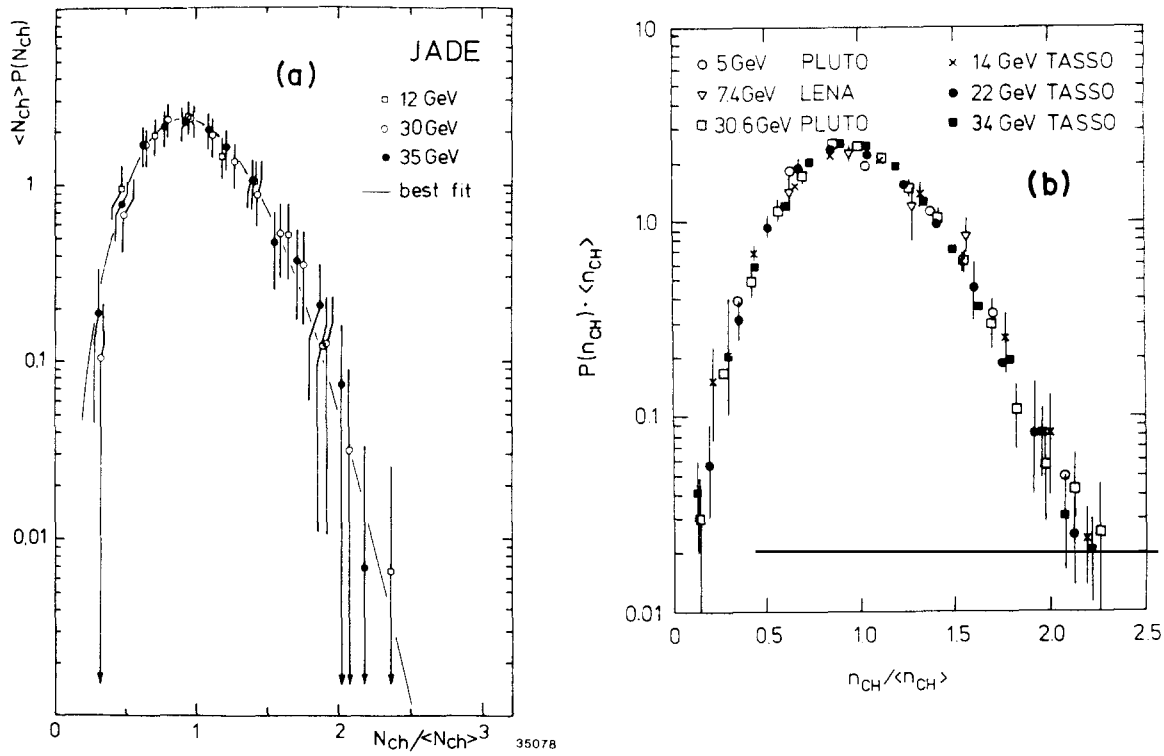

Fig. 4.3. KNO [4.9] plot of the charged multiplicity distributions from (a) JADE [4.2] and from (b) TASSO [4.1], PLUTO [4.3] and LENA [4.6].

The difference $\rho_N - \rho_\gamma$ is the fraction of energy carried by long-lived hadrons and neutrinos. The long-lived hadrons include K_L, n and $\bar{n}$. Using available data at PETRA, these contributions can be estimated and in this way we obtain

ρ_ν = the energy fraction carried by neutrinos .

The JADE result [4.10] are plotted in fig. 4.4 and the corrected means ρ_γ, ρ_N and ρ_ν from JADE are listed in table 4.2. No difference is seen between two-jet events and planar events.

The most interesting feature of the result is that the fraction of energy carried by neutrinos is quite small. This excludes the Pati–Salam model [4.12] where multihadron final states arise via quarks of integer charge which decay into hadrons and neutrinos, giving rise to a neutrino energy fraction ρ_ν between 18% and 28%.

The distribution from CELLO [4.11] of the corrected photonic energy fraction ρ_γ per event is shown in fig. 4.5. The average is found to be

$$\rho_\gamma = 0.268 \pm 0.003 \text{ (stat.)} \pm 0.045 \text{ (syst.)} .$$

This average includes in particular the photons resulting from π^0's from K_s^0 decays, and is in agreement with the JADE value.

Table 4.2
The corrected gamma ray, neutral particle and neutrino energy fractions from JADE [4.10]

W (GeV)		ρ_γ	ρ_N	ρ_ν
12.00	All events	0.25 ± 0.04	0.37 ± 0.04	0.00 ± 0.06
	Planar	0.21 ± 0.05	0.32 ± 0.05	-0.01 ± 0.07
30.30	All events	0.28 ± 0.03	0.36 ± 0.04	-0.03 ± 0.05
	Planar	0.28 ± 0.03	0.36 ± 0.04	-0.03 ± 0.06
34.89	All events	0.30 ± 0.03	0.38 ± 0.04	-0.02 ± 0.05
	Planar	0.32 ± 0.03	0.41 ± 0.04	-0.02 ± 0.06

4.3. Inclusive cross section of charged hadrons and scale breaking

The single-particle inclusive cross section easiest to measure experimentally is that for charged hadrons. In this case, there is no need to differentiate between, for example, π^+ and K^+. The PETRA data from TASSO [4.13] are shown in fig. 4.6. In this figure the corrected scaled particle cross sections $s\, d\sigma_{ch}/dx_p$ are presented for c.m. energies of 14, 22 and 34 (= average over 30.0–36.7) GeV. The error bars shown include the statistical as well as the systematic errors except for the overall normalization uncertainty of 4.5%, which is common to all data shown in fig. 4.6.

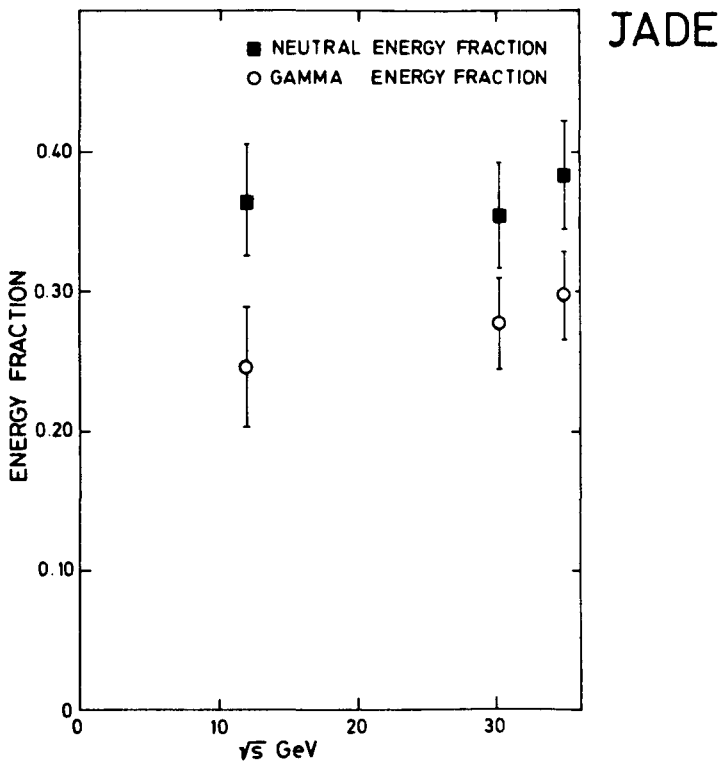

Fig. 4.4. Neutral and gamma-ray energy fractions as a function of the c.m. energy from JADE [4.10].

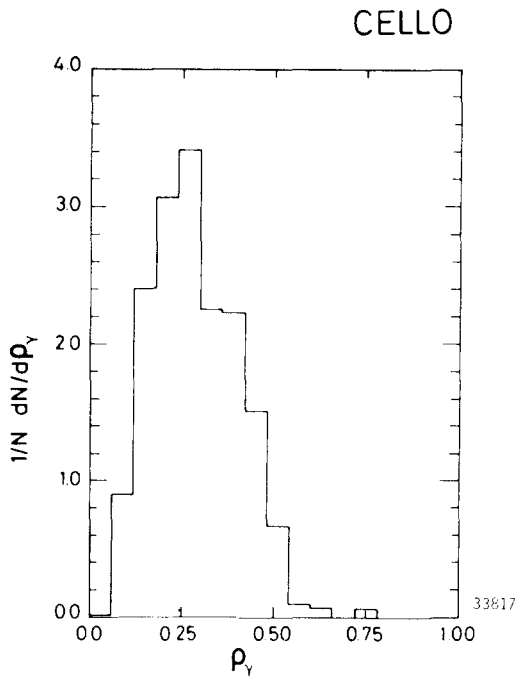

Fig. 4.5. CELLO [4.11] distribution of the fraction ρ_γ of the total center-of-mass energy carried by photons in an event.

As seen from fig. 4.6, this single-particle inclusive cross section $s\,\mathrm{d}\sigma_{\mathrm{ch}}/\mathrm{d}x_p$ for charged hadrons decreases steeply as a function of x_p, but, for given x_p, depends relatively weakly on s. This justifies the term "scaled cross section". In order to show the s dependence more clearly, this quantity is plotted in fig. 4.7a for fixed x_p intervals as a function of s. At small x_p, $x_p \leqq 0.1$, a rapid rise is seen with s which is responsible for the observed growth of the charged-particle multiplicity with s. For $x_p \geqq 0.2$ the data show a slow significant decrease with s. Fig. 4.7b shows the normalized cross section $(1/\sigma_{\mathrm{tot}})\,\mathrm{d}\sigma_{\mathrm{ch}}/\mathrm{d}x_p$, which has smaller systematic errors, and a possible contribution from the weak neutral current (expected to change σ_{tot} at $W = 35$ GeV by 2–3%) is subtracted. The s dependence observed is similar to that for the scaled cross section. The observed scaling violation is in agreement with the data presented by MARK II [4.14] and JADE [4.2]. In order to quantify the amount of scale breaking the data of TASSO between $W = 12.0$ and 36.7 GeV are fitted to a form suggested by QCD [4.15]

$$s\,\mathrm{d}\sigma_{\mathrm{ch}}/\mathrm{d}x_p = b[1 + c_1 \ln(s/s_0)]$$

and

$$(1/\sigma_{\mathrm{tot}})\,\mathrm{d}\sigma_{\mathrm{ch}}/\mathrm{d}x_p = d[1 + c_2 \ln(s/s_0)]\,,$$

where s_0 is taken to be 1 GeV^2. The fits yield the results shown in table 4.3. In each one of the four x_p intervals above $x_p = 0.2$, the observed scale breaking is at the level of a 4 to 10 s.d. effect. Going from $W = 14$ to $W = 35$ GeV $s\,\mathrm{d}\sigma_{\mathrm{ch}}/\mathrm{d}x_p$ on the average is reduced by ~20%.

In the quark–parton model, the fragmentation functions of the quarks are expected to depend only on the fractional energy, $x_E = 2E/W$ carried by the hadron. However, the observed scale breaking is

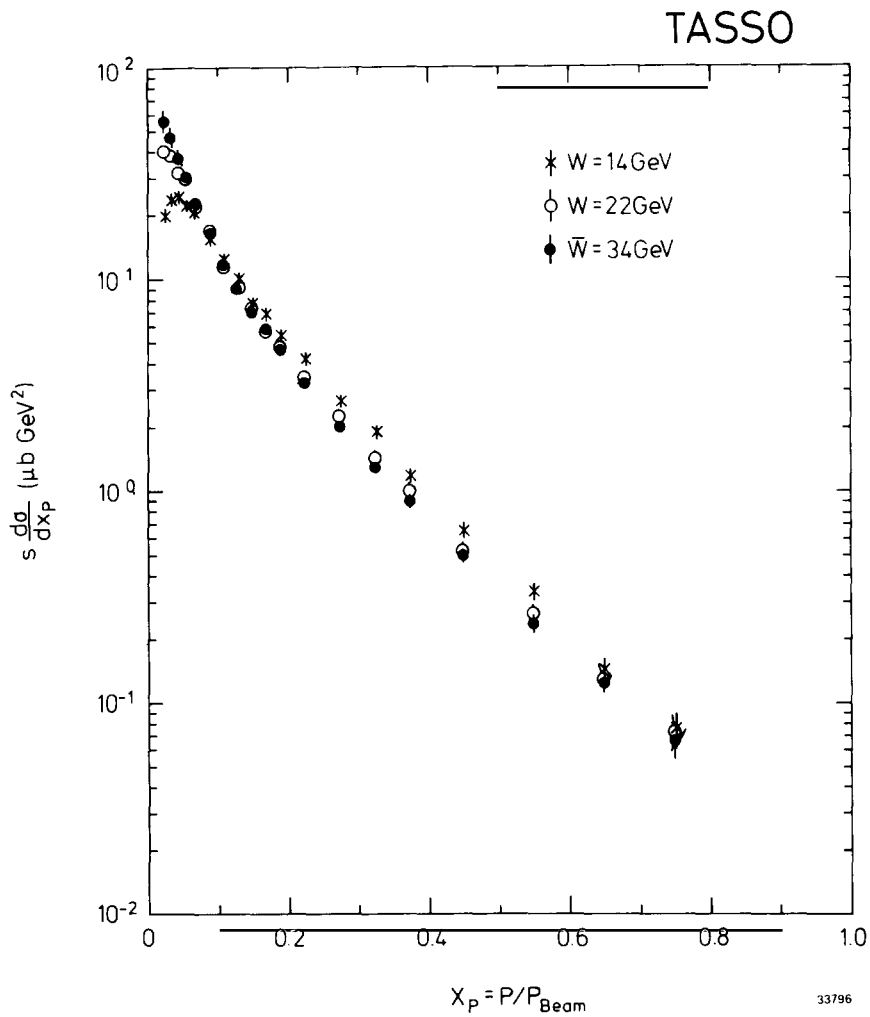

Fig. 4.6. The TASSO [4.13] scaled cross section $s\,d\sigma/dx_p$ ($x_p = 2p/W$) for inclusive charged-particle production measured at W = 14, 22 and 34 GeV. The errors shown include the statistical as well as the systematic uncertainties except for an overall normalization uncertainty of 4.5%.

expected in QCD where at high W gluon emission depletes the particle yield at large x and increases it at small x. Scale-breaking effects are better studied with the cross sections for specific particle types (π, K, p, ...) rather than with the unseparated cross sections which at lower energies are strongly affected by mass effects. For instance, proton production passes its phase-space maximum only at a momentum of 1 GeV/c (see section 4.5 below) which corresponds to an x_p value of 0.4 at W = 5 GeV.

4.4. Charged-particle inclusive distribution with respect to the jet axis

The distributions presented in the preceding section are functions of two variables, namely s and p (or equivalently x_p). As discussed in chapter 2, most of the hadronic events are of the form of two jets. Therefore, the natural next level of sophistication in treating inclusive distributions is to consider it as a function of three variables; s, p_L and p_T, where the parallel and the perpendicular components are taken with respect to the jet axis.

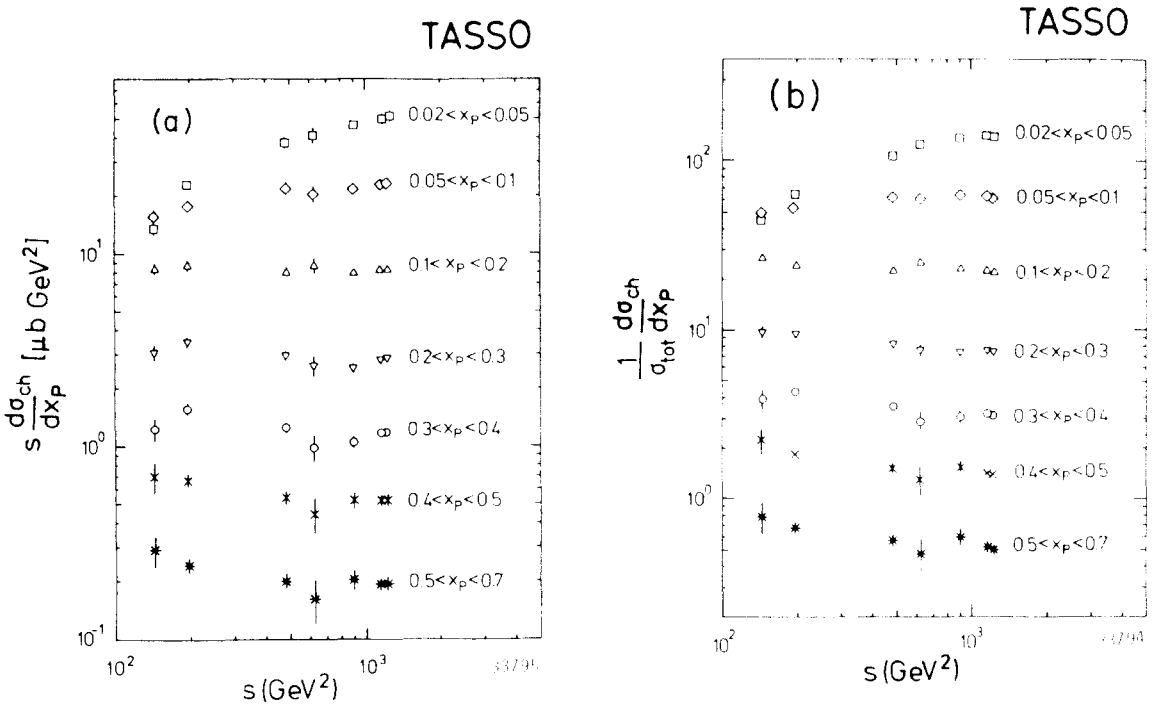

Fig. 4.7. The TASSO [4.13] inclusive charged particle production. (a) The scaled cross section $s\,d\sigma_{ch}/dx_p$ versus the square of the c.m. energy $s = W^2$. The errors shown include the statistical as well as the systematic uncertainties except for an overall normalization uncertainty of 4.5%. (b) The normalized cross section $(1/\sigma_{tot})\,d\sigma_{ch}/dx_p$ versus s. The errors shown include the statistical as well as the systematic uncertainties.

A preliminary step in this direction is to consider the rapidity distribution. The rapidity y is defined in terms of the particle energy E and its longitudinal momentum $p_\parallel$ with respect to the jet axis by $y = 0.5 \ln\{(E + p_\parallel)/(E - p_\parallel)\}$. Fig. 4.8a shows the rapidity distributions normalized to the total cross section as measured by TASSO [4.1] between 14 and 34 GeV. The thrust axis was taken as the jet axis. To compute y, the particles were assumed to be pions. One observes a plateau near $y = 0$ that broadens with increasing c.m. energy. The height of the plateau is not constant, but rises approximately logarithmically with increasing energy (see insert in fig. 4.8b). In the fragmentation region (y close to $y_{max} = 0.5 \ln(s/m^2)$) the particle yield is a steeply descending function of y. The width of the fragmentation region is roughly one unit. The energy dependences of the plateau and fragmentation regions

Table 4.3
Scale-breaking parameters as suggested by QCD. The parameters b and c_1 are obtained by fitting the TASSO data [4.13] on $s\,d\sigma_{ch}/dx_p$, while d and c_2 are obtained from the same data expressed as $(1/\sigma_{tot})\,d\sigma_{ch}/dx_p$

x_p	b (μb GeV^2)	c_1	d	c_2
0.1–0.2	8.6 ± 1.3	−0.008 ± 0.020	28.7 ± 1.5	−0.033 ± 0.007
0.2–0.3	4.3 ± 0.6	−0.053 ± 0.013	15.1 ± 0.8	−0.071 ± 0.005
0.3–0.4	2.1 ± 0.3	−0.063 ± 0.013	7.3 ± 0.6	−0.081 ± 0.006
0.4–0.5	0.96 ± 0.18	−0.065 ± 0.016	3.0 ± 0.4	−0.075 ± 0.010
0.5–0.7	0.37 ± 0.07	−0.069 ± 0.017	1.1 ± 0.2	−0.074 ± 0.013

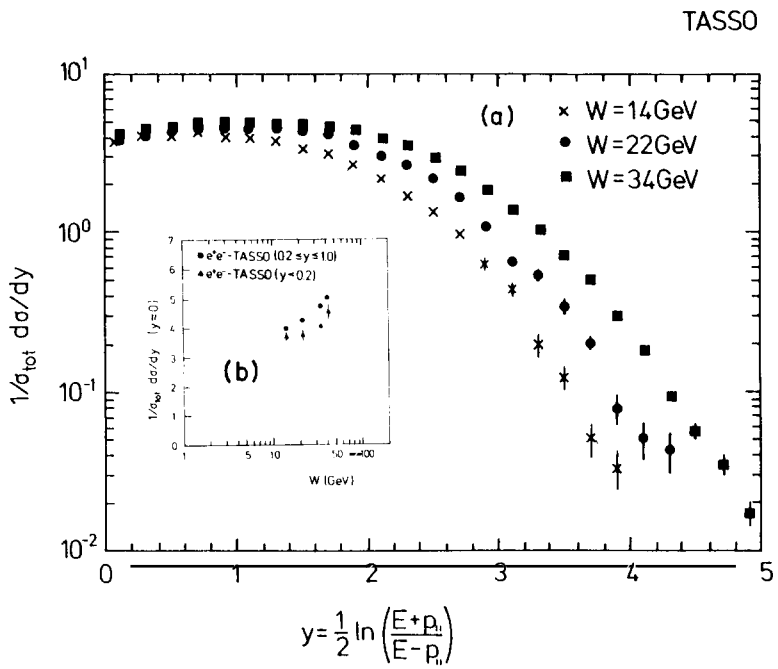

Fig. 4.8. (a) The TASSO [4.1] normalized differential cross section for the rapidity $y = \frac{1}{2}\ln\{(E + P_\parallel)/(E - P_\parallel)\}$ folded around zero for W = 14, 22 and 34 GeV. The thrust axis was used as the jet axis. (b) The height of the rapidity yield near $y = 0$ as a function of the c.m. energy W.

show that the faster than logarithmic growth of the average multiplicity at high energies is correlated with a rise of the plateau which is due to low-energy particles.

Fig. 4.9a shows the transverse momentum distributions $(1/\sigma_{tot})\, d\sigma/dp_T^2$ from TASSO [4.1] for W = 14, 22, 34 and 41.5 GeV. The p_T^2 distributions near $p_T^2 = 0$ are of the form $d\sigma/dp_T^2 \sim \exp(-ap_T^2)$ and these distributions broaden with increasing c.m. energy. Fig. 4.9b displays the distributions of the average squared transverse momenta *in* and *out* of the event plane (see section 3.2.1), $\langle p_{T\,in}^2 \rangle$ and $\langle p_{T\,out}^2 \rangle$ which are defined as

$$\langle p_{T\,in}^2 \rangle = Q_2 \sum p_j^2/N, \qquad \langle p_{T\,out}^2 \rangle = Q_1 \sum p_j^2/N$$

where Q_1 and Q_2 are defined in section 2.5 and N is the number of charged particles in an event. As W increases the $\langle p_{T\,in}^2 \rangle$ distribution develops a long tail to high values of $\langle p_{T\,in}^2 \rangle$. Such a tail is not seen for $\langle p_{T\,out}^2 \rangle$.

4.5. Particle identification and over-all view

The knowledge of particle composition of the final state in e^+e^- annihilation is important for understanding the fragmentation of quarks and gluons into hadrons. The following types of particles

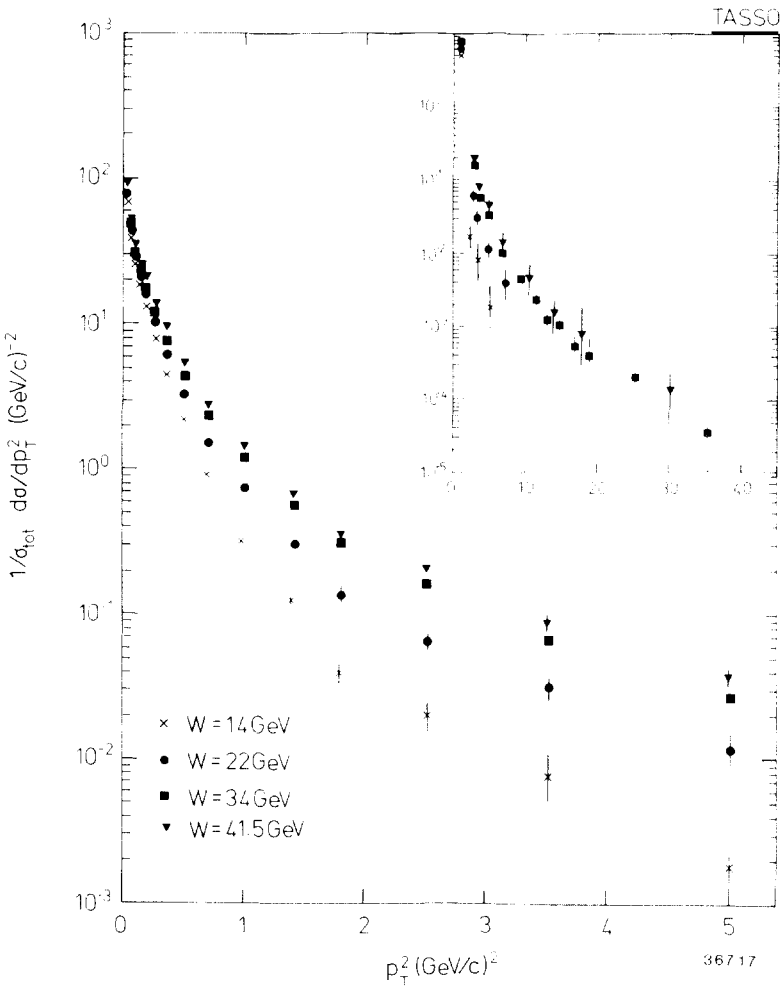

Fig. 4.9a. TASSO [4.1] normalized differential cross section for the square of the momentum component transverse to the jet axis (= sphericity axis), p_T^2, for W = 14, 22, 34 and 41.5 GeV.

have been identified in jets at PETRA and their inclusive cross sections measured and published:

π^0:	TASSO [4.17], CELLO [4.18, 4.19],
$\pi^\pm$:	TASSO [4.20, 4.21, 4.22],
$K^\pm$:	TASSO [4.20, 4.22],
K_s^0:	TASSO [4.23], PLUTO [4.24], JADE [4.2],
ρ^0:	TASSO [4.25],
$p, \bar{p}$:	TASSO [4.20, 4.22], JADE [4.26],
$\Lambda, \bar{\Lambda}$:	JADE [4.26], TASSO [4.27],
$\Xi^-, \bar{\Xi}^-$:	TASSO [4.28],
$D^{*\pm}$:	TASSO [4.29],
	(and MARK II, HRS [4.30] at PEP and CLEO [4.31] at CESR).

These hadrons have been arranged in order of increasing mass.

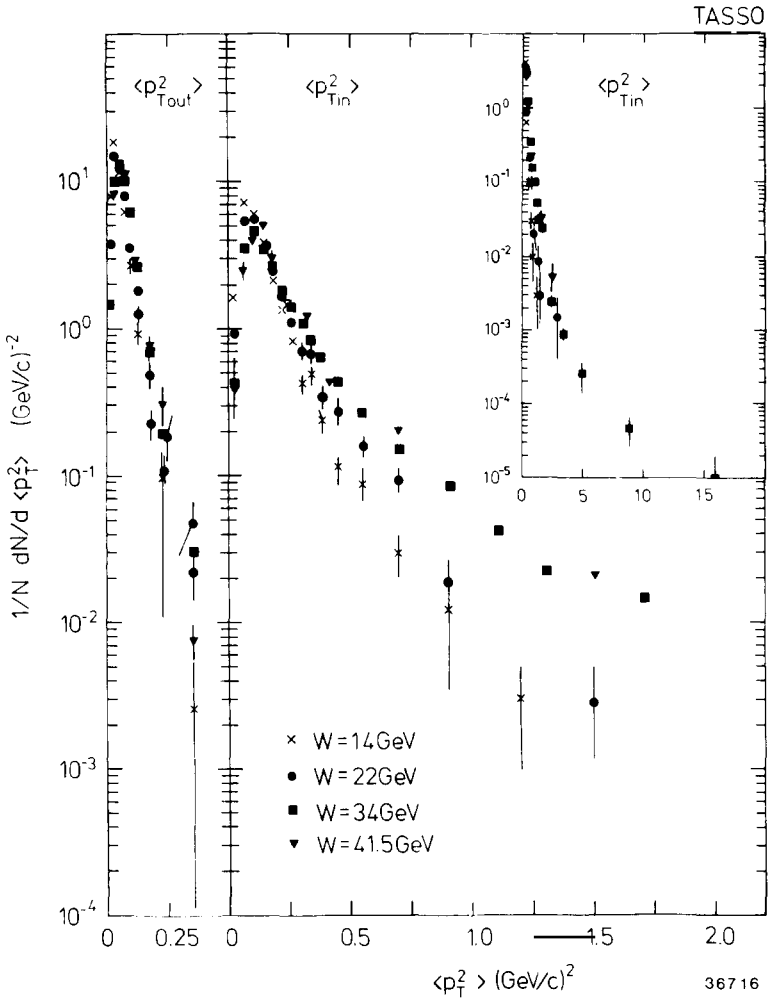

Fig. 4.9b. TASSO [4.1] distribution of the transverse momentum in and out of the event plane averaged over one event, $\langle p^2_{T\,in} \rangle$ and $\langle p^2_{T,\,out} \rangle$, at W = 14, 22, 34 and 41.5 GeV.

The cross sections are discussed separately beginning in the next section. A great variety of techniques have been used in identifying these particles. The stable or long-lived charged particles may be identified by time-of-flight (TOF), Čerenkov counters, or the method of dE/dx. The short-lived particles all must be identified by their decays:

$$\pi^0 \to \gamma\gamma$$
$$K^0_s \to \pi^+\pi^-$$
$$\rho^0 \to \pi^+\pi^-$$
$$\Lambda \to p\pi$$
$$\Xi^- \to \Lambda\pi^-$$

and

$$D^{*+} \to D^0\pi^+ \text{ with } D^0 \to K^-\pi^+ .$$

However, a great deal of ingenuity is needed and has been applied in the study of these decay modes. The techniques used and the momentum ranges covered by the TASSO, JADE, PLUTO and CELLO Collaborations are listed in table 4.4.

So far as particle identification is concerned, the TASSO detector is the best one at PETRA. The identification of the neutral K through the decay $K_S^0 \to \pi^+\pi^-$ was first achieved [4.23] with this detector, and as seen from table 4.4, the TASSO detector can reach the highest momenta in most of the cases of π^0, $\pi^\pm$, ρ^0, $K^\pm$, p, $\bar{p}$, Λ, $\bar{\Lambda}$ and $D^{*\pm}$. Indeed, when the experiments were originally proposed and accepted on October 19th, 1976, the ability to identify particles was a main feature of TASSO. For these reasons, our attention will be focused mostly on TASSO in the remainder of this chapter.

As a preview of the data to be presented below, fig. 4.10a summarizes the TASSO data on the

Table 4.4
Methods of hadron identification used and momentum ranges in GeV/c covered by the CELLO, JADE, PLUTO and TASSO Collaborations

Type of particle	CELLO	JADE	PLUTO	TASSO
π^0	Liquid argon above 0.9 GeV/c			Liquid argon 0.5–4 GeV/c
$\pi^\pm$				TOF & Čerenkov above 0.3 GeV/c
$K^\pm$				TOF & Čerenkov 0.4–2.0, 3–6 and above 10 GeV/c
$K^0, \bar{K}^0$		$K_S^0 \to \pi^+\pi^-$ all p	$K_S^0 \to \pi^+\pi^-$ all p	$K_S^0 \to \pi^+\pi^-$ all p
ρ^0				$\rho^0 \to \pi^+\pi^-$ 1.7–12 GeV/c
p, $\bar{p}$		dE/dx 0.3–0.9 GeV/c ($\bar{p}$ only)		TOF & Čerenkov 0.4–2.0, 3–6 and above 10 GeV/c
Λ, $\bar{\Lambda}$		dE/dx & $\bar{\Lambda} \to \bar{p}\pi^+$ 0.4–1.4 GeV/c		$\Lambda \to p\pi^-$ 1–10 GeV/c
Ξ^-, $\bar{\Xi}^+$				$\Xi^- \to \Lambda\pi^-$ 1–6 GeV/c
D^{*+}				$D^{*+} \to D^0\pi^+$ $D^0 \to K^-\pi^+$ above 5 GeV/c

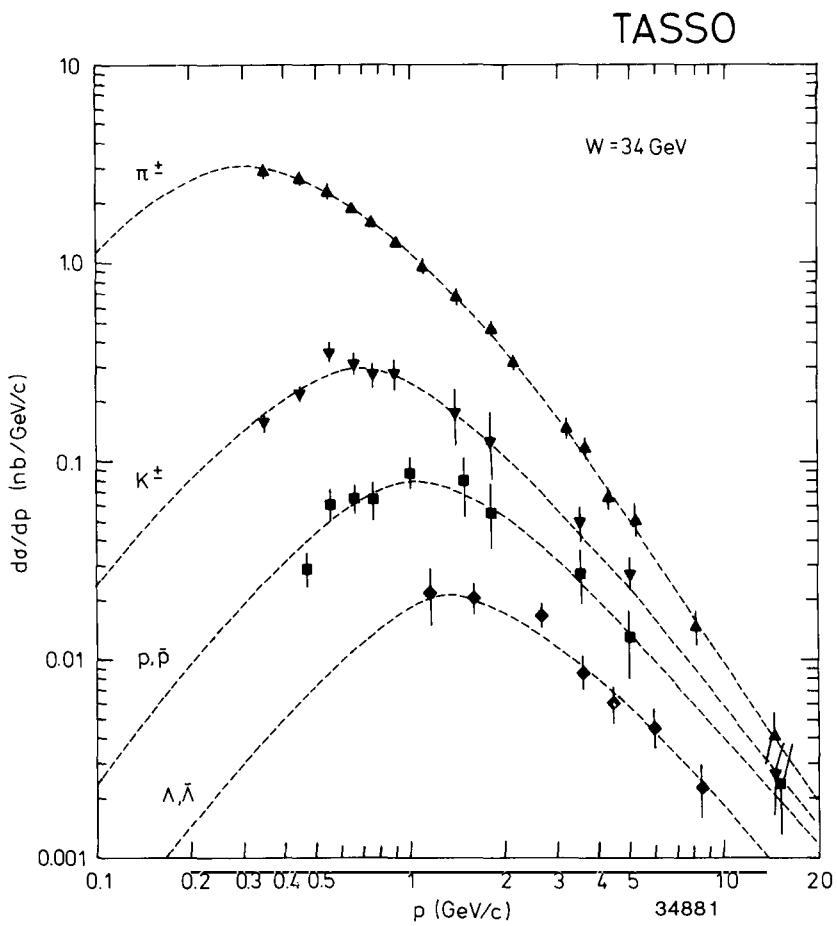

Fig. 4.10a. The differential cross sections for the inclusive production of $(\pi^+ + \pi^-)$, $(K^+ + K^-)$, $(p + \bar{p})$ and $(\Lambda + \bar{\Lambda})$ from TASSO at $W = 34$ GeV. The dashed curves are drawn to guide the eye.

differential cross sections $d\sigma/dp$ for $\pi^\pm$, $K^\pm$, p, $\bar{p}$, Λ and $\bar{\Lambda}$ at $W = 34$ GeV. The curves are drawn merely to guide the eye. As seen from this figure, the $\pi^\pm$ yield dominates for momenta below about 1 GeV/c. For example, the ratios $\pi^\pm : K^\pm : p, \bar{p}$ is approximately 100 : 10 : 1 at 0.5 GeV/c, but decrease to about 4 : 2 : 1 at 6 GeV/c. As seen from eq. (4.3) all differential cross sections $d\sigma/dp$ must approach zero as $p \to 0$, and hence must have maxima before dropping off. The position of the maximum increases with the particle mass: it appears to be below 0.4 GeV/c for pions, around 0.7 GeV/c for kaons and near 1 GeV/c for p and Λ.

The scaled inclusive cross section for $(\pi^+ + \pi^-)$, $(K^+ + K^-)$, $(p + \bar{p})$ and $(\Lambda + \bar{\Lambda})$ as determined by TASSO [4.22, 4.27] are shown in fig. 4.10b. Note that the cross section for $(K^+ + K^-)$, for example, is defined to be the sum of the cross section for K^+ and the cross section for K^-, not the cross section for the production of both a K^+ and a K^- in the same event. It is seen from fig. 4.10b that the scaled cross sections for the various particles are rather similar in shape as functions of x_E.

The average number of hadrons per event n_i is calculated according to

$$\langle n_i \rangle = \int_0^{p_{max}} \left(\frac{d\sigma}{dp}\right)_i dp \Big/ \sigma_{tot} \tag{4.14}$$

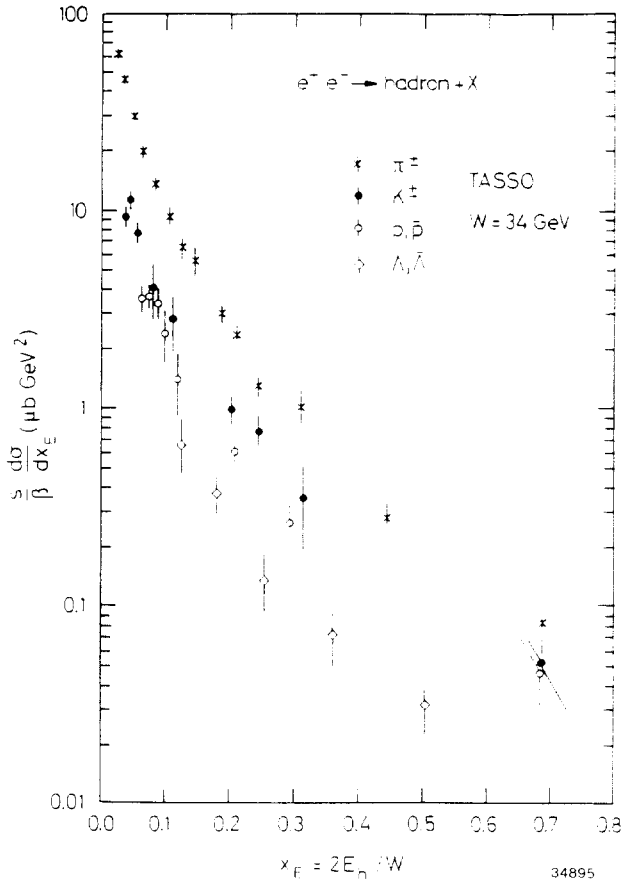

Fig. 4.10b. The TASSO scaled cross sections at $W = 34$ GeV for the inclusive production of $(\pi^+ + \pi^-)$, $(K^+ + K^-)$, $(p + \bar{p})$ and $(\Lambda + \bar{\Lambda})$ [4.22, 4.27].

where σ_{tot} is the total hadronic cross section. The extrapolation of $(d\sigma/dp)_i$ to zero momentum as well as the interpolation over the momentum intervals for which particles were not identified, was done by parametrizing the invariant cross sections in the form [4.22]

$$(E_i/4\pi p_i^2)\,(d\sigma/dp)_i = \sum_m A_{im} \exp(-B_{im}E_i)\,. \tag{4.15}$$

The average particle multiplicities for hadronic events at 34 GeV are tabulated in table 4.5. The majority of the $\pi^\pm$, $K^\pm$, ... presumably result from the decay of heavier-mass particles. Thus about 35% of the protons and antiprotons come from the decays of Λ and $\bar{\Lambda}$. In the case of ρ^0, integration over the measure range of $0.1 < x < 0.7$ gives $0.41 \pm 0.04 \pm 0.08$ ρ^0 per event, and extrapolation to all x yields the value given in table 4.5.

Since $\rho^0 \to \pi^+ + \pi^-$, there are 0.73 π^+ and 0.73 π^- per event from ρ^0 decay alone. If the productions of ρ^+, ρ^0 and ρ^- are assumed to be equal, then the decay of ρ gives 1.46 π^+, 1.46 π^0 and 1.46 π^- per event. In other words, approximately 30% of the π's come from ρ decay.

The average particle yields are compared with lower-energy data for ρ^0 in fig. 4.11, and for $\pi^\pm$, $K^\pm$,

Table 4.5
The average number of various particles contained in a hadronic event at 34 GeV. The number of $\pi^\pm$ contains those from the decay of ρ^0, and that for $p+\bar{p}$ contains those from the decay of $\Lambda + \bar{\Lambda}$. The data are from TASSO

Particle	$\langle n_i \rangle$	
π^0	6.1 ±2.0	[4.17]
$\pi^\pm$	10.3 ±0.4	[4.22]
$K^\pm$	2.0 ±0.2	[4.22]
$K^0 + \bar{K}^0$	1.6 ±0.1	[4.23]
ρ^0	0.73 ± 0.06	[4.25]
$p+\bar{p}$	0.8 ±0.1	[4.22]
$\Lambda + \bar{\Lambda}$	0.28 ± 0.04	[4.27]
$\Xi^- + \bar{\Xi}^-$	0.026 ± 0.008	[4.28]
$D^{*\pm}$	0.31 ± 0.08	[4.29]

and p, $\bar{p}$ in fig. 4.12. Here R_{ρ^0} is defined as

$$R_{\rho^0} = \sigma(e^+e^- \to \rho^0 X)/\sigma(e^+e^- \to \mu^+\mu^-)\,. \tag{4.16}$$

Recent results from DELCO and TPC are consistent with those of TASSO. In all cases, the increase is roughly proportional to that of the total multiplicity.

Another way to present the data is to show the particle fraction as function of the hadron momentum. The recent TASSO data [4.22] are shown in fig. 4.13. For low momenta, most of the particles are pions, as already discussed. At $W = 34$ GeV, the ratios $\pi^\pm : K^\pm : p, \bar{p}$ are 0.55 : 0.30 : 0.15 at 5 GeV/c and 0.45 : 0.30 : 0.25 above 10 GeV/c. Also included in these figures are results from other experiments at lower energies [4.32 to 4.34].

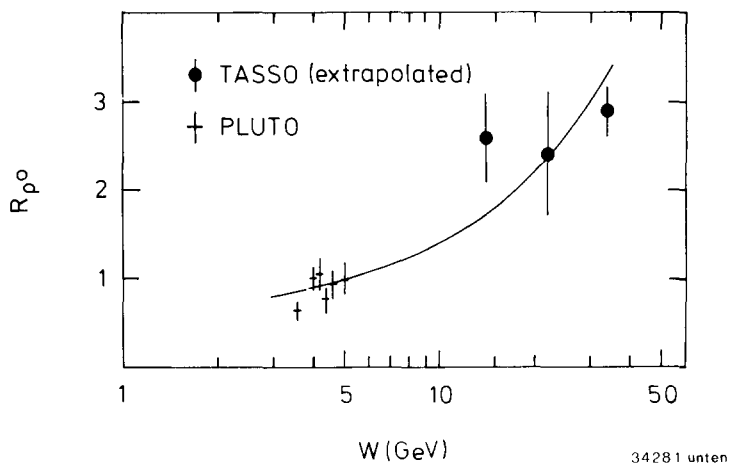

Fig. 4.11. $R_{\rho 0}$ for $e^+e^- \to \rho^0 +$ hadrons as a function of W (errors shown are statistical only). The curve shows a fit to the TASSO [4.25] charged particle multiplicity in $e^+e^- \to$ hadrons normalized to $R_{\rho 0}$ measured at 5 GeV.

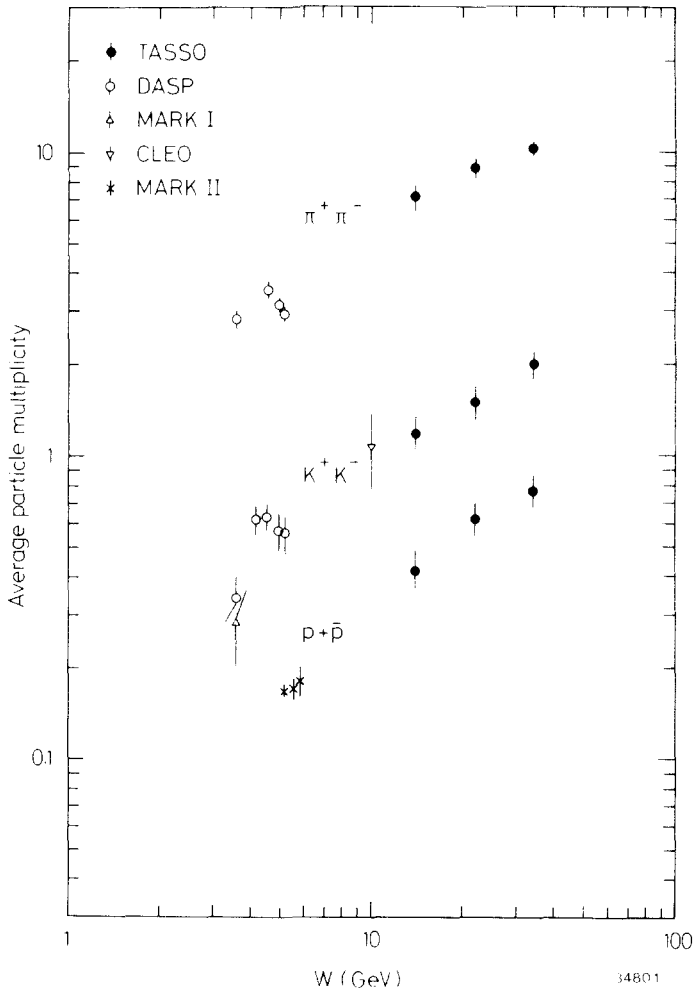

Fig. 4.12. Average particle multiplicities for $\pi^{\pm}$, $K^{\pm}$, and $p, \bar{p}$ as functions of the center-of-mass energy W.

4.6. *Inclusive cross section of* π^0

We begin with the hadron of the lowest mass, namely π^0. The only way to detect π^0 is through its decay product of two gammas. At TASSO and CELLO the photons are detected in the liquid argon calorimeters. We shall summarize the results from both TASSO and CELLO here, but with the technical details from TASSO given as an example.

In TASSO photons have been detected by a pattern recognition program scanning the information of the calorimeter for clusters. A cluster is defined as a group of adjacent front towers with energy deposit, separated from any other cluster by front towers with shower energy below 20 MeV. The back towers associated with the front tower cluster are found and their energy is added to that measured by the front towers. Using the strip information the precise position of the cluster is determined. Taking the event vertex as the origin, the θ and ϕ coordinates are computed. All charged tracks seen in the central detector are followed to see whether they can be linked to any of the clusters. Clusters for which the

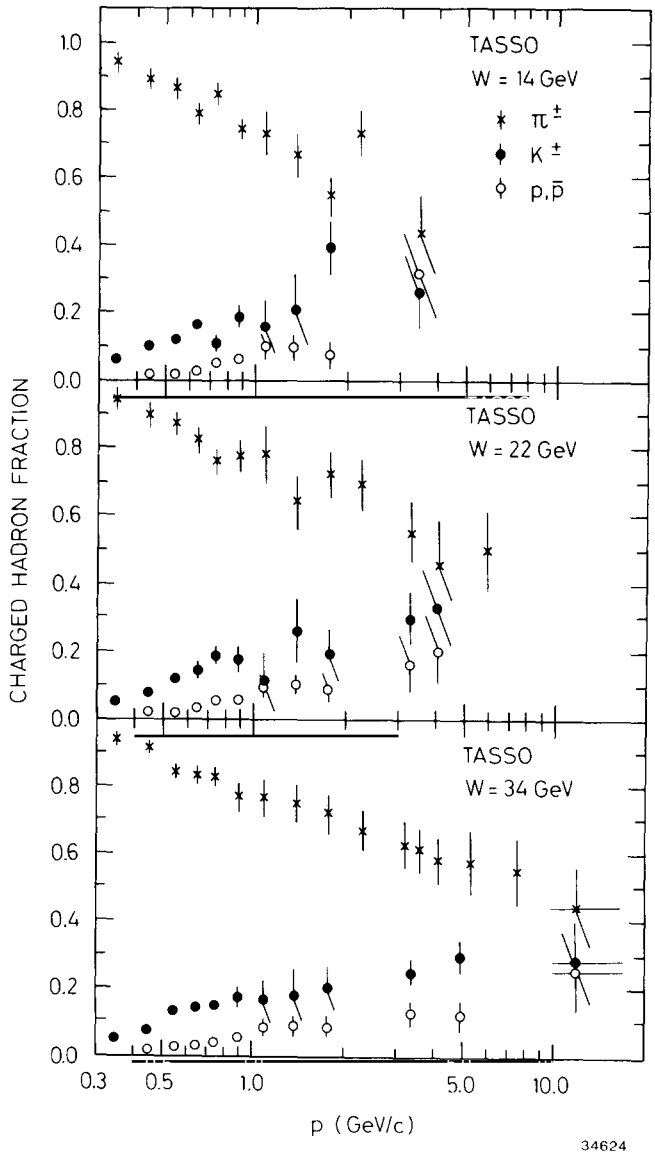

Fig. 4.13. Fractions of $\pi^{\pm}$, $K^{\pm}$, and p, $\bar{p}$ as functions of particle momentum at center-of-mass energy W = 14, 22 and 34 GeV. These data are from TASSO [4.22].

measured direction agrees with that predicted for a given charged track to better than 0.05 rad are called charged clusters and are ignored in the further analysis.

The remaining clusters have been assumed to originate from photons. The measured energy has been corrected for energy loss through absorption and leakage with the correction functions determined by the Monte Carlo program EGS [4.35] which simulates the shower development in the absorber and the calorimeter stack. Correction functions have been determined as a function of incident photon energy and angles applying the same cluster analysis as used for the data. The resulting energy resolution for

photons at normal incidence can be approximated by (see section 1.8.4)

$$\sigma_E/E = \left(0.11 + \frac{0.02}{E - 0.5}\right)\Big/\sqrt{E} \qquad \text{for } E > 1\,\text{GeV}.$$

The energy calibration is monitored by Bhabha scattering $e^+e^- \to e^+e^-$ detected in the calorimeter. The angular resolution for photons of energy near 1 GeV is $\sigma_\phi = 4$ mrad, $\sigma_\theta = 6$ mrad as determined by Monte Carlo studies; the measured angular resolution for high energy ($E > 10$ GeV) electrons is $\sigma_\phi \approx \sigma_\theta = 3$ mrad. The detection efficiency for photons as determined from EGS studies is 50% at 55 MeV rising to >90% above 160 MeV.

For each event all possible pairs of photons have been formed and their effective mass $m_{\gamma\gamma}$ and total energy $E_{\gamma\gamma}$ have been calculated. Fig. 4.14 shows the $m_{\gamma\gamma}$ distributions obtained at $W = 14$ GeV and 34 GeV for $0.5 < E_{\gamma\gamma} < 4$ GeV requiring each γ to have at least $E_{\min} = 0.15$ GeV energy. A clear π^0 signal is observed. The π^0 r.m.s. mass resolution of $\sigma_m = 0.023$ (0.031) GeV is obtained at 14 (34) GeV.

Fig. 4.15 shows the differential cross section $d\sigma/dp$ for π^0 production and the scaled cross section $(s/\beta)\,d\sigma/dx_E$ (see section 4.1(v)) for $W = 14$ and 34 GeV. The error bars include the statistical error as

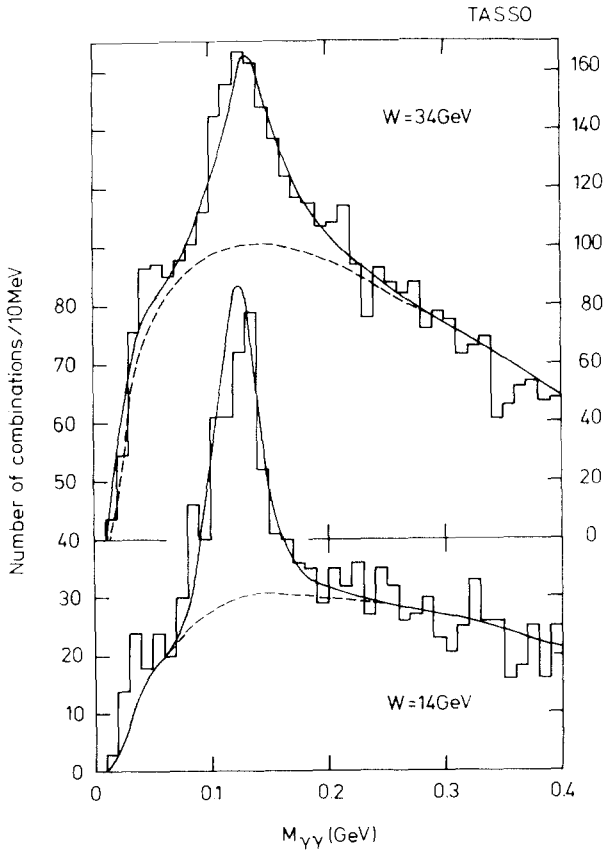

Fig. 4.14. The $\gamma\gamma$ mass distributions measured at 14 and 34 GeV for $0.5 < E_{\gamma\gamma} < 4$ GeV and photon energies $E_\gamma > 0.15$ GeV. The dashed curves indicate the background contribution as computed from Monte Carlo. The solid curves show the sum of the contributions from π^0 production and background.

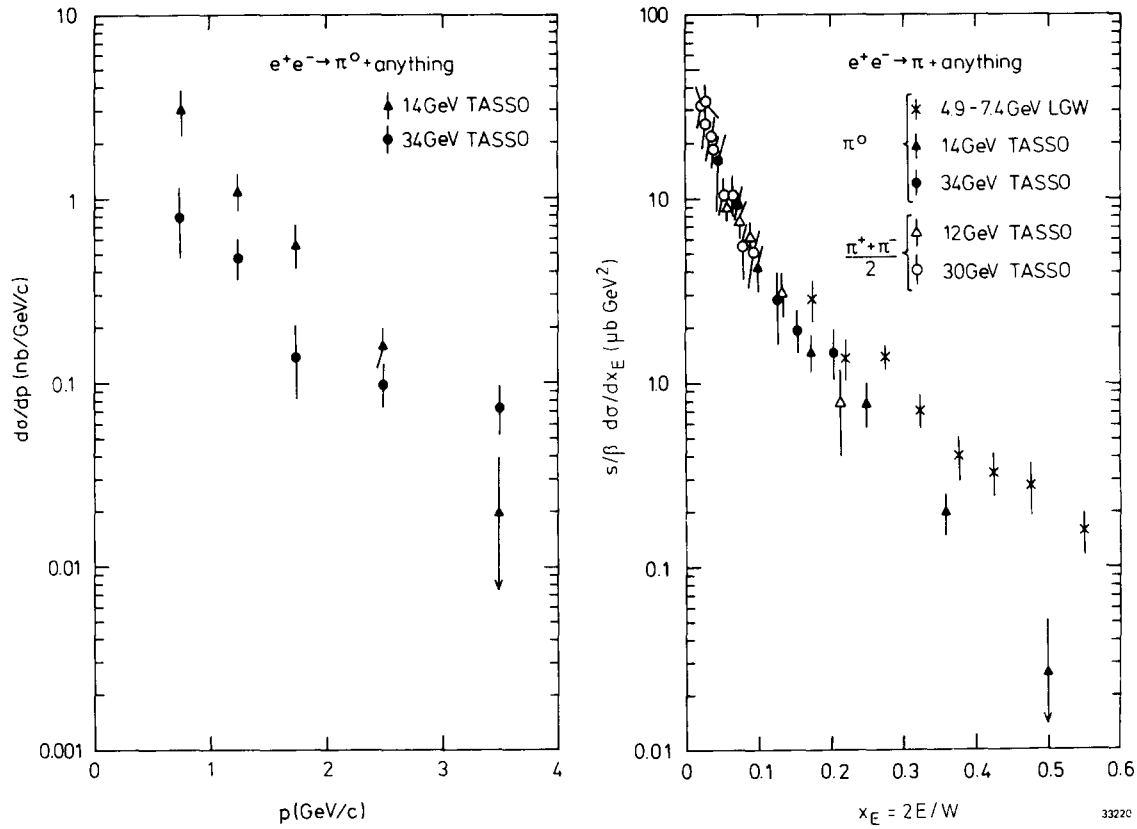

Fig. 4.15. (a) The TASSO [4.17] differential cross section $d\sigma/dp$ for $e^+e^- \to \pi^0$ + anything at $W = 14$ and 34 GeV. π^0's from K decay are excluded. (b) The TASSO [4.17] scaled cross section $(s/\beta)\, d\sigma/dx_E$ for $e^+e^- \to \pi^0$ + anything at $W = 14$ and 34 GeV (π^0's from K decay are excluded), and at 4.9–7.4 GeV by ref. [4.36]. Also shown are the averages of π^+ and π^- production, $0.5(\sigma(\pi^+) + \sigma(\pi^-))$, as measured at 12 and 30 GeV [4.20].

well as the uncertainties in background subtraction (typically of the order of 10%), acceptance (8%), efficiency of the calorimeter (5%) and cross section normalization (8%) which have been added in quadrature. Fig. 4.15b also exhibits the averages of the π^+ and π^- cross section $(\sigma(\pi^+) + \sigma(\pi^-))/2$ measured previously at $W = 12$ and 30 GeV by TASSO [4.20]. They agree well with the π^0 cross sections.

Fig. 4.15b shows that the scaled π^0 cross sections for W at 14 and 34 GeV agree within errors in the x_E region where both sets overlap ($x_E = 0.1$–0.2). However, the comparison of the TASSO data with those measured [4.36] at lower energy (4.9–7.4 GeV) suggests a sizeable scaling violation (see fig. 4.15b): for x_E between 0.2 and 0.6 the low-energy data are roughly a factor of 2 above those from 14 GeV.

Recently, the CELLO Collaboration [4.19] has obtained the inclusive cross section of π^0 for the entire momentum range >0.9 GeV/c. The data used correspond to 1.3 pb^{-1} at $W = 14$ GeV, 2.5 pb^{-1} at 22 GeV, and 7.9 pb^{-1} at 34 GeV. The neutral-particle analysis uses the barrel liquid argon calorimeter which has a solid angle acceptance of 86% of 4π. Each of the 16 calorimeter modules samples the energy deposited by particles up to 17 times in depth leading to spatial measurements in six layers up to a maximum depth of 20 radiation lengths. Each layer consists of channels in three orientations. They obtain an energy resolution of $\sigma(E)/E = 13\%/\sqrt{E}$ (GeV) and an angular resolution of 4 mrad. The

jet-structure of the multihadronic final states causes a substantial overlap between clusters of deposited charge from different photons, and from photons and charged tracks. Therefore, the actual resolution obtained in a multihadronic event depends on the γ-energy and event topology and can vary by up to a factor of 2.

Two distinct methods of analysis are used. In the first method [4.18], two photon clusters are combined, and all invariant mass combinations $m_{\gamma\gamma}$ of two photons in a given event are constructed. Fig. 4.16 shows the distribution of these masses for the three c.m. energies. A fit to the data using a Gaussian plus a background term, given by a second order polynomial, yields a width of the π^0 peak of $\sigma = 16 \pm 4$, 23 ± 3 and 23 ± 5 (MeV/c^2) at $W = 14$, 22 and 34 GeV respectively. This first method of analysis is useful up to a π^0 momentum of about 8 GeV/c.

In order to reach higher π^0 momenta, a second method [4.19] is used. The efficiency to reconstruct high energy π^0's from the two decay photons depends strongly on the probability to resolve two nearby photons in the liquid argon calorimeter. Given the granularity of the CELLO liquid argon calorimeter, this reconstruction efficiency decreases rapidly in the momentum interval $6.0 < P_{\pi^0} < 8.0$ GeV/c. In this second method of analysis, only one single neutral shower is detected in the calorimeter.

With Monte Carlo generated events CELLO obtained an acceptance matrix A_{ij} by determining the probability for a π^0 from an energy bin E_i to be reconstructed as a single neutral shower into an energy bin E_j within a cone of 5 degrees around the original π^0 direction of flight. Using this A_{ij}, the π^0 cross sections are calculated from the yield of single neutral showers in the data.

The recent CELLO results [4.19] for the invariant cross sections $(s/\beta)\,\mathrm{d}\sigma/\mathrm{d}x_E$ for inclusive π^0-production are shown in figs. 4.17 and 4.18. The errors include the statistical and systematic ones added in quadrature. The results for small x at $W = 34$ GeV are somewhat lower than the previous CELLO result based on the same data [4.18]. This is attributed to improved evaluation of detector acceptance. Comparison with the TASSO data [4.21] on $\pi^\pm$ to be described in the next section yields the ratio $2\pi^0/(\pi^+ + \pi^-) = 1.21 \pm 0.42$, 0.96 ± 0.40 and 1.01 ± 0.35 at $W = 14$, 22 and 34 GeV respectively. Finally, the TASSO [4.17] and CELLO results on the inclusive cross section for π^0 are found to be in good agreement at $W = 34$ GeV in the x-range of overlap $x < 0.2$, but, at $W = 14$ GeV, the CELLO result is higher than, but still compatible with, the TASSO result.

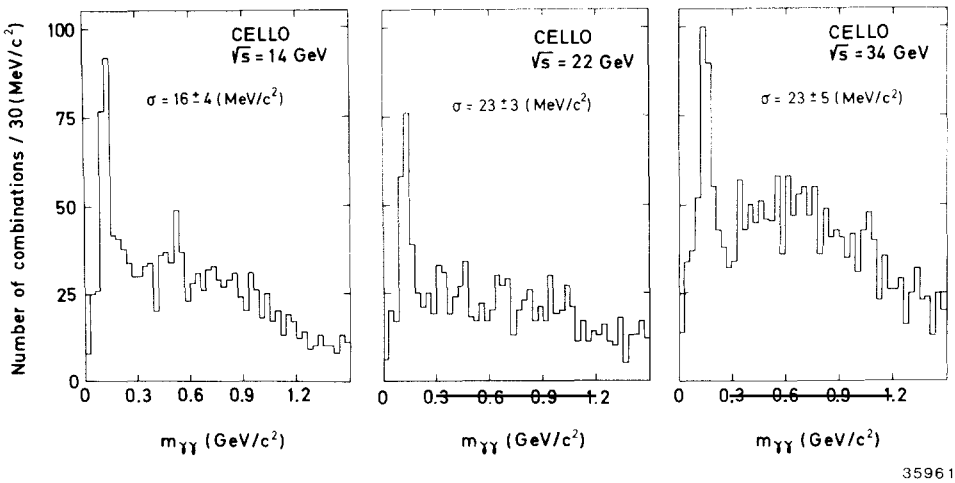

Fig. 4.16. CELLO [4.19] distribution of the invariant mass combinations of all photon pairs at $W = 14$, 22 and 34 GeV.

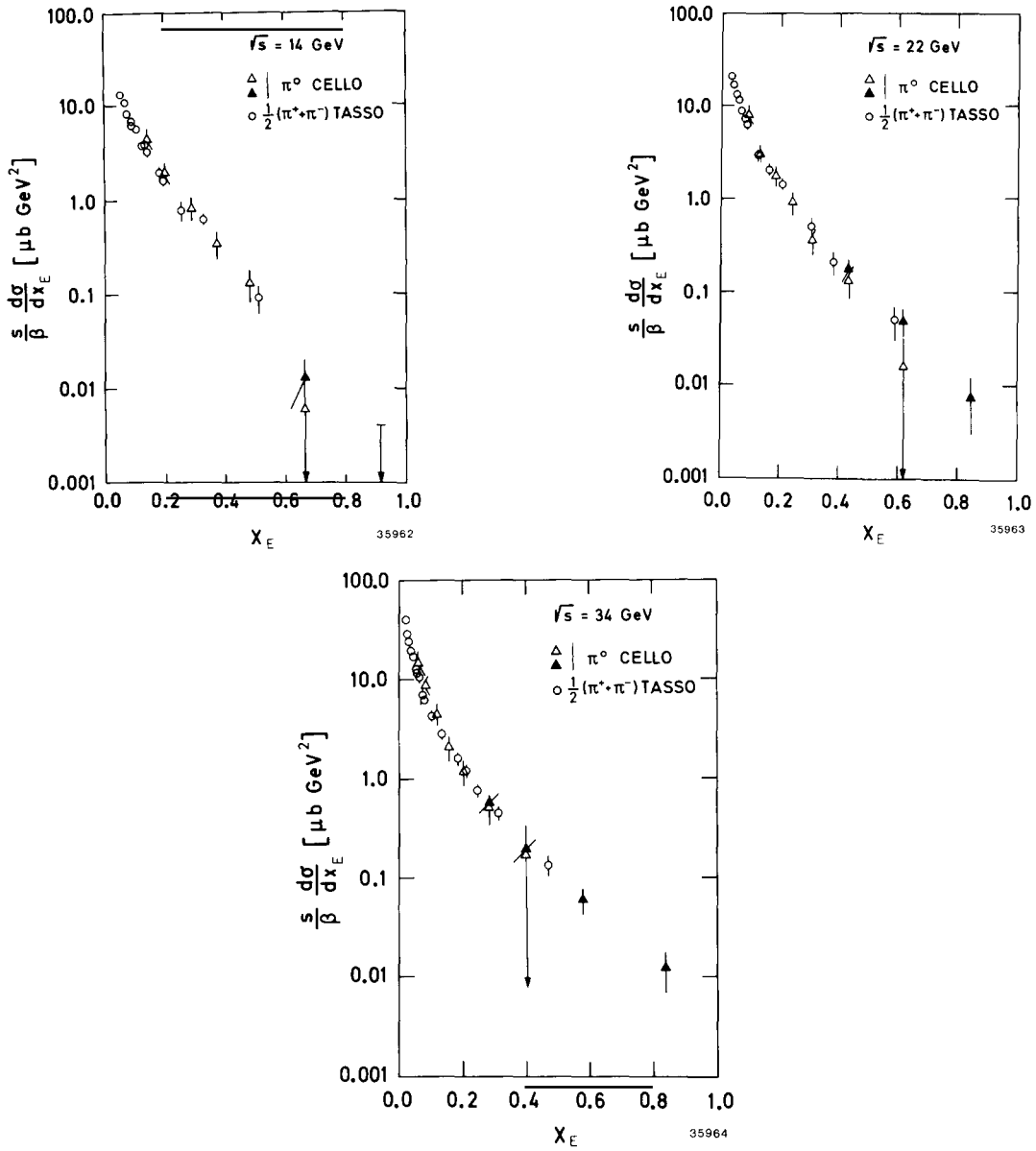

Fig. 4.17. Comparison of the CELLO [4.19] inclusive cross sections $(s/\beta)\,d\sigma/dx_E$ for π^0 production at W = 14, 22 and 34 GeV with one half of the TASSO [4.21] inclusive cross sections for $\pi^\pm$. For the CELLO data, the open and full triangles refer to the results obtained by the first and second methods of analysis respectively.

4.7. Inclusive cross section of $\pi^\pm$

At TASSO, the separation of the charged particles $\pi^\pm$, $K^\pm$, and p, $\bar{p}$ is performed with the inner and the hadron-arm time-of-flight counters and with Čerenkov counters [4.20 to 4.22, 4.37]. The inner time-of-flight system (ITOF) is located at a radial distance of 132 cm from the beam axis. It consists of 48 counters viewed by phototubes at both ends and covers a solid angle of 82% of 4π. The r.m.s. time

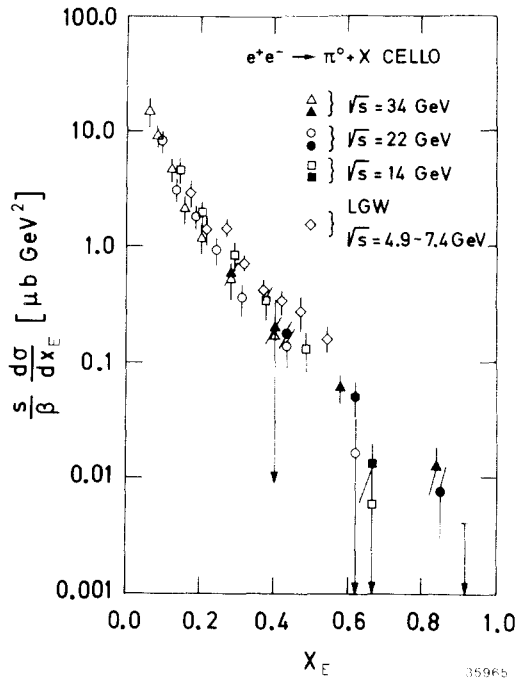

Fig. 4.18. CELLO [4.19] inclusive cross sections $(s/\beta)\,d\sigma/dx_E$ for π^0 production at W = 14, 22 and 34 GeV. In addition π^0 inclusive data from lower energies [4.36] are also shown. For the CELLO data, the open and full symbols refer to the results obtained by the first and second methods of analysis respectively.

resolution is 0.45 ns for particles passing through the center of the counters, improving approximately linearly to 0.27 ns for particles passing through near the end of the scintillators. Averaged over the whole data sample, the r.m.s. time resolution was 0.38 ns. The hadron-arm time-of-flight system (HATOF) is located at an average distance of 5.5 m from the interaction point and covers a solid angle of 20% of 4π. The average r.m.s. time resolution in the HATOF counters was 0.45 ns. Fig. 4.19(a and b) shows the scatter plot of particle velocity β versus momentum in the ITOF and HATOF counters respectively. Clear pion, kaon and proton bands can be seen.

Three types of Čerenkov counters, arranged sequentially and subtending a solid angle of 19% of 4π, were used for particle identification at higher momenta. The radiators are silica aerogel [4.38], Freon 114 and CO_2 with threshold momenta for pions of 0.7, 2.7 and 4.8 GeV/c, for kaons of 2.3, 9.5 and 17 GeV/c, and for protons of 4.4, 18 and 32 GeV/c respectively.

The momentum ranges where charged particle separation has been achieved at TASSO with these three systems are listed in table 4.6.

The performance of the Čerenkov counter system is shown in fig. 4.20 at W = 34 GeV. Fig. 4.20a shows the normalized aerogel counter rate $f_A = N_{\text{aerogel}}/N_{\text{tot}}$, i.e. the number of particles in a given momentum interval which produce light in aerogel divided by the total number of particles selected for particle identification in that interval. The data shown are corrected for background due to electrons and non-recognized showers. A steep rise is observed above 0.6 GeV/c showing the pion threshold in aerogel. This is followed by a plateau region between 1.2 and 2.3 GeV/c and then a second rise is observed above the K threshold. The curve in fig. 4.20a shows the pion contribution to f_A which is calculated from the measured pion fractions [4.21] multiplied by the efficiency of the aerogel counters.

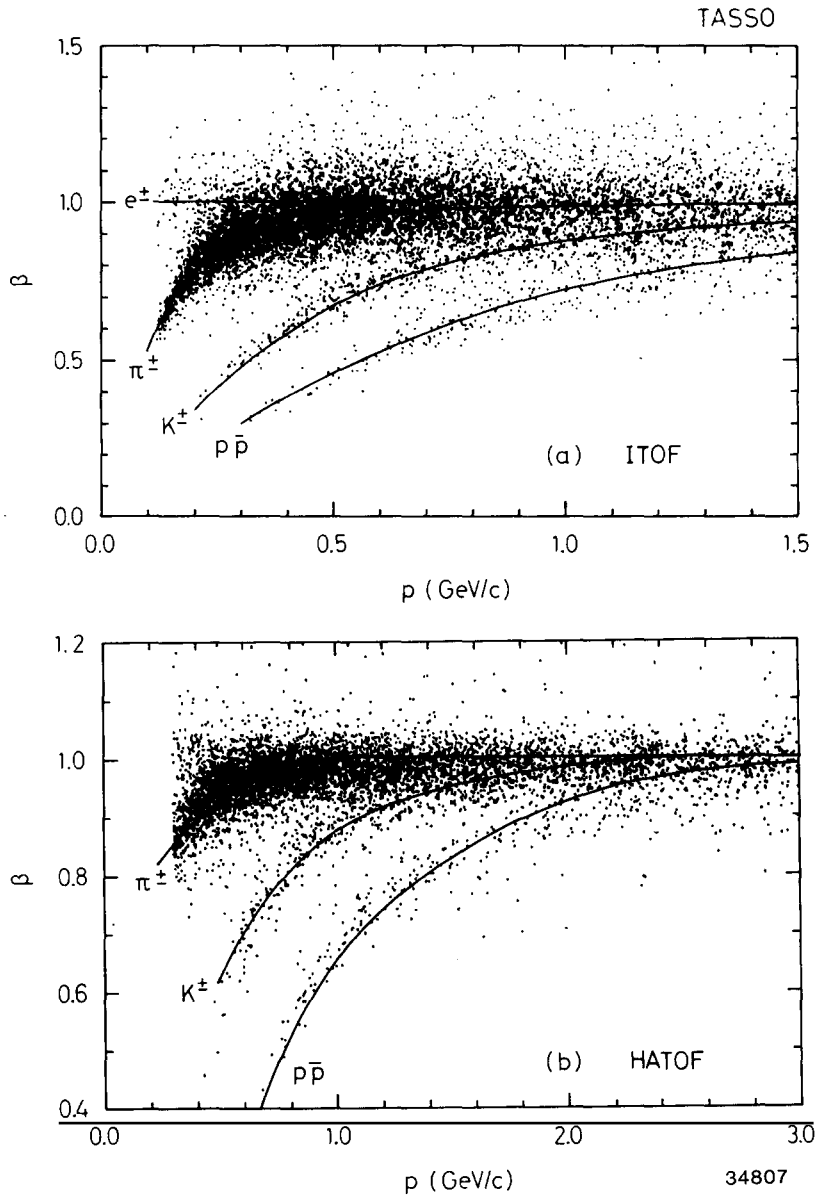

Fig. 4.19. Particle velocity versus momentum from TASSO [4.22] for charged tracks from multihadronic events: (a) inner time-of-flight counters, and (b) hadron-arm time-of-flight counters. The solid lines give $p = mc\beta(1-\beta^2)^{-1/2}$.

The difference between f_A and this curve is shown in fig. 4.20b for all momenta above 0.8 GeV/c. The rise above the K threshold is observed more clearly than in f_A, since the pion fraction drops with increasing momentum. With the amount of data used, the proton threshold above 4.5 GeV/c is not observed.

The normalized rates of the Freon counters $f_F = N_{Freon}/N_{tot}$ and of the CO_2 counters $f_C = N_{CO_2}/N_{tot}$ are shown in fig. 4.20c. The pion thresholds between 2.7 and 3 GeV/c in Freon and between 5 and 7 GeV/c in CO_2 are clearly seen.

Table 4.6
Momentum ranges for $\pi^\pm/K^\pm/p, \bar{p}$ separation for the various systems in the TASSO detector

	Momentum range in GeV/c for	
	$\pi^\pm/K^\pm$ separation	$K^\pm/p, \bar{p}$ separation
Inner time-of-flight system	0.3–1.0	0.4–1.4
Hadron-arm time-of-flight system	0.5–1.5	1.0–2.0
Čerenkov counter system	Above 0.8	3–6 and above 10
Combined	Above 0.3	0.4–2.0, 3–6 and above 10

The detection efficiencies of the Čerenkov counters for the different particle species are calculated as a function of momentum, using the efficiency plateau values as obtained from cosmic ray muons and taking into account the momentum resolution of the detector and the measured hadron momentum spectrum [4.13]. The efficiencies are listed in table 4.7.

In the momentum range 3–6 GeV/c, pions are identified by the Freon counters whereas kaons and protons are separated on a statistical basis making use of their different detection efficiencies in the aerogel counters.

The numbers of $\pi^\pm$, $K^\pm$, and p, $\bar{p}$ are corrected for the decay of pions and kaons, for nuclear interactions in the material in front of the counters, and for the contamination due to muons. Within statistical errors equal numbers of positive and negative particles are observed for each species at all momenta and c.m. energies. It is also verified that the tracks selected for particle identification have the same spectra in total momentum and transverse momentum with respect to the sphericity axis as all central detector tracks. Furthermore, the events in which tracks are selected for particle identification have the same sphericity and multiplicity distribution as the total hadronic event sample. The results of the ITOF, HATOF and Čerenkov analyses are in good agreement in the regions of overlap and are combined.

The measured charged-particle fractions have already been discussed in section 4.5. The cross section for the inclusive production of charged hadrons, $e^+e^- \to h^\pm X$ where $h^+ = \pi^+, K^+$, and p, $\bar{p}$, is obtained by multiplying the inclusive cross section for all charged hadrons (see section 4.3) by this particle fraction. The resulting scaled cross sections $(s/\beta)\,d\sigma/dx_E$ for $\pi^\pm$ at $W = 14$, 22 and 34 GeV are shown in fig. 4.21. For $x_E \leqq 0.1$, these cross sections do not show any significant energy variation between 14 and 34 GeV. However, for larger x_E values, one observes higher cross sections at 14 GeV than at 34 GeV. This effect becomes quite pronounced in comparison with the 5.2 GeV data from DASP [4.32].

4.8. Inclusive cross section of $K^\pm$

The TASSO [4.22] system of separating $\pi^\pm$, $K^\pm$, and p, $\bar{p}$ has already been described in the preceding section. In particular, the identification of $K^\pm$ requires both $\pi^\pm/K^\pm$ and $K^\pm/p, \bar{p}$ separations. The momentum ranges for both of these separations have been summarized in table 4.6.

The TASSO [4.22] scaled cross section $(s/\beta)\,d\sigma/dx_E$ for $K^\pm$ is shown in fig. 4.22 for $W = 14$, 22 and 34 GeV. In both fig. 4.21 and fig. 4.22, all statistical and systematic errors are included in the error bars

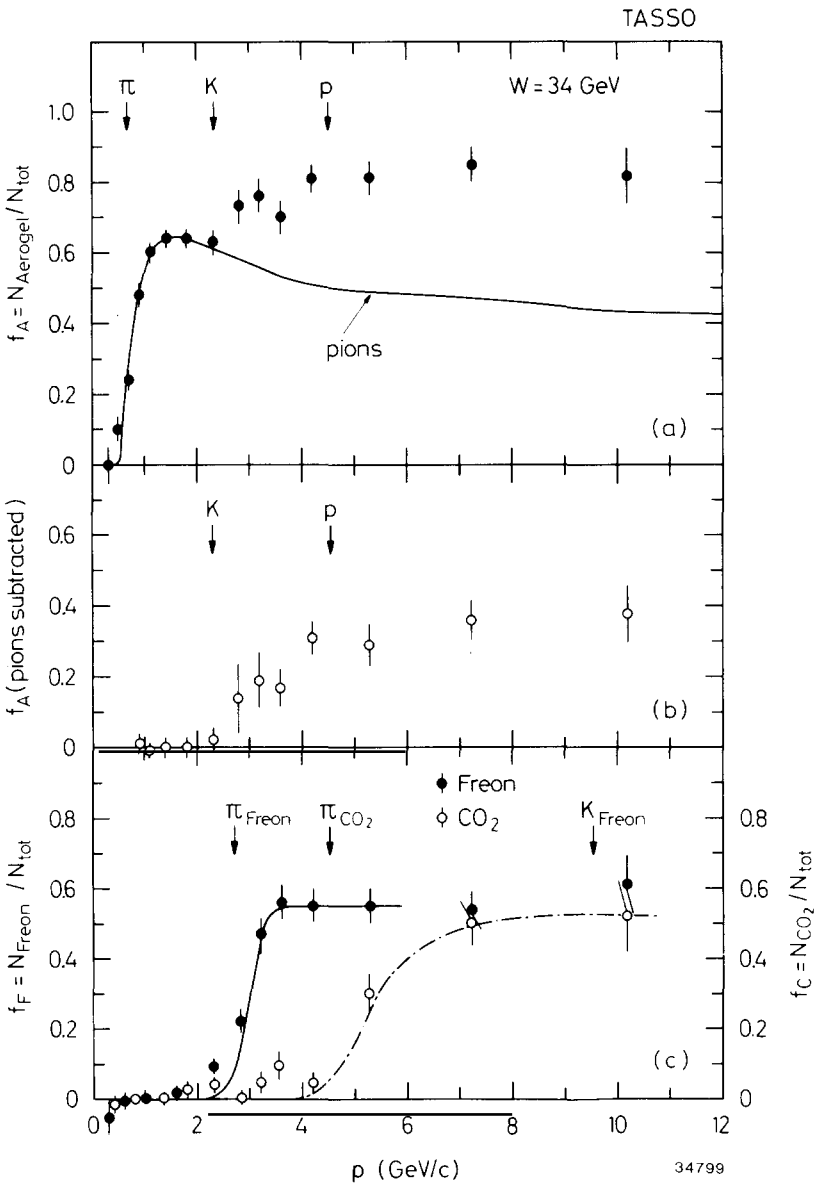

Fig. 4.20. Fraction of tracks selected for particle identification by TASSO [4.22] from multihadronic events at $W = 34$ GeV which produce light in the Čerenkov counters. The data are corrected for background due to electrons and non-recognized electromagnetic showers. The error bars include all statistical and systematic errors. The arrows indicate the pion, kaon and proton thresholds. (a) Aerogel counters. The solid line is the pion contribution. (b) The same as in (a), but with the pion contribution subtracted. The error bars contain also the uncertainties resulting from the error of the pion fraction. (c) Freon counters (closed circles) and CO_2 counters (open circles). The solid and dash-dotted lines are calculated pion threshold curves assuming a constant pion fraction of 0.55 in the momentum range of 2.0 to 12.0 GeV/c. Errors as in (a).

except for an overall normalization of 8.5% at $W = 14$ GeV, 6.3% at $W = 22$ GeV, and 5.5% at $W = 34$ GeV. Unlike fig. 4.21 for $\pi^{\pm}$, there is no clear indication in fig. 4.22 of any decrease in the scaled cross section from $W = 14$ GeV to 34 GeV, even for large values of x_E. However, a comparison with the DASP data [4.32] at lower energy of 5.2 GeV shows that such a decrease in the scaled cross section with increasing W is present for $K^{\pm}$ as well as $\pi^{\pm}$. Such a scale violation is expected from QCD since gluon emission should lead to a depletion of hadrons at large x_E, as discussed in section 4.3.

Table 4.7
Mean detection efficiency of the Čerenkov counters for pions, kaons and protons (antiprotons) in the momentum regions $3.0 < p < 6.0$ GeV/c and $10.0 < p < 17.0$ GeV/c. The uncertainty in the efficiency is ±0.05 in the threshold regions and ±0.02 (±0.01) for the aerogel (Freon and CO_2) counters in the plateau region

Momentum range (GeV/c)	Detection efficiency					
	Aerogel			Freon		CO_2
	π	K	p	π	K	π
3.0–3.4	0.90	0.69	-	0.77	-	-
3.4–3.8	0.90	0.76	-	0.95	-	-
3.8–4.6	0.90	0.81	0.09	0.99	-	0.04
4.6–6.0	0.91	0.85	0.46	>0.99	-	0.44
10.0–17.0	0.91	0.90	0.84	>0.99	0.54	0.96

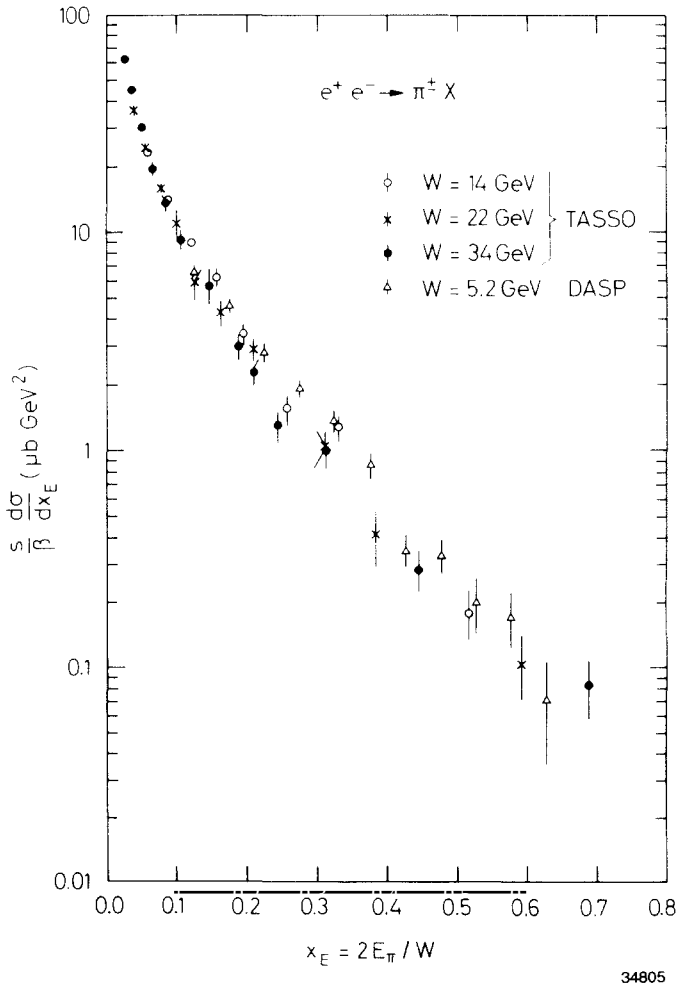

Fig. 4.21. TASSO [4.22] scaled cross section $(s/\beta)\,d\sigma/dx_E$ for $\pi^\pm$ as a function of x_E for c.m. energies W = 14, 22 and 34 GeV. Also shown are the DASP data at W = 5.2 GeV.

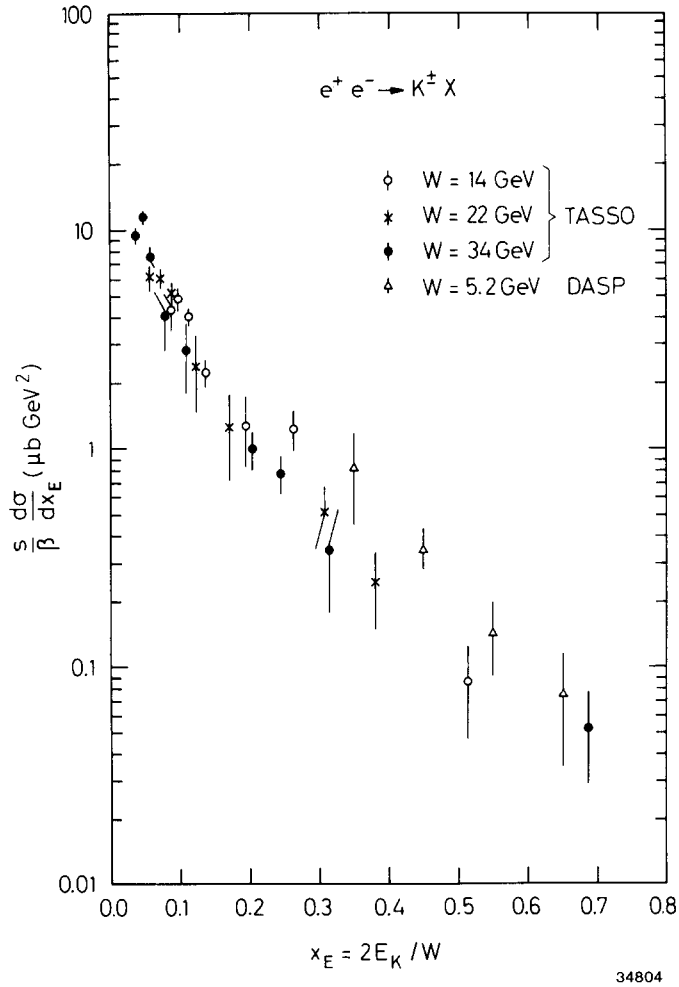

Fig. 4.22. TASSO [4.22] scaled cross section $(s/\beta)\,d\sigma/dx_E$ for $K^\pm$ as a function of x_E for c.m. energies W = 14, 22 and 34 GeV. Also shown are the DASP data at W = 5.2 GeV.

4.9. Inclusive cross section of K^0

At PETRA, K_L^0 has not been detected and K_s^0 is detected through the charged decay mode $K_s^0 \rightarrow \pi^+\pi^-$. Therefore the inclusive cross sections of K^0 and $\bar{K}^0$ are always taken to be equal and also equal to the inclusive cross section of K_s^0 which is the actual quantity measured.

This inclusive cross section was first measured by TASSO [4.23], followed by PLUTO [4.24], and more recently JADE [4.2]. As already discussed in section 4.7, at TASSO $\pi^\pm$ can be identified in the hadron arms but only up to 1 GeV/c outside the hadron arms. Therefore, in this measurement of the inclusive cross section for K_s^0, this $\pi^\pm$ identification is not used. Instead, the method used by all three Collaborations consists of identifying the decay $K_s^0 \rightarrow \pi^+\pi^-$ by locating the decay vertex and verifying that the line joining the intersection point to the decay vertex agrees in direction (in the transverse plane) with the sum of the momenta of the two charged tracks. This is feasible because the K_s^0 lifetime when multiplied by c is $c\tau = 2.7$ cm. With cuts based on this consideration, the charged tracks of

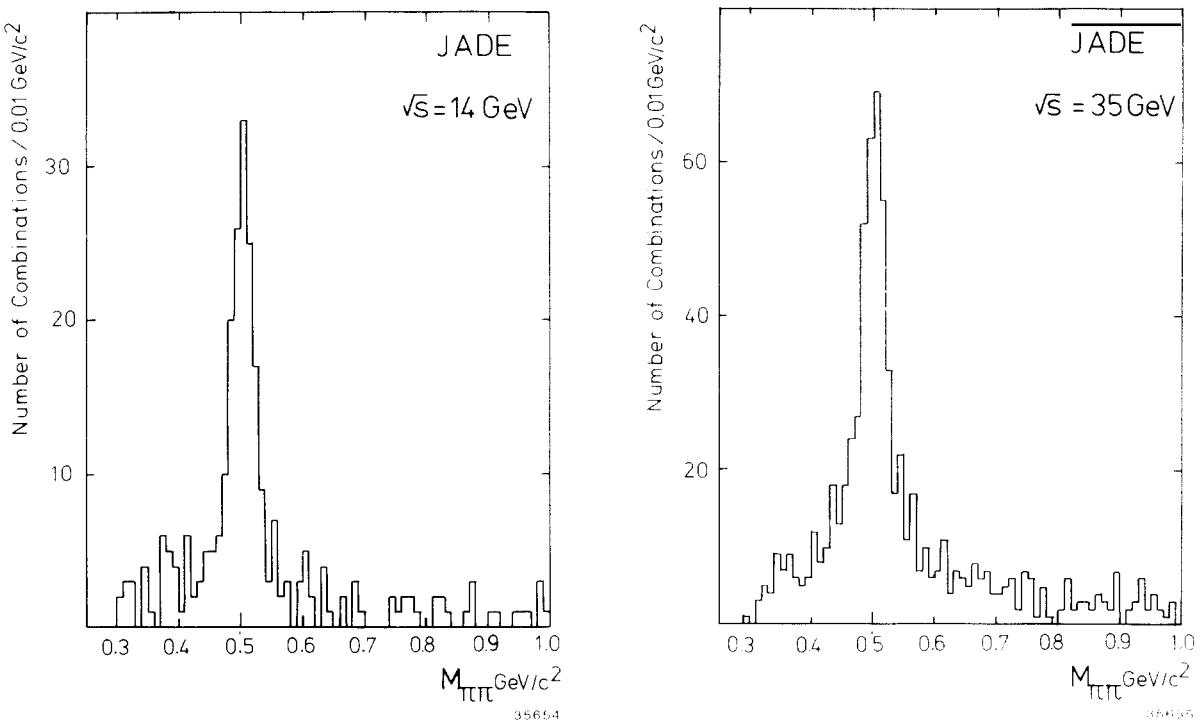

Fig. 4.23. JADE [4.2] invariant mass distribution of oppositely charged tracks satisfying the selection criteria. Correction for energy loss is made and pion masses are assumed. The width of the peak obtained by a Gaussian fit is 17.3 MeV/c^2(σ) at 14 GeV and 21.3 MeV/c^2(σ) at 35 GeV.

opposite signs are assumed to be pions and the invariant mass is calculated. The K^0_s peak is quite pronounced, as shown in fig. 4.23 from the JADE data. The observed value of the K^0_s lifetime agrees with the usual value. The PETRA results are shown in fig. 4.24.

The total K^0 yield is shown in fig. 4.25 and compared with other data [4.24, 4.39]. The increase is quite significant, and is comparable to that of multiplicity, as seen from fig. 4.1.

4.10. Inclusive cross section of ρ^0

The inclusive cross section of ρ^0 has been measured by the TASSO Collaboration [4.25] at W = 14, 22 and 34 GeV. We discuss the analysis at 34 GeV.

Since π/K separation is not used, each charged particle is treated both as pion and kaon. The invariant mass spectra for $\pi^-\pi^+$ and $K^\mp\pi^\pm$ are assumed to be given by the corresponding like-sign spectra plus a sum of contributions from ρ^0, K^{*0}, K^0 and ω meson decay products (or reflections resulting from wrong mass assignments) and an additional linear term. The like-sign spectra are normalized to the region $1.7 < m_{\pi\pi} < 2.7$ GeV and $2.0 < m_{K\pi} < 3.0$ GeV. Standard masses and widths folded with the apparatus resolution are used in the fit. The reflections resulting from wrong mass assignments are not strongly momentum dependent and are described by a fixed shape for each decay mode. The result of the fit to the $m_{\pi^+\pi^-}$ spectrum, integrated over the range $0.1 < x_E < 0.7$, is shown in fig. 4.26.

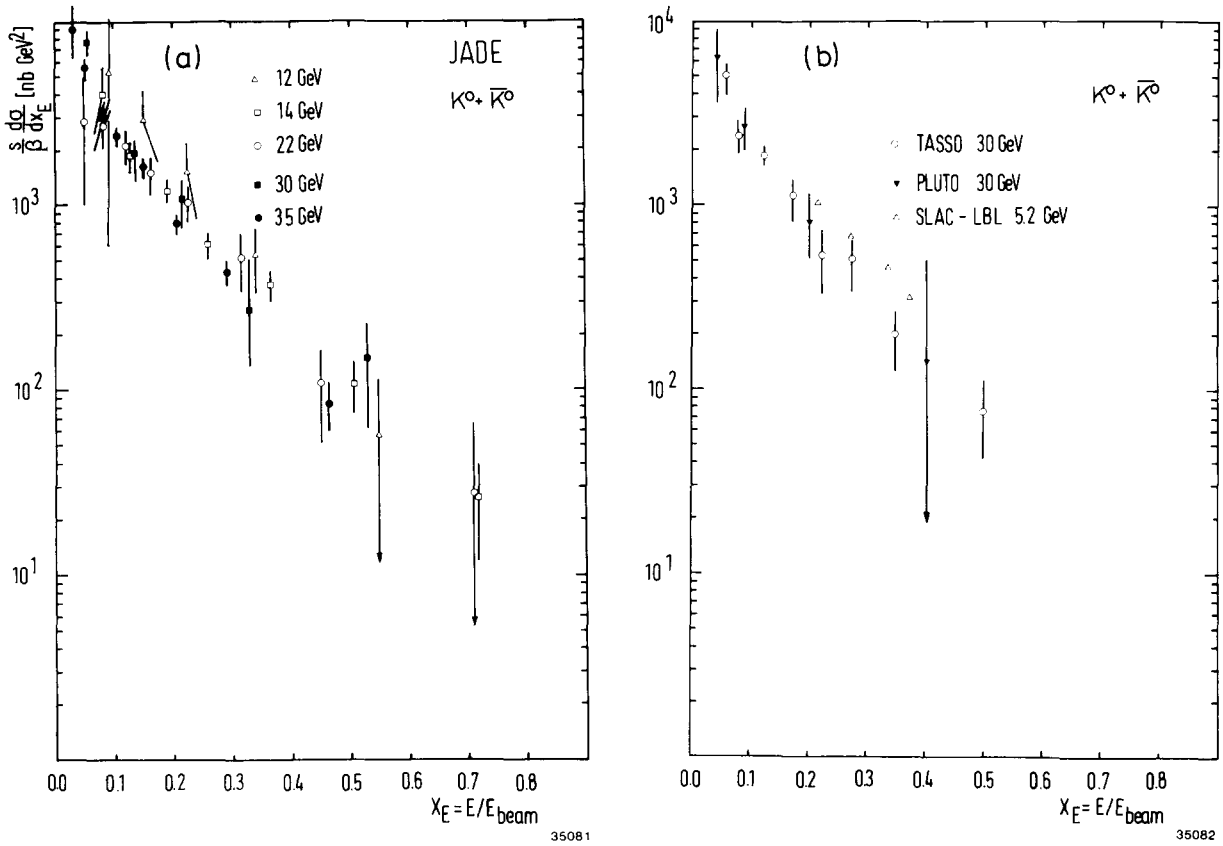

Fig. 4.24. The PETRA [4.2] scaled cross section for neutral kaons.

The data in the range of x_E from 0.1 to 0.7 are analyzed in four x_E bins. The scaled inclusive differential cross section $(s/\beta)\,d\sigma/dx_E$ for ρ^0 production is shown in fig. 4.27. The errors shown are statistical only and do not include the 20% systematic error determined by using different background calculations. Integration of the differential cross section gives $(0.41 \pm 0.04 \pm 0.08)$ ρ^0 per event in the range $0.1 < x_E < 0.7$, as already discussed in section 4.5. Also shown in fig. 4.27 is the $\pi^\pm$ cross section measured [4.21] at the same energy. In the range $0.1 < x_E < 0.4$, the ratio $\sigma(\rho^0)/\sigma(\pi^+ + \pi^-)$ is found to be $0.24 \pm 0.03 \pm 0.05$. Due to limited statistics and reduced acceptance, the data for $W = 14$ and 22 GeV have each been analyzed in only a single bin. In the region $0.2 < x_E < 0.7$, the number of ρ^0 per event is found to be $0.33 \pm 0.06 \pm 0.07$ $(0.22 \pm 0.06 \pm 0.05)$ at $W = 14$ (22) GeV.

The parameters in the Field–Feynman fragmentation models have been described in section 2.10. The rate of ρ^0 production is determined mainly by the parameter $P/(P + V)$. From the measured rate of ρ^0 production in the range $0.2 < x_E < 0.7$ at $W = 34$ GeV, TASSO has obtained

$$P/(P + V) = 0.42 \pm 0.08 \pm 0.15\,, \tag{4.17}$$

which is consistent within error with the value given in (2.26). In this model, in addition to direct production, only ρ^0 production via η' decay is significant (12% of the total ρ^0 production). The full curve shown in fig. 4.27 is the Field–Feynman result assuming $P/(P + V) = 0.42$. There is good agreement with

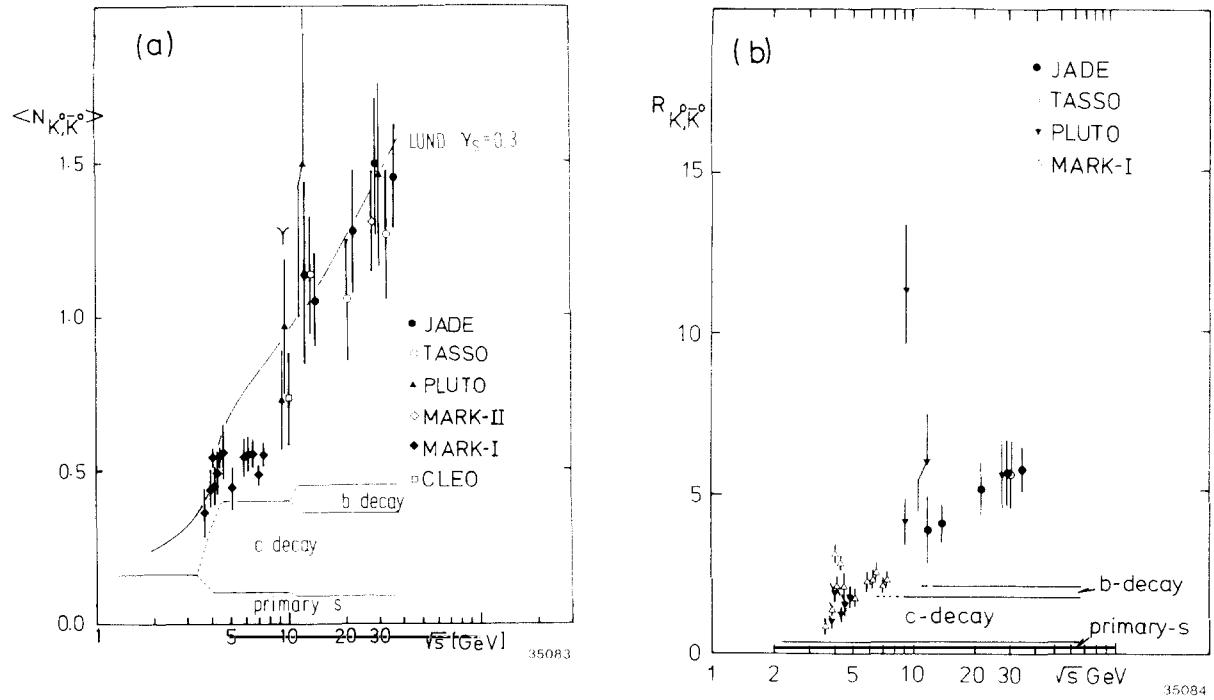

Fig. 4.25. (a) Dependence of the number of neutral kaons per event on the center-of-mass energy W. Systematic errors are included except for the PLUTO data. (b) Dependence of $R(K^0, \bar{K}^0) = [\sigma(K^0) + \sigma(\bar{K}^0)]/\sigma_{\mu\mu}$ on W. When W reaches the threshold of open charm or open bottom, contributions from the weak decay of the heavy quarks are switched on. In the energy region far above the bottom threshold, most of the neutral kaons come from the fragmentation process. This figure is from [4.2].

the data, and the measured rates of ρ^0 production at $W = 14$ and 22 GeV in the region $0.2 < x_E < 0.7$ are also consistent with this value of $P/(P + V)$.

Integration of the differential cross section allows a measure of R_{ρ^0}. At $W = 34$ GeV, the regions not measured, $x_E < 0.1$ and $x_E > 0.7$, are estimated to contribute ~40% and ~3% of the total cross section respectively. At $W = 14$ (22) GeV, the regions $x < 0.2$ and $x > 0.7$ contribute 43 (59)% and 6 (4)% of

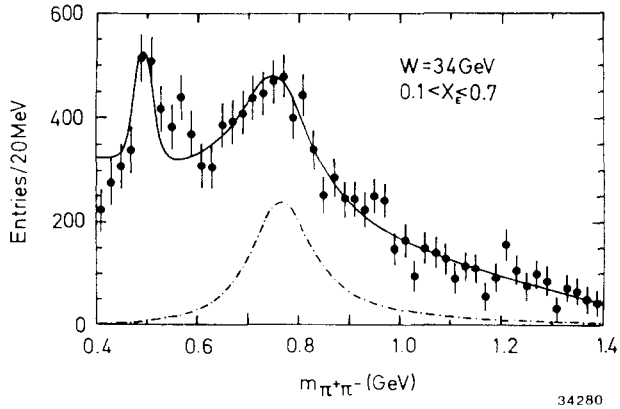

Fig. 4.26. The TASSO [4.25] $m_{\pi^+\pi^-}$ spectrum following subtraction of the like-sign spectrum for $W = 34$ GeV. The solid curve shows the result of the fit and the dash-dotted curve the ρ^0 contribution.

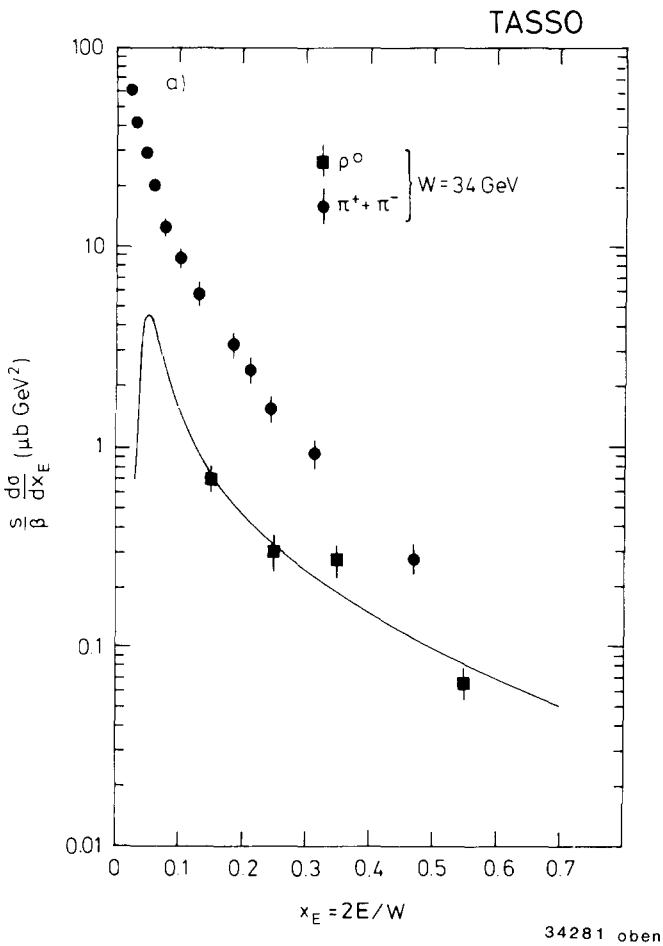

Fig. 4.27. The TASSO [4.25] scaled cross section $(s/\beta)\,d\sigma/dx_E$ for ρ^0 production at $W = 34$ GeV. Also shown is the cross section for $\pi^+ + \pi^-$ production at this energy. The smooth curve is the Field–Feynman Monte Carlo prediction for ρ^0 production assuming $P/(P + V) = 0.42$.

the total cross section respectively. The results are shown in fig. 4.11. The errors shown are statistical only. Also shown in fig. 4.11 are measurements at lower energy [4.40].

4.11. Inclusive cross section of proton

One of the major excitements at PETRA is the observation of the copious production of baryons. Over three years ago, TASSO [4.20] observed the inclusive production of protons and antiprotons. JADE [4.26] then confirmed the inclusive antiproton spectrum to about 1 GeV/c and also observed the inclusive anti-Λ spectrum to about 1.4 GeV/c, while TASSO [4.27] obtained the Λ and $\bar{\Lambda}$ spectrum all the way up to 10 GeV/c in momentum.

The TASSO TOF and Čerenkov systems for particle identification have already been described in section 4.7. JADE, on the other hand, concentrates entirely on the antiprotons, which are identified by means of a simultaneous measurement of momentum and energy loss (dE/dx) in the drift chamber, a special feature of the JADE detector (see section 1.5.3). $\bar{p}$ candidates are selected in the momentum

range 0.3 to 0.9 GeV/c where the only source of background is protons entering the jet chamber from the outside and moving towards the center of the detector and causing a misidentification as antiprotons.

The TASSO [4.22] inclusive cross section for p and $\bar{p}$ at $W = 34$ GeV has already been shown in figs. 4.9 and 4.10. In fig. 4.28, these cross sections are given for $W = 14$, 22 and 34 GeV, and compared with the DASP result [4.32] at $W = 5.2$ GeV. The JADE results, over smaller momentum ranges, are compatible.

The JADE Collaboration [4.26] has initiated the study of a possible baryon–antibaryon correlation within the same event. Although they find an interesting anticorrelation in the azimuthal angle $\Delta\phi$ formed by the baryon–antibaryon momenta projected onto the plane perpendicular to the event axis, this anticorrelation is not verified by TASSO with much larger statistics. We describe briefly the TASSO result [4.22]. With the momenta of p and $\bar{p}$ restricted to the range 0.4–1.2 GeV/c, TASSO has found nearly 100 events with 2p, 2$\bar{p}$, or p + $\bar{p}$. The precise number of events is shown in table 4.8. On the basis of the 75 events with at least one p and one $\bar{p}$, the results are shown in fig. 4.29. In particular, it is seen from fig. 4.29b that the data are consistent with no correlation in $\Delta\phi$.

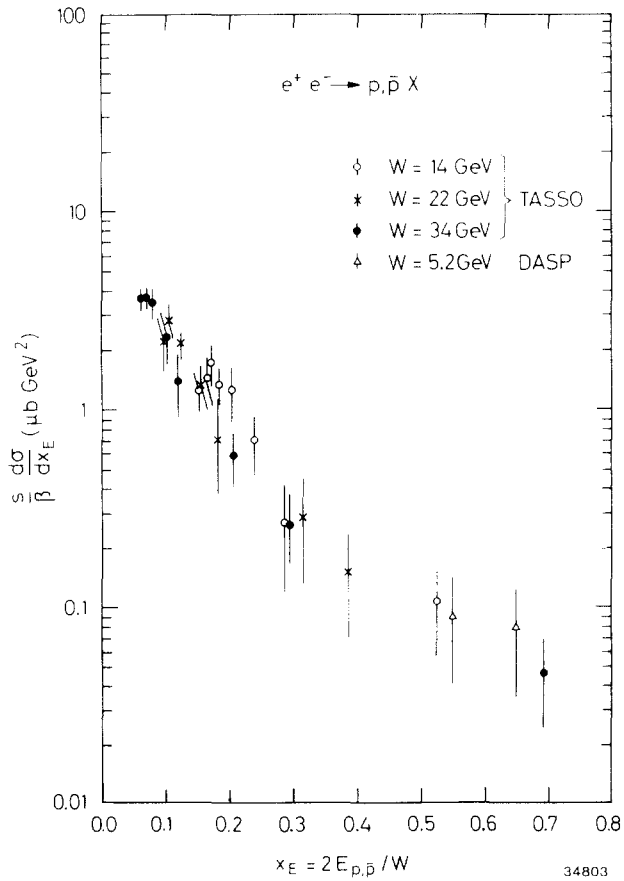

Fig. 4.28. The TASSO [4.22] scaled cross section $(s/\beta)\,d\sigma/dx_E$ for p, $\bar{p}$ as a function of x_E for c.m. energies $W = 14$, 22 and 34 GeV. Also shown are the DASP data at $W = 5.2$ GeV.

Table 4.8
Number of events with two or more protons and/or antiprotons detected (TASSO) [4.22]

W (GeV/c)	Total number of hadronic events	(p + $\bar{p}$) events	(2p) or (2$\bar{p}$) events	(2p + 1$\bar{p}$) or (1p + 2$\bar{p}$) events
14	2 704	19	3	0
22	2 120	6	1	1
34	19 679	47	18	2

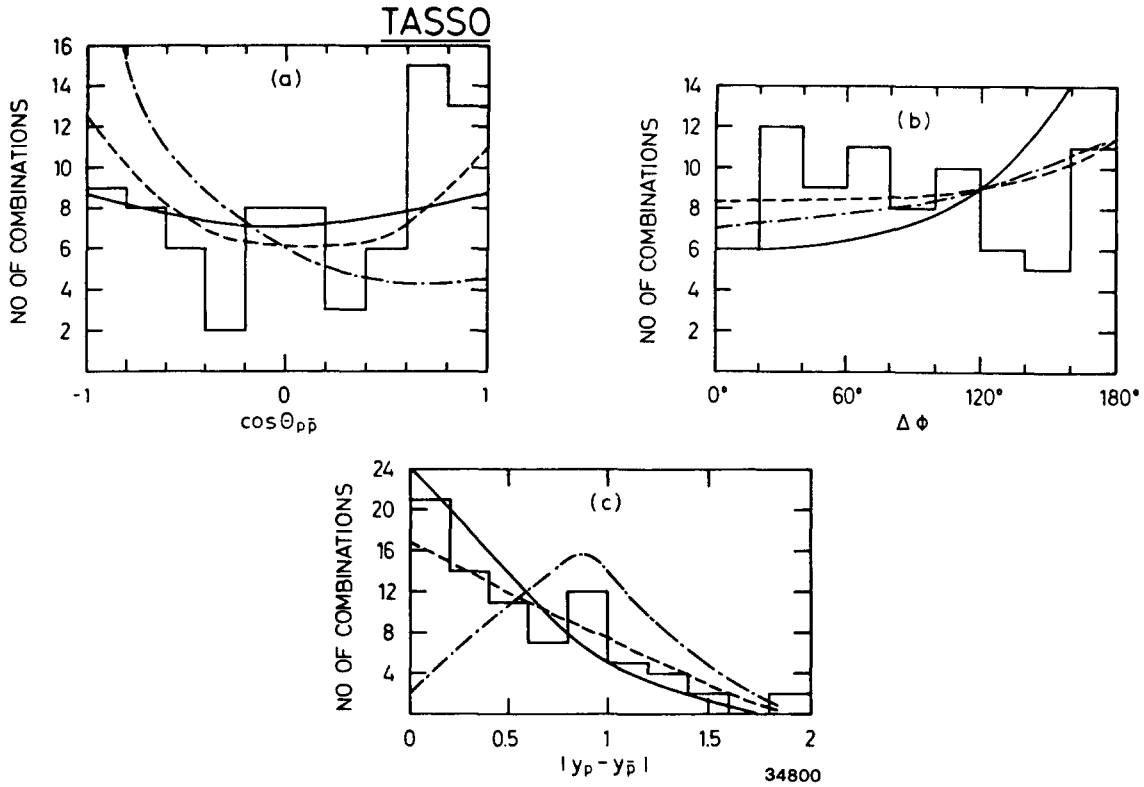

Fig. 4.29. TASSO [4.22] proton–antiproton correlations for events with at least one observed proton and antiproton. The data from all three c.m. energies W = 12, 22 and 34 GeV have been combined. For events with 2p + 1$\bar{p}$ or 1p + 2$\bar{p}$ both p$\bar{p}$ combinations are plotted. (a) cos $\theta_{p\bar{p}}$, where $\theta_{p\bar{p}}$ is the angle between p and $\bar{p}$, (b) difference of azimuthal angle $\Delta\phi$ of p and $\bar{p}$, measured in the plane perpendicular to the jet axis, (c) difference of p and $\bar{p}$ in rapidity. The curves are the prediction of various models referred to in ref. [4.22].

4.12. Inclusive cross section of Λ

As mentioned in the preceding section, Λ production at PETRA was first measured by the JADE Collaboration [4.26] in the momentum range 0.4–1.4 GeV/c, and then shortly thereafter by the TASSO Collaboration [4.27] in the much larger momentum range 1–10 GeV/c. Both experiments are to be described in some detail in this section.

JADE has identified $\bar{p}$ using dE/dx technique in the momentum range 0.3–0.9 GeV/c. A sample of events with $\bar{p}$ candidates identified by ionization loss in the enlarged momentum range 0.3–1.3 GeV/c is scanned for antilambdas ($\bar{\Lambda}$) using the decay mode $\bar{\Lambda} \to \bar{p}\pi^+$. The enlarged sample contains particles of ambiguous mass assignment (e^- or $\bar{p}$), but due to the narrow width of the lambda, these could eventually be subtracted from the lambda sample.

The following criteria have to be satisfied:

(i) The closest approaches, d_0, of both tracks to the beam line must be greater than 2 mm.

(ii) The momentum of the π^+-candidate is less than 40% of the momentum of the $\bar{p}$-candidate. This essentially removes any remaining K^0_S candidates.

(iii) The two tracks have a common origin in space.

(iv) The main vertex and the decay vertex are separated by more than 10 mm and less than 200 mm in the plane perpendicular to the beam.

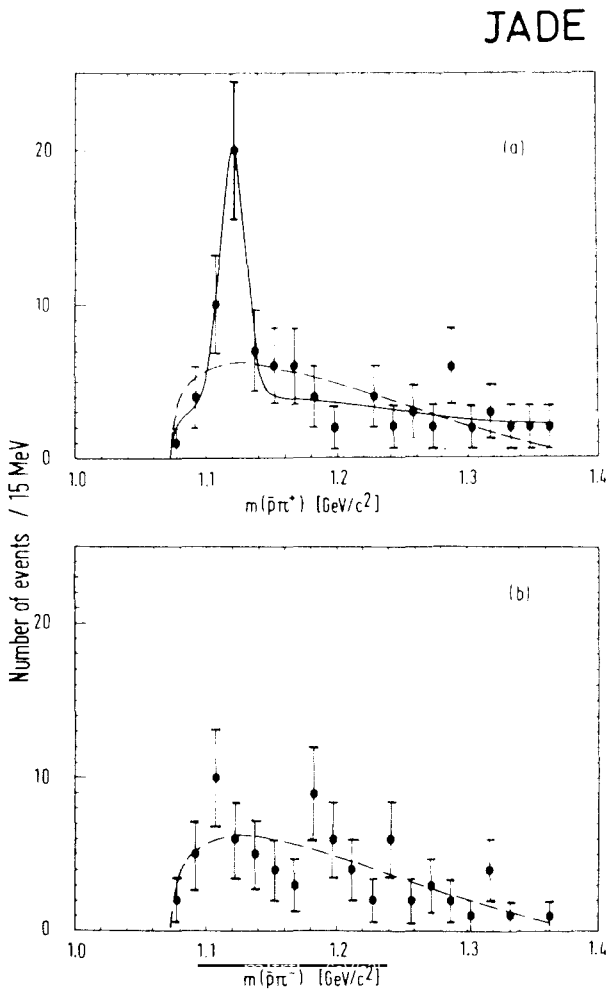

Fig. 4.30. Fit to the $\bar{p}\pi^+$ mass spectrum from JADE [4.26] (a) and to the $\bar{p}\pi^-$ mass spectrum (b). The dashed line represents a fit to the $\bar{p}\pi$ spectrum and is shown on the $\bar{p}\pi^+$ spectrum for comparison.

The invariant masses of the selected $\bar{\Lambda}$ candidates are shown in fig. 4.30a where a prominent $\bar{\Lambda}$ signal is visible over a broad background. The mass distribution of the wrong charge combinations $\bar{p}\pi^-$ does not show any peak structure [fig. 4.30b] as expected.

In the TASSO experiment [4.27], the protons and antiprotons are not identified, and the candidates for $\Lambda \to p\pi^-$ and $\bar{\Lambda} \to \bar{p}\pi^+$ are first selected as follows:

(i) Only particles with $p_T > 0.1$ GeV/c and $|\cos\theta| < 0.87$ are considered.

(ii) All pairs of oppositely charged trajectories are required to satisfy a three-dimensional fit which demands that they intersect at a point in space. The higher-momentum particle is considered to be the proton (antiproton).

(iii) Pairs consisting of tracks with more hits in the tracking chambers in front of the decay point than could be considered accidental or with more than 3 hits missing following the decay point are rejected.

(iv) The direction of the line joining primary vertex and decay point has to agree with the direction of the Λ momentum vector within 3° in the projection perpendicular to the beam.

(v) Electron pairs are moved from the sample by demanding that the effective mass of the pair be greater than 50 MeV if the particles are considered to be electrons.

After these cuts, the remaining events are further treated by two different methods, method 1 that is designed for lower-momentum and method 2 for higher-momentum Λ and $\bar{\Lambda}$. The requirements in method 1 consist mainly of d_0 cut, momentum-dependent minimum and maximum distance between the primary vertex and the Λ ($\bar{\Lambda}$) decay point, and the removal of the majority of $K^0_s \to \pi^+\pi^-$ decays by rejecting candidates with $|m_{\pi\pi} - M_{K^0}| < 15$ MeV where $m_{\pi\pi}$ is the effective mass if both tracks are considered to be pions. The resulting Λ and $\bar{\Lambda}$ peaks are shown in fig. 4.31. In method 2, the Λ ($\bar{\Lambda}$) decay points are required to be at a radius greater than 20 cm but less than 45 cm and hence be further from the primary vertex than the first tracking chamber. This assures that only genuine V^0's, i.e. track pairs not originating at the primary vertex, are accepted. The masses $m_{\pi\pi}$ and $m_{p\pi}$ for these candidates are displayed in fig. 4.32. Except for a very small background this sample consists of either $\Lambda \to \pi p$ or $K^0_s \to \pi^+\pi^-$ decays.

One way to express the TASSO results on Λ and $\bar{\Lambda}$ is, at $W = 34$ GeV,

$$\frac{\sigma(e^+e^- \to \Lambda X) + \sigma(e^+e^- \to \bar{\Lambda} X)}{\sigma(e^+e^- \to \mu^+\mu^-)} = 1.12 \pm 0.15 \pm 0.17 \tag{4.18}$$

where as usual the first error is statistical while the second one is systematic. Here extrapolation has been carried out to cover also the unobserved range of 0–1 GeV/c, which contributes 13% of this value. In this extrapolation, the form (4.15) with one term is used over the momentum range from 1 to 5 GeV/c. The inclusive cross section of Λ and $\bar{\Lambda}$, as a function of x_E at $W = 34$ GeV, has already been compared in fig. 4.10 with those of $\pi^\pm$, $K^\pm$ and p, $\bar{p}$ which exhibit similar features: the cross section falls exponentially with a break in slope around $x_E = 0.1$.

How are the baryons formed? Until recently, the popular model of hadron production in electron–positron annihilation did not include baryons at all [4.7, 4.41]. The reason is that it takes three quarks to form a baryon, and this has been considered to be difficult. Another way of saying this is that the color tube has to double back on itself in order to bring three quarks together. Since the observation of baryons at PETRA there have been several attempts to include baryons in the previously developed models. In all cases, diquarks are introduced as entities distinct from quarks. In the LUND version [4.8], it is assumed that diquark pairs are produced by the color force field in addition to quark pairs

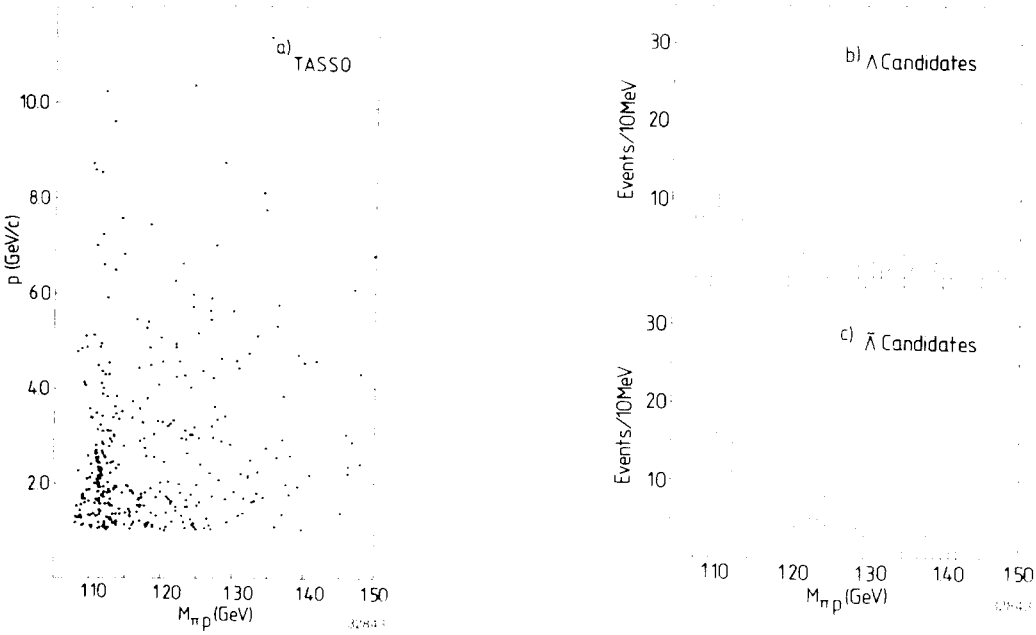

Fig. 4.31. TASSO [4.27] identification of Λ. (a) Total momentum for particle pairs versus the $p\pi$ invariant mass for pairs satisfying the cuts of method 1 (see text). (b) $M_{p\pi}$ projection for Λ candidates. (c) $M_{\bar{p}\pi^+}$ projection for $\bar{\Lambda}$ candidates.

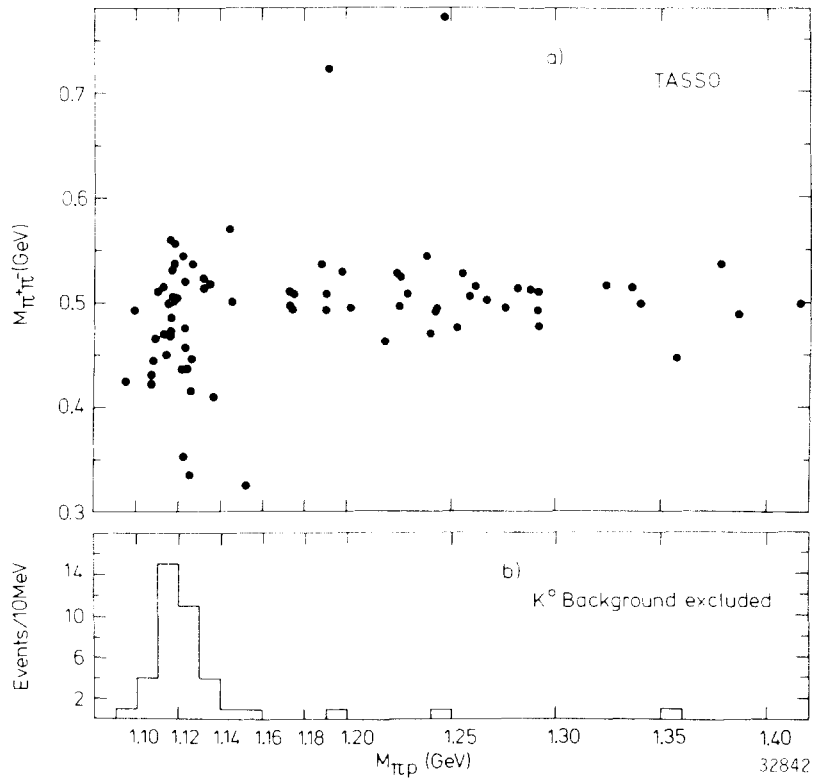

Fig. 4.32. TASSO [4.27] identification of Λ. (a) Invariant mass assuming pion masses versus invariant mass assuming $p\pi^-$ or $\bar{p}\pi^+$ masses for particle pairs satisfying the cuts of method 2 (see text). (b) Mass spectrum of $M_{p\pi^-}$ or $M_{\bar{p}\pi^+}$ with K^0 background excluded.

with a relatively low probability

$$\text{Prob(qq)/Prob(q)} = 0.065\,.$$

This ratio was extracted from SPEAR data [4.42] in the 4 GeV center of mass region. In the version of Meyer [4.43], the Field–Feynman scheme [4.7] [fig. 4.33a] is used to include diquark pairs with a similar probability

$$P_{B1} = \frac{\text{Prob(qq)}}{\text{Prob(q)} + \text{Prob(qq)}} = 0.075 \tag{4.19}$$

based on TASSO data [4.20]. This is shown schematically in fig. 4.33b. The ratios of u, d and s quark pairs are taken to be 2:2:1, and the ratios of diquark pairs are taken similarly. The results of these two procedures are shown in fig. 4.34. For the solid curve of Meyer in this figure, a second mechanism for diquark pair production, described by a probability P_{B2} defined similarly as (4.19), has been added as shown in fig. 4.33c. The data are not sensitive enough to support this second mechanism, which in the simplest form tends to increase e^+e^- total hadronic cross section in contradiction with the PETRA data.

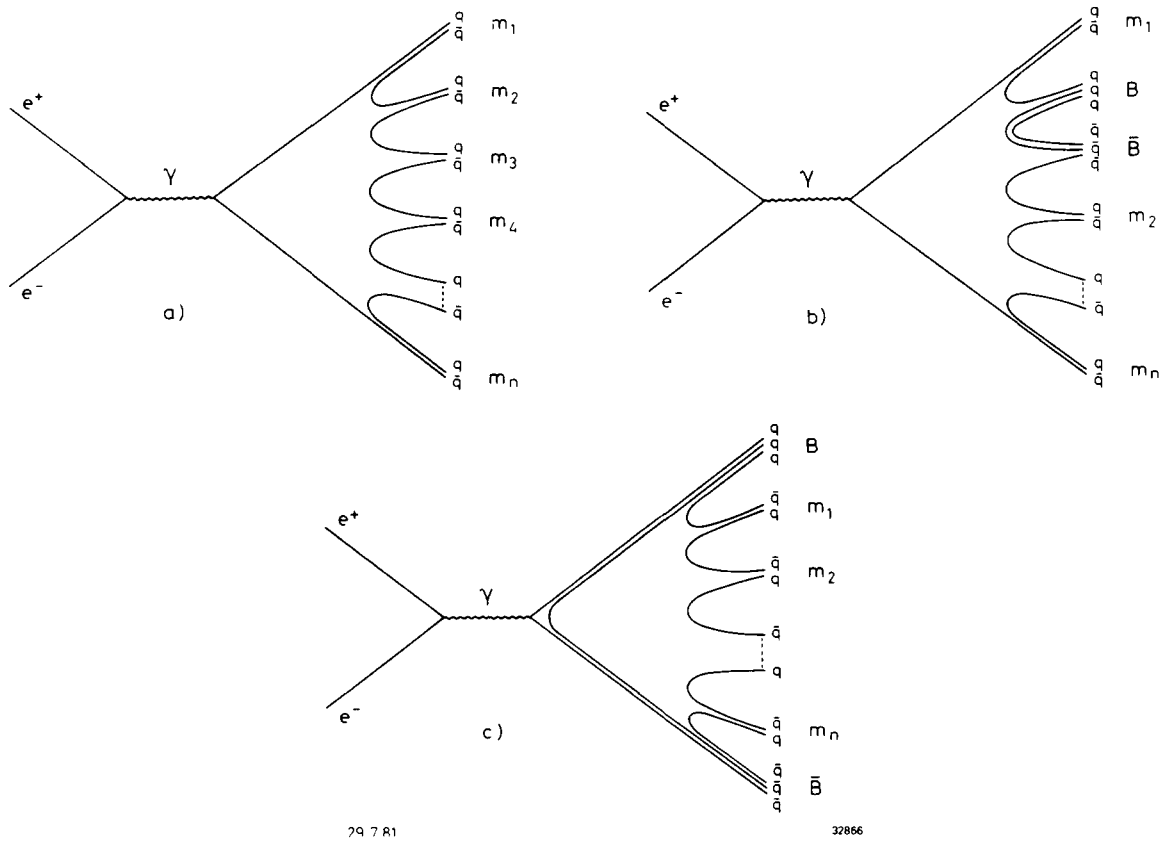

Fig. 4.33. (a) Diagram for $e^+e^- \to$ mesons. (b) Diagram for $e^+e^- \to$ mesons and baryons. (c) Diagram for $e^+e^- \to$ mesons and baryons with leading baryons in each jet.

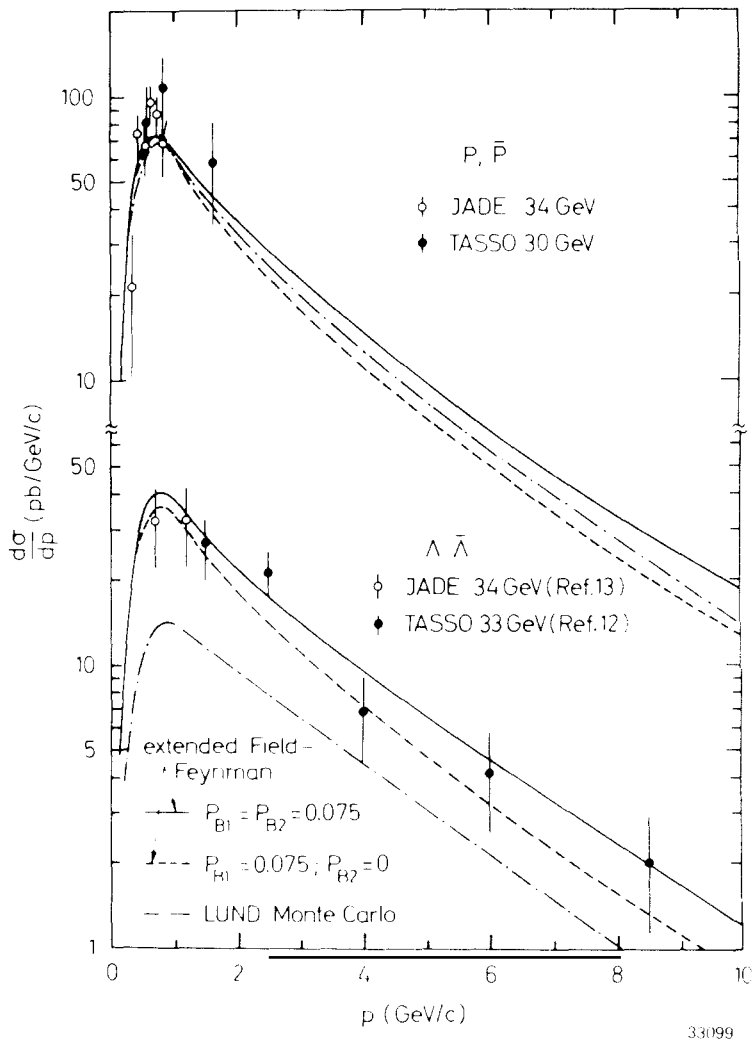

Fig. 4.34. Inclusive spectra of p, $\bar{p}$, Λ, $\bar{\Lambda}$. Data by the TASSO [4.20, 4.27] and the JADE [4.26] Collaborations. (All data points have been scaled with s^{-1} to the energy of 33 GeV.) Solid curves: $P_{B1} = P_{B2} = 0.075$ (Meyer [4.43]). Dashed curves: $P_{B1} = 0.075$, $P_{B2} = 0$ (Meyer [4.43]). Dash-dotted curves: LUND model.

4.13. Inclusive cross section of Ξ

We describe briefly the very recent measurement of the inclusive cross section of Ξ^- by the TASSO Collaboration [4.28]. For this purpose, the Λ candidates are first obtained by the method of the preceding section with slightly different cuts. To select Ξ^-'s, a search is carried out for the intersection of an additional charged track with the Λ. The requirements are that:

(i) the additional charged track satisfies $p_T > 0.1$ GeV/c and $|\cos\theta| < 0.87$;

(ii) the intersection of the additional track with the Λ should be more than 1 cm away from the intersection point in the r–ϕ plane and in front of the Λ decay point;

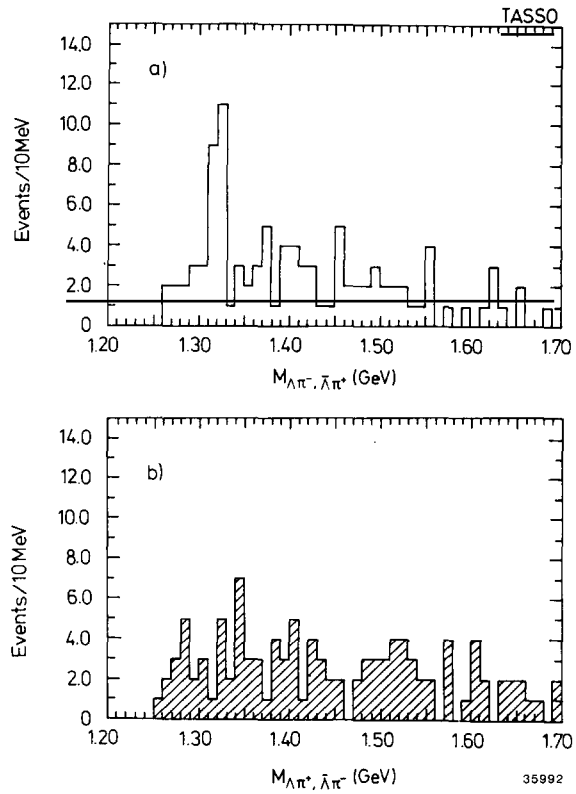

Fig. 4.35. (a) The TASSO [4.28] invariant $\Lambda\pi^-$, $\bar{\Lambda}\pi^+$ mass spectrum. (b) The invariant $\Lambda\pi^+$, $\bar{\Lambda}\pi^-$ mass spectrum.

(iii) the angle between the reconstructed direction of flight of the $\Lambda\pi^-$ combination and its momentum vector is smaller than 5°; and

(iv) the momentum of the $\Lambda\pi^-$ combination is greater than 1 GeV/c.

The resulting $\Lambda\pi^-$ mass spectrum is shown in fig. 4.35a. A narrow peak around the Ξ^- mass (1.321 GeV) is visible. No similar structure is visible in fig. 4.35b, where the Λ's are combined with tracks of the wrong charge ("Ξ^{+}"). Furthermore, by assigning the kaon mass to the additional charged track and computing the ΛK mass spectrum, no enhancement in the Ω^- region is seen. The width of the Ξ^- signal in fig. 4.35a is in agreement with the expected r.m.s. resolution of $\sigma = 8$ MeV obtained from Monte Carlo calculations. From fig. 4.35a TASSO has obtained 20 candidates ($11\Xi^-$ and $5\overline{\Xi^-}$ above total background of 4) with a mass $1.310\,\text{GeV} < M(\Lambda\pi) < 1.330\,\text{GeV}$.

On the basis of 14 of these 20 candidates with center-of-mass energy $W > 30$ GeV (the average energy being $\bar{W} = 34.4$ GeV), the scaled inclusive cross section of Ξ^- is shown in fig. 4.36. The total yield of Ξ^-, $\overline{\Xi^-}$ per hadronic event is found to be

$$0.026 \pm 0.008\ (\text{stat.}) \pm 0.009\ (\text{syst.})\,.$$

The systematic error stems mainly from uncertainties in the efficiency and in the extrapolation to low momenta.

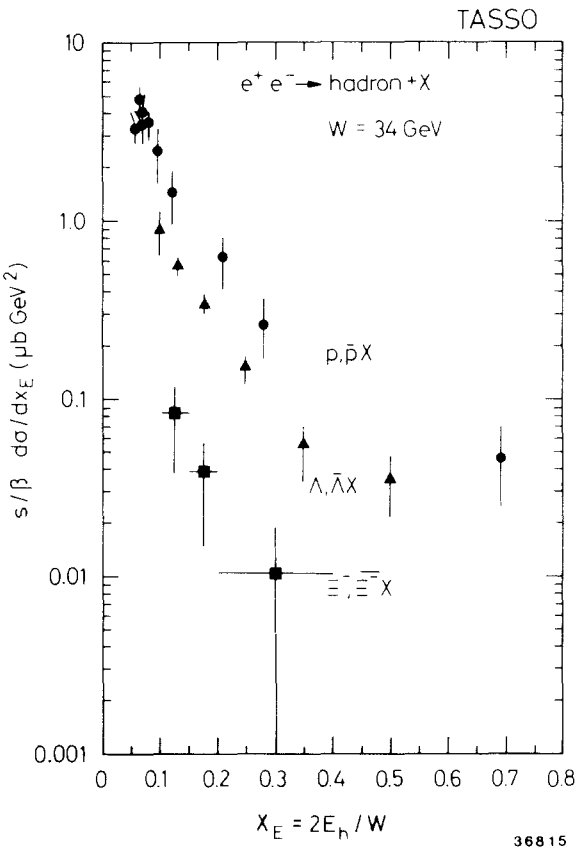

Fig. 4.36. The TASSO [4.28] scaled cross section $(s/\beta)\,d\sigma/dx_E$ for $e^+e^- \rightarrow \Xi^-, \bar{\Xi}^- X$ at $W = 34.4$ GeV.

4.14. *Inclusive cross section of* $D^{*\pm}$

The $D^{*\pm}$ mesons are identified by TASSO [4.29] using a procedure previously applied by the MARK II [4.30] and CLEO [4.31] Collaborations. It is based on the fact that the Q value of the decay $D^{*+} \rightarrow \pi^+ D^0$ is only 5.8 MeV. As a result, the direction of the π^+ relative to that of the D^0 and the momentum of the π^+ are severely restricted. The D^0 is detected in the decay mode $D^0 \rightarrow K^-\pi^+$. For brevity we shall indicate only the particle states; the analysis also includes the antiparticle states.

The data used are collected at c.m. energies W between 30.0 and 36.7 GeV with an average $\bar{W} = 34.3$ GeV for a total luminosity of 79 pb^{-1} and a total of 22 356 hadron events. Using the average beam position as a constraint in the track reconstruction, the momentum resolution is $\sigma_p/p = 0.010\sqrt{2.9 + p^2}$, p in GeV/c, as determined from μ-pair events. For each event all possible $(K^-\pi^+)$ and $(K^-\pi^+)\pi^+$ mass combinations ($M_{K^-\pi^+}$, $M_{K^-\pi^+\pi^+}$) are formed assuming each particle in turn to be a kaon and a pion. The particles forming the $(K^-\pi^+)$ system are required to have each a momentum $p > 0.8$ GeV/c, and the lone π^+ to have $p > 0.3$ GeV/c. Fig. 4.37a shows the distribution of the mass difference $\Delta M = M_{K^-\pi^+\pi^+} - M_{K^-\pi^+}$ for those combinations where $M_{K^-\pi^+}$ is in the D^0 mass region (1.744–1.984 GeV) and for which $x_E > 0.5$, where $x_E = 2E_{K^-\pi^+\pi^+}/W$ is the fractional energy of the $K^-\pi^+\pi^+$ system. A narrow peak is seen centered around $\Delta M = 0.145$ GeV which is indicative of the

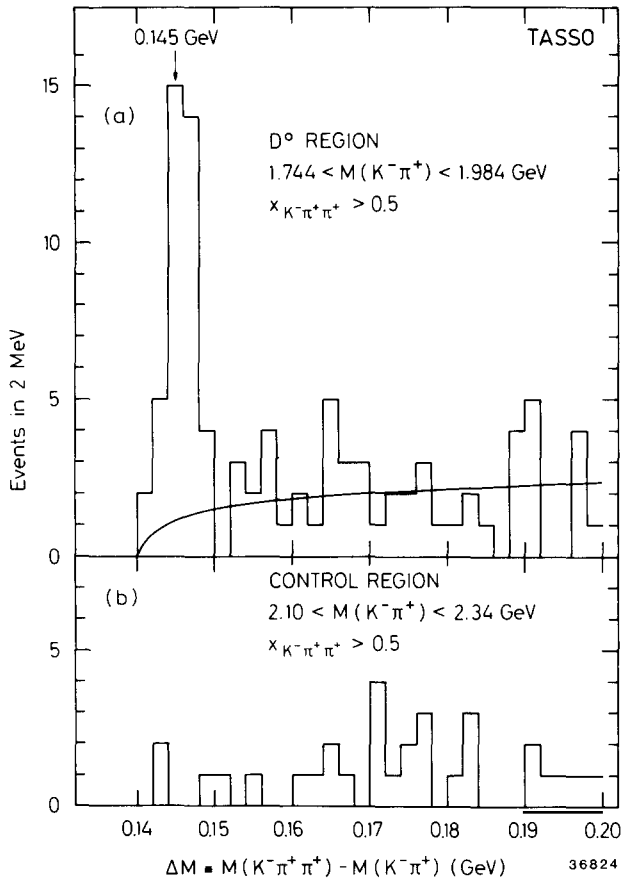

Fig. 4.37. TASSO [4.29] identification of $D^{*\pm}$. (a) The spectrum of the mass difference $\Delta M = M_{(K^-\pi^+)\pi^+} - M_{(K^-\pi^+)}$ for $x_E > 0.5$ and $(K^-\pi^+)$ combinations in the D^0 mass region (1.744–1.984 GeV). The curve shows the expected background contribution. (b) The ΔM spectrum for $x_E > 0.5$ and $(K^-\pi^+)$ combinations in the control region (2.10–2.34 GeV).

decay $D^{*+} \to \pi^+ D^0$. The r.m.s. width of the peak, $\sigma_{\Delta M} = 1.5$ MeV, is consistent with the expected resolution. No such peak is observed when $M_{K^-\pi^+}$ is required to be in a control region outside of the D^0 mass (2.10–2.34 GeV) as shown by fig. 4.37b. In fig. 4.38 the distribution of $M_{K^-\pi^+}$ is shown for all $K^-\pi^+\pi^+$ combinations with $\Delta M < 0.150$ GeV. A clear D^0 signal centered at 1.87 GeV is observed with a r.m.s. width of $\sigma_M = 0.075$ GeV in agreement with the TASSO resolution. There is a second mass peak centered around 1.62 GeV. As was pointed out by Goldhaber [4.44] this so-called satellite enhancement S^0 in the $K^-\pi^+$ mass distribution arises from the decays

$$D^0 \to K^-\rho^+ \quad (\rho^+ \to \pi^+\pi^0) \qquad \text{and} \qquad D^0 \to \pi^+ K^{*-} \quad (K^{*-} \to K^-\pi^0) .$$

The spin of the $\rho^+(K^{*-})$ is perpendicular to the direction of the recoiling $K^-(\pi^+)$ leading to a decay distribution $\sim\cos^2\theta_H$ where θ_H is the angle between the decay $\pi^+(K^-)$ and the recoiling $K^-(\pi^+)$ in the rest system of the $\rho^+(K^{*-})$. This produces peaks in the $K^-\pi^+$ mass distribution near 1.62 GeV and at low $K^-\pi^+$ masses. The shape and magnitude of the S^0 peak are consistent with what one expects from the measured [4.45] branching ratios for the $D^0 \to K^-\rho^+$ and $D^0 \to \pi^+ K^{*-}$ decays.

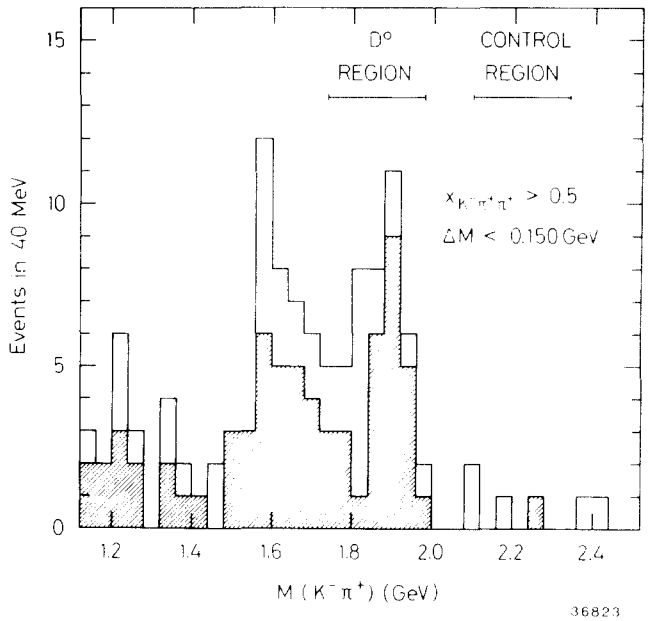

Fig. 4.38. The TASSO [4.29] ($K^-\pi^+$) mass spectrum for $(K^-\pi^+)\pi^+$ combinations with $\Delta M < 0.15$ GeV and $x_E > 0.5$. The dashed histogram shows the mass spectrum obtained with the more strict cuts of $W > 35$ GeV and each of the particles forming the ($K^-\pi^+$) system having momenta greater than 1.4 GeV. The D^0 peak is clearly visible, and the additional peak to the right is satellite enhancement S^0.

The inclusive cross section of D^{*+} is obtained as follows. The number of D^{*+}'s is determined as a function of x_E from the number of D^0 candidates defined by $1.744 < M_{K\pi} < 1.984$ GeV and $\Delta M < 0.15$ GeV. For small x_E, $0.3 < x_E < 0.5$, no clear D^0 signal is observed: There are 19 D^0 candidates of which 17 are estimated to be due to background. For $x_E > 0.5$ there are 40 $D^{*+} \to D^0\pi^+$ candidates with a background of 8 events of which 2 come from the S^0. The background is estimated by generating Monte Carlo events according to $e^+e^- \to \bar{q}q$, $\bar{q}qg \to$ hadrons and applying the same cuts as for the D^{*+} selection. The event acceptance, detection efficiency and radiative corrections are calculated by the same Monte Carlo program. The detection efficiency for the decay $D^{*+} \to \pi^+D^0 \to K^-\pi^+\pi^+$ varies between 32 and 45% for $x_E > 0.3$. The branching ratios [4.46] $B(D^{*+} \to D^0\pi^+) = 44 \pm 10\%$ and $B(D^0 \to K^-\pi^+) = 3.0 \pm 0.6\%$ are used to compute the cross section.

Fig. 4.39 shows the inclusive cross section $(s/\beta)\, d\sigma/dx_E$ as a function of x_E (note that the cross section includes both D^{*+} and D^{*-} productions). The overall normalization uncertainty of ±35% is due mainly to those in the D^{*+} and D^0 branching ratios. The TASSO cross section is consistent with that of MARK II [4.30] at 29 GeV but is somewhat lower than that measured by CLEO [4.31] at 10.4 GeV. Note that all three experiments use the same values for the D^{*+} and D^0 branching ratios. Qualitatively, all three experiments observe similar behaviors: the D^* mesons are concentrated at large x_E values, the maximum being at $x_E = 0.6$–0.7. The integration of the measured $D^{*\pm}$ cross section over $x_E > 0.3$ yields relative to the μ-pair cross section, $\sigma_{\mu\mu}$,

$$R_{D^{*\pm}}(x_E > 0.3) = \{\sigma_{D^{*+}}(x_E > 0.3) + \sigma_{D^{*-}}(x_E > 0.3)\}/\sigma_{\mu\mu}$$
$$= 1.25 \pm 0.32\ (\text{stat.}) \pm 0.44\ (\text{syst.}).$$

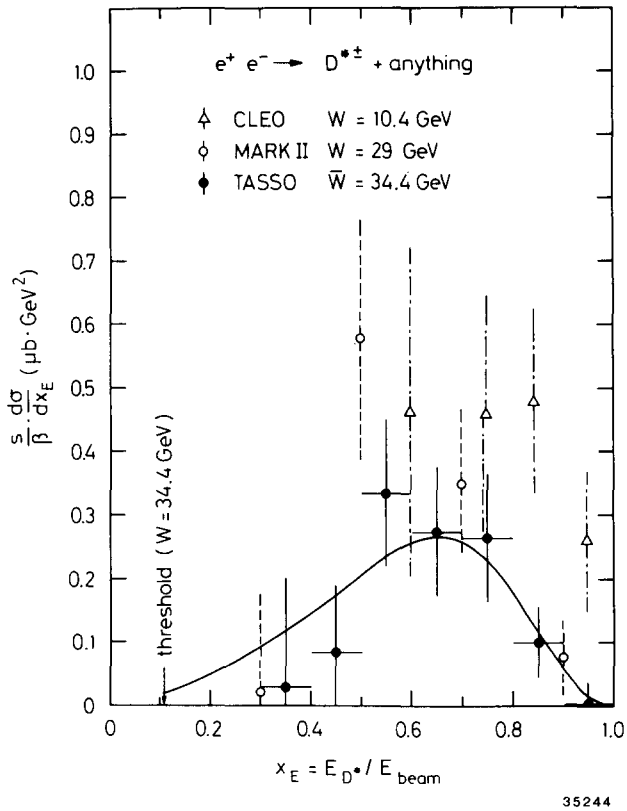

Fig. 4.39. The inclusive cross section $(s/\beta)\,d\sigma/dx_E$ for $e^+e^- \to D^{*\pm}X$. The errors shown are statistical, and a ±35% normalization uncertainty is not included.

Assuming equal rates for charged and neutral D*'s the total D* production is found to be

$$R_{D^*}(x_E > 0.3) = 2.50 \pm 0.64 \pm 0.88\,.$$

This can be compared with the expected total inclusive primary charm quark and antiquark yield of

$$R_c = 2 \cdot \tfrac{4}{3} \cdot (1 + \alpha_s/\pi) \approx 2.80$$

assuming for the strong coupling $\alpha_s = 0.17$. The data indicate that a large fraction of charm quark production proceeds via D* formation.

4.15. Fragmentation functions for heavy quarks

As already discussed in section 2.4, high-energy electron–positron annihilation into hadrons proceeds predominately via quark-pair formation $e^-e^+ \to q\bar{q}$. In the case of the light quarks u, d and s, the identification of the final-state hadron that carries the primary quark (antiquark) appears to be rather difficult, since many other low-mass hadrons are produced in addition. For the heavy quarks charm and bottom, the situation is different: a fast charmed or bottom hadron will most likely contain the primary

charm or bottom quark, since the production of charmed and bottom hadrons from the sea is expected to be negligible at PETRA energies. Moreover, the charmed hadrons originating from the decays of bottom hadrons should have lower momenta.

The inclusive cross section of $D^{*\pm}$, therefore, gives direct information about the fragmentation function for the charm quark c. As seen in section 4.14, a large fraction of charm quark fragmentation yields $D^{*\pm}$. If we make the additional assumptions that fragmentations into D and D^* have the same shape and that the contributions from the bottom mesons are negligible, then the normalized inclusive cross section of $D^{*\pm}$ is the fragmentation function for c. This agrees with the results obtained by the CDHS Collaboration [4.47] and the EMC Collaboration [4.48] using neutrinos and muons respectively, and also with theoretical expectations [4.49]. For comparison, the average values from CDHS and EMC are respectively $\langle x_D \rangle = 0.68 \pm 0.08$ and $\langle x_D \rangle = 0.59 \pm 0.03 \pm 0.03$.

The corresponding information about the bottom quark b does not exist: so far no one at PETRA has been able to reconstruct a bottom meson. Therefore, all information about the b fragmentation function at PETRA energies is indirect, and comes from inclusive lepton spectra. A practical prerequisite to use the lepton spectra for this purpose is to have a simple parametrization for the fragmentation function, which we shall discuss now.

The parametrization proposed by Peterson et al. [4.50] for heavy quark fragmentation is

$$\left\{ x_E \left(1 - \frac{1}{x_E} - \frac{\varepsilon}{1 - x_E} \right) \right\}^{-1} . \tag{4.20}$$

If this form is used for $(s/\beta)\, d\sigma/dx_E$, a fit to the TASSO $D^{*\pm}$ data yields

$$\varepsilon_c = 0.18 \pm 0.07$$

for charm quark; the resulting curve is shown in fig. 4.39. The rationale for (4.20) is as follows [4.50].

With reference to the schematic picture in fig. 4.40, Q and $H = (Q\bar{q})$ are expected to carry almost the same energy, since attaching a light antiquark $\bar{q}$ to the heavy quark Q decelerates Q only slightly in the fragmentation process. Thus the gross features of the amplitude $Q \to H + q$ is determined by the value of the energy transfer $\Delta E = E_H + E_q - E_Q$:

$$\text{amplitude } (Q \to H + q) \propto \Delta E^{-1} . \tag{4.21}$$

Expanding the energies about the (transverse) particle masses ($m_H \simeq m_Q$ for simplicity),

$$\begin{aligned} \Delta E &= (m_Q^2 + x_E^2 P^2)^{1/2} + (m_q^2 + (1 - x_E)^2 P^2)^{1/2} - (m_Q^2 + P^2)^{1/2} \\ &\propto 1 - 1/x_E - \varepsilon/(1 - x_E) \end{aligned} \tag{4.22}$$

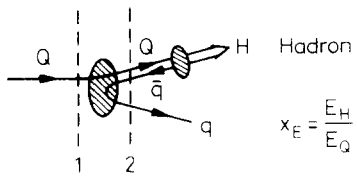

Fig. 4.40. The fragmentation of a heavy quark Q into a meson $H(Q\bar{q})$. Dashed lines are time slices used in the derivation of eq. (4.20).

and taking a factor x_E^{-1} for longitudinal phase space, we get (4.20). Furthermore, it is seen from (4.22) that the value of ε is proportional to m_Q^{-2}; therefore,

$$\varepsilon_b = (m_c/m_b)^2 \varepsilon_c \,. \tag{4.23}$$

Accepting the form (4.20), MARK II and MAC at PEP and MARK J at PETRA have analyzed the inclusive lepton spectra for the purpose of determining ε_b. MARK II uses electrons, while both MAC and MARK J use muons. The results are

$$\varepsilon_b = \begin{cases} 0.030^{+0.032+0.023}_{-0.018-0.014} & \text{(MARK II [4.51])} \\ 0.008^{+0.037}_{-0.008} & \text{(MAC [4.52])} \\ 0.023^{+0.010+0.018}_{-0.008-0.013} & \text{(MARK J [4.53])} \,. \end{cases}$$

[The value given by MARK J is actually $\sqrt{\varepsilon_b} = 0.15 \pm 0.03 \pm 0.05$.] It is questionable whether these values can be directly compared, because the corresponding values ε_c for the charm quark are vastly different: 0.25 for MARK II (which is already higher than the TASSO result from $D^{*\pm}$) and 0.64 for MARK J with very small errors. The experimental data are not yet accurate enough to decide whether the theoretical relation (4.23) is correct.

5. Electroweak interaction

5.1. Introduction

We now come to one of the most exciting results from PETRA, the observation of weak and electromagnetic interference. Indeed, it was one of the main original purposes of building PETRA to observe such effects, especially the presence of forward–backward asymmetry in electron–positron annihilation [5.1].

The JADE [5.2] and TASSO [5.3] Collaborations are respectively the first and second groups to observe such an asymmetry. The process they studied is the creation of μ pairs:

$$e^-e^+ \to \mu^-\mu^+ \,.$$

Since the asymmetry increases rapidly with energy, such experimental results require both high energy and high statistics. In as much as the published results do not include the entire data set available now, in this chapter we shall update the experimental data whenever possible.

As of now, the statistically most significant data on weak and electromagnetic interference are still from this process of the creation of μ pairs. The processes $e^-e^+ \to \tau^-\tau^+$ [5.4] and $e^-e^+ \to c\bar{c}$ [5.5, 5.6] have also been measured. The asymmetry measurements on these three processes are described respectively in sections 5.6, 5.7 and 5.10. Readers especially interested in this topic can go directly to these sections.

Since the neutral intermediate vector boson Z^0 [5.5, 5.7] has not only axial vector but also vector coupling to fermions, this forward–backward asymmetry is not the only manifestation of electroweak

interaction for electron–positron annihilation. In particular, there are also modifications on the total rate and on the angular distributions, which can be used to determine the vector coupling of Z^0. Results from leptons are summarized in section 5.8.

5.2. Standard model

Before describing the experimental procedure, we review briefly the standard model, which is the elegant scheme for the unification of the weak and electromagnetic interactions developed by Glashow, Weinberg and Salam [5.5]. In this model there are three families of quarks and leptons:

$$\begin{pmatrix} u \\ d \\ \nu_e \\ e \end{pmatrix} \quad \begin{pmatrix} c \\ s \\ \nu_\mu \\ \mu \end{pmatrix} \quad \begin{pmatrix} t \\ b \\ \nu_\tau \\ \tau \end{pmatrix}$$

and the electromagnetic and weak interactions are transmitted by the vector bosons γ, Z^0 and $W^\pm$. Of course, this model is also applicable if the number of families is more than three.

The process

$$e^-e^+ \to f\bar{f}$$

can proceed not only through one-photon annihilation (fig. 5.1a), but also through one-Z^0 annihilation (fig. 5.1b) where f can be any fundamental fermion in the three families, including the yet unobserved top quark t (see section 7.2).

The couplings of the fermion f, including the electron e, to the photon and the Z^0 are explicitly shown in fig. 5.1. While the coupling to γ involves as usual only the vector current, that to the Z^0 is a

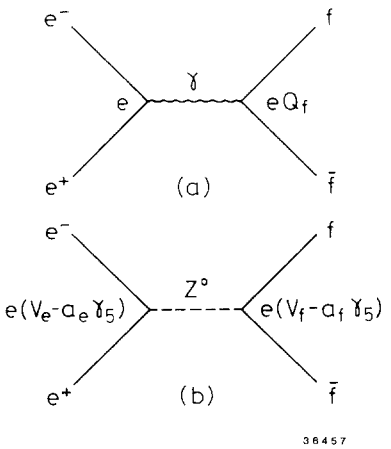

Fig. 5.1. The process $e^-e^+ \to f\bar{f}$ in the standard model.

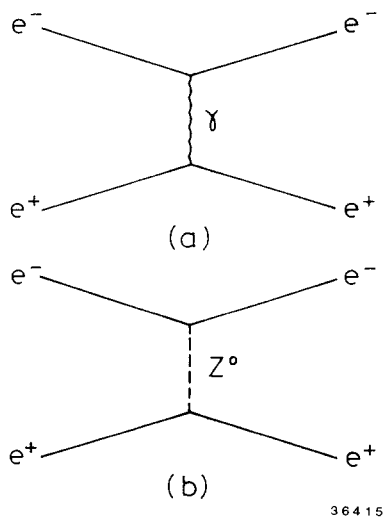

Fig. 5.2. Further second-order diagrams for Bhabha scattering $e^+e^- \to e^+e^-$ in the standard model. These are in addition to those of fig. 5.1.

Table 5.1
Values of v_f and a_f in the standard model

f	e^-, μ^-, τ^-	ν_e, ν_μ, ν_τ	d, s, b	u, c, t
Q_f	-1	0	$-\frac{1}{3}$	$\frac{2}{3}$
v_f	$-1+4\sin^2\theta_w$	1	$-1+\frac{4}{3}\sin^2\theta_w$	$1-\frac{8}{3}\sin^2\theta_w$
a_f	-1	1	-1	1

weak coupling and has both a vector and an axial vector part. The interference between the axial vector coupling to Z^0 and the vector coupling to both γ and Z^0 is responsible for the forward–backward asymmetry. The values of the vector coupling v_f and the axial vector coupling a_f as defined in fig. 5.1 for various fermions are given in table 5.1 in terms of the Weinberg angle θ_w [5.5]. Since the Weinberg angle is fairly accurately known from other experiments, the standard model gives unambiguous predictions for this forward–backward asymmetry. Thus a measurement of this asymmetry gives a direct test of the standard model.

Which fermion is most suitable for the measurement of this asymmetry? The neutrinos are clearly out, since they have no electromagnetic coupling. The quarks are also less suitable because, in order to identify the flavor of the underlying quark from the observed jets, there is a large loss in statistics. Thus there are only three possible choices: e, μ or τ. Of these three, e cannot be easily used because the Bhabha process [5.8] $e^+e^- \to e^+e^-$ also proceeds via Møller scattering [5.9], i.e. the exchange of a photon or a Z^0 in the cross channel as shown in fig. 5.2, which gives a huge asymmetry. We are therefore left with just two candidates, μ and τ.

There is, however, an additional complication. The lowest-order radiative correction to the diagram of fig. 5.1a contains a part due to two-photon annihilation. The two diagrams of this process are shown in fig. 5.3. The interference of the diagrams of fig. 5.1a and of fig. 5.3 gives also a forward–backward asymmetry. Fortunately, this purely QED asymmetry is completely and reliably calculable and hence can be subtracted. Furthermore, this QED asymmetry is about 1.5%, significantly smaller than the expected asymmetry at PETRA energies from the standard model.

On the basis of the two diagrams of fig. 5.1, the differential cross section for $e^-e^+ \to f\bar{f}$ is, in the

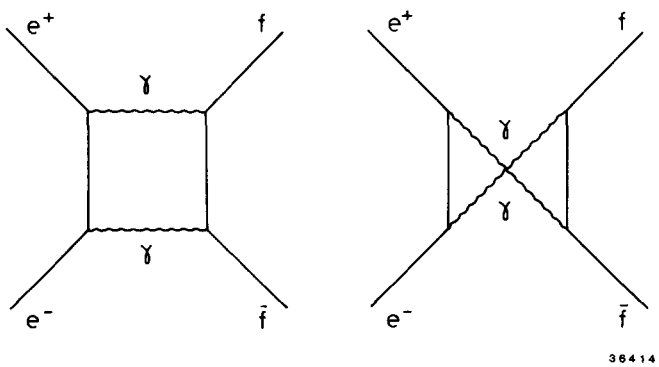

Fig. 5.3. Two-photon annihilation diagrams for $e^+e^- \to f\bar{f}$. The interference of the contributions from these diagrams and from those of fig. 5.1 gives an asymmetry of known amount.

standard model with the quark mass neglected [5.10]:

$$\frac{d\sigma(e^-e^+\to f\bar{f})}{d\cos\theta}=\frac{\pi\alpha^2}{2s}\left\{Q_f^2(1+\cos^2\theta)-\frac{2Q_fgs(s/M_z^2-1)[v_ev_f(1+\cos^2\theta)+2a_ea_f\cos\theta]}{(s/M_z^2-1)^2+\Gamma_z^2/M_z^2}\right.$$
$$\left.+\frac{s^2g^2[(v_e^2+a_e^2)(v_f^2+a_f^2)(1+\cos^2\theta)+8v_ea_ev_fa_f\cos\theta]}{(s/M_z^2-1)^2+\Gamma_z^2/M_z^2}\right\} \tag{5.1}$$

where M_z and Γ_z are the mass and width of Z^0, and

$$g=\frac{\sqrt{2}\,G_F}{4e^2}=\frac{\sqrt{2}\,G_F}{16\pi\alpha} \tag{5.2}$$

in terms of the Fermi weak coupling constant G_F. Integration over θ gives in particular:

$$R_f=Q_f^2-\frac{2Q_fgs(s/M_z^2-1)v_ev_f-s^2g^2(v_e^2+a_e^2)(v_f^2+a_f^2)}{(s/M_z^2-1)^2+\Gamma_z^2/M_z^2}. \tag{5.3}$$

In writing down these formulas, the diagrams of fig. 5.2 have not been included. Therefore, they are not valid for Bhabha scattering. As they stand, (5.1) and (5.3) are valid for μ and τ. They are also valid for the quarks provided that the right-hand sides are multiplied by the color factor 3.

The asymmetry $A(\theta)$, as a function of θ, is defined by

$$A_f(\theta)=\frac{d\sigma(e^-e^+\to f\bar{f})/d\cos\theta|_\theta-d\sigma(e^-e^+\to f\bar{f})/d\cos\theta|_{\pi-\theta}}{d\sigma(e^-e^+\to f\bar{f})/d\cos\theta|_\theta+d\sigma(e^-e^+\to f\bar{f})/d\cos\theta|_{\pi-\theta}}. \tag{5.4}$$

It therefore follows from (5.1) that the angular dependence of $A(\theta)$ is very simply

$$A_f(\theta)=A_f(0)\frac{2\cos\theta}{1+\cos^2\theta} \tag{5.5}$$

and $A_f(0)$, the asymmetry at $\theta=0$, is explicitly

$$A_f(0)=\frac{-2Q_fgs(s/M_z^2-1)a_ea_f+4s^2g^2v_ea_ev_fa_f}{Q_f^2[(s/M_z^2-1)^2+\Gamma_z^2/M_z^2]-2Q_fgs(s/M_z^2-1)v_ev_f+s^2g^2(v_e^2+a_e^2)(v_f^2+a_f^2)}. \tag{5.6}$$

If the acceptance is 4π, then by (5.5) the average asymmetry is

$$\langle A_f\rangle=\frac{\sigma(\theta<\pi/2)-\sigma(\theta>\pi/2)}{\sigma(\theta<\pi/2)+\sigma(\theta>\pi/2)}=\tfrac{3}{4}A_f(0). \tag{5.7}$$

Since the acceptance is actually less than 4π, $\langle A_f\rangle$ is somewhat smaller in magnitude. The formulas (5.5), (5.6) and (5.7) are valid for all fundamental fermions, both leptons and quarks, with the exception of the electron.

Using the measured Weinberg angle of [5.11]

$$\sin^2 \theta_w = 0.228\,, \tag{5.8}$$

this average asymmetry $\langle A_f \rangle$ of (5.7) is plotted in fig. 5.4, in the PETRA energy range for the various fermions. Note that, for these fermions, the total cross section is more sensitive to v than to a, while the forward–backward asymmetry is more sensitive to a than to v.

To get a better physical feeling for this asymmetry, we get a simple approximate formula of high accuracy from (5.6) for PETRA energies. First, since the Fermi coupling constant is

$$G_F = 1.1663 \times 10^{-5}\,\mathrm{GeV}^{-2}$$

it follows from (5.2) that

$$g = 4.4967 \times 10^{-5}\,\mathrm{GeV}^{-2}\,.$$

Thus, for example, at the PETRA energy of $\sqrt{s} = 36.6\,\mathrm{GeV}$, $gs \sim 0.06$ is quite small. In the standard model, the Z^0 mass is given by

$$M_z = (2\sqrt{g}\,\sin 2\theta_w)^{-1} \tag{5.9}$$

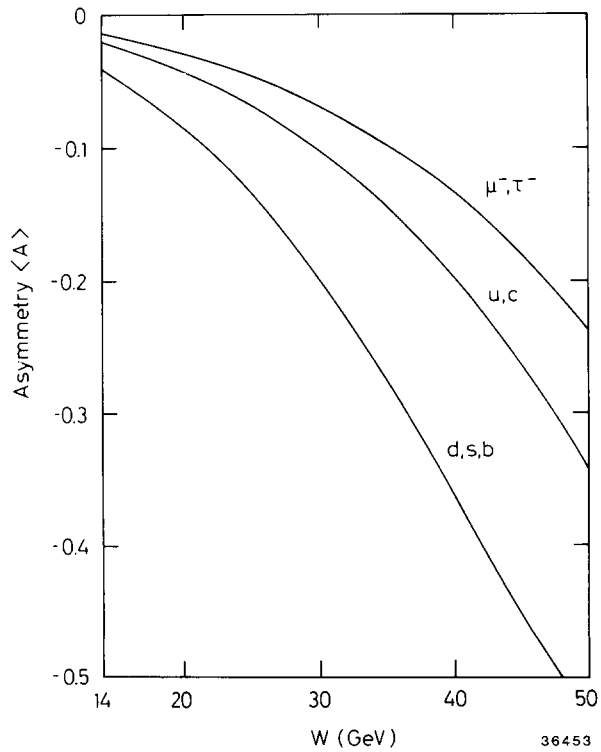

Fig. 5.4. Average asymmetry on the basis of the standard model.

and hence the value (5.8) of $\sin\theta_w$ gives (radiative corrections increase M_z by a few percent)

$$M_z = 88.9\,\text{GeV}\,. \tag{5.10}$$

In the standard model, Z^0 has a width Γ_z of about 3 GeV. Thus the term Γ_z^2/M_z^2 in (5.6) can be omitted. Finally, because of (5.8), v_e from table 5.1

$$v_e = -0.088 \tag{5.11}$$

is quite small. Neglecting $2gsv_e \sim -0.01$, (5.6) simplifies considerably to

$$A_f(0) \sim \frac{2gsa_ea_f}{Q_f(1 - s/M_z^2)}\,. \tag{5.12}$$

The appearance of Q_f in the denominator means that the asymmetry is larger for the quarks than for the charged leptons, while the factor s favors higher energies. In particular, for μ and τ, (5.12) is simply

$$A_\mu(0) = A_\tau(0) \sim -\frac{9\times 10^{-5}\,s}{1 - s/7900} \tag{5.13}$$

with s in GeV^2. From eq. (5.7), the average asymmetry is $\frac{3}{4}A_\mu(0) = \frac{3}{4}A_\tau(0)$.

For completeness, we give here the differential cross section for Bhabha scattering taking into account all four second-order diagrams of fig. 5.1 and fig. 5.2 [5.12]:

$$\frac{d\sigma(e^-e^+\to e^-e^+)}{d\cos\theta} = \frac{\pi\alpha^2}{4s}\left[4B_1 + B_2(1-\cos\theta)^2 + B_3(1+\cos\theta)^2\right] \tag{5.14}$$

where

$$B_1 = (s/t)^2\left|1 + (v_e^2 - a_e^2)R_t\right|^2 \tag{5.15}$$

$$B_2 = \left|1 + (v_e^2 - a_e^2)R_s\right|^2 \tag{5.16}$$

$$B_3 = \frac{1}{2}\left[\left|1 + \frac{s}{t} + (v_e + a_e)^2\left(R_s + \frac{s}{t}R_t\right)\right|^2 + \left|1 + \frac{s}{t} + (v_e - a_e)^2\left(R_s + \frac{s}{t}R_t\right)\right|^2\right], \tag{5.17}$$

$$R_s = \frac{gsM_z^2}{s - M_z^2 + i\Gamma_zM_z}\,, \tag{5.18}$$

and

$$R_t = \frac{gtM_z^2}{t - M_z^2 + i\Gamma_zM_z}\,, \tag{5.19}$$

with

$$t = -\tfrac{1}{2}s(1-\cos\theta)\,. \tag{5.20}$$

It is interesting to note that (5.1) with $Q_f = -1$ can be obtained from the above formula for Bhabha scattering by taking the limit $t \to \infty$. The reason is that, in this limit of $t \to \infty$, the contributions from the diagrams of fig. 5.2, which involve the exchange of a photon or a Z^0 in the t channel, become zero. For both (5.1) and (5.14), the electron and the positron beams are assumed to be unpolarized.

5.3. *Bhabha scattering* $e^-e^+ \to e^-e^+$

We begin the discussion of the various experimental results. Bhabha scattering, both at small angles and at large angles, is often used as a luminosity monitor. The selected events are required to have two oppositely charged tracks of sufficiently high momenta within acceptance and with an acollinearity angle of typically less than 10°. The tracks have to originate close to the intersection point, and cosmic ray backgrounds are further reduced by measurement of the time of flight. Contaminations from μ pairs and τ pairs are subtracted statistically.

Even at the highest energies the loss resulting from events having two tracks with the same charge assignment is small, less than 1% in the various experiments. This problem will be discussed in further detail in section 5.6 on $e^-e^+ \to \mu^-\mu^+$. A much more serious problem is that the electrons and positrons from the Bhabha events tend to produce secondary particles due to showering in the beam pipe and

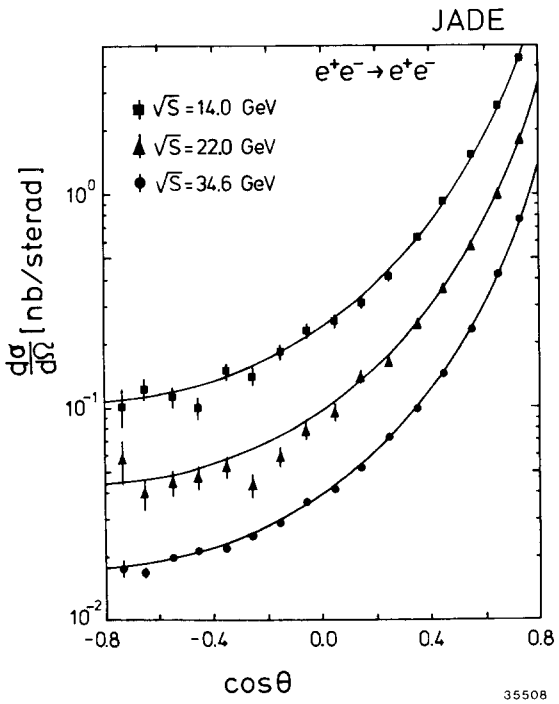

Fig. 5.5. JADE [5.17] differential cross sections for the reaction $e^+e^- \to e^+e^-$ for c.m. energies 14, 22 and 34.6 GeV. The lines show the QED expectations.

other materials. For the TASSO detector for example, this material before the tracking chambers amounts to 0.13 radiation length. Therefore the restriction to events with exactly two charged tracks leads to losses which are around 13% and further are dependent on the polar angle θ. Taking into account radiative effects and shower formation, the resulting acceptance is found to be almost flat for $|\cos\theta| < 0.5$ with a value of 0.80 and falls to 0.72 at $|\cos\theta| = 0.7$. Monte Carlo simulation is used to correct for this and other effects, such as the detector efficiency.

All PETRA data on Bhabha scattering are in good agreement with QED [5.13 to 5.26]. As an example, the JADE [5.17] results are shown in fig. 5.5. For the purpose of looking for weak effects, it is more useful to plot instead the ratio

$$\frac{\mathrm{d}\sigma^{\mathrm{exp}}/\mathrm{d}\cos\theta}{\mathrm{d}\sigma^{\mathrm{QED}}/\mathrm{d}\cos\theta}. \tag{5.21}$$

Such plots from CELLO [5.14] and TASSO [5.26] are shown in figs. 5.6 and 5.7 respectively and compared with the standard model of Glashow, Weinberg and Salam. It is seen that these data on

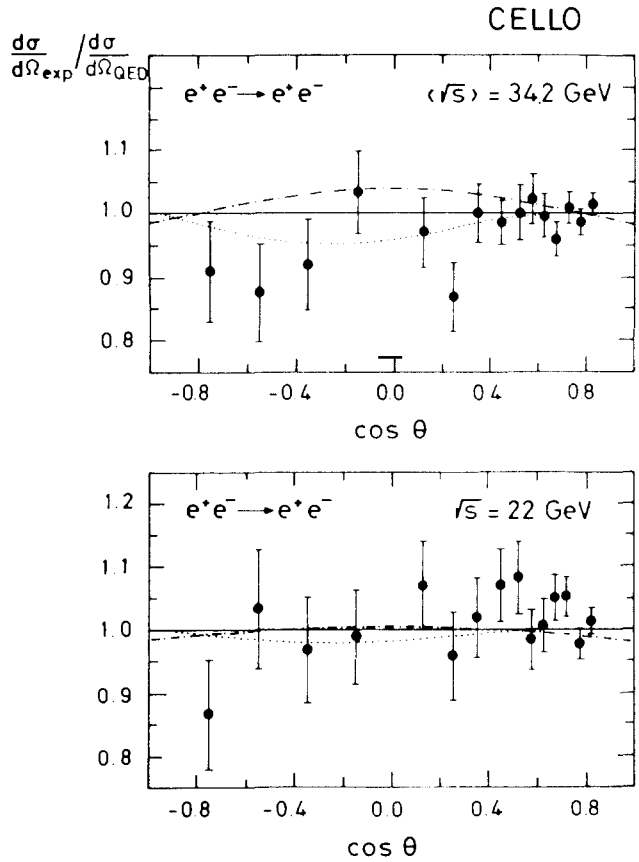

Fig. 5.6. The CELLO [5.14] differential cross section $\mathrm{d}\sigma/\mathrm{d}\Omega$ for Bhabha scattering at $\langle\sqrt{s}\rangle = 34.2$ GeV and $\sqrt{s} = 22$ GeV normalized to the QED cross section. The full line is the QED prediction. The dotted line represents the best fit for a^2 and v^2. The dot-dashed line shows the prediction for the second solution for neutrino-electron scattering ($v^2 = 1.08$, $a^2 = 0.0$).

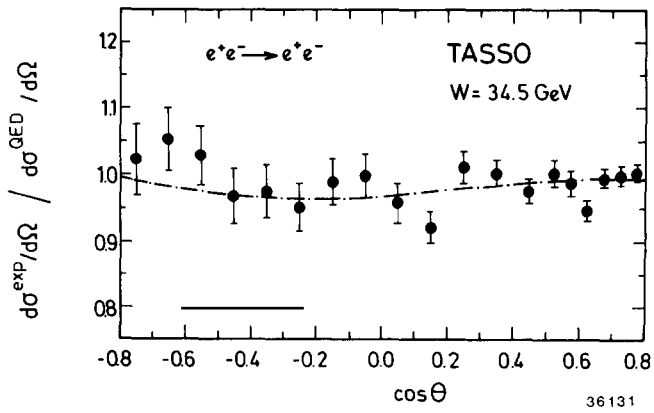

Fig. 5.7. The TASSO [5.26] differential cross section divided by the QED expectation for the reaction $e^+e^- \to e^+e^-$. The curve shows the fit to the data of the Glashow–Weinberg–Salam theory with $\sin^2\theta_w = 0.26$.

Bhabha scattering, taken by themselves, are not sufficiently accurate to differentiate between pure quantum electrodynamics and the standard model. They will, however, be used together with those from $e^-e^+ \to \mu^-\mu^+$ and $e^-e^+ \to \tau^-\tau^+$ to determine the vector and axial vector coupling in section 5.8.

For Bhabha scattering the ratio (5.21) is more sensitive to v_e than a_e, while for pair production it is more sensitive to the axial–vector couplings than to the vector couplings. This is most clearly seen by considering the rough approximation where we keep gs only to the first order and neglect both s and Γ_z^2 as compared with M_z^2. In this approximation, it follows from eqs. (5.1) and (5.14) that the ratio can be expressed in the form

$$\frac{d\sigma(e^-e^+ \to f\bar{f})/d\cos\theta}{d\sigma^{QED}(e^-e^+ \to f\bar{f})/d\cos\theta} = 1 + 2Q_f^{-1}gs\left[v_e v_f + a_e a_f \frac{2\cos\theta}{1+\cos^2\theta}\right] \tag{5.22}$$

and

$$\frac{d\sigma(e^-e^+ \to e^-e^+)/d\cos\theta}{d\sigma^{QED}(e^-e^+ \to e^-e^+)/d\cos\theta} = 1 + 2gs[v_e^2 S_v(\cos\theta) + a_e^2 S_a(\cos\theta)], \tag{5.23}$$

where

$$S_v(\cos\theta) = \frac{3\sin^2\theta}{3+\cos^2\theta} \tag{5.24}$$

and

$$S_a(\cos\theta) = \frac{-\sin^2\theta\,(5 - 8\cos\theta - \cos^2\theta)}{(3+\cos^2\theta)^2}. \tag{5.25}$$

Accordingly, in this approximation, for pair production the vector couplings of Z^0 changes only the normalization while the axial–vector couplings give the asymmetry in angular distribution. For Bhabha scattering, the effects are more complicated. The functions S_v and S_a, which give the sensitivities to v_e and a_e

respectively, are plotted in fig. 5.8. It is seen that S_v is everywhere larger than S_a in absolute values, but, except near the forward direction, the magnitudes are not very different.

5.4. Total cross section of μ-pair creation

Fig. 5.9 shows the results obtained for the measurements of R_μ, as a function of s, by the four PETRA groups [5.27]: CELLO, JADE, MARK J and TASSO. Again, no deviation from QED is observed.

From the standard model, the total cross section for μ-pair production is given by (5.3) with $f = \mu$:

$$R_\mu = 1 + gs\,\frac{2(s/M_z^2 - 1)v_e v_\mu + gs(v_e^2 + a_e^2)(v_\mu^2 + a_\mu^2)}{(s/M_z^2 - 1)^2 + \Gamma_z^2/M_z^2}. \tag{5.26}$$

Since gs is small at PETRA energies, deviation from 1 gives a measure of the quantity $v_e v_\mu$. Therefore the data shown in fig. 5.9 imply that $v_e v_\mu$ is small.

5.5. Total cross section for $e^-e^+ \to \tau^-\tau^+$ and branching ratios

Fig. 5.10 shows the results obtained at PETRA [5.27] for the measurements of R_τ as a function of s. Again, no deviation from QED is observed. The standard model again gives (5.26) for R_τ, provided that the couplings v_μ and a_μ are replaced by v_τ and a_τ respectively.

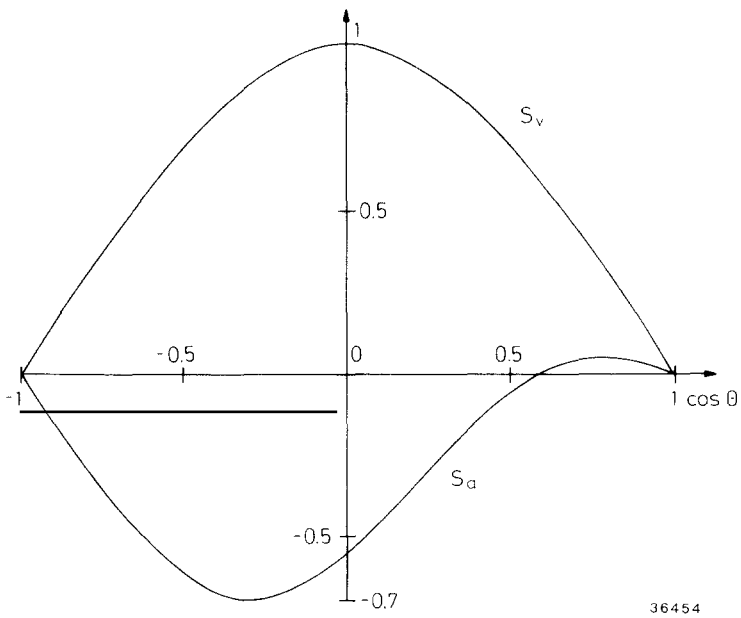

Fig. 5.8. Sensitivity of the Bhabha scattering cross section divided by the QED prediction to the vector and axial-vector couplings of Z^0.

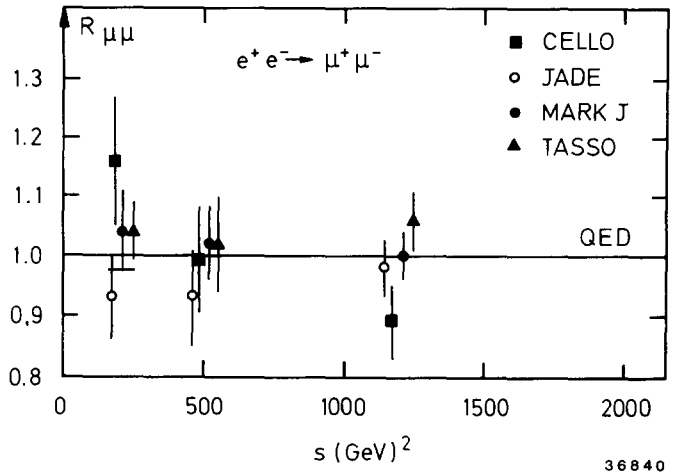

Fig. 5.9. Measured R_μ for $e^-e^+ \to \mu^-\mu^+$ from CELLO, JADE, MARK J and TASSO [5.27].

Among the detectors at PETRA, CELLO has the largest acceptance for $e^-e^+ \to \tau^-\tau^+$ [5.4, 5.28]. We therefore discuss in more detail the results from CELLO [5.29, 5.30].

Event candidates are selected on the basis of the relatively low multiplicity and the distinct back-to-back topology of $\tau^-\tau^+$ events. More precisely, the cuts are as follows:

- For all events: at least two tracks satisfying

(a) $p_T > 350$ MeV/c with respect to the beam axis.

(b) $|\cos\theta| < 0.86$.

- For two-prong events

(c) $|\boldsymbol{p}_1| + |\boldsymbol{p}_2| > 5$ GeV/c.

(d) Total momentum transverse to the beam >300 MeV/c.

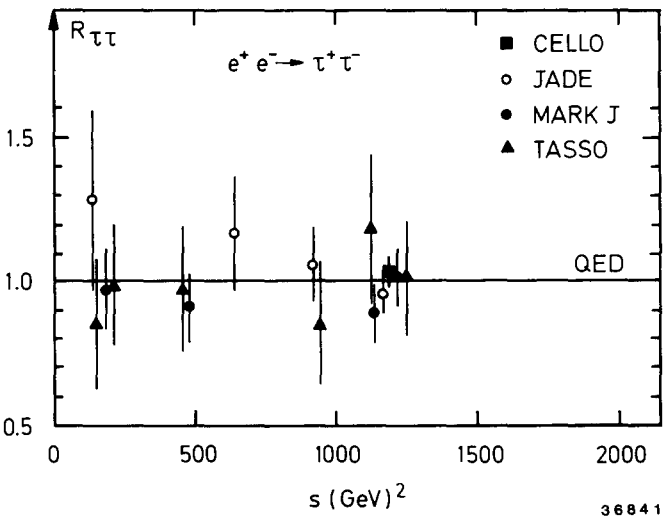

Fig. 5.10. Measured R_τ for $e^-e^+ \to \tau^-\tau^+$ from CELLO, JADE, MARK J and TASSO [5.27].

(e) Acolinearity in space >20 mrad and <0.7 rad.

(f) Angle between the prongs in the projection containing the beam direction >3.5 mrad.

(g) Angle between the prongs in the projection transverse to the beam >10 mrad.

– For ≧ four-prong events

(h) $\Sigma |\boldsymbol{p}| > 4$ GeV/c.

(i) At least one track in two back-to-back sectors 80° wide in the projection transverse to the beam direction.

(j) Number of tracks ≦8.

The acolinearity cuts (e), (f), (g) suppress contributions from Bhabhas, μ pairs and cosmic muons. Background due to 2γ processes is removed by the cuts (c), (d) and (e). Multihadronic events are significantly rejected by the multiplicity cut (j), residual beam-gas events by the back-to-back requirement (i) and energy cut (h). The polar angle cut ensures a high efficiency for the charged trigger and also that the tracks enter the sensitive region of the liquid argon barrel calorimeter.

In addition, most Bhabha events are suppressed by the requirement of an energy deposition <15 GeV in at least one of the two back-to-back calorimeter modules corresponding to the direction of the final particles.

After these candidates are double scanned in order to remove the remaining background events, a total of 526 $\tau^-\tau^+$ events survive, corresponding to the CELLO integrated luminosity of 11.2 pb^{-1} at a center-of-mass energy of 34 GeV. The following decay channels have been studied:

(1) $\tau \to \rho\nu$, characterized by one-prong decay with one or two photons in the same hemisphere,

(2) $\tau \to \mu\nu\bar{\nu}$, where a particle momentum larger than 2 GeV/c and an associated hit in the muon chambers are required,

(3) $\tau \to e\nu\bar{\nu}$, where the e, with momentum larger than 1 GeV/c, is identified by the characteristic shower pattern in the calorimeter, and

(4) $\tau \to \pi\nu$, where the shower pattern is required to be consistent with a minimum ionizing particle.

For these four decay channels, the efficiencies and background contributions are tabulated in table 5.2.

The resulting branching ratios are given in table 5.3 and compared with the world average [5.11]. From the momentum spectra of the observed decay products, CELLO has initiated the study of τ polarization asymmetry. No such asymmetry has yet been observed, the result being $(1 \pm 22)\%$.

Table 5.2
Summary of the four decay samples and their respective efficiencies and background contributions, from CELLO [5.30]

	ρ	π	e	μ
No. of events	101	34	60	47
Efficiency	0.45 ± 0.04	0.48 ± 0.04	0.73 ± 0.04	0.70 ± 0.06
Contamination from:				
μ	0	1.4 ± 1.4	0	-
e	0	0.5 ± 0.5	-	0
π	0		0.7 ± 0.7	2.0 ± 1.0
ρ	-	5.4 ± 1.2	0	0
$\pi\pi^0\pi^0$	15.4 ± 8.4	0	0	0
K, K*	2.3 ± 1.1	3.6 ± 1.4	0	0

Table 5.3
τ branching ratio in %

	CELLO [5.30]	World average [5.11]
BR($\tau \to \rho\nu$)	$22.8 \pm 2.5 \pm 2.1$	21.6 ± 3.6
BR($\tau \to \mu\nu\bar{\nu}$)	$17.6 \pm 2.6 \pm 2.1$	18.5 ± 1.2
BR($\tau \to e\nu\bar{\nu}$)	$18.3 \pm 2.4 \pm 1.9$	16.2 ± 1.0
BR($\tau \to \pi\nu$)	$9.9 \pm 1.7 \pm 1.3$	10.7 ± 1.6

5.6. *Forward–backward asymmetry in* $e^-e^+ \to \mu^-\mu^+$

We now come to the most exciting topic of the observation of weak and electromagnetic interference in the process $e^-e^+ \to \mu^-\mu^+$. This process has the great advantage that the systematic error in the asymmetry is certainly less than 1%, because the backgrounds (due to misidentified Bhabha events, cosmic rays, two-photon process, and τ pairs) can be kept small and do not produce artificial asymmetry.

As already mentioned in section 5.3, the loss resulting from events having two tracks with the same charge assignment is small. In fig. 5.11, the MARK J plot [5.31] is shown on the measured normalized reciprocal momentum p_{beam}/p_μ for the forward-going muon versus that of the backward-going muon. The sign of this reciprocal momentum is defined as the charge determined from the track curvature. The events are concentrated in the vicinities of the two points $(1, -1)$ and $(-1, 1)$, corresponding to the

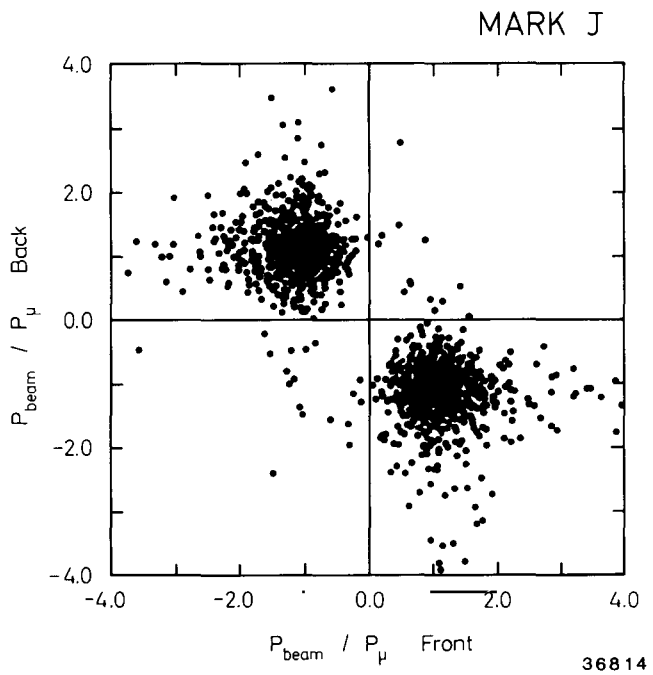

Fig. 5.11. The MARK J [5.31] normalized reciprocal momentum p_{beam}/p_μ for the forward and the backward muons in the reaction $e^-e^+ \to \mu^-\mu^+$. The sign of this reciprocal momentum is defined as the charge determined from the track curvature.

two cases of μ^+ forward, μ^- backwards and vice versa. It is seen from this figure that the percentage of events misidentified as $\mu^+\mu^+$ and $\mu^-\mu^-$ is indeed small.

Higher order α^3 QED corrections [5.32], due to the interference of contributions from the diagrams of fig. 5.3 with those from fig. 5.1, are applied to the experimental data. Within the acceptance of most detectors, $|\cos\theta| < 0.80$ or slightly more, this correction corresponds to a positive asymmetry of $\sim 1.5\%$. Checks of this procedure have been performed by investigating distributions which are generated by radiative effects, for example, the acolinearity distribution between the two muons. No correction has been applied in the data for higher order weak-electromagnetic effects. The angular distributions for $e^-e^+ \to \mu^-\mu^+$ as presented by the various PETRA Collaborations are given in fig. 5.12 [5.33]. It is seen from these high-energy data that there is a distinct deviation from the symmetrical angular distribution predicted by QED.

Table 5.4 summarizes the results on the μ-pair asymmetry at PETRA with the data from CELLO [5.34], JADE [5.2], MARK J [5.35], PLUTO [5.34] and TASSO [5.26] but updated to the time of the 1983 Cornell Conference [5.36]. Each of the three high-statistics experiments JADE, TASSO and MARK J shows an effect of four or more standard deviations, in agreement with the standard model. If

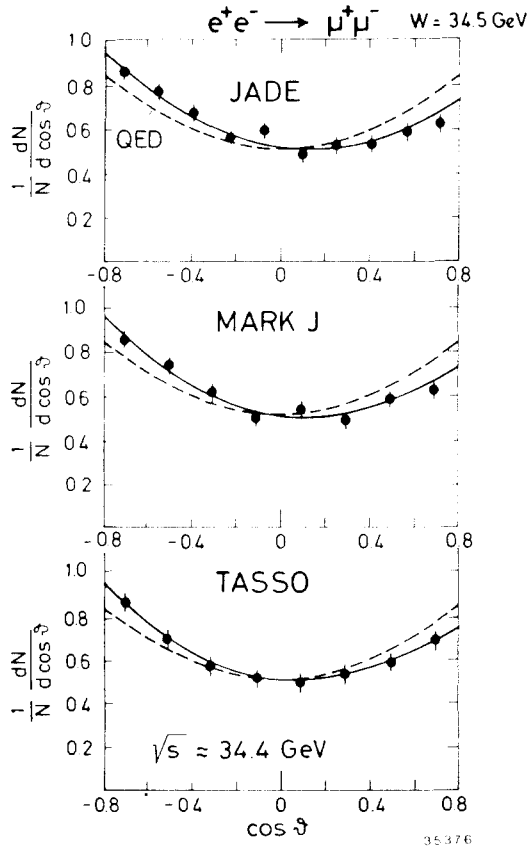

Fig. 5.12. Angular distribution for μ-pair production $e^-e^+ \to \mu^-\mu^+$ measured by the PETRA experiments [5.33]. The data have been corrected for QED radiative effects. The dashed lines are the lowest-order QED prediction of $1 + \cos^2\theta$, while the solid lines are the fits to the data using eq. (5.1) of the standard model.

Table 5.4
PETRA data on μ-pair asymmetry [5.36]

Experiment	$\sqrt{s}$ (GeV)	$\langle A_\mu \rangle$ (%)	$\langle A_\mu \rangle_{GWS}$ (%)
CELLO	34.2	-6.4 ± 6.4	−9.2
JADE	34.4	-11.0 ± 1.8	−9.3
MARK J	34.6	-11.7 ± 1.7	−9.5
PLUTO	34.7	-12.4 ± 3.1	−9.5
TASSO	34.5	-9.1 ± 2.3	−9.5
combined	34.5	-10.8 ± 1.1	−9.4

the five results are averaged according to their statistical significance, then the result at $W = 34.5$ GeV is [5.36]

$$\langle A_\mu \rangle_{av} = (-10.8 \pm 1.1)\% ,$$

to be compared with the prediction −9.4% of the standard model. Note that the experimental value has not been corrected for radiative effects from diagrams containing Z^0.

Thus the weak-electromagnetic interference has been observed unambiguously at PETRA. For the sake of visual display, the combined fit to the angular distributions is shown in fig. 5.13 [5.36].

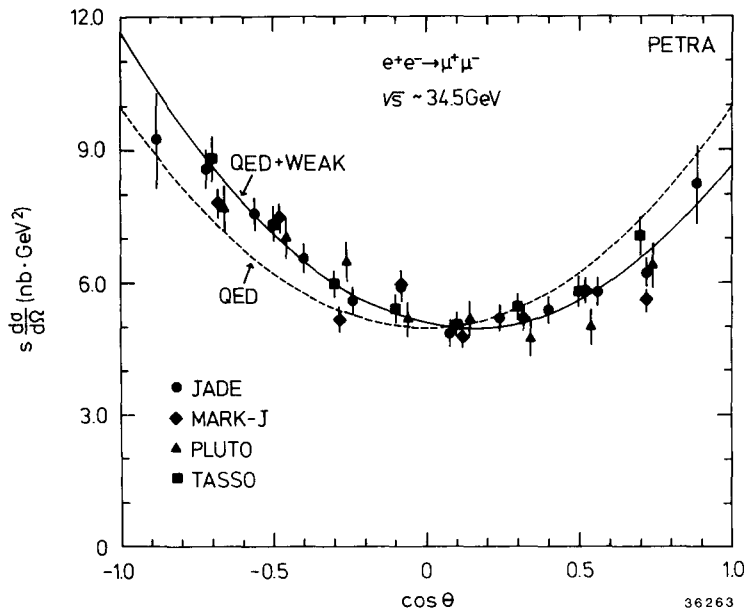

Fig. 5.13. Compilation [5.36] of PETRA high-energy data for the angular distribution of $e^+e^- \to \mu^+\mu^-$ at $\sqrt{s} \sim 34.5$ GeV. The data are corrected for effects α^3. The full curve shows a fit to the data allowing for an asymmetry; the dashed curve is the symmetric QED prediction.

5.7. Forward–backward asymmetry in $e^+e^- \to \tau^+\tau^-$

In the standard model, the Z^0 couplings to μ and τ [5.4] are identical, as shown in table 5.1. Therefore, the asymmetries are theoretically identical for the processes $e^+e^- \to \mu^+\mu^-$ and $e^+e^- \to \tau^+\tau^-$.

The experimental problems of measuring these two asymmetries, however, are quite different. The selection and identification of events for $e^+e^- \to \tau^+\tau^-$ have already been discussed in section 5.5. Compared with the μ pairs, the backgrounds for τ pairs are larger, arising from Bhabha events with bremsstrahlung in the beam pipe, two-photon processes, multihadron events, etc. The contamination due to Bhabha scattering requires special attention, since it produces a positive asymmetry, thereby counteracting the expected negative asymmetry due to weak and electromagnetic interference. The effects of these backgrounds depend on the ability to identify correctly the final states. The resulting systematic uncertainty is about 2%. Although this is significantly larger than the $<1\%$ for μ pairs, it is not a serious problem at PETRA because it is still less than the statistical uncertainty.

The experimental data are treated in a way similar to that for $e^+e^- \to \mu^+\mu^-$, described in the preceding section. There are only two journal publications from PETRA on this asymmetry; they are:

TASSO [5.3] $\quad (-4 \pm 6)\%$

and

CELLO [5.25] $\quad (-10.3 \pm 5.2)\%$.

The combined fit to the updated angular distributions from the PETRA groups is shown in fig. 5.14 taken from the 1983 Cornell Conference. Taken individually, none of these results can be said to have established a significant asymmetry. However, every one is in the expected direction in the sense of having a negative value, and a 4 standard-deviation effect is obtained if the values presented at the Cornell Conference [5.36] are averaged statistically. The combined experimental asymmetry is

$$\langle A_\tau \rangle_{\mathrm{av}} = (-7.6 \pm 1.9)\%$$

to be compared with the theoretical prediction of -9.4%.

5.8. Overall fit of the leptonic vector and axial-vector weak couplings

As already discussed in section 5.6, the best evidence at PETRA for weak and electromagnetic interference comes from the forward–backward asymmetry in μ-pair production $e^+e^- \to \mu^+\mu^-$. All observations are consistent with the prediction of the standard model that

$$v_e = v_\mu = v_\tau \tag{5.27}$$

and

$$a_e = a_\mu = a_\tau . \tag{5.28}$$

On the assumption of this universality, overall fits have been carried out by the various PETRA

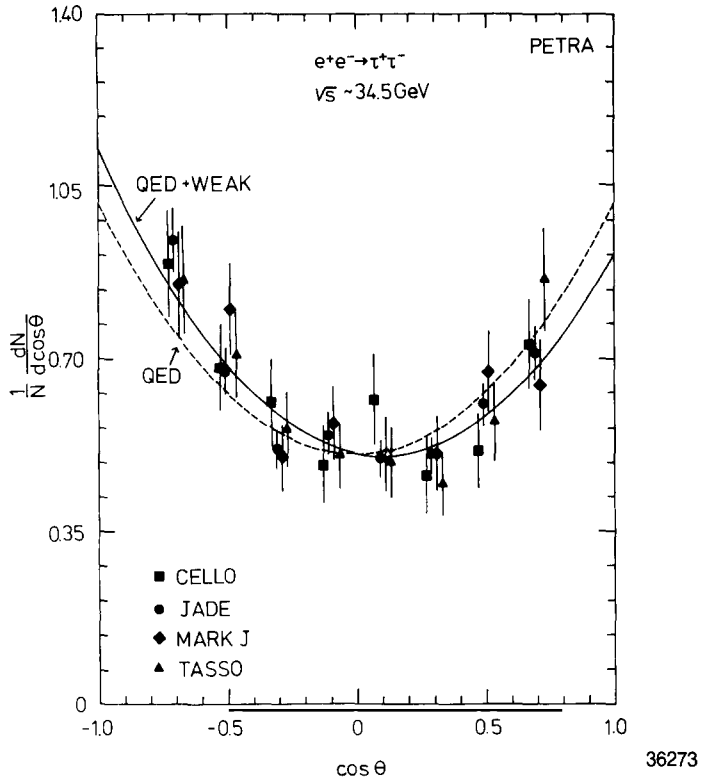

Fig. 5.14. Compilation [5.36] of PETRA high-energy data for the angular distribution of $e^+e^- \to \tau^+\tau^-$ at $\sqrt{s} \sim 34.5$ GeV. The data are corrected for effects α^3. The full curve shows a fit to the data allowing for an asymmetry; the dashed curve is the symmetric QED prediction.

Collaborations to the leptonic data on $e^-e^+ \to e^-e^+$, $e^-e^+ \to \mu^-\mu^+$ and $e^-e^+ \to \tau^-\tau^+$. Each Collaboration uses its own data; the choice of data and the results of the overall fits are tabulated in table 5.5, where v and a mean the quantities (5.27) and (5.28) respectively. The CELLO data are from [5.14], the JADE and MARK J data from [5.2] and [5.35] respectively but updated to the time of the Paris Conference [5.27] and the TASSO data from [5.26]. Table 5.5 gives results from two separate overall fits, one for the values of v^2 and a^2, while the other is a direct fit for $\sin^2\theta_w$ on the basis of the standard model.

Table 5.5
Overall fit of $e^+e^- \to$ lepton pairs

Experiment	Data used	a^2	v^2	$\sin^2\theta_w$
CELLO [5.14]	ee, $\mu\mu$, $\tau\tau$	1.22 ± 0.47	-0.12 ± 0.33	$0.21^{+0.14}_{-0.09}$
JADE [5.27]	$\mu\mu$	1.17 ± 0.24	0.20 ± 0.32	
MARK J [5.27]	ee, $\mu\mu$, $\tau\tau$	1.12 ± 0.24	-0.08 ± 0.20	0.26 ± 0.09
TASSO [5.26]	ee, $\mu\mu$	0.88 ± 0.22	-0.14 ± 0.21	0.26 ± 0.07
Average		1.06 ± 0.13	-0.06 ± 0.12	

The errors on the vector coupling and the axial–vector coupling constants are correlated. As an example of this correlation, the TASSO data is shown in fig. 5.15a with 95% confidence level contours using the definition of $g_V = v/2$ and $g_A = a/2$. In that figure, the shaded areas show the two solutions of νe experiments. It is an impressive feat of the PETRA experiments to obtain a determination of the weak neutral–current coupling constants at these high energies with an accuracy comparable to that from the neutrino–electron scattering experiments at much lower energies. The combined data from the PETRA groups are shown in fig. 5.15b [5.36].

5.9. *Determination of the Weinberg angle θ_w from the total hadronic cross section*

So far in this chapter, only the experimental data on the production of lepton pairs have been discussed. In this and the next section, attention is focused on weak effects in the hadronic events at PETRA.

In the standard model, when eq. (5.3) is summed over the various quarks, the result for the total hadronic cross section is

$$R = 3\left[\sum_q Q_q^2 - \frac{2gs(s/M_z^2 - 1)v_e \Sigma_q Q_q v_q - s^2 g^2 (v_e^2 + a_e^2)\Sigma_q (v_q^2 + a_q^2)}{(s/M_z^2 - 1)^2 + \Gamma_z^2/M_z^2}\right]. \tag{5.29}$$

For the PETRA energy range, the quarks that should be taken into account are: d, u, s, c and b. In (5.29) radiative corrections due to gluons have not been included. For energies away from the thresholds of production for new quark flavors and much below M_z, the inclusion of these radiative corrections leads approximately to an additional factor of $1 + \alpha_s/\pi$.

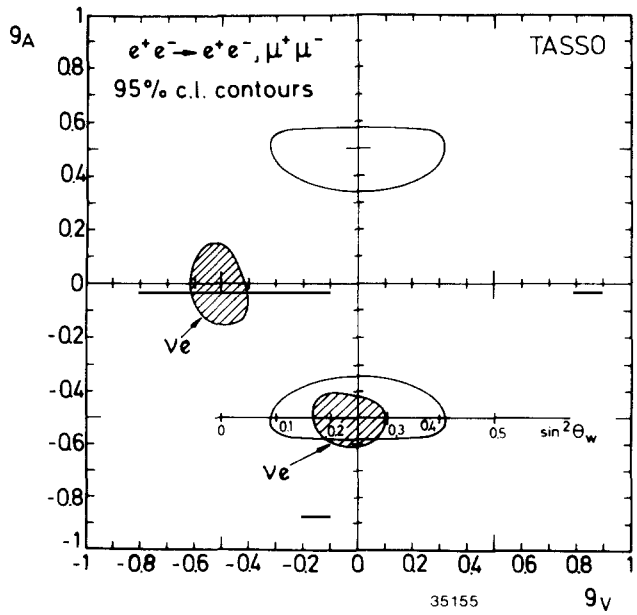

Fig. 5.15a. TASSO result [5.26] of a fit to g_V and g_A with 95% c.l. contours [$g_V = v/2$, $g_A = a/2$]. The shaded areas show the two solutions of the 95% confidence level contours from a common fit to the νe data. Indicated is also the prediction of the standard model.

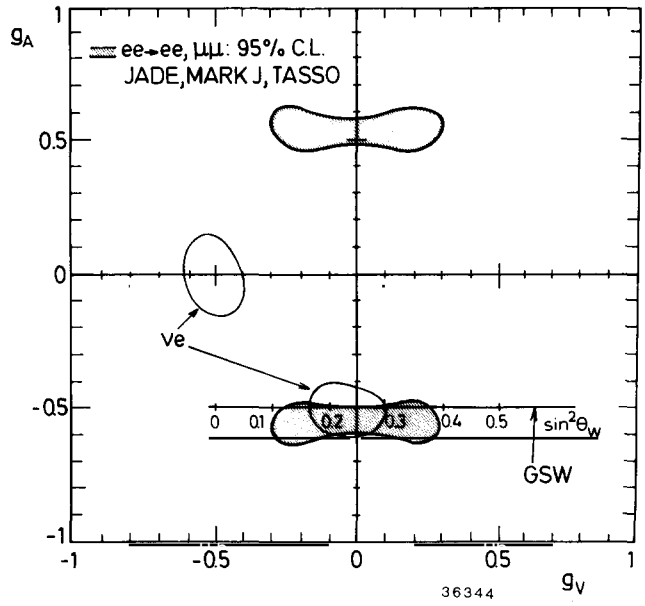

Fig. 5.15b. 95% confidence level contours [5.36] for g_V and g_A from $e^+e^- \to \mu^+\mu^-$ and $e^+e^- \to e^+e^-$ from JADE, MARK J and TASSO (shaded area) [$g_V = v/2$, $g_A = a/2$]. The open areas are the 95% confidence level contours from a common fit to all νe data. Indicated is also the prediction of the standard model.

The precise measurement of R at PETRA has already been presented in section 2.2, fig. 2.6 for TASSO [5.37], and fig. 2.7 for JADE [5.38]. One of the main motivations for these precise measurements is that, as seen from (5.29) with this factor of $1 + \alpha_s/\pi$, R as a function of the center-of-mass energy gives unambiguous determination [5.21, 5.37 to 5.39], independent of fragmentation, of the quark–gluon coupling constant α_s and the Weinberg angle θ_w for electroweak interaction. MARK J [5.21] obtains

$$\sin^2 \theta_w = 0.27^{+0.34}_{-0.08}$$

independent of the value of α_s. Both TASSO [5.37] and JADE [5.38] Collaborations have performed simultaneous fits to the data on the total cross section by varying the two fundamental constants α_s and θ_w. The TASSO results are

$$\alpha_s = 0.18 \pm 0.03 \pm 0.14 \qquad \text{for } s = 1000\ \text{GeV}^2$$

and

$$\sin^2 \theta_w = 0.40 \pm 0.16 \pm 0.02\,.$$

The resulting R with these parameters are shown as the solid line in fig. 2.6. The more accurate JADE results are

$$\alpha_s = 0.20 \pm 0.08 \qquad \text{for } s = 900\ \text{GeV}^2$$

and

$$\sin^2 \theta_w = 0.23 \pm 0.05$$

where the errors include both statistical and systematic contributions, and give the one-standard deviation limits when the other parameters are left free. The resulting R with these parameters are shown as the solid line in fig. 2.7.

5.10. Forward–backward asymmetry in $e^-e^+ \to c\bar{c}$

The inclusive spectrum for $D^{*\pm}$ has been presented in section 4.14. Through this $D^{*\pm}$ we identify events from $e^-e^+ \to c\bar{c}$, and can, in particular, give an experimental determination of the forward–backward asymmetry for these events.

The decays used for D^{*+} by TASSO [5.40] are

$$D^{*+} \to D^0\pi^+$$

with two modes for D^0:

$$D^0 \to K^-\pi^+ \quad \text{and} \quad D^0 \to K^-\pi^+\pi^0$$

through either ρ^+ or K^{*+} with the neutral pion not detected. These two modes for D^0 are referred to as D^0 and S^0, as already discussed in section 4.14. The corresponding charge-conjugate modes are used for D^{*-}.

For the determination of the angular distribution of the $D^{*\pm}$, the D^0 and S^0 candidates are required to satisfy:

a) $1.50\,\text{GeV} < M(K^-\pi^+) < 1.984\,\text{GeV}$;
b) $M(K^-\pi^+\pi^+) - M(K^-\pi^+) < 0.15\,\text{GeV}$;

and

c) $E(K^-\pi^+\pi^+)/E_{\text{beam}} > 0.5$.

In order to enhance the sensitivity to the weak contribution, only events with $W > 34\,\text{GeV}$ are accepted, the average W being 35 GeV. The background under the D^0 and S^0 peaks is reduced by requiring the momenta of each of the particles forming the $(K^-\pi^+)$ system to have $p > 1.4\,\text{GeV}/c$. In total there are 51 D* candidates with an estimated background of 5. The angle θ is taken to be the angle between the incoming e^- and the $K^-\pi^+\pi^+$ system. Fig. 5.16 shows the D^{*+} angular distribution. The acceptance is uniform over the range $|\cos\theta| < 0.8$. The angular distribution is consistent with the form

$$d\sigma/d\cos\theta \sim 1 + a\cos\theta + \cos^2\theta\,.$$

Fitting this form to the data for $|\cos\theta| < 0.8$ and extrapolating to $\cos\theta = \pm 1$ yields for the asymmetry

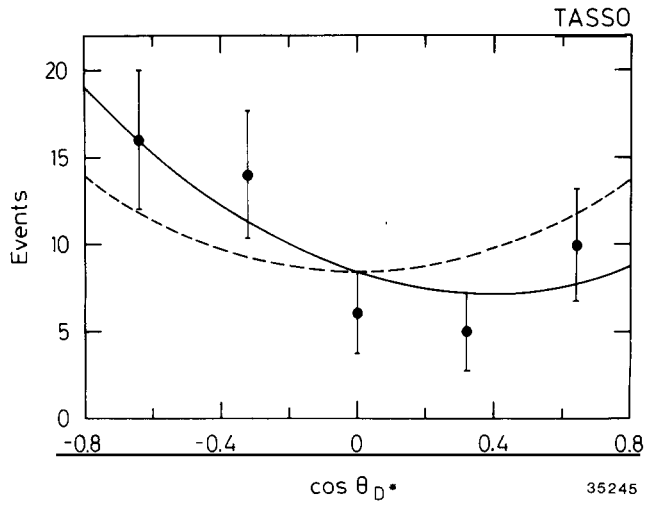

Fig. 5.16. The TASSO [5.40] $D^{*\pm}$ production angular distribution; θ is the angle between the e^- beam and the $K^-\pi^+\pi^+$ ($K^+\pi^-\pi^-$) system. The full curve indicates the fit $d\sigma/d\cos\theta \sim 1 + a\cos\theta + \cos^2\theta$. The dashed curve is proportional to $1 + \cos^2\theta$.

$A_c = \frac{3}{8}a = -0.28 \pm 0.13$. No correction is applied for the background. Assuming the latter to be forward–backward symmetric would change A_c to -0.31 after correction. The fraction of $D^{*\pm}$ mesons coming from bottom hadrons is estimated to be ~4% and gives a negligible contribution to the measured asymmetry. This measured asymmetry is to be compared with the standard-model value of -0.14, which is 50% larger than A_μ because of the smaller quark charge [see eq. (5.12)].

This result is the first indication for a weak-current contribution to charm production $e^-e^+ \to c\bar{c}$. From the value of $A_c = -0.28 \pm 0.13$, it follows that $a_e a_c = -1.96 \pm 0.92$. This is consistent with the standard-model value of -1. If, furthermore, the experimental value of $a_e^2 = 1.06 \pm 0.13$ from table 5.5 is used, then $|a_c| = 1.90 \pm 0.90$, to be compared with the standard-model value of 1.

5.11. QED tests and search for a second neutral intermediate vector boson

We briefly discuss in this section two unrelated topics: QED tests and comparison of the experimental data with models with two neutral intermediate vector bosons.

QED predictions are based on the validity of Maxwell's equations and on the assumption that leptons are point-like objects without excited states. The procedure used at PETRA to compare the data with the QED predictions is as follows:

(a) the data are corrected for weak effects on the basis of the standard model.

(b) the data are also corrected for radiative effects and effects due to hadron vacuum polarization.

(c) the corrected cross sections are compared to the QED predictions, and deviations are parametrized in terms of form factors [5.41]

$$F_\pm = 1 \mp \frac{q^2}{q^2 - \Lambda_\pm^2}. \tag{5.30}$$

Table 5.6 gives the 95% confidence level lower limits for $\Lambda_\pm$ for various processes. On the basis of the largest value in that table, QED is found to be valid to the extremely short distance of 10^{-16} cm.

Table 5.6
QED parameters: 95% confidence lower limits in GeV/c

Experiment	$e^-e^+ \to e^-e^+$		$e^-e^+ \to \mu^-\mu^+$		$e^-e^+ \to \tau^-\tau^+$		$e^-e^+ \to \gamma\gamma$	
	Λ_+	Λ_-	Λ_+	Λ_-	Λ_+	Λ_-	Λ_+	Λ_-
CELLO	83	155	186	101	142	121	59	48
	[5.13]	[5.13]	[5.33]	[5.33]	[5.29]	[5.29]	[5.13]	[5.13]
JADE	178	200	142	126	111	93	61	57
	[5.17]	[5.17]	[5.47]	[5.47]	[5.47]	[5.47]	[5.17]	[5.17]
MARK J	128	161	192	163	100	127	58	38
	[5.31]	[5.31]	[5.42]	[5.35]	[5.42]	[5.42]	[5.43]	[5.47]
PLUTO	80	234	107	101	79	63	46	36
	[5.22]	[5.22]	[5.45]	[5.45]	[5.45]	[5.45]	[5.46]	[5.46]
TASSO	155	251	222	187	104	189	34	42
	[5.26]	[5.26]	[5.26]	[5.26]	[5.47]	[5.47]	[5.24]	[5.24]

Finally, we discuss the possible modification of the standard model by including more than one neutral intermediate vector boson, say Z_1 and Z_2. Since copious production of Z_1 (where the convention is that $M_{z_1} < M_{z_2}$) via the process

$$e^-e^+ \to \gamma Z_1 \tag{5.31}$$

as shown in fig. 2.2b has not been seen at the highest PETRA energy, the value of M_{z_1} must be at least 42 GeV. A more refined comparison is based on the fact that the presence of two or more Z's leads to a change of the vector coupling constant [5.48]:

$$v^2(Z_1, Z_2) = v^2 + 16C, \tag{5.32}$$

where v^2 is the value for the standard model. Table 5.7 gives the upper limits of C as obtained by the various PETRA Collaborations.

The relation between the value of C and the masses of Z_1 and Z_2 is model dependent. On the basis of the TASSO data [5.26], for example, the mass limits are shown in fig. 5.17 for the two models $SU(2) \times U(1) \times U'(1)$ and $SU(2) \times U(1) \times SU'(2)$. In both of these models, Z_1 is lighter than, while Z_2 is heavier than, the mass of Z^0 in the standard model.

Table 5.7
95% confidence upper limit for the parameter C

CELLO [5.14]	0.031
JADE [5.17]	0.031
MARK J [5.25]	0.021
PLUTO [5.23]	0.060
TASSO [5.26]	0.012
Combined	0.010

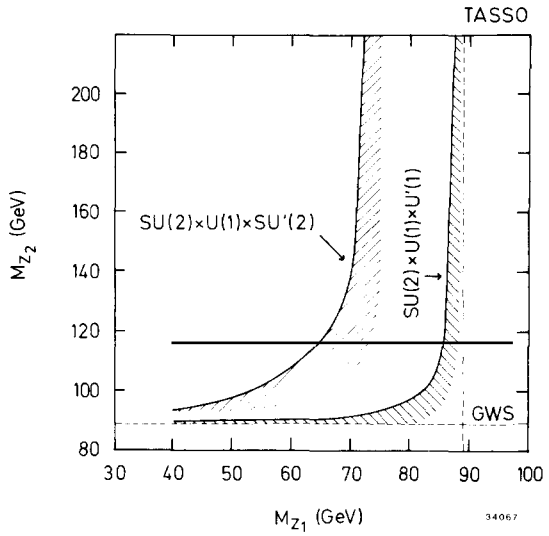

Fig. 5.17. TASSO [5.24] limits on the Z^0 masses for models with two Z^0 bosons. The allowed masses of Z_1 and Z_2 are confined to the region (partially shaded) between the solid curve and the dashed lines.

6. Two-photon physics

By two-photon physics, we mean the study of processes of the type [6.1]

$$e^+e^- \to e^+e^- + \text{hadrons} \tag{6.1}$$

shown in fig. 2.1 (3h). The assumed mechanism is that the positron and the electron each emit a photon, and the two photons interact to produce the hadrons. The details of the process are shown diagrammatically in fig. 6.1.

Before discussing the physical significance of such processes, let us say a word about the notation. In this chapter, the symbol W will be used to denote the invariant mass of the two photons, or equivalently that of the hadron system, while s retains the meaning of the square of the center-of-mass energy of the incoming system of the electron and the positron. Thus $W \neq \sqrt{s}$, and this W should not be confused with the W used in the other chapters.

6.1. Physical significance

There are at least four independent reasons why two-photon physics is important.

(A) At high energies, the total cross section for the process (6.1) is large.

For the purpose of orientation, let us give a very rough order-of-magnitude estimate for the cross section for the process (6.1) by comparing it with the one-photon hadronic process

$$e^+e^- \to \text{hadrons} \tag{6.2}$$

studied in chapters 2, 3 and 4. As seen from fig. 6.1, the electromagnetic coupling appears four times for

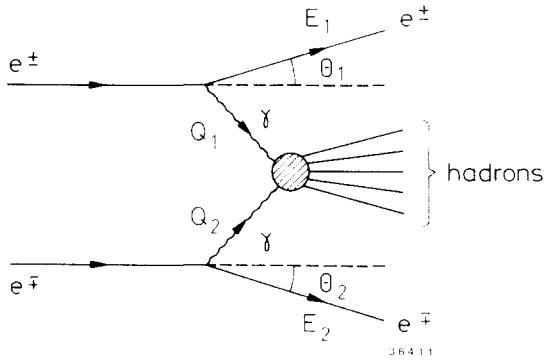

Fig. 6.1. Diagram for $e^+e^- \to e^+e^-$ + hadrons.

(6.1), and hence its cross section, compared with that of (6.2), is reduced by a factor of α^2. This is roughly a reduction of five orders of magnitude. Fortunately, there are enhancements from two different sources.

(i) For a given hadronic state, the cross section for the two-photon process (6.1) behaves like s^0 in the high-energy limit [6.1], while that for (6.2) behaves like s^{-1}. The process (6.1) is therefore enhanced by a factor of

$$s/W^2 .$$

For example, if $\sqrt{s}$ is 35 GeV and $W \sim 1$ GeV (such as the η' meson), this gain is three orders of magnitude.

(ii) The two-photon process can proceed with the final electron and positron near the original beam directions. In such cases, both Q_1^2 and Q_2^2 of fig. 6.1 are quite small, being of the order of magnitude of m^2, where m is the electron mass. This gain is of the form

$$(\ln(p_T/m))^2 ,$$

where p_T is some typical transverse momentum. For example, if p_T is 300 MeV/c, this gain is about 40.

Therefore, very roughly, the cross section for (6.1) can be a sizeable fraction of that of (6.2) at PETRA energies. The actual situation is somewhat more complicated. Note that the enhancement factor (i) increases with energy; there is roughly another factor of 5 going from the present PETRA energy to Z^0.

(B) The charge-conjugation quantum number for a two-photon state is +1, and hence the hadrons can be a $C = +1$ resonance such as f^0. Because of this charge conjugation quantum number, such resonances do not appear directly in one-photon annihilation (6.2) of e^+ and e^-.

In principle, the two-photon process gives a way to search for new $C = +1$ resonances. In practice, this has not been accomplished at PETRA. Instead, experimental results are limited to some of the known low-lying resonances. In table 6.1 a part of the listing for $C = +1$ mesons with well-known decay modes is reproduced from 1982 Review of Particle Properties [6.2].

Of the mesons listed in table 6.1, four have been clearly seen at PETRA through the two-photon process: η', f^0, A_2 and f'. The experimental results on these four mesons will be described respectively in

Table 6.1
Properties of $C = +1$ mesons, including their major decay modes, from the 1982 Review of Particle Properties

	$I^G(J^P)C_n$ – estab.	Mass M (MeV)	Full width Γ (MeV)	M^2 $\pm\Gamma M$ (GeV^2)	Partial decay mode	
					Mode	Fraction (%)
π^0	$1^-(0^-)+$	134.96	7.95 eV ±0.55 eV	0.018215	$\gamma\gamma$ γe^+e^-	98.787 ± 0.030 1.213 ± 0.030
η	$0^+(0^-)+$	548.8 ±0.6	0.83 keV ±0.12 keV	0.301 ±0.000	$\gamma\gamma$ $3\pi^0$ $\pi^+\pi^-\pi^0$ $\pi^+\pi^-\gamma$	39.1 ±0.8 31.8 ±0.8 23.7 ±0.5 4.91 ± 0.13
$\eta'(958)$	$0^+(0^-)+$	957.57 ±0.25	0.28 ±0.10	0.917 ±0.0003	$\eta\pi\pi$ $\rho^0\gamma$ $\omega\gamma$ $\gamma\gamma$	65.3 ± 1.6 30.0 ± 1.6 2.8 ± 0.5 1.9 ± 0.2
S*(975)	$0^+(0^+)+$	975 ±4	33 ±6	0.951 ±0.032	$\pi\pi$ $K\bar{K}$	78 ± 3 22 ± 3
f(1270)	$0^+(2^+)+$	1273 ±5	179 ±20	1.62 ±0.23	$\pi\pi$ $2\pi^+2\pi^-$ $K\bar{K}$	83.1 ± 1.9 2.8 ± 0.4 2.9 ± 0.2
$A_1(1270)$	$1^-(1^+)+$	1275 ±30	315 ±45	1.63 ±0.40	$\rho\pi$	dominant
D(1285)	$0^+(1^+)+$	1283 ±5	26 ±5	1.65 ±0.03	$K\bar{K}\pi$ $\eta\pi\pi$ $\delta\pi$ 4π (prob. $\rho\pi\pi$)	11 ± 3 49 ± 6 36 ± 7 40 ± 7
$\varepsilon(1300)$	$0^+(0^+)+$	~1300	200–600		$\pi\pi$ $K\bar{K}$	~90 ~10
$A_2(1320)$	$1^-(2^+)+$	1318 ±5	110 ±5	1.74 ±0.14	$\rho\pi$ $\eta\pi$ $\omega\pi\pi$ $K\bar{K}$	70.1 ± 2.2 14.5 ± 1.2 10.6 ± 2.5 4.8 ± 0.5
f'(1515)	$0^+(2^+)+$	1520 ±10	75 ±10	2.31 ±0.11	$K\bar{K}$	dominant

sections 6.5, 6.6, 6.7 and 6.8. In addition, some other hadronic states have also been measured, including $\rho^0\rho^0$ and $p\bar{p}$, to be described in sections 6.9 and 6.10 respectively.

(C) Just as $e^+e^- \to q\bar{q}$ is similar to $e^+e^- \to \mu^+\mu^-$, the pair-creation process $\gamma\gamma \to q\bar{q}$ is entirely similar to $\gamma\gamma \to \mu^+\mu^-$, as shown in fig. 6.2.

On the basis of this very simple quark picture, contrary to proton antiproton annihilation for example, high p_T jets are expected to occur with high probability. This may seem startling at first sight, and is to be discussed in section 6.11.

In connection with the process $\gamma\gamma \to q\bar{q}$, the following comments may be useful.

(i) As $\gamma\gamma \to q\bar{q}$ is analogous to $e^+e^- \to q\bar{q}$, the analog of $e^+e^- \to q\bar{q}g$ discussed extensively in chapter 3

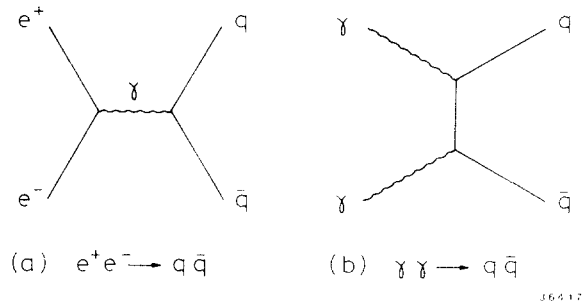

Fig. 6.2. Diagrams for the creation of $q\bar{q}$ pair.

is

$$\gamma\gamma \to q\bar{q}g\,. \tag{6.3}$$

The diagrams for (6.3) are shown in fig. 6.3. Unlike the three-jet events of chapter 3, this (6.3) in the form of

$$e^+e^- \to e^+e^- + \text{three jets} \tag{6.4}$$

has not yet been seen at PETRA. The difficulty is as follows. Since three-jet events were first discovered after the c.m. energy of PETRA reached 27 GeV, events of the type (6.4) require a relatively high rest mass for the $\gamma\gamma$ system, say 10 or 15 GeV at least. By (Ai), such events are rather rare. These rare but interesting events may be identified by studying three-jet events with the following properties (which are not independent):

(α) The momenta of the three jets as calculated from the angles between the jets (see, for example, fig. 3.1a) do not agree with the observed momenta from the hadrons in the jet. This includes in particular events with $\theta_3 > \pi$.

(β) The missing momentum is predominantly in the direction of the beam axis.

Of course, the measurement of the momenta of the neutrals is highly desirable if not essential. Backgrounds due to

$$e^+e^- \to \gamma + \text{three jets} \tag{6.5}$$

need to be subtracted.

(ii) While $e^+e^- \to q\bar{q}$ can be used to describe well the bulk of the data on $e^+e^- \to$ hadrons, $\gamma\gamma \to q\bar{q}$

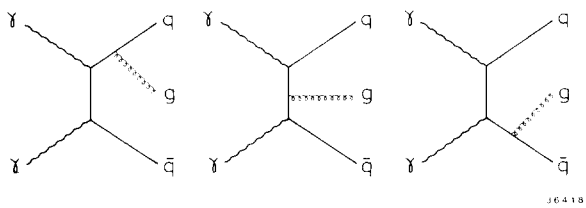

Fig. 6.3. Diagrams for the production of $q\bar{q}g$ by two photons.

cannot be expected to describe by itself most of the data on two-photon physics, even when the c.m. energy of $\gamma\gamma$ is high. The reason is that, while $e^+e^- \to$ hadrons through the intermediary of one photon is necessarily a hard process at high energies and hence well described by quarks, $\gamma\gamma \to$ hadrons can be a soft process as well as a hard process. An example of a soft process is shown in fig. 6.4 in the language of vector dominance [6.3]; the hadrons may be produced through either elastic scattering or diffractive dissociation. Thus $\gamma\gamma \to q\bar{q}$ is expected to give an adequate description only for high p_T jets. Accordingly it would be very interesting to measure the angular distributions of sphericity and/or thrust axes in the center-of-mass system of the two photons.

(D) Deep inelastic electron–photon scattering

$$e + \gamma \to e + \text{hadrons} \tag{6.6}$$

provides an additional opportunity to test quantum chromodynamics.

Experimentally, this deep inelastic electron–photon scattering is observed through the two-photon process (6.1) by selecting final states where the electron (or positron) has a large scattering angle while the positron (or electron) has a small scattering angle. With reference to fig. 6.1, this means that θ_1 is large while θ_2 is small, or vice versa. Since (6.6) is precisely the deep inelastic electron–proton scattering with the proton replaced by the photon, it is convenient and natural to express the result in terms of the photon structure functions. This interesting and ongoing investigation is discussed in section 6.12.

Finally, we discuss here briefly the subtle point of the relation between the two-photon process (6.1) and the corresponding process $\gamma\gamma \to$ hadrons. That there is an intimate relation is clear from the fact that, for most of the two-photon events, the two photons are both close to the mass shell. Physically, the point is that, since a charged particle has its own Coulomb field, by Lorentz transformation an ultra-relativistic charged particle, such as an electron or positron, carries with it a sharp pulse of electromagnetic field. For processes due to this pulse, the replacement of an electron or positron beam by a photon beam in the same direction is known as the Weizsäcker–Williams approximation [6.4]. For example, this approximation can be applied to give accurate information about γp processes from inelastic ep scattering. If the electron or positron beam is unpolarized, then by symmetry the photon beam is also unpolarized. For the two-photon process (6.1), this approximation needs to be applied twice, once to the electron beam and again to the positron beam. Accordingly, even if the electron beam and the positron beams are both unpolarized, there is still a correlation between the polarizations of the two-photon beams [6.5]. This correlation is neglected in the double Weizsäcker–Williams approximation.

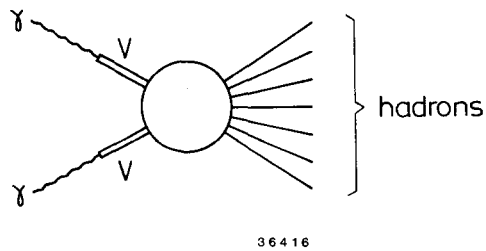

Fig. 6.4. Vector-meson dominance diagram for $\gamma\gamma \to$ hadrons.

6.2. Kinematics

Let $(E_1, \boldsymbol{p}_1)$ and $(E_2, \boldsymbol{p}_2)$ be the energies and momenta of the outgoing electron and positron, then, with reference to fig. 6.1, it is seen that

$$|Q_1^2| = -(E_b - E_1)^2 + [(E_b^2 - m^2)^{1/2} - (E_1^2 - m^2)^{1/2} \cos\theta_1]^2 + (E_1^2 - m^2)\sin^2\theta_1 ,$$

where E_b is the beam energy and m is the electron mass. This relation can be written in the form

$$|Q_1^2| = 2[E_b E_1 - m^2 - \sqrt{E_b^2 - m^2}\sqrt{E_1^2 - m^2}\cos\theta_1] . \tag{6.7}$$

Since the electron mass m, being about 0.5 MeV, is very small compared with E_b and E_1, expansion of the square roots gives

$$\begin{aligned} |Q_1^2| &= 2E_b E_1 - 2m^2 - 2E_b E_1 \cos\theta_1 + m^2 (E_b/E_1 + E_1/E_b)\cos\theta_1 \\ &= 4E_b E_1 \sin^2\frac{\theta_1}{2} + m^2 \left[\frac{(E_b - E_1)^2}{E_b E_1}\cos\theta_1 - 4\sin^2\frac{\theta_1}{2}\right] . \end{aligned} \tag{6.8}$$

Again because of the smallness of the electron mass m, the second term in (6.8) is negligible compared with the first unless θ_1 is very small. Therefore, the approximation of small θ_1 can always be used in the square brackets, leading to $\cos\theta_1 \sim 1$ and $\sin^2(\theta_1/2) \sim 0$. Therefore the formula

$$|Q_1^2| = 4E_b E_1 \sin^2(\theta_1/2) + m^2 (E_b - E_1)^2/E_b E_1 \tag{6.9}$$

is always accurate. Of course

$$|Q_2^2| = 4E_b E_2 \sin^2(\theta_2/2) + m^2 (E_b - E_2)^2/E_b E_2 . \tag{6.10}$$

In particular, the first term and the second term of (6.9) are equal at an angle

$$\theta_1 = \theta_0 = m(E_b - E_1)/E_b E_1 . \tag{6.11}$$

If E is 15 GeV, then this θ_0 is about 0.5 mrad even for a very low value of $E_1 = 1$ GeV. Therefore, for θ_1 much above 1 mrad, the effect of the electron mass is negligible.

We discuss next the energy and momentum of the hadron system produced in the two-photon process. By energy-momentum conservation, they are respectively $2E_b - E_1 - E_2$ and $-\boldsymbol{p}_1 - \boldsymbol{p}_2$. Let θ_{12} be the angle between $\boldsymbol{p}_1$ and $-\boldsymbol{p}_2$. The invariant mass of this hadron system is given by

$$W^2 = (2E_b - E_1 - E_2)^2 - (\boldsymbol{p}_1 + \boldsymbol{p}_2)^2 . \tag{6.12}$$

In this quantity the electron mass can be neglected altogether, leading to

$$W^2 = 4[(E_b - E_1)(E_b - E_2) - E_1 E_2 \sin^2(\theta_{12}/2)] . \tag{6.13}$$

In some applications, the second term is negligible because of the smallness of θ_{12}. However, when W is relatively small, say around or below about 1 GeV, the second term can often be important. For example, take $E_b = 15$ GeV, $E_1 = E_2 = 14$ GeV and $\theta_{12} = 100$ mrad, then the second term is about half of the first term, and $W = 1.43$ GeV.

For the discussion of the two-photon physics, we shall use the following terminology. By a single-tagged event, we mean that the outgoing electron or the positron is observed in the forward detector. By an untagged or no-tag event, we mean that neither the electron nor the positron is detected in the forward detector.

The forward detector covers an angular range of typically a few degrees, as described in chapter 1. For CELLO, JADE, PLUTO and TASSO, this angular range is respectively from 25 to 50 mrad, from 34 to 75 mrad, from 23 to 260 mrad, and from 24 to 60 (recently increased to 110) mrad. For PLUTO, there are actually two forward detectors in each direction, a small-angle tagger between 23 and 70 mrad, and a large-angle tagger between 70 and 260 mrad – see section 1.7.5. Because of the logarithmic dependence of the event rate on the angle, the rates of single-tagged events are about the same for the small-angle tagger and the large-angle tagger. For a single-tagged event, θ_1 is in the range of a few degrees while θ_2 is small. In other words, $|Q_2^2|$ is small but $|Q_1^2|$ is not so small. As an example, for $E_b = 15$ GeV, $E_1 = E_2 = 7$ GeV, $\theta_1 = 40$ mrad and $\theta_2 = 0$, then by (6.9) and (6.10)

$$|Q_1^2| = 0.17\ \text{GeV}^2 \qquad \text{and} \qquad |Q_2^2| = 0.16\ \text{MeV}^2 . \tag{6.14}$$

Similarly, for most of the untagged events, both θ_1 and θ_2 are small, and hence both $|Q_1^2|$ and $|Q_2^2|$ are small. Needless to say, the rate for untagged events is much higher than the single-tagged events, but the single-tagged events are much better identified as due to the two-photon process (6.1). However, in tagging the photon we also pay another price: as seen from (6.14), the value of $|Q_1^2|$ is sizeable, and extrapolation to smaller values of $|Q_1^2|$ is often necessary. In principle, there are also doubly-tagged events. Their rates are even smaller, and they have not yet been used at PETRA to yield any interesting physics result.

6.3. QED tests

Beginning in the next section, the various PETRA results on two-photon physics are described. As shown in fig. 2.1, the processes 3e and 3ℓ bear a great deal of similarity to 3h, which is (6.1). They, 3e and 3ℓ, are well-known QED processes and can be calculated accurately. Therefore, in principle, a measure of these processes gives QED tests in addition to those of chapter 5.

For this comparison with the predictions of QED, one of the 3ℓ processes, namely

$$e^+e^- \to e^+e^-\mu^+\mu^-$$

has been used by MARK J [6.6], PLUTO [6.7] and CELLO [6.8], and the process 3e

$$e^+e^- \to e^+e^-e^+e^-$$

by PLUTO [6.7] and CELLO [6.8]. In the theoretical calculations, the diagrams included are those shown in fig. 6.5, and the program of Vermaseren [6.9] is used. These diagrams give cross sections of the order of α^4. No higher-order radiative corrections, which are estimated to be small [6.10], are included.

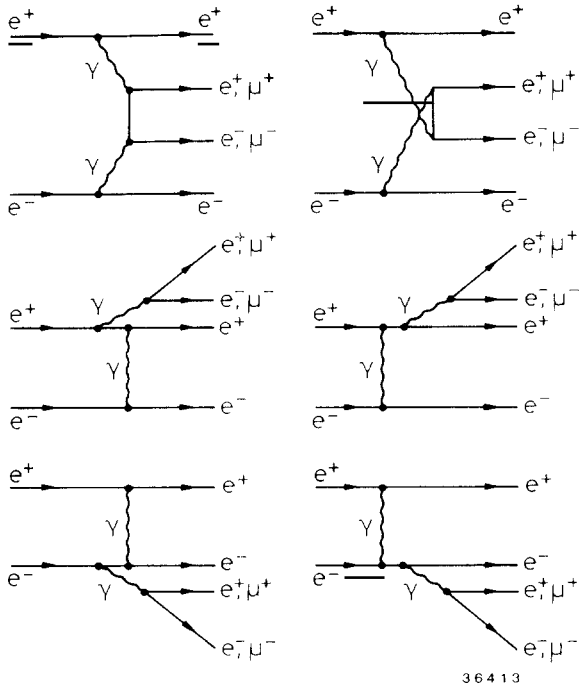

Fig. 6.5. Feynman diagrams for $e^-e^+ \to e^+e^-e^+e^-$ and $e^+e^- \to e^+e^-\mu^+\mu^-$.

For these QED tests at PETRA, the events used by MARK J, PLUTO and CELLO correspond respectively to integrated luminosities of 30, 2.6 and 7.5 pb^{-1}. In figs. 6.6, 6.7 and 6.8, the data are compared respectively with the QED predictions. The agreement is good in every case. It is seen from fig. 6.6 of the MARK J data that QED is correct to α^4 and up to $W^2 \sim 100\,GeV^2$ and $p_\perp^2 \sim 50\,GeV^2/c^2$, so far as the process $e^+e^- \to e^+e^-\mu^+\mu^-$ is concerned. The selection of events is somewhat different for the three experiments. In the CELLO study, one of the outgoing electrons is tagged using the end-cap liquid argon electromagnetic calorimeter (see section 1.4.4) with polar angles ranging between 130 and 400 mrad. The average Q^2 is $9.5\,GeV^2/c^2$.

We must add that the nature of the present QED test is quite different from those of section 5.11. There, the point of the test is to see the extent which QED can be pushed to small distances, and accordingly the results are expressed in terms of suitable cutoff parameters Λ (see table 5.6). Here, although the processes studied are of higher order in the fine-structure constant α, the propagators are comparatively less far off the mass shell. Therefore, it is essentially inconceivable for QED not to hold accurately.

6.4. $\gamma\gamma$ total cross section

Following the guiding philosophy of going from the general features to the specific channels as stated at the beginning of chapter 2, we study in connection with two-photon physics first the topic of $\gamma\gamma$ total cross section. Ten years ago, when vector-meson dominance [6.3] was generally accepted, the process

$$\gamma\gamma \to \text{hadrons} \tag{6.15}$$

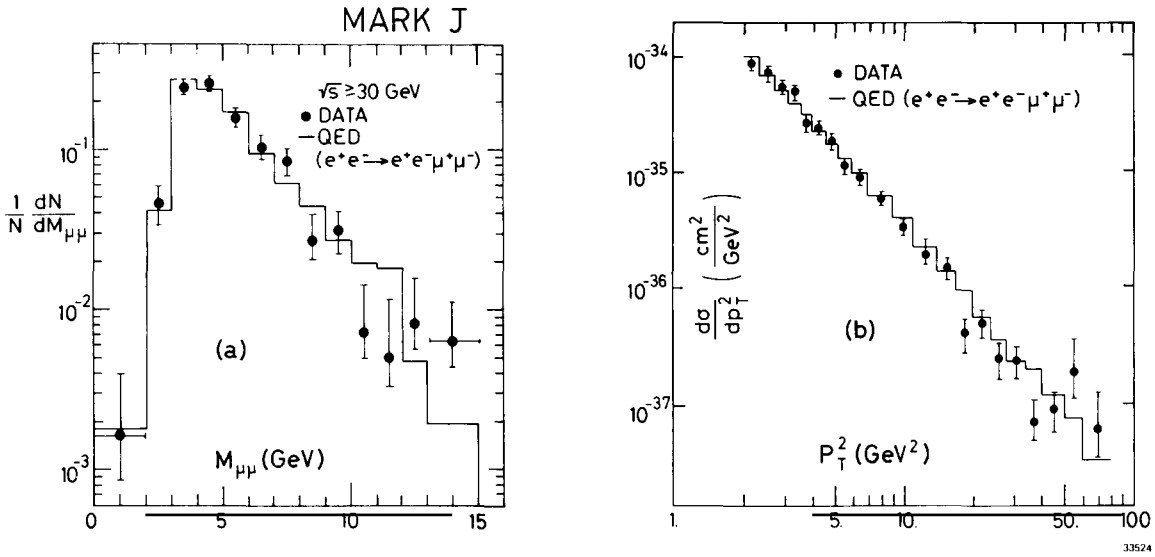

Fig. 6.6. MARK J data [6.6] on (a) invariant-mass distribution for muon pairs under no-tag condition, and (b) $d\sigma/dp_T^2$ as a function of p_T^2 for the sample obtained with use of one entry for each muon. The lines are QED calculations.

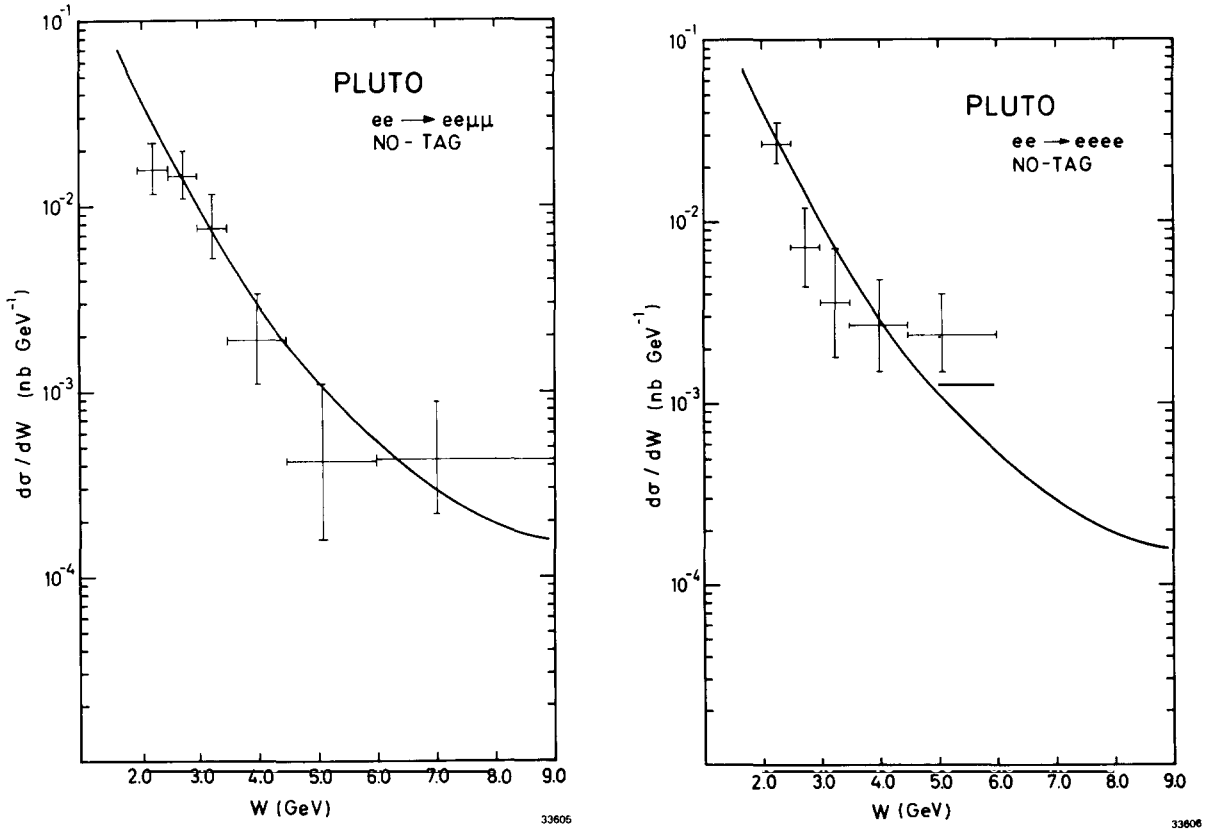

Fig. 6.7. Continued on next page.

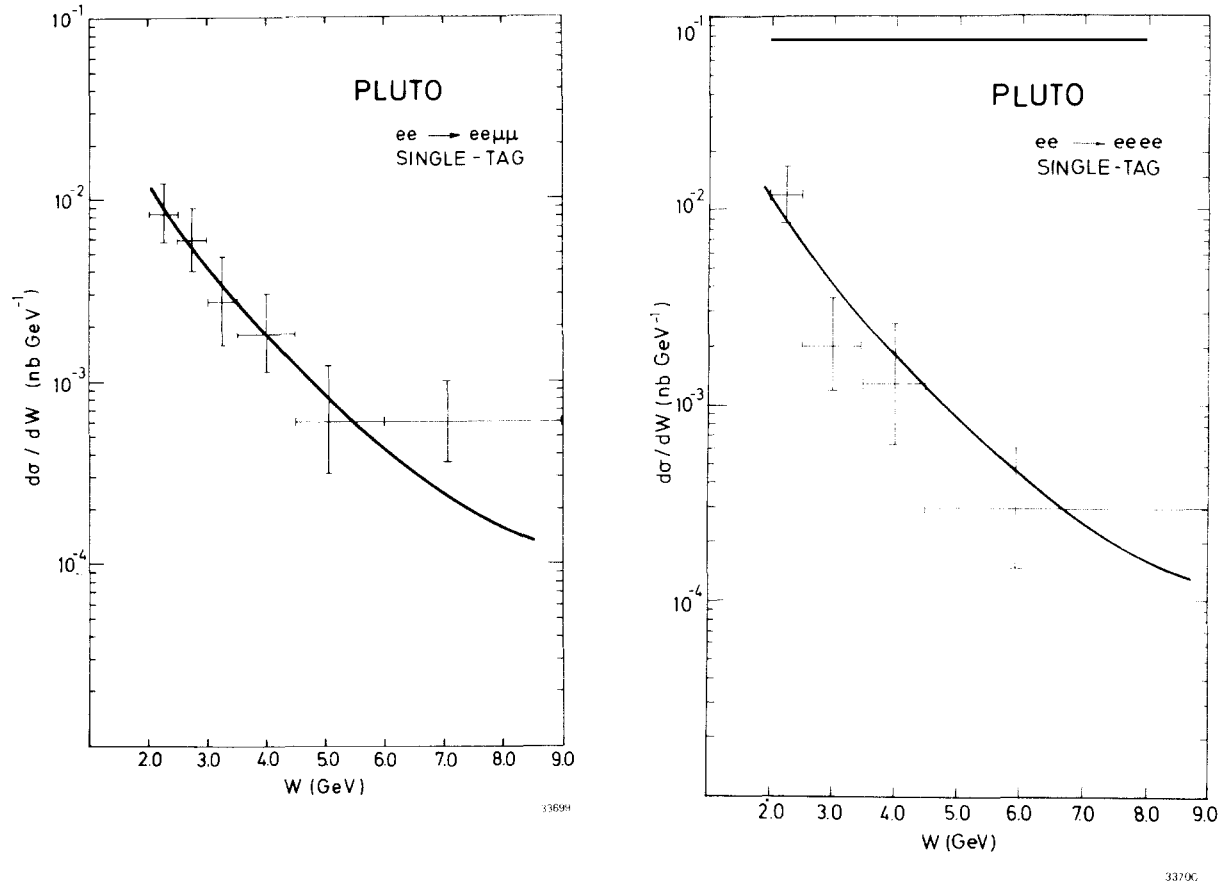

Fig. 6.7. PLUTO [6.7] data on the differential cross sections in the invariant mass W for muon and electron pairs in the untagged and the single-tagged regions. The solid curves are the absolute QED predictions.

was believed to proceed via the diagram of fig. 6.4, where each photon was first turned into a vector meson, either ρ, ω or ϕ. We know now that this cannot be the whole story. As already mentioned in section 6.1(C), (6.15) is also expected to proceed via the formation of two quark jets as shown in fig. 6.2b.

Through unitarity the total cross section for (6.15) is given by the imaginary part of $\gamma\gamma \to \gamma\gamma$ forward scattering, with electromagnetic effects due to electron, muon and tau loops subtracted. Thus the diagram of fig. 6.4 leads to those of fig. 6.9a, where either a Pomeron P or some other Regge pole R is exchanged between the vector mesons. Similarly, the diagram of fig. 6.2b leads to the quark diagrams of fig. 6.9b, where a third diagram with no imaginary part in the forward direction has been omitted. In order to determine the importance of the quark diagrams in the $\gamma\gamma$ total cross section, the PLUTO Collaboration [6.11, 6.12] has measured this total cross section and compared with the expectations of vector-meson dominance. In vector-meson dominance, the cross section for two real photons can be estimated using Pomeron factorization

$$\sigma_{\gamma\gamma} \cdot \sigma_{pp} = (\sigma_{\gamma p})^2$$

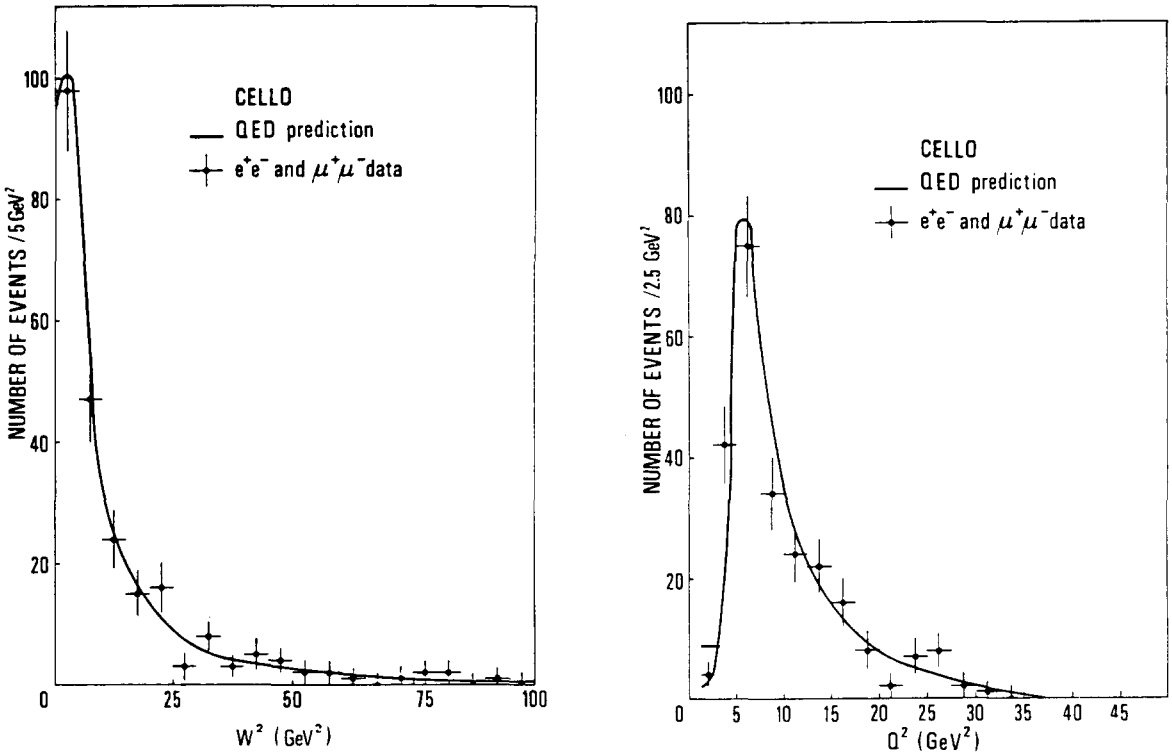

Fig. 6.8. CELLO [6.8] data on (a) W^2 distribution of lepton pairs, and (b) Q^2 distribution. The data on $e^+e^- \to e^+e^-e^+e^-$ and $e^+e^- \to e^+e^-\mu^+\mu^-$ have been combined. The curves are the QED predictions.

and Regge exchange to be [6.13]

$$\sigma^{\mathrm{VMD}}(W) = 240\ \mathrm{nb} + \frac{270\ \mathrm{nb\ GeV}}{W}. \tag{6.16}$$

Since the untagged events clearly cannot be used for the measurement of this $\gamma\gamma$ total cross section,

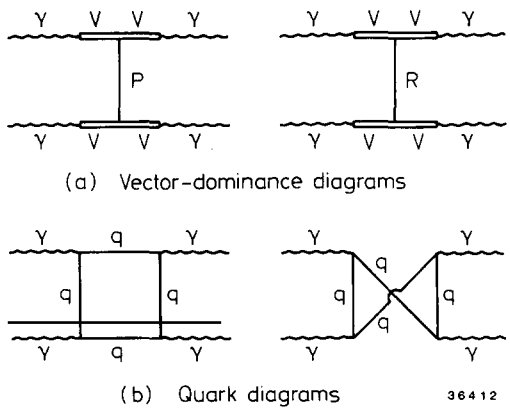

Fig. 6.9. Diagrams for the total cross section $\gamma\gamma \to$ hadrons.

the single-tagged events are analyzed for this purpose. As shown in the example (6.14), the Q^2 for the photon from the tagged electron or positron is not negligible compared with mass squared of the vector meson even for the small-angle tagger of PLUTO. Extrapolation to $Q^2 = 0$ is therefore necessary. An extrapolation using a ρ-pole form factor [6.12]

$$\sigma_t(W, Q^2) = \sigma_{\gamma\gamma}(W)\left(\frac{m_\rho^2}{m_\rho^2 + Q^2}\right)^2 \tag{6.17}$$

is made to the results of PLUTO. Fig. 6.10 shows the results of $\sigma_{\gamma\gamma}(W)$ as a function of W. The data are seen to be larger than the expectations of the vector-dominance model (σ^{VDM}), and are therefore fitted to a form:

$$\sigma_{\gamma\gamma}(W) = A\sigma^{\mathrm{VMD}}(W) + \frac{B}{W^2} = A\left(240\ \mathrm{nb} + \frac{270\ \mathrm{nb\ GeV}}{W}\right) + \frac{B}{W^2}. \tag{6.18}$$

The result of the fit is $A = 0.97 \pm 0.16$ and $B = 2250 \pm 500\ \mathrm{nb\ GeV^2}$. The term $1/W^2$ is expected from point-like contribution [quark diagrams of fig. 6.9b]. The statistical error is indicated by the hatched band in fig. 6.10.

In this figure, systematic error is not shown. The cross section as a function of W depends on the unfolding of W from the visible hadronic energy W_{vis}. Since this unfolding is sensitive to the Monte Carlo model used, the systematic error is expected to be large. The steep rise for W below 3 GeV, which is the most prominent feature of fig. 6.10, needs to be confirmed by the improved data from the new PLUTO configuration (see fig. 1.21).

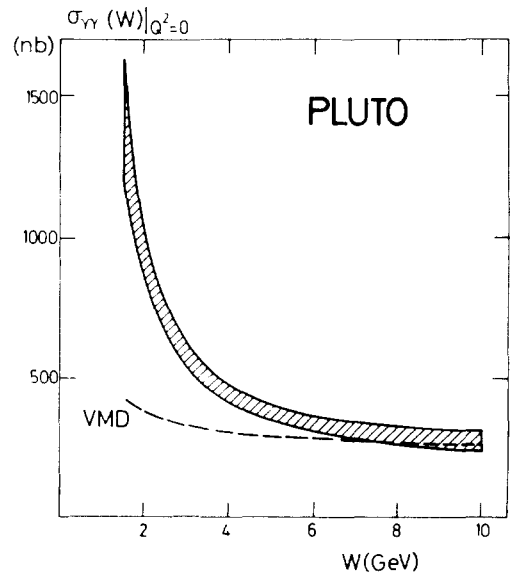

Fig. 6.10. The PLUTO [6.12] total photon–photon cross section extrapolated to $Q^2 = 0$, versus the true invariant mass W. The hatched band represents the 1 standard deviation limits as obtained from the fit. The VMD prediction is given by the dashed line.

6.5. $e^+e^- \to e^+e^-\eta'$

The first theoretical discussion of two-photon physics (6.1) was given by Low [6.14] over twenty years ago. He studied the process

$$e^+e^- \to e^+e^-\pi^0 .$$

However, there is no data from PETRA on this process. In this and the next three sections, the PETRA data on the two-photon production of the $C = +1$ mesons η', f^0, A_2 and f' are presented. These sections are arranged in order of increasing masses of the mesons.

At PETRA, the process

$$e^+e^- \to e^+e^-\eta'(958)$$

has been investigated through the decay mode

$$\eta' \to \gamma\rho^0$$
$$\quad\quad \hookrightarrow \pi^+\pi^-$$

by the JADE Collaboration [6.15] and the CELLO Collaboration [6.16] at an average center-of-mass energy of 34 GeV. The photons are detected respectively in the lead glass counters (JADE) and the liquid argon counters (CELLO).

The JADE data is shown in fig. 6.11 which give the invariant mass spectra of the $\pi^+\pi^-$ system and the $\pi^+\pi^-\gamma$ system. In fig. 6.11b the additional requirement $m(\pi^+\pi^-) < 1.0$ GeV has been imposed. Prominent ρ^0 and η' signals are seen. The association of the ρ^0 with the η' signal is evident in the shaded histogram of fig. 6.11b, which is obtained by restricting the $\pi^+\pi^-$ mass to the ρ^0 band defined by $0.60 < m(\pi^+\pi^-) < 0.85$ GeV.

The CELLO data on the $\pi^+\pi^-\gamma$ mass distribution is shown in fig. 6.12. With the cut of $0.6 < m(\pi^+\pi^-) < 0.9$ GeV, a clean η' signal is seen.

The values of the radiative width $\Gamma_{\gamma\gamma}(\eta')$ measured by JADE and CELLO are given in table 6.2 together with the previous result from the MARK II Collaboration [6.17] at SPEAR. These values agree with the theoretical prediction of 6 keV on the basis of the quark model with a small octet–singlet mixing angle [6.18].

6.6. $e^+e^- \to e^+e^-f^0$

The first meson seen at PETRA through the two-photon process (6.1) is the f^0, whose mass and width are (from table 6.1)

$$M(f^0) = (1273 \pm 5)\,\text{MeV}, \qquad \Gamma(f^0) = (179 \pm 20)\,\text{MeV}, \tag{6.19}$$

and which decays predominately into two pions with a branching ratio of $(83.1 \pm 1.9)\%$. The charged decay mode

$$f^0 \to \pi^+\pi^-$$

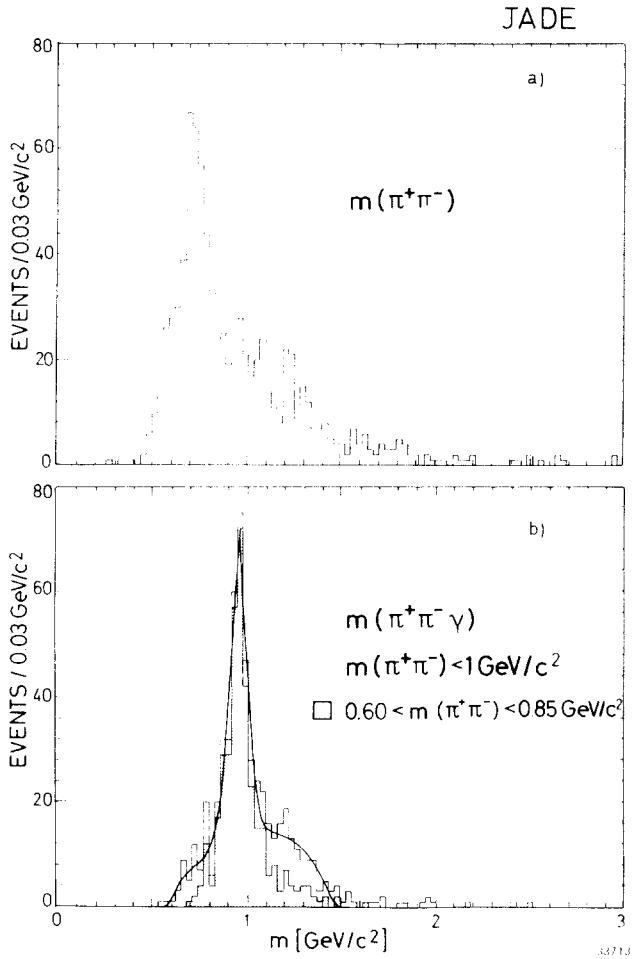

Fig. 6.11. (a) Mass distribution of the $\pi^+\pi^-$ system from JADE [6.15]. (b) Mass distribution of the $\pi^+\pi^-\gamma$ system, with the restriction that $m(\pi^+\pi^-) < 1.0\,\mathrm{GeV}/c^2$. In the shaded histogram the mass of the $\pi^+\pi^-$ system is further restricted to the ρ^0 band, $0.60 < m(\pi^+\pi^-) < 0.85\,\mathrm{GeV}/c^2$.

is used by both the PLUTO Collaboration [6.19] and the TASSO Collaboration [6.20].

The important point is that, with this decay mode, every particle in the final state is charged. Therefore the process

$$e^+e^- \to e^+e^-f^0$$

has been studied under both the no-tag and the single-tag conditions. Because of statistics, the no-tag condition gives by far the more useful data.

Under the no-tag condition, candidates for $e^+e^- \to e^+e^-\pi^+\pi^-$ are selected by requiring two oppositely charged tracks that are non-colinear but coplanar with the beam direction. Furthermore, since the transverse momenta of the outgoing e^+ and e^- are small as discussed in section 6.2, those for the oppositely charged tracks must cancel. Thus, for example, the TASSO Collaboration uses a cut

$$|\boldsymbol{p}_{T1} + \boldsymbol{p}_{T2}| < 0.3\,\mathrm{GeV}/c\,.$$

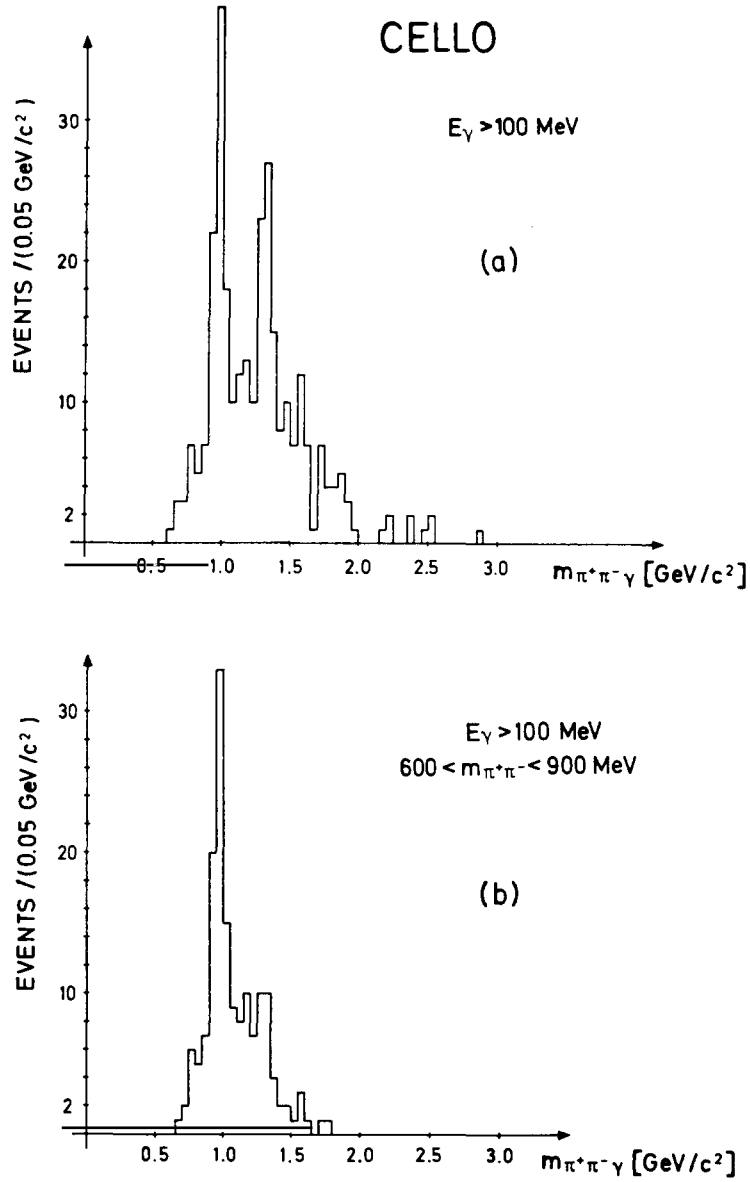

Fig. 6.12. (a) The CELLO [6.16] distribution of $\pi^+\pi^-\gamma$ effective mass. (b) Distribution of $\pi^+\pi^-\gamma$ effective mass with the additional cut $600 < m_{\pi^+\pi^-} < 900\,\mathrm{MeV}/c^2$.

Table 6.2
Experimental results on the radiative width of η'

Collaboration	Decay channel	$\Gamma_{\gamma\gamma}(\eta') \pm$ stat. $\pm$ syst. errors	Ref.
JADE	$\rho^0\gamma$	$5.0 \pm 0.5 \pm 0.9$ keV	[6.15]
CELLO	$\rho^0\gamma$	$6.2 \pm 1.1 \pm 0.8$ keV	[6.16]
MARK II	$\rho^0\gamma$	$5.8 \pm 1.1 \pm 1.2$ keV	[6.17]

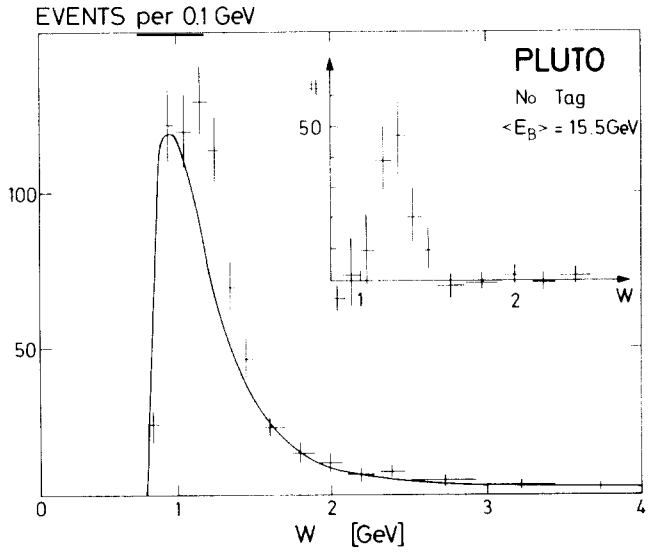

Fig. 6.13. Invariant mass distribution of the two-prong events from PLUTO [6.19]. The solid curve is an absolute QED prediction. The insert shows the difference between data and QED background.

The no-tag data from PLUTO [6.19] and TASSO [6.20] are shown respectively in fig. 6.13 and figs. 6.14–6.15, where the number of events are given as functions of the invariant mass W of the two observed charged tracks, both assumed to be pions. The data are to be compared with the absolute QED predictions for the processes

$$e^+e^- \to e^+e^-e^+e^-$$

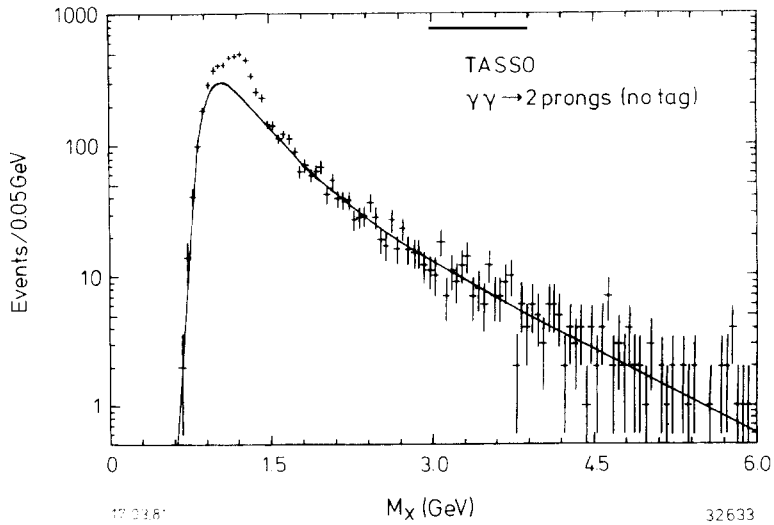

Fig. 6.14. $e^+e^- \to e^+e^-$ + two charged particles (no tag): TASSO [6.20] invariant mass distribution of the two charged particles assuming pion masses; the curve is the prediction for QED lepton-pair production. Note the logarithmic scale for the number of events.

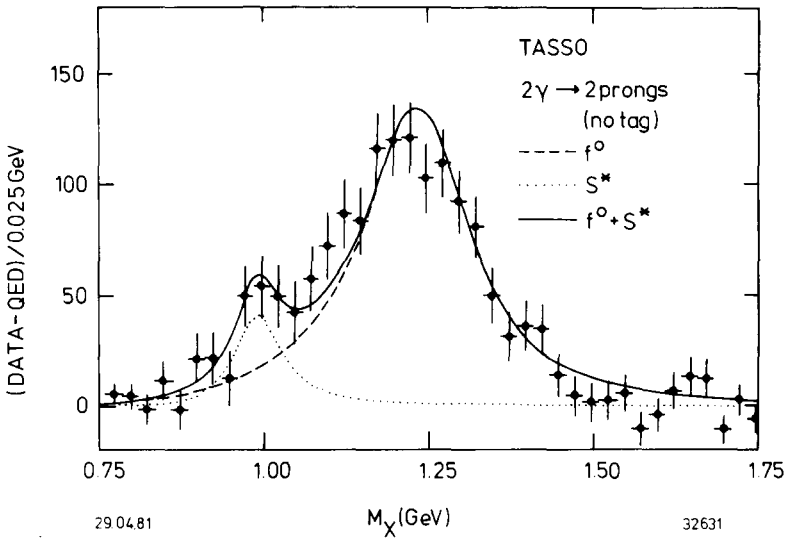

Fig. 6.15. Same as in fig. 6.14 but with the QED contribution subtracted. The curves show fits for f^0 and S* production with the f^0, S* parameters taken from the 1980 Review of Particle Properties.

and

$$e^+e^- \to e^+e^-\mu^+\mu^- .$$

The diagrams taken into account in this QED calculation are those of fig. 6.5. PLUTO has also included a small (15% of QED) contribution from the non-resonant $e^+e^- \to e^+e^-\pi^+\pi^-$. The theoretical results are shown as the solid curves in fig. 6.13 and fig. 6.14. For $W > 1.5$ GeV the data and the theoretical results are in good agreement. The excess of events below 1.5 GeV is shown in fig. 6.13 (insert) and fig. 6.15 for PLUTO and TASSO respectively. The peaks are interpreted as the f^0.

PLUTO [6.19] and TASSO [6.20] have also obtained data under single-tag conditions, as shown in figs. 6.16 and 6.17 respectively. It is seen that the f^0 peak is much less pronounced. The average $|Q^2|$ of the tagged photons are respectively 0.28 and 0.35 $(\text{GeV}/c)^2$.

On the basis of the no-tag data and using the known branching ratio for $f^0 \to \pi^+\pi^-$, the radiative width $\Gamma_{\gamma\gamma}(f^0)$ can be obtained under the assumption of the dominance of the helicity 2 production. The PETRA data are compared with those from MARK II [6.21] and the Crystal Ball [6.22] at SPEAR in table 6.3. It is seen that all four results agree well within the errors. The average is close to $\Gamma_{\gamma\gamma}(f^0) = 3$ keV.

We now turn to an interesting aspect of the process $e^+e^- \to e^+e^-f^0$. The TASSO Collaboration finds that the f^0 with the standard parameters (6.19) gives a rather poor fit to their data and an excess of events below the f^0 peak [6.20]. Leaving the resonance parameters free to vary leads to the values

$$M(f^0) = (1240 \pm 7)\,\text{MeV}, \qquad \Gamma(f^0) = (245 \pm 21)\,\text{MeV} \tag{6.20}$$

which are inconsistent with the established parameters (6.19). This result of TASSO is later confirmed

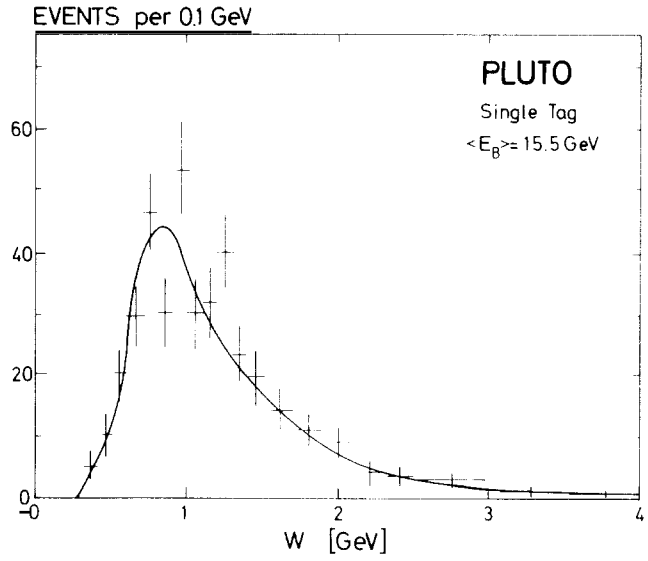

Fig. 6.16. The PLUTO [6.19] invariant mass distribution of the two-prong events with a single tag in the small-angle tagger.

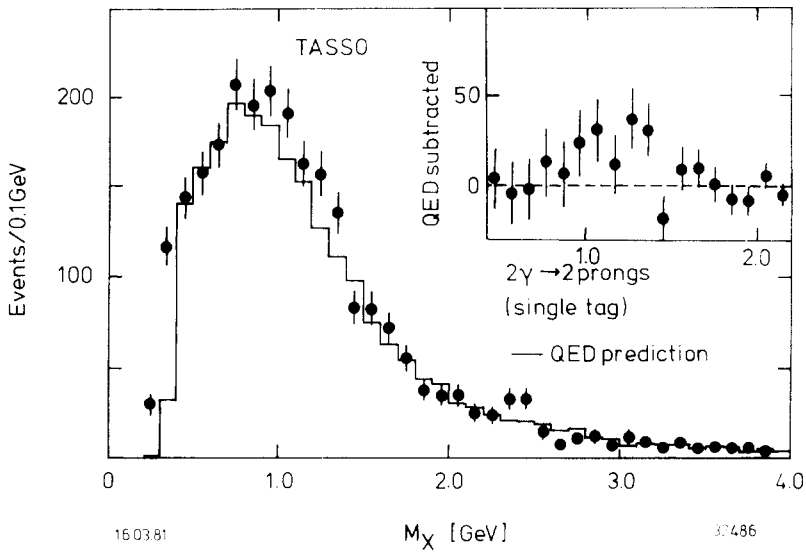

Fig. 6.17. $e^+e^- \to e^+e^-$ + two charged particles (single tag): Invariant mass distribution of TASSO [6.20] of the two-prongs assuming pion masses. The histogram shows the QED prediction for lepton-pair production. The insert shows the mass distribution with the QED contribution subtracted.

Table 6.3
Experimental results on the radiative width of f^0

Collaboration	Decay channel	$\Gamma_{\gamma\gamma}(f^0) \pm$ stat. $\pm$ syst. error	Ref.
PLUTO	$\pi^+\pi^-$	$2.3 \pm 0.5 \pm 0.35$ keV	[6.19]
TASSO	$\pi^+\pi^-$	$3.2 \pm 0.2 \pm 0.6$ keV	[6.20]
MARK II	$\pi^+\pi^-$	$3.6 \pm 0.3 \pm 0.5$ keV	[6.21]
Crystal Ball	$\pi^0\pi^0$	$2.7 \pm 0.2 \pm 0.6$ keV	[6.22]

by the Crystal Ball Collaboration using the neutral decay mode $f^0 \to \pi^0\pi^0$. Their values are [6.22]

$$M(f^0) = (1238 \pm 14)\,\text{MeV}, \qquad \Gamma(f^0) = (248 \pm 38)\,\text{MeV},$$

in agreement with (6.20). Therefore, additional contributions are necessary to explain the data. Several possibilities have been suggested in the literature [6.20 to 6.22].

6.7. $e^+e^- \to e^+e^- A_2$

In order of increasing mass, the next meson that has been reported at PETRA via the two-photon process is A_2. As seen from table 6.1, the most prominent decay mode of the neutral A_2^0 is

$$A_2^0(1320) \to \pi^{\mp}\rho^{\pm} \hookrightarrow \pi^{\pm}\pi^0 \tag{6.21}$$

leading to the final state $\pi^+\pi^-\pi^0$. A less prominent mode is

$$A_2^0(1320) \to \pi^0\eta \hookrightarrow \gamma\gamma \tag{6.22}$$

with a branching ratio of approximately $14.5\% \cdot 39.1\% = 5.7\%$.

The CELLO data, already given in fig. 6.12, shows in addition to the η' signal a peak at $m(\pi^+\pi^-\gamma) = 1.3$ GeV. This peak is interpreted as evidence for the two-photon production of A_2^0, where A_2^0 decays in the mode (6.21) with one low-energy photon from the π^0 not detected. Assuming a pure helicity 2 state, CELLO obtains the radiative width of A_2^0 as given in table 6.4. Also shown in table 6.4 is the earlier result from the Crystal Ball Collaboration [6.22] using the decay mode (6.22) leading to a 4γ final state. The results are in agreement with each other. The ratio $\Gamma_{\gamma\gamma}(A_2^0):\Gamma_{\gamma\gamma}(f^0)$ from tables 6.3 and 6.4 is in rough agreement with the theoretical expectation of 0.36 under the assumption of ideal mixing in the 2^{++} nonet [6.23].

6.8. $e^+e^- \to e^+e^- f'$

In the three preceding sections on the two-photon production of η', f^0 and A_2^0, charged tracks are always assumed to be pions. With the ability to identify particles, the TASSO Collaboration has measured the two-photon production of f′ [6.24]. As seen from table 6.1, this f′(1515) decays

Table 6.4
Experimental results on the radiative width of A_2^0

Collaboration	Decay channel	$\Gamma_{\gamma\gamma}(A_2^0) \pm$ stat. $\pm$ syst. errors	Ref.
CELLO	$\pi^+\pi^-\pi^0$	$0.81 \pm 0.19^{+0.42}_{-0.11}$ keV	[6.16]
Crystal Ball	4γ	$0.77 \pm 0.18 \pm 0.27$ keV	[6.22]

predominantly into $K\bar{K}$. The two decay modes

$$f' \to K^+K^- \tag{6.23}$$

and

$$f' \to K_s^0 K_s^0 \to \pi^+\pi^-\pi^+\pi^- \tag{6.24}$$

are used, both under no-tag condition.

For the decay mode (6.23), events with two tracks of opposite signs coplanar with the beam axis are selected provided that the cut

$$|\boldsymbol{p}_{T1} + \boldsymbol{p}_{T2}| < 0.1 \text{ GeV}/c$$

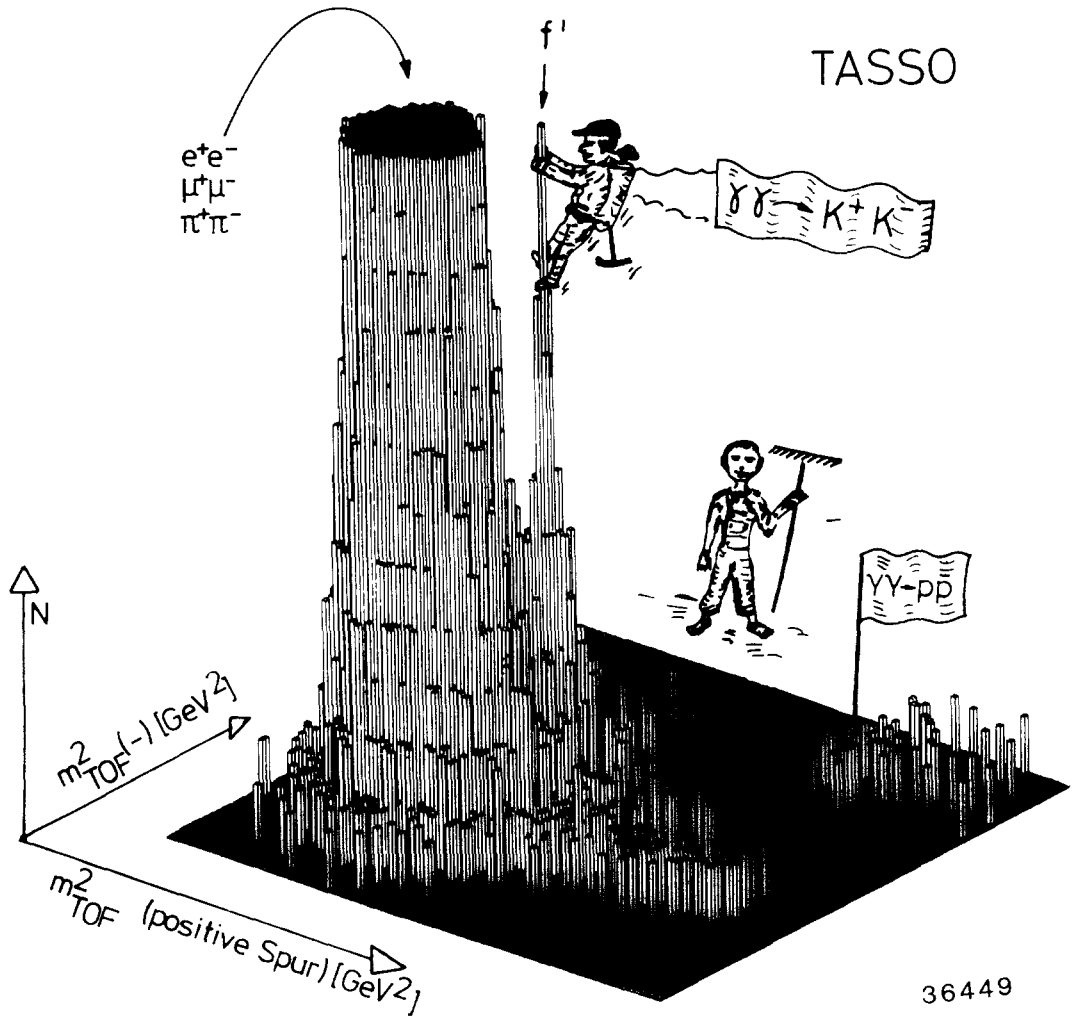

Fig. 6.18. TASSO [6.24] histogram of m^2_{TOF} of the negative particle and m^2_{TOF} of the positive one for two-photon events with two charged particles after a cut of $|\Sigma \boldsymbol{p}_T| < 0.1$ GeV/c has been applied.

is satisfied. Since the TOF separation of kaons from the lighter particles (see section 4.7 and table 4.6) deteriorates with increasing particle momentum, only events with both tracks having momenta lower than 0.9 GeV/c are taken for the analysis. The square of the mass, called m^2_{TOF}, is then calculated from the measured track length, the momentum, and the time of flight. The resulting two-dimensional histogram is shown in fig. 6.18. While most of the events – electron, muon, and pion pairs – cluster around zero, about 0.8% of the entries are K^+K^- pairs. On the right-hand side of fig. 6.18, there is also a well-separated cluster of $p\bar{p}$ events; they are to be discussed in section 6.10. The TASSO invariant mass distribution of the 419 K^+K^- events is shown in fig. 6.19. A clear enhancement in the region of f′ is seen.

For the decay mode (6.24), events with two positive and two negative tracks are selected. Most of these events are due to $\rho^0\rho^0$ production, to be described in the next section. Assuming all the tracks are due to pions, there is a clear indication of K^0_s production. The events are fitted to the $K^0_sK^0_s$ hypothesis (2 constraint fit), and 156 events with a fitted $|\Sigma \boldsymbol{p}_T| < 0.15$ GeV/c yield an acceptable chi-square probability. The $M(K^0_sK^0_s)$ distribution for these events is shown in fig. 6.20, where a clear signal at the f′(1515) is again seen.

The contribution of the 2^{++} nonet resonances to the $\gamma\gamma \to K\bar{K}$ cross section can be expressed as a coherent sum of the f^0, A_2 and f′ amplitudes [6.24, 6.25]

$$\sigma_{\gamma\gamma\to K\bar{K}}(W) = 40\pi W^{-2}|[\Gamma_{\gamma\gamma}(f^0)\,B(f^0\to K\bar{K})]^{1/2}\,\mathrm{BW}(f^0) \pm [\Gamma_{\gamma\gamma}(A_2)\,B(A_2\to K\bar{K})]^{1/2}\,\mathrm{BW}(A_2) + [\Gamma_{\gamma\gamma}(f')\,B(f'\to K\bar{K})]^{1/2}\,\mathrm{BW}(f')|^2 . \quad (6.25)$$

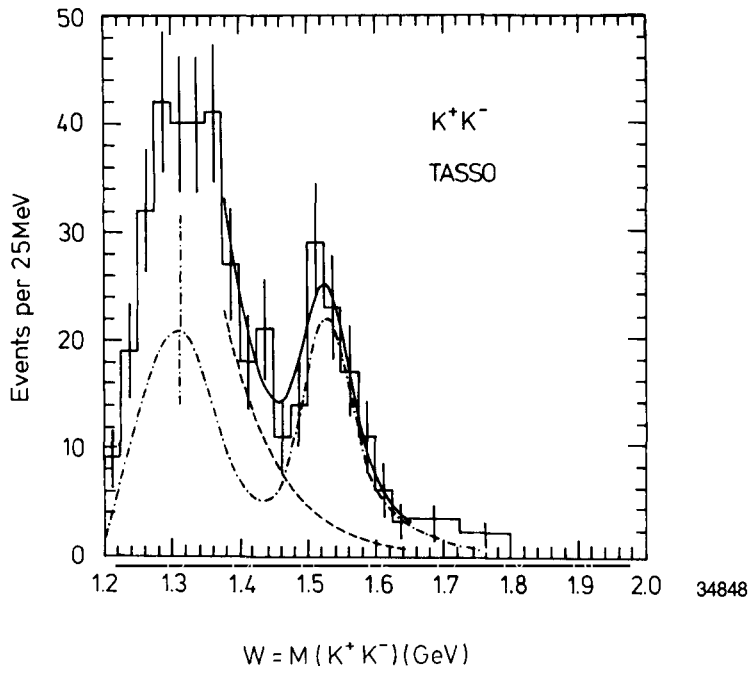

Fig. 6.19. TASSO [6.24] event distribution in the invariant mass $M(K^+K^-)$ of the observed K^+ and K^-. The full curve is the result of a fit as described in the text. The dash-dotted curve is the contribution from the interfering f^0, A_2 and f′ resonances. The background contribution is given by the dashed line. The error on the dash-dotted curve reflects the uncertainty in the $\gamma\gamma$ partial widths and $K\bar{K}$ branching ratios of f^0 and A_2.

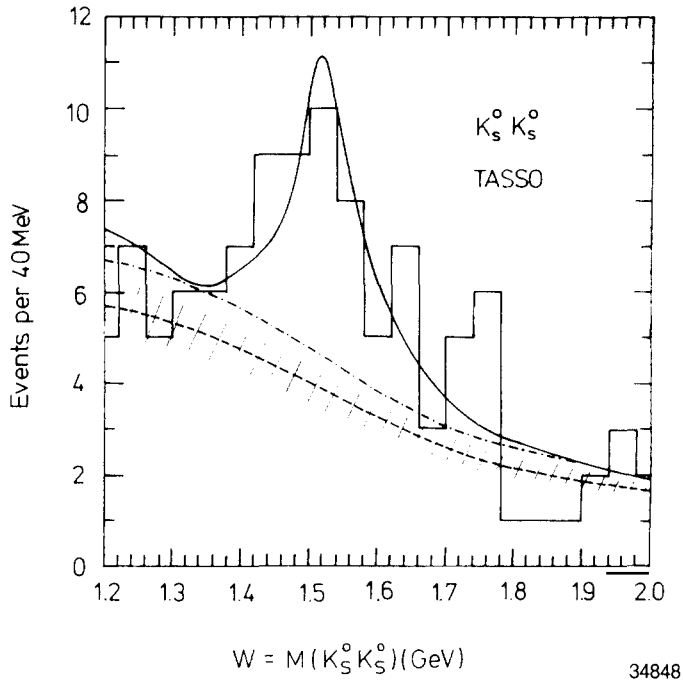

Fig. 6.20. TASSO [6.24] $M(K_S^0K_S^0)$ distribution for events with fitted $|\Sigma \boldsymbol{p}_T| < 0.15\,\mathrm{GeV}/c$. The full curve is the result of a fit to a sum of the interfering f^0, A_2 and f′ resonances and a background (dash-dotted line). The dashed curve is the estimate of the absolute background not due to $K_S^0K_S^0$ production, with an uncertainty given by the shaded area.

$\mathrm{BW}(R) = M\sqrt{\Gamma}/(M^2 - W^2 - \mathrm{i}M\Gamma)$ is a relativistic Breit–Wigner amplitude, where M is the mass and Γ is the energy dependent width of the resonance R. According to SU(3) predictions [6.25] the '+' sign of the second term applies to the K^+K^- final state; the '−' sign applies to $K^0\bar{K}^0$.

In analyzing the data of fig. 6.19, non-resonant K^+K^- production has to be taken into account in addition to the resonances as described by (6.25). The result of the fit is shown as the full curve in fig. 6.19. In this fit, the parameter

$$\tilde{\Gamma}_{\gamma\gamma}(\mathrm{f}') = \Gamma_{\gamma\gamma}(\mathrm{f}')\, B(\mathrm{f}' \to \mathrm{K}\bar{\mathrm{K}}),$$

which appears in (6.25) is treated as free. This leads to the value of $\tilde{\Gamma}_{\gamma\gamma}(\mathrm{f}')$ given in the upper line of table 6.5.

Similar analysis is applied to the decay mode (6.24), where the dominant background is due to $\rho^0\rho^0$ production. The result of the radiative width of f′ is shown in the lower line of table 6.5. The two results are in good agreement with each other. In both analyses, acceptance effects are included assuming a helicity $\lambda = 2$ angular distribution.

Since the branching ratio $B(\mathrm{f}' \to \mathrm{K}\bar{\mathrm{K}})$ is not known (see table 6.1), it is not possible to get the radiative width of f′ from the result listed in table 6.5. Assuming that this branching ratio is at least 0.5 [6.26], then the TASSO result yields the following limits on the SU(3) mixing angle

$$25.4° < \theta_{\mathrm{M}} < 34.7° \qquad (95\%\ \mathrm{CL}),$$

Table 6.5
Experimental results on the radiative width of f'(1515)

Collaboration	Decay channel	$\tilde{\Gamma}_{\gamma\gamma}(f') \pm$ stat. $\pm$ syst. errors*	Ref.
TASSO	K^+K^-	$0.11 \pm 0.02 \pm 0.04$ keV	[6.24]
TASSO	$K_s^0K_s^0$	$0.11 \pm 0.03 \pm 0.04$ keV	[6.24]

*This is the radiative width $\Gamma_{\gamma\gamma}(f')$ multiplied by the branching ratio $B(f' \to K\bar{K})$.

which is close to the ideal mixing value of 35.3°, and which includes the mixing angle of $28° \pm 3°$ given by the Gell-Mann–Okubo (GMO) quadratic mass formula.

Finally, the TASSO data also give an upper limit on the radiative width of $\theta(1640)$, which has been studied at SPEAR [6.27]. Assuming $J^{PC} = 2^{++}$ for this $\theta(1640)$, $\lambda = 2$, and no interference with the other 2^{++} states, the upper limit is

$$\Gamma_{\gamma\gamma}(\theta)\, B(\theta \to K\bar{K}) < 0.3\,\text{keV} \qquad (95\%\ \text{CL}). \tag{6.26}$$

6.9. $e^+e^- \to e^+e^-\rho^0\rho^0$

The two-photon production of η', f^0, A_2^0 and f', described in the last four sections, are all theoretically expected, and their rates can all be roughly estimated. There is no surprise.

The TASSO Collaboration is the first to study the two-photon production of the exclusive 4π state

$$e^+e^- \to e^+e^-\pi^+\pi^-\pi^+\pi^-,$$

as already mentioned in the preceding section. This reaction proceeds predominantly through the two-photon production of a pair of ρ^0 [6.28]. More recently, the TASSO Collaboration has given a detailed analysis of the angular correlation on the basis of a larger data sample [6.29]. The results have also been confirmed by the MARK II Collaboration [6.30]. The cross section for this process [6.28], shown in fig. 6.21, is much larger than the estimate from the vector-meson dominance model. It is theoretically unexpected and has lead to various theoretical speculations [6.31, 6.32], which in most cases explain the enhancement by the formation of a resonance decaying into $\rho^0\rho^0$.

The events are selected with the cut $|\Sigma\, \boldsymbol{p}_T| < 0.15$ GeV/c. Fig. 6.22 contains in the left column the scatter plots of the one $\pi^+\pi^-$ mass versus the other (two entries per event) for different W intervals. For W larger than the $\rho^0\rho^0$ threshold [fig. 6.22(g and i)], one observes a strong enhancement in the $\rho^0\rho^0$ mass region. This is not seen in the corresponding scatter plots, in the right column, of the like-sign combinations (one entry per event) shown in fig. 6.22(h and j). Below the $\rho^0\rho^0$ threshold the enhancement in the opposite-sign mass combinations [fig. 6.22(a, c and e)] is shifted towards smaller masses because of phase-space limitations. By comparison, these scatter plots do not show clearly the $K_s^0K_s^0$ final state discussed in the preceding section.

The result on the study of the angular correlation [6.29] is shown in fig. 6.23 for the mass range $1.4 < M_{4\pi} < 1.6$ GeV. In this figure, those events are considered which have both $\pi^+\pi^-$ masses in the ρ^0 band for at least one $\pi^+\pi^-$–$\pi^+\pi^-$ combination. If both $\pi^+\pi^-$–$\pi^+\pi^-$ combinations are within this cut, they both appear in the plots. The polar angle θ_ρ of the ρ^0 production axis [fig. 6.23a] is defined in the $\gamma\gamma$ c.m. system with the z axis along the $\gamma\gamma$ axis. For the fig. 6.23(b and c), the angles θ_π and ϕ_π

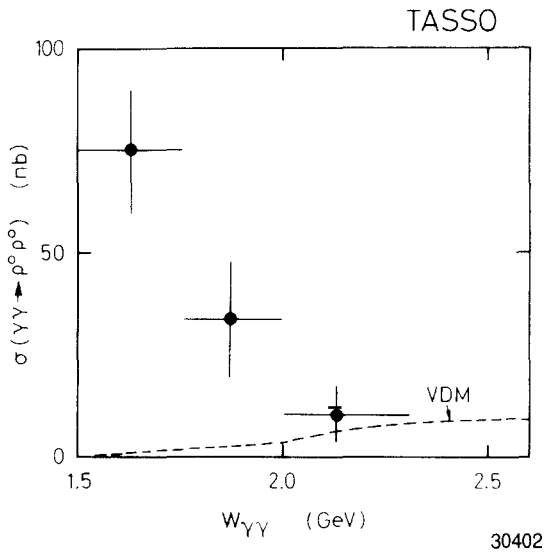

Fig. 6.21. First measurement of the cross section for the reaction $\gamma\gamma \to \rho^0\rho^0$ by the TASSO Collaboration [6.28]. The curve is the prediction of the vector-meson dominance model.

describing the ρ^0 decay are taken in the ρ^0 helicity frames, which are the ρ^0 rest systems with the positive z axis in the direction of flight of one of the ρ^0's. θ_π is the polar angle of the π^+ from a ρ^0 [fig. 6.23b], $\Delta\phi = \phi_{\pi a} - \phi_{\pi b}$ is the angle between the decay planes of the 2 ρ^0's (denoted as a and b). θ_{ab} is the opening angle between the two π^+ directions, each defined in its respective ρ^0 c.m. frame [fig. 6.23d].

It is seen from fig. 6.23 that the $J^P = 0^-$ and 2^- states are predicted to show distinct features which are not observed in the data. Thus the dominance of negative parity states suggested by several authors [6.31] to explain the large $\rho^0\rho^0$ cross section at low W is excluded. The results on the positive parity states can be summarized as follows. For $W = M_{4\pi} < 1.7$ GeV, the fitted $\rho^0\rho^0$ contribution has dominantly $J^P = 0^+$ while the 2^+ fraction is small. At higher W, the 2^+ contribution appears to become dominant.

Similar to (6.26), TASSO gives the upper limit for $\theta(1640)$ [6.27]

$$\Gamma_{\gamma\gamma}(\theta)\, B(\theta \to \rho^0\rho^0) < 1.2\,\text{keV} \qquad (95\%\ \text{CL}). \tag{6.27}$$

For the glueball candidate $\iota(1440)$ [6.33], the corresponding limit is

$$\Gamma_{\gamma\gamma}(\iota)\, B(\iota \to \rho^0\rho^0) < 1.0\,\text{keV} \qquad (95\%\ \text{CL}). \tag{6.28}$$

6.10. $e^+e^- \to e^+e^-p\bar{p}$

The TASSO Collaboration is also the first one at PETRA to observe the two-photon production of proton–antiproton pairs [6.34]. Recently, they have reported their result with an increase in statistics by a factor of 10 [6.35]. Some of these events have already been shown in fig. 6.18. The cuts used are the same as those of section 6.8 for K^+K^- pairs, except the momentum of each track is now required to be

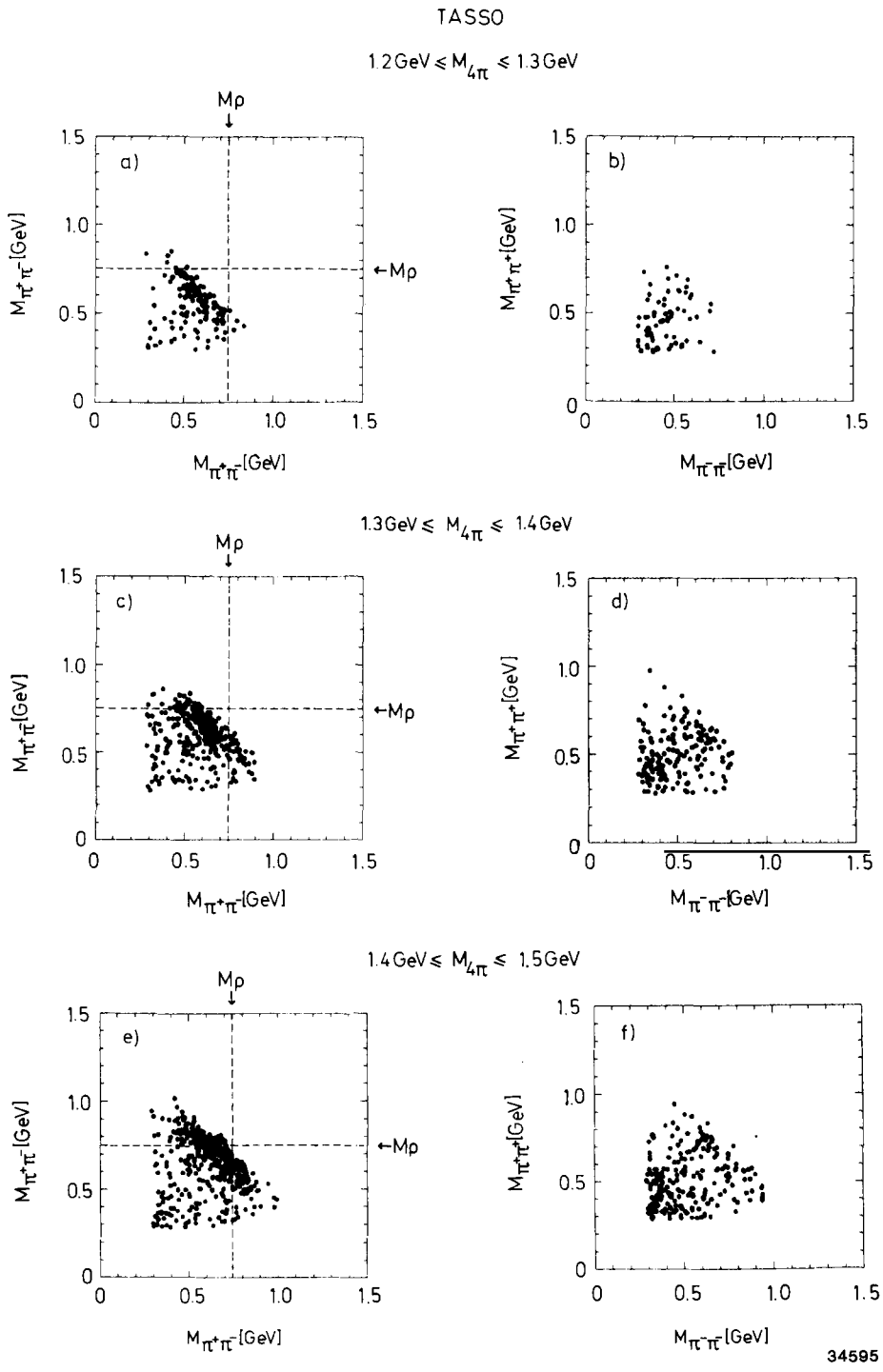

Fig. 6.22. Continued on next page.

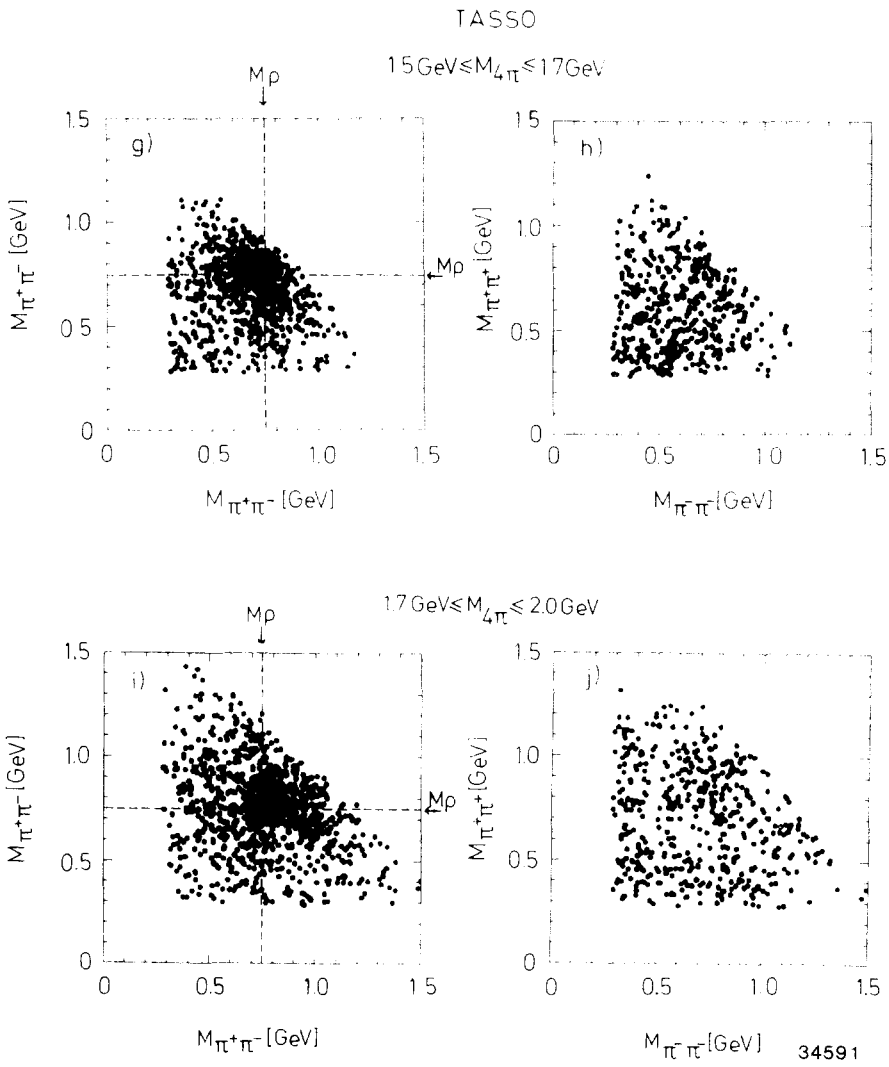

Fig. 6.22. Left column (a, c, e, g, i): $\pi^+\pi^-$ mass versus $\pi^-\pi^-$ mass from TASSO [6.29] for five different $W = M_{4\pi}$ intervals. Right column (b, d, f, h, j): $\pi^+\pi^+$ mass versus $\pi^-\pi^-$ for the same intervals.

lower than 1.6 GeV/c corresponding roughly to a 2σ (3σ) TOF separation of kaons (pions) from protons. With this more relaxed cut, the total number of $e^+e^- \to e^+e^-p\bar{p}$ events from TASSO is 72, with an estimated background of 5.

The uncorrected invariant mass distribution of these 72 events is given in fig. 6.24a, and the cross section integrated over the angular range $|\cos\theta^*| \leqq 0.6$ in fig. 6.24b. The integrated cross section is comparatively large above threshold and decreases rapidly with increasing W; it is about 4 nb at 2 GeV and smaller than 0.5 nb above 3 GeV. The uncorrected $\cos\theta^*$-distributions of the events for the two mass bins ($2.0\,\text{GeV} \leqq W \leqq 2.4\,\text{GeV}$ and $2.4\,\text{GeV} < W \leqq 2.8\,\text{GeV}$) are given in fig. 6.25(a and b) together with the detection efficiency. The detection efficiency is largest for $\cos\theta^* = 0$ and decreases smoothly toward forward angles reaching zero at $|\cos\theta^*| \geqq 0.8$ because of the cuts. The differential cross section $d\sigma/d\cos\theta^*$ is shown in fig. 6.25(c and d) for both mass regions. These differential cross sections

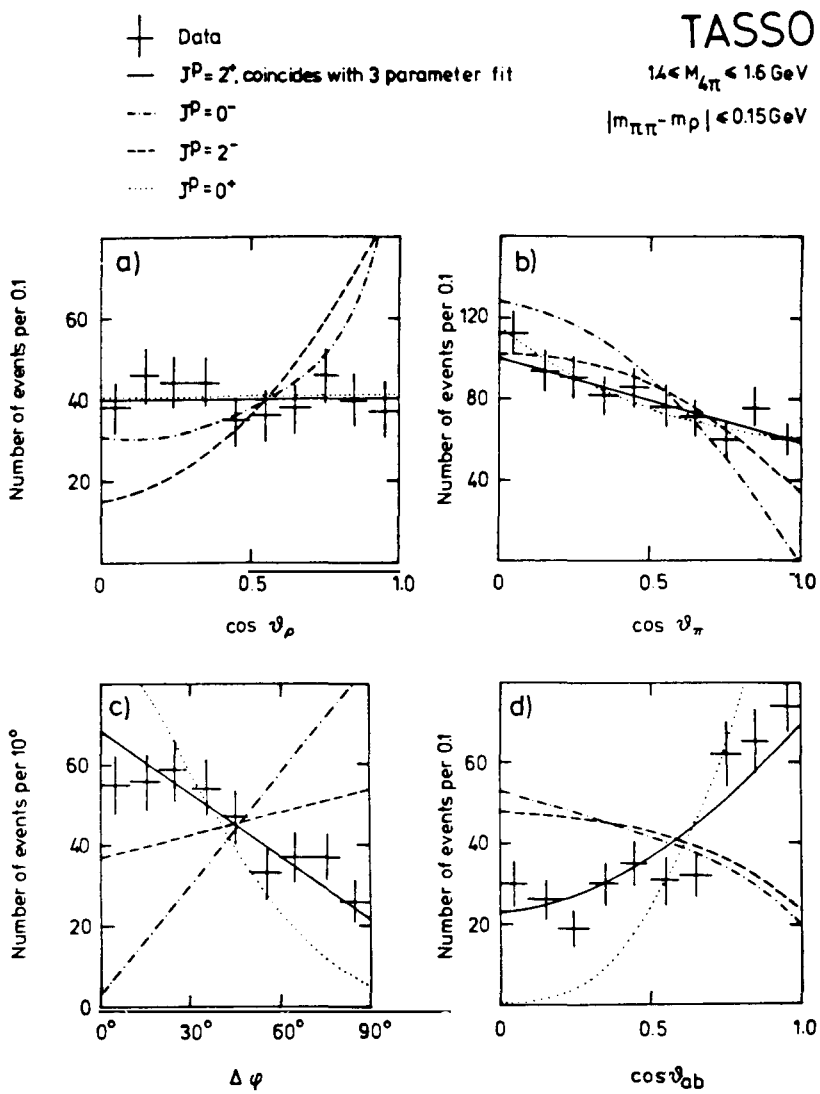

Fig. 6.23. TASSO [6.29] angular distributions for $1.4 < M_{4\pi} < 1.6$ GeV. The angles are explained in the text. The solid curve is the result of the 3-parameter fit, the other curves are Monte Carlo predictions for $\rho^0\rho^0$ production with $J^P = 2^-$ (dashed line), $J^P = 0^-$ (dash-dotted line) or $J^P = 0^+$ (dotted). The distribution for $J^P = 2^+$ coincides with the curve for the isotropic case (result of the 3-parameter fit).

are roughly one order of magnitude less than the Born approximation assuming the protons to be point-like Dirac particles with a pure QED coupling to the photons. Recently the differential cross section of $\gamma\gamma \to p\bar{p}$ has been calculated within the framework of QCD [6.36]. When this theoretical result is extrapolated from the J/ψ mass region into the W range of the experimental data, the result is given as the shaded areas in fig. 6.25(c and d) corresponding to different choices of the distribution function. The theoretical cross section is of the same order of magnitude as the data.

Since the only established particle with even C-parity in the mass range covered by this TASSO experiment is the η_c at 2.984 ± 0.004 GeV [6.37], and no event is observed there with the detector

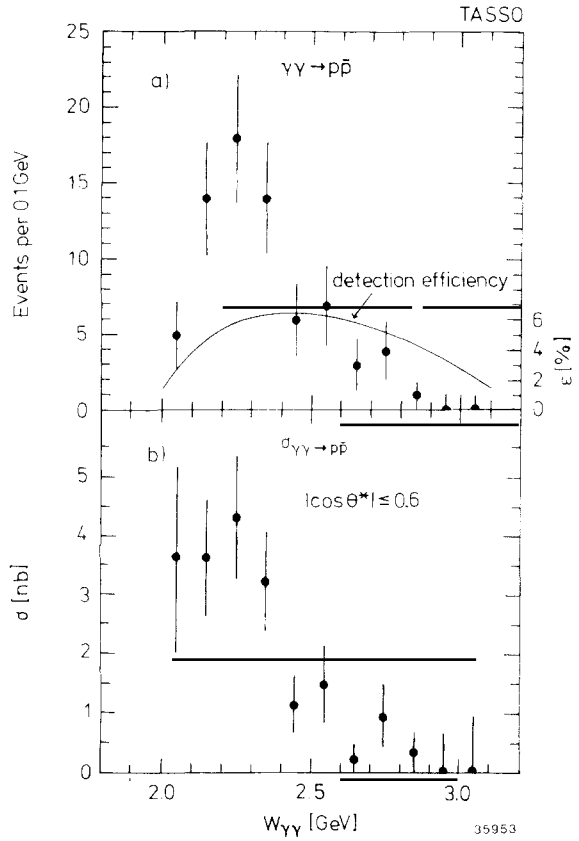

Fig. 6.24. TASSO [6.35] data on the two-photon process $e^+e^- \to e^+e^-p\bar{p}$ under no-tag condition: (a) Uncorrected invariant mass distribution of $p\bar{p}$ events and energy dependence of the detection efficiency (full line). (b) Cross section for $\gamma\gamma \to p\bar{p}$ integrated over the angular range $|\cos\theta^*| \leqq 0.6$, where θ^* is the scattering angle in the two-photon center-of-mass system.

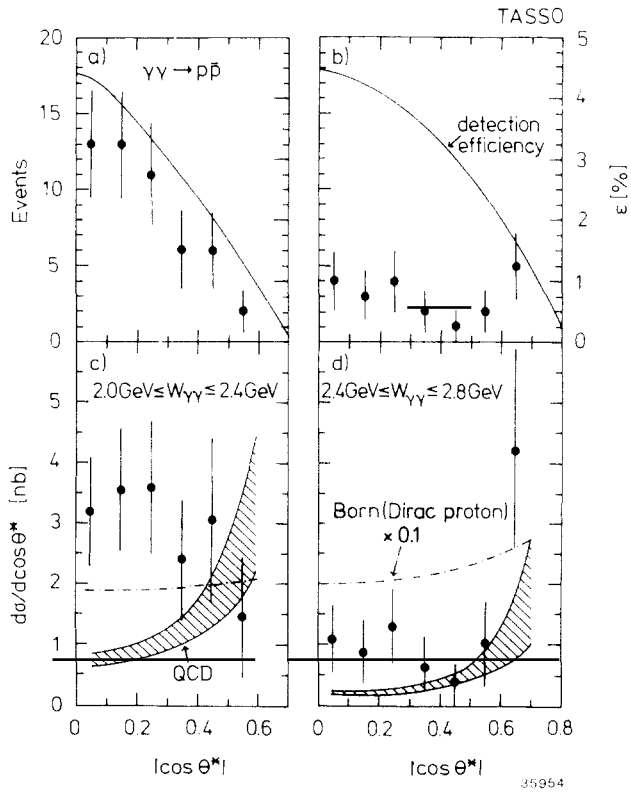

Fig. 6.25. TASSO [6.35] data on the two-photon process $e^+e^- \to e^+e^-p\bar{p}$ under no-tag condition. For angular distribution the data has been divided into two bins as shown. (a) & (b) Uncorrected distribution of the proton scattering angle in the $\gamma\gamma$ c.m. system and the angular dependence of the detection efficiency (full line). (c) & (d) Differential cross section $d\sigma/d\cos\theta^*$ of $\gamma\gamma \to p\bar{p}$ for 2.0 GeV $\leqq W \leqq$ 2.4 GeV and 2.4 GeV $< W \leqq$ 2.8 GeV. The data are compared to theoretical calculations as explained in the text.

resolution taken in account, the upper limit

$$\Gamma_{\gamma\gamma}(\eta_c)\, B(\eta_c \to p\bar{p}) < 0.32\ \text{keV} \qquad (95\%\ \text{CL})$$

is obtained.

6.11. *High p_T jets*

As discussed in section 6.1 (Cii), the two-photon process can proceed via two distinct mechanisms: soft process where the virtual photons behave like hadrons [as for example shown in fig. 6.4] and hard process where the virtual photons couple in a point-like way to quarks [as shown in figs. 6.2b and 6.3]. Experimental evidence for this hard process has been obtained by the JADE and TASSO Collaborations [6.38, 6.39].

Since, as we have learned in detail in chapter 2, quarks and antiquarks hadronize into jets, the events selected for the present purpose are

$$e^+e^- \to e^+e^- + \text{two jets}\,. \tag{6.29}$$

Such an event with a single tag from TASSO is shown in fig. 6.26. As a general characteristic of two-photon events, the jets are not colinear but are coplanar with the beam direction.

The hard scattering diagram of fig. 6.2b has the following two main characteristics:

(A) The first characteristic is the ratio [6.18, 6.40] (Q_i = quark charge)

$$\frac{\sigma(\gamma\gamma \to q\bar{q})}{\sigma(\gamma\gamma \to \mu^+\mu^-)} = 3 \sum_{u,d,s,c} Q_i^4 = \frac{34}{27} \tag{6.30}$$

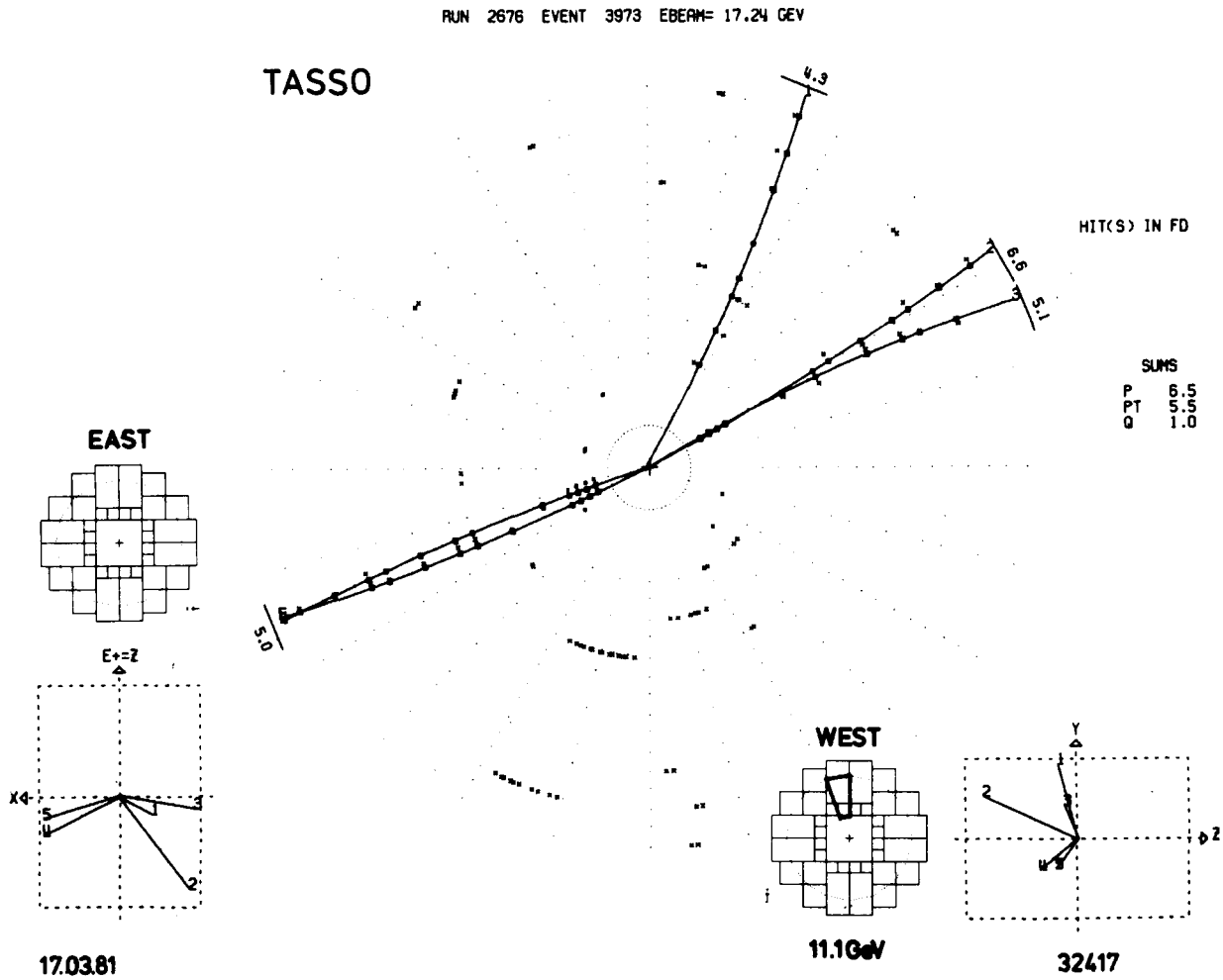

Fig. 6.26. $\gamma\gamma \to$ 2-jet events of TASSO at $E_{\text{c.m.}} = 34.5$ GeV. The energy of the single-tagged e^- is 11 GeV.

if the first four quark flavors are included. Note that u and c are responsible for 94% of this ratio. An experimental determination of this ratio is a test of the quark charges.

(B) Secondly, similar to $\gamma\gamma \to \mu^+\mu^-$, the differential cross section $d\sigma/dp_T^2$ falls roughly as p_T^{-4}, where p_T is the transverse momentum of each hadronic jet with respect to the beam direction. This is a much slower decrease than that exhibited by pp and πp cross sections.

One has to be careful, however, in applying this p_T^{-4} behavior to the two-photon process (6.29). The reason is that, given a two-photon invariant mass W, the behavior for $\gamma\gamma \to q\bar{q}$ is p_T^{-4} until near the kinematic limit, then falls faster due to phase space, and is of course zero beyond the kinematic limit. Therefore, the average over the two-photon invariant mass gives a somewhat steeper decrease.

The higher the energy, the clearer the jet structure becomes (see for example fig. 2.8). Thus the most desirable events are those with high W. Experimentally however, unless tagged, these two-photon events look similar to the more numerous 1γ hadronic events of chapter 2. It is for this compelling reason that both JADE and TASSO have used only the single-tagged events to study (6.29).

We discuss in some detail the event selection used by JADE. The cuts are (i) single tagging of at least 4 GeV; (ii) four or more particles (charged or neutral) in the two jets; (iii) a well-defined vertex (of at least two charged tracks) within 8 cm of the interaction point; and (iv) a total visible energy E_{vis} (assuming all particles to be pions and photons) of at least 3 GeV plus the momentum component $P_{vis,z}$ along the beam line. The visible energy spectrum of the events selected in this way is shown in fig. 6.27a, where those above 20 GeV have been deleted. The important point is that even for tagged events

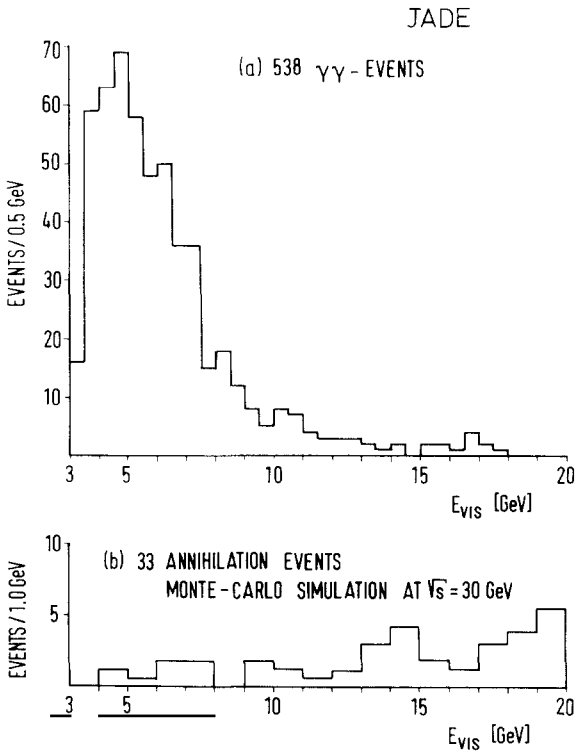

Fig. 6.27. JADE [6.38] histogram versus the visible energy of (a) single-tag multihadron two-photon events and (b) Monte Carlo simulated annihilation events with a radiated photon heading toward one of the tagging counters.

a contamination from 1γ annihilation must be considered. In fig. 6.27b we show the energy spectrum of simulated annihilation events with a radiated photon heading towards one of the tagging counters. Since electrons and photons cannot be distinguished in the tagging counter, all two-photon events above 15 GeV can be associated with annihilation processes. One then obtains for the region from 3 to 10 GeV an upper limit of 2% for the annihilation background and from 10 to 15 GeV an upper limit of 20%.

The result from JADE [6.38] is shown in fig. 6.28 and compared with the prediction from $\gamma\gamma \to q\bar{q}$, and the corresponding result from TASSO [6.39] in fig. 6.29. It is interesting to note from both fig. 6.28 and fig. 6.29 that even at the highest p_T^2 the experimental data tend to be somewhat higher, by a factor of about 1.5 than the expectation evaluation from the diagram of fig. 6.2b. The reason may be the contributions from QCD corrections, from 3- and 4-jet processes, and from higher twist diagrams.

TASSO [6.39] has also given an inclusive p_T distribution for charged hadrons on the basis of their single-tag events. The result of fig. 6.30 shows a steep exponential fall-off at low p_T and a long tail towards high p_T. It has been analyzed by fitting the function

$$d\sigma/dp_T^2 = c_1 \exp(-ap_T) + c_2(p_T)^{-b} \tag{6.31}$$

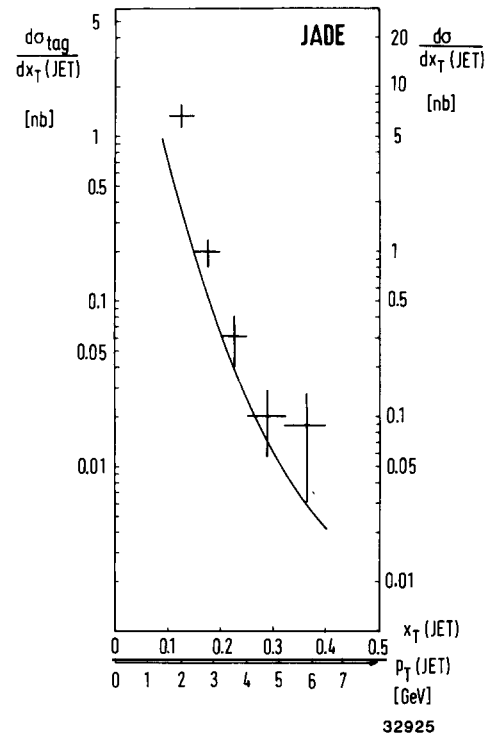

Fig. 6.28. JADE [6.38] transverse momentum distribution of jets for single-tag data compared with absolute predictions for fractional charged quarks (curve). $x_T(\text{jet}) = p_T(\text{jet})/E_{\text{beam}}$ is taken with respect to the center-of-mass direction of motion. The cross section is given for the JADE tagging condition on the left-hand scale and integrated over all electron angles and energies on the right-hand scale.

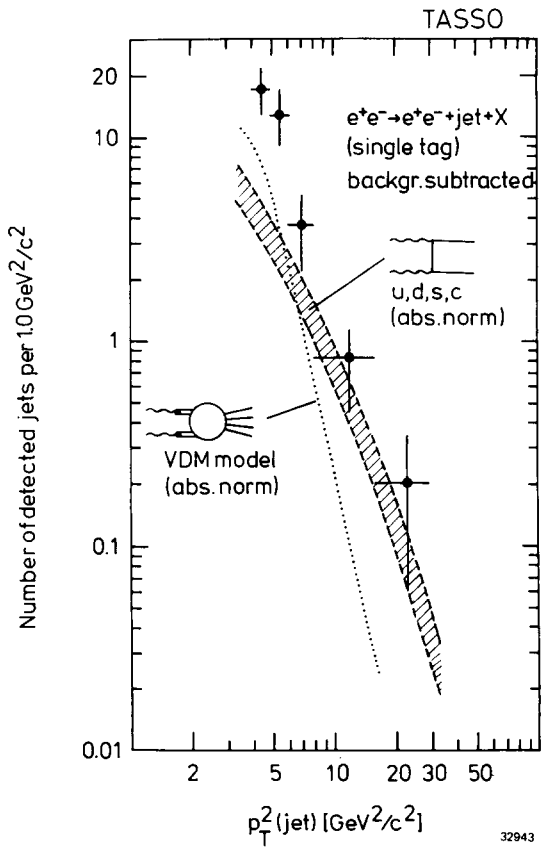

Fig. 6.29. The TASSO [6.39] p_T^2(jet) distribution from single-tagged data for $e^+e^- \to e^+e^-$ + jet + X, compared to a $e^+e^- \to e^+e^-$ + $q\bar{q}$ calculation with four different types of fragmentation models (shaded band) and to VDM (dotted line).

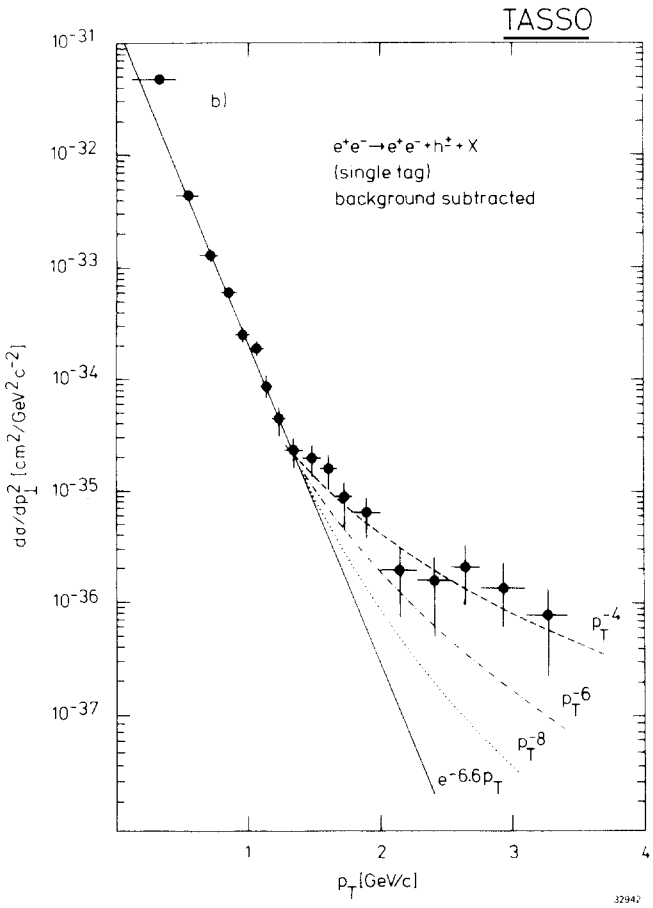

Fig. 6.30. TASSO [6.39] inclusive differential cross section as a function of the single-particle momentum perpendicular to the beam direction.

to the data yielding $b = 3.9 \pm 0.6$ for the exponent, in good agreement with the expectation of p_T^{-4}.

6.12. Deep inelastic eγ *scattering*

The PLUTO Collaboration is the first group to obtain interesting results on the structure function of the photon by studying at PETRA deep inelastic electron–photon scattering [6.41]. More recent results in this connection are due to the JADE Collaboration [6.42] and the CELLO Collaboration [6.43]. In these experiments, one of the outgoing electron or positron is observed. Since the other electron or positron is not tagged, the second photon is nearly on mass shell. Therefore, as already discussed in section 6.1(D), under this configuration the observed $e^+e^- \to e^+e^-$ hadrons is closely related to the deep inelastic eγ scattering as shown in fig. 6.31a, analogous to deep inelastic ep scattering.

There are several contributions to the diagram of fig. 6.31a. Vector-meson dominance model gives the diagram of fig. 6.31b, while the QCD process $\gamma\gamma \to q\bar{q}$ of fig. 6.2b leads to fig. 6.31c, and higher-order QCD corrections give diagrams such as that of fig. 6.31d.

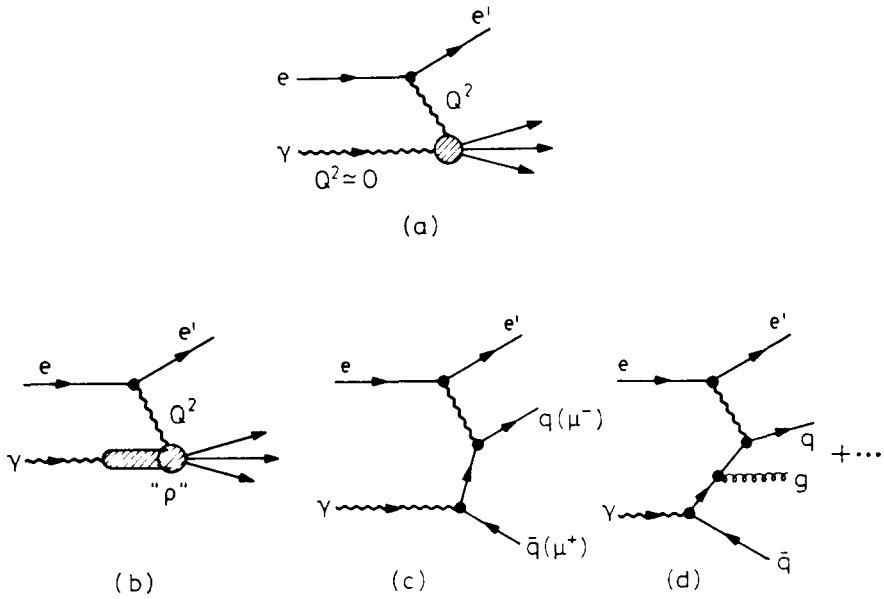

Fig. 6.31. Diagrams contributing to $e\gamma \to e'$ hadrons.

The usual scaling variables x and y are defined as (see fig. 6.1)

$$x = \frac{|Q_1^2|}{|Q_1^2| + W^2} \quad \text{and} \quad y = 1 - \frac{E_1}{E}\cos^2\frac{\theta_1}{2}, \tag{6.32}$$

and the structure functions F_1 and F_2 are related to the cross section by

$$\left.\frac{d\sigma}{dx\,dy}\right|_{e\gamma\to eX} = \frac{16\pi\alpha^2 EE_\gamma}{Q^4}\left[(1-y)F_2(x, Q^2) + xy^2 F_1(x, Q^2)\right], \tag{6.33}$$

where $Q^2 = |Q_1^2|$ and E_γ is the energy of the nearly on shell 'target' photon in the laboratory system. With the experimental acceptances at PETRA, xy^2 is small (except for the post-1981 configuration of PLUTO). Thus the cross section is well approximated by

$$\left.\frac{d\sigma}{dx\,dy}\right|_{e\gamma\to eX} = \frac{16\pi\alpha^2 EE_\gamma}{Q^4}(1-y)F_2(x, Q^2). \tag{6.34}$$

This approximation is used to extract information about the photon structure function $F_2(x, Q^2)$. In the quark parton model x is the relative momentum fraction of the quark and F_2 is a measure of the momentum weighted quark content of the photon target.

The PETRA experimental results are shown in figs. 6.32 and 6.33. We describe first the data points and then the theoretical curves in these two figures. Since the outgoing electron or the outgoing positron is measured, but not both, there is no direct way to determine W, the invariant mass of the two photons. Instead, the quantity measured by each of the three Collaborations is W_{vis}, the invariant mass

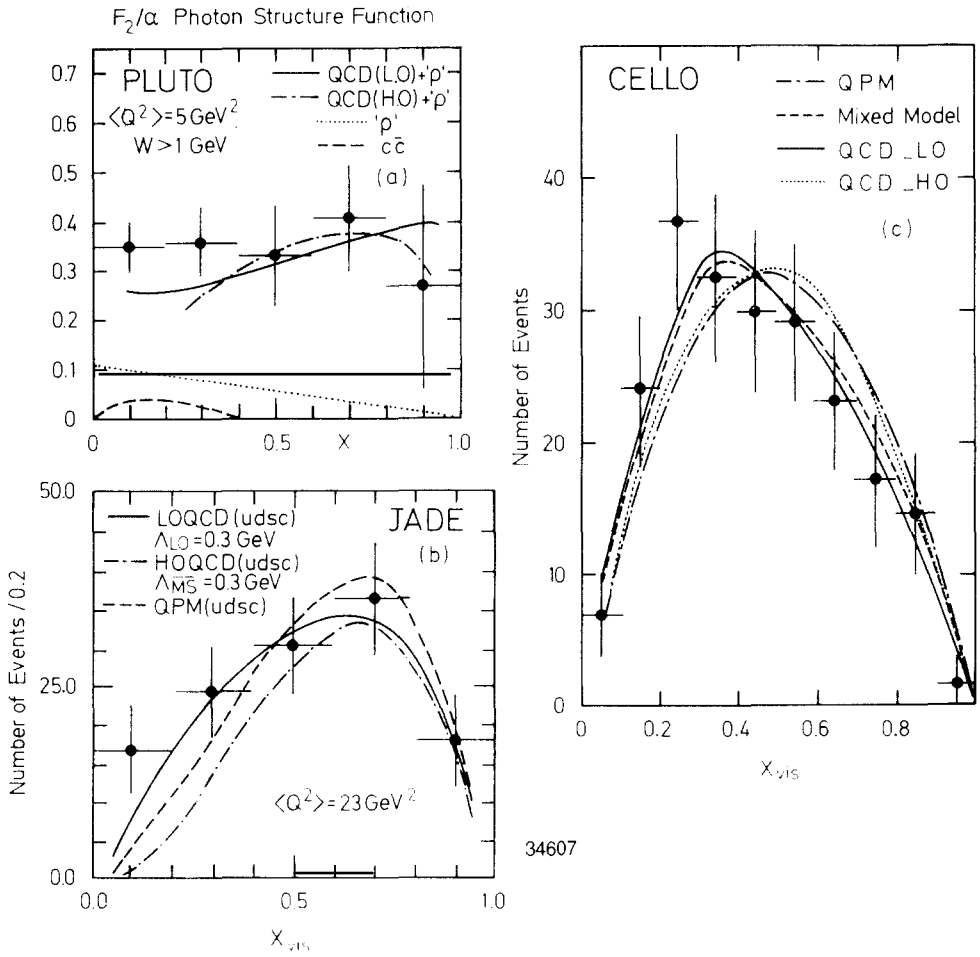

Fig. 6.32. PETRA experimental data on the photon structure function: (a) PLUTO [6.41], (b) JADE [6.42], and (c) CELLO [6.43]. Curves based on various theories are also shown for comparison.

of the visible hadrons and photons. Of course W_{vis} is in general somewhat smaller than W, and furthermore depends on the properties of the detector. From this W_{vis}, the variable x_{vis} is obtained through (6.32) as

$$x_{vis} = \frac{|Q_1^2|}{|Q_1^2| + W_{vis}^2}. \tag{6.35}$$

In principle, the x_{vis} distribution can be converted into an x distribution by proper unfolding. The result of the unfolding has only been reported by PLUTO. Thus fig. 6.32 shows the distributions averaged over Q^2 of PLUTO [6.41] as a function of x, and of JADE [6.42] and CELLO [6.43] as functions of x_{vis}. In fig. 6.33, the photon structure function is averaged over x but shown as a function of Q^2. Actually, it is averaged over x_{vis} since unfolding is unnecessary for this purpose. In this figure, the data points are from the following references: open triangle from PLUTO [6.41]; open circle from JADE [6.42]; closed circle from CELLO [6.43]; and closed square from CELLO [6.44], where 18 events are observed of

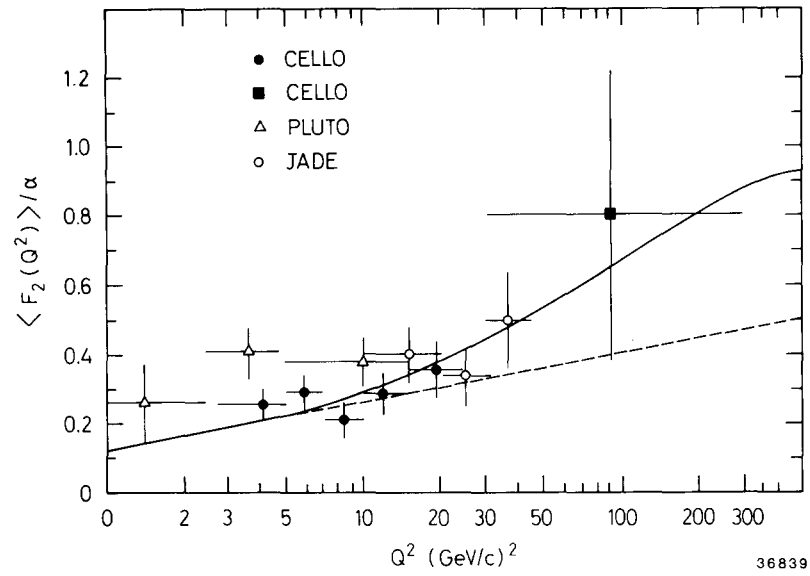

Fig. 6.33. $(1/\alpha)\langle F_2(x)\rangle$ as a function of Q^2. Solid curve: QCD.LO (u, d, s, c) with $\Lambda_{LO} = 0.3$ GeV. Dashed curve: QCD.LO (u, d, s). These data are taken from PLUTO [6.41], JADE [6.42] and CELLO [6.43, 6.44].

topologically isolated energetic electrons (or positrons) at $\sqrt{s} = 34$ GeV, leading to large values of Q^2. Clearly the data available so far are compatible with a logarithmic variation, without demonstrating the existence of such a dependence on Q^2.

In figs. 6.32 and 6.33, a variety of theoretical curves are also shown. Briefly, they are: quark parton model (QPM); leading order QCD (QCD-LO or equivalently LOQCD), which contains one parameter Λ_{LO}; higher order QCD (QCD-HO or equivalently HOQCD), which also contains one parameter $\Lambda_{\overline{MS}}$ where MS stands for minimal subtraction; a version of the vector-meson dominance model ('ρ') [6.45]; and the mixed model where leading order QCD is used for the u, d and s quarks while the quark parton model is applied to the c quark.

While there is no discrepancy between theory and experiment, this subject of the photon structure function cannot be considered to have been completely clarified and is being further pursued at PETRA. The underlying complication is due to the fact that the photon structure function is truly a function of the two variables x and Q^2, and does not satisfy any simple scaling law. In addition, there are difficulties on both the theoretical and the experimental sides. On the experimental side, a major problem is the determination of x, as already mentioned. In the near future, further results are expected from the PLUTO Collaboration, using their new forward spectrometer (see section 1.7.5 and fig. 1.21).

The theoretical investigation of the photon structure function in the QCD framework is pioneered by Witten [6.46], who obtains the asymptotic behavior for large Q^2 in a beautiful form that contains no parameter at all. His investigation is followed by those of many others [6.47]. Briefly, the difficulty is as follows. Since the Q^2 at PETRA is not in the asymptotic region, correction terms to the Witten result have to be found before a meaningful comparison can be made with the experimental data. These correction terms are found to be large, and also not parameter free. Most of the investigations on these correction terms have been carried out on the basis of the Altarelli–Parisi equation [6.47]. Unfortunately, the Altarelli–Parisi equation is an integro-differential equation, and boundary conditions

are needed in the form of one or more functions. Therefore, a great deal of further work is needed on the photon structure function, not only from experimentalists but also from theoreticians.

In summary, we have seen three separate types of evidence that the process $\gamma\gamma \to q\bar{q}$ is important: from the exclusive two-photon processes, the high p_T jets, and the photon structure function. Since two-photon physics at such high energies has been investigated only for a short time, further understanding and clarification can certainly be expected in the near future.

7. Search for new particles

7.1. Introduction

In this chapter we give most of the unsuccessful searches for new particles carried out at PETRA.

All these searches are motivated by theoretical considerations. Some of the considerations are well founded, the best example being the standard model that predicts the existence of the top quark t. Section 7.2 is devoted to the search for this top quark. There are other cases where the theory cannot be considered to be so reliable but, on the basis of such a theory, the properties of the particle, including its mass, can be reasonably well predicted. The case of the charged technipion is such an example, and is discussed in section 7.3. That search turns out to apply not only to charged technipions but also to charged Higgs. Another theory that is very beautiful but has so far no experimental support is the theory of supersymmetry, which predicts a large number of new particles as partners to the known ones. The search for these supersymmetric particles is summarized in section 7.4. The last two sections of this chapter are devoted to the searches for new leptons of various types, free quarks and magnetic monopoles.

The two most common reasons for not being able to observe a particle are:

(a) the mass is too high;

(b) the production cross section is too low.

Thus the experimental result takes the form of an upper limit on the production cross section as a function of the assumed mass of the particle. In many cases, however, a reliable estimate of the production cross section can be obtained. Then the experimental result can be given as a lower limit for the mass. There are other cases where an assumption needs to be made about the properties of the particle being looked for. In such cases care must be taken in giving meaning to the experimental results.

7.2. Search for the top quark

7.2.1. Top quark

Experimentally we know the existence and properties of five quarks (u, d, s, c and b) and six leptons (e, μ, τ and their associated neutrinos). So far as charge, baryon number and color are concerned, these eleven fermions fall into four classes:

e, μ and τ – integer charge, no baryon number and no color;

ν_e, ν_μ and ν_τ – no charge, no baryon number and no color;

d, s and b – charge = $-\frac{1}{3}$, baryon number = $\frac{1}{3}$ and color triplet;

u and c – charge = $\frac{2}{3}$, baryon number = $\frac{1}{3}$ and color triplet.

From this classification, it is tempting to postulate the existence of a sixth quark, called the top quark t, similar to u and c so that there are three numbers in each of these four classes.

With this hypothetical top quark, there are thus three families of quarks and leptons:

$$\begin{pmatrix} u \\ d \\ \nu_e \\ e^- \end{pmatrix} \quad \begin{pmatrix} c \\ s \\ \nu_\mu \\ \mu^- \end{pmatrix} \quad \begin{pmatrix} t \\ b \\ \nu_\tau \\ \tau^- \end{pmatrix} \tag{7.1}$$

as already discussed in section 5.2 on the standard model [7.1]. In each family there are in order a quark of baryon number $\frac{1}{3}$ and charge $\frac{2}{3}$, a quark of baryon number $\frac{1}{3}$ and charge $-\frac{1}{3}$, a neutral lepton, and a charged lepton. The quarks are available in three colors, while the leptons are color singlets. This arrangement has a number of nice features theoretically.

At PETRA, all experimental groups have searched for this top quark [7.2 to 7.10]. Four different methods have been used, falling into two broad categories.

(A) Search for top quark jets via $e^+e^- \to t\bar{t}$. This is sometimes described as the search for the open top. Three distinct properties of the final states from $t\bar{t}$ have been used.

(A1) R. Since the charge of the top quark is $\frac{2}{3}$, its contribution to R is large. Significantly above the top threshold, its contribution is $\Delta R = \frac{4}{3}$ compared with the sum of contributions $R = \frac{11}{3}$ from the already observed u, d, s, c and b quarks.

(A2) Event shape. Because of the expected large mass of the top quark, the resulting hadrons from $t\bar{t}$ must distribute in a more spherical and less planar way.

(A3) Muon yield. In the Kobayashi–Maskawa model [7.11] the top quark is expected to decay predominately into the b quark which subsequently decays into a c quark, etc. In this cascade there is an appreciable probability of $\sim 10\%$ that each of these decays yields a muon. Hence top quark production is a rich source of prompt muons.

(B) Search for a $t\bar{t}$ bound state. This is sometimes referred to as the search for the hidden top. Analogous to the J/ψ from a $c\bar{c}$ bound state and the upsilon from a $b\bar{b}$ bound state, several $t\bar{t}$ bound states with charge conjugation -1 are expected to exist. Search for such bound states requires the accelerator to scan in energy.

The next two subsections are devoted to some of the data obtained from these methods (A1), (A2), (A3) and (B).

7.2.2. Search for the open top

As already shown in figs. 2.3, 2.6 and 2.7, the observed R at PETRA is essentially a constant above the upsilon region. Therefore, the method (A1) of looking for a step in R yields no sign of a top quark.

The next method, (A2), of looking for events of a different shape is more sensitive. If a pair of particles are produced by e^-e^+ annihilation not far above threshold, their velocities are relatively low, and hence the decay products tend to distribute more or less isotropically in the laboratory system. Such events tend to have not only large sphericity but also large aplanarity. A study of such events is a more sensitive way to detect the possible presence of a $t\bar{t}$ threshold than R, which treats all hadronic events equally.

Analysis of event shape is carried out at PETRA whenever a new energy region becomes available. An example of the comparison between experimental data and Monte Carlo results in the triangular

plot is shown in fig. 7.1 [7.12]. It is clearly seen that the Monte Carlo distribution from $e^+e^- \to t\bar{t}$ gives a much larger number of events with large sphericity and aplanarity.

In connection with method (A3), PLUTO [7.13], JADE [7.14], and MARK J [7.15] and CELLO [7.16] Collaborations have measured the muon yield at different center-of-mass energies. In fig. 7.2, the cross section from CELLO of prompt muons in hadronic events is shown. The data fit nicely with the expectation of a five-flavor Monte Carlo simulation.

We compare these three methods of searching for the open top and also with the search for the hidden top to be described in the next subsection.

The search for a step in R is most straightforward and independent of the detailed properties of the top quark. With the accelerator running smoothly, systematic errors from the two sides of the step are likely to cancel to a large extent. However, since all hadronic events are treated equally, this method is less sensitive than the method of event shape.

The method of event shape emphasizes the non-planar events characteristic of $e^+e^- \to t\bar{t}$. Although more sensitive, the quantitative comparison with Monte Carlo requires detailed assumptions about the decay of mesons with top quantum number. The method of muon yield is most likely going to serve the purpose of verifying the results of these two other methods.

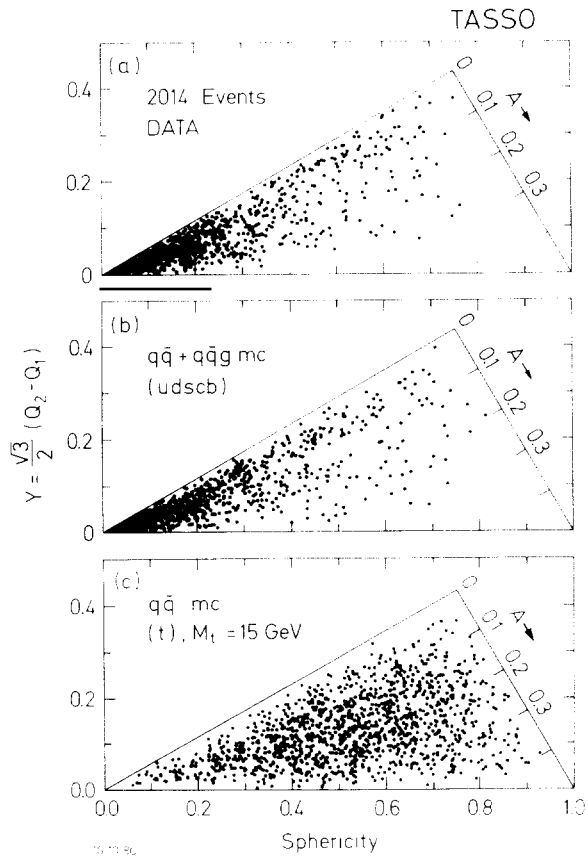

Fig. 7.1. (a) The event distribution in aplanarity and sphericity observed by the TASSO Collaboration between 27.4 GeV and 36.6 GeV in c.m. energy. Monte Carlo created events in aplanarity and sphericity at 30 GeV in c.m. for (b) $e^+e^- \to q\bar{q}g$ with q = u, d, s, c and b; (c) $e^+e^- \to t\bar{t}$ with m_t = 15 GeV and a c.m. energy of 35 GeV.

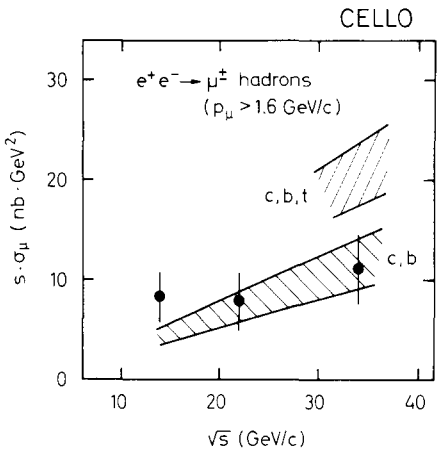

Fig. 7.2. The CELLO [7.16] cross section of prompt muons with $p > 1.6$ GeV/c at the three c.m. energies, compared to MC expectations. The error bars include both statistical and systematic uncertainties.

Since the production of the top quark is likely to occur only at the upper limit of the machine energy, energy scan makes it possible to reach an additional couple of GeV, which may be crucial. From the binding energy of the upsilon, it is safe to assume that the binding energy of the $t\bar{t}$ resonance is at least 1 GeV. When this method of energy scan was first proposed, there was understandably some reluctance for various reasons such as a loss of integrated luminosity. However, by now energy scan is considered to be a routine operation, including changing the energy by varying the magnet current without refilling. Therefore this method of energy scan is to be described in detail in the following subsection.

7.2.3. Search for the hidden top

At PETRA three periods of energy scans have been performed, the energy ranges covered being $27 < W < 31.6$ GeV, $33 < W < 38.6$ GeV and $40 < W < 43.1$ GeV. The energy steps used are 10 MeV per beam for the lower energy ranges and 15 MeV per beam for the highest energy ranges. In fig. 7.3, the MARK J [7.6] result is shown for the range 37 to 38.6 GeV. No $t\bar{t}$ resonance is seen.

The conclusion is therefore reached that up until now no evidence for the t quark has been seen at PETRA. The search will continue, especially after the further increase in PETRA energy scheduled for the later part of 1983. Since this method of energy scan is considered to be the best method of search for this t quark, we discuss here in some detail this particular method.

The basic idea of this analysis was already used with the original SPEAR data on the J/ψ: Since the total width of a 1^- heavy $q\bar{q}$ state is small compared with the machine width, the important quantity is the integrated cross sections. Applied to the toponium $t\bar{t}$ state of mass M, the integrated cross sections are given by [7.17]

$$\int \sigma_f(W)\,\mathrm{d}W = \frac{6\pi^2}{M^2}\frac{\Gamma_{ee}\Gamma_f}{\Gamma} \tag{7.2}$$

where Γ_{ee} is partial width for the decay $(t\bar{t}) \to e^-e^+$, Γ_f for the decay process $(t\bar{t}) \to f$ whose cross section σ_f is being measured, and Γ is the total width of the toponium $(t\bar{t})$. The integration is performed over the toponium resonance.

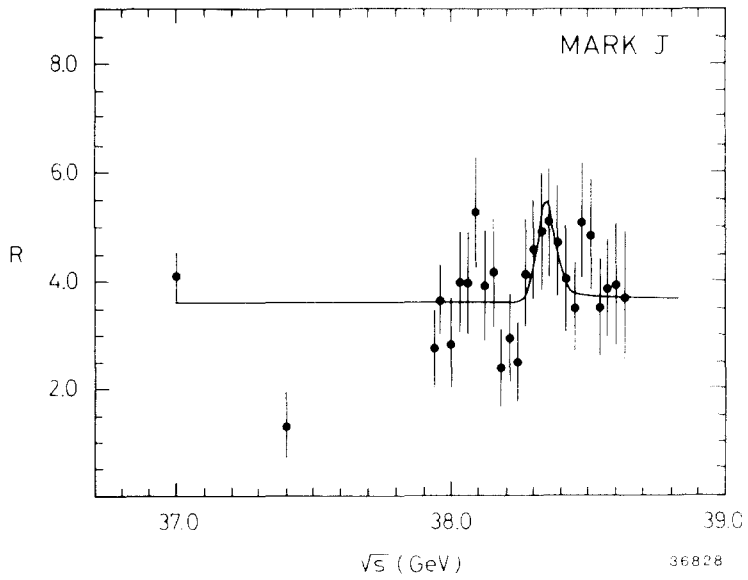

Fig. 7.3. The MARK J [7.6] relative hadronic cross section R as a function of $\sqrt{s}$ in the range 37 to 38.63 GeV. The curve is the best fit to the largest deviations found in the entire scan.

Special cases of (7.2) include

$$\int \sigma_{\text{total}}(W)\,\mathrm{d}W = \frac{6\pi^2}{M^2}\Gamma_{ee} \tag{7.3}$$

$$\int \sigma_{\text{h}}(W)\,\mathrm{d}W = \frac{6\pi^2}{M^2}\frac{\Gamma_{ee}\Gamma_{\text{h}}}{\Gamma} \tag{7.4}$$

$$\int \sigma_{ee}(W)\,\mathrm{d}W = \frac{6\pi^2}{M^2}\frac{\Gamma_{ee}^2}{\Gamma} \tag{7.5}$$

and

$$\int \sigma_{\mu\mu}(W)\,\mathrm{d}W = \frac{6\pi^2}{M^2}\frac{\Gamma_{ee}\Gamma_{\mu\mu}}{\Gamma}\,. \tag{7.6}$$

Here σ_{total} and σ_{h} are respectively the total cross section for $e^+e^- \to (t\bar{t})$ and the cross section for $e^+e^- \to (t\bar{t}) \to$ hadrons. Thus σ_{total} gives directly Γ_{ee} from (7.3), and then σ_{ee} gives the total width Γ. These integrated cross sections are insensitive to the machine width.

It is, however, incorrect to divide this integrated cross section by the machine width to get the expected peak cross section. The reason is that, because of the small machine width, radiative effects are very large. Suppose that PETRA is running at a center-of-mass energy W that is equal to the toponium mass M, then the incident electron, or the incident positron, or both may emit a photon of energy larger than the machine width. When this happens, the electron and/or positron no longer has

enough energy to produce the toponium. Thus the observed cross section at the toponium peak is reduced due to the radiative effects [7.18].

In order to appreciate the importance of this effect, let us consider the case of J/ψ from SPEAR [7.19]. In that case, the observed cross section of 2300 nb for hadrons should be compared with

$$\frac{\text{right-hand side of (7.4)}}{\sqrt{2\pi}\,\Delta W}, \tag{7.7}$$

where the factor $\sqrt{2\pi}$ is needed because ΔW is the Gaussian machine width. Using $M = 3.097$ GeV, $\Gamma_{ee} = 4.7$ keV, the hadronic branching ratio $\Gamma_h/\Gamma = 0.85$, and the machine width of

$$\Delta W = \sqrt{2}\,\Delta E_{\text{beam}} = \sqrt{2}\,(0.56\,\text{MeV}) \tag{7.8}$$

for SPEAR, (7.7) gives 4970 nb. Thus the radiative effect reduces the observed peak cross section by a factor of 2.2.

To have some feeling as to what to expect in this search for the toponium at PETRA, we give the following rough estimate. First, the beam spread at PETRA is [7.20]

$$\Delta E_{\text{beam}} = 6.08 \times 10^{-5}\,E^2_{\text{beam}} \tag{7.9}$$

in units of GeV. Under the reasonable assumption that the partial width Γ_{ee} into electron–positron pairs is the same for J/ψ and ($t\bar{t}$), and the less accurate assumption that the radiative effects are also the same, then the expected peak cross section for toponium is given by

$$\frac{2300\text{ nb}}{0.85} \cdot \left(\frac{3.097}{M}\right)^2 \frac{0.56}{0.0608\,(M/2)^2} = \frac{9.56 \times 10^5\,\text{nb}}{M^4}, \tag{7.10}$$

where M is in GeV. For the range of M between 36 GeV and 50 GeV, the machine beam width ΔE_{beam} for PETRA and this peak cross section are tabulated in table 7.1. This peak cross section includes both hadronic and leptonic events.

Table 7.1
Estimated cross sections, number of events, and statistical standard deviations for each experiment in connection with the search for toponium at PETRA. The statistical significance can be somewhat improved by adding together data from neighboring points

$W = M_{t\bar{t}}$ (GeV)	Machine width ΔE_{beam} (MeV)	Peak cross section (nb)	Total no. of events for 50 nb^{-1}	Background no. of events for 50 nb^{-1}	Standard deviation for 50 nb^{-1}
36	19.7	0.57	29.3	9.4	6.5
38	22.0	0.46	24.5	8.4	5.5
40	24.3	0.37	20.7	7.6	4.7
42	26.8	0.31	17.6	6.9	4.1
44	29.4	0.26	15.2	6.3	3.6
46	32.2	0.21	13.2	5.7	3.1
48	35.0	0.18	11.6	5.3	2.7
50	38.0	0.15	10.2	4.9	2.4

In order to estimate the expected number of events and the background, we make the following further assumptions: the R for the background via the five known quarks is 4 (see section 2.2), and the detection efficiency for both the toponium signal and the background is taken to be 0.7. For an integrated luminosity of $50\,\mathrm{nb}^{-1}$ for each point in the energy scan, the expected number N_b of background events, the total number N_t of events including both the toponium signal and the background, and the resulting statistical significance are listed in table 7.1 and plotted in figs. 7.4 and 7.5 (upper curve). The statistical significance means

$$(N_t - N_b)/\sqrt{N_b}\,.$$

This statistical significance is for each PETRA experiment, and can be somewhat improved by adding together the number of events for neighboring points in the energy scan. Better yet, it can be improved by a factor of 2 by combining the data from the four PETRA experiments running simultaneously. Although it is usually dangerous to combine data from different experiments, it is justified in this case because this is a straightforward search for a peak.

We discuss briefly the reliability of the various assumptions used in this estimate. First, the assumption of equal electronic width for J/ψ and for $t\bar{t}$ is likely to be accurate for a toponium mass in the PETRA range. The assumption of the same radiative effect is, however, on the pessimistic side. This is readily seen by comparing the ratio $M/\Delta E_{\mathrm{beam}}$, which is 5500 for SPEAR but only 1650 for PETRA with $M = 40\,\mathrm{GeV}$. Thus the radiative effect must be significantly smaller at PETRA with a resulting

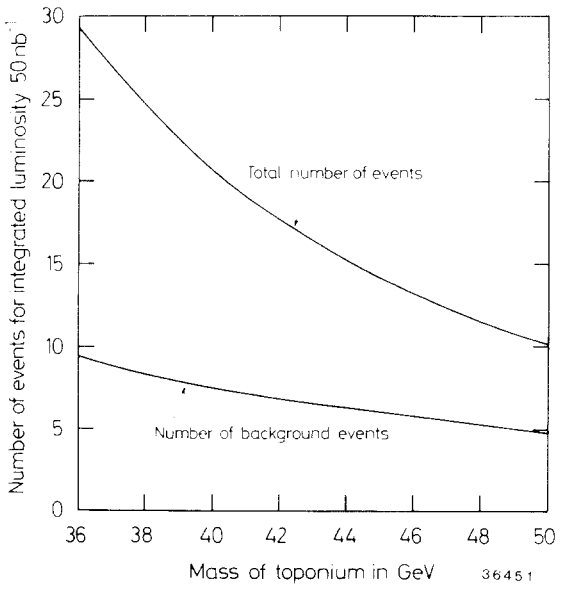

Fig. 7.4. Number of events at toponium peak corresponding to an integrated luminosity of $50\,\mathrm{nb}^{-1}$ at PETRA for various assumed values of the toponium mass.

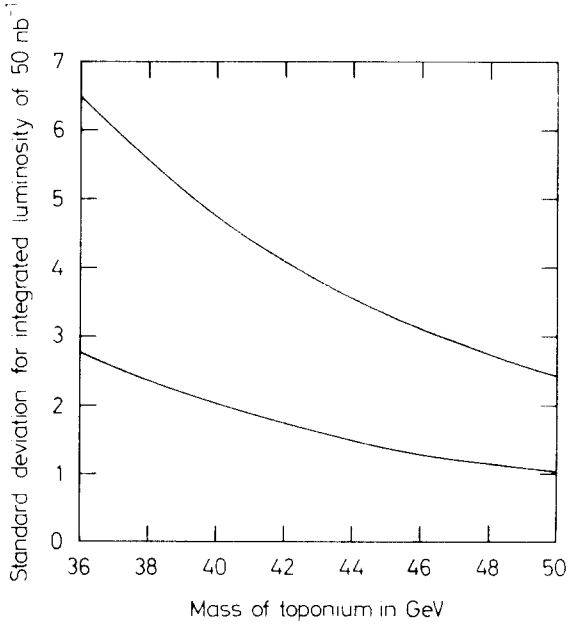

Fig. 7.5. Statistical significance at toponium peak corresponding to an integrated luminosity of $50\,\mathrm{nb}^{-1}$ at PETRA for various assumed values of the toponium mass. The upper curve is for the lowest 1^- toponium state with an electronic width Γ_{ee} of 4.7 keV, and the lower curve is for an excited state with $\Gamma_{ee} = 2\,\mathrm{keV}$.

larger peak cross section. The assumption of 70% detection efficiency is arrived at in the following way: it is not only the detector coverage for the two-jet events via the known quarks, but also the branching ratio Γ_h/Γ for toponium decay into hadrons. Thus this assumption is on the optimistic side. Taking all those points into account, this rough estimate is reasonably realistic.

It should be clearly understood that this estimate applies only to the lowest 1^- toponium state. Because of the larger spread of the wave function, the higher 1^- toponium states have much smaller electronic width Γ_{ee}. Using the value of $\Gamma_{ee} = 2\,\text{keV}$ from $\psi(3685)$, the statistical significance for the second 1^- toponium state is shown in fig. 7.5 (lower curve). In this case, with an integrated luminosity of $50\,\text{nb}^{-1}$ per point, it is necessary to combine the data from the four PETRA experiments. Even then, the signal is marginal at best.

7.3. Search for charged technipions and Higgs

7.3.1. Theoretical considerations

In current theories of weak interactions, spin-zero particles are needed in order to generate masses for the intermediate vector bosons W and Z^0. In the original Higgs mechanism [7.21] used in the Weinberg–Salam theory [7.1], the spin-zero particle is elementary and has no charged partner. If there are charged partners, these charged Higgs [7.22] can be pair produced in e^+e^- annihilation and, similar to the neutral Higgs, decay predominately into the heaviest quarks and leptons that are kinematically allowed. If, in contrast to the standard model, these spin-zero particles arise from dynamical symmetry breaking, then they are composite. While the concept of dynamical symmetry breaking is very attractive, specific additional assumptions are needed before concrete theoretical predictions can be obtained. At the present time, the most popular theory of this type is based on technicolor [7.23] and predicts the existence of spin-zero bosons of relatively low masses, called technipions. The mass of the charged technipions has been predicted to be in the range of 5 to 14 GeV [7.24]. The decays into the heaviest kinematically allowed quarks and leptons are favored. The ratio of the leptonic and hadronic decay rates can be substantial or very small depending on the specific assumptions used [7.25]. If the leptonic decay mode is substantial, then the search for such spin-zero particles can be accomplished by studying the processes

$$e^+e^- \to H^+H^- \to (\tau\nu)\,(\text{hadrons}) \text{ and } (\tau^-\bar{\nu})(\tau^+\nu)\,, \tag{7.11}$$

where the symbol $H^\pm$ is used for both charged Higgs and technipions. In order to avoid any assumption about the size of the leptonic branching ratio, it is necessary to study also

$$e^+e^- \to H^+H^- \to \text{hadrons}\,. \tag{7.12}$$

The experimental investigation of these processes are discussed respectively in sections 7.3.3 and 7.3.4.

7.3.2. Kinematics

The search for charged scalar particles through pair production is hampered by the small production cross section [7.26],

$$\frac{d\sigma}{d\Omega} = \frac{\alpha^2}{8s}\beta^3 \sin^2\theta_H \tag{7.13}$$

and

$$R_{H^+H^-} = \frac{\sigma(e^+e^- \to H^+H^-)}{\sigma(e^+e^- \to \mu^+\mu^-)} = \tfrac{1}{4}\beta^3 \tag{7.14}$$

where β is the velocity of $H^\pm$ in the c.m. system and θ_H is the production angle with respect to the beam axis. These are to be compared with the corresponding cross section for a fermion pair of the same charge:

$$\frac{d\sigma}{d\Omega} = \frac{\alpha^2}{8s}\beta\,(3-\beta^2)\,(1+\cos^2\theta_f) \tag{7.15}$$

and

$$R_{f^+f^-} = \frac{\sigma(e^-e^+ \to f^-f^+)}{\sigma(e^-e^+ \to \mu^-\mu^+)} = \tfrac{1}{2}\beta(3-\beta^2)\,. \tag{7.16}$$

In (7.14) and (7.16), the masses of $H^\pm$ and $f^\pm$ are much larger than the μ mass. Therefore, not only the cross section for the scalar pair is smaller by a factor of 4, but also the rise above threshold is much slower, as shown in fig. 7.6. For these reasons, in the search for the charged technipion and Higgs, it is not sufficient to study R, and more powerful methods of analysis have been used.

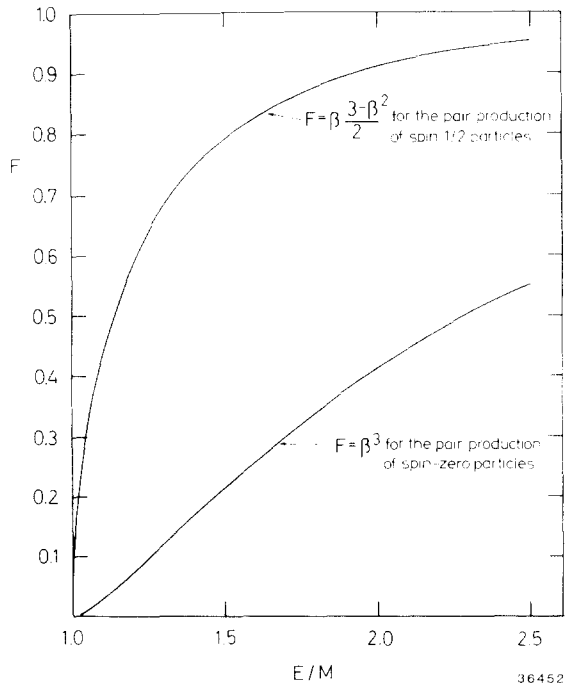

Fig. 7.6. Threshold behavior for the production cross sections of point-like spin-zero and spin $\frac{1}{2}$ particles in e^-e^+ annihilation.

7.3.3. Leptonic mode

JADE Collaboration [7.27] is the first in carrying out a search for the charged technipion of Higgs through the leptonic and mixed modes (7.11). We describe in some detail the cuts that they used for the mixed mode $e^+e^- \to H^+H^- \to (\tau\nu)$ (hadrons). On the basis of the thrust axis $\hat{n}_T$, the observed particles are separated into two hemispheres as shown in fig. 7.7. Define θ_T as the angle between $\hat{n}_T$ and the incident e^+ direction, and E_h, M_h and E_τ, M_τ as the energies and invariant masses of the hadron and $\tau\nu$ hemispheres respectively. The initial cuts are

(1) $|\cos\theta_T| < 0.65$.

(2) Existence of at least one track on the $(\tau\nu)$ side inside a 70° cone around the thrust axis.

(3) $E_h > 0.6\,E_{beam}$ and $E_\tau < 0.4\,E_{beam}$.

After these initial cuts, the experimental data are analyzed in two different ways, one efficient for low and the other for high m_H.

(A1) $(\tau\nu)$ (hadrons)-mode, low m_H.

(4) All tracks other than the one on the $\tau\nu$-side must be on the hadron side within a cone of 60° from $\hat{n}_T$, i.e. an isolated track with or without neutrals recoiling against a narrow hadron jet.

(5) $M_\tau < 2$ GeV.

(6) $M_h > 2.5$ GeV.

(A2) $(\tau\nu)$ (hadrons)-mode, high m_H.

(4′) A high invariant hadron mass: $M_h > 0.3\,E_{beam}$.

(5′) $\Delta\phi > 30°$, where $\Delta\phi$ is the angle between the following two planes: one formed by the initial beam direction $\hat{z}$ and the vector sum of the momenta of the observed particles in the hadron hemisphere, and the other formed by the same $\hat{z}$ and the corresponding sum in the $\tau\nu$ hemisphere.

The rationale for the choice of these cuts is qualitatively understandable and is discussed in some detail by JADE.

No event survives either cuts. The significance of these null results is assessed using Monte Carlo simulation of the process under consideration, where the hadronic decay of $H^\pm$ is taken to be due to $c\bar{s}$, $\bar{c}s$, $c\bar{b}$ or $\bar{c}b$, and the experimental data for the τ branching ratios are used. Comparison with the Monte Carlo result then leads to, for each value of the mass m_H, an upper limit for the product of branching ratios $B_{\tau\nu}B_{had}$ (95% confidence level, say). These excluded ranges are of course symmetrical under the exchange $B_{\tau\nu} \leftrightarrow B_{had}$ of the branching ratios. The results are shown in fig. 7.8.

In order to study the possibility that the charged technipion or Higgs decays almost exclusively into leptons, JADE has studied also the process $e^+e^- \to H^+H^- \to (\tau^+\nu)(\tau^-\bar{\nu})$ of (7.11). With a suitable choice of cuts of a similar nature, again no event survives, and the excluded region is also shown in fig. 7.8, which

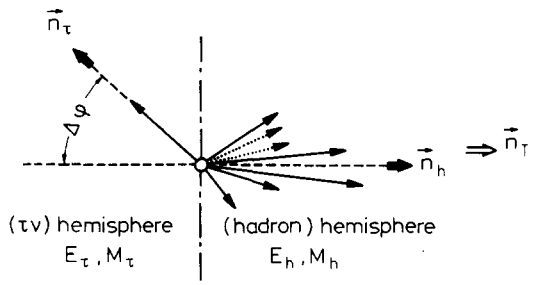

Fig. 7.7. A typical $(\tau\nu)$(hadrons) event seen in the view normal to the $e^\pm$ beam. The full and the dotted lines represent the momentum vectors of charged particles and the γ rays respectively.

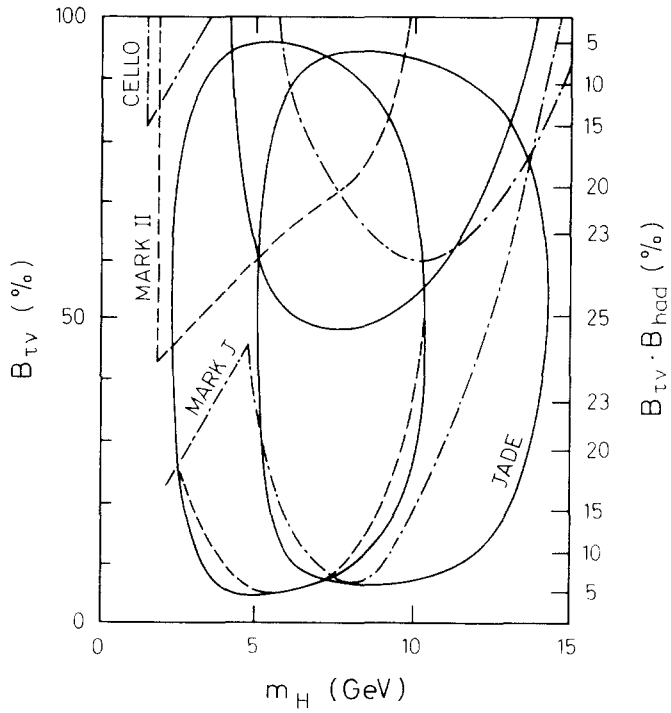

Fig. 7.8. Experimental bounds on the mass of charged Higgs or technipions $H^\pm$ as a function of the leptonic and hadronic branching ratios. The areas included by the curves are excluded with 90% C.L.

contains not only the JADE results, but also the later ones from CELLO [7.28], MARK J [7.29] and MARK II [7.30].

7.3.4. Hadronic mode

With these results on the leptonic and mixed modes, it was urgent to decide between the following two possibilities:

(1) The charged technipion and Higgs do not exist in the mass range accessible to PETRA, or

(2) They exist in the mass range but decay predominately into hadrons.

The challenge to decide between these two possibilities was taken up by the TASSO Collaboration [7.31] by studying the process (7.12).

The final state from this process (7.12) consists of four hadronic jets, for example from c, $\bar{s}$, $\bar{c}$ and s. Therefore the fast four-jet analysis [7.32] (see section 3.2.7), involving the repeated application of the three-jet analysis [7.33] (see section 3.2.1) can be used. However, the jet masses cannot be neglected in this case because they may be comparable to the masses of $H^\pm$. This generalization of including the non-zero jet masses in the four-jet analysis is applied to both the experimental data and the Monte Carlo event simulation [7.31]. Two decay processes are studied:

Case (A) $$e^+e^- \to H^+H^-, \quad H^- \to \bar{c}s, \quad H^+ \to c\bar{s}$$

i.e. $H^{\pm}$ decay exclusively into $c\bar{s}$ quarks;

$$\text{Case (B)}\qquad e^+e^- \to H^+H^-,\quad H^- \to \bar{c}s \text{ or } \bar{c}b,\quad H^+ \to c\bar{s} \text{ or } c\bar{b}$$

with $H^{\pm}$ decaying equally into $c\bar{s}$ and $c\bar{b}$.

The data were subjected to a number of cuts in order to maximize the signal of $e^+e^- \to H^+H^-$ over the background contribution from QCD processes. First, good four-jet candidates are selected by applying cuts in the total visible energy of the event, the minimum observed jet energy, the minimum reconstructed jet energy, and the opening angle between the jets from the same $H^{\pm}$ decay. After these cuts, each event is described in terms of the three variables

$$\Delta E = E_1 + E_2 - E_{\text{beam}}\,, \qquad m_{\text{av}} = \tfrac{1}{2}(m_{12} + m_{34})\,, \qquad \text{and} \qquad \theta_{\text{av}} = \tfrac{1}{2}(\theta_{12} + \theta_{34})\,,$$

where the various variables are shown in fig. 7.9. Roughly speaking, in these three variables, the events fill an ellipsoid whose size and orientation depends on m_H. By a linear transformation on the three variables, the tilted ellipsoid is transformed into a sphere of radius R. The cut $R < R_{\text{rms}}$ is introduced to suppress the QCD background.

The analysis is repeated in steps of 100 MeV for m_H between 5 GeV and 14.5 GeV. With the cuts described above, the experimental data are compared with the Monte Carlo expectation in fig. 7.10. The surviving events above 13 GeV are consistent with QCD expectation. Note that fig. 7.10 is really a compilation of many similar but independent analyses, each corresponding to a different value of m_H. In particular, the surviving event in the range of m_H between 6.3 GeV and 6.9 GeV is the same event. Finally, the region of hadronic branching ratio excluded by this TASSO result is shown in fig. 7.11. Combined with the JADE result of section 7.3.3, at the 95% confidence level there is no point-like

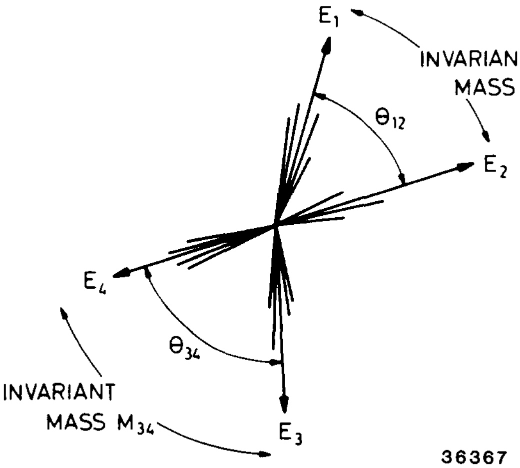

Fig. 7.9. Some of the kinematic variables for a four-jet event from the pair production of $H^{\pm}$. The jets 1 and 2 are from the decay of one H, and jets 3 and 4 are from the other H.

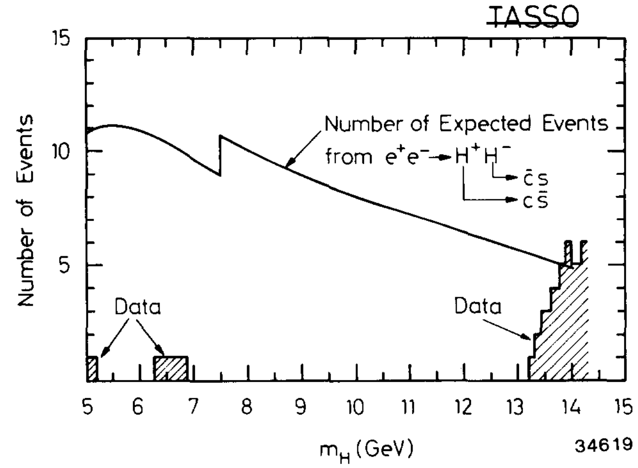

Fig. 7.10. Number of expected events after all the cuts as a function of m_H for $e^+e^- \to H^+H^-$ with $H^+ \to c\bar{s}$, $H^- \to \bar{c}s$. Also shown is the number of events observed by TASSO as a function of m_H.

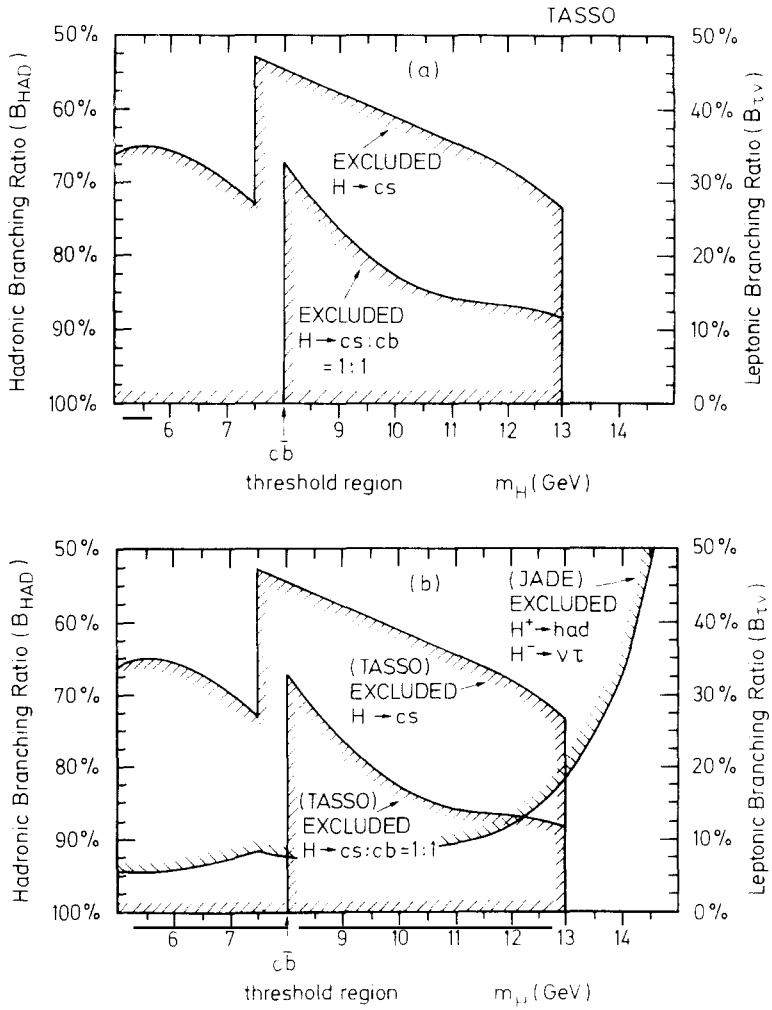

Fig. 7.11. (a) Limits on the hadronic branching ratio (B_{had}) as a function of $H^\pm$ mass from TASSO for case (A) $e^+e^- \to H^+H^-$ with $H^+ \to c\bar{s}$, $H^- \to \bar{c}s$ and for case (B) $e^+e^- \to H^+H^-$ with $(H \to cs):(H \to cb) = 1:1$. The shaded area is excluded at the 95% confidence level. The vertical scale on the right-hand side of the figure indicates the corresponding leptonic branching ratios ($B_{\tau\nu}$) if the sum of $B_{had} + B_{\tau\nu} = 1$. (b) Limits on the leptonic branching ratio from JADE for $H^+ \to \tau^+\nu$, $H^- \to \tau^-\bar{\nu}$ or $H^+ \to \tau^+\nu$, $H^- \to$ hadrons superimposed on (a).

spin-zero charged particle in the mass range of 5 to 13 GeV. In particular, if the theoretical mass prediction does not change, the standard technicolor scheme is essentially ruled out.

7.4. Search for supersymmetric particles

7.4.1. Supersymmetry

Supersymmetry refers to symmetry between bosons and fermions [7.34]. The study of supersymmetry has theoretical, but not experimental, motivation, and it is not possible to judge now whether it will eventually become a useful concept in particle physics [7.35]. Nevertheless, it is interesting because it introduces a very large number of new particles. At present, there are many possible versions of supersymmetric theories, but most of them contain new particles as follows:

Table 7.2
Supersymmetric partners of known and expected particles. The spin is shown in the brackets

Particle	Supersymmetric partner
photon γ [1]	photino λ_γ [1/2]
lepton ℓ [1/2]	scalar lepton s_ℓ, t_ℓ [0]
quark q [1/2]	scalar quark s_q, t_q [0]
gluon g [1]	gluino $\tilde{g}$ [1/2]
$W^\pm$ [1], Z^0 [1] and Higgs [0]	supersymmetric heavy leptons [1/2]

(a) supersymmetric partners of known particles, as listed in table 7.2;
(b) goldstino λ_g due to the enlargement of the gauge group.

Counting the internal degrees of freedom, the number of supersymmetric partners and the number of the original known particles are the same. Therefore, to each lepton ℓ of spin $\frac{1}{2}$, there are two scalar leptons. Furthermore, the scalar quarks are color triplets, and the gluino is a color octet.

All the new particles are massive. Among them, the lightest particle is expected to be either the photino or the goldstino. Thus for example a scalar lepton decays into the corresponding lepton plus either a photino or goldstino.

7.4.2. Pair production of scalar leptons

Point-like scalar leptons, which have charges $\pm e$, are pair produced in e^+e^- annihilation with the angular distribution (7.13) and integrated cross section (7.14), just like charged technipions. The decay is different: scalar leptons (sometimes called sleptons) decay rapidly as shown in fig. 7.12. Therefore the

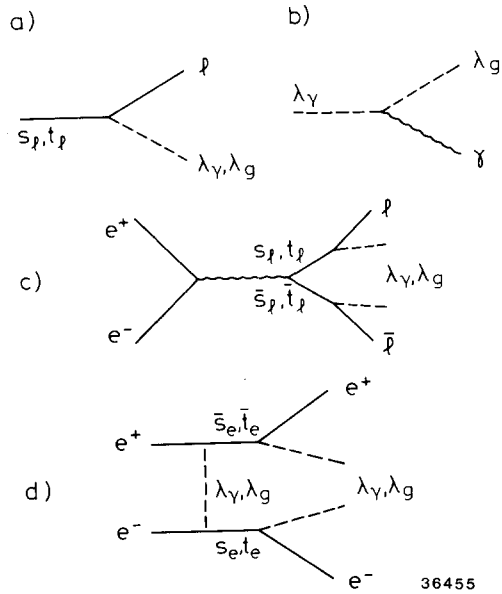

Fig. 7.12. Production and decay of some supersymmetric particles: (a) scalar lepton decay; (b) model-dependent photino decay; (c) pair production and decay of scalar leptons in e^-e^+ annihilation; and (d) additional diagram for the production and decay of scalar electrons.

cross section is known, and the signature for the three types of scalar leptons s_e, t_e; s_μ, t_μ; and s_τ, t_τ are

$$e^-e^+ \to e^-e^+ \text{ (acolinear)} + \cdots \tag{7.17}$$

$$e^-e^+ \to \mu^-\mu^+ \text{ (acolinear)} + \cdots \tag{7.18}$$

and

$$e^-e^+ \to \tau^-\tau^+ \text{ (acolinear)} + \cdots \tag{7.19}$$

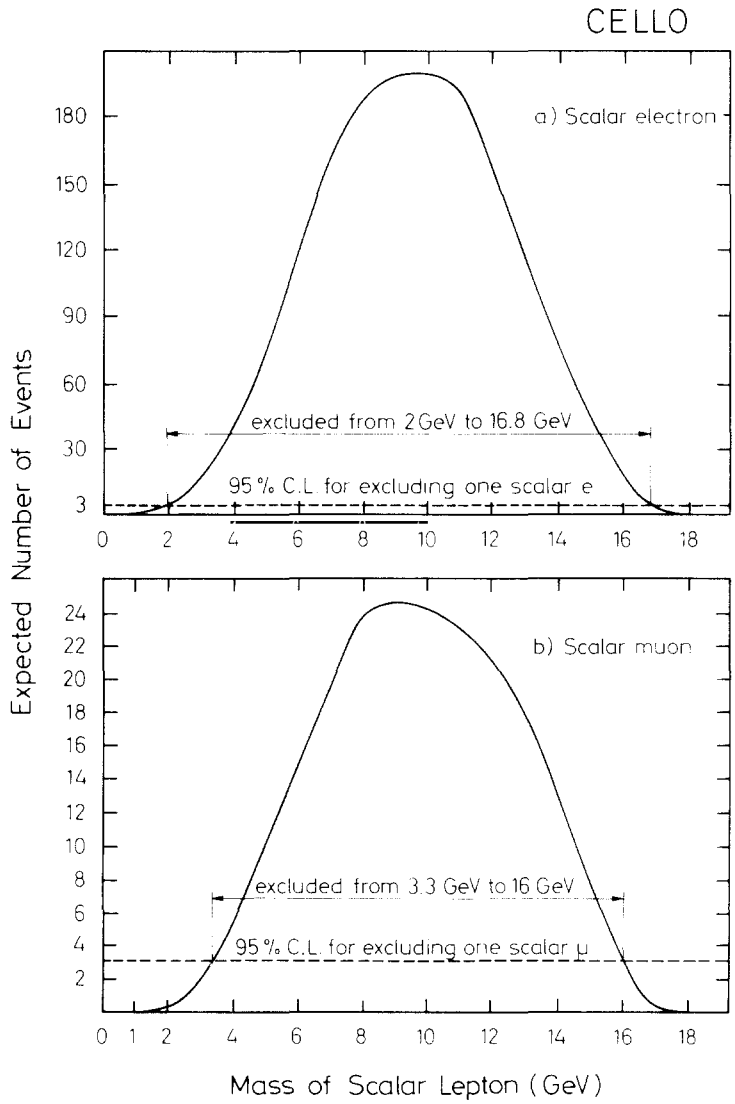

Fig. 7.13. CELLO [7.28] limits on the masses of (a) scalar electrons and (b) scalar muons. The larger number of expected events in detector for the scalar electron is due to the diagram of fig. 7.12d.

While the diagram of fig. 7.12c applies to all three processes, the diagram of fig. 7.12d, involving the exchange of the photino and the goldstino, has the consequence that the cross section for (7.17) is much larger than those for (7.18) and (7.19). The additional particles in these processes, shown as . . . , may include photons due to the decay of photinos and goldstinos, whichever have the higher mass.

Since the cross section for the pair production of scalar leptons is of the order of α^2, there is no difficulty in subtracting out radiative pair production of ordinary leptons. CELLO [7.28], MARK J [7.29, 7.36] and TASSO [7.37] at PETRA have all carried out this search for scalar leptons, and the results of CELLO and MARK J are shown in figs. 7.13 and 7.14 respectively. The experimental lower limits on the masses from the various PETRA Collaborations are summarized in table 7.3.

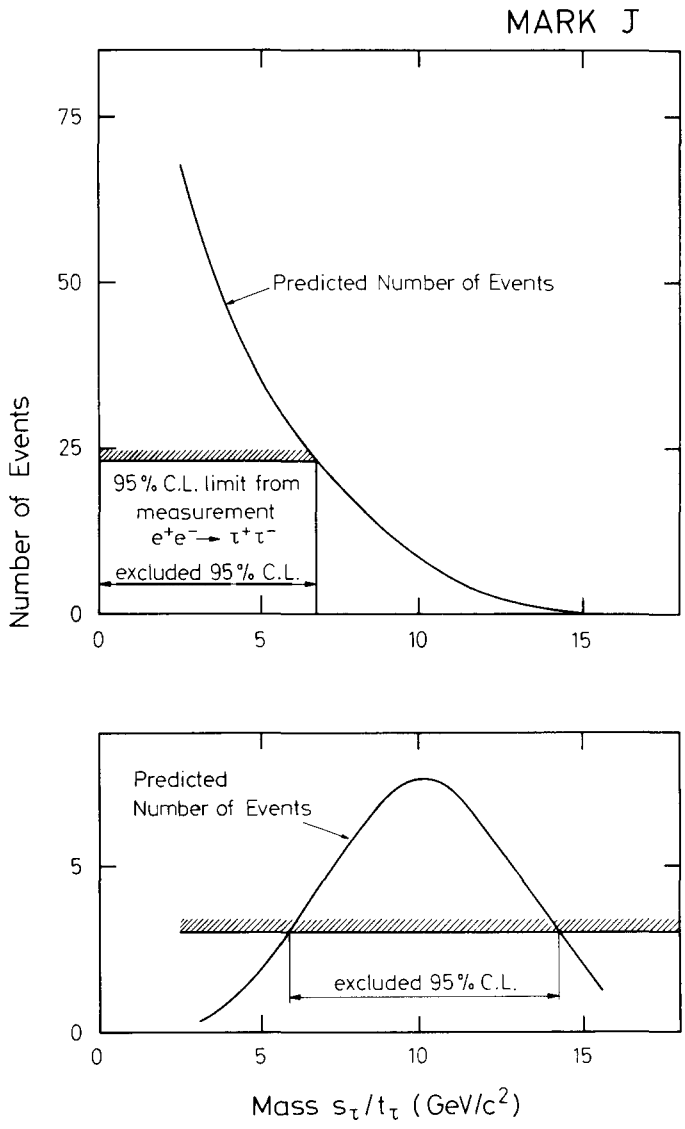

Fig. 7.14. MARK J [7.29] limits on the mass of scalar τ.

Table 7.3
Experimental lower limits on the masses of scalar leptons in GeV (95% C.L.)

	$\tilde{e}_e$	$\tilde{\mu}_\mu$	$\tilde{\tau}_\tau$	Ref.
CELLO	16.8	16	15.3	[7.28]
MARK J		15	14	[7.36, 7.29]
TASSO	16.6	16.4		[7.37]

7.4.3. Photinos

We consider next the supersymmetric analog of the e^-e^+ annihilation into two photons, namely

$$e^-e^+ \to \lambda_\gamma \lambda_\gamma . \tag{7.20}$$

This process is impossible to observe experimentally if the photino is stable, which could occur if it has a lower mass than the goldstino or if there is no goldstino at all. Although in principle possible, it is difficult to observe the radiative correction to (7.20):

$$e^-e^+ \to \lambda_\gamma \lambda_\gamma \gamma . \tag{7.21}$$

This has not been accomplished so far at either PETRA or PEP, but there have been proposals to investigate (7.21) experimentally.

On the other hand, if the photino decays into a goldstino and a photon as shown in fig. 7.12b, then (7.20) leads to two acolinear photons in the final state with additional invisible goldstinos. CELLO [7.38] has searched for two photon events with missing energy to yield an upper limit for the production of neutral particles which decay into a photon and a non-interacting particle, and this search applies in particular to the unstable photino. Assuming that the mass of the photino is much larger than that of the goldstino, then the photino lifetime as given by fig. 7.12b is [7.39]

$$\tau_{\lambda_\gamma} = 8\pi d^2 / m_{\lambda_\gamma}^5 \tag{7.22}$$

where m_{λ_γ} is the photino mass and d is a parameter characterizing the symmetry breaking, which is unknown. For the CELLO search, this lifetime must be such that the decays occur inside the detector. The cross section for the process depends on the mass of the scalar electron, which is also unknown. In the CELLO analysis, this mass of the scalar electron is assumed to be 40 GeV. However, a change of this mass by ±50% alters the lower bound of the photino mass by less than 20%. No photino is found, and the range of photino mass excluded is shown in fig. 7.15 together with the bounds from cosmological considerations [7.39, 7.40] and from the J/ψ decay [7.41]. For example, assuming that $d = (100\ \text{GeV})^2$, the photino mass range excluded by CELLO is from 100 MeV to 13 GeV.

7.5. Search for new heavy leptons

7.5.1. Sequential leptons

It was less than a decade ago when one of the major problems of elementary particle physics was:

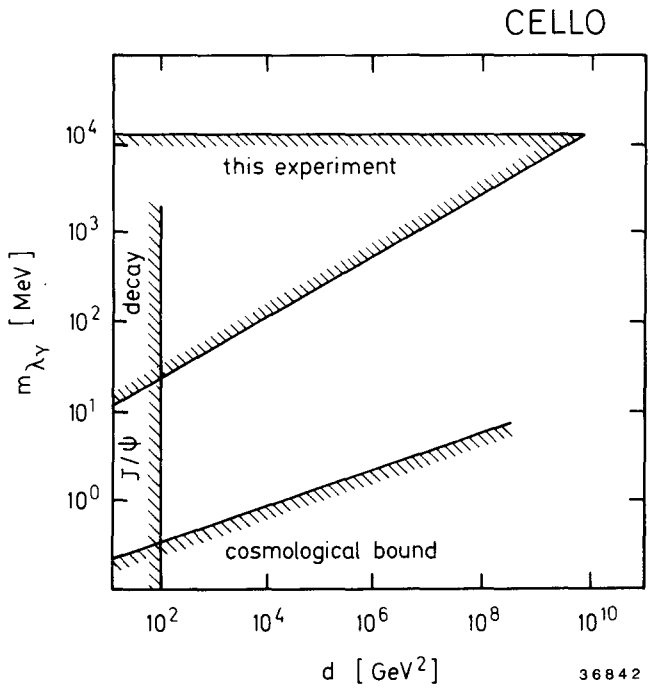

Fig. 7.15. CELLO [7.38] 95% C.L. limits on the mass of the photino versus the scale parameter d for supersymmetric breaking. The mass of the scalar electron is assumed to be 40 GeV. The cosmological bound and the limit from J/ψ decay is also shown.

Why is there a muon? It is an indication of the rapid progress of the field that this problem has been changed to: Why are there three generations of quarks and leptons? As seen from (7.1), for each of these three known generations, the first particle discovered experimentally is the charged lepton. The reason is undoubtedly that the charged lepton is not as heavy as the quark and not as elusive as the associated neutrino. Therefore the most reasonable and practical way to locate a fourth generation is to try to detect a lepton heavier than the τ.

Properties of such a sequential lepton are clearly known. The angular distribution and cross section for pair production in e^+e^- annihilation, as shown in fig. 7.16a, are given by (7.15) and (7.16). The major decay modes are given in fig. 7.16b. With the phase-space factors neglected, the branching ratios can be estimated from the color factors:

$$B(L^- \to \nu_L d\bar{u}) \sim B(L^- \to \nu_L s\bar{c}) \sim 3B(L^- \to \nu_L \ell \bar{\nu}_\ell)\,. \tag{7.23}$$

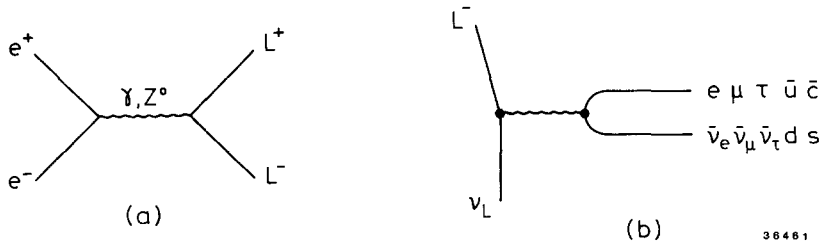

Fig. 7.16. Production and major decay modes of a heavy sequential lepton.

The result is that

$$B(L^- \to \nu_L e \bar{\nu}_e) \sim B(L^- \to \nu_L \mu \bar{\nu}_\mu) \sim B(L^- \to \nu_L \tau \bar{\nu}_\tau) \sim 11\% , \tag{7.24}$$

and

$$B(L^- \to \nu_L d\bar{u}) \sim B(L^- \to \nu_L s\bar{c}) \sim 32\% , \tag{7.25}$$

together with small branching ratios, perhaps 1% to 2%, for

$$B(L^- \to \nu_L s\bar{u}), \quad B(L^- \to \nu_L d\bar{c}) \quad \text{and} \quad B(L^- \to \nu_L b\bar{c}).$$

Some of these decays lead to distinct signatures that can be used in the search for the next sequential lepton.

(a) Approximately 10% of all $L\bar{L}$ pairs result in a final state $e^+e^- \to e^\pm \mu^\mp$ + neutrinos. The muon and the electron are in general acolinear and the total energy visible in the event is less than the available center-of-mass energy. This configuration is shown schematically in fig. 7.17a.

(b) $e^+e^- \to L\bar{L} \to e^\pm(\mu^\mp)$ + (hadrons)$^\pm$ + neutrinos. In this final state the electron (muon) is recoiling against a low multiplicity hadron jet. The electron (muon) and the jet axis are in general acolinear and some of the available energy is carried off by neutrinos. Roughly 40% of all new sequential lepton pairs will populate these final states. This configuration is shown in fig. 7.17b.

(c) $e^+e^- \to L\bar{L} \to$ (hadrons)$^+$ + (hadrons)$^-$ + neutrinos. The two low-multiplicity hadron jets will in general be acolinear and a fraction of the c.m. energy is carried off by neutrinos. This is shown in fig. 7.17c.

These and similar topologies have been used by MARK J [7.36], TASSO [7.42], PLUTO [7.43] and JADE [7.44] at PETRA to search for sequential leptons heavier than the τ. The results are negative: the experimental mass limits and the methods used are listed in table 7.4.

7.5.2. Excited muon

The searches for other varieties of heavy leptons are to be given in this and the next three subsections. Specifically, these further searches are for: excited muon, excited electron, stable heavy charged lepton, and heavy neutral lepton.

Over the years, there have been many theoretical discussions as to whether leptons are composite particles so that excited states exist [7.45]. By definition an excited muon decays to a muon and a

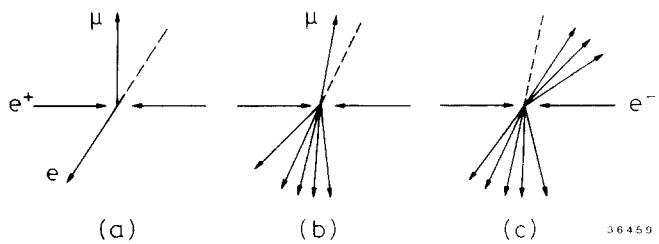

Fig. 7.17. Three different experimental signatures for the production of a pair of heavy sequential leptons.

Table 7.4
Mass limit on new sequential leptons

Group	Lower limit 95% C.L.	Signature	Ref.
MARK J	16.0 GeV	Single muon recoiling against many hadrons	[7.36]
TASSO	15.5 GeV	Single charged particle recoiling against many hadrons	[7.42]
PLUTO	14.5 GeV	Single muon recoiling against many hadrons	[7.43]
JADE	18.0 GeV	Two acolinear jets	[7.44]

photon

$$\mu^{*\pm} \to \mu^{\pm}\gamma . \tag{7.26}$$

Since this decay is electromagnetic, the lifetime of $\mu^{*\pm}$ is very short. Thus the search for an excited muon consists of looking for μ and γ. Obviously, the two possible production processes are:

$$e^-e^+ \to \mu^{*-}\mu^{*+} \tag{7.27}$$

and

$$e^-e^+ \to \mu^{*-}\mu^{+} \text{ or } \mu^{-}\mu^{*+} . \tag{7.28}$$

Fig. 7.18 shows these two processes together with the subsequent decays according to (7.26).

Searches have been performed at PETRA by MARK J [7.46] through both of these production processes. These searches consist of detecting the $\mu^-\mu^+\gamma\gamma$ and $\mu^-\mu^+\gamma$ final states and compare with the predictions from quantum electrodynamics. No deviation from QED has been seen in this way. For example, for the $\mu^-\mu^+\gamma$ final state, MARK J observed 108 events, while QED predicts 116. Therefore there is no evidence of any production of an excited muon at PETRA.

In order to deduce any limit from this absence of events, however, detailed assumptions are necessary about the production processes (7.27) and (7.28). The assumptions used are as follows:

(1) For the μ^* pair production (7.27), the angular distribution (7.15) and the cross section (7.16) are

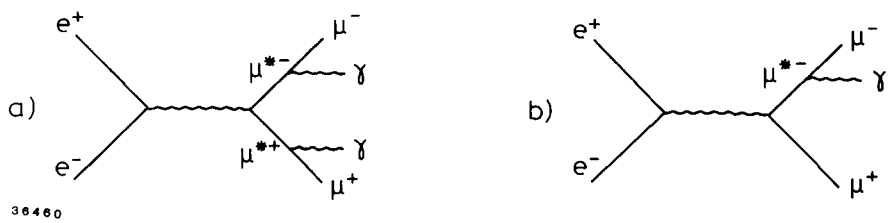

Fig. 7.18. Production of the excited muon in e^-e^+ annihilation.

used. Since the momentum transfer is more than twice the excitation energy, the correctness of this assumption of point-like excited state is not obvious.

(2) For the process (7.28), the model-dependent $\mu^*\mu\gamma$ vertex is parametrized by [7.47]

$$\frac{e\lambda}{M_{\mu^*}}\bar{\psi}_{\mu^*}\sigma_{\beta\alpha}\psi_{\mu}F^{\beta\alpha}, \tag{7.29}$$

where $F^{\beta\alpha}$ is the electromagnetic field tensor, and λ is an unknown effective coupling constant. With (7.29), the angular distribution and cross section for (7.28) are given by

$$\frac{d\sigma}{d\Omega} = \lambda^2\alpha^2\frac{(s-M_{\mu^*}^2)^2}{s^3}[(s+M_{\mu^*}^2)-(s-M_{\mu^*}^2)\cos^2\theta] \tag{7.30}$$

and hence

$$\sigma = \frac{8\pi\alpha^2}{3}\lambda^2(1-M_{\mu^*}^2/s)^2(1+2M_{\mu^*}^2/s). \tag{7.31}$$

With these assumptions, the MARK J search via the process (7.27) gives a lower limit for the mass of the excited muon

$$M_{\mu^*} > 10\,\text{GeV} \qquad (95\%\ \text{CL}).$$

Using the same method, MAC [7.48] has later obtained the lower limit

$$M_{\mu^*} > 14.5\,\text{GeV} \qquad (90\%\ \text{CL}).$$

Note the difference in confidence level and that the MAC data have been taken at a lower energy. The search through the process (7.28) excludes certain regions in the M_{μ^*}–λ plane. See the discussion in section 7.1. In fig. 7.19, the MARK J limit from (7.28) is shown together with [7.49] the limit obtained from the anomalous magnetic moment of the muon [7.50].

7.5.3. Excited electron

We discuss very briefly the search for an excited electron. This is carried out through $e^+e \to \gamma\gamma$, where an e^* may be exchanged in addition to the e, as shown in fig. 7.20. Again, there is no evidence for an excited electron, and the limits have already been given in table 5.6 as Λ for $\gamma\gamma$ by PLUTO [7.51], TASSO [7.52], CELLO [7.53, 7.38], MARK J [7.46] and JADE [7.54].

7.5.4. Stable charged heavy lepton

JADE [7.55] and MARK J [7.46] have searched for stable charged heavy leptons. The rationale is as follows. For the three generations of quarks and leptons, the neutrinos are known to be massless or nearly massless. Accordingly, in the search for the possible fourth generation via the charged heavy lepton as discussed in section 7.5.1, it is implicitly assumed that the charged lepton is significantly heavier than the corresponding neutrino. If the reverse is true [7.56], i.e., if the neutrino is heavier than the charged lepton, then the charged lepton is stable and the search in section 7.5.1 fails. Instead,

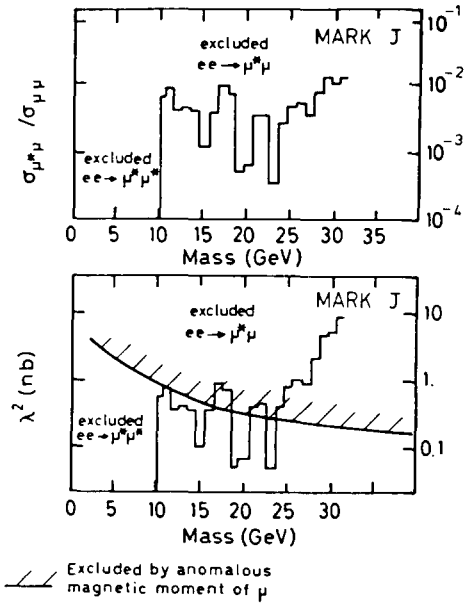

Fig. 7.19. MARK J [7.46] experimental limits on the production of excited muons μ^* together with limits from the anomalous magnetic moment of the muon.

pair-produced stable charged heavy leptons would behave like additional "μ pair with low momenta".

The mass limits from JADE and MARK J are

$$M_{L^\pm} > \begin{matrix} 12\,\text{GeV} & \text{(JADE)} \\ 14\,\text{GeV} & \text{(MARK J)} \end{matrix}$$

for such particles. The MARK J data is shown in fig. 7.21.

7.5.5. Neutral heavy lepton

Heavy neutral leptons [7.57] are not required in the standard theory. Indeed, they were proposed before the observation of weak and electromagnetic interference at PETRA, as discussed in chapter 5. The JADE Collaboration has searched for an electron-type neutral heavy lepton E_0, which forms a

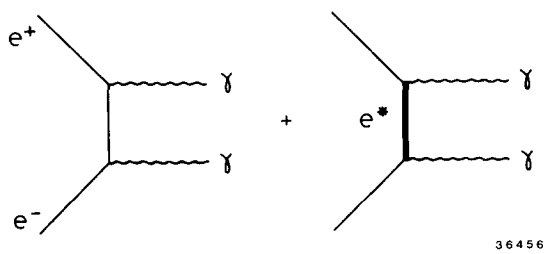

Fig. 7.20. Possible contributions to $e^+e^- \to \gamma\gamma$.

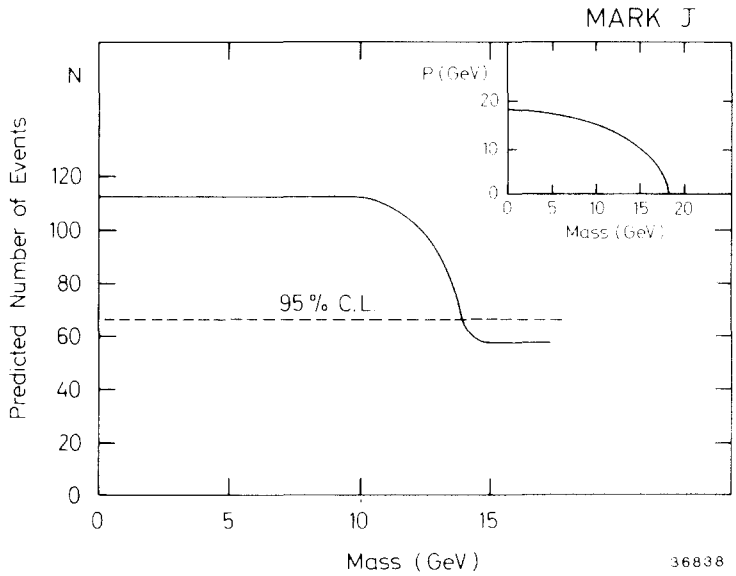

Fig. 7.21. Experimental limit from MARK J [7.46] on the production of stable charged leptons.

doublet

$$\begin{pmatrix} E_0 \\ e^- \end{pmatrix}$$

with the electron. Possible production and decay mechanism for E_0 are shown in fig. 7.22(a, b and c). This E_0 can be pair-produced via the neutral weak current and singly produced via the charged weak current. Charged current production dominates at present energies provided the interaction has the usual weak strength. The decay modes $E_0 \to e\ W^+$ can lead to a pure leptonic final state or to a jet consisting of an electron and hadrons, as shown in fig. 7.22d.

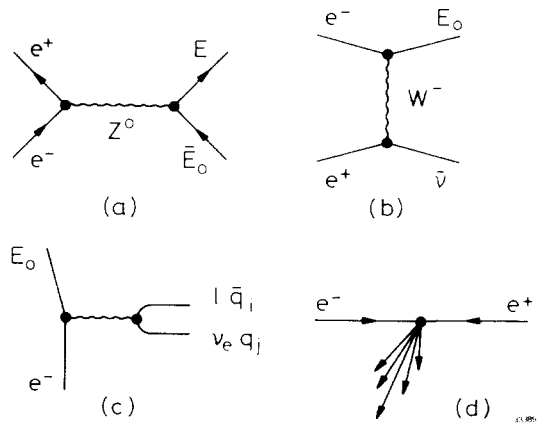

Fig. 7.22. Heavy electron-like neutral lepton. (a) & (b) Production mechanism via the neutral weak and the charged weak current. (c) Decay modes. (d) Final state in $e^+e^- \to E^0\bar{E}$.

The JADE Collaboration [7.44] has carried out two separate analyses, one for high E_0 mass and one for low E_0 mass. In the high-mass analysis, the number of actual observed events surviving the cuts they use is two, giving 6.3 events as 95% C.L. limit. The origin of the two events is unknown. However, the two events are consistent with the contribution from the process $e^+e^- \to$ hadrons + hard photon, where the photon escaped through a gap of the lead glass counter between the barrel and the end cap. The beam energies of the two events are 16.993 and 16.996 GeV. As seen from fig. 7.23, the resulting 95% C.L. lower mass limits for E_0 are

$$M(E_0) > 24.5\,\text{GeV} \quad \text{for V + A},$$
$$M(E_0) > 22.5\,\text{GeV} \quad \text{for V - A}.$$

7.6. *Search for magnetic monopoles and free quarks*

7.6.1. *Magnetic monopoles*

We conclude this chapter by describing two searches which would have profound effects on our understanding of particle physics had they been successful.

The magnetic monopole was first discussed by Dirac [7.58] over half a century ago. He showed that the magnetic charge g of a monopole is related to the electric charge e by

$$eg = n\tfrac{1}{2}\hbar c, \tag{7.32}$$

where $n = \pm 1, \pm 2, \pm 3, \ldots$. The PETRA search [7.59] for this monopole makes use of a detector that consists of 7 cylindrical layers of Kapton foils, 40 cm long, 18.4 cm diameter, 75 μ thick, placed at the SW interaction region inside the vacuum chamber of the storage ring. The solid angle covered is 85% of 4π, using a length of 30 cm of the foils.

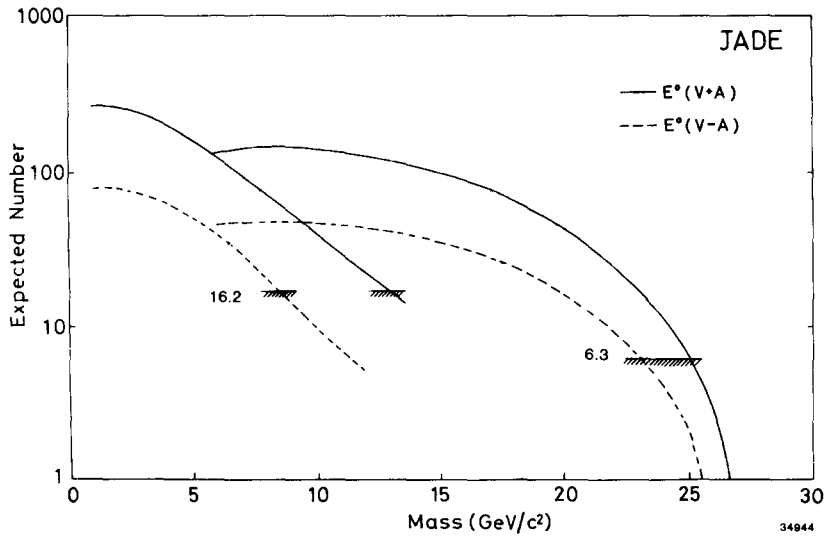

Fig. 7.23. JADE [7.44] search for an electron-type neutral heavy lepton. The curves show the expected number of events for V + A coupling (solid line) and V - A coupling (dashed line). The 95% C.L. limits are also shown, as hatched lines.

No magnetic monopole is found. Assuming monopole pair production and using the Ahlen–Kinoshita theory [7.60] of monopole ionization, the experimental mass limits are shown in fig. 7.24 for $|n| = 1, 2, 3, 4$ and 5. If this pair production is isotropic, then the upper limit for the cross section is found to be

$$\sigma < 4 \times 10^{-38}\,\mathrm{cm}^2 \qquad (95\%\ \mathrm{C.L.})\,.$$

Similar work has been done at PEP [7.61].

7.6.2. *Free quark*

The concept of quarks [7.62, 7.63] is a most useful one in particle physics, especially at PETRA energies. Conflicting results on the existence of free quarks have been reported from searches in bulk material.

The JADE Collaboration [7.55] has carried out a free quark search at PETRA using both the inclusive and the exclusive channels

$$e^-e^+ \to q\bar{q} \qquad \text{and} \qquad e^-e^+ \to q\bar{q}X\,.$$

They rely on the measurement of specific ionization, which is assumed to depend on the charge Q_q in the form

$$\mathrm{d}E/\mathrm{d}x = Q_q^2\, f(\beta)\,. \tag{7.33}$$

It is by no means clear whether such an ionization formula is applicable to quarks [7.64].

No free quark is found. In the inclusive search, the analysis has been carried out using two different

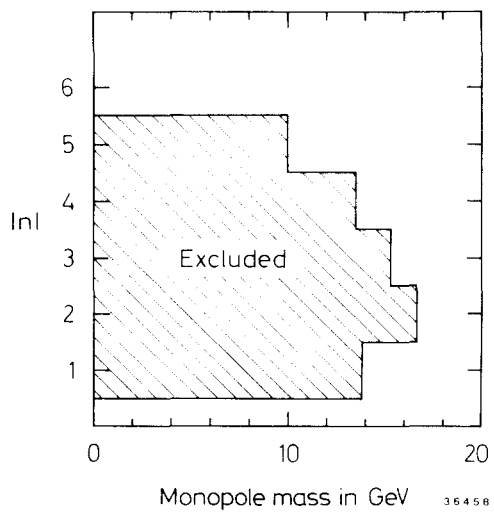

Fig. 7.24. Experimental lower limit for the mass of the magnetic monopole for various values of $n = 2eg/\hbar c$.

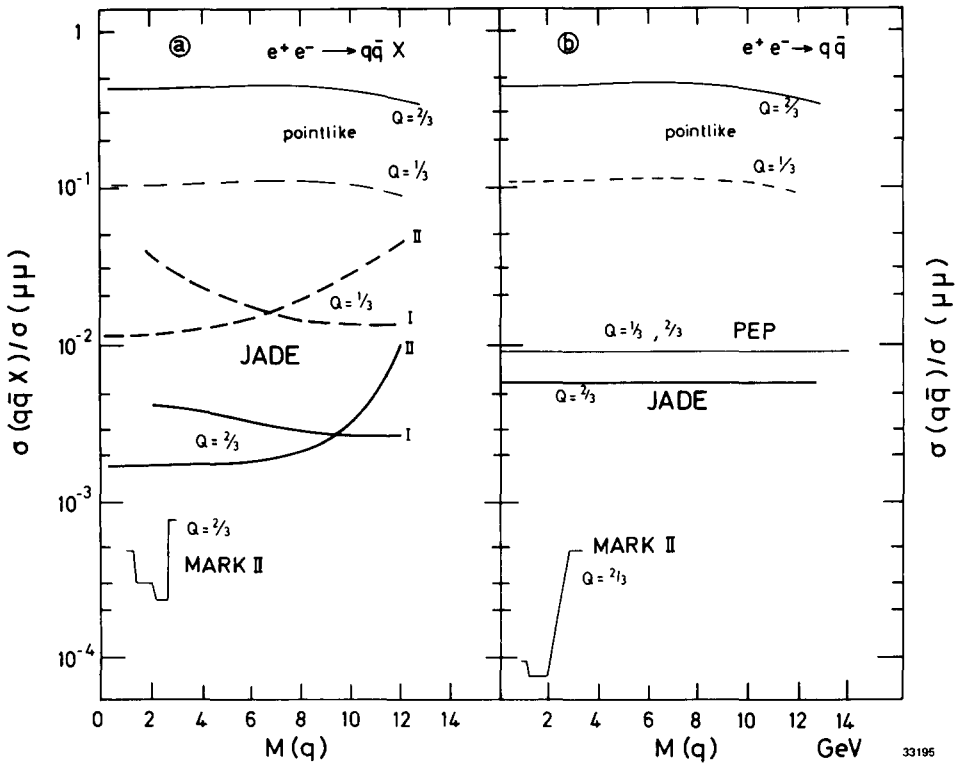

Fig. 7.25. The 90% upper limit on the cross sections for (a) inclusive quark production $e^+e^- \to q\bar{q}X$ and (b) exclusive quark production $e^+e^- \to q\bar{q}$ plotted versus quark mass. The curves marked I or II in (a) show the limit obtained by JADE for two different assumptions or the momentum distributions of the quarks.

momentum distributions for the free quarks:

$$\frac{1}{\sigma(q\bar{q})} E\left(\frac{d^3\sigma}{dp^3}\right) = A \exp(-3.5\, E)$$

$$\frac{1}{\sigma(q\bar{q})} E\left(\frac{d^3\sigma}{dp^3}\right) = \text{constant}\,.$$

The resulting 90% C.L. cross sections for inclusive quark production, with the assumption (7.33), is plotted [7.12] in fig. 7.25 together with the similar data from SPEAR [7.65] and PEP [7.66].

Acknowledgements

I wish to thank M. Jacob and M. Perl for their encouragement in writing this report. I am most grateful to J. Ellis, E. Lohrmann, P. Söding, V. Sörgel, B. Wiik, G. Wolf, T.T. Wu and G. Zobernig for numerous discussions and constructive comments. I would also like to thank D. Degèle and R. Kose for

useful comments regarding the machine PETRA, and E. Hilger on two-photon physics. I am indebted to M. Cherney for his valuable assistance in preparing this report and K. Heide for her dedicated effort in typing the manuscript. Most of all I would like to thank the DESY directorate, P. Söding, V. Sörgel and G. Voss, and also G. Söhngen for their hospitality extended to me while working at DESY and for providing an excellent opportunity to do exciting physics. This work is in part supported by the U.S. Department of Energy contract number DE-AC02-76ER00881.

References

Chapter 1

[1.1] Deutsches Elektronen-Synchrotron, PETRA - a proposal for extending the storage-ring facilities at DESY to higher energies, DESY, Hamburg, November 1974;
Deutsches Elektronen-Synchrotron, PETRA - updated version of the PETRA proposal, DESY, Hamburg, February 1976.
[1.2] PETRA Storage Ring Group, D. Degèle et al., DESY M-83-20 (1983) and Proc. 12th Intern. Conf. on High-Energy Accelerators, Fermilab., August 1983.
[1.3] K. Robinson and G.A. Voss, CEA Report CEA-TM-149 (1965);
K. Steffen, DESY Internal Report DESY M-79/07 (1979);
K. Steffen, DESY Internal Report DESY HERA-80/03 (1980);
K. Steffen and G.A. Voss, DESY Internal Report DESY M-81/17 (1981);
A. Piwinski, DESY 81-066 (1981);
Micro-beta: K. Steffen, G.A. Voss and G. Wolf, DESY Internal Report DESY M-81/20 (1981).
[1.4] A. Piwinski, G. Ripken and A. Wrulich, DESY Internal Report, DESY M80-03 (1980).
[1.5] DESY, Wissenschaftlicher Jahresbericht (1981) p. 109 ff;
DESY, Wissenschaftlicher Jahresbericht (1982).
[1.6] R.D. Kohaupt, DESY Internal Report DESY M-83-07 (1983) and Proc. 1983 Particle Accelerator Conf. Santa Fe, New Mexico, March 1983.
[1.7] W. Bauer et al., Proc. 1983 Particle Accelerator Conf., Santa Fe, New Mexico, March 1983;
H. Lengeler, Proc. 12th Intern. Conf. on High-Energy Accelerator, Fermilab, August 1983.
[1.8] A.A. Sokolov and I.M. Ternov, Soviet Physics - Doklady 8 (1964) 1203;
V.N. Baier, Soviet Physics - Uspekhi 14 (1972) 695;
J.D. Jackson, Rev. Mod. Phys. 48 (1976) 417.
[1.9] K. Steffen, DESY Internal Report, DESY M-82-25 (1982);
H.D. Bremer, J. Kewisch, H.C. Lewin, H. Mais, R. Rossmanith and R. Schmidt, DESY 82-026 (1982);
H.D. Bremer, J. Kewisch, H.C. Lewin, H. Mais, G. Ripken, R. Rossmanith, R. Schmidt and D.P. Barber, DESY Internal Report, DESY M-82-26 (1982);
D.P. Barber, J. Kewisch, H. Mais, G. Ripken, R. Rossmanith and R. Schmidt, DESY 82-076 (1982);
D.P. Barber, H.D. Bremer, J. Kewisch, H.C. Lewin, T. Limberg, H. Mais, G. Ripken, R. Rossmanith and R. Schmidt, DESY 83-065 (1983);
H. Mais, G. Ripken, DESY Internal Report, DESY M-82-17 (1982);
R. Neumann and R. Rossmanith, Nucl. Instr. Meth. 204 (1982) 29.
[1.10] CELLO Collaboration, H.-J. Behrend et al., Phys. Scripta 23 (1981) 610.
[1.11] DESY, PETRA Bulletin No. 14, April 1979.
[1.12] JADE Collaboration, Proposal for a Compact Magnetic Detector at PETRA (1976).
[1.13] J. Heintze, Nucl. Instr. Meth. 156 (1978) 227;
W. Farr et al., Nucl. Meth. 156 (1978) 283;
W. Farr and J. Heintze, Nucl. Instr. Meth. 156 (1978) 301;
H. Drumm et al., IEEE Trans. Nucl. Sci. 26 (1979) 81;
H. Drumm et al., Nucl. Instr. Meth. 176 (1980) 333;
J. Heintze, Proc. Intern. Symp. on Nuclear Radiation Detectors, March 1981, Tokyo, Japan;
J. Heintze, Nucl. Instr. Meth. 196 (1982) 293;
A. Wagner, Proc. Intern. Conf. on Instrumentation for Colliding Beam Physics (SLAC, 1982) SLAC-Report 250, p. 76.
[1.14] JADE Collaboration, W. Bartel et al., Phys. Lett. 92B (1980) 206;
JADE Collaboration, W. Bartel et al., Z. Phys. C, Particles and Fields 19 (1983) 197.
[1.15] JADE Collaboration, W. Bartel et al., Phys. Lett. 99B (1981) 277.
[1.16] JADE Collaboration, W. Bartel et al., Phys. Lett. 88B (1979) 171.

[1.17] MARK J Collaboration, Proposal to Build a 4π Electromagnetic Detector to Study Weak and Electromagnetic Interactions and to Search for New Particles at PETRA (1976);
MARK J Collaboration, Phys. Report 63 (1980) 337.
[1.18] MARK J Collaboration, B. Adeva et al., Phys. Rev. Lett. 48 (1982) 1701.
[1.19] L. Criegee and G. Knies, DESY 81-044 (1981) and Phys. Report 83 (1982) 151.
[1.20] PLUTO Collaboration, Proposal for Experiments at PETRA with PLUTO (1976).
[1.21] TASSO Collaboration, Proposal for a Large 4π Magnetic Detector for PETRA (1976).
[1.22] TASSO Collaboration, R. Brandelik et al., Phys. Lett. 94B (1980) 259;
TASSO Collaboration, R. Brandelik et al., Phys. Lett. 110B (1982) 173.
[1.23] TASSO Collaboration, R. Brandelik et al., Phys. Lett. 107B (1981) 290.
[1.24] TASSO Collaboration, R. Brandelik et al., Phys. Lett. 83B (1979) 261.
[1.25] H. Boerner et al., Nucl. Instr. Meth. 176 (1980) 151.
[1.26] TASSO Collaboration, M. Althoff et al., Phys. Lett. 126B (1983) 493.
[1.27] TASSO Collaboration, M. Althoff et al., Z. Phys. C, Particles and Fields 17 (1983) 5.
[1.28] A. Ladage, Proc. Intern. Conf. on Instrumentation for Colliding Beam Physics (SLAC, 1982) SLAC-Report 250, p. 180.
[1.29] TASSO Collaboration, R. Brandelik et al., Phys. Lett. 108B (1982) 71.
[1.30] H. Burkhardt et al., Nucl. Instr. Meth. 184 (1981) 319;
G. Poelz and R. Riethmüller, Nucl. Instr. Meth. 195 (1982) 491.

Chapter 2

[2.1] H.J. Bhabha, Proc. Roy. Soc. (London) A154 (1935) 195.
[2.2] S.L. Glashow, Nucl. Phys. 22 (1961) 579;
S. Weinberg, Phys. Rev. Lett. 19 (1967) 1264;
A. Salam, Proc. Eighth Nobel Symp., May 1968, ed. N. Svartholm (Wiley, 1968) p. 367;
S.L. Glashow, J. Iliopoulos and L. Maiani, Phys. Rev. D2 (1970) 1285.
[2.3] M.L. Perl et al., Phys. Rev. Lett. 35 (1975) 1489 and Phys. Lett. 63B (1976) 466;
G.J. Feldman et al., Phys. Rev. Lett. 38 (1977) 117.
[2.4] UA1 Collaboration, G. Arnison et al., Phys. Lett. 126B (1983) 398;
UA2 Collaboration, G. Bagnaia et al., Phys. Lett. 129B (1983) 130.
[2.5] P. Söding and G. Wolf, Ann. Rev. Nucl. Part. Sci. 31 (1981) 231;
TASSO Collaboration, M. Althoff et al., DESY 83-130 (1983) and Z. Phys. C, Particles and Fields (to be published);
TASSO Collaboration, M. Althoff et al., DESY 84-001 (1984) and Phys. Lett. (to be published).
[2.6] A. Quenzer, Thesis, Orsay Report LAL (1977) 1294;
A. Cordier et al., Phys. Lett. 81B (1979) 389;
J. Perez-Y-Jorba, Proc. XIX Int. Conf. on High Energy Physics, Tokyo (1978) 277;
R.F. Schwitters, XVIII Int. Conf. on High Energy Physics, Tbilisi (1976) B34;
J. Burmester et al., Phys. Lett. 66B (1977) 395;
R. Brandelik et al., Phys. Lett. 76B (1978) 361;
C. Bacci et al., Phys. Lett. 86B (1979) 234;
P. Bock et al., Z. Phys. C, Particles and Fields 6 (1980) 125.
[2.7] J.J. Aubert et al., Phys. Rev. Lett. 33 (1974) 1404;
J.-E. Augustin et al., Phys. Rev. Lett. 33 (1974) 1406;
C. Bacci et al., Phys. Rev. Lett. 33 (1974) 1408;
G.S. Abrams et al., Phys. Rev. Lett. 33 (1974) 1453 and 34 (1975) 1181;
P. Rapidis et al., Phys. Rev. Lett. 39 (1977) 526.
[2.8] S.W. Herb et al., Phys. Rev. Lett. 39 (1977) 252;
W.R. Innes et al., Phys. Rev. Lett. 39 (1977) 1240;
Ch. Berger et al., Phys. Lett. 76B (1978) 243;
C.W. Darden et al., Phys. Lett. 76B (1978) 246;
D. Andrews et al., Phys. Rev. Lett. 44 (1980) 1108 and 45 (1980) 219;
T. Böhringer et al., Phys. Rev. Lett. 44 (1980) 1111;
G. Finocchiaro et al., Phys. Rev. Lett. 45 (1980) 222.
[2.9] CELLO Collaboration, H.J. Behrend et al., DESY 81-029 (1981).
[2.10] JADE Collaboration, W. Bartel et al., Phys. Lett. 88B (1979) 171;
JADE Collaboration, W. Bartel et al., Phys. Lett. 89B (1979) 136;
JADE Collaboration, W. Bartel et al., Phys. Lett. 91B (1980) 152;
JADE Collaboration, W. Bartel et al., Phys. Lett. 100B (1981) 364.

[2.11] JADE Collaboration, W. Bartel et al., Phys. Lett. 129B (1983) 145.
[2.12] MARK J Collaboration, D.P. Barber et al., Phys. Rev. Lett. 42 (1979) 1113;
MARK J Collaboration, D.P. Barber et al., Phys. Rev. Lett. 43 (1979) 901;
MARK J Collaboration, D.P. Barber et al., Phys. Lett. 85B (1979) 463;
MARK J Collaboration, D.P. Barber et al., Phys. Rev. Lett. 44 (1980) 1722;
MARK J Collaboration, Phys. Rev. Lett. 50 (1983) 799.
[2.13] PLUTO Collaboration, Ch. Berger et al., Phys. Lett 81B (1979) 410;
PLUTO Collaboration, Ch. Berger et al., Phys. Lett. 86B (1979) 413.
[2.14] TASSO Collaboration, R. Brandelik et al., Phys. Lett. 83B (1979) 261;
TASSO Collaboration, R. Brandelik et al., Z. Phys. C, Particles and Fields 4 (1980) 87;
TASSO Collaboration, R. Brandelik et al., Phys. Lett. 88B (1979) 199.
[2.15] TASSO Collaboration, R. Brandelik et al., DESY 82-010 (1982) and Phys. Lett. 113B (1982) 499.
[2.16] G. Hanson et al., Phys. Rev. Lett. 35 (1975) 1609.
[2.17] M. Gell-Mann, Phys. Lett. 8 (1964) 214;
G. Zweig, CERN-Report TH 401 and TH 412 (1964).
[2.18] C.N. Yang and R.L. Mills, Phys. Rev. 96 (1954) 191.
[2.19] D.J. Gross and F. Wilczek, Phys. Rev. Lett. 30 (1973) 1343;
H.D. Politzer, Phys. Rev. Lett. 30 (1973) 1346;
T. Applequist and H. Georgi, Phys. Rev. D8 (1973) 4000;
A. Zee, Phys. Rev. D8 (1973) 4038.
[2.20] J.D. Bjorken and S.J. Brodsky, Phys. Rev. D1 (1970) 1416.
[2.21] PLUTO Collaboration, Ch. Berger et al., Phys. Lett. 82B (1979) 449;
K. Hagiware, Nucl. Phys. B137 (1978) 164.
[2.22] Sau Lan Wu and Georg Zobernig, Z. Phys. C. Particles and Fields 2 (1979) 107.
[2.23] E. Farhi, Phys. Rev. Lett. 39 (1977) 1587.
[2.24] S. Brandt et al., Phys. Lett. 12 (1964) 57.
[2.25] G. Sterman and S. Weinberg, Phys. Rev. Lett. 39 (1977) 1436.
[2.26] K.H. Mess and B.H. Wiik, DESY Report 82-011 (1982) and Les Houches, Session XXXVIII, 1981, Gauge theories in high energy physics, eds. M.K. Gaillard and R. Stora (North-Holland Publishing Company, 1983).
[2.27] R.D. Field and R.P. Feynman, Nucl. Phys. B136 (1978) 1.
[2.28] T. Meyer, Program Write-Up (1979) for TASSO Collaboration, unpublished.
[2.29] TASSO Collaboration, R. Brandelik et al., Phys. Lett. 94B (1980) 437.
[2.30] TASSO Collaboration, R. Brandelik et al., Phys. Lett. 100B (1981) 357.
[2.31] Sau Lan Wu, DESY Report 81-003 (1981) and Physica Scripta 25 (1981) 212.

Chapter 3

[3.1] Sau Lan Wu and Georg Zobernig, Z. Phys. C, Particles and Fields 2 (1979) 107;
Sau Lan Wu and Georg Zobernig, TASSO Note No. 84, June 26, 1979.
[3.2] B.H. Wiik, Proc. Intern. Conf. on neutrinos, weak interactions and cosmology, Bergen, Norway, 18–22 June 1979, p. 113.
[3.3] P. Söding, Proc. European Physical Society Intern. Conf. on High Energy Physics, Geneva, Switzerland, 27 June–4 July, 1979, p. 271.
[3.4] TASSO Collaboration, R. Brandelik et al., Phys. Lett. 86B (1979) 243 [received on August 29, 1979].
[3.5] MARK J Collaboration, D.P. Barber et al., Phys. Rev. Lett. 43 (1979) 830 [received on August 31, 1979].
[3.6] PLUTO Collaboration, Ch. Berger et al., Phys. Lett. 86B (1979) 418 [received on September 13, 1979].
[3.7] JADE Collaboration, W. Bartel et al., Phys. Lett. 91B (1980) 142 [received on December 7, 1979].
[3.8] J. Ellis, M.K. Gaillard and G.G. Ross, Nucl. Phys. B111 (1976) 253 [Errata: B130 (1977) 516];
T.A. DeGrand, Y.J. Ng and S-H. Tye, Phys. Rev. D16 (1977) 3251;
A. De Rujula, J. Ellis, E.G. Floratos and M.K. Gaillard, Nucl. Phys. B138 (1978) 387;
J. Ellis, Comments Nucl. Part. Phys. 9 (1981) 153.
[3.9] G. Hanson et al., Phys. Rev. Lett. 35 (1975) 1609.
[3.10] TASSO Collaboration, R. Brandelik et al., Phys. Lett. 94B (1980) 437.
[3.11] S. Brandt and H.D. Dahmen, Z. Phys. C, Particles and Fields 1 (1979) 61.
[3.12] JADE Collaboration, W. Bartel et al., Phys. Lett. 101B (1981) 129.
[3.13] J. Ellis and I. Karliner, Nucl. Phys. B148 (1979) 141.
[3.14] TASSO Collaboration, R. Brandelik et al., Phys. Lett. 97B (1980) 453;
For higher statistics in gluon spin analysis from TASSO, see Sau Lan Wu, DESY Report 83-007 and Proc. Summer Institute on Particle Physics, August 1982, SLAC, Stanford, California.

[3.15] M.R. Anderberg, Cluster Analysis for Applications (Academic Press, New York, 1973).
[3.16] K. Lanius, DESY 80-36 (1980).
[3.17] J. Dorfan, Z. Phys. C, Particles and Fields 7 (1981) 349.
[3.18] H.J. Daum, H. Meyer and J. Bürger, Z. Phys. C, Particles and Fields 8 (1981) 167.
[3.19] K. Lanius, H.E. Roloff and H. Schiller, Z. Phys. C, Particles and Fields 8 (1981) 251.
[3.20] C.T. Zahn, IEEE Trans. Computers C-20 (1971) 68.
[3.21] PLUTO Collaboration, Ch. Berger et al., Phys. Lett. 97B (1980) 459.
[3.22] JADE Collaboration, W. Bartel et al., Phys. Lett. 119B (1982) 239.
[3.23] A. De Rujula et al., Nucl. Phys. B138 (1978) 387.
[3.24] MARK J Collaboration, D.P. Barber et al., Phys. Lett. 108B (1982) 63.
[3.25] Sau Lan Wu, Z. Phys. C, Particles and Fields 9 (1981) 329.
[3.26] TASSO Collaboration, M. Althoff et al., Phys. Lett. 126B (1983) 493.
[3.27] JADE Collaboration (presented by S. Orito);
MARK J Collaboration (presented by H. Newman);
PLUTO Collaboration (presented by Ch. Berger);
TASSO Collaboration (presented by G. Wolf);
Proc. 1979 Intern. Symp. on Lepton and Photon Interactions at High Energies, Fermilab, Batavia, Illinois, August 23–29, 1979.
[3.28] R.D. Field and R.P. Feynman, Nucl. Phys. B136 (1978) 1;
A. Ali, J.G. Körner, G. Kramer and J. Willrodt, Z. Phys. C, Particles and Fields 1 (1979) 203 and 269;
T. Meyer, Program Write-Up for TASSO Collaboration (1979).
[3.29] MARK J Collaboration, Phys. Report 63 (1980) 337;
The claim that the "first statistically relevent results, establishing the 3-jet pattern from $q\bar{q}g$ of a sample of hadronic events, were presented by the MARK J Collaboration" is not justified [see last paragraph of section 3.3.2].
[3.30] P. Söding and G. Wolf, Ann. Rev. Nucl. Part. Sci. 31 (1981) 231.
[3.31] CELLO Collaboration, H.J. Behrend et al., Phys. Lett. 110B (1982) 329.
[3.32] MARK J Collaboration, D.P. Barber et al., Phys. Lett. 89B (1979) 139.
[3.33] PLUTO Collaboration, Ch. Berger et al., Phys. Lett. 99B (1981) 292.
[3.34] CELLO Collaboration, H.J. Behrend et al., Phys. Lett. 113B (1982) 427.
[3.35] CELLO Collaboration, H.J. Behrend et al., Z. Phys. C, Particles and Fields 14 (1982) 95.
[3.36] JADE Collaboration, W. Bartel et al., Phys. Lett. 119B (1982) 239.
[3.37] CELLO Collaboration, H.J. Behrend et al., Nucl. Phys. B218 (1983) 269.
[3.38] MARK J Collaboration, B. Adeva et al., Phys. Rev. Lett. 50 (1983) 2051.
[3.39] P. Hoyer, P. Osland, H.G. Sander, T.F. Walsh and P.M. Zerwas, Nucl. Phys. B161 (1979) 349.
[3.40] A. Ali, E. Pietarinen, G. Kramer and J. Willrodt, Phys. Lett. 93B (1980) 155.
[3.41] R.K. Ellis, D.A. Ross and A.E. Terrano, Phys. Rev. Lett. 45 (1980) 1226 and Nucl. Phys. B178 (1981) 421.
[3.42] K.J.F. Gaemers and J.A.M. Vermaseren, Z. Phys. C, Particles and Fields 7 (1980) 81;
J.A.M. Vermaseren, K.J.F. Gaemers and S.J. Oldham, Nucl. Phys. B187 (1981) 301.
[3.43] K. Fabricius, G. Kramer, G. Schierholz, I. Schmitt, Phys. Lett. 97B (1981) 431 and Z. Phys. C, Particles and Fields 11 (1982) 315;
A. Ali, J.G. Körner, G. Kramer, Z. Kunszt, E. Pietarinen, G. Schierholz, and J. Willrodt, Phys. Lett. 82B (1979) 285, and Nucl. Phys. B167 (1980) 454.
[3.44] B. Andersson, G. Gustafson and T. Sjöstrand, Z. Phys. C, Particles and Fields 6 (1980) 235;
T. Sjöstrand, Lund Preprint, LU TP 80-3 (1980), LU TP 82-3 (1982);
B. Andersson, G. Gustafson and T. Sjöstrand, Nucl. Phys. B197 (1982) 45.
[3.45] L.W. Mo and Y.S. Tsai, Rev. Mod. Phys. Mod. Phys. 41 (1969) 205;
G. Bonneau and F. Martin, Nucl. Phys. B27 (1971) 381;
F.A. Berends, K.J.F. Gaemers and R. Gastmans, Nucl. Phys. B57 (1973) 381;
F.A. Berends, K.J.F. Gaemers and R. Gastmans, Nucl. Phys. B63 (1973) 381;
Y.S. Tsai, Rev. Mod. Phys. 46 (1974) 815;
F.A. Berends and G.J. Komen, Phys. Lett. 63B (1976) 432;
F.A. Berends and R. Kleiss, Nucl. Phys. B178 (1981) 141.
[3.46] C.L. Basham, L.S. Brown, S.D. Ellis and S.T. Love, Phys. Rev. Lett. 41 (1978) 1585; Phys. Rev. D17 (1978) 2298; D19 (1979) 2018; Phys. Lett. 85B (1979) 297;
L.S. Brown and S.D. Ellis, Phys. Rev. D24 (1981) 2383.
[3.47] PLUTO Collaboration, Ch. Berger et al., Phys. Lett. 99B (1981) 292;
D. Schlatter et al., Phys. Rev. Lett. 49 (1982) 521;
CELLO Collaboration, H.J. Behrend et al., Z. Phys. C, Particles and Fields 14 (1982) 95.
[3.48] Sau Lan Wu, DESY Report 81-003 (1981) and Physica Scripta 25 (1981) 212.
[3.49] JADE Collaboration, W. Bartel et al., Z. Phys. C, Particles and Fields 9 (1981) 315.

[3.50] JADE Collaboration, W. Bartel et al., Phys. Lett. 123B (1983) 460.
[3.51] PLUTO Collaboration, Ch. Berger et al., Phys. Lett. 100B (1981) 351;
PLUTO Collaboration, Ch. Berger et al., Z. Phys. C, Particles and Fields 12 (1982) 297.
[3.52] O. Nachtmann and A. Reiter, Z. Phys. C, Particles and Fields 16 (1982) 45;
A. Reiter, QCD-Untersuchungen zur Elektron-Positron Annihilation in 4 jets, University of Heidelberg Report, HD-THEP-81-10 (1981).
[3.53] JADE Collaboration, W. Bartel et al., Phys. Lett. 115B (1982) 338.

Chapter 4

[4.1] TASSO Collaboration, R. Brandelik et al., Phys. Lett. 89B (1980) 418;
TASSO Collaboration, M. Althoff et al., DESY 83-130 (1983) and Z. Phys. C, Particles and Fields (to be published).
[4.2] JADE Collaboration, W. Bartel et al., Z. Phys. C, Particles and Fields 20 (1983) 187.
[4.3] PLUTO Collaboration, Ch. Berger et al., Phys. Lett. 95B (1980) 313.
[4.4] C. Bacci et al., Phys. Lett. 86B (1979) 234.
[4.5] J.L. Siegrist, Ph.D. thesis SLAC-225 (1980);
M.S. Alam et al., Phys. Rev. Lett. 49 (1982) 357.
[4.6] LENA Collaboration, B. Niczyporuk et al., Z. Phys. C, Particles and Fields 9 (1981) 1.
[4.7] R.D. Field and R.P. Feynman, Nucl. Phys. B136 (1978) 1.
[4.8] B. Andersson, G. Gustafson and T. Sjöstrand, Z. Phys. C, Particles and Fields 6 (1980) 235;
T. Sjöstrand, Lund Preprint, LU TP 80-3 (1980), LU TP 82-3 (1982);
B. Andersson, G. Gustafson and T. Sjöstrand, Nucl. Phys. B197 (1982) 45.
[4.9] Z. Koba, H.B. Nielsen and P. Olesen, Nucl. Phys. B40 (1972) 317.
[4.10] JADE Collaboration, W. Bartel et al., Z. Phys. C, Particles and Fields 9 (1981) 315.
[4.11] CELLO Collaboration, H.J. Behrend et al., Z. Phys. C, Particles and Fields 14 (1982) 189.
[4.12] J.C. Pati and A. Salam, Nucl. Phys. B144 (1978) 445.
[4.13] TASSO Collaboration, R. Brandelik et al., Phys. Lett. 114B (1982) 65.
[4.14] J.F. Patrick et al., Phys. Rev. Lett. 49 (1982) 1232.
[4.15] R. Baier and K. Fey, Z. Phys. C, Particles and Fields 2 (1979) 339;
G. Altarelli et al., Nucl. Phys. B160 (1979) 301.
[4.16] G.G. Hanson, XIII Rencontre de Moriond (1978), ed. J. Tran Thanh Van, Vol. II, p. 15.
[4.17] TASSO Collaboration, R. Brandelik et al., Phys. Lett. 108B (1982) 71.
[4.18] CELLO Collaboration, H.J. Behrend et al., Z. Phys. C, Particles and Fields 14 (1982) 189.
[4.19] CELLO Collaboration, H.J. Behrend et al., Z. Phys. C, Particles and Fields 20 (1983) 207.
[4.20] TASSO Collaboration, R. Brandelik et al., Phys. Lett. 94B (1980) 444.
[4.21] TASSO Collaboration, R. Brandelik et al., Phys. Lett. 113B (1982) 98.
[4.22] TASSO Collaboration, M. Althoff et al., Z. Phys. C, Particles and Fields 17 (1983) 5.
[4.23] TASSO Collaboration, R. Brandelik et al., Phys. Lett. 94B (1980) 91.
[4.24] PLUTO Collaboration, Ch. Berger et al., Phys. Lett. 104B (1981) 79.
[4.25] TASSO Collaboration, R. Brandelik et al., Phys. Lett. 117B (1982) 135.
[4.26] JADE Collaboration, W. Bartel et al., Phys. Lett. 104B (1981) 325.
[4.27] TASSO Collaboration, R. Brandelik et al., Phys. Lett. 105B (1981) 75.
[4.28] TASSO Collaboration, M. Althoff et al., Phys. Lett. 130B (1983) 340.
[4.29] TASSO Collaboration, M. Althoff et al., Phys. Lett. 126B (1983) 493.
[4.30] J.M. Yelton et al., Phys. Rev. Lett. 49 (1982) 430.
[4.31] C. Bebek et al., Phys. Rev. Lett. 49 (1982) 610.
[4.32] DASP Collaboration, R. Brandelik et al., Nucl. Phys. B148 (1979) 189;
D.G. Aschman et al., Phys. Rev. Lett. 41 (1978) 445;
H. Albrecht et al., Phys. Lett. 102B (1981) 291.
[4.33] M. Piccolo et al., Phys. Lett. 86B (1979) 220;
A. Brody et al., Phys. Rev. Lett. 48 (1982) 1070.
[4.34] G.S. Abrams et al., Phys. Rev. Lett. 44 (1980) 10;
M.W. Coles et al., Phys. Rev. D26 (1982) 2190.
[4.35] R.L. Ford and W.R. Nelson, SLAC Report 210 (1978).
[4.36] D.L. Scharre et al., Phys. Rev. Lett. 41 (1978) 1005.
[4.37] H. Burkhardt et al., Nucl. Instr. Meth. 184 (1981) 319.
[4.38] G. Poelz and R. Riethmüller, Nucl. Instr. Meth. 195 (1982) 491.
[4.39] V. Lüth et al., Phys. Lett. 70B (1977) 120;
MARK II Collaboration, J. Dorfan, Proc. Summer Institute on Particle Physics, July 27–August 7, 1981, SLAC, Stanford, California;
CLEO Collaboration, A. Brody et al., Phys. Rev. Lett. 48 (1982) 1070.

[4.40] J. Bürger, Proc. XIII Rencontre de Moriond, II (1978) 133.
[4.41] J. Andersson, G. Gustafson and C. Peterson, Nucl. Phys. B135 (1978) 273;
P. Hoyer, P. Osland, H.G. Sander, T.F. Walsh and P.M. Zerwas, Nucl. Phys. B161 (1979) 349;
A. Ali, E. Pietarinen, G. Kramer and J. Willrodt, Phys. Lett. 93B (1980) 155;
J.B. Andersson, G. Gustafson and T. Sjöstrand, Phys. Lett. 94B (1980) 211.
[4.42] M. Piccolo et al., Phys. Rev. Lett. 39 (1977) 1503;
G.S. Abrams et al., Phys. Rev. Lett. 44 (1980) 10.
[4.43] T. Meyer, Z. Phys. C, Particles and Fields 12 (1982) 77.
[4.44] G. Goldharber, private communication.
[4.45] R.H. Schindler et al., Phys. Rev. D24 (1981) 78.
[4.46] J.M. Yelton et al., Phys. Rev. Lett. 49 (1982) 430.
[4.47] H. Abramowicz et al., Z. Phys. C, Particles and Fields 15 (1982) 19;
N. Ushida et al., Phys. Lett. 121B (1983) 292.
[4.48] EMC Collaboration, J.J. Aubert et al., Nucl. Phys. 213B (1983) 31.
[4.49] J.D. Bjorken, Phys. Rev. D17 (1978) 171;
M. Suzuki, Phys. Lett. 71B (1977) 139.
[4.50] C. Peterson, D. Schlatter, I. Schmitt and P.M. Zerwas, Phys. Rev. D27 (1983) 105.
[4.51] MARK II Collaboration, M.E. Nelson et al., Phys. Rev. Lett. 50 (1983) 1542.
[4.52] MAC Collaboration, E. Fernandez et al., Phys. Rev. Lett. 50 (1983) 2054.
[4.53] MARK J Collaboration, B. Adeva et al., Phys. Rev. Lett. 51 (1983) 443.

Chapter 5

[5.1] CELLO Collaboration, Proposal for a 4π Magnetic Detector for PETRA;
JADE Collaboration, Proposal for a Compact Magnetic Detector at PETRA (1976);
MARK J Collaboration, A Simple Detector to measure e^-e^+ Reactions at High Energies (1976);
PLUTO Collaboration, Proposal for Experiments at PETRA with PLUTO (1976);
TASSO Collaboration, Proposal for a Large 4π Magnetic Detector for PETRA (1976).
[5.2] JADE Collaboration, W. Bartel et al., Phys. Lett. 108B (1982) 140.
[5.3] TASSO Collaboration, R. Brandelik et al., Phys. Lett. 110B (1982) 173.
[5.4] M.L. Perl et al., Phys. Rev. Lett. 35 (1975) 1489; Phys. Lett. 63B (1976) 466;
G.J. Feldman et al., Phys. Rev. Lett. 38 (1977) 117.
[5.5] S.L. Glashow, Nucl. Phys. 22 (1961) 579;
S. Weinberg, Phys. Rev. Lett. 19 (1967) 1264;
A. Salam, Proc. Eighth Nobel Symp., May 1968, ed. N. Svartholm (Wiley, 1968) p. 367;
S.L. Glashow, J. Iliopoulos and L. Maiani, Phys. Rev. D2 (1970) 1285.
[5.6] M.K. Gaillard, B.W. Lee and J.L. Rosner, Rev. Mod. Phys. 47 (1975) 277.
[5.7] UA1 Collaboration, G. Arnison et al., Phys. Lett. 126B (1983) 398;
UA2 Collaboration, P. Bagnaia et al., Phys. Lett. 129B (1983) 130.
[5.8] H.J. Bhabha, Proc. Roy. Soc. (London) A154 (1935) 195.
[5.9] C. Møller, Ann. Phys. 14 (1932) 531.
[5.10] N. Cabibbo and R. Gatto, Phys. Rev. 124 (1961) 1577;
T. Kinoshita, J. Pestieau, P. Roy and H. Terazawa, Phys. Rev. D2 (1970) 910;
J. Godine and A. Hankey, Phys. Rev. D6 (1972) 3301;
R. Budny, Phys. Lett. 45 (1973) 340.
[5.11] Particle Data Group, M. Roos et al., Review of Particle Properties, Phys. Lett. 111B (1982).
[5.12] R. Budny, Phys. Lett. 55B (1975) 227.
[5.13] CELLO Collaboration, H.J. Behrend et al., Phys. Lett. 103B (1981) 148;
CELLO Collaboration, H.J. Behrend et al., Phys. Lett. 123B (1983) 127.
[5.14] CELLO Collaboration, H.J. Behrend et al., Z. Phys. C, Particles and Fields 16 (1983) 301.
[5.15] JADE Collaboration, W. Bartel et al., Phys. Lett. 92B (1980) 206.
[5.16] JADE Collaboration, W. Bartel et al., Phys. Lett. 99B (1981) 281.
[5.17] JADE Collaboration, W. Bartel et al., Z. Phys. C, Particles and Fields 19 (1983) 197.
[5.18] MARK J Collaboration, D.P. Barber et al., Phys. Rev. Lett. 42 (1979) 1110.
[5.19] MARK J Collaboration, D.P. Barber et al., Phys. Rev. Lett. 43 (1979) 1915.
[5.20] MARK J Collaboration, D.P. Barber et al., Phys. Lett. 95B (1980) 149.
[5.21] MARK J Collaboration, D.P. Barber et al., Phys. Rev. Lett. 46 (1981) 1663.
[5.22] PLUTO Collaboration, Ch. Berger et al., Z. Phys. C, Particles and Fields 4 (1980) 269.
[5.23] PLUTO Collaboration, Ch. Berger et al., Z. Phys. C, Particles and Fields 7 (1981) 289.

[5.24] TASSO Collaboration, R. Brandelik et al., Phys. Lett. 94B (1980) 259;
TASSO Collaboration, R. Brandelik et al., Phys. Lett 117B (1982) 365.
[5.25] A. Böhm, DESY Report 82-084 and Proc. SLAC Summer Institute on Particle Physics, Stanford, California, August 1982.
[5.26] TASSO Collaboration, M. Althoff et al., DESY 83-089 (1983) and Z. Phys. C, Particles and Fields 22 (1984) 13.
[5.27] M. Davier, Proc. XXI Intern. Conf. on High Energy Physics, Paris, July 1982, p. C3-471.
[5.28] Y.S. Tsai, Phys. Rev. D4 (1971) 2821;
H.B. Thacker and J.J. Sakurai, Phys. Lett. 36B (1971) 103.
[5.29] CELLO Collaboration, H.J. Behrend et al., Phys. Lett. 114B (1982) 282.
[5.30] CELLO Collaboration, H.J. Behrend et al., Phys. Lett. 127B (1983) 270.
[5.31] J.G. Branson, MIT-LNS Technical Report Number 133 and Lectures at the Intern. School of Subnuclear Physics, Erice (1982).
[5.32] F.A. Berends, K.J.F. Gaemers and R. Gastmans, Nucl. Phys. B63 (1973) 381 and B68 (1974) 541;
F.A. Berends and R. Gastmans, Nucl. Phys. B61 (1973) 414;
F.A. Berends and R. Kleiss, Nucl. Phys. B178 (1981) 141;
F.A. Berends, R. Kleiss and S. Jadach, Nucl. Phys. B202 (1982) 63;
M. Böhm and W. Hollik, DESY 83-060 (1983).
[5.33] A. Böhm, Proc. Intern. Europhysics Conf. on High Energy Physics, Brighton, UK, July 1983.
[5.34] CELLO Collaboration, H.J. Behrend et al., Z. Phys. C, Particles and Fields 14 (1982) 283;
PLUTO Collaboration, Ch. Berger et al., Z. Phys. C, Particles and Fields 21 (1983) 53.
[5.35] MARK J Collaboration, B. Adeva et al., Phys. Rev. Lett. 48 (1982) 1701.
[5.36] B. Naroska, Proc. 1983 Intern. Symp. on Lepton and Photon Interactions at High Energies, Cornell University, Ithaca, NY, August 1983.
[5.37] TASSO Collaboration, R. Brandelik et al., Phys. Lett. 113B (1982) 499.
[5.38] JADE Collaboration, W. Bartel et al., Phys. Lett. 129B (1983) 145.
[5.39] JADE Collaboration, W. Bartel et al., Phys. Lett. 101B (1981) 361.
[5.40] TASSO Collaboration, M. Althoff et al., Phys. Lett. 126B (1983) 493.
[5.41] R.P. Feynman, Phys. Rev. 76 (1949) 769;
V.B. Berestetskii, O.N. Krokhin and A.K. Khlebnikov, ZETF 30 (1956) 788 [English transl. Soviet Physics – JETP 3 (1956) 761];
S.D. Drell, Ann. Phys. 4 (158) 75;
B. De Tollis, Nuovo Cim. 16 (1960) 203;
J.A. McClure and S.D. Drell, Nuovo Cim. 37 (1965) 1638.
[5.42] MARK J Collaboration, D.P. Barber et al., Phys. Rev. Lett. 45 (1980) 1904.
[5.43] MARK J Collaboration, B. Adeva et al., Phys. Rev. Lett. 48 (1982) 967.
[5.44] MARK J Collaboration, Phys. Report 63 (1980) 337.
[5.45] PLUTO Collaboration, Ch. Berger et al., Phys. Lett. 99B (1981) 489.
[5.46] PLUTO Collaboration, Ch. Berger et al., Phys. Lett. 94B (1980) 87.
[5.47] K.H. Mess and B.H. Wiik, DESY Report 82-011 (1982) and Les Houches, Session XXXVII, 1981, Gauge theories in high energy physics, eds. M.K. Gaillard and R. Stora (North-Holland, Amsterdam, 1983).
[5.48] P.Q. Hung and J.J. Sakurai, Nucl. Phys. B143 (1978) 81;
J.D. Bjorken, Phys. Rev. D19 (1979) 335;
E.H. de Groot, G.J. Gounaris and D. Schildknecht, Phys. Lett. 85B (1979) 399; 90B (1980) 427; Z. Phys. C, Particles and Fields 5 (1980) 127;
D. Schildknecht, Proc. Intern. School of Subnuclear Physics (Erice, 1980); Bielefeld preprint BI-TP 81/12;
V. Barger, W.Y. Keung and E. Ma, Phys. Rev. Lett. 44 (1980) 1169; Phys. Rev. D22 (1980) 727; Phys. Lett. 94B (1980) 377.

Chapter 6

[6.1] N. Arteaga-Romero, A. Jaccarini and P. Kessler, C.R. Acad. Sci. Ser. B296 (1969) 153 and 1133;
H. Cheng and T.T. Wu, Phys. Rev. Lett. 23 (1969) 1311;
S.J. Brodsky, T. Kinoshita and H. Terazawa, Phys. Rev. Lett. 25 (1970) 972;
B. Schrempp-Otto, F. Schrempp and T.F. Walsh, Phys. Lett. B36 (1971) 463;
B. Renner, Nucl. Phys. B30 (1971) 634;
G. Schierholz and K. Sundermeyer, Nucl. Phys. B40 (1972) 125;
D. Faiman, H.J. Lipkin and H.R. Rubinstein, Phys. Lett. 59B (1975) 269;
J. Babcock and J.L. Rosner, Phys. Rev. D14 (1976) 1286;
M. Greco and Y. Srivastava, Nuovo Cim. 43A (1978) 88;
V.M. Budnev and A.E. Kaloshin, Phys. Lett. 86B (1979) 351;
V.M. Budnev, I.F. Ginzburg and V.G. Serbo, Phys. Lett. 96B (1980) 387;
J.H. Field, E. Pietarinen and K. Kajantie, Nucl. Phys. B171 (1980) 377.
[6.2] Particle Data Group, M. Roos et al., Review of Particle Properties, Phys. Lett. 111B (1982).
[6.3] J.J. Sakurai, Ann. Phys. 11 (1960) 1.
[6.4] C.F. v. Weizsäcker, Z. Phys. 88 (1934) 612;
E.J. Williams, Kgl. Dansk Videnskab. Selskab 13 (1935) No. 4.

[6.5] H. Cheng and T.T. Wu, Nucl. Phys. B32 (1971) 461.
[6.6] MARK J Collaboration, B. Adeva et al., Phys. Rev. Lett. 48 (1982) 721.
[6.7] PLUTO Collaboration, Ch. Berger et al., Nucl. Phys. B202 (1982) 189.
[6.8] CELLO Collaboration, H.J. Behrend et al., Phys. Lett. 126B (1983) 384.
[6.9] J.A.M. Vermaseren, Program Write-Up (1978) and Proc. Intern. Workshop on $\gamma\gamma$ Collisions (Amiens, France, 1980), Lecture notes in physics, Vol. 134 (Springer, 1980).
[6.10] M. Defrise, Z. Phys. C, Particles and Fields 9 (1981) 41;
M. Defrise, S. Ong, J. Salva and C. Carimalo, Phys. Rev. D23 (1981) 663.
[6.11] PLUTO Collaboration, Ch. Berger et al., Phys. Lett. 89B (1979) 120.
[6.12] PLUTO Collaboration, Ch. Berger et al., Phys. Lett. 99B (1981) 287.
[6.13] T.F. Walsh, J. de Phys. C2 Suppl. 3 (1974) 77;
S.J. Brodsky, J. de Phys. C2 Suppl. 3 (1974) 69;
J.L. Rosner, in: ISABELLE Physics Prospects, BNL report 17552 (1972) 316.
[6.14] F. Low, Phys. Rev. 120 (1960) 582.
[6.15] JADE Collaboration, W. Bartel et al., Phys. Lett. 113B (1982) 190.
[6.16] CELLO Collaboration, H.J. Behrend et al., Phys. Lett. 114B (1982) 378 [Errata: 125B (1983) 518].
[6.17] MARK II Collaboration, G. Abrams et al., Phys. Rev. Lett. 43 (1979) 477;
P. Jenni, Proc. Intern. Workshop on $\gamma\gamma$ collisions (Amiens, France, 1980).
[6.18] H. Suura, T.F. Walsh and B.-L. Young, Nuovo Cim. Lett. 4 (1972) 505.
[6.19] PLUTO Collaboration, Ch. Berger et al., Phys. Lett. 94B (1980) 254.
[6.20] TASSO Collaboration, R. Brandelik et al., Z. Phys. C, Particles and Fields 10 (1981) 117.
[6.21] A. Roussarie et al., Phys. Lett. 105B (1981) 304.
[6.22] C. Edwards et al., Phys. Lett. 110B (1982) 82.
[6.23] F.J. Gilman, Proc. 1979 Conf. on Two-photon interactions (Lake Tahoe) p. 215.
[6.24] TASSO Collaboration, M. Althoff et al., Phys. Lett. 121B (1983) 216;
Lutz Köpke, Ph.D thesis (1983), BONN-IR-83-16, Bonn University, Bonn, Germany.
[6.25] H.J. Lipkin, Nucl. Phys. B7 (1968) 321, Proc. EPS Int. Conf. on High Energy Physics, Palermo 1975, p. 609;
D. Faiman, H.J. Lipkin and H.R. Rubenstein, Phys. Lett. 59B (1975) 269.
[6.26] N. Samios, M. Goldberg and B.T. Meadows, Rev. Mod. Phys. 46 (1974) 49;
L. Montanet, Reports on Progress in Physics 46 (1983) 337.
[6.27] C. Edwards et al., Phys. Rev. Lett. 48 (1982) 458.
[6.28] TASSO Collaboration, R. Brandelik et al., Phys. Lett. 97B (1980) 448.
[6.29] TASSO Collaboration, M. Althoff et al., Z. Phys. C, Particles and Fields 16 (1982) 13.
[6.30] D.L. Burke et al., Phys. Lett. 103B (1981) 153.
[6.31] H. Goldberg and T. Weiler, Phys. Lett. 102B (1981) 63;
J. Layssac and F.M. Renard, Seminar on $\gamma\gamma$ Physics, Clermont-Ferrand, March 1981.
[6.32] R.M. Godbole and K.V.L. Sarma, Phys. Lett. 109B (1982) 504;
S. Minami, Lett. Nuovo Cim. 34 (1982) 125;
Bing An Li and K.F. Liu, Phys. Lett. 118B (1982) 435;
N.N. Achasov, S.A. Devyanin, and G.N. Shestakov, Phys. Lett. 108B (1982) 134;
K. Biswal and S.P. Misra, Phys. Rev. D26 (1982) 3020.
[6.33] C. Edwards et al., Phys. Rev. Lett. 49 (1982) 259.
[6.34] TASSO Collaboration, R. Brandelik et al., Phys. Lett. 108B (1982) 67.
[6.35] TASSO Collaboration, M. Althoff et al., Phys. Lett. 130B (1983) 449.
[6.36] P.H. Damgaard, Nucl. Phys. B211 (1983) 435.
[6.37] T.M. Himel et al., Phys. Rev. Lett. 45 (1980) 1146;
R. Partridge et al., Phys. Rev. Lett. 45 (1980) 1150.
[6.38] JADE Collaboration, W. Bartel et al., Phys. Lett. 107B (1981) 163;
R. Partridge et al., Phys. Rev. Lett. 45 (1980) 1150.
[6.39] TASSO Collaboration, R. Brandelik et al., Phys. Lett. 107B (1981) 290.
[6.40] S.M. Berman, J.D. Bjorken and J.B. Kugot, Phys. Rev. D4 (1971) 3388;
S. Brodsky, T.A. DeGrand, J.F. Gunion and J.H. Weis, Phys. Rev. D19 (1979) 1418.
[6.41] PLUTO Collaboration, Ch. Berger et al., Phys. Lett. 107B (1981) 168.
[6.42] JADE Collaboration, W. Bartel et al., Phys. Lett. 121B (1983) 203.
[6.43] CELLO Collaboration, H.J. Behrend et al., Phys. Lett. 126B (1983) 391.
[6.44] CELLO Collaboration, H.J. Behrend et al., Phys. Lett. 118B (1982) 211.
[6.45] C. Peterson, T.F. Walsh and P.M. Zerwas, Nucl. Phys. B174 (1980) 424.
[6.46] E. Witten, Nucl. Phys. B120 (1977) 189.

[6.47] G. Altarelli and G. Parisi, Nucl. Phys. B126 (1977) 298;
W.A. Bardeen and A.J. Buras, Phys. Rev. D20 (1979) 166;
D.W. Duke and J.F. Owens, Phys. Rev. D22 (1980) 2280;
S.J. Brodsky, Proc. Summer Inst. Particle Phys., SLAC Report No. 224 (1980) p. 133;
M.K. Chase, Nucl. Phys. B189 (1981) 461.

Chapter 7

[7.1] S.L. Glashow, Nucl. Phys. 22 (1961) 579;
S. Weinberg, Phys. Rev. Lett. 19 (1967) 1264;
A. Salam, Proc. Eighth Nobel Symp., May 1968, ed. N. Svartholm (Wiley, 1968) p. 367;
S.L. Glashow, J. Iliopoulos and L. Maiani, Phys. Rev. D2 (1970) 1285.
[7.2] CELLO Collaboration, H.J. Behrend et al., DESY 81-029 (1981);
[7.3] JADE Collaboration, W. Bartel et al., Phys. Lett. 88B (1979) 171;
JADE Collaboration, W. Bartel et al., Phys. Lett. 89B (1979) 136;
JADE Collaboration, W. Bartel et al., Phys. Lett. 91B (1980) 152;
JADE Collaboration, W. Bartel et al., Phys. Lett. 100B (1981) 364.
[7.4] JADE Collaboration, W. Bartel et al., Phys. Lett. 129B (1983) 145.
[7.5] MARK J Collaboration, D.P. Barber et al., Phys. Rev. Lett. 42 (1979) 1113;
MARK J Collaboration, D.P. Barber et al., Phys. Rev. Lett. 43 (1979) 901;
MARK J Collaboration, D.P. Barber et al., Phys. Lett. 85B (1979) 463;
MARK J Collaboration, D.P. Barber et al., Phys. Rev. Lett. 44 (1980) 1722.
[7.6] MARK J Collaboration, B. Adeva et al., Phys. Rev. Lett. 50 (1983) 799.
[7.7] PLUTO Collaboration, Ch. Berger et al., Phys. Lett. 81B (1979) 410;
PLUTO Collaboration, Ch. Berger et al., Phys. Lett. 86B (1979) 413.
[7.8] PLUTO Collaboration, Ch. Berger et al., Phys. Lett. 91B (1980) 148.
[7.9] TASSO Collaboration, R. Brandelik et al., Phys. Lett. 83B (1979) 261;
TASSO Collaboration, R. Brandelik et al., Z. Phys. C, Particles and Fields 4 (1980) 87;
TASSO Collaboration, R. Brandelik et al., Phys. Lett. 88B (1979) 199.
[7.10] TASSO Collaboration, R. Brandelik et al., Phys. Lett. 113B (1982) 499.
[7.11] M. Kobayashi and K. Maskawa, Prog. Theor. Phys. 49 (1973) 652.
[7.12] B.H. Wiik, DESY Report 80-124 (1980) and Proc. XXth Intern. Conf. on High Energy Physics, University of Wisconsin, Madison, Wisconsin, July 1980.
[7.13] PLUTO Collaboration, Ch. Berger et al., Phys. Rev. Lett. 45 (1980) 1533.
[7.14] JADE Collaboration, W. Bartel et al., Phys. Lett. 99B (1981) 277.
[7.15] MARK J Collaboration, B. Adeva et al., Phys. Rev. Lett. 51 (1983) 443.
[7.16] CELLO Collaboration, H.J. Behrend et al., Z. Phys. C, Particles and Fields 19 (1983) 291.
[7.17] H.T. Nieh, T.T. Wu and C.N. Yang, Phys. Rev. Lett. 34 (1975) 49.
[7.18] J.D. Jackson and D.L. Scharre, Nucl. Instr. Meth. 128 (1975) 13.
[7.19] J.-E. Augustin et al., Phys. Rev. Lett. 33 (1974) 1406.
[7.20] Deutsches Elektronen-Synchrotron, PETRA – updated version of the PETRA proposal, DESY Hamburg, February 1976.
[7.21] P.W. Higgs, Phys. Lett. 12 (1964) 132; Phys. Rev. Lett. 13 (1964) 508; Phys. Rev. 145 (1966) 1156;
F. Englert and R. Brout, Phys. Rev. Lett. 13 (1964) 321;
G.S. Guralnik, C.R. Hagen and T.W.B. Kibble, Phys. Rev. Lett. 13 (1964) 585;
T.W.B. Kibble, Phys. Rev. 155 (1967) 1554.
[7.22] E. Golowich and T.C. Yang, Phys. Lett. 80B (1979) 245;
L.N. Chang and J.E. Kim, Phys. Lett. 81B (1979) 233;
H.E. Haber, G.L. Kane and T. Sterling, Nucl. Phys. B161 (1979) 493;
G. Barbiellini et al., DESY 79-027 (1979), and references therein.
[7.23] S. Weinberg, Phys. Rev. D13 (1976) 974; D19 (1979) 1277;
L. Susskind, Phys. Rev. D20 (1979) 2619;
S. Dimopoulos and L. Susskind, Nucl. Phys. B155 (1979) 237;
E. Eichten and K.D. Lane, Phys. Lett. 90B (1980) 125;
M.A.B. Beg, H.D. Politzer and P. Ramond, Phys. Rev. Lett. 43 (1979) 1701;
S. Dimopoulos, Nucl. Phys. B168 (1980) 69;
M.E. Peskin, Nucl. Phys. B175 (1980) 197;
S. Dimopoulos, S. Raby and P. Sikivie, Nucl. Phys. B176 (1980) 449;
S. Dimopoulos, S. Raby and G.L. Kane, Nucl. Phys. B182 (1981) 77;
E. Fahri and L. Susskind, Phys. Reports 74 (1981) 277;

A. Ali, DESY 81-032 (1981);
G. Barbiellini et al., DESY 81-064, and references therein.
[7.24] S. Dimopoulos, Nucl. Phys. B168 (1980) 69;
M.E. Peskin, Nucl. Phys. B175 (1980) 197;
J. Preskill, Nucl. Phys. B177 (1981) 21;
S. Chadha and M.E. Peskin, Nucl. Phys. B185 (1981) 61 and B187 (1981) 541.
[7.25] J. Ellis, M.K. Gaillard, D.V. Nanopoulos and P. Sikivie, Nucl. Phys. B182 (1981) 529.
[7.26] N. Cabibbo and R. Gatto, Phys. Rev. 124 (1961) 1577.
[7.27] JADE Collaboration, W. Bartel et al., Phys. Lett. 114B (1982) 211.
[7.28] CELLO Collaboration, H.J. Behrend et al., Phys. Lett. 114B (1982) 287.
[7.29] MARK J Collaboration, B. Adeva et al., Phys. Lett. 115B (1982) 345.
[7.30] MARK II Collaboration, C.A. Blocker et al., Phys. Rev. Lett. 49 (1982) 517.
[7.31] TASSO Collaboration, M. Althoff et al., Phys. Lett. 122B (1983) 95.
[7.32] Sau Lan Wu, Z. Phys. C, Particles and Fields 9 (1981) 329.
[7.33] Sau Lan Wu and Georg Zobernig, Z. Phys. C, Particles and Fields 2 (1979) 107.
[7.34] Yu. A. Gol'fand and E.P. Likhtman, JETP Lett. 13 (1971) 323;
D.V. Volkov and V.P. Akulov, Phys. Lett. 46B (1973) 109;
J. Wess and B. Zumino, Nucl. Phys. B70 (1974) 39;
A. Salam and J. Strathdee, Nucl. Phys. B76 (1974) 477.
[7.35] P. Fayet, Phys. Lett. 69B (1977) 489;
D.V. Nanopoulos, A. Savoy-Navarro and Ch. Tao (organizers), Proc. Workshop on Supersymmetry versus Experiment, CERN, Geneva, Switzerland, April 1983.
[7.36] MARK J Collaboration, D.P. Barber et al., Phys. Rev. Lett. 45 (1980) 1904.
[7.37] TASSO Collaboration, R. Brandelik et al., Phys. Lett. 117B (1982) 365.
[7.38] CELLO Collaboration, H.J. Behrend et al., Phys. Lett. 123B (1983) 127.
[7.39] N. Cabibbo, G.R. Farrar and K. Maiani, Phys. Lett. 105B (1981) 155.
[7.40] J.E. Gunn et al., Astrophys. J. 223 (1978) 1015.
[7.41] P. Fayet, Phys. Lett. 84B (1979) 421.
[7.42] TASSO Collaboration, R. Brandelik et al., Phys. Lett. 99B (1981) 163.
[7.43] PLUTO Collaboration, Ch. Berger et al., Phys. Lett. 99B (1981) 489.
[7.44] JADE Collaboration, W. Bartel et al., Phys. Lett. 123B (1983) 353.
[7.45] J.C. Pati and A. Salam, Phys. Rev. D10 (1974) 275;
J.C. Pati, Phys. Lett. 98B (1981) 40;
H. Terazawa, Y. Chikashige and K. Akama, Phys. Rev. D15 (1977) 480;
H. Terazawa, Institut des Sciences Nucleaires Report No. 401, 1981;
S. Glashow, Harvard University Report No. HUTP-77/A005, 1977;
Y. Ne'eman, Phys. Lett. 82B (1979) 69;
A. Hariri and N. Sieberg, Phys. Lett. 98B (1981) 269;
M.A. Shupe, Phys. Lett. 86B (1979) 87;
R. Casalbuoni and R. Gatto, Phys. Lett. 93B (1980) 47, and Université de Genève Report No. UGBA-DPT981/06-272;
S.H. Albright, B. Schrempp and F. Schrempp, DESY 81-038 (1981);
M.E. Peskin, in: Proc. Intern. Symp. on Lepton and Photon Interactions at High Energies, Bonn, 1981, ed. W. Pfeill (Physikalisches Institut, Universität, Bonn, 1981);
T.D. Lee, Particle Physics and Introduction to Field Theory (Harwood Academic, New York, 1981) p. 825.
[7.46] MARK J Collaboration, B. Adeva et al., Phys. Rev. Lett. 48 (1982) 967.
[7.47] A. Litke, Ph.D. thesis, Harvard University, 1970 (unpublished).
[7.48] MAC Collaboration, W.T. Ford et al., Phys. Rev. Lett. 51 (1983) 257.
[7.49] G. Flügge, Proc. DESY 1982 Workshop, DESY, Hamburg, September 1982.
[7.50] H. Pietschmann and H. Stremnitzer, Universität Wien Report UWTH Ph-1982-13.
[7.51] PLUTO Collaboration, Ch. Berger et al., Phys. Lett. 94B (1980) 87.
[7.52] TASSO Collaboration, R. Brandelik et al., Phys. Lett. 94B (1980) 259.
[7.53] CELLO Collaboration, H.J. Behrend et al., Phys. Lett. 103B (1981) 148.
[7.54] JADE Collaboration, W. Bartel et al., Z. Phys. C, Particles and Fields 19 (1983) 197.
[7.55] JADE Collaboration, W. Bartel et al., Z. Phys. C, Particles and Fields 6 (1980) 295.
[7.56] H. Fritzsch, Phys. Lett. 67B (1977) 451.
[7.57] J.D. Bjorken and C. Llewellyn Smith, Phys. Rev. D7 (1973) 887;
A. Ali, Phys. Rev. D10 (1974) 2801;
F. Bletzacker and H.T. Nieh, Phys. Rev. D16 (1977) 2115.
[7.58] P.A.M. Dirac, Proc. Roy. Soc. (London) 133A (1931) 60.
[7.59] P. Musset, M. Price and E. Lohrmann, Phys. Lett. 128B (1983) 333.

[7.60] S.P. Ahlen, Phys. Rev. D17 (1978) 229;
S.P. Ahlen and K. Kinoshita, Phys. Rev. D26 (1982) 2347;
For small values of β, see S. Drell et al., Phys. Rev. Lett. 50 (1983) 644.
[7.61] K. Kinoshita, P.B. Price and D. Fryberger, Phys. Rev. Lett. 48 (1982) 77.
[7.62] M. Gell-Mann, Phys. Lett. 8 (1964) 214.
[7.63] G. Zweig, CERN-Report TH 401 and TH 412 (1964).
[7.64] B.M. McCoy and T.T. Wu, Phys. Lett. 72B (1977) 219.
[7.65] J.M. Weiss et al., Phys. Lett. 101B (1981) 439.
[7.66] A. Marini et al., Phys. Rev. Lett. 48 (1982) 1649.

Appendix

(Publications appeared after July 15, 1983 are mostly not covered by this report.)

A1. Publications of the CELLO collaboration

(1) *CELLO: A new detector at PETRA.*
By CELLO Collaboration, H.J. Behrend et al.,
DESY 80-128, December 1980,
Phys. Scripta 23 (1981) 610.

(2) *Measurement of* $e^+e^- \to e^+e^-$ *and* $e^+e^- \to \gamma\gamma$ *at energies up to* 36.7 *GeV.*
By CELLO Collaboration, H.J. Behrend et al.,
DESY 81-021, May 1981,
Phys. Lett. 103B (1981) 148.

(3) *Search for narrow quarkonium states and pair production of new heavy quarks at c.m. energies from* 33 *GeV to* 36.7 *GeV.*
By CELLO Collaboration, H.J. Behrend et al.,
DESY 81-029, June 1981.

(4) *Topology of hadronic* e^+e^- *annihilation events at* 22 *GeV and* 34 *GeV c.m. energy.*
By CELLO Collaboration, H.J. Behrend et al.,
DESY 81-080, November 1981,
Phys. Lett. 110B (1982) 329.

(5) *Determination of the radiative widths of the* η' *and* A_2 *from two photon exchange production.*
By CELLO Collaboration, H.J. Behrend et al.,
DESY 82-008, February 1982,
Phys. Lett. 114B (1982) 378 (Erratum: Phys. Lett. 125B (1983) 518).

(6) *An analysis of the charged and neutral energy flow in* e^+e^- *hadronic annihilation at* 34 *GeV, and a determination of the QCD effective coupling constant.*
By CELLO Collaboration, H.J. Behrend et al.,
DESY 82-017, March 1982,
Phys. Lett. 113B (1982) 427.

(7) *Measurement of inclusive γ and π^0 spectra and a comparison of the neutral and charged components in hadronic events in e^+e^- annihilation at 34 GeV.*
By CELLO Collaboration, H.J. Behrend et al.,
DESY 82-018, March 1982,
Z. Phys. C, Particles and Fields 14 (1982) 189.

(8) *Measurement of the reaction $e^+e^- \to \mu^+\mu^-$ for $14 \leq \sqrt{s} \leq 36.4$ GeV.*
By CELLO Collaboration, H.J. Behrend et al.,
DESY 82-019, March 1982,
Z. Phys. C, Particles and Fields 14 (1982) 283.

(9) *Measurement of $e^+e^- \to \tau^+\tau^-$ at high energy and properties of the τ lepton.*
By CELLO Collaboration, H.J. Behrend et al.,
DESY 82-020, April 1982,
Phys. Lett. 114B (1982) 282.

(10) *Scalar lepton search with the CELLO detector at PETRA.*
By CELLO Collaboration, H.J. Behrend et al.,
DESY 82-021, April 1982,
Phys. Lett. 114B (1982) 287.

(11) *Analysis of the energy weighted angular correlations in hadronic e^+e^- annihilations at 22 GeV and 34 GeV.*
By CELLO Collaboration, H.J. Behrend et al.,
DESY 82-022, April 1982,
Z. Phys. C, Particles and Fields 14 (1982) 95.

(12) *Observation of topologically isolated energetic electrons in e^+e^- interactions.*
By CELLO Collaboration, H.J. Behrend et al.,
DESY 82-055, August 1982,
Phys. Lett. 118B (1982) 211.

(13) *Measurement of the τ lifetime.*
By CELLO Collaboration, H.J. Behrend et al.,
DESY 82-056, August 1982,
Nucl. Phys. B211 (1983) 369.

(14) *The influence of fragmentation models on the determination of the strong coupling constant in e^+e^- annihilation into hadrons.*
By CELLO Collaboration, H.J. Behrend et al.,
DESY 82-061, September 1982,
Nucl. Phys. B218 (1983) 269.

(15) *Coupling strengths of weak neutral currents from leptonic final states at 22 GeV and 34 GeV.*
By CELLO Collaboration, H.J. Behrend et al.,
DESY 82-063, September 1982,
Z. Phys. C, Particles and Fields 16 (1983) 301.

(16) *Investigation of two photon final states in* e^+e^- *annihilation at* $\langle\sqrt{s}\rangle = 34.2$ *GeV.*
By CELLO Collaboration, H.J. Behrend et al.,
DESY 82-080, December 1982,
Phys. Lett. 123B (1983) 127.

(17) *Lepton pair production in deep inelastic* $e\gamma$ *scattering.*
By CELLO Collaboration, H.J. Behrend et al.,
DESY 83-017, March 1983,
Phys. Lett. 126B (1983) 384.

(18) *Experimental study of the hadronic photon structure function.*
By CELLO Collaboration, H.J. Behrend et al.,
DESY 83-018, March 1983,
Phys. Lett. 126B (1983) 391.

(19) τ *branching ratios and polarization limits in* e^+e^- *interactions at* $\sqrt{s} = 34$ *GeV.*
By CELLO Collaboration, H.J. Behrend et al.,
DESY 83-019, March 1983,
Phys. Lett. 127B (1983) 270.

(20) *Inclusive production of electrons and muons in multihadronic events at PETRA.*
By CELLO Collaboration, H.J. Behrend et al.,
DESY 83-034, May 1983,
Z. Phys. C, Particles and Fields 19 (1983) 291.

(21) *Inclusive* γ *and* π^0 *production in* e^+e^- *annihilation at* 14, 22 *and* 34 *GeV c.m. energy*
By CELLO Collaboration, H.J. Behrend et al.,
DESY 83-066, July 1983,
Z. Phys. C, Particles and Fields 20 (1983) 207.

(22) *Measurement of the reaction* $\gamma\gamma \to \pi^+\pi^+\pi^-\pi^-$ *at PETRA.*
By CELLO Collaboration, H.J. Behrend et al.,
DESY 83-081, September 1983,
Z. Phys. C, Particles and Fields 21 (1984) 205.

(23) *On the model dependence of the determination of the strong coupling constant in second order QCD from* e^+e^- *annihilation into hadrons.*
By CELLO Collaboration, H.J. Behrend et al.,
DESY 83-127, December 1983,
Phys. Lett. 138B (1984) 311.

(24) *Production of the* f^0 *meson in photon photon collisions.*
By CELLO Collaboration, H.J. Behrend et al.,
DESY 84-007, January 1984,
Z. Phys. C, Particles and Fields.

(25) *New data on semihadronic decays of the τ lepton.*
By CELLO Collaboration, H.J. Behrend et al.,
DESY 84-008, January 1984,
Phys. Lett.

(26) *Limits on spin 0 bosons in* e^+e^- *annihilation up to 45.2 Ge V c.m. energy.*
By CELLO Collaboration, H.J. Behrend et al.,
DESY 84-020, February 1984,
Phys. Lett. 140B (1984).

(27) *Observation of a multiparticle event with 2 isolated energetic muons in* e^+e^- *interactions.*
By CELLO Collaboration, H.J. Behrend et al.,
DESY 84-024, March 1984,
Phys. Lett.

A2. Publications of the JADE Collaboration

(1) *Total cross section for hadron production by* e^+e^- *annihilation at PETRA energies.*
By JADE Collaboration, W. Bartel et al.,
DESY 79-64, October 1979,
Phys. Lett. 88B (1979) 171.

(2) *Search for new flavor production at PETRA.*
By JADE Collaboration, W. Bartel et al.,
DESY 79-70, October 1979,
Phys. Lett. 89B (1979) 136.

(3) *Observation of planar three-jet events in* e^+e^- *annihilation and evidence for gluon bremsstrahlung.*
By JADE Collaboration, W. Bartel et al.,
DESY 79-80, December 1979,
Phys. Lett. 91B (1980) 142.

(4) *Search for narrow resonances in* e^+e^- *annihilation at c.m. energies between 29.90 GeV and 31.46 GeV.*
By JADE Collaboration, W. Bartel et al.,
DESY 80-04, January 1980,
Phys. Lett. 91B (1980) 152.

(5) *Test of quantum electrodynamics at PETRA.*
By JADE Collaboration, W. Bartel et al.,
DESY 80-14, March 1980,
Phys. Lett. 92B (1980) 206.

(6) *Search for fractional charge and heavy stable particles at PETRA.*
By JADE Collaboration, W. Bartel et al.,
DESY 80-71, July 1980,
Z. Phys. C, Particles and Fields 6 (1980) 295.

(7) *Prompt muons in multiparticle events from* e^+e^- *annihilation at PETRA.*
By JADE Collaboration, W. Bartel et al.,
DESY 80-86, September 1980,
Phys. Lett. 99B (1981) 277.

(8) *Experimental limits on the strength of weak neutral currents in lepton pair production at PETRA energies.*
By JADE Collaboration, W. Bartel et al.,
DESY 80-123, December 1980,
Phys. Lett. 99B (1981) 281.

(9) *Search for narrow resonances in* e^+e^- *annihilation at c.m. energies between* 33.0 *GeV and* 36.72 *GeV.*
By JADE Collaboration, W. Bartel et al.,
DESY 81-006, January 1981,
Phys. Lett. 100B (1981) 364.

(10) *Experimental study of jets in electron–positron annihilation.*
By JADE Collaboration, W. Bartel et al.,
DESY 81-009, February 1981,
Phys. Lett. 101B (1981) 129.

(11) *A determination of quark weak couplings at PETRA energies.*
By JADE Collaboration, W. Bartel et al.,
DESY 81-015, March 1981,
Phys. Lett. 101B (1981) 361.

(12) *Energy carried by gamma rays and neutral particles in multihadron final states at PETRA.*
By JADE Collaboration, W. Bartel et al.,
DESY 81-025, June 1981,
Z. Phys. C, Particles and Fields 9 (1981) 315.

(13) *Baryon production in* e^+e^- *annihilation at PETRA.*
By JADE Collaboration, W. Bartel et al.,
DESY 81-028, June 1981,
Phys. Lett. 104B (1981) 325.

(14) *Observation of high-*p_T *jets in two-photon interactions.*
By JADE Collaboration, W. Bartel et al.,
DESY 81-048, August 1981,
Phys. Lett. 107B (1981) 163.

(15) *Observation of a charge asymmetry in* $e^+e^- \to \mu^+\mu^-$.
By JADE Collaboration, W. Bartel et al.,
DESY 81-072, October 1981,
Phys. Lett. 108B (1982) 140.

(16) *A measurement of the reaction* $e^+e^- \to e^+e^-\eta'$ *and the radiative width* $\Gamma_{\eta'} \to \gamma\gamma$ *at PETRA.*
By JADE Collaboration, W. Bartel et al.,
DESY 82-007, February 1982,
Phys. Lett. 113B (1982) 190.

(17) *Upper limit on beauty lifetime and lower limit on weak mixing angles.*
By JADE Collaboration, W. Bartel et al.,
DESY 82-014, March 1982,
Phys. Lett. 114B (1982) 71.

(18) *Observation of four-jet structure in* e^+e^- *annihilation at* $\sqrt{s} = 33$ *GeV.*
By JADE Collaboration, W. Bartel et al.,
DESY 82-016, March 1982,
Phys. Lett. 115B (1982) 338.

(19) *A search for charged scalar particles pair produced in* e^+e^- *annihilation.*
By JADE Collaboration, W. Bartel et al.,
DESY 82-023, April 1982,
Phys. Lett. 114B (1982) 211.

(20) *Differential three-jet cross section in* e^+e^- *annihilation and comparison with second-order predictions of QCD and Abelian vector theory.*
By JADE Collaboration, W. Bartel et al.,
DESY 82-060, September 1982,
Phys. Lett. 119B (1982) 239.

(21) *Experimental study of the photon structure function* F_2 *in the high* Q^2 *region.*
By JADE Collaboration, W. Bartel et al.,
DESY 82-064, September 1982,
Phys. Lett. 121B (1983) 203.

(22) *Experimental evidence for differences in* $\langle p_\perp \rangle$ *between quark jets and gluon jets.*
By JADE Collaboration, W. Bartel et al.,
DESY 82-086, December 1982, Dedicated to the memory of Peter Dittmann,
Phys. Lett. 123B (1983) 460.

(23) *A search for new heavy leptons at PETRA.*
By JADE Collaboration, W. Bartel et al.,
DESY 83-002, January 1983,
Phys. Lett. 123B (1983) 353.

(24) *Measurement of the processes* $e^+e^- \to e^+e^-$ *and* $e^+e^- \to \gamma\gamma$ *at PETRA.*
By JADE Collaboration, W. Bartel et al.,
DESY 83-035, May 1983,
Z. Phys. C, Particles and Fields 19 (1983) 197.

(25) *Charged particle and neutral kaon production in* e^+e^- *annihilation at PETRA.*
By JADE Collaboration, W. Bartel et al.,
DESY 83-042, June 1983,
Z. Phys. C, Particles and Fields 20 (1983) 187.

(26) *Precise measurement of total cross sections for the process* $e^+e^- \to$ *multihadrons in the c.m. energy range between* 12.0 *and* 36.4 *GeV.*
By JADE Collaboration, W. Bartel et al.,
DESY 83-050, June 1983,
Phys. Lett. 129B (1983) 145.

(27) *A search for flavor-changing neutral currents in* b *decay at PETRA.*
By JADE Collaboration, W. Bartel et al.,
DESY 83-049, July 1983,
Phys. Lett. 132B (1983) 241.

(28) *Observation of inclusive* η *production in* e^+e^- *annihilation at c.m. energies of* 34 *GeV.*
By JADE Collaboration, W. Bartel et al.,
DESY 83-063, July 1983,
Phys. Lett. 130B (1983) 454.

(29) *Particle distribution in 3-jet events produced by* e^+e^-*-annihilation.*
By JADE Collaboration, W. Bartel et al.,
DESY 83-080, August 1983,
Z. Phys. C, Particles and Fields 21 (1983) 37.

(30) *Test of fragmentation models by comparison with 3-jet events produced in* $e^+e^- \to$ *hadrons.*
By JADE Collaboration, W. Bartel et al.,
DESY 83-079, August 1983,
Phys. Lett. 134B (1984) 275.

(31) *A search for massive photinos at PETRA.*
By JADE Collaboration, W. Bartel et al.,
DESY 84-016, February 1984,
Phys. Lett. 139B (1984) 327.

A3. Publications of the MARK J Collaboration

(1) *Measurement of the relative total hadronic cross section R at PETRA.*
By MARK J Collaboration, D.P. Barber et al.,
MIT/LNS Report 100,
Phys. Rev. Lett. 42 (1979) 1113.

(2) *Test of quantum electrodynamics at* $s^{1/2} = 13$ *and* 17 *GeV.*
By MARK J Collaboration, D.P. Barber et al.,
MIT/LNS Report 101,
Phys. Rev. Lett. 42 (1979) 1110.

(3) *Study of electron–positron collisions at center-of-mass energies of* 27.4 *and* 27.7 *GeV at PETRA.*
By MARK J Collaboration, D.P. Barber et al.,
MIT/LNS Report 103,
Phys. Rev. Lett. 43 (1979) 901.

(4) *Study of electron–positron collisions at the highest PETRA energy.*
By MARK J Collaboration, D.P. Barber et al.,
MIT/LNS Report 104,
Phys. Lett. 85B (1979) 463.

(5) *Test of universality of charged leptons.*
By MARK J Collaboration, D.P. Barber et al.,
MIT/LNS Report 105,
Phys. Rev. Lett. 43 (1979) 1915.

(6) *Discovery of three-jet events and a test of quantum chromodynamics at PETRA.*
By MARK J Collaboration, D.P. Barber et al.,
MIT/LNS Report 106,
Phys. Rev. Lett. 43 (1979) 830.

(7) *Physics with high energy electron–positron colliding beams with the MARK J detector* (1*st year of MARK J*).
By MARK J Collaboration,
MIT/LNS Report 107,
Phys. Reports 63 (1980) 337.

(8) *Tests of quantum chromodynamics and a direct measurement of the strong coupling constant* α_s *at* $\sqrt{s} = 30$ *GeV.*
By MARK J Collaboration, D.P. Barber et al.,
MIT/LNS Report 108,
Phys. Lett. 89B (1979) 139.

(9) *Search for the production of a new quark flavor at the c.m.-system energies between* 33 *and* 35.8 *GeV.*
By MARK J Collaboration, D.P. Barber et al.,
MIT/LNS Report 110,
Phys. Rev. Lett. 44 (1980) 1722.

(10) *Unique solution for the weak neutral current coupling constants in purely leptonic interactions.*
By MARK J Collaboration, D.P. Barber et al.,
PITHA 80/8,
Phys. Lett. 95B (1980) 149.

(11) *Experimental study of heavy charged leptons and search for scalar partners of muons at PETRA* ($12\ GeV \leqq E_{c.m.} \leqq 36.7\ GeV$).
By MARK J Collaboration, D.P. Barber et al.,
MIT/LNS Report 113,
Phys. Rev. Lett. 45 (1980) 1904.

(12) *Experimental study of electroweak parameters at PETRA energies* ($12 \leqq E_{c.m.} \leqq 36.7$ *GeV*).
By MARK J Collaboration, D.P. Barber et al.,
PITHA 81/07,
Phys. Rev. Lett. 46 (1981) 1663.

(13) *Measurements of hadron production and three-jet event properties at PETRA.*
By MARK J Collaboration, D.P. Barber et al.,
MIT/LNS Report 115,
Phys. Lett. 108B (1982) 63.

(14) *Experimental tests of higher order quantum electrodynamics at small distances.*
By MARK J Collaboration, B. Adeva et al.,
MIT/LNS Report 122,
Phys. Rev. Lett. 48 (1982) 721.

(15) *Experimental limits on the production of excited leptons and stable heavy leptons.*
By MARK J Collaboration, B. Adeva et al.,
MIT/LNS Report 123,
Phys. Rev. Lett. 48 (1982) 967.

(16) *Measurement of charge asymmetry in* $e^+e^- \to \mu^+\mu^-$.
By MARK J Collaboration, B. Adeva et al.,
MIT/LNS Report 124,
Phys. Rev. Lett. 48 (1982) 1701.

(17) *Search for charged Higgs, scalar taus and a test of technicolor models.*
By MARK J Collaboration, B. Adeva et al.,
MIT/LNS Report 125,
Phys. Lett. 115B (1982) 345.

(18) *Search for top quark and a test of models without top quark up to* 38.54 *GeV at PETRA.*
By MARK J Collaboration, B. Adeva et al.,
MIT/LNS Report 128,
Phys. Rev. Lett. 50 (1983) 799.

(19) *A model-independent second-order determination of the strong coupling constant* α_s.
By MARK J Collaboration, B. Adeva et al.,
MIT/LNS Report 132,
Phys. Rev. Lett. 50 (1983) 2051.

(20) *Experimental study of inclusive muon spectra at PETRA from electron-positron collisions in the energy region* $33 \leq \sqrt{s} \leq 38.54$ *Ge V.*
By MARK J Collaboration, B. Adeva et al.,
DESY 83-029, April 1983,
Phys. Rev. Lett. 51 (1983) 443.

(21) *Search for new particles in* e^+e^- *annihilation from* 39.79 *to* 45.22 *GeV.*
By MARK J Collaboration, B. Adeva et al.,
MIT/LNS Report 134 (1984).

A4. Publications of the PLUTO Collaboration at PETRA

(1) *First observation of hadron production in* e^+e^- *collisions at* 13 *and* 17 *GeV c.m. energy with the PLUTO detector at PETRA.*
By PLUTO Collaboration, Ch. Berger et al.,
DESY 79-11, February 1979 (updated version of DESY 79-06),
Phys. Lett. 81B (1979) 410.

(2) *Search for a "top" threshold in hadronic* e^+e^- *annihilation at energies between* 22 *GeV and* 31.6 *GeV.*
By PLUTO Collaboration, Ch. Berger et al.,
DESY 79-56, September 1979,
Phys. Lett. 86B (1979) 413.

(3) *Evidence for gluon bremsstrahlung in* e^+e^- *annihilations at high energies.*
By PLUTO Collaboration, Ch. Berger et al.,
DESY 79-57, September 1979,
Phys. Lett. 86B (1979) 418.

(4) *Hadron production from photon–photon interactions in the c.m. energy range from* 1 *to* 5 *GeV.*
By PLUTO Collaboration, Ch. Berger et al.,
DESY 79-65, October 1979,
Phys. Lett. 89B (1979) 120.

(5) *Two-particle correlations in* e^+e^- *annihilation.*
By PLUTO Collaboration, Ch. Berger et al.,
DESY 79-83, December 1979,
Phys. Lett. 90B (1980) 312.

(6) *Test of QED in the reactions* $e^+e^- \to e^+e^-$ *and* $e^+e^- \to \mu^+\mu^-$ *at c.m. energies from* 9.4 *GeV to* 31.6 *GeV.*
By PLUTO Collaboration, Ch. Berger et al.,
DESY 80-01, January 1980,
Z. Phys. C, Particles and Fields 4 (1980) 269.

(7) *Search for narrow resonances in* e^+e^- *annihilation at PETRA.*
By PLUTO Collaboration, Ch. Berger et al.,
DESY 80-02, January 1980,
Phys. Lett. 91B (1980) 148.

(8) *Lepton and hadron pair production in two photon reactions.*
By PLUTO Collaboration, Ch. Berger et al.,
DESY 80-34, April 1980,
Phys. Lett. 94B (1980) 254.

(9) *Measurement of the reaction* $e^+e^- \to \gamma\gamma$ *at c.m. energies from* 9.4 *GeV to* 31.6 *GeV.*
By PLUTO Collaboration, Ch. Berger et al.,
DESY 80-35, April 1980,
Phys. Lett. 94B (1980) 87.

(10) *Inclusive muon production at c.m. energies* 12 *to* 31.6 *GeV.*
By PLUTO Collaboration, Ch. Berger et al.,
DESY 80-47, June 1980,
Phys. Rev. Lett. 45 (1980) 1533.

(11) *Multiplicity distributions in* e^+e^- *annihilations at PETRA energies.*
By PLUTO Collaboration, Ch. Berger et al.,
DESY 80-69, July 1980,
Phys. Lett. 95B (1980) 313.

(12) *A study of multijet events in* e^+e^- *annihilation.*
By PLUTO Collaboration, Ch. Berger et al.,
DESY 80-93, October 1980,
Phys. Lett. 97B (1980) 459.

(13) *Inelastic electron–photon scattering at moderate four momentum transfers.*
By PLUTO Collaboration, Ch. Berger et al.,
DESY 80-94, October 1980,
Phys. Lett. 99B (1981) 287.

(14) *Energy–energy correlations in* e^+e^- *annihilation into hadrons.*
By PLUTO Collaboration, Ch. Berger et al.,
DESY 80-78, November 1980,
Phys. Lett. 99B (1981) 292.

(15) *Observation of QCD effects in transverse momenta of* e^+e^- *jets.*
By PLUTO Collaboration, Ch. Berger et al.,
DESY 80-111, November 1980,
Phys. Lett. 100B (1981) 351.

(16) *Experimental test of electroweak effects at PETRA energies.*
By PLUTO Collaboration, Ch. Berger et al.,
DESY 80-116, November 1980,
Z. Phys. C, Particles and Fields 7 (1981) 289.

(17) *Lepton pair production and search for a new heavy lepton in* e^+e^- *annihilation.*
By PLUTO Collaboration, Ch. Berger et al.,
DESY 81-001, January 1981,
Phys. Lett. 99B (1981) 489.

(18) *Inclusive* K^0 *production in* e^+e^- *annihilation for* $9.3\ GeV < \sqrt{s} < 31.6\ GeV$.
By PLUTO Collaboration, Ch. Berger et al.,
DESY 81-018, April 1981,
Phys. Lett. 104B (1981) 79.

(19) *First measurement of the photon structure function* F_2.
By PLUTO Collaboration, Ch. Berger et al.,
DESY 81-051, August 1981,
Phys. Lett. 107B (1981) 168.

(20) *Energy dependence of jet measures in* e^+e^- *annihilation.*
By PLUTO Collaboration, Ch. Berger et al.,
DESY 81-081, November 1981,
Z. Phys. C, Particles and Fields 12 (1982) 297.

(21) *A study of the two-photon production of two-body final states with invariant mass greater than* 2.0 *GeV.*
By PLUTO Collaboration, Ch. Berger et al.,
DESY 82-004, February 1982,
Nucl. Phys. B202 (1982) 189.

(22) *A measurement of charge properties of quark jets at PETRA.*
By PLUTO Collaboration, Ch. Berger et al.,
DESY 82-058, August 1982,
Nucl. Phys. B214 (1983) 189.

(23) *Energy moments for quark jets at PETRA.*
By PLUTO Collaboration, Ch. Berger et al.,
DESY 83-040, June 1983,
Z. Phys. C, Particles and Fields 19 (1983) 205.

(24) *Measurement of the muon pair asymmetry in* e^+e^- *annihilation at* $\sqrt{s} = 34.7\ GeV$.
By PLUTO Collaboration, Ch. Berger et al.,
DESY 83-084, September 1983,
Z. Phys. C, Particles and Fields 21 (1983) 53.

(25) *Measurement of transverse momenta in* e^+e^- *annihilation jets at PETRA.*
By PLUTO Collaboration, Ch. Berger et al.,
DESY 83-054, June 1983,
Z. Phys. C, Particles and Fields 22 (1984) 103.

(26) *Exclusive production of hadron pairs at large momentum transfer in photon–photon interactions.*
By PLUTO Collaboration, Ch. Berger et al.,
DESY 83-122, November 1983,
Phys. Lett. 137B (1984) 267.

A5. Publications of the TASSO Collaboration

(1) *Properties of hadron final states in* e^+e^- *annihilation at* 13 *GeV and* 17 *GeV center-of-mass energies.*
By TASSO Collaboration, R. Brandelik et al.,
DESY 79-14, February 1979,
Phys. Lett. 83B (1979) 261.

(2) *Evidence for planar events in* e^+e^- *annihilation at high energies.*
By TASSO Collaboration, R. Brandelik et al.,
DESY 79-53, August 1979,
Phys. Lett. 86B (1979) 243.

(3) e^+e^- *annihilation at high energies and search for the* t*-quark continuum contribution.*
By TASSO Collaboration, R. Brandelik et al.,
DESY 79-74, November 1979,
Z. Phys. C, Particles and Fields 4 (1980) 87.

(4) *Energy scan for narrow states in* e^+e^- *annihilation at c.m. energies between* 29.90 *GeV and* 31.46 *GeV.*
By TASSO Collaboration, R. Brandelik et al.,
DESY 79-75, November 1979,
Phys. Lett. 88B (1979) 199.

(5) *Rapid growth of charged particle multiplicity in high-energy* e^+e^- *annihilations.*
By TASSO Collaboration, R. Brandelik et al.,
DESY 79-73, November 1979,
Phys. Lett. 89B (1980) 418.

(6) *Production and properties of the* τ *lepton in* e^+e^- *annihilation at c.m. energies from* 12 *GeV to* 31.6 *GeV.*
By TASSO Collaboration, R. Brandelik et al.,
DESY 80-12, February 1980,
Phys. Lett. 92B (1980) 199.

(7) K^0 *production in* e^+e^- *annihilations at* 30 *GeV center-of-mass energy.*
By TASSO Collaboration, R. Brandelik et al.,
DESY 80-39, May 1980,
Phys. Lett. 94B (1980) 91.

(8) *Test of QED in* e^+e^- *annihilation at energies between* 12 *GeV and* 31.6 *GeV.*
By TASSO Collaboration, R. Brandelik et al.,
DESY 80-33, April 1980,
Phys. Lett. 94B (1980) 259.

(9) *Comparison of* e^+e^- *annihilation with QCD and determination of the strong coupling constant.*
By TASSO Collaboration, R. Brandelik et al.,
DESY 80-40, May 1980,
Phys. Lett. 94B (1980) 437.

(10) *Charged pion, kaon, proton and antiproton production in high-energy* e^+e^- *annihilation.*
By TASSO Collaboration, R. Brandelik et al.,
DESY 80-49, June 1980,
Phys. Lett. 94B (1980) 444.

(11) *Rho–rho production by two photon scattering.*
By TASSO Collaboration, R. Brandelik et al.,
DESY 80-77, July 1980,
Phys. Lett. 97B (1980) 448.

(12) *Evidence for a spin-*1 *gluon in three jet events.*
By TASSO Collaboration, R. Brandelik et al.,
DESY 80-80, August 1980,
Phys. Lett. 97B (1980) 453.

(13) *Search for new sequential leptons in* e^+e^- *annihilation at PETRA energies.*
By TASSO Collaboration, R. Brandelik et al.,
DESY 80-108, November 1980,
Phys. Lett. 99B (1981) 163.

(14) *Evidence for charged primary partons in* $e^+e^- \rightarrow$ *two jets.*
By TASSO Collaboration, R. Brandelik et al.,
DESY 81-005, January 1981,
Phys. Lett. 100B (1981) 357.

(15) *Two-photon excitation of the tensor meson* $f^0(1270)$.
By TASSO Collaboration, R. Brandelik et al.,
DESY 81-026, June 1981,
Z. Phys. C, Particles and Fields 10 (1981) 117.

(16) $\Lambda, \bar{\Lambda}$ *production in* e^+e^- *annihilation at* 33 *GeV center-of-mass energy.*
By TASSO Collaboration, R. Brandelik et al.,
DESY 81-039, July 1981,
Phys. Lett. 105B (1981) 75.

(17) *High p_T hadron production in photon–photon collisions.*
By TASSO Collaboration, R. Brandelik et al.,
DESY 81-053, August 1981,
Phys. Lett. 107B (1981) 290.

(18) *Exclusive proton–antiproton production in two-photon collisions.*
By TASSO Collaboration, R. Brandelik et al.,
DESY 81-058, September 1981,
Phys. Lett. 108B (1982) 67.

(19) *π^0 production by e^+e^- annihilation at 14 GeV and 34 GeV c.m. energy.*
By TASSO Collaboration, R. Brandelik et al.,
DESY 81-069, October 1981,
Phys. Lett. 108B (1982) 71.

(20) *Charge asymmetry and weak interaction effects in $e^+e^- \to \mu^+\mu^-$ and $e^+e^- \to \tau^+\tau^-$.*
By TASSO Collaboration, R. Brandelik et al.,
DESY 82-002, January 1982,
Phys. Lett. 110B (1982) 173.

(21) *Charged pion production in e^+e^- annihilation at 14 GeV, 22 GeV and 34 GeV c.m. energy.*
By TASSO Collaboration, R. Brandelik et al.,
DESY 82-009, February 1982,
Phys. Lett. 113B (1982) 98.

(22) *A measurement of σ^{tot} ($e^+e^- \to$ hadrons) for c.m. energies between 12.0 GeV and 36.7 GeV.*
By TASSO Collaboration, R. Brandelik et al.,
DESY 82-010, February 1982,
Phys. Lett. 113B (1982) 499.

(23) *Scale breaking in inclusive charged particle production by e^+e^- annihilation.*
By TASSO Collaboration, R. Brandelik et al.,
DESY 82-013, March 1982,
Phys. Lett. 114B (1982) 65.

(24) *Inclusive ρ^0 production in e^+e^- annihilation at high energy.*
By TASSO Collaboration, R. Brandelik et al.,
DESY 82-046, July 1982,
Phys. Lett. 117B (1982) 135.

(25) *Electroweak coupling constants in the leptonic reactions $e^+e^- \to e^+e^-$ and $e^+e^- \to \mu^+\mu^-$ and search for scalar leptons.*
By TASSO Collaboration, R. Brandelik et al.,
DESY 82-032, May 1982,
Phys. Lett. 117B (1982) 365.

(26) *Angular correlations in* $\gamma\gamma \to \rho^0\rho^0$ *near threshold.*
By TASSO Collaboration, M. Althoff et al.,
DESY 82-062, September 1982,
Z. Phys. C, Particles and Fields 16 (1982) 13.

(27) *Production of* $K\bar{K}$*-pairs in photon–photon collisions and the excitation of the tensor meson* f'(1515).
By TASSO Collaboration, M. Althoff et al.,
DESY 82-071, November 1982,
Phys. Lett. 121B (1983) 216.

(28) *Search for charged Higgs and technipions at PETRA.*
By TASSO Collaboration, M. Althoff et al.,
DESY 82-069, October 1982,
Phys. Lett. 122B (1983) 95.

(29) *Charged hadron composition of the final state in* e^+e^- *annihilation at high energies.*
By TASSO Collaboration, M. Althoff et al.,
DESY 82-070, October 1982,
Z. Phys. C, Particles and Fields 17 (1983) 5.

(30) $D^{*\pm}$ *production by* e^+e^- *annihilation near* 34.4 *GeV c.m. energy*
By TASSO Collaboration, M. Althoff et al.,
DESY 83-010, February 1983,
Phys. Lett. 126B (1983) 493.

(31) *Differential cross sections for* $\gamma\gamma \to p\bar{p}$ *in the c.m. energy range from* 2.0 *to* 3.1 *GeV.*
By TASSO Collaboration, M. Althoff et al.,
DESY 83-064, July 1983,
Phys. Lett. 130B (1983) 449.

(32) *Observation of* Ξ^-, $\overline{\Xi^-}$ *production in* e^+e^- *annihilation.*
By TASSO Collaboration, M. Althoff et al.,
DESY 83-071, August 1983,
Phys. Lett. 130B (1983) 340.

(33) *An improved measurement of electroweak couplings from* $e^+e^- \to e^+e^-$ *and* $e^+e^- \to \mu^+\mu^-$.
By TASSO Collaboration, M. Althoff et al.,
DESY 83-089, September 1983,
Z. Phys. C, Particles and Fields 22 (1984) 13.

(34) *Properties of charm jets in* e^+e^- *annihilation near* 34 *GeV.*
By TASSO Collaboration, M. Althoff et al.,
DESY 83-114, November 1983,
Phys. Lett. 135B (1984) 243.

(35) *Observation of hard processes in collisions of two quasi-real photons.*
By TASSO Collaboration, M. Althoff et al.,
DESY 83-115, November 1983,
Phys. Lett. 138B (1984) 219.

(36) *Observation of* F *meson production in high energy* e^+e^- *annihilation.*
By TASSO Collaboration, M. Althoff et al.,
DESY 83-119, November 1983,
Phys. Lett. 136B (1984) 130.

(37) *Production and muonic decay of heavy quarks in* e^+e^- *annihilation at* 34.5 *GeV.*
By TASSO Collaboration, M. Althoff et al.,
DESY 83-121, November 1983,
Z. Phys. C, Particles and Fields.

(38) *Jet production and fragmentation in* e^+e^- *annihilation at* 12–43 *GeV.*
By TASSO Collaboration, M. Althoff et al.,
DESY 83-130, December 1983,
Z. Phys. C, Particles and Fields.

(39) *Measurement of R and search for the top quark in* e^+e^- *annihilation between* 39.8 *and* 45.2 *GeV.*
By TASSO Collaboration, M. Althoff et al.,
DESY 84-001, January 1984,
Phys. Lett.

(40) *Evidence for local compensation of baryon number in* e^+e^- *annihilation.*
By TASSO Collaboration, M. Althoff et al.,
DESY 84-004, January 1984,
Phys. Lett. 139B (1984) 126.

(41) *Experimental test of the flavor independence of the quark–gluon coupling constant.*
By TASSO Collaboration, M. Althoff et al.,
DESY 84-005, January 1984,
Phys. Lett. 138B (1984) 317.

(42) *Observation of the reaction* $\gamma\gamma \to p\bar{p}\pi^+\pi^-$.
By TASSO Collaboration, M. Althoff et al.,
DESY 84-015, February 1984,
Phys. Lett.

(43) *Determination of the* τ *lifetime in high energy* e^+e^- *annihilations.*
By TASSO Collaboration, M. Althoff et al.,
DESY 84-017, February 1984,
Phys. Lett.

(44) *A determination of* α_s *in first and second order QCD from* e^+e^- *annihilation into hadrons.*
By TASSO Collaboration, M. Althoff et al.,
DESY 84-
Z. Phys. C, Particles and Fields.